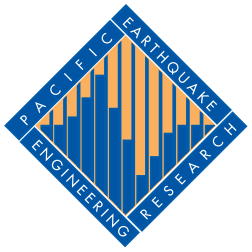

PACIFIC EARTHQUAKE ENGINEERING
RESEARCH CENTER

Seismic Performance of an Instrumented Tilt-up Wall Building

James C. Anderson
University of Southern California

Vitelmo V. Bertero
University of California, Berkeley

Contributors:
Mohsen Kargahi
Mohamed Al Satari

University of Southern California

Sponsor:
California Energy Commission

PEER 2004/04
JULY 2004

Seismic Performance of an Instrumented Tilt-up Wall Building

James C. Anderson
University of Southern California

Vitelmo V. Bertero
University of California, Berkeley

Contributors:

Mohsen Kargahi
Graduate Research Assistant, USC

Mohamed Al-Satari
Graduate Research Assistant, USC

Sponsor:
California Energy Commission

PEER Report 2004/04
Pacific Earthquake Engineering Research Center
College of Engineering
University of California, Berkeley

July 2004

ABSTRACT

The seismic response of an instrumented tilt-up wall building is initially investigated under the action of four earthquake ground motions that were recorded at the site. The strongest base acceleration was 0.18g recorded during the Big Bear, California, earthquake. Building response was obtained from nine sensors located in the building, and these data were used to evaluate the behavior of the building and the accuracy of the numerical calculations obtained from a three-dimensional building model. A site visit indicated that the response of the walls to the recorded ground motions had been primarily linear elastic; however, minor cracking had occurred in some walls and pilasters due to the strongest ground motions. Since the building was occupied, it was difficult to inspect the roof diaphragm and connections to the walls. Fourier spectra analysis of the recorded response indicated an increase in the fundamental period of the building during each of the four ground motions.

Initial elastic dynamic analyses compared the calculated accelerations and displacements with those obtained from corresponding sensor locations. In general, these comparisons were quite good. Base shear demands from recorded ground motions were compared with the design base shear used for the original design as well as with the current requirements of the 1997 UBC. Force demands on the roof to wall connections were also determined and plotted. Force contours including in-plane shear, in-plane moment, and out-of-plane moment were plotted and used to estimate maximum stresses in the reinforced concrete walls and timber diaphragm. These results indicate that in-plane shear in the diaphragm is critical followed in importance by the glulam beam to pilaster connection and the out-of-plane moment in the wall. The in-plane shear capacity of the walls is well above the minimum required by the codes and also well above that demanded by the four recorded ground motions.

Following these analyses, the effects on the building of three stronger ground motions having pulse-type displacement characteristics were evaluated. The base shear demands of these ground motions exceed the minimum code design requirements in both principal directions. A comparison of the forces in the connections and force contours in the walls and diaphragm with their capacities indicates that of these, only the in-plane shear capacity of the walls has sufficient capacity to remain elastic. As in the case of the ground motions recorded at the site, the critical demand is the in-plane shear in the roof diaphragm.

With these results, a nonlinear three-dimensional model of the building was developed within the constraints of the computer program (SAP2000). Nonlinear elements were incorporated for the connections of the roof diaphragm to the glulam beams and purlins, and the nonlinear behavior of the diaphragm was modeled using a Hrennikoff model of the continuum. Inelastic characteristics for these components were obtained from the results of a limited number of component tests conducted at the University of California at Irvine. This modeling permitted consideration of both old and new connections to the pilasters, along with the effects of dense and sparse nailing in the diaphragm. Static pushover analyses and dynamic time history analyses were conducted. The results of these analyses indicate that nonlinear behavior can have a significant effect on the force and displacement demands of the different components. The use of the new connections, along with the dense nailing in the diaphragm, produces the best results; however, the displacement (ductility) demands may require additional strengthening of the critical roof diaphragm.

Inclusion of the vertical ground accelerations in the analyses of the elastic model with nonlinear connections had a significant effect on the vertical shear force component of the glulam to pilaster connections, with increases of more than 100% being obtained under pulse-type ground motions. However, this connection force component, including the increase, is approximately 33% of the more dominant axial force component. Moreover, this increase, and the fact that two of the force components are perpendicular to the grain, indicate the need to test these critical connections under triaxial loading.

ACKNOWLEDGMENTS

This study was sponsored by the Pacific Earthquake Engineering Research Center's Program of Applied Earthquake Engineering Research of Lifeline Systems supported by the California Energy Commission, the California Department of Transportation, and the Pacific Gas and Electric Company.

This work made use of the Earthquake Engineering Research Centers Shared Facilities supported by the National Science Foundation under award number EEC-9701568 through the Pacific Earthquake Engineering Research Center (PEER).

Any opinions, findings, and conclusions or recommendations expressed in this material are those of the authors and do not necessarily reflect those of the National Science Foundation.

This report was prepared as a result of work sponsored by the California Energy Commission ("the Commission"). It does not necessarily represent the views of the Commission, its employees, or the State of California. The Commission, the State of California, its employees, contractors, and subcontractors make no warranty, express or implied, and assume no legal liability for the information in this report; nor does any party represent that the use of this information will not infringe upon privately owned rights. This report has not been approved or disapproved by the Commission nor has the Commission passed upon the accuracy or adequacy of the information in this report.

Mr. Kent Ferre (of PG&E) served as the technical monitor for this project, and Mr. Chris Poland (of Degenkolb Engineers) served as project consultant. Their interest and constructive comments were greatly appreciated and made significant contributions to the results of this report. In addition to doctoral students Mohsen Kargahi and Mohamed Al-Satari, Ms. Zwei Zhang participated in the early stages of this study. Without their help, this study could not have been completed. Thanks are also due Dr. Tony Shakal and Dr. Moh Huang of the California Strong Motion Instrumentation Program for their assistance in providing much of the data used in this study.

CONTENTS

LIST OF FIGURES

LIST OF TABLES

1 Introduction

Tilt-up construction is widely used for low-rise commercial and industrial buildings. The walls are poured in the horizontal position on the ground slab and after curing are raised or "tilted" to their final vertical position where they are stabilized with temporary shoring. The wall panels are tied to the floor slab and to the foundation with precast reinforcing and a finish slab. The roof generally consists of a system of glulam-beams, purlins, subpurlins and blocking capped with plywood, and is connected to the walls to form a lateral load-resisting diaphragm. In some cases steel metal decks are used without a concrete topping slab. This construction is generally known as a "rigid wall-flexible diaphragm structure." It has been estimated that there are 20,000 tilt-up wall (TUW) buildings in Southern California. Although economical to build, this type of construction has been subject to significant damage in recent earthquakes.

Problems with this type of construction observed following the San Fernando earthquake (1971) led to major revisions in the 1973, 1976, and 1979 editions of the Uniform Building Code. Included in these changes were provisions for a positive, direct connection of the concrete walls to the wood roof and floor diaphragms. The seismic coefficient, C_p, used in the formula, $F_p = ZIC_pW_p$, was also increased by 50% (from 0.2 to 0.3) to increase the lateral design forces for the tilt-up panels and their connections. Additional changes were included in the 1991 Uniform Building Code as a result of performance studies of this type of construction following the Morgan Hill (1987), the Whittier Narrows (1987), and the Loma Prieta (1989) earthquakes. Included in these modifications was the provision to increase the seismic design forces for wall to flexible diaphragm connections by 50% (Cp = 0.45) in the center half of the diaphragm span.

The Northridge earthquake (1994) provided a critical test of both the old and new code provisions for buildings with tilt-up walls. It was estimated that of the 1,200 TUW buildings in the San Fernando Valley, more than 400 had significant structural damage including partial collapse of roofs and collapse of exterior walls. This behavior was largely due to the failure of the out-of-plane connections between the roof diaphragm and the concrete wall panels. Steel ties

between the beams and concrete panels failed by pulling out of the wall, fracturing at the wall face, and fracturing through the first bolt hole. Shear failures occurred in the pilasters directly below the support connections at the glulam beams, leading to partial roof collapses. These failures resulted in significant economic loss and indicate a need to develop improved procedures for evaluating the seismic forces that are developed at the connections between the TUW panels and the roof diaphragm.

In order to improve the design of new facilities and to select efficient strategies for the seismic upgrading of existing facilities, it is necessary to predict the dynamic behavior of such facilities in a reliable manner when subjected to earthquake ground accelerations. This requires the development of an analytical model that accurately represents the structural system, and the comparison of the results obtained from this model with the results of large-scale experiments. The best large-scale experiment is when an earthquake occurs and properly placed instruments record the response of the building to ground accelerations recorded at the base. This report summarizes the studies conducted on one TUW warehouse building instrumented with 12 accelerometers that have recorded the response of the building to four strong ground motions.

2 Building Description

The design of the tilt-up warehouse in Redlands, California, was completed in the fall of 1971 following the San Fernando earthquake in February. Most likely, it was designed for the lateral force provisions of the 1969 Building Code. Construction was completed the following year. The building plan is 232 feet by 90 feet with the longitudinal dimension oriented in the north-south direction. A view of the east side of the building showing the access door near the south end of the building and the office located near the center is presented in Figure 2.1. An isometric drawing of the building is shown in Figure 2.2. The building is divided into two sections by a bearing stud partition that is located 132 feet from the south end (100 feet from the north end) as shown in the plan view of the roof in Figure 2.3. Small offices are located on each side of this partition on the east side of the building. Also, the east side of the building contains two large overhead doors (12 feet by 14 feet), one in the south section and one in the north, as can be seen in the east elevation (Fig. 2.4**)**. There are no openings in the tilt-up walls of the other three sides of the building.

The concrete wall panels are 7 inches thick and have widths of 22.5 feet, 22 feet, and 20 feet depending on location. Cast-in-place pilasters create a continuous connection between adjacent wall panels. Panel reinforcement is assumed to consist of a single curtain of #4 bars spaced at 12 inches on center (o.c.) in each direction. This is similar to the minimum steel requirement as specified in the building code. Two #5 bars are added on the three sides of the door openings.

The main support for the roof diaphragm is provided by glulam beams that are cambered by 3 feet and span in the transverse direction between the pilasters. Purlins that are 4 inches by 14 inches deep span between the glulam beams and are spaced at 8 feet o.c. Rafters consisting of 2 inch x 4 inch beams span the purlins at 2 feet o.c. Sheathing for the diaphragm is provided by ½ inch structural plywood.

Drilled caissons that are 3 feet in diameter and 12 feet deep are used to support the pilasters. A mat consisting of a five-inch slab on grade is connected to the wall panels and pilasters at the base level. The existing soil beneath the slab was removed to a depth of 4 feet and recompacted to 95% of optimum density.

Fig. 2.1 View of tilt-up wall building looking west

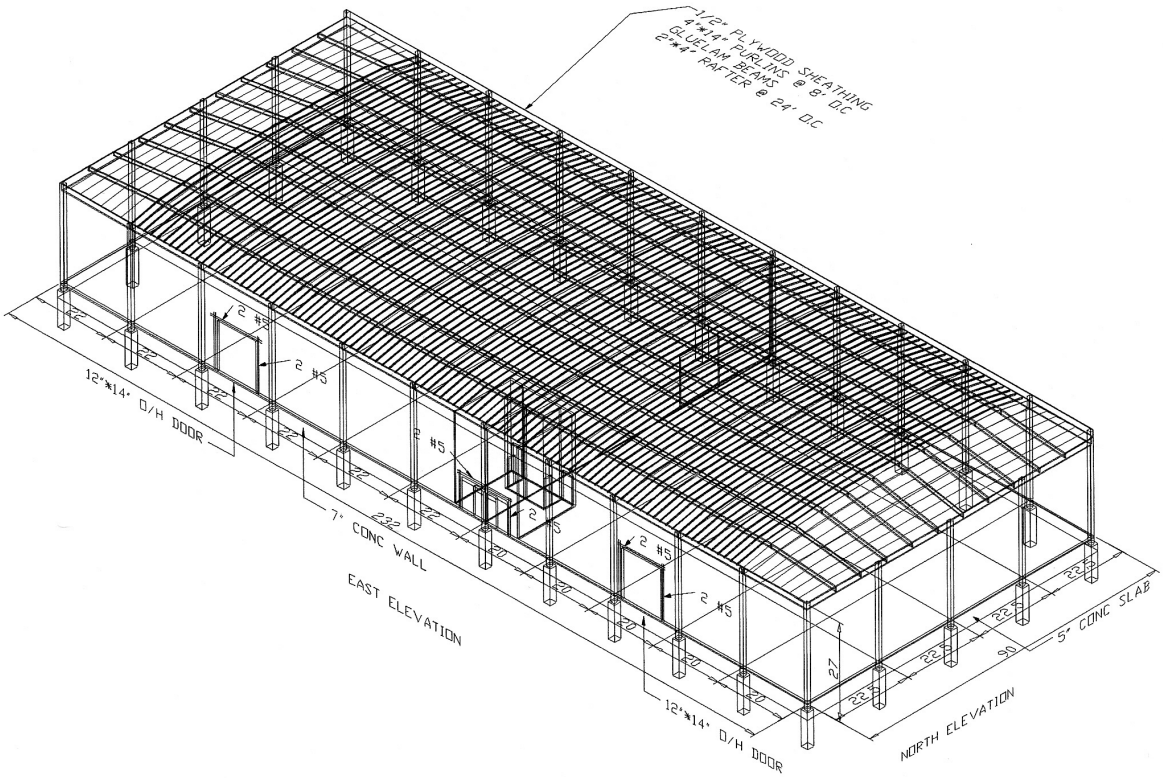

Fig. 2.2 Isometric drawing of tilt-up wall building

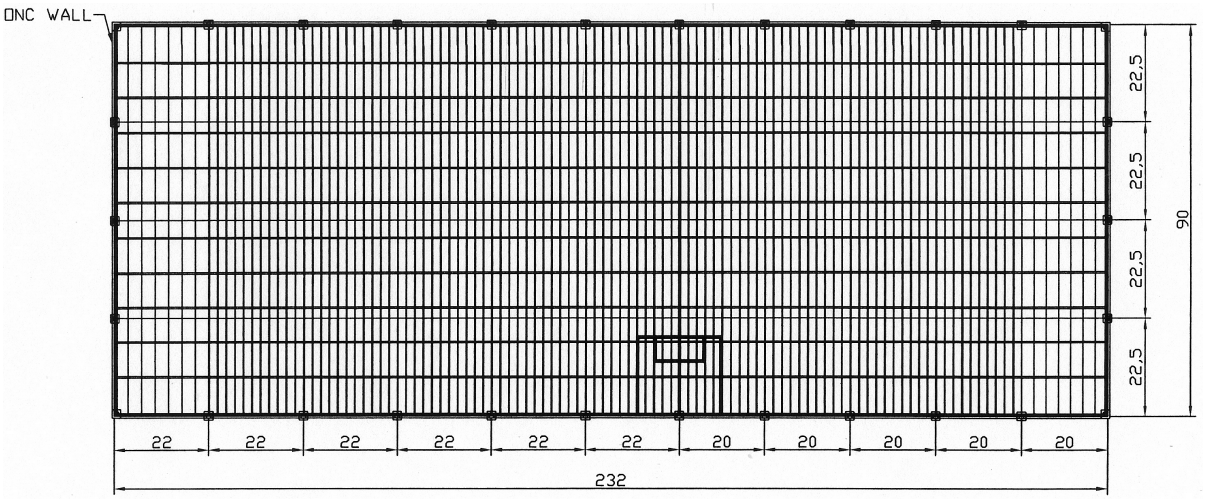

Fig. 2.3 Roof plan

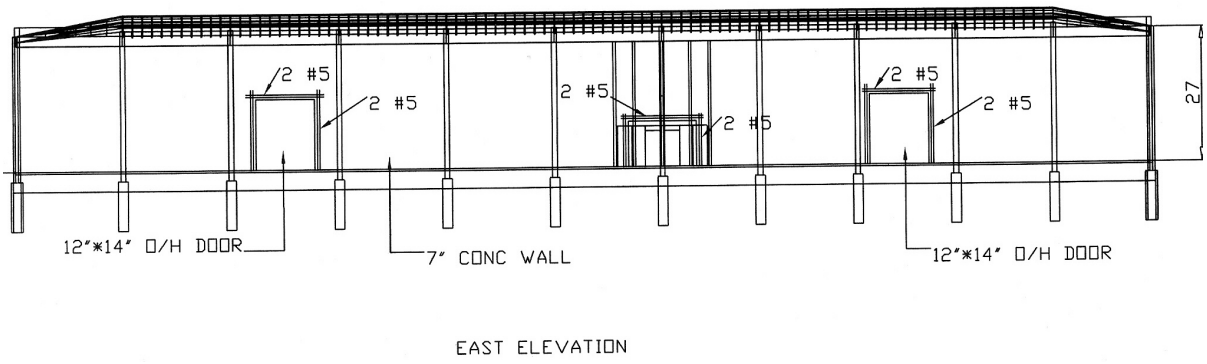

Fig. 2.4 East elevation

3 Instrumentation and Recorded Seismic Response

As part of the California Strong Motion Instrumentation Program (CSMIP), the building was instrumented with 12 strong motion accelerometers. The location of these instruments is shown in Figure 3.1. The installation of sensors 1, 11, and 12 on the floor slab is shown in Figure 3.2 to the right of the bearing stud partition. Sensor 2 is mounted at the midheight of the west wall just to the right of the partition (Fig. 3.3). Sensor 4 is mounted on the glulam beam at the partition and all other sensors are mounted on the walls just under the roof diaphragm. The instrumentation in this building, located almost midway between the San Jacinto and San Andreas fault systems, has recorded the response of the building to several earthquakes. Four of the strongest recorded ground motions were recorded during the following earthquakes: Palm Springs (July 8, 1986), Landers (June 28, 1992), Big Bear (June 28, 1992), and Northridge (January 17, 1994). The responses of the building under these ground motions are considered in this study. The site is 10 km (6.2 miles) miles from the epicenter of the Palm Springs earthquake, 74 km (46 miles) west of the epicenter of the Landers earthquake, 39 km (24 miles) west of the epicenter of the Big Bear earthquake, and 123 km (76 miles) southeast of the epicenter of the Northridge earthquake. Peak recorded accelerations in the building for these ground motions are summarized in Table 3.1 and corresponding displacements in Table 3.2.

An examination of the recorded accelerations (Table 3.1) indicates that the values developed by the Big Bear earthquake are the strongest of this ensemble of earthquake motions. In the longitudinal (N-S) direction, the peak base acceleration was recorded at 0.132g. This resulted in an out-of-plane acceleration of 0.439g at the top of the south wall and in-plane accelerations of 0.133g and 0.132g at the top of the west and east walls, respectively. This indicates that there is a substantial out-of-plane amplification (3.3x) of the base acceleration and almost zero in-plane amplification. A similar result is obtained in the transverse (E-W) direction where the peak recorded base acceleration was 0.177g. The peak recorded out-of-plane

acceleration at the top of the west wall was 0.616g for an amplification of 3.5 times the base. In-plane accelerations of 0.166g and 0.181g were recorded at the top of the south and north walls respectively.

The displacement data obtained from the recorded accelerations are given in Table 3.2. These data indicate that the largest displacements in the N-S direction are due to the Big Bear ground motions; however, the largest displacements in the E-W direction are due to the Landers ground motions. The amplified acceleration and the drift obtained from the recorded data are summarized in Table 3.3. Here it can be seen that the largest amplification of acceleration occurs out-of-plane in the E-W direction and has a maximum value of 5.65 under the Palm Springs ground motion. It can also be seen that there is very little amplification of acceleration in the plane of the wall, with the maximum being 1.2. The largest drift is shown to occur out-of-plane in the E-W direction and has a maximum value of 0.81 inches under the Big Bear ground motion. The in-plane drift is very small with the maximum occurring in the N-S direction, having a value of 0.028 inches.

Table 3.1 Recorded seismic acceleration response (g)

Sensor I.D.	Palm Springs	Landers	Big Bear	Northridge
1 (UP)	0.023	0.046	0.062	0.017
2 (EW)	0.094	0.238	0.377	0.106
3 (EW)	0.123	0.337	0.616	0.160
4 (EW)	0.119	0.330	0.601	0.154
5 (EW)	0.243	0.493	0.598	0.191
6 (EW)	0.039	0.127	0.166	0.044
7 (EW)	0.048	0.116	0.181	0.043
8 (NS)	0.041	0.120	0.133	0.072
9 (NS)	0.112	0.419	0.439	0.178
10 (NS)	0.038	0.122	0.132	0.070
11 (NS)	0.039	0.117	0.132	0.070
12 (EW)	0.043	0.106	0.177	0.045

Table 3.2 Recorded seismic displacement response (cm)

Sensor I.D.	Palm Springs	Landers	Big Bear	Northridge
1 (UP)	0.260	0.78	0.973	0.34
2 (EW)	0.742	3.68	2.566	1.20
3 (EW)	0.778	4.23	3.174	1.31
4 (EW)	0.795	4.39	3.334	1.36
5 (EW)	1.086	4.75	3.962	1.54
6 (EW)	0.564	3.24	1.974	1.07
7 (EW)	0.599	3.23	1.972	0.97
8 (NS)	0.520	1.96	3.251	1.11
9 (NS)	0.544	2.48	3.831	1.20
10 (NS)	0.488	1.91	3.201	1.08
11 (NS)	0.491	1.84	3.257	1.08
12 (EW)	0.548	3.21	1.915	1.02

Table 3.3 Maximum amplified acceleration and drift (in.)

	Amplified Acceleration					Drift (in.)			
	Out-of-plane		In-plane			Out-of-plane		In-plane	
Earthquake	E-W	N-S	E-W	N-S		E-W	N-S	E-W	N-S
Palm Springs	5.65	2.87	0.907	0.970		0.21	0.02	0.006	0.001
Landers	4.65	3.58	1.20	1.04		0.61	0.25	0.012	0.028
Big Bear	3.48	3.33	0.94	1.00		0.81	0.23	0.023	0.022
Northridge	4.24	2.54	0.98	1.00		0.21	0.05	0.02	0.00

Redlands - 1-story Warehouse
(CSMIP Station No. 23495)

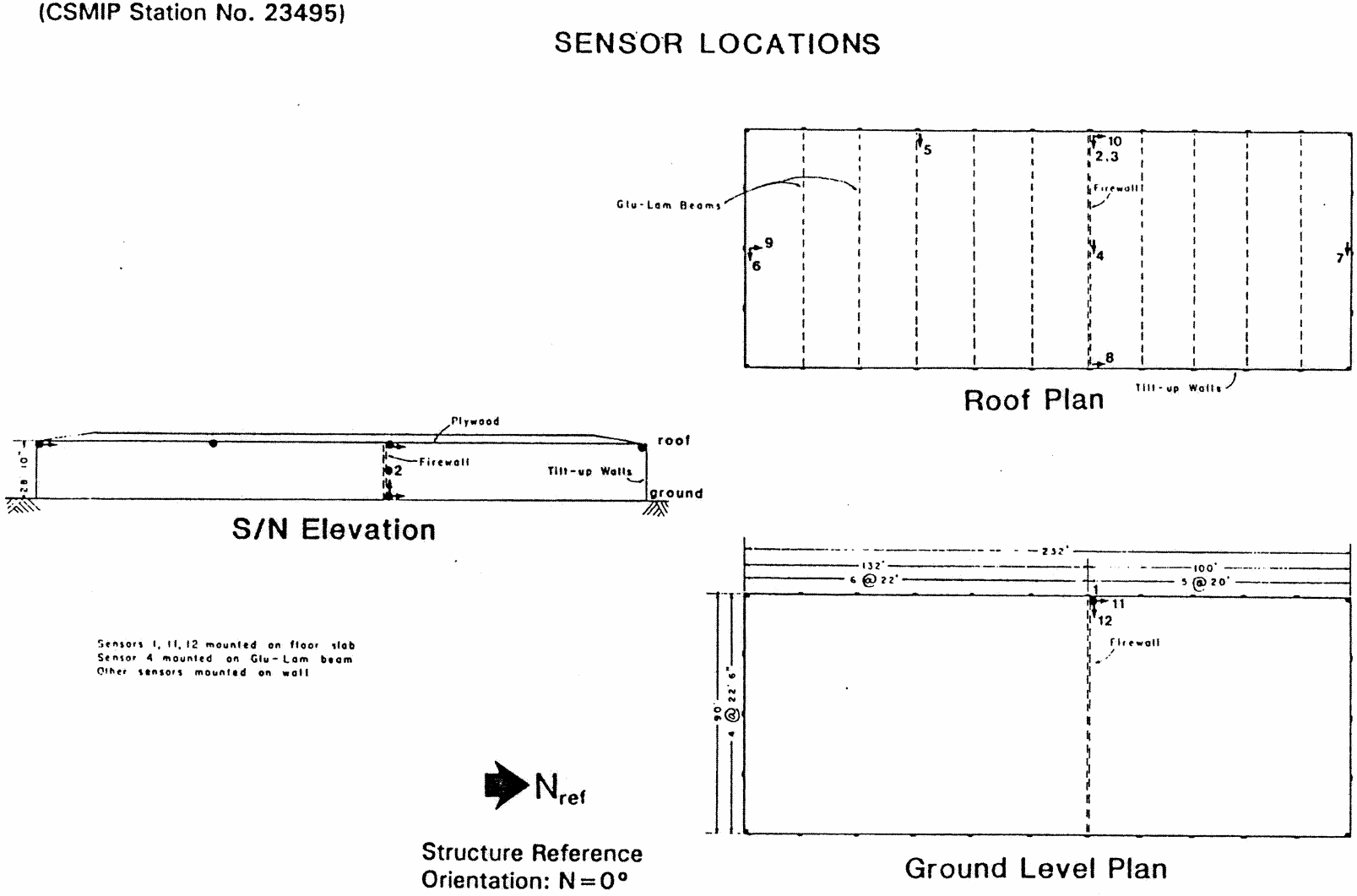

Figure 3.1 Sensor locations

Fig. 3.2 Sensors 1, 11, 12 adjacent to fire wall

Fig 3.3 Sensor 2, Midheight of west wall

4 Observed Damage

On August 15, 2001, the authors conducted an inspection of the TUW building in an effort to determine any degree of damage resulting from the four strongest ground motions recorded at the site discussed previously. Some minor cracking was observed in the tilt-up walls but was not considered to be structurally important because it could not result in yielding of the reinforcement, and no crushing of the concrete was observed. Although a close inspection of the roof diaphragm and its connection to the TUW was not possible, it appeared that no significant structural damage had occurred, based on observations from inside the building at several locations. This was also confirmed in the discussion the authors had with the person in charge of the warehouse operation. He informed us that the function of the warehouse had not been affected in any of the strongest earthquakes considered, although boxes and furniture fell down from the storage shelves. Thus the following discussion considers only the observed damage in the TUW, and attempts will be made to evaluate it quantitatively.

4.1 DAMAGE TO TILT-UP WALLS

It was noted that the degree of observed damage (cracking) (Figs. 4.1–4.2) had been more severe along the west and north walls than that observed along the east and south walls, respectively. This poses the question why? While structurally the north and south walls seem to be the same, there is a difference between the east and west walls. The main structural difference is their geometric configurations. The east wall has some significant openings that include two overhead doors for access to the warehouse, whereas, the west wall has no opening. Thus the in-plane stiffness of the west wall is higher than that of the east wall, and under the effects of the north-south components of the ground motions, the west wall in its elastic response will attract and develop higher inertial forces. This fact could be the reason for the development of some minor shear (diagonal) cracks in the west wall, as shown in Figure 4.2, and horizontal cracks in the pilasters of the north wall, as shown in Figure 4.3.

As illustrated in Figure 4.1, although a large number of small horizontal cracks occurred in the outside of the pilasters located in the north wall, similar cracks were not observed in the pilasters of the east wall. While there is no doubt that these cracks were a consequence of the flexural behavior of the pilasters, out of the plane of the wall, what was surprising at first sight is that such cracks were observed only at the outside of the pilasters of the west wall. To find the reasons for this particular pattern of damage, a series of simple analytical calculations were conducted based on different assumptions regarding the possible response of these longitudinal walls.

4.2 ESTIMATION OF TUW BEHAVIOR

Analysis of the ground motions recorded at the site indicates that the Big Bear earthquake induced the highest peak ground acceleration. Furthermore, an analysis of the responses recorded by the other sensors in the building, particularly those that recorded the response normal to the plane of the TUW, also indicated that the recorded accelerations were the highest for the motions induced by the Big Bear earthquake. Therefore, it was decided to conduct an initial series of estimations using the accelerations recorded during this earthquake. The following three cases were considered for the boundary conditions of each of the TUW: (A) Each TUW is simply supported only at the bottom and at 27 feet from the bottom (roof level); (B) Each TUW is simply supported not only as in (A) but also by the pilasters; and (C) Each TUW is simply supported as in (A) and rigidly connected at the pilasters with the pilasters simply connected at their bottom and at the roof level. For these three cases it was assumed that the inertial forces that were developed are those due to the accelerations recorded at sensors 12 (bottom), 2 (midheight) and 3 (roof). The values recorded at these three locations were 0.17g, 0.43g, and 0.75g, respectively. These are the values given in Figure 4.4, which are uncorrected values and differ somewhat from those given in Table 3.1. Furthermore, for these cases it is assumed that the wall response to the effects of the induced inertial forces is in its elastic range, assuming an uncracked cross section.

CASE A. Based on the previous assumptions and the assumed approximate uniform accelerations indicated in Figure 4.5, it can be assumed that the maximum moment developed in the wall will be close to

$$M_{max} \cong m(0.43g)(27)^2/8 \text{ where m is the mass per unit length (say, 1 ft).}$$

Then, considering a unit (1 ft) strip of wall, the mass will be

m = (1.0′*7″÷12/′)*150 pcf÷(12″/′g)= 87.5 lbs/ft/g and the moment becomes

M_{max}/ft = 87.5 lbs/ft* 0.43g* $(27)^2$/8g = 3428 lbs-ft/ft (3.43 k-in./in.) and

the maximum flexural stress becomes $\sigma_{max} = M_{max}/S = 6 * 3.43$ kip-in./7^2 = 0.42 ksi.

Considering that the modulus of rupture of concrete is 7.5√ f′c, the required concrete strength to avoid cracking of the wall would be $(420 \text{ psi}/7.5)^2$ = 3136 psi. As it is doubtful that in 1969 the TUW had been cast with a concrete that in 1992 reached a compressive strength of 3163 psi, the above estimation indicates that the TUW should have cracked, but this was not observed during the inspection. Thus either the concrete strength was higher than 3136 psi, which is doubtful, or the TUW did not behave as a beam on a simply supported span with supports only at the bottom and the roof levels. Due to the presence of the pilasters and their connection with the TUW, the pilasters will offer at least a simple support along their length, as considered in CASE B.

It is of interest to note that as discussed and illustrated in Chapter 6, Section 6.5, and in Figure 6.91b, respectively, the contours of the TUW considered as separated wall segments show that the maximum value at the panel located near the center of the west wall is in the range of 3.0 to 3.6 kips/in., which is in close agreement with the above-estimated value of 3.43 kip-in./in. strip.

CASE B. Each TUW is approximately a square plate (20′ or 21′ x 27′) with simple supports along its four edges (boundaries). It is obvious that due to the inertial forces that act out of its plane, its behavior will be close to that of a square two-way plate with simple supports along the edges. Therefore, the maximum moment will be somewhat smaller than half of the value estimated for CASE A, (i.e., smaller than (3.43/2) = 1.71 kip-in.). The contours of the out-of-plane moment in the vertical direction (Fig. 6.91a), which was obtained through a linear elastic analysis of the model that considered the TUW panels connected through the pilasters, show that the maximum value of the moment could reach 1.25 kip-in./in. Therefore it can be concluded that under the assumptions made for this case, the TUW could not have suffered any flexural cracking, which is in agreement with the observations made in the field inspection of the building.

CASE C. The main purpose for considering this case is to attempt to justify the damage observed in the outside of the pilaster located in the west wall and in the outside of the pilasters located in the north wall. This type of damage is illustrated in the photos of Figures 4.1 and 4.3. Two different kinds of models for analyzing the behavior of the pilaster have been considered:

(1) The pilaster acted as a separated element from the TUW and is simply supported at the bottom and at the roof level and (2) the pilaster acted together with the connected TUW panels, and the entire wall system was simply supported at the bottom (ground slab) and at the top (roof) level.

In the two models analyzed it was assumed that the pilaster has a 12″ x 24″ cross section; however the actual cross section was later realized to be 14″ x 24″. The importance of this change in cross section will be discussed.

4.3 ESTIMATION BASED ON MODEL (1)

Based on assumptions made for CASE A, but considering the pilaster rather than the TUW panel, and using the accelerations shown in Figure 4.5:

$(M_{max})_{pilaster} = (m_{pil})(0.43g)*27^2/8 = (1'x2') * (150\ pcf/g)*(0.43g)(91.125\ ft^2) \cong 11{,}755$ lbs-ft 11.75 kip-ft.

$$\sigma_{max} = 11{,}755* 12 \text{ kip-in.}*6/(12x24^2) = 122 \text{ psi} < 7.5\sqrt{f'_c}$$

This would have required a compressive strength of only 265 psi to prevent cracking, and hence, it can be concluded that no flexural cracking could have occurred under the assumed model. Thus, as could be expected, this model is not a realistic one and the use of a 14″ x 24″ cross section does not affect these results.

4.4 ESTIMATION BASED ON MODEL (2)

This estimate is based on the assumptions made for CASE A regarding the accelerations acting along the longitudinal wall (Fig. 4.5) but considering that the wall is composed of the TUW and the pilaster with the cross section (Fig. 4.6). Therefore the tributary mass to the total inertial force per foot of height is

m = (20*7/12 + 1*2) *(150/g) = 2,050/g lb/ft and the maximum demanded moment is

$$M_{max} = (2{,}050/g) \text{ x } (0.43g) \text{ x } 27^2/8 = 80{,}327 \text{ lb-ft}$$

As the neutral axis of the cross section (Fig. 4.6b**)** is located at 0.3 inches above the thickness of the wall, the resulting I_{xx} is about 27,560 in.^{4} and the section modulus becomes

$$S_{outside} = 27{,}560/(17.0\text{-}0.3) = 1{,}650 \text{ in.}^3 \quad \text{and} \quad S_{inside} = 27{,}560/(7 + 0.3) = 3{,}775 \text{ in.}^3$$

$$\text{and } (\sigma_t)_{outside} = 80{,}327*12/1650 = 584 \text{ psi}$$

Considering the modulus of rupture, the concrete would have cracked for any concrete with a compressive strength of less than 6,063 psi. Since it is doubtful that the concrete of the pilaster could have such a high strength, it is concluded that the pilaster at the west wall could have suffered the observed outside cracks under the effects of the recorded ground motions induced by the Big Bear earthquake. However, the following two questions remain: (1) *Why were no cracks observed on the inside of the pilasters and* (2) *Why were no cracks observed in the outside of the pilasters located in the east wall*?

Question (1): The answer can be obtained by estimating the stress on the inside of the wall as $\sigma_{inside} = 80{,}327 \times 12/3{,}775 = 255$ psi

In order to crack the concrete under this stress, the compressive strength of the concrete would have to be less than $(255/7.5)^2 = 1156$ psi, which does not seem reasonable; thus no cracking could occur.

Question (2): A possible reason for the absence of cracking on the outside of the pilaster of the east wall is that the recorded component of the ground motions in the E-W direction only induced a severe acceleration response in one direction, in this case the west direction. An analysis of the recorded acceleration response as well as of the calculated displacements out of plane seems to indicate that this was the case. Regarding the possibility that the width of the pilasters was 14 inches, rather than the assumed 12 inches in the above estimation, will not change the conclusions and answers offered.

4.5 ANALYSIS OF CASE C BASED ON STRESS CONTOURS

The calculated out-of-plane bending moment at the midheight of the pilaster located at the middle of the longitudinal wall is 22.5 ft-kips as shown in Figure 4.7. From the contours of bending moments out of plane along the TUW panels adjacent to the pilaster, it can be seen that the values of these moments vary from 0.80 to 1.50 in.-kips/in. Based on these values it can be considered that approximately the total moment that has to be resisted by the Tee-shaped pilaster section of Figure 4.6 can be estimated as follows:

$M_{max} = 22.5 \times 12$ (in.-kips) + (0.80+1.5)*0.5*240 (in.-kips) = 546 in.-kips

Based on this M_{max} the tensile stresses would be

$(\sigma_t)_{outside} = 546{,}000/1650 = 331$ psi.

Therefore, the compressive strength for flexural cracking would have to be less than 1,948 psi. As it is doubtful that the concrete would have such a low value, it would appear that according to the linear elastic analysis of the 3D model developed for this analysis, the pilaster could not have cracked under the effects of the ground motions recorded during the Big Bear earthquake.

In view of these analytical results the following question has been raised: "*Could the damage have occurred during any of the ground motions that have been recorded in the previous earthquakes*?"

The Landers earthquake occurred on the same day as the Big Bear earthquake. An analysis of the recorded responses originated by the Landers earthquake indicates that in spite of smaller peak ground accelerations, the spectral responses (PSA, PSV, and SD) in the period range of 0.4–0.5 seconds are significantly higher than those for the Big Bear earthquake. This is particularly true for those values corresponding to the sensors measuring the responses in the E-W direction. Considering these results and also those obtained taking into account the change in period as a consequence of a decrease in stiffness as clearly indicated by the results obtained applying Fourier transfer functions and Fourier moving window analyses, it appears that the existing damage (cracks) on the outside of the pilasters located in the west wall started during the Landers earthquake.

Regarding the above observation, it must be noted that even if the compressive strength of the concrete was 3,600 psi, the modulus of rupture would have been 450 psi. When this value is compared with the value estimated from Big Bear (331 psi), an increase in the moment of only 36% (450/331 = 1.36) will be required to cause cracking. According to the above discussion of the severity of the Landers response spectra with respect to the Big Bear response spectra, this increase could easily have been attained under the effects of the Landers ground motions. It also has to be noted that as the tensile stress on the inside of the pilaster would be 3,775/1,650 = 2.29 times smaller than the tensile stress on the outside, no cracks would have occurred in the inside surface of the pilasters.

Fig. 4.1 Horizontal cracks in pilaster, north wall

Fig. 4.2 Diagonal shear crack, west wall

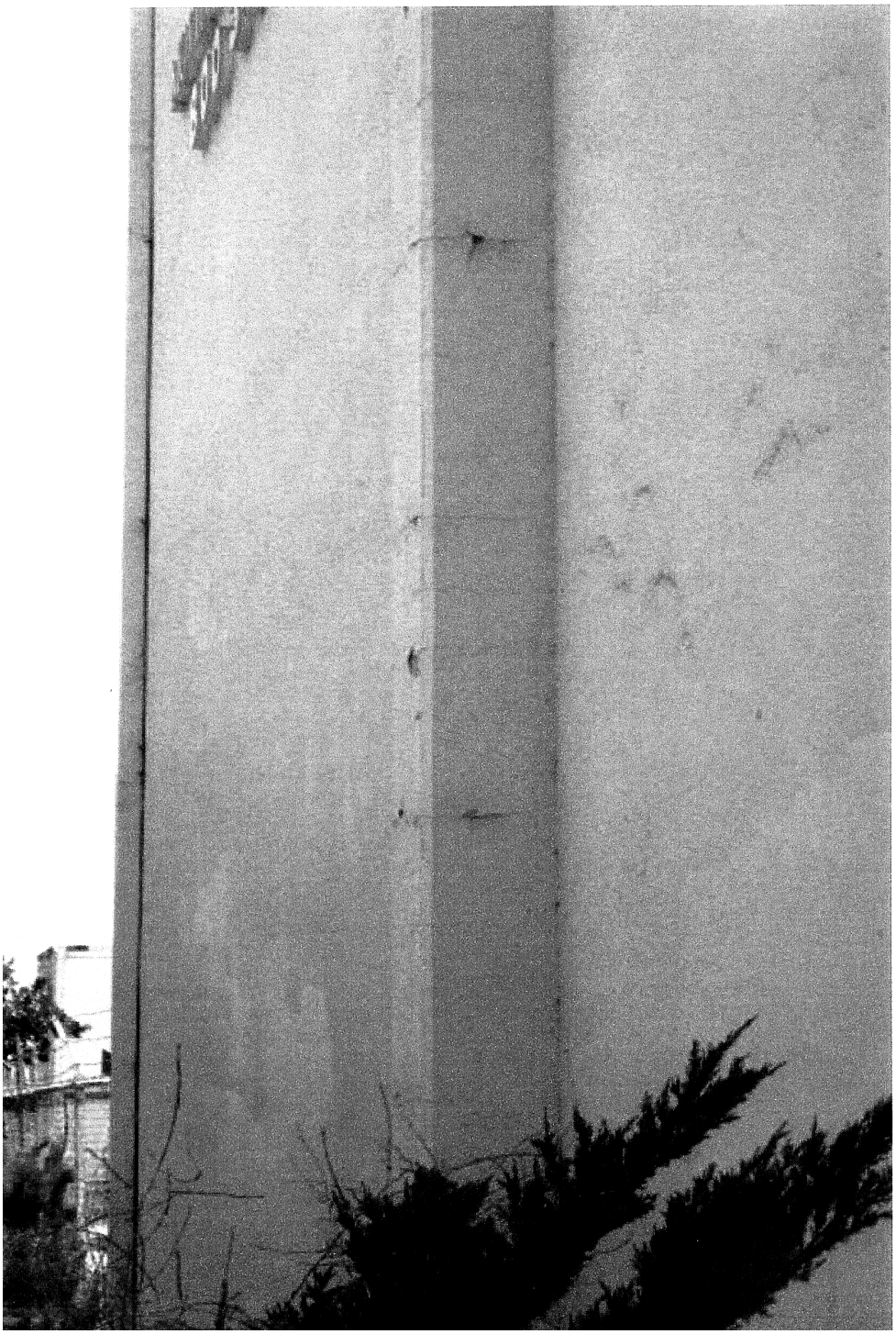

Fig. 4.3 Pilaster cracks, north wall

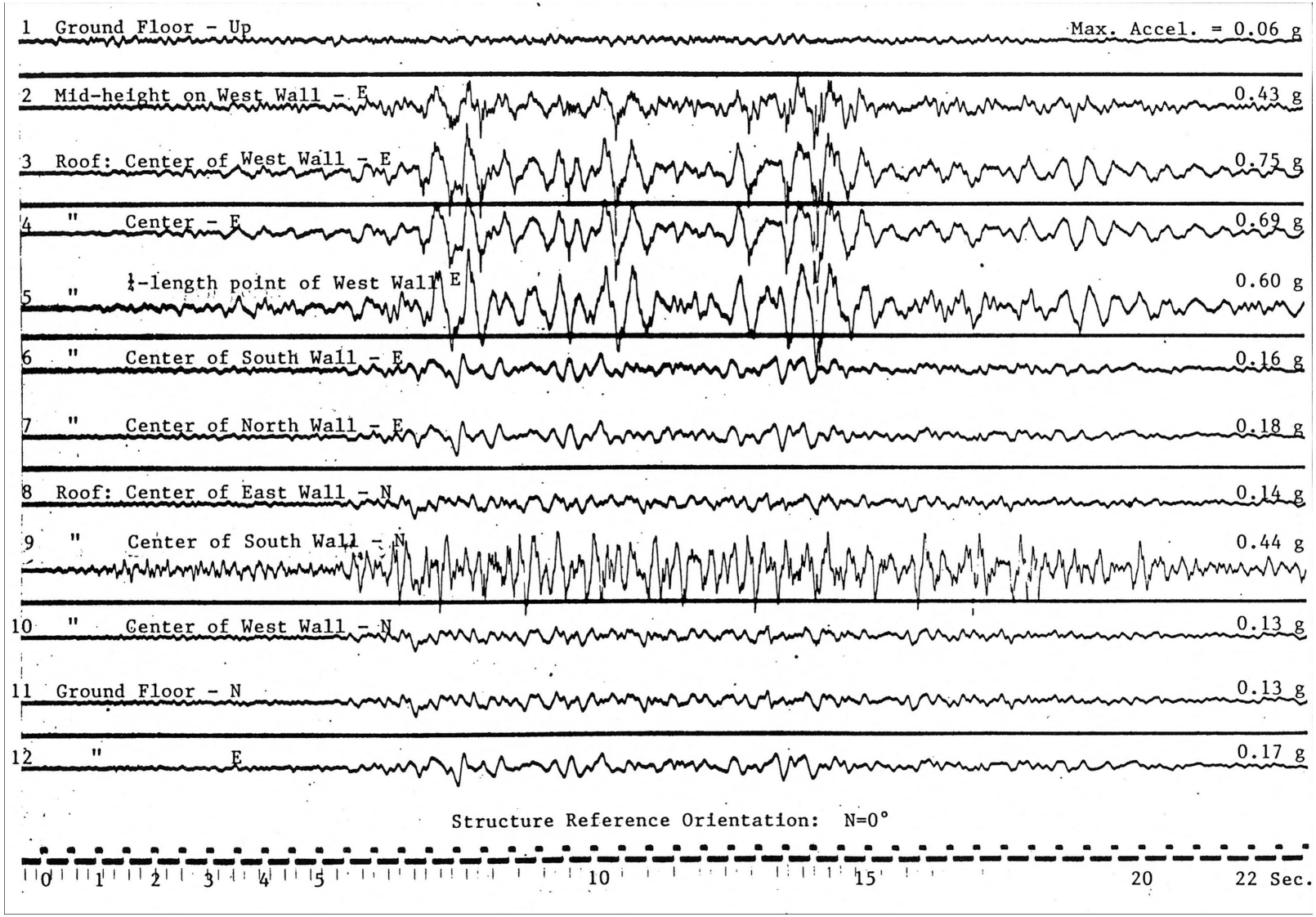

Fig. 4.4 Uncorrected recorded accelerations, Big Bear

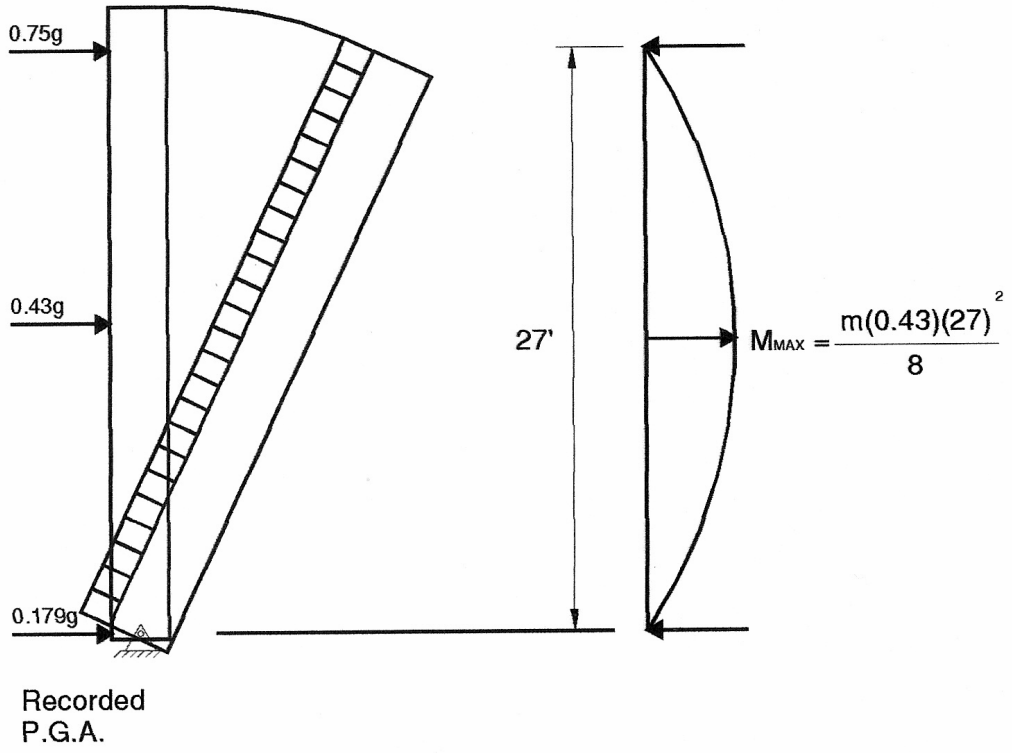

Fig. 4.5 Approximate accelerations and moments in wall

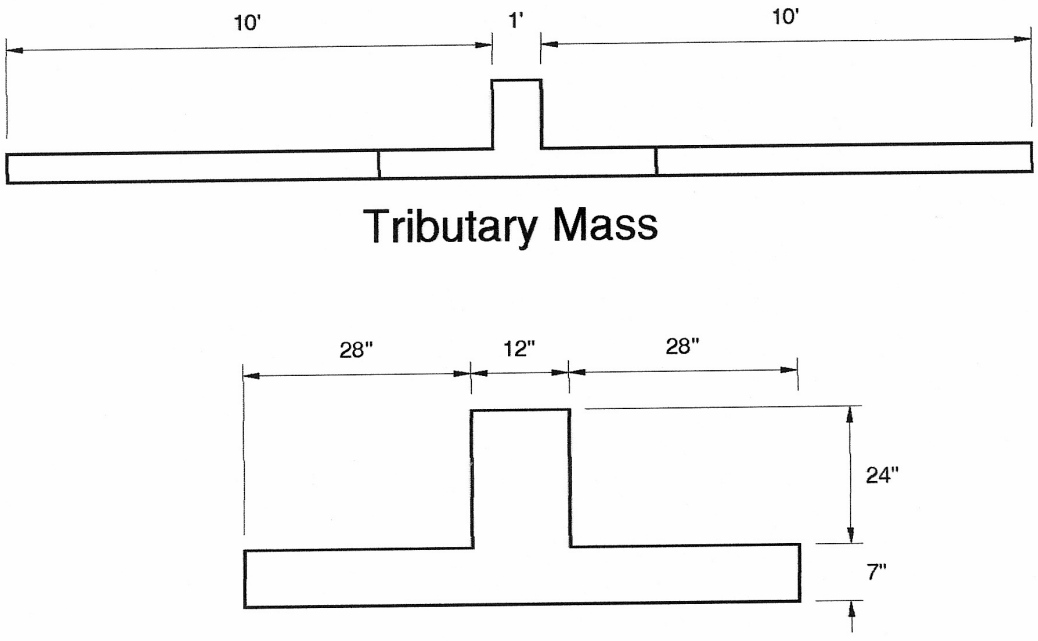

Fig. 4.6 Tributary mass and resisting pilaster section

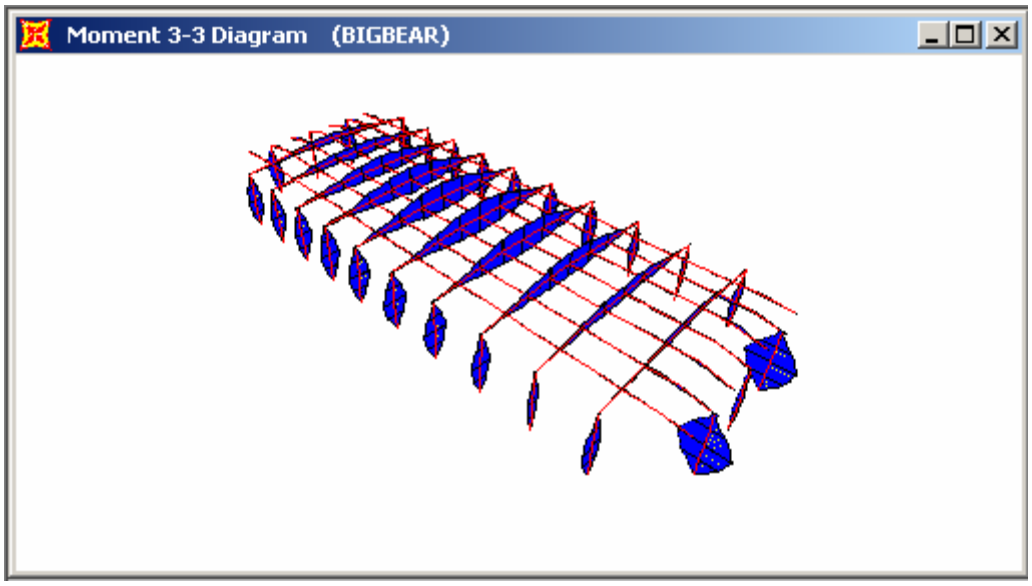

(a)

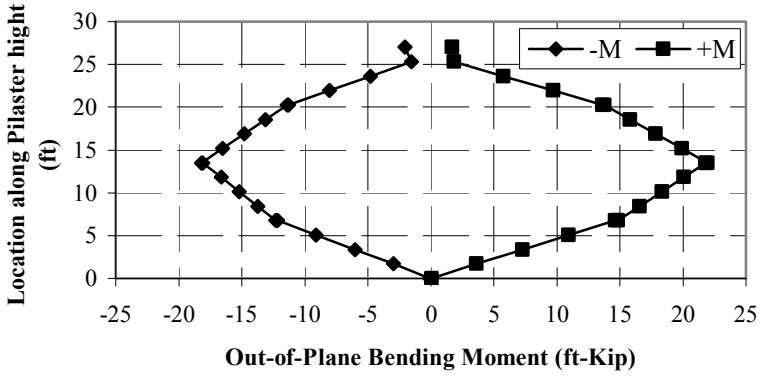

(b)

Fig. 4.7 Out-of-plane bending moments in pilasters (a) and critical pilasters (b), Big Bear

5 Spectral Analysis of Recorded Data

5.1 RESPONSE SPECTRA

Passing the recorded acceleration record through a single-degree-of-freedom system having 5% of critical damping and a variable circular frequency generated linear elastic response spectra. Comparisons were then made between spectra at critical locations in the building to evaluate some of the dynamic response characteristics.

The response spectrum obtained from sensor 5 in the transverse (E-W) direction during the Landers earthquake is shown in Figure 5.1. A distinctive peak occurs at a period of 0.4 seconds indicating the fundamental period of the building in this direction. Also shown is the response spectrum obtained from the accelerations recorded from sensor 12 at the base of the wall. A comparison of these two spectra at the first significant transverse period indicates the amount of out-of-plane amplification of the ground acceleration (1.2/0.36=3.3) in the wall. The response spectrum obtained from sensor 9 in the longitudinal (N-S) direction at the roof is shown in Figure 5.2. This figure indicates that the fundamental period in this direction is 0.35 seconds. Also shown is the spectrum obtained from sensor 11 at the base. As before, the difference in the spectra indicates the amount of out-of-plane amplification of the motion in the wall.

The variation of acceleration in the transverse direction at the roof level along the west wall is shown by comparing the response spectrum obtained from sensor 5 with that from sensor 3 in Figure 5.3. Although the amplification recorded by sensor 5 is slightly above that recorded by sensor 3 in the higher frequency range, the two responses are quite similar. In Figure 5.4, the response spectrum obtained in the east-west direction (sensor 6) at the top of the south wall is compared with the response spectrum at the base in the east-west direction (sensor 12). It can be seen that these two responses are almost identical.

5.2 FOURIER TRANSFER FUNCTIONS

In the four figures that follow, Fourier transfer functions (FTFs) in the north-south direction are calculated using sensor 9 at the roof and sensor 11 at the base. Transfer functions are calculated for each of the four recorded earthquake motions in chronological sequence. The FTF for the Palm Springs earthquake is shown in Figure 5.5. The fundamental frequency occurs at a value of 2.9 hertz for a period of 0.35 seconds. This value agrees well with the response spectrum analysis and is representative of the building in its initial condition. The FTF for the Landers earthquake is shown in Figure 5.6 and has a fundamental frequency of 3.02 hertz and a corresponding period of 0.33 seconds. Since there is almost no change in the period in this direction, linear behavior might be assumed in this direction under these two earthquakes. As mentioned in the previous section, the Big Bear earthquake produced the strongest ground shaking and structural response for this building. The calculated FTF for the Big Bear earthquake is shown in Figure 5.7, where a fundamental frequency of 1.33 hertz is indicated along with a corresponding period of 0.75 seconds. Hence this earthquake has caused the period to more than double, indicating inelastic behavior that may be due in part to loosening of the nails and connectors in the timber diaphragm. The FTF for the final record, Northridge, is shown in Figure 5.8. Recall that the recorded motions at this location due to the Northridge earthquake were not too severe. The fundamental frequency obtained from this earthquake is indicated to be 1.67 hertz with a corresponding period of 0.6 seconds. The reduction in period may have been due to some remedial work performed after the Big Bear earthquake.

In the next four figures, FTFs in the east-west direction are calculated using sensor 5 at the roof and sensor 12 at the base for the same four earthquakes. As before, the first of this series of earthquakes was Palm Springs, and the FTF is shown in Figure 5.9. The fundamental frequency can be seen to be 2.5 hertz and the corresponding period 0.4 seconds. The FTF for the next earthquake, Landers, is shown in Figure 5.10. In this case the fundamental frequency is 2.17 hertz and the corresponding period is 0.46 seconds for an increase of 15%. The third earthquake in the sequence is Big Bear; the FTF for this earthquake is shown in Figure 5.11. The figure indicates a fundamental frequency of 1.86 hertz and a corresponding period of 0.54 seconds. The final earthquake is Northridge, and the FTF for this record is shown in Figure 5.12. Here the fundamental frequency is indicated as 1.48 hertz, which corresponds to a period of 0.67 seconds.

These results are summarized in Table 5.1. A similar reduction in stiffness has been noted by others [Bouwkamp et al., 1994] in a study of an instrumented tilt-up building in Hollister, California, that recorded responses from the Morgan Hill (1984), Hollister (1986), and Loma Prieta earthquakes.

Table 5.1 Observed changes in frequency, period, and stiffness

Longitudinal Direction (N-S)

Seismic Event	Fundamental Frequency (hz)	Fundamental Period (sec)	Relative Stiffness	Percent Stiffness Reduction
Palm Springs	2.90	0.35	1.00	0%
Landers	3.02	0.33	1.12	0%
Big Bear	1.33	0.75	0.22	78%
Northridge	1.67	0.60	0.34	66%

Transverse Direction (E-W)

Seismic Event	Fundamental Frequency (hz)	Fundamental Period (sec)	Relative Stiffness	Percent Stiffness Reduction
Palm Springs	2.50	0.40	1.00	0%
Landers	2.17	0.46	0.75	25%
Big Bear	1.86	0.54	0.55	45%
Northridge	1.48	0.67	0.35	65%

5.3 MOVING WINDOW FOURIER TRANSFER FUNCTIONS

Moving window Fourier transfer function (MWFTF) analyses were conducted using the recorded base and roof motions in both the N-S and E-W directions to see if any permanent changes in the fundamental period of the structure could be identified. The recorded acceleration data from sensors 9 and 11 were used for the N-S direction and data from sensors 5 and 12 were used for the E-W direction. The MWFTFs have been calculated for ten-second window lengths with five-second window shifts, embedding zeros to obtain good resolution in the spectra. These results are presented in Figures 5.13–5.16. Under the E-W component of the Palm Springs ground motion (Fig. 5.13), the period remains relatively constant at 0.4 seconds for the full 50-second duration of the recordings. A decrease in period at 20 seconds into the record may indicate an interaction with either the partition wall or the warehouse contents. Storage racks extend to the roof line of the warehouse and may interfere with the out-of-plane deformation of

the tilt-up walls. In the N-S direction, the period averages approximately 0.33 seconds over the 50-second duration.

Similar MWFTFs for the recorded Landers earthquake motion are shown in Figure 5.14. In the E-W direction, the period starts at 0.4 seconds, lengthens to 0.48 seconds during the strong motion portion of the record, and then returns to 0.40 seconds. Lengthening of the period during the time of strong ground motion may be due to loosening of the connections and some micro-cracking in the tilt-up walls, as noted in the previous section. Analyses for the stronger Big Bear ground motions, shown in Figure 5.15, indicate a further lengthening of the period in the E-W direction during the strong motion portion of the record, to 0.52 seconds. However, the period returns to 0.4 seconds at the end of the record. Therefore, the lengthening is most likely due to loosening of the connections, particularly the nailed connections, and micro-cracking of the walls. Once the stronger ground motion subsides, any slippage in the connections also subsides and the opening and closing of micro-cracks diminishes. This behavior also implies that there was no yielding of the reinforcing steel in the walls.

The MWFTF results for the recorded Northridge ground motion are shown in Figure 5.16. In general, these results show no new behavior from that discussed previously. In the transverse (E-W) direction the period starts at 0.4 seconds and ends, lengthens to 0.47 seconds during the strong motion, and returns to 0.4 seconds at the end. In the longitudinal direction, the period remains approximately constant at an average value of 0.32 seconds. These results indicate that that the damage discussed in the previous section most likely occurred during the Landers and/or Big Bear earthquakes.

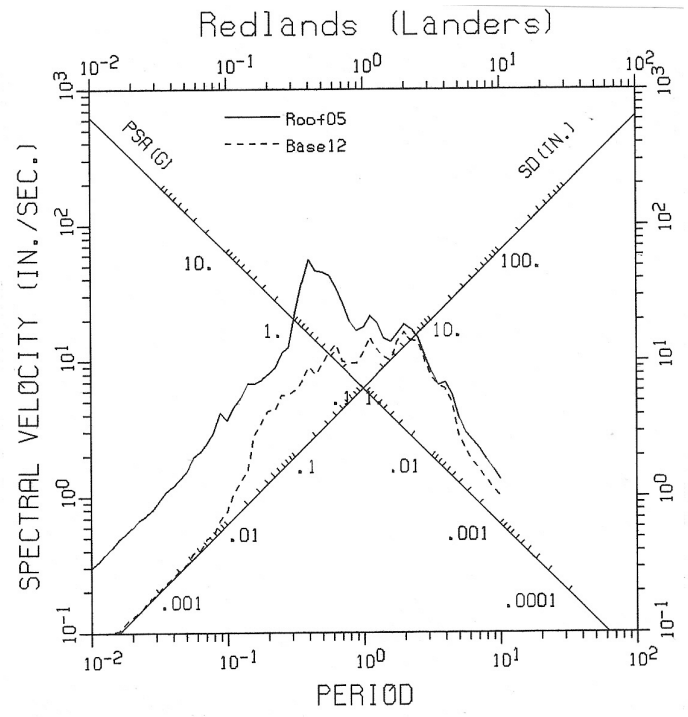

Fig. 5.1 Response spectra, roof (05) vs. base (12), Landers

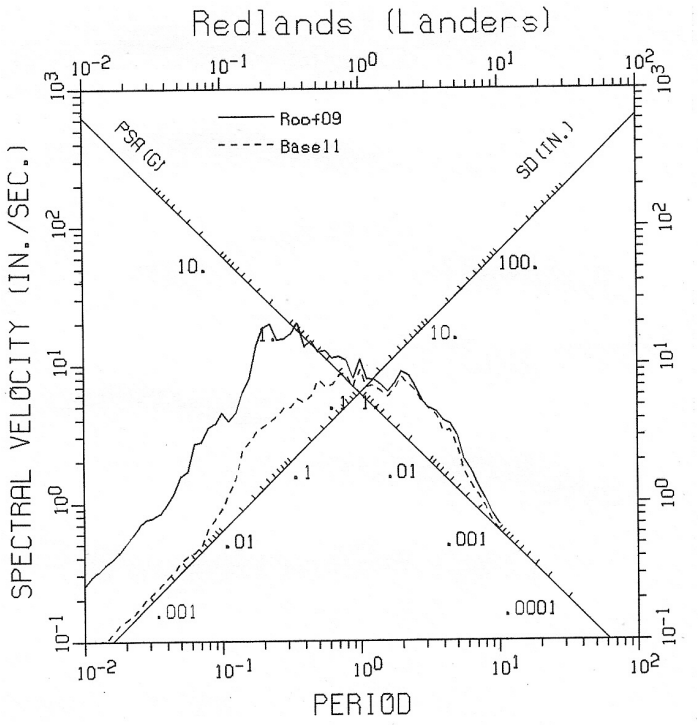

Fig. 5.2 Response spectra, roof (09) vs. base (11), Landers

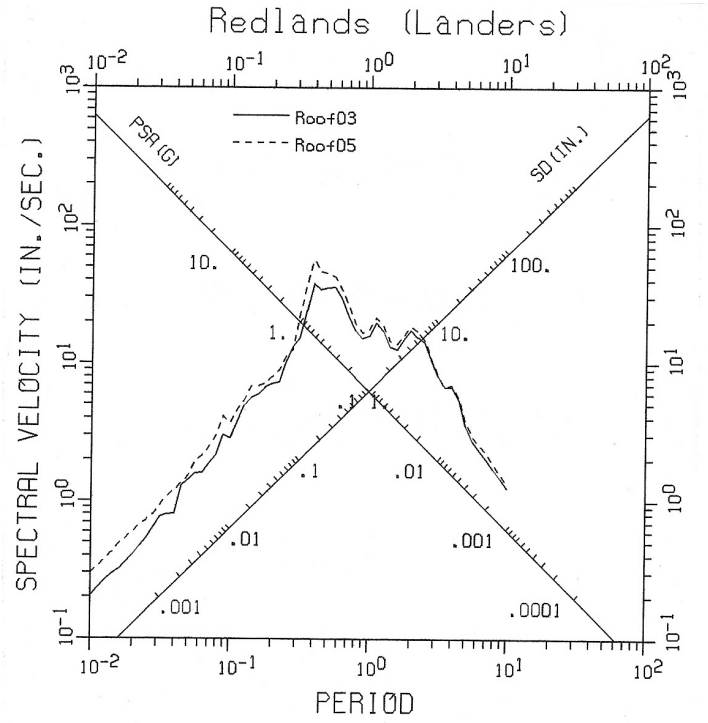

Fig. 5.3 Response spectra, roof (03) vs. roof (05), Landers

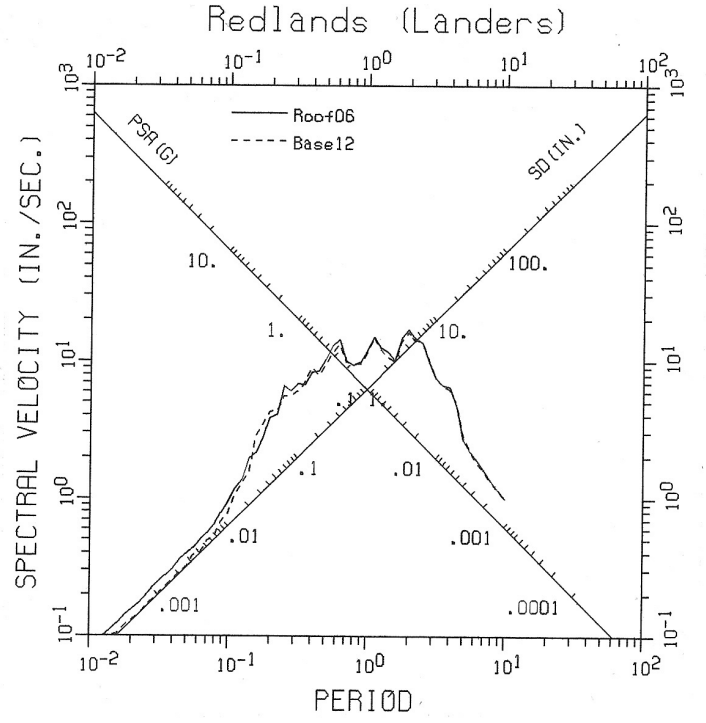

Fig. 5.4 Response spectra, roof (06) vs. base (12), Landers

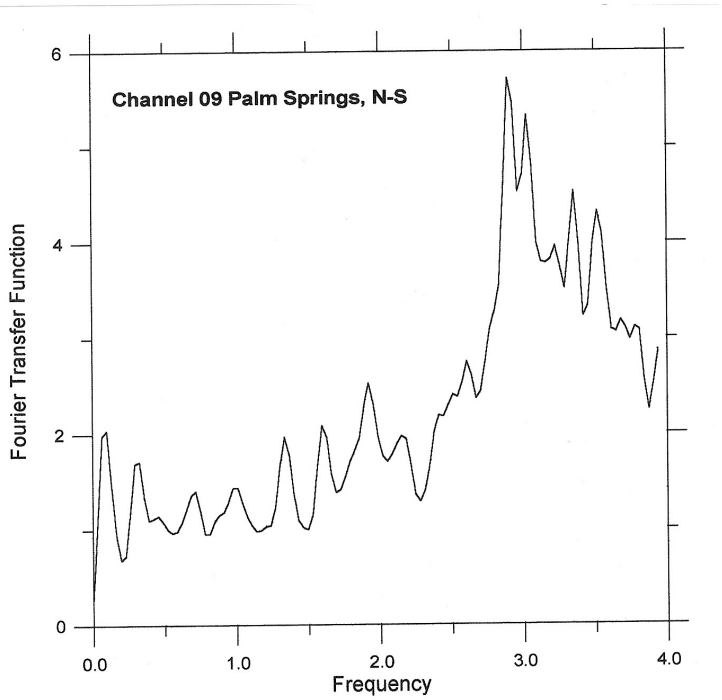

Fig. 5.5 Fourier transfer function, N-S, Palm Springs

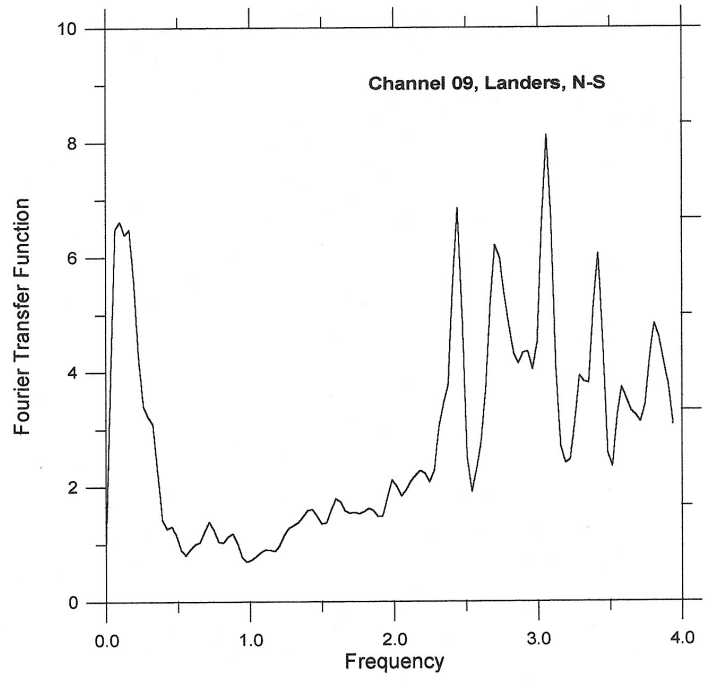

Fig. 5.6 Fourier transfer function, N-S, Landers

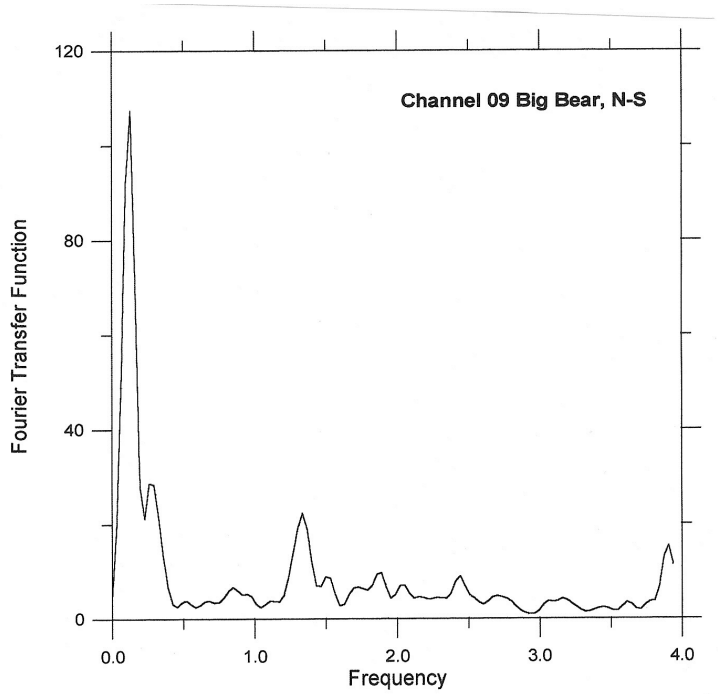

Fig. 5.7 Fourier transfer function, N-S, Big Bear

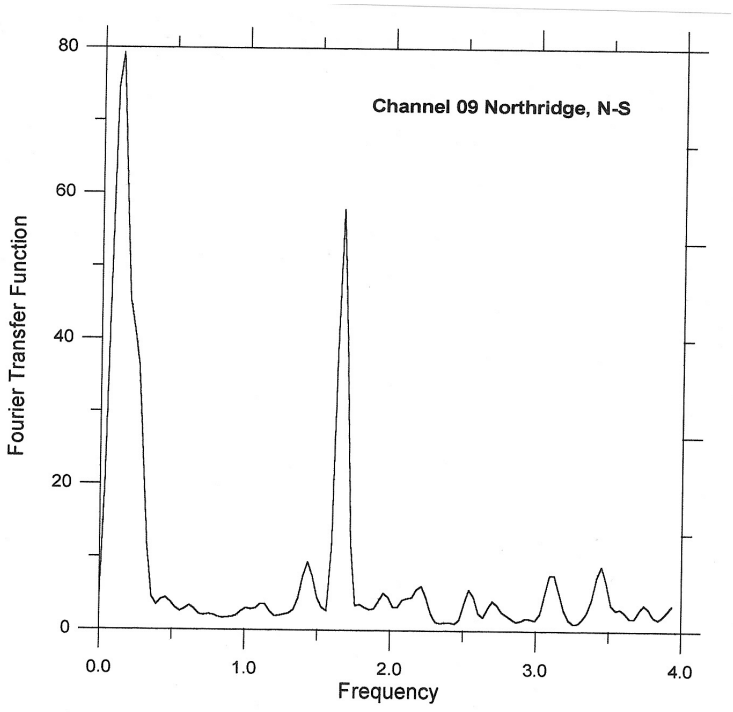

Fig. 5.8 Fourier transfer function, N-S, Northridge

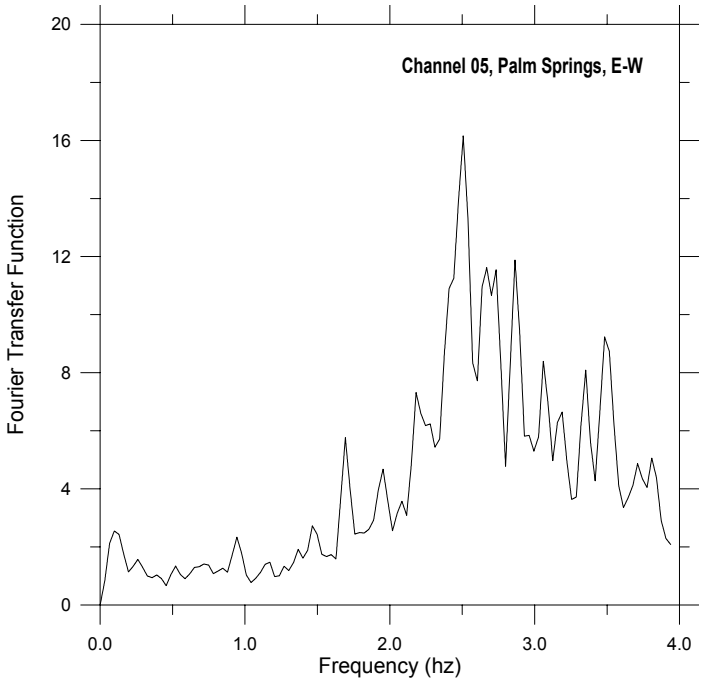

Fig. 5.9 Fourier transfer function, E-W, Palm Springs

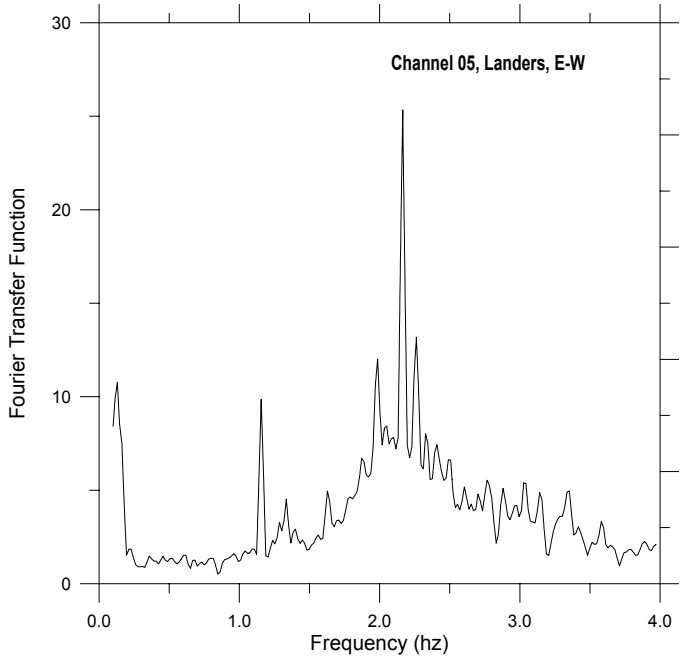

Fig. 5.10 Fourier transfer function, E-W, Landers

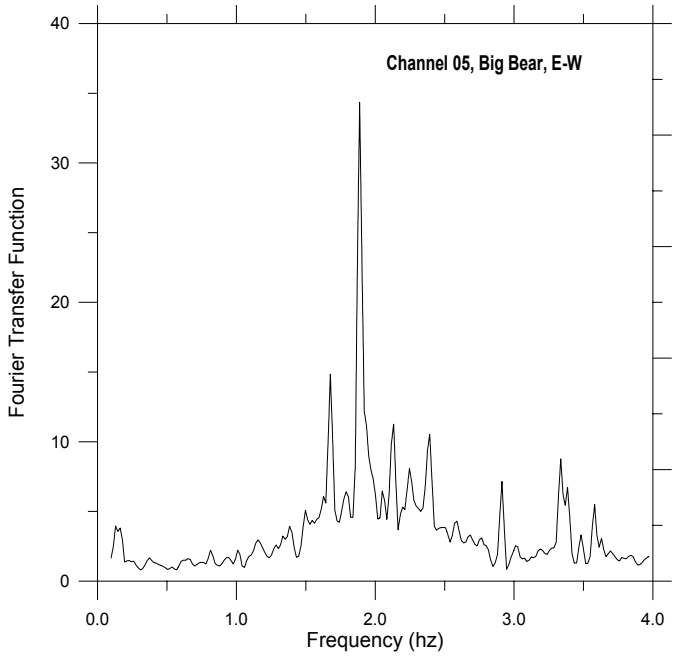

Fig. 5.11 Fourier transfer function, E-W, Big Bear

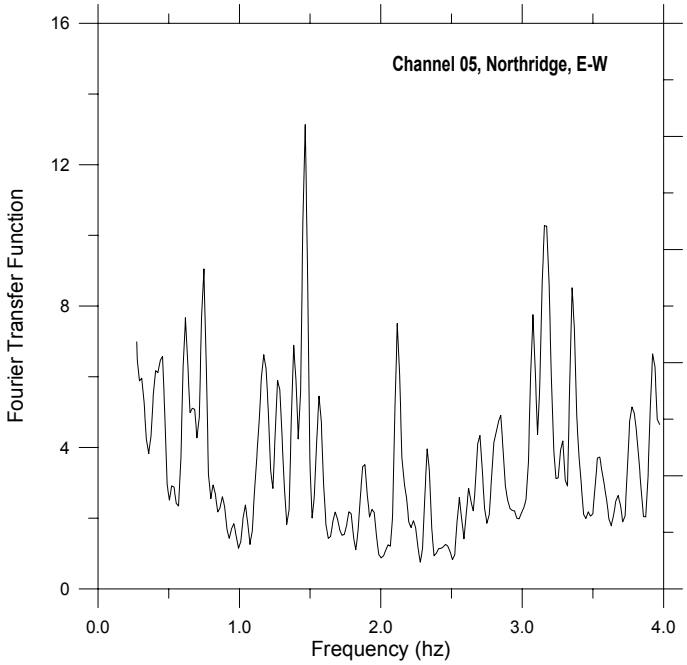

Fig. 5.12 Fourier transfer function, E-W, Northridge

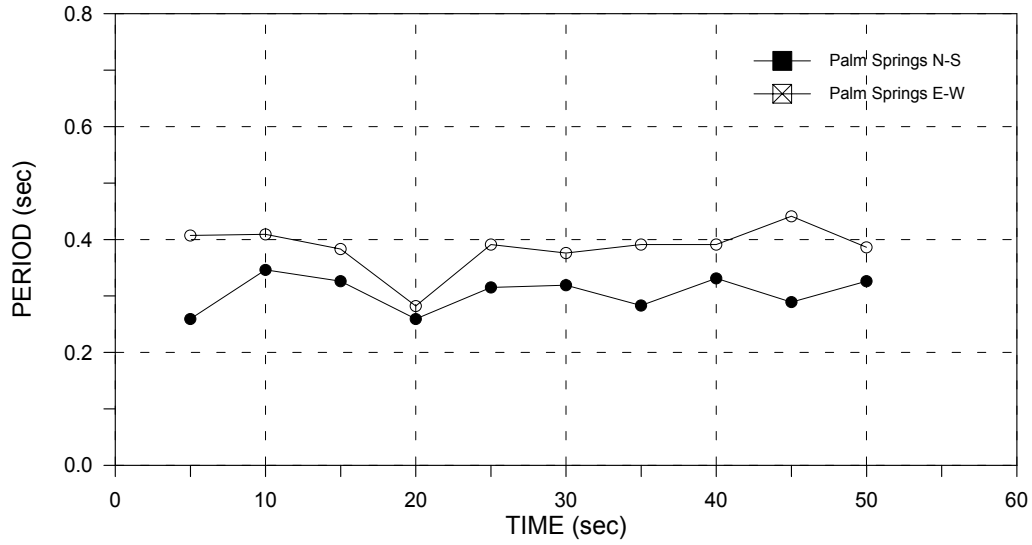

Fig. 5.13 Moving window analysis, Palm Springs

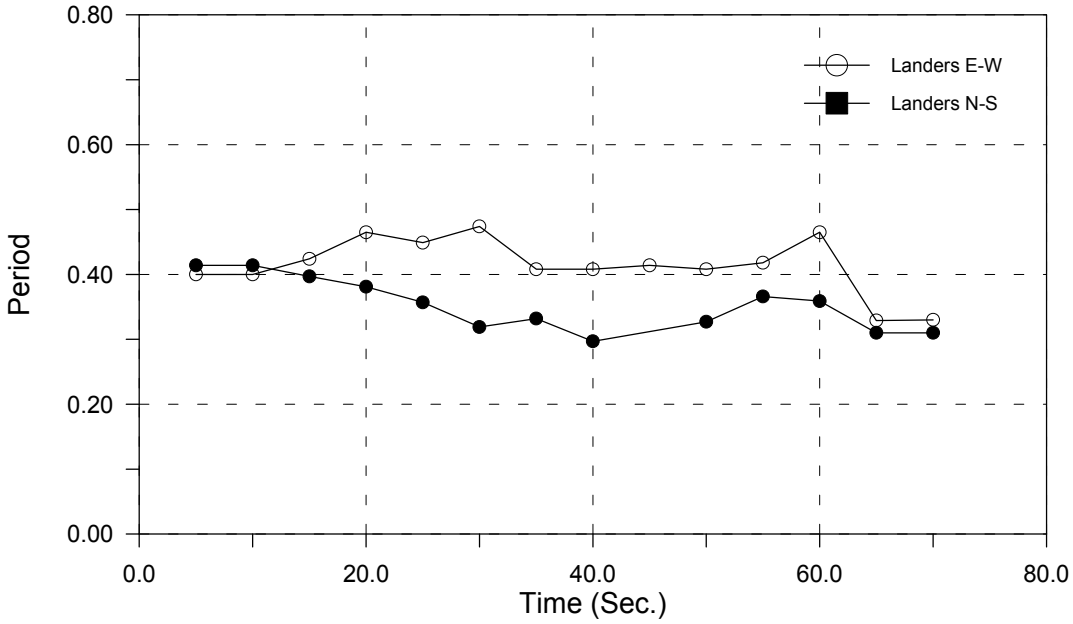

Fig. 5.14 Moving window analysis, Landers

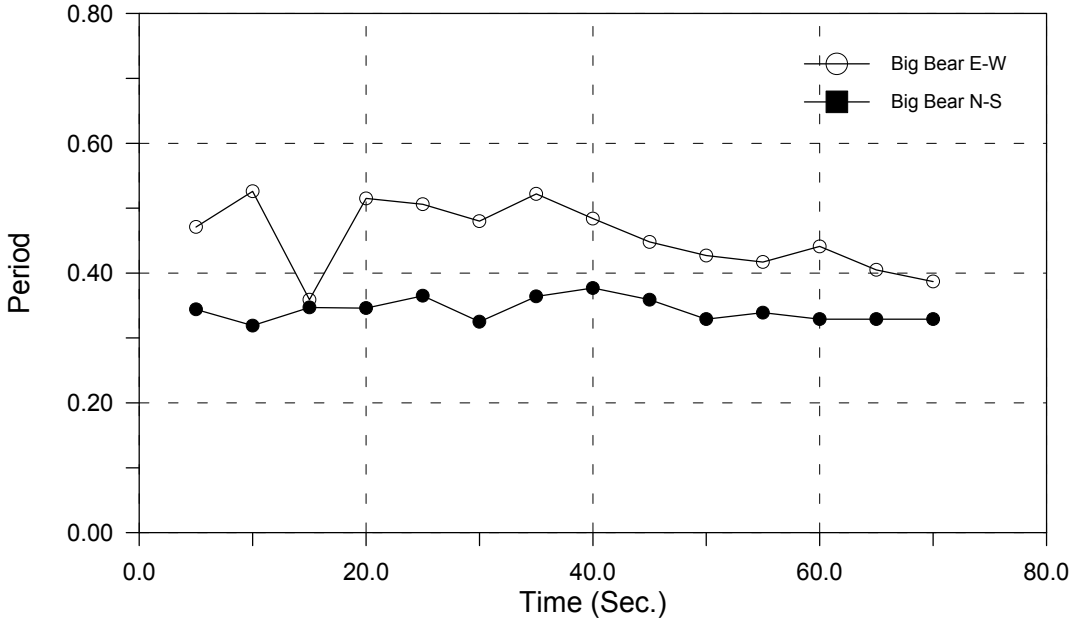

Fig. 5.15 Moving window analysis, Big Bear

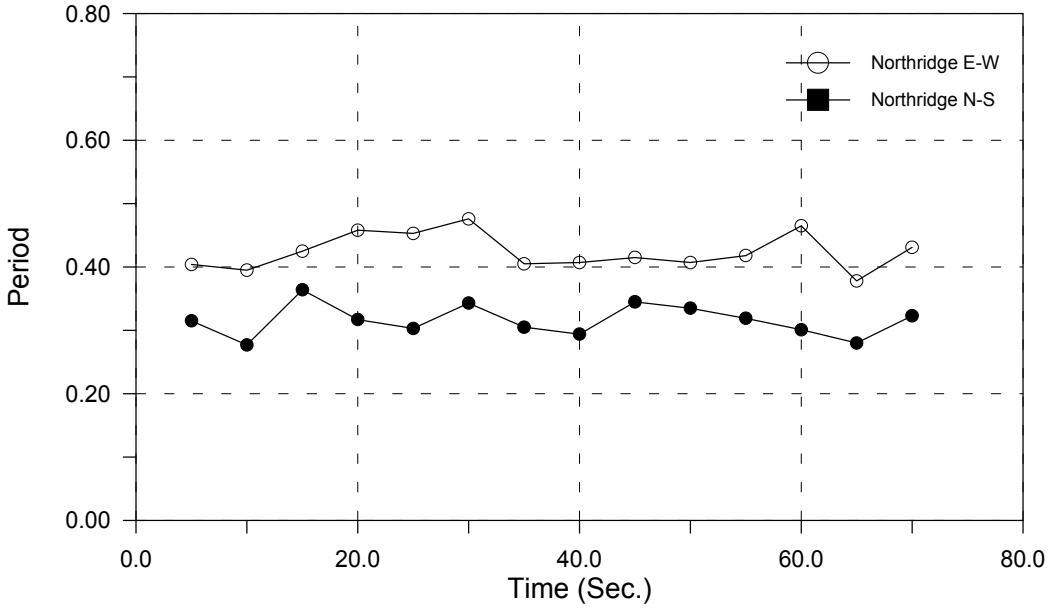

Fig. 5.16 Moving window analysis, Northridge

6 Elastic Dynamic Analyses

Relatively few detailed three-dimensional analyses have been conducted on these building systems. Three-dimensional dynamic analyses of building structures have traditionally not been done for more conventional structures due to the amount of time required to develop the analytical model and the high computational demands and storage requirements. However, with the dramatic improvements in software and increases in computational capabilities now available to engineering offices, such analyses may be used for more conventional systems. The sponsors of this research required that the computer programs used for the analyses be readily available commercial programs. For this reason, the SAP2000 program was selected. The nonlinear version of this program has some limited nonlinear analysis capabilities that will be discussed in a later section and used for the nonlinear dynamic analyses conducted as part of this study. Only a limited number of drawings (4) were available for this building and these provided few details. Therefore, when details needed to be considered, assumptions had to be made and standard details for this type of construction were used. The original elastic model is a detailed model of the tilt-up warehouse as built. Two additional models are included to investigate variations of the basic configuration that are used in current building practice for this type of structure. The first of these considers the effect of lack of continuity at the four corners of the building. The second variation considers the removal of the pilasters and the segmentation of the building walls with the glulam beams located at the center of the individual wall segments.

6.1 ORIGINAL ELASTIC MODEL

The original elastic model consists of the following structural members: (a) concrete slab on grade supported by linear elastic springs representing the soil, (b) concrete walls, (c) concrete pilasters, (d) timber glulam beams, (e) timber roof purlins, and (f) plywood roof diaphragm. The glulam beams and roof purlins are represented by beam elements in the analytical model. The

concrete walls and floor slab are represented by shell elements, and the plywood roof panels are also represented by shell elements. These elements can be seen in the isometric view of the model shown in Figure 6.1. The slab on grade is normal weight concrete (E=3,600 ksi) with an actual thickness of 5 inches and an effective thickness of 2 inches. The tilt-up walls are also normal weight concrete (E=3,600 ksi) with an actual thickness of 7 inches used for mass calculation and an effective thickness of 5.5 inches used for stiffness calculation. Pilasters are normal weight concrete (E=3,600 ksi) with 14″ x 24″ cross section. The roof diaphragm is structural plywood (E=1,300 ksi) with a 0.5 inch nominal thickness used for mass calculations and an effective stiffness of 0.2 inches used for stiffness calculations. The glulams are glued laminated timbers (E=1,400 ksi) 30 inches deep and 10-¾ inches wide. Purlins are structural timber with 4″ x 14″ nominal size. The overall model consists of 1000 beam elements, 2000 shell elements, and 500 spring elements.

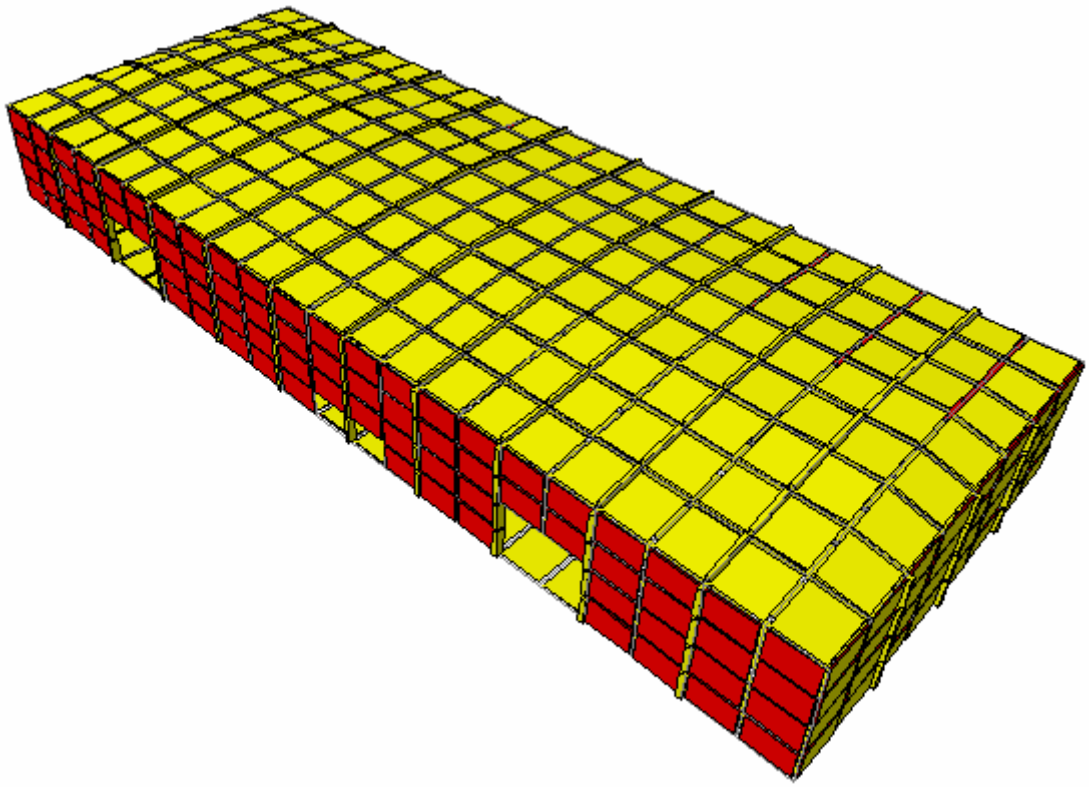

Fig. 6.1 Elastic finite element model (SAP 2000)

6.1.1 Modal Analyses

Modal analyses were conducted using the above model and considering 35 modes of vibration. The modal periods and mass participation ratios for these modes of vibration are summarized in Table 6.1. Considering the contributions of the individual modes, the first significant mode in the transverse (E-W) direction is the sixth mode, which has a period of 0.39 seconds. In a similar manner, the first significant mode in the longitudinal (N-S) direction is the ninth mode, having a period of 0.29 seconds. These results are compared with the results of the spectral analyses in Table 6.2. The first mode, having a period of 0.72 seconds, is a vertical mode.

Table 6.1 Modal periods and mass participation, elastic model

MODE	PERIOD	INDIVIDUAL MODE (PERCENT)			CUMULATIVE MODE (PERCENT)		
		UX	UY	UZ	UX	UY	UZ
1	0.717918	0.001	0	4.0217	0.001	0	4.0217
2	0.590654	0	0.0393	0.0043	0.001	0.0393	4.026
3	0.582274	0	0	0.0691	0.001	0.0393	4.0951
4	0.499461	0.0001	0	0.0624	0.0011	0.0393	4.1575
5	0.471977	0.0031	0	0.4764	0.0043	0.0393	4.6339
6	0.390846	40.819	0.0001	0.0001	40.8233	0.0394	4.634
7	0.388876	0.0041	0.5616	0	40.8274	0.6009	4.634
8	0.330793	0	0.0002	0.1492	40.8274	0.6011	4.7832
9	0.291661	0	3.1424	0.0001	40.8274	3.7435	4.7833
10	0.261067	0	0.0004	0.0081	40.8275	3.7439	4.7915
11	0.23621	0	5.44	0.0001	40.8275	9.1839	4.7915
12	0.232412	0.0031	0.001	0	40.8306	9.185	4.7915
13	0.212977	0.0003	0.023	0.0263	40.8309	9.2079	4.8179
14	0.199515	2.5242	0.0001	0.0007	43.3551	9.208	4.8186
15	0.195342	0	4.7827	0	43.3551	13.9907	4.8186
16	0.193709	0.1664	0	0.0001	43.5215	13.9907	4.8187
17	0.192708	1.09	0.0003	0.0004	44.6115	13.991	4.819
18	0.188556	0.0716	0.0001	0.0001	44.6831	13.991	4.8191
19	0.184965	0.0239	0.0008	0.0156	44.707	13.9918	4.8347
20	0.184788	0.001	0.0027	0	44.708	13.9945	4.8347
21	0.184353	0.0117	0.0216	0.0662	44.7197	14.0161	4.9009
22	0.18411	0.0188	0.0036	0.017	44.7385	14.0196	4.9179
23	0.180608	0.016	0.0002	0.0001	44.7545	14.0198	4.918
24	0.179955	0.1119	0.0214	0.0056	44.8664	14.0412	4.9236
25	0.175921	0.4594	0.002	0.0301	45.3258	14.0431	4.9537

Table 6.2 Fundamental period comparisons

Analysis Procedure	Transverse (E-W)	Longitudinal (N-S)
Response spectrum	0.40 seconds	0.35 seconds
Fourier transfer function	0.40 seconds	0.33 seconds
SAP2000 3D model	0.39 seconds	0.29 seconds

It should be noted that the mass participation in the fundamental mode of the transverse (E-W) direction is 41%, and with the inclusion of all 35 modes the mass participation only increases to 46%. This compares with a value of 49% for a wall segment that is simply supported on four sides and has an aspect ratio of 22′/27′ = 0.8 [Norris, et al., 1959]. In the longitudinal direction (N-S) the mass participation in the fundamental mode is only 3.1%, and with the inclusion of the first 35 modes it increases to only 15-½%. This implies that for equal accelerations in both directions, the base shear in the E-W direction will be three times that in the N-S direction.

The deflected shape of the fundamental mode in the transverse (E-W) direction is shown in Figure 6.2, and the deflected shape of the fundamental mode in the longitudinal (N-S) direction in Figure 6.3**.** In this mode, the deformation of the roof diaphragm is large relative to the deformation of the walls, resulting in a somewhat distorted shape for the mode.

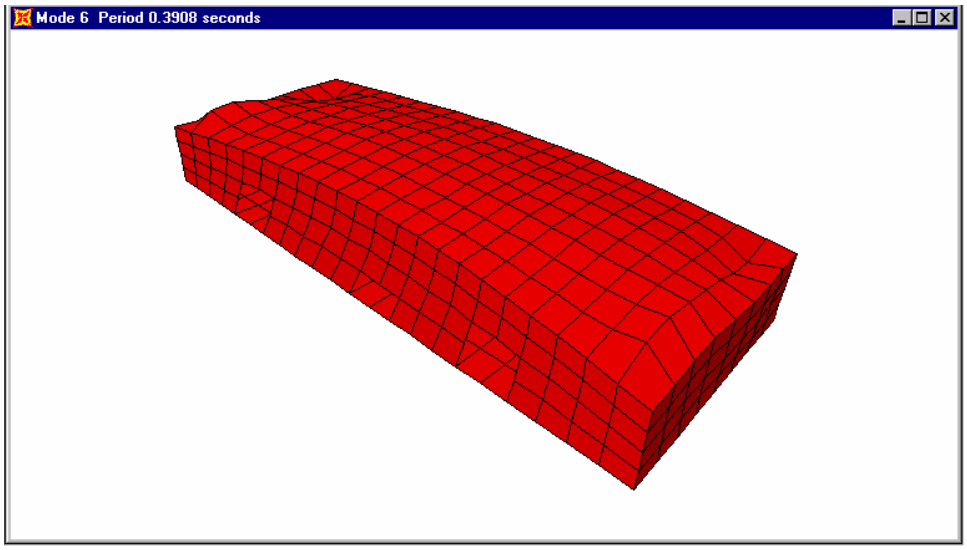

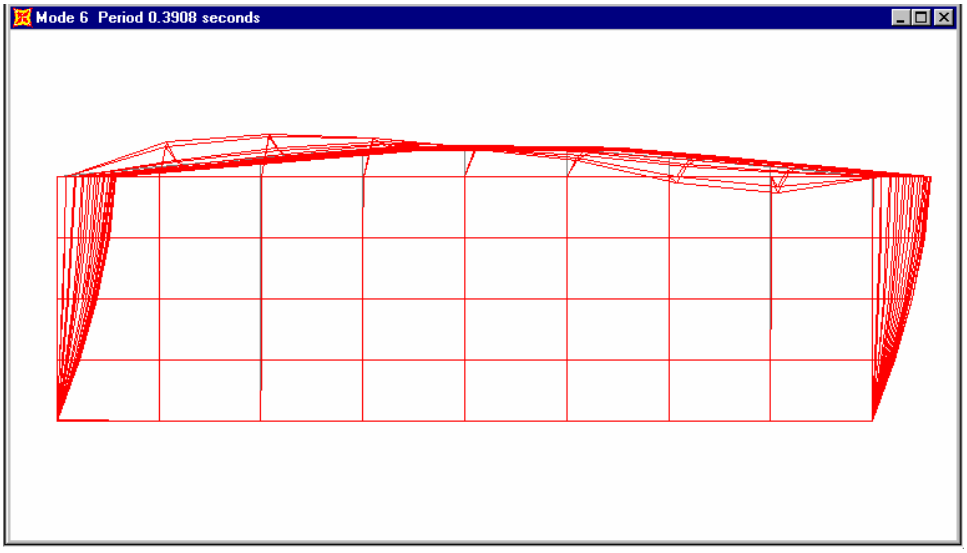

Fig. 6.2 Transverse fundamental mode shape

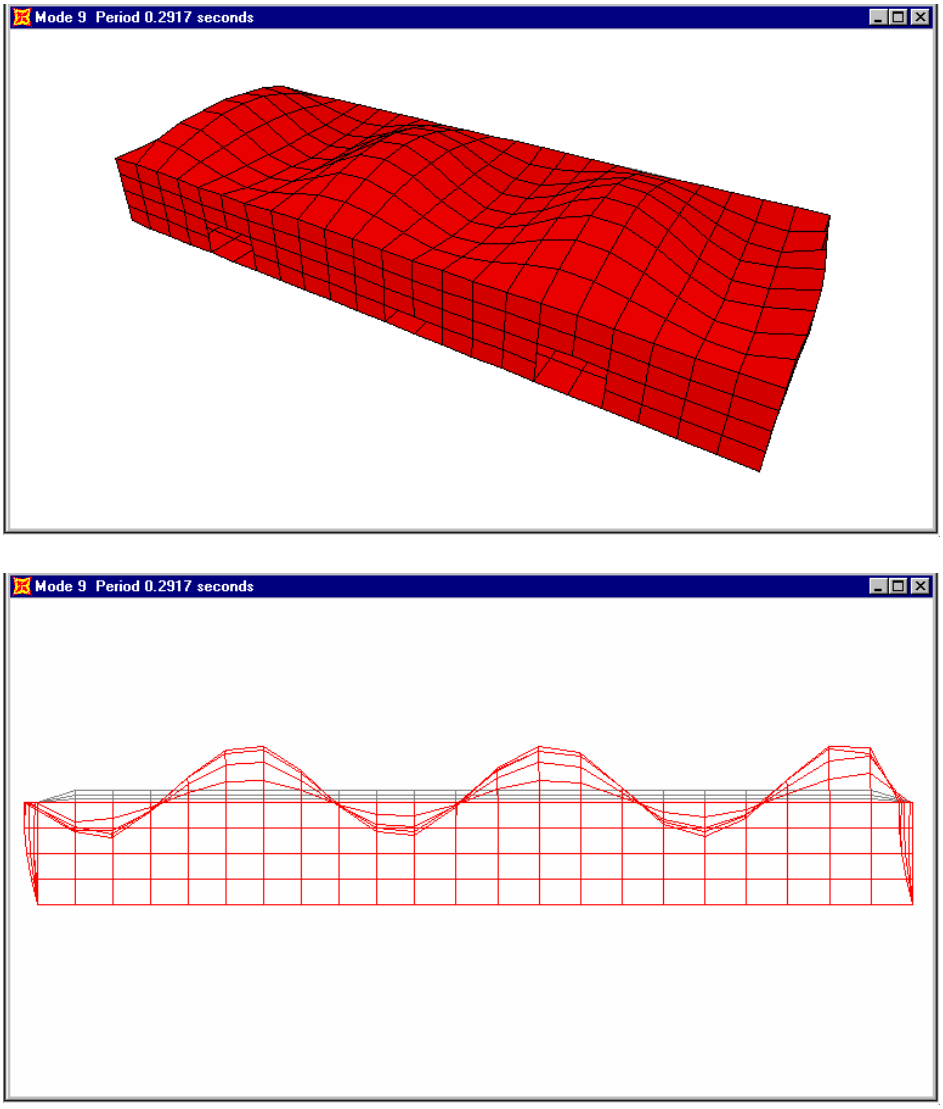

Fig. 6.3 Longitudinal fundamental mode shape

6.1.2 Calculated versus Recorded Response

In order to verify the capability of the analytical model to reproduce the accelerations and displacements in the building with acceptable accuracy, the recorded acceleration response from four earthquakes was used for making critical comparisons. The four earthquakes that produced the recorded data were Palm Springs (1986), Landers (1992), Big Bear (1992), and Northridge (1994). For each time history earthquake analysis, the two horizontal acceleration components were applied simultaneously at the base of the building. The data at the base was recorded on channel 12 (E-W) and channel 11 (N-S). The recorded accelerations measure the total

acceleration, which is integrated numerically to obtain the total displacement. Similar calculations are performed for the calculated acceleration and displacement.

Time histories of the recorded accelerations for the Palm Springs earthquake and corresponding displacements are compared with those calculated using the analytical model in Figures 6.4–6.9. The out-of-plane acceleration data for channel 2, located midheight of the west wall, are shown in Figure 6.4a. Here it can be seen that the peak acceleration reaches a value of 0.19g at 10 seconds. However, the peak acceleration measured at this location was only 0.094g (Table 3.1). The maximum calculated displacement was 0.38 inches (Fig. 6.4b) compared with a recorded value of 0.30 inches. Channel 3 is located at the top of the west wall and recorded a peak out-of-plane acceleration of 0.123g, as shown in Figure 6.5a, compared with a calculated value of 0.27g. The maximum displacement based on the recorded acceleration is 0.31 inches compared with a calculated value of 0.59 inches (Fig. 6.5b). These two instruments were located on the tilt-up wall adjacent to the bearing stud partition (fire wall) that was not included in the analytical model due to lack of details. Interaction between these two walls may have influenced the comparison of peak values at these locations. Time histories for channel 5, located at the roof level on the west wall midway between the fire wall and the south wall are shown in Figure 6.6. The out-of-plane acceleration time history (Fig. 6.6a) indicates a calculated peak acceleration of 0.22g, which compares with a peak recorded value of 0.24g (Table 3.1). The calculated displacement time history (Fig. 6.6b) indicates a peak displacement of 0.5 inches, whereas the peak recorded displacement is 0.43 inches. Channel 6 is located at the roof level in the middle of the south wall. The calculated in-plane acceleration at this location is shown in Figure 6.8a and indicates a peak value of 0.042g compared with a recorded value of 0.039g. The calculated peak displacement (Fig. 6.8b) is 0.23 inches compared with the 0.24 inches recorded. Channel 9 measures out-of-plane acceleration at the roof level at the midpoint of the south wall. The calculated peak acceleration, shown in Figure 6.7a, is 0.075g compared with 0.11g recorded. The calculated peak displacement (Fig. 6.7b) is 0.25 inches compared with 0.22 inches recorded (Table 3.1). In-plane accelerations at the roof level of the west wall are obtained from channel 10. The calculated peak acceleration, shown in Figure 6.9a, is 0.38g compared with a recorded value of 0.39g. The calculated peak displacement (Fig. 6.9b) is 0.2 inches compared with the recorded value of 0.23 inches.

These results indicate that the calculated displacement time histories show a better correlation with the displacement time histories derived from the recorded acceleration data than the calculated accelerations with the recorded acceleration data. This is usually the case, since the displacements are determined by integrating the acceleration data twice, which produces a smoothing effect and eliminates high-frequency peaks that occur in the acceleration data. It should also be noted that the frequency of the displacements is primarily the frequency of the ground motion.

The recorded and calculated accelerations and displacements for the Landers earthquake record are presented and compared in Figures 6.10–6.15. These results are not significantly different from those just discussed for the Palm Springs earthquake. Therefore in the following paragraph, the results from the strongest of the recorded earthquakes, Big Bear, will be discussed in detail.

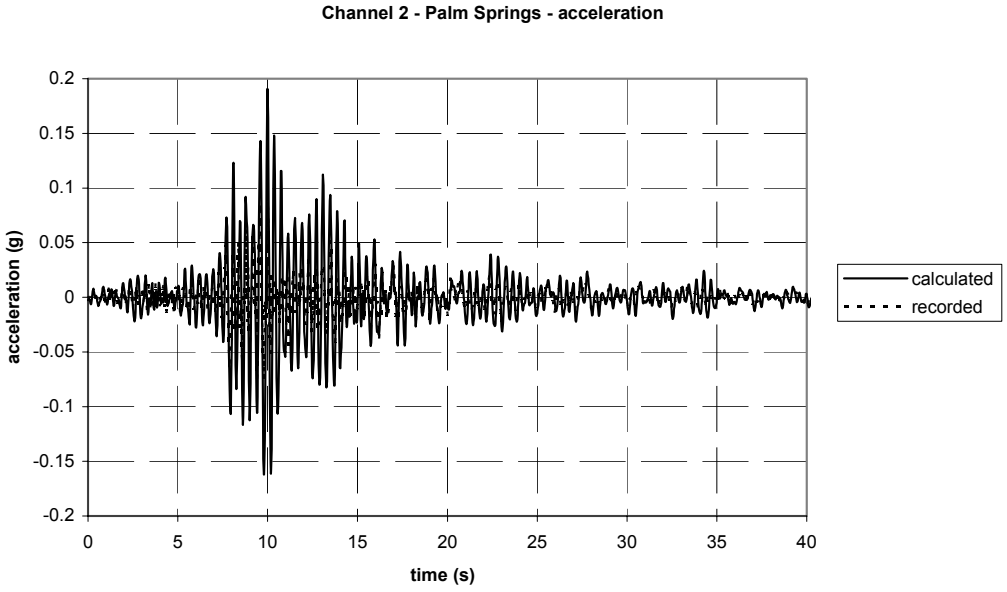

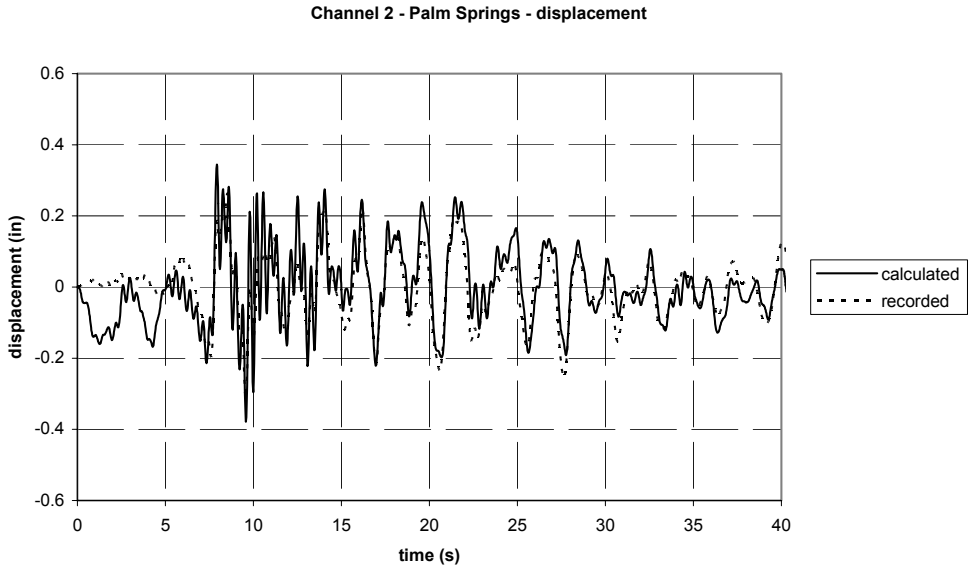

Fig. 6.4 Response comparisons, ch. 2, Palm Springs

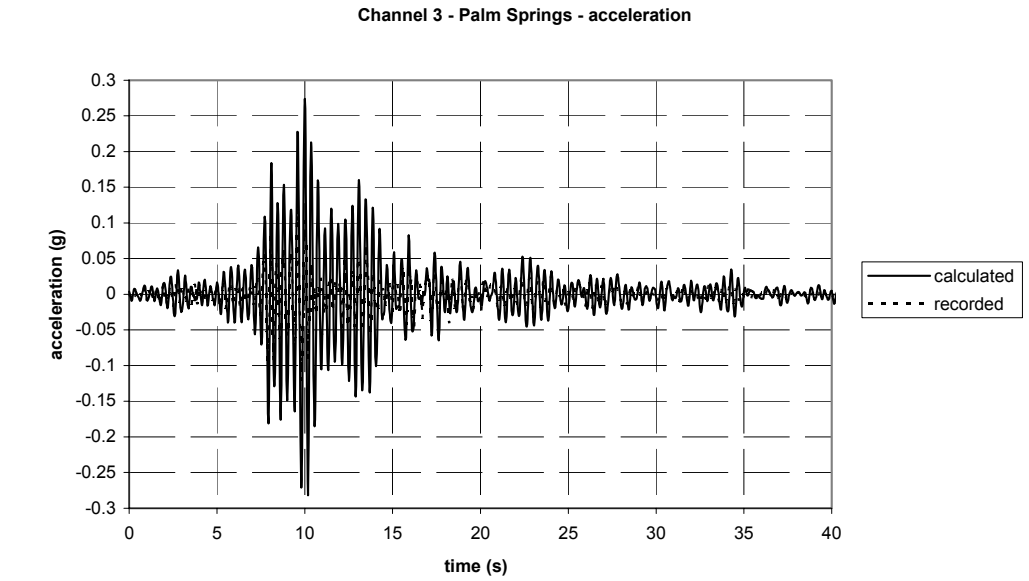

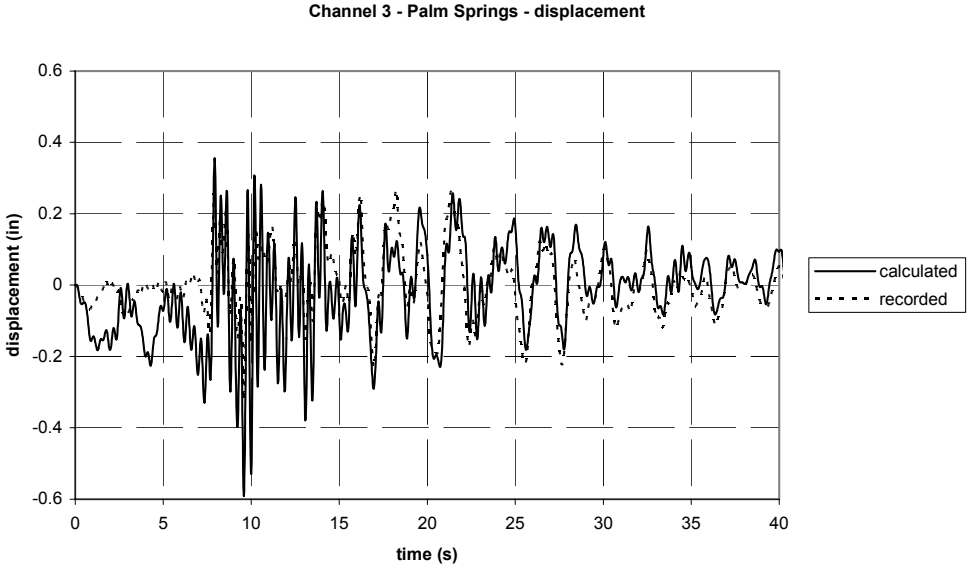

Fig. 6.5 Response comparisons, ch. 3, Palm Springs

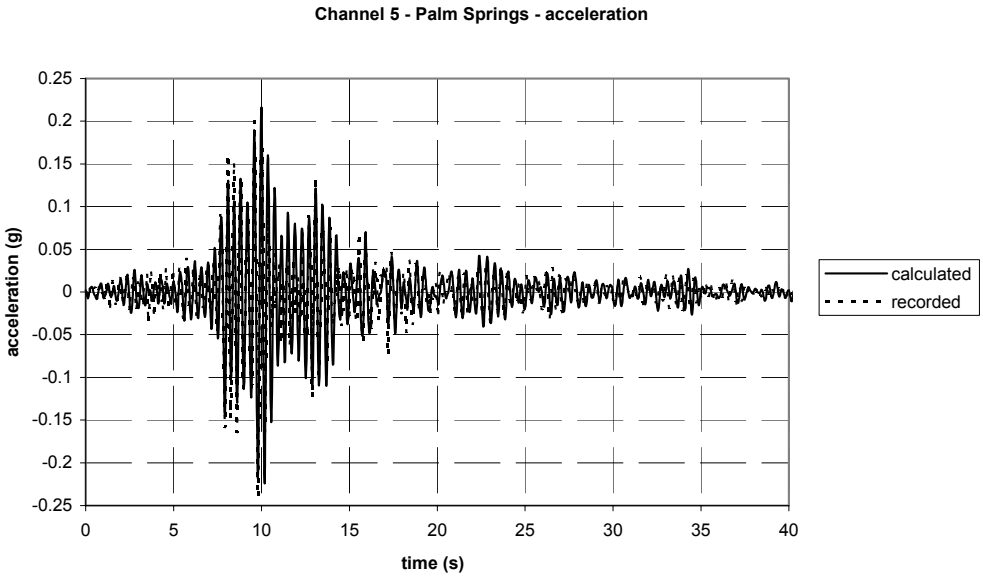

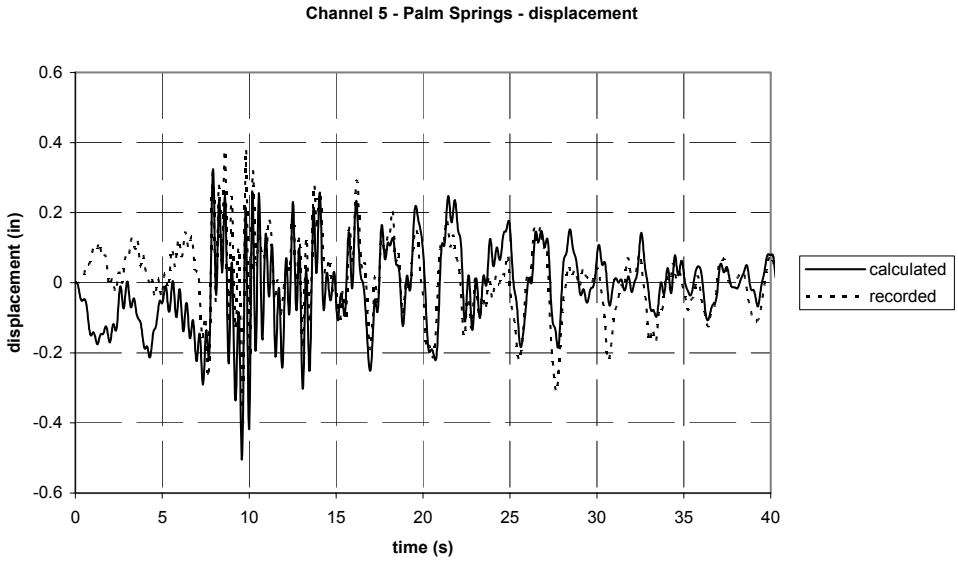

Fig. 6.6 Response comparisons, ch. 5, Palm Springs

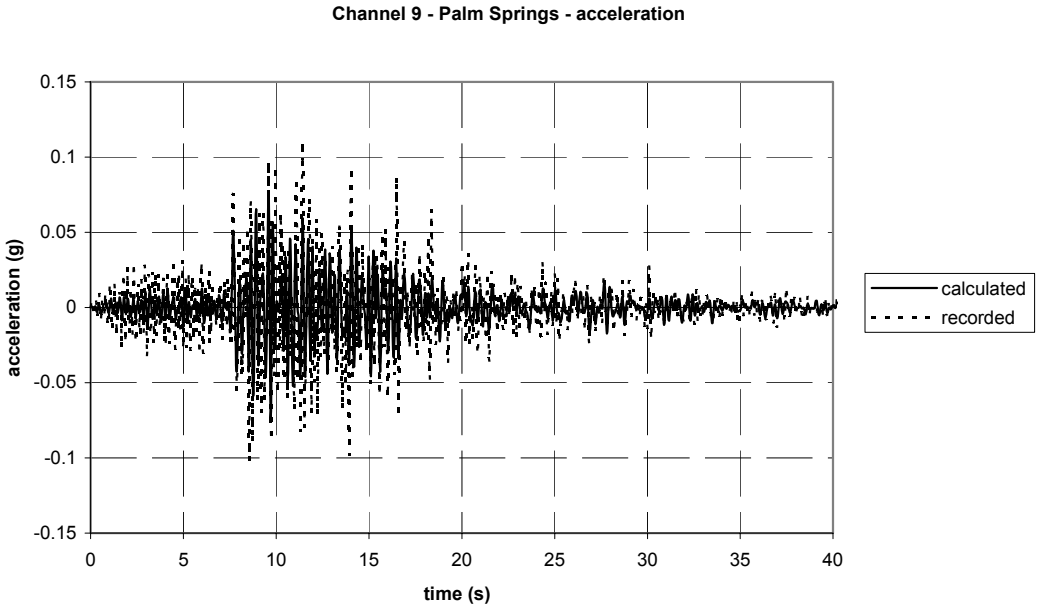

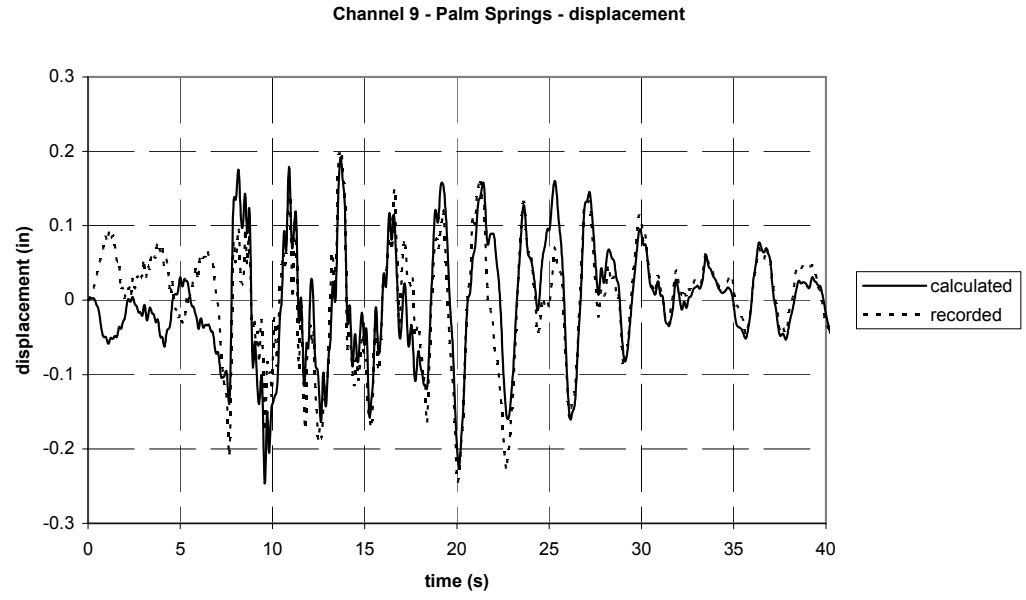

Fig. 6.7 Response comparisons, ch. 9, Palm Springs

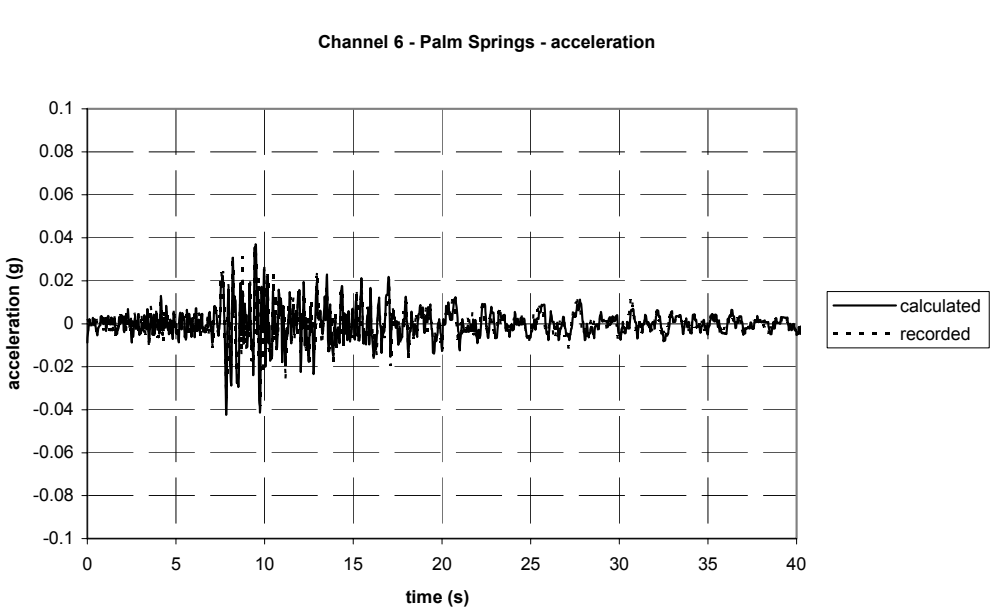

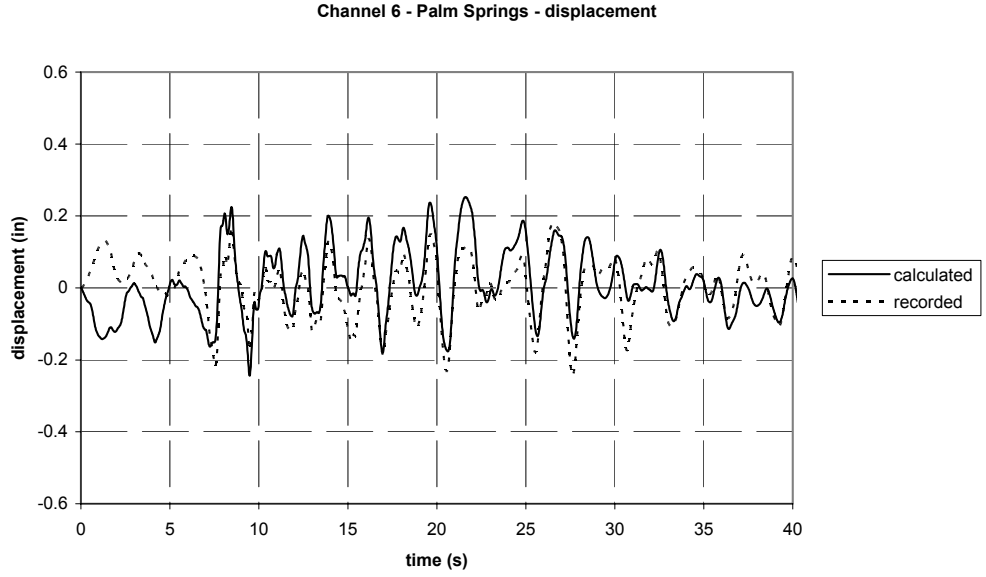

Fig. 6.8 Response comparisons, ch. 6, Palm Springs

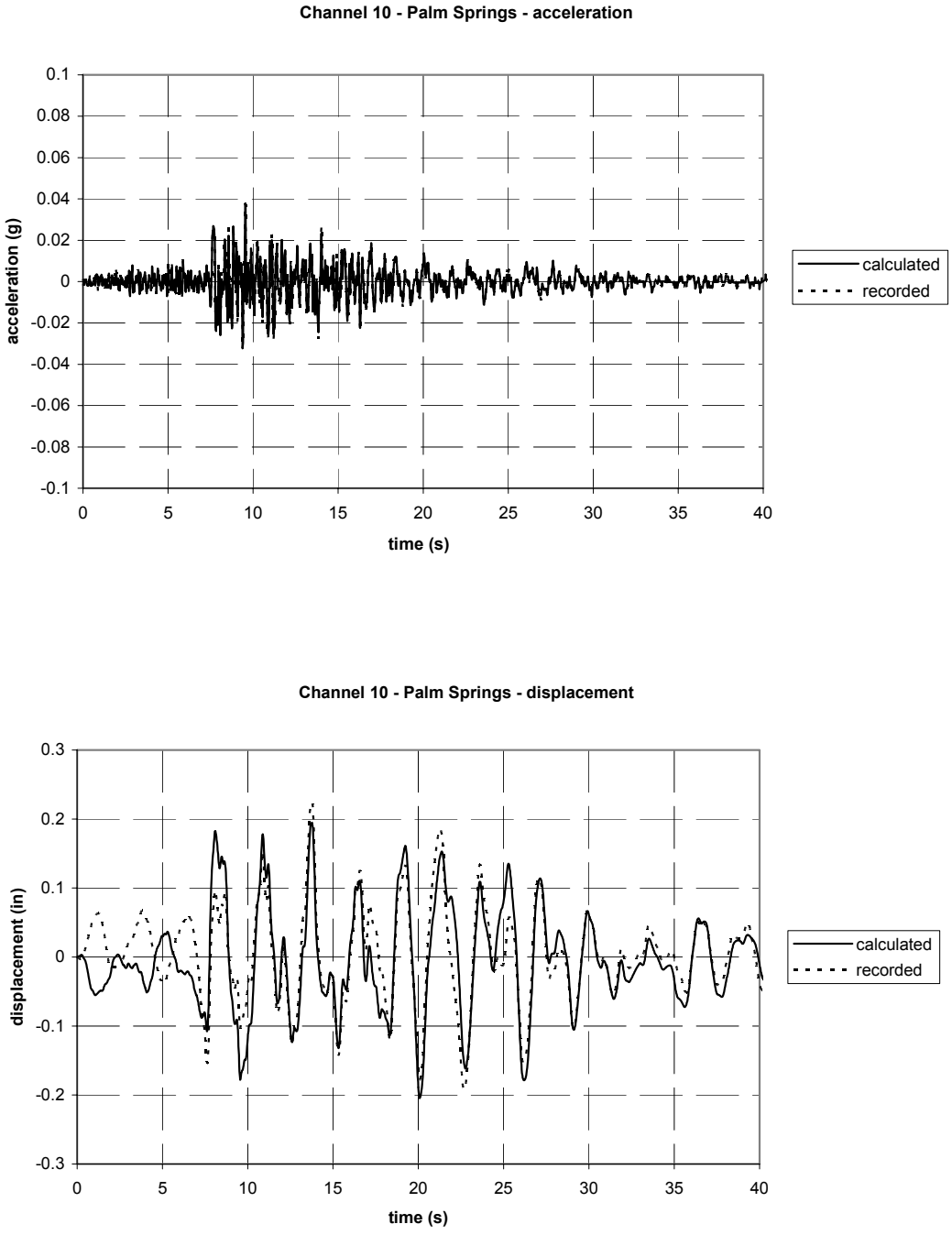

Fig. 6.9 Response comparisons, ch. 10, Palm Springs

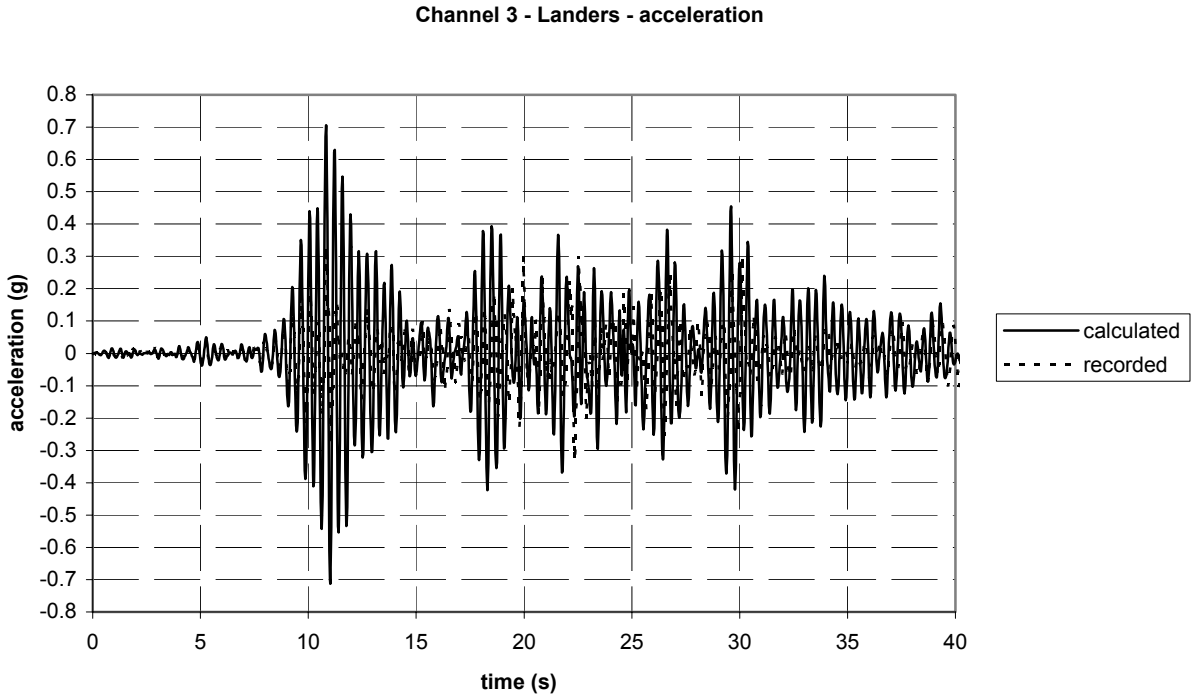

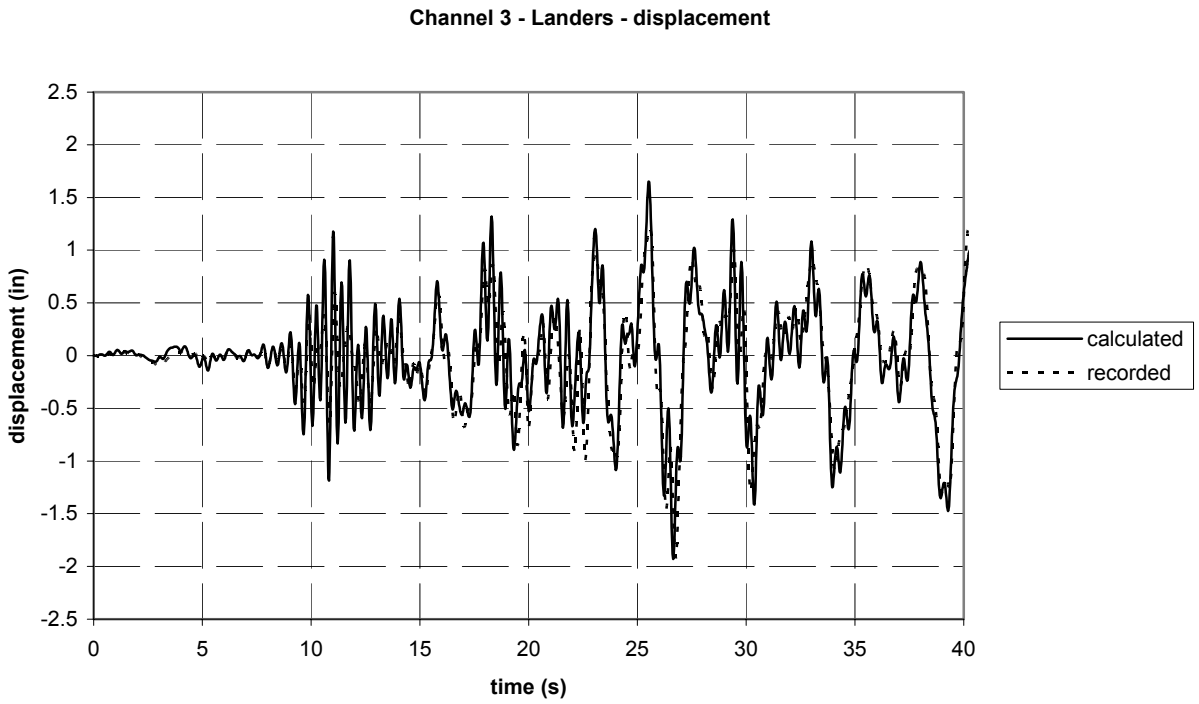

Fig. 6.10 Response comparisons, ch. 3, Landers

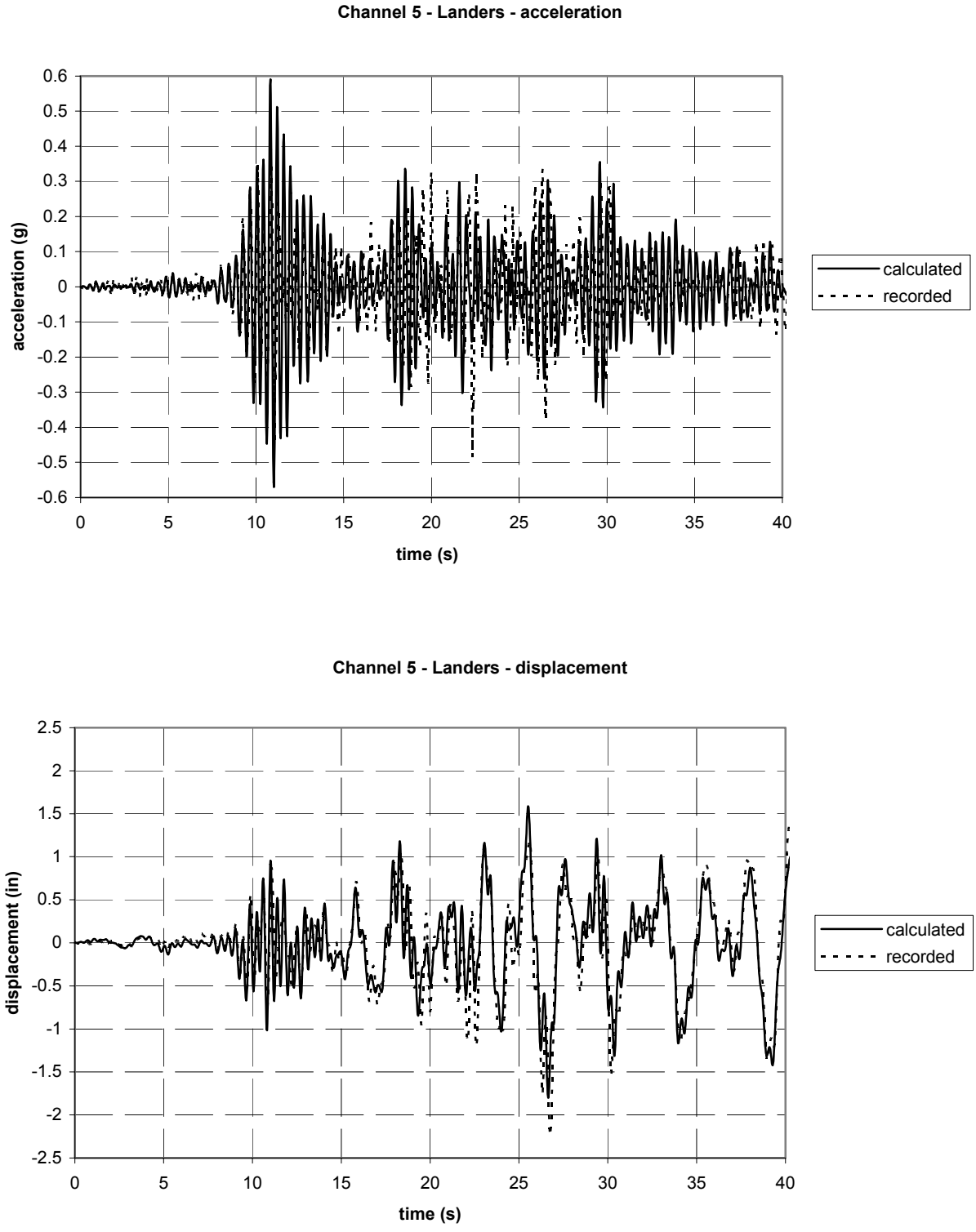

Fig. 6.11 Response comparisons, ch. 5, Landers

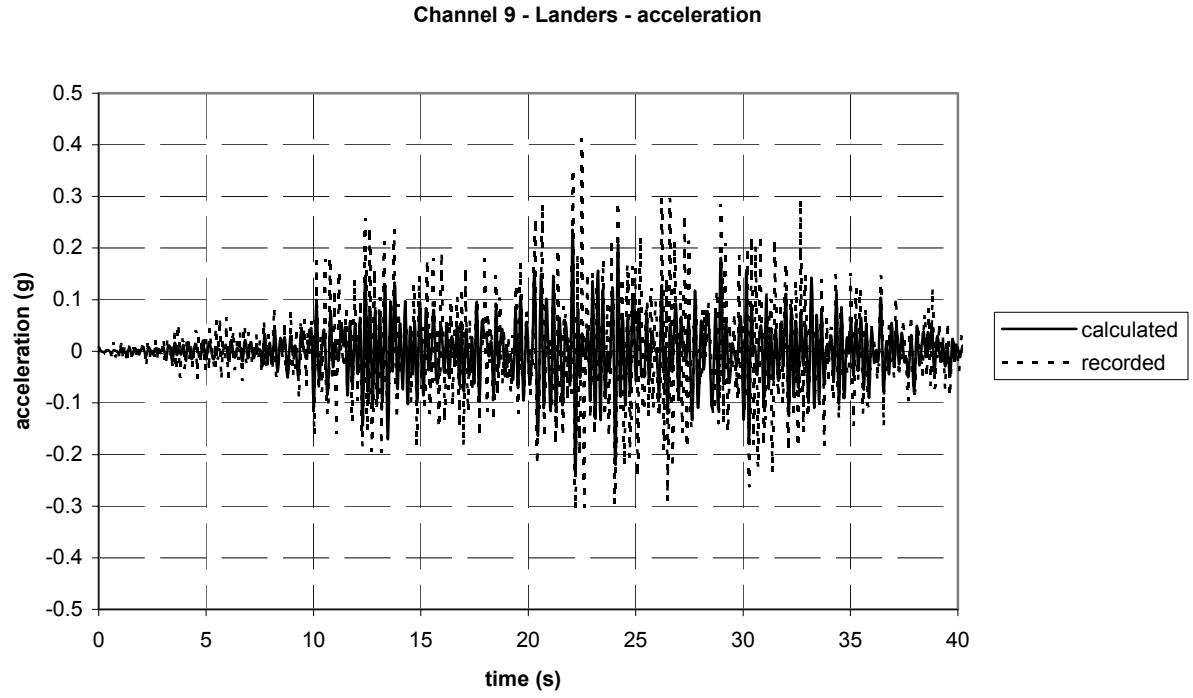

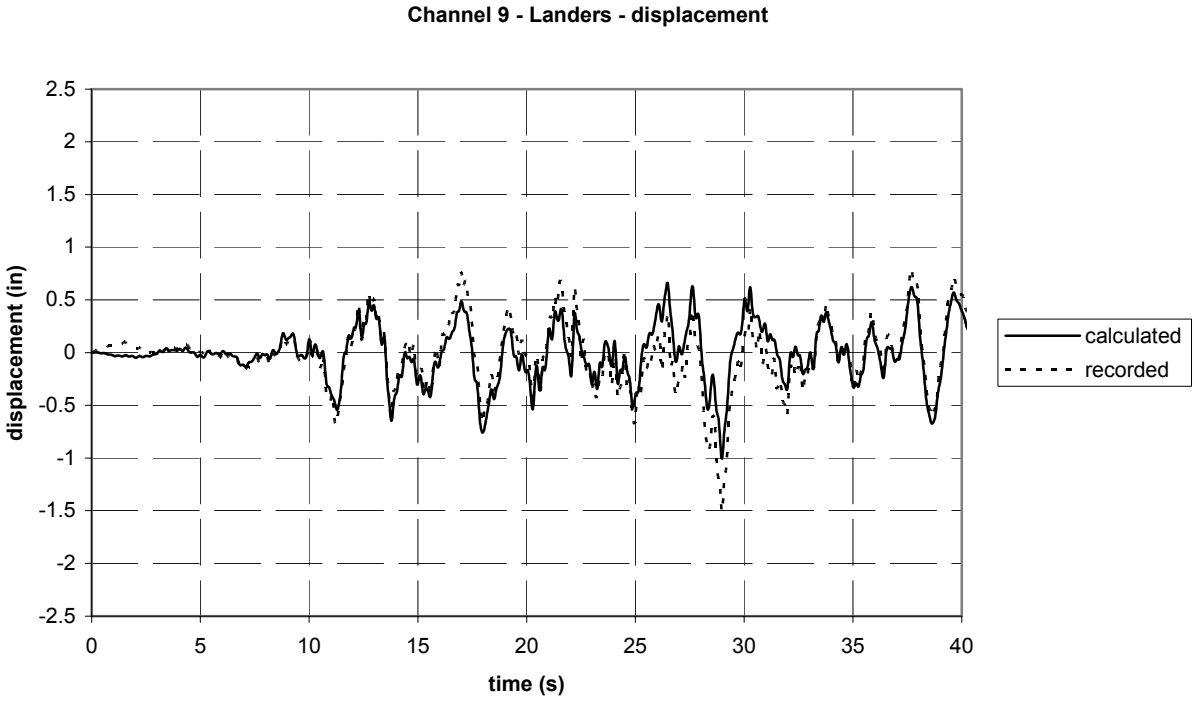

Fig. 6.12 Response comparisons, ch. 9, Landers

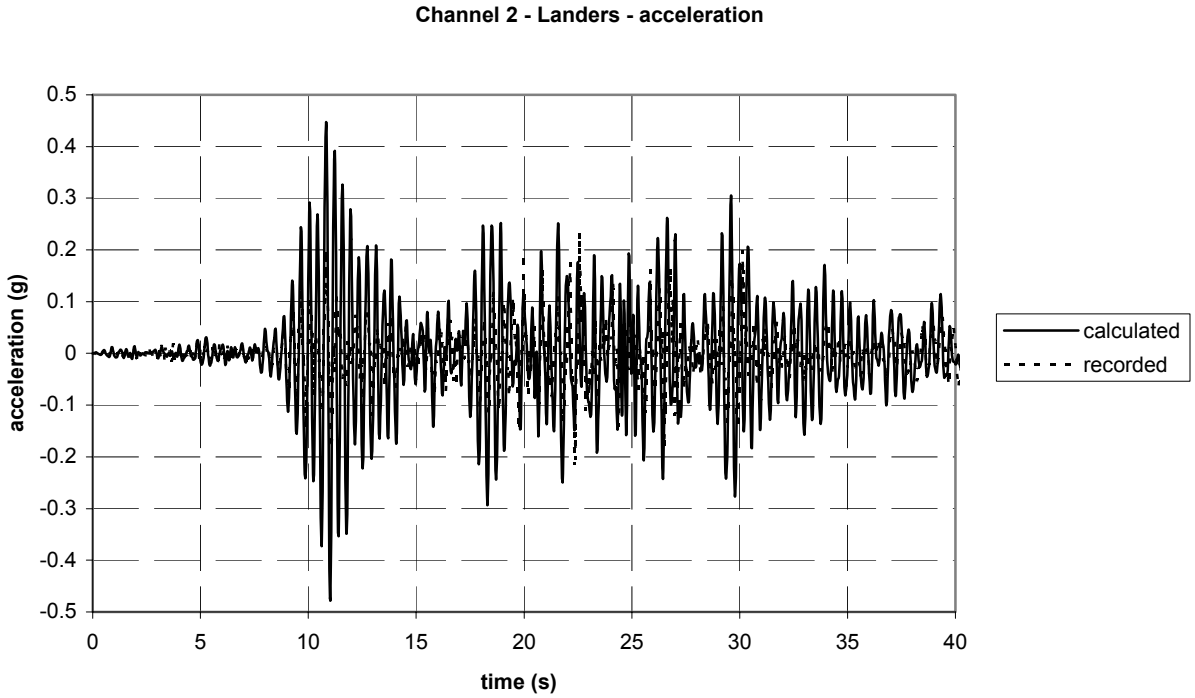

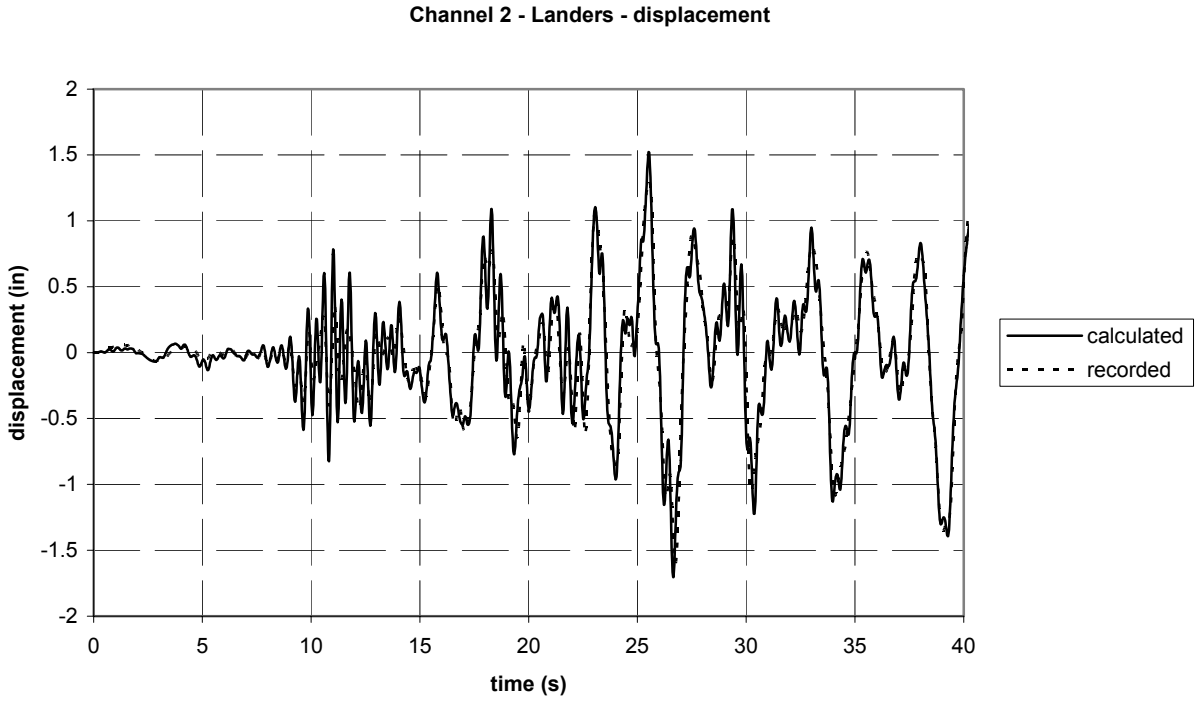

Fig. 6.13 Response comparisons, ch. 2, Landers

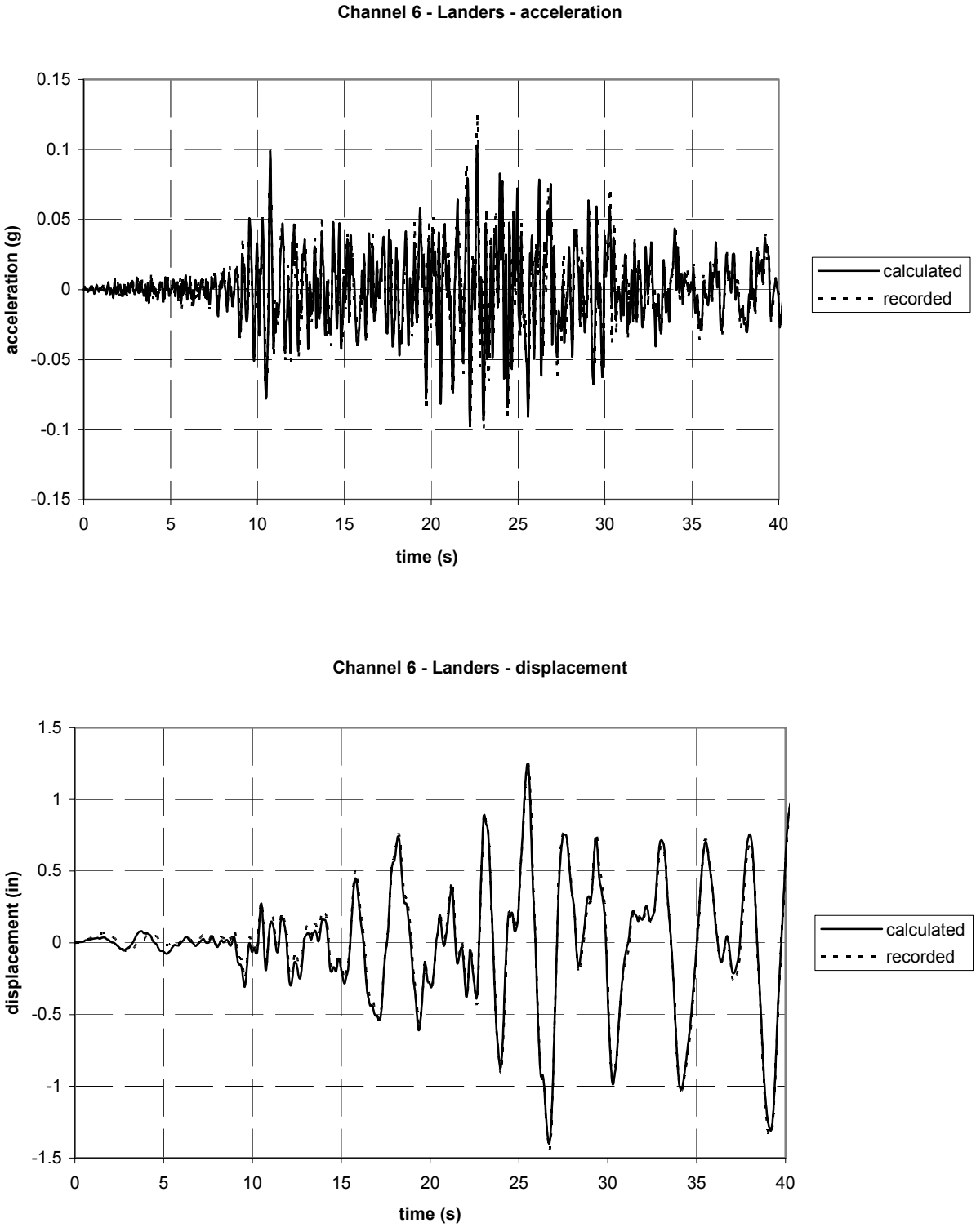

Fig. 6.14 Response comparisons, ch. 6, Landers

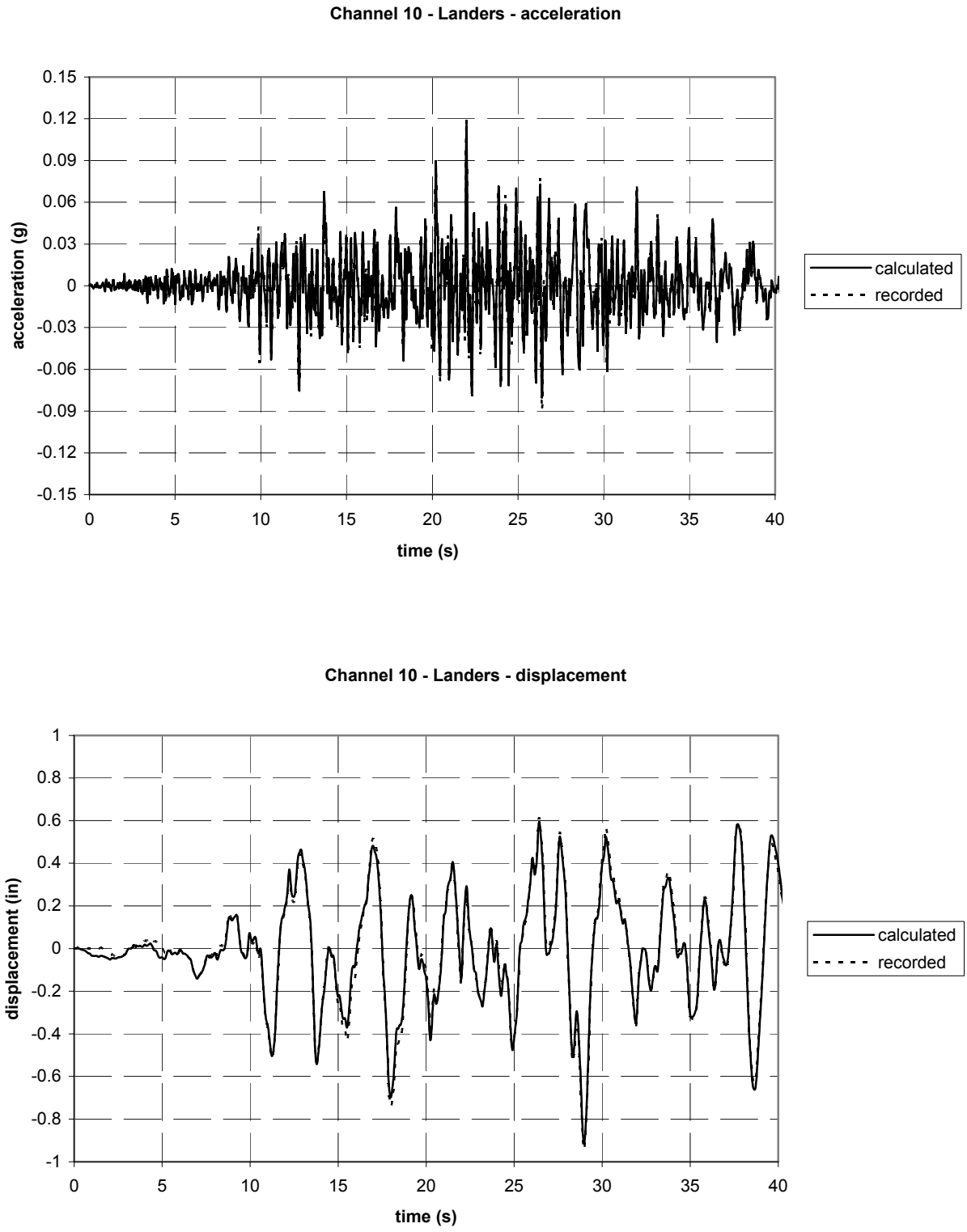

Fig. 6.15 Response comparisons, ch. 10, Landers

Time histories of the recorded accelerations and corresponding displacements for the Big Bear earthquake are compared with the matching calculated values in Figures 6.16–6.21. The out-of-plane acceleration data for channel 2, located at midheight of the west wall, are shown in Figure 6.16a. Here it can be seen that the calculated peak acceleration reaches a value of 0.51g at 14 seconds. However, the peak acceleration measured at this location was only 0.38g (Table 3.1). The maximum calculated displacement was 1.4 inches (Fig. 6.16b) compared with a recorded value of 1.0 inches. Channel 3 is located at the top of the west wall and recorded a peak out-of-plane acceleration of 0.62g compared with a calculated value of 0.77g as shown in Fig. 6.17a. The maximum displacement based on the recorded acceleration is 1.25 inches compared with a calculated value of 1.8 inches (Fig. 6.17b). Recall that these two instruments were located on the tilt-up wall adjacent to the bearing stud partition (fire wall) that was not included in the analytical model. Interaction between these two walls may have influenced the comparison of peak values at these two locations.

Time histories for channel 5, located at the roof level midway between the fire wall and the south wall are shown in Figure 6.18. The out-of-plane acceleration time history (Fig. 6.18a) indicates a calculated peak acceleration of 0.60g, which is the same as the peak recorded value of 0.60g (Table 3.1). The calculated displacement time history (Fig. 6.18b) indicates a peak displacement of 1.55 inches, whereas the peak recorded displacement is 1.56 inches. Channel 6 is located at the roof level in the middle of the south wall. The calculated in-plane acceleration at this location is shown in Figure 6.19a and indicates a peak value of 0.17g compared with a recorded value of 0.17g. The calculated peak displacement (Fig. 6.19b) is 0.80 inches compared with 0.78 inches recorded. Channel 9 measures out-of-plane acceleration at the roof level at the midpoint of the south wall. The calculated peak acceleration, shown in Figure 6.20a, is 0.21g compared with 0.44g recorded. The calculated peak displacement of 1.50 inches (Fig. 6.20b), is close to the 1.51 inches recorded (Table 3.1). In-plane accelerations at the roof level of the west wall are obtained from channel 10. The peak calculated acceleration of 0.13g, shown in Figure 6.21a, is equal to that recorded. The peak calculated displacement (Fig. 6.21b) is 1.30 inches compared with the recorded value of 1.28 inches. It is concluded that the response comparisons are well within acceptable limits.

The recorded and calculated accelerations and displacements for the Northridge earthquake records are presented and compared in Figures 6.22–6.27. These results are not

significantly different from those discussed for the previous two earthquake records and therefore will not be discussed here.

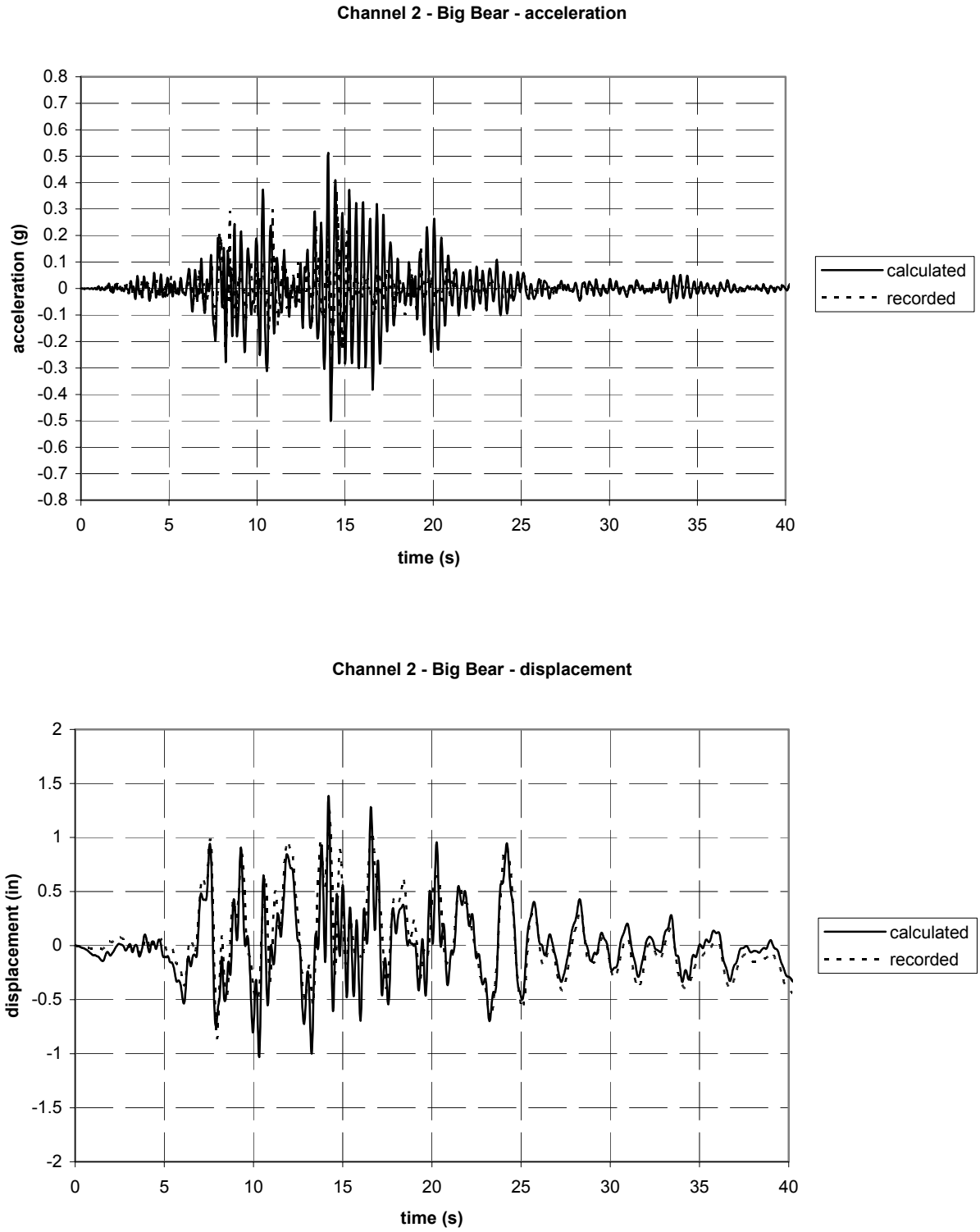

Fig. 6.16 Response comparisons, ch. 2, Big Bear

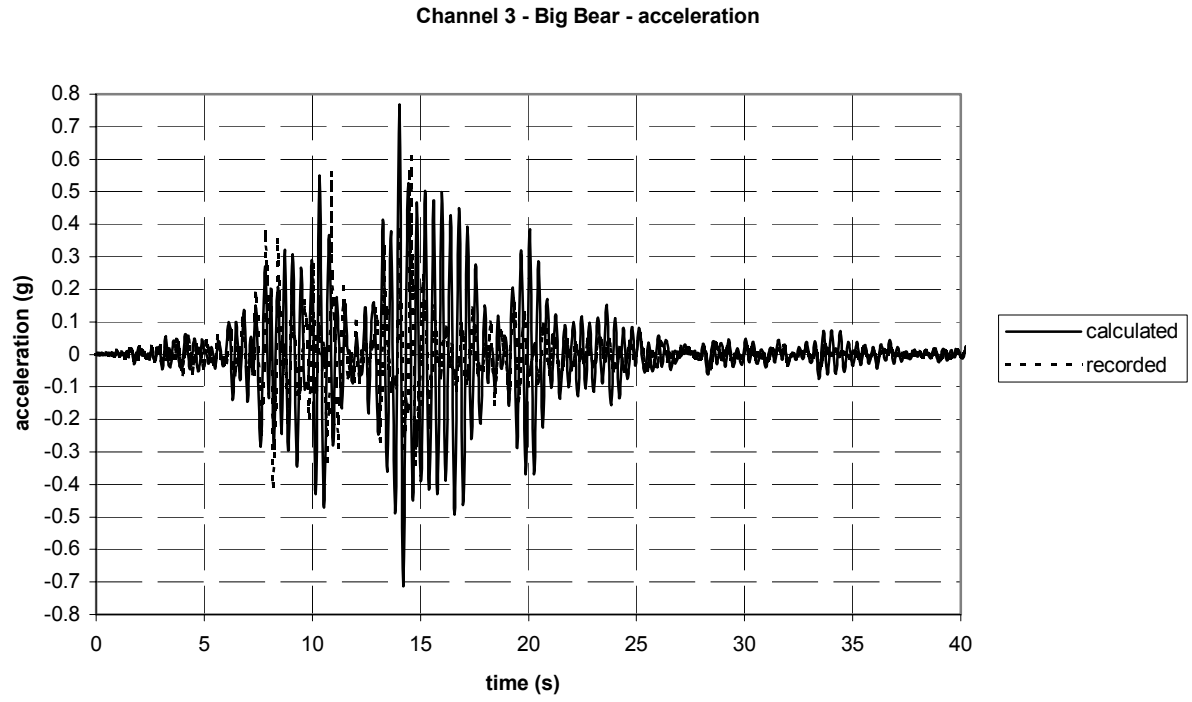

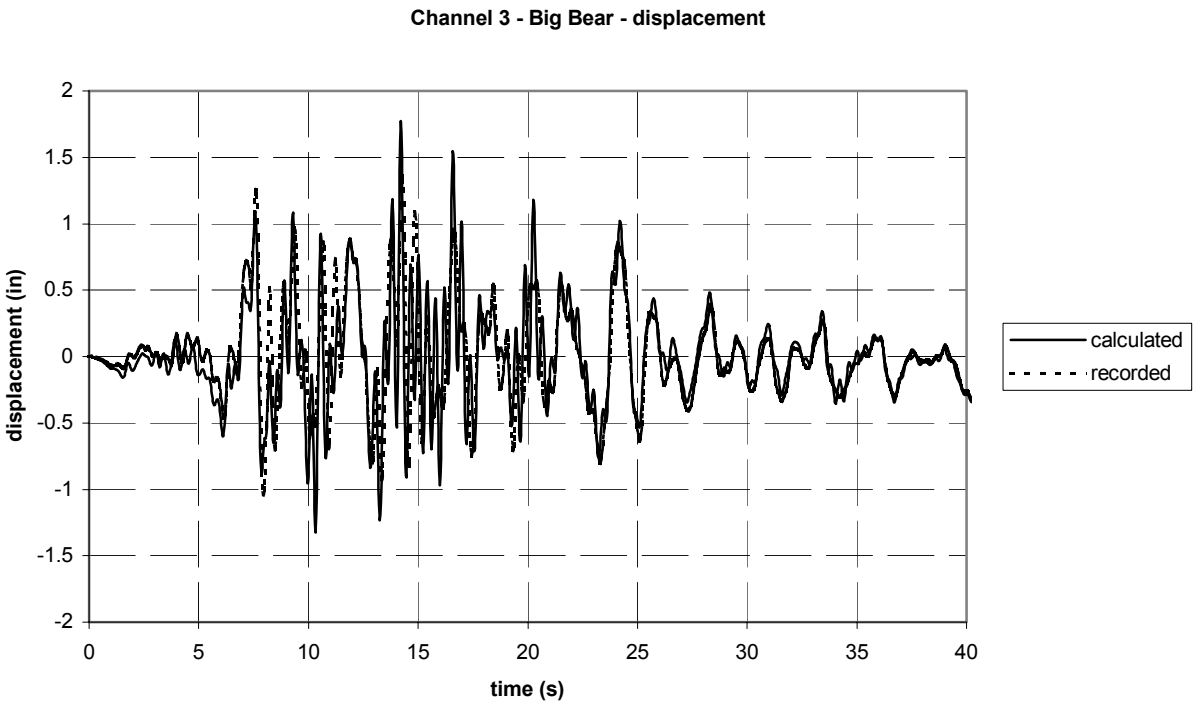

Fig. 6.17 Response comparisons, ch. 3, Big Bear

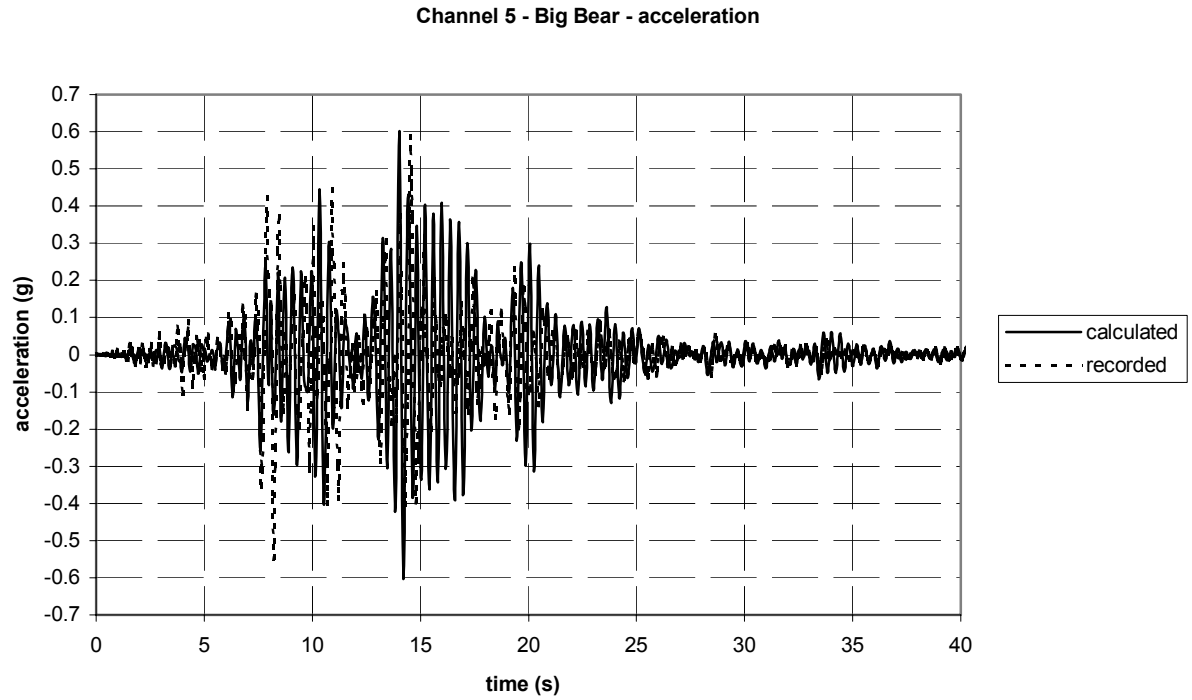

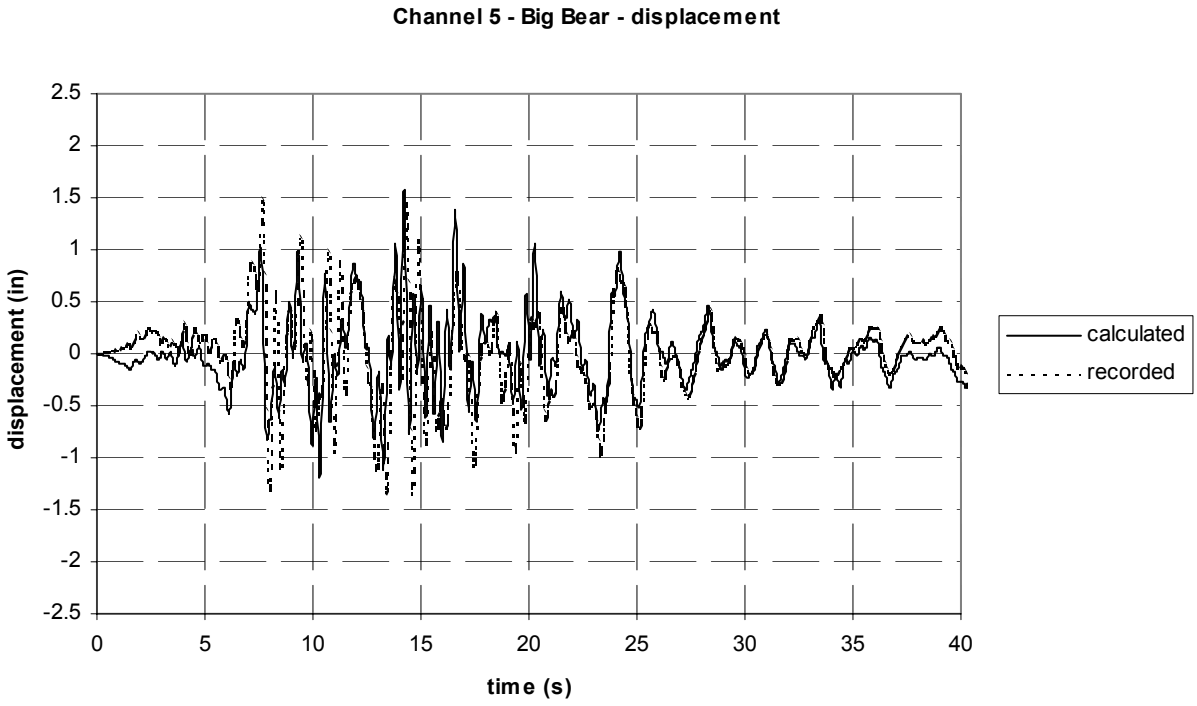

Fig. 6.18 Response comparisons, ch. 5, Big Bear

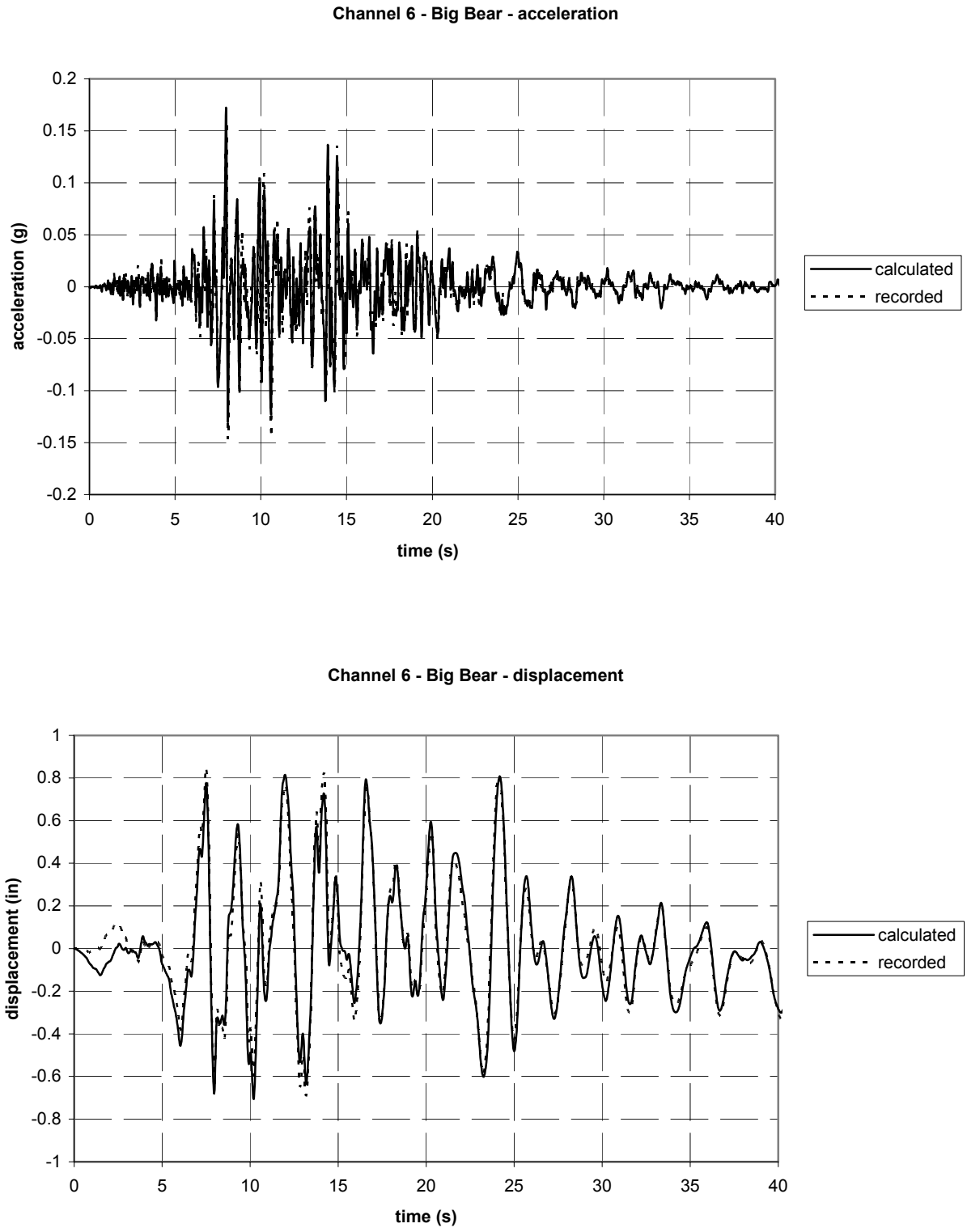

Fig. 6.19 Response comparisons, ch. 6, Big Bear

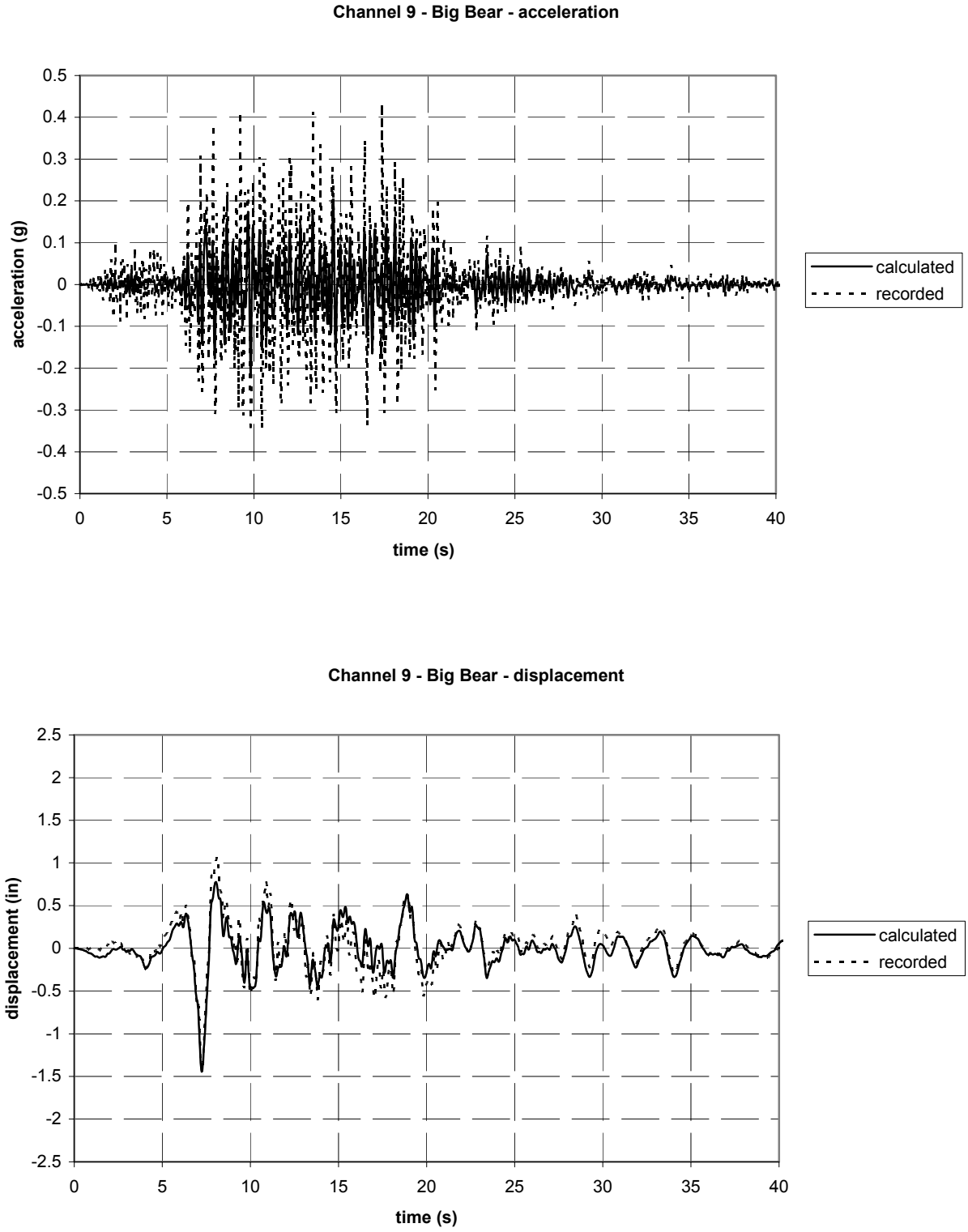

Fig. 6.20 Response comparisons, ch. 9, Big Bear

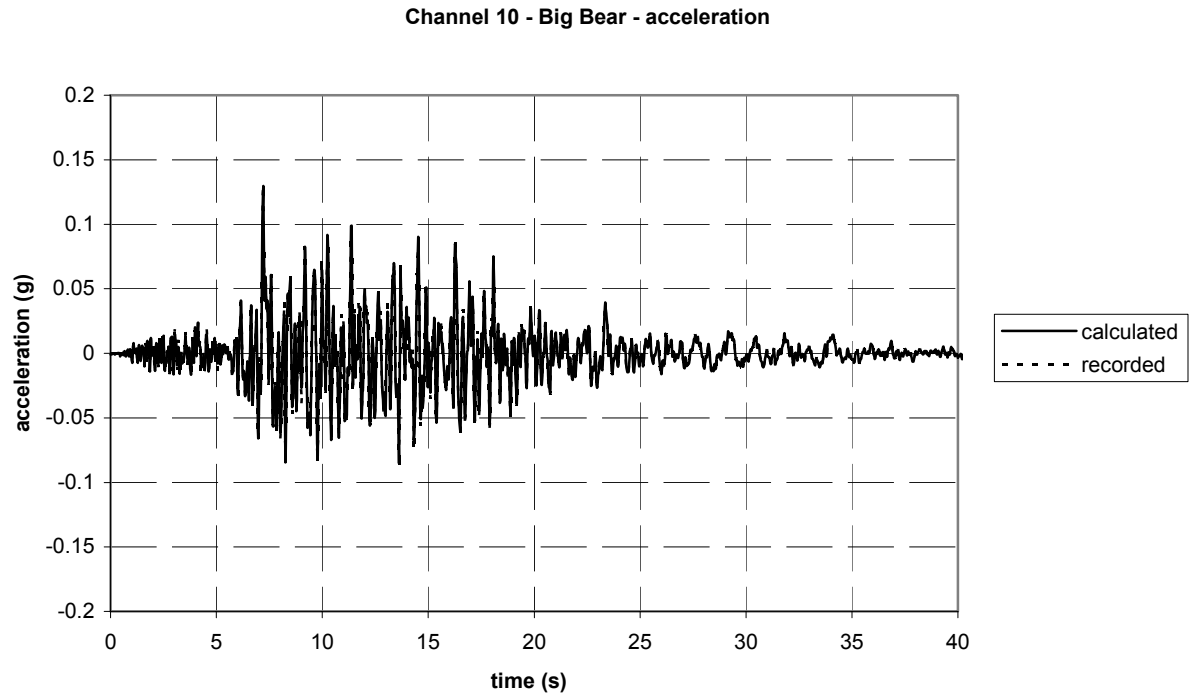

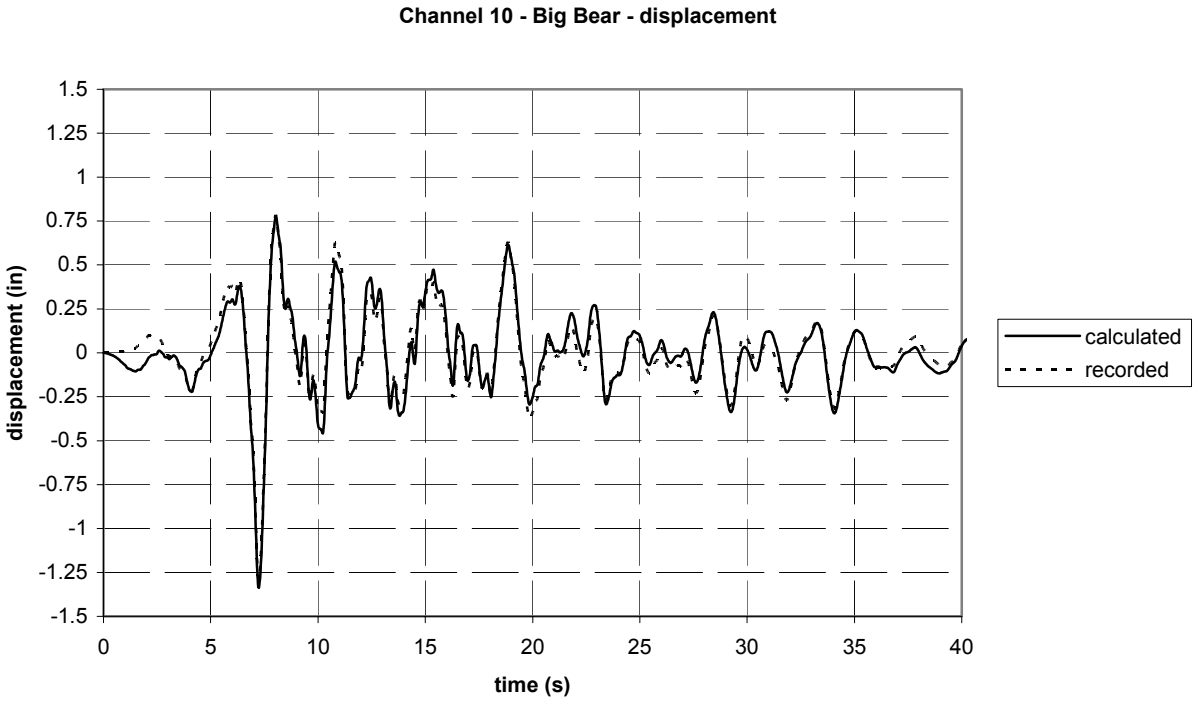

Fig. 6.21 Response comparisons, ch. 10, Big Bear

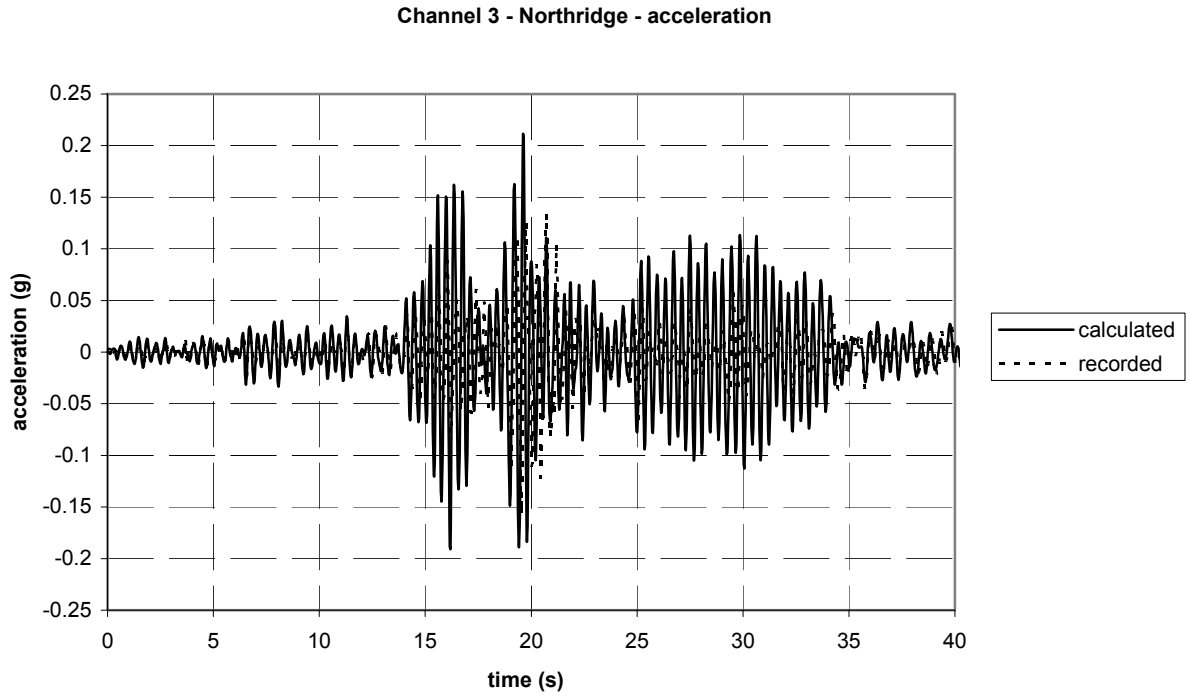

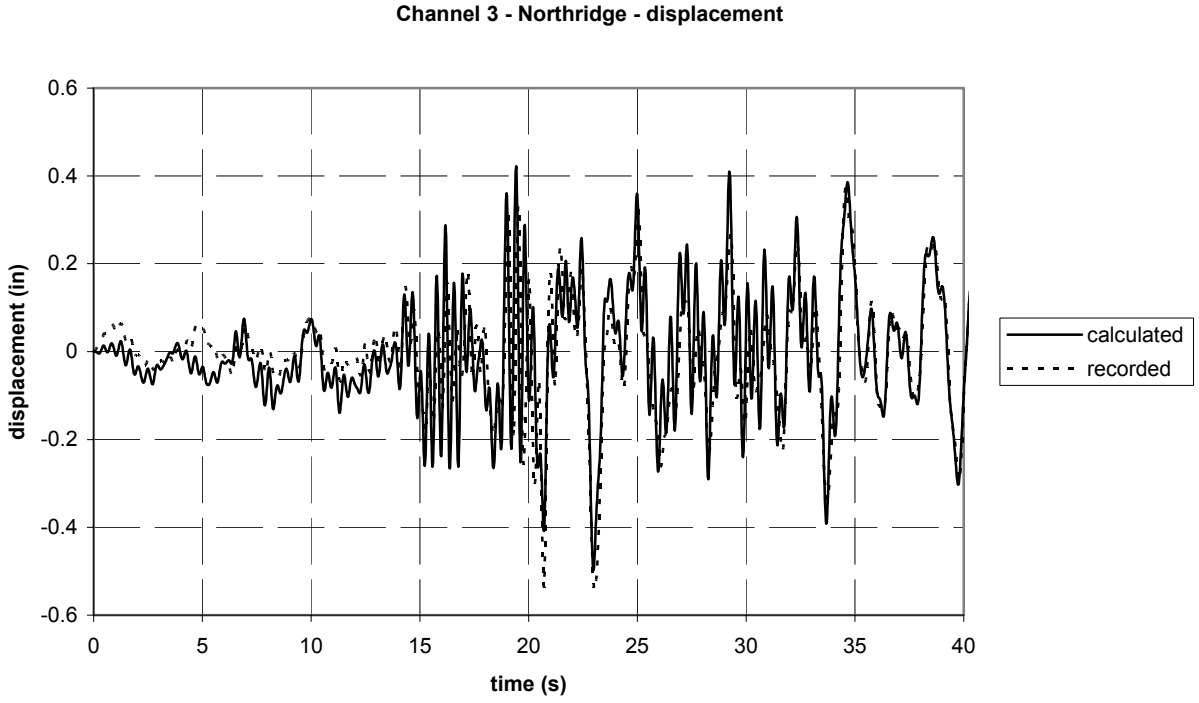

Fig. 6.22 Response comparisons, ch. 3, Northridge

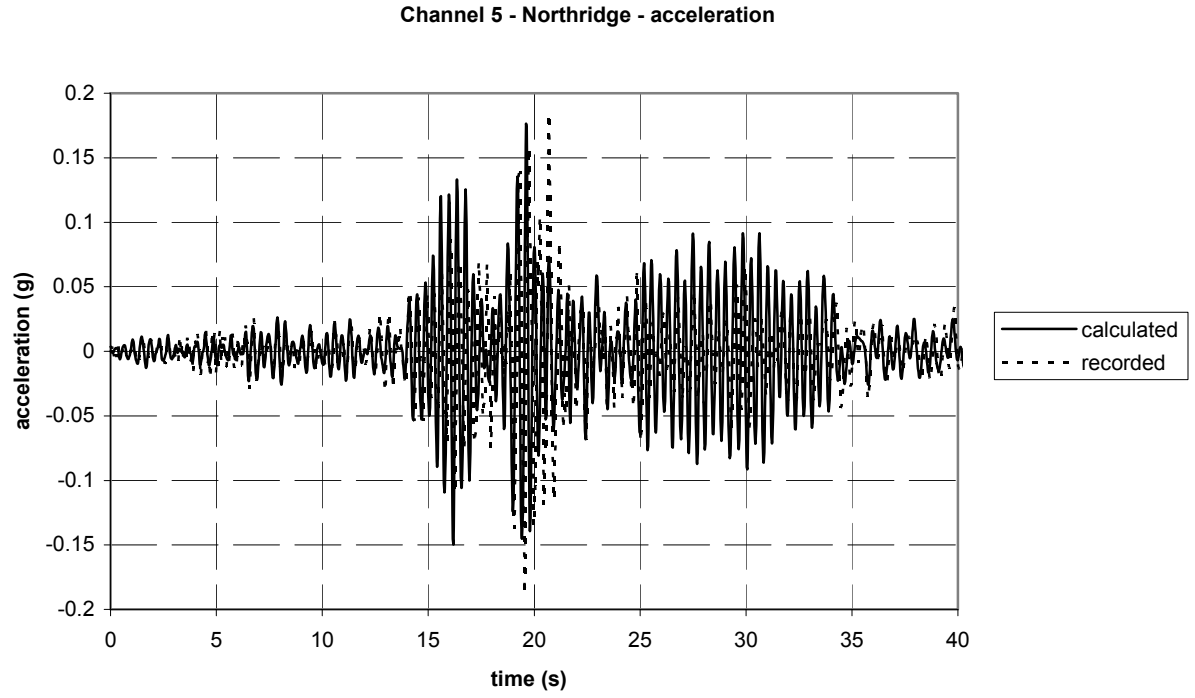

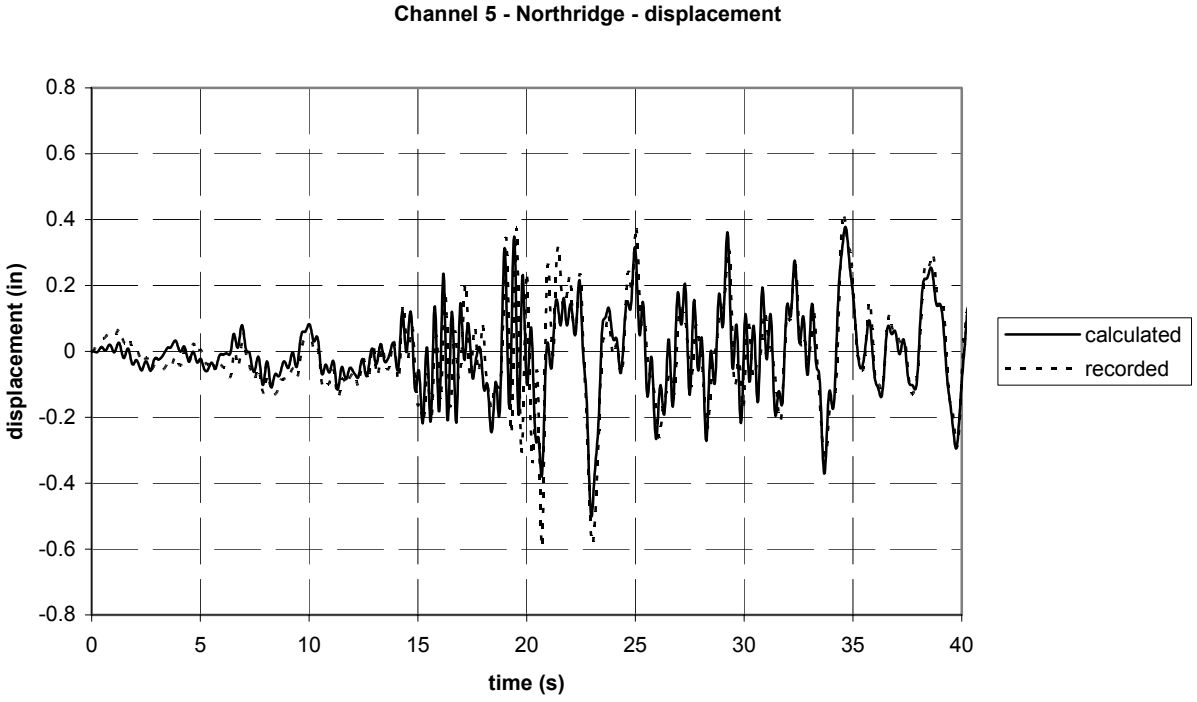

Fig. 6.23 Response comparisons, ch. 5, Northridge

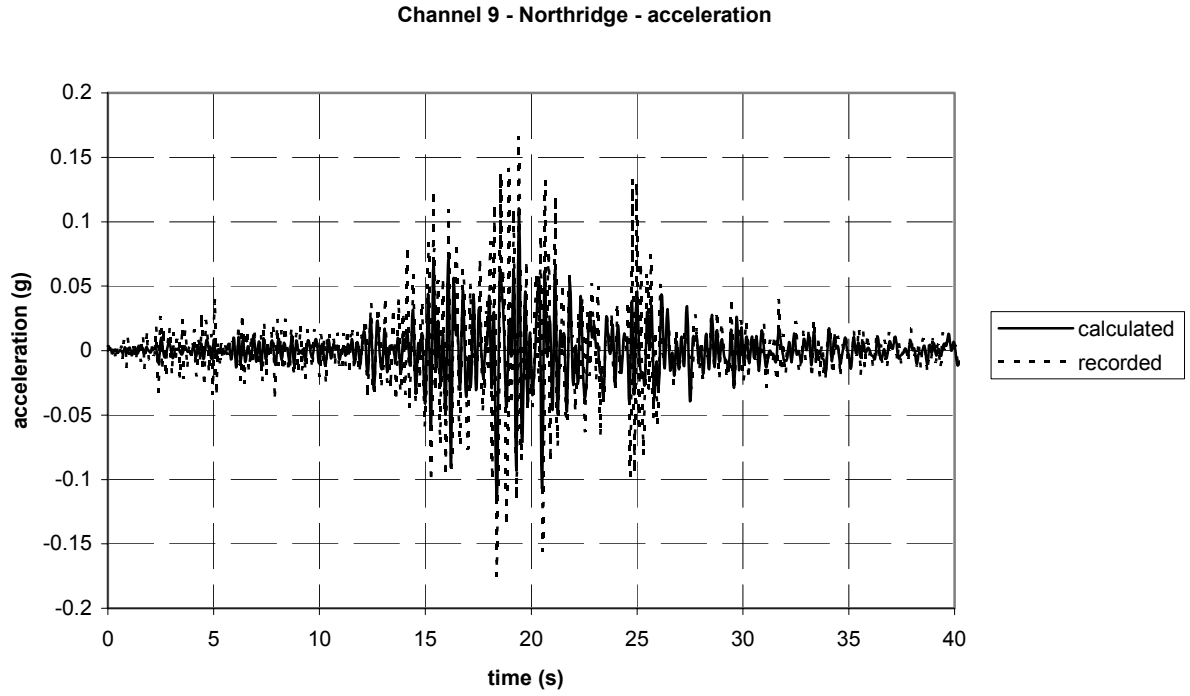

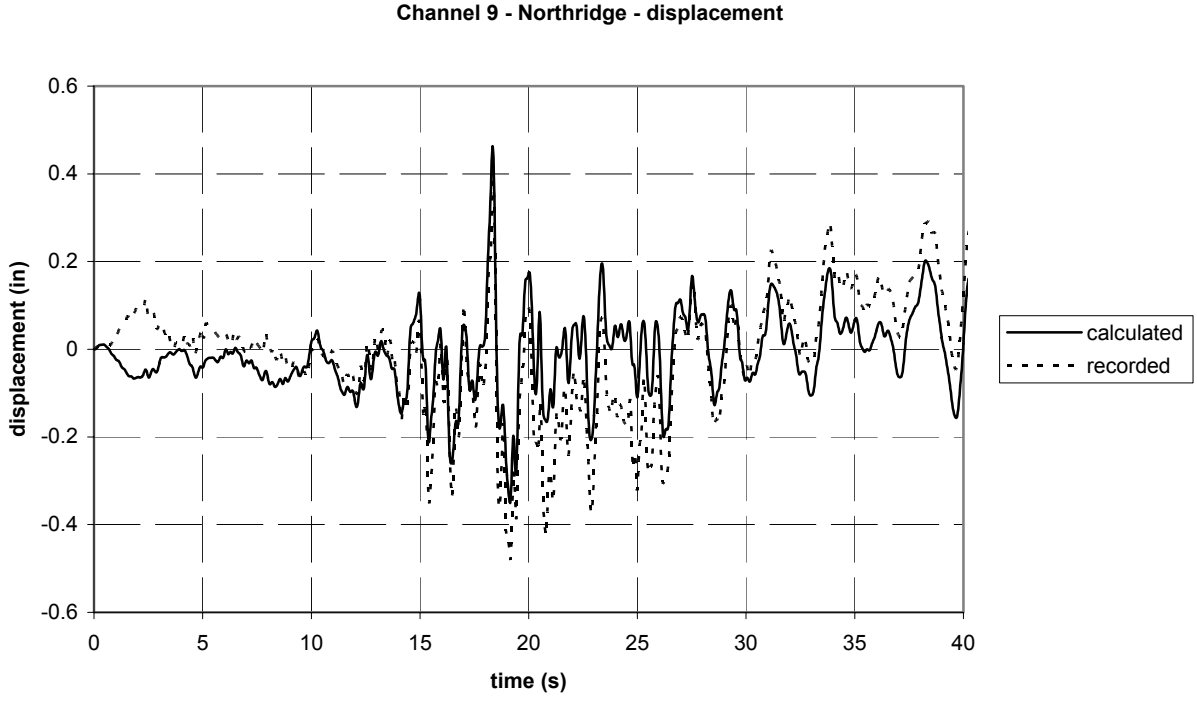

Fig. 6.24 Response comparisons, ch. 9, Northridge

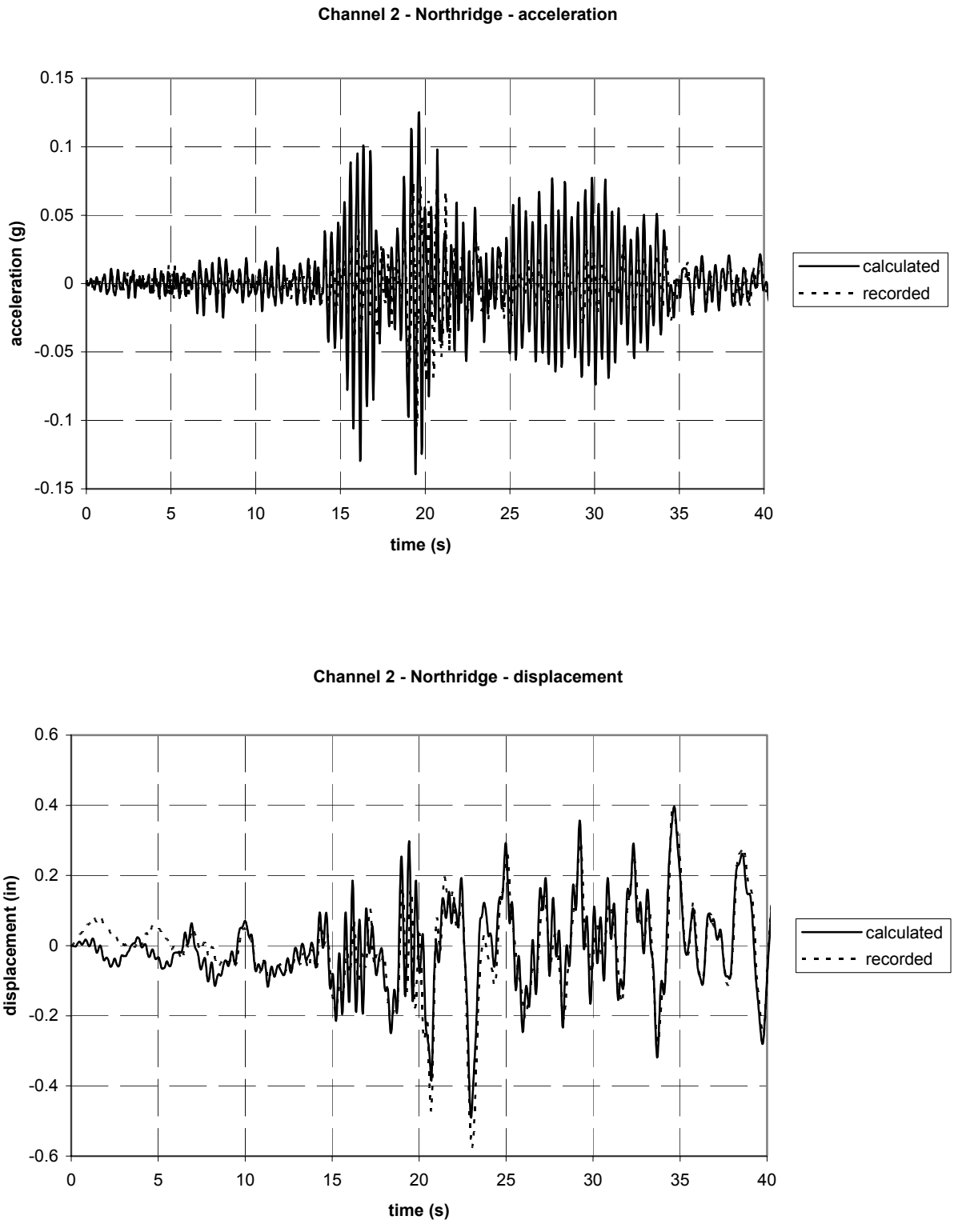

Fig. 6.25 Response comparisons, ch. 2, Northridge

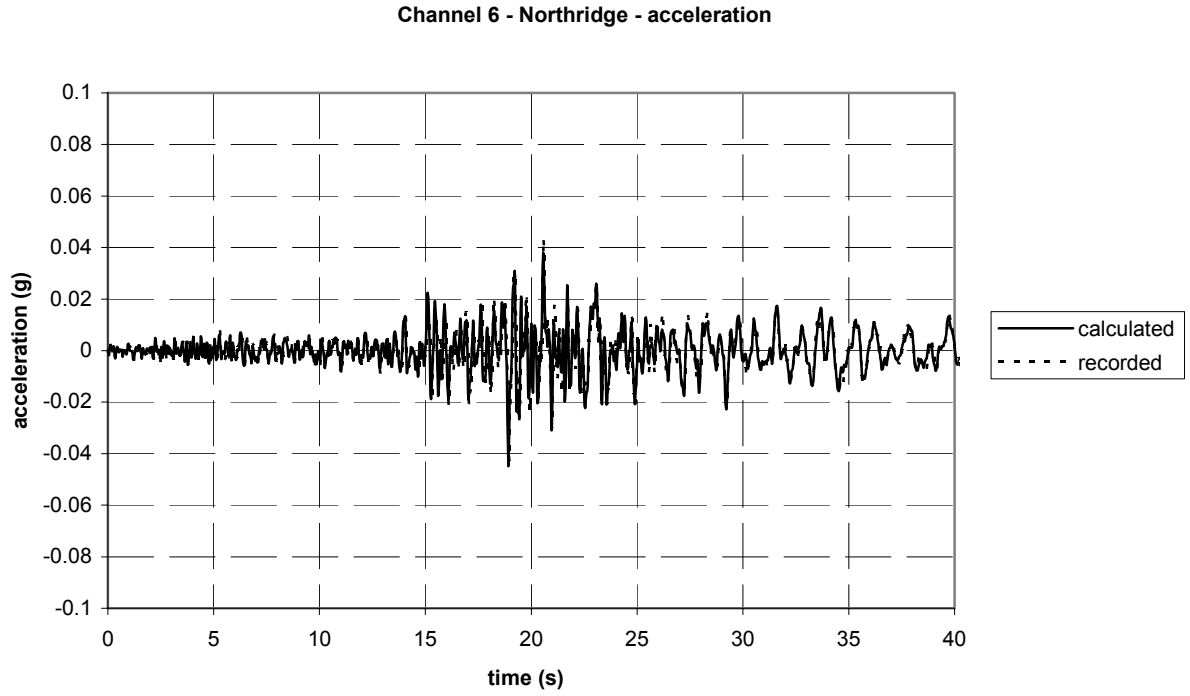

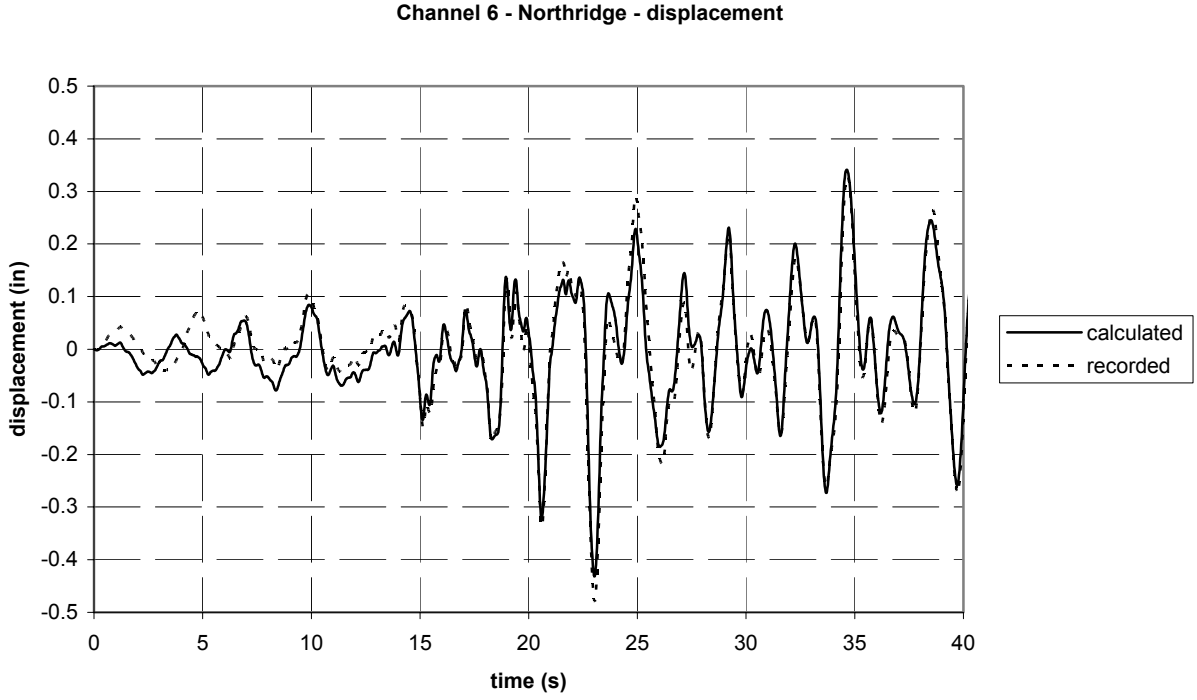

Fig. 6.26 Response comparisons, ch. 6, Northridge

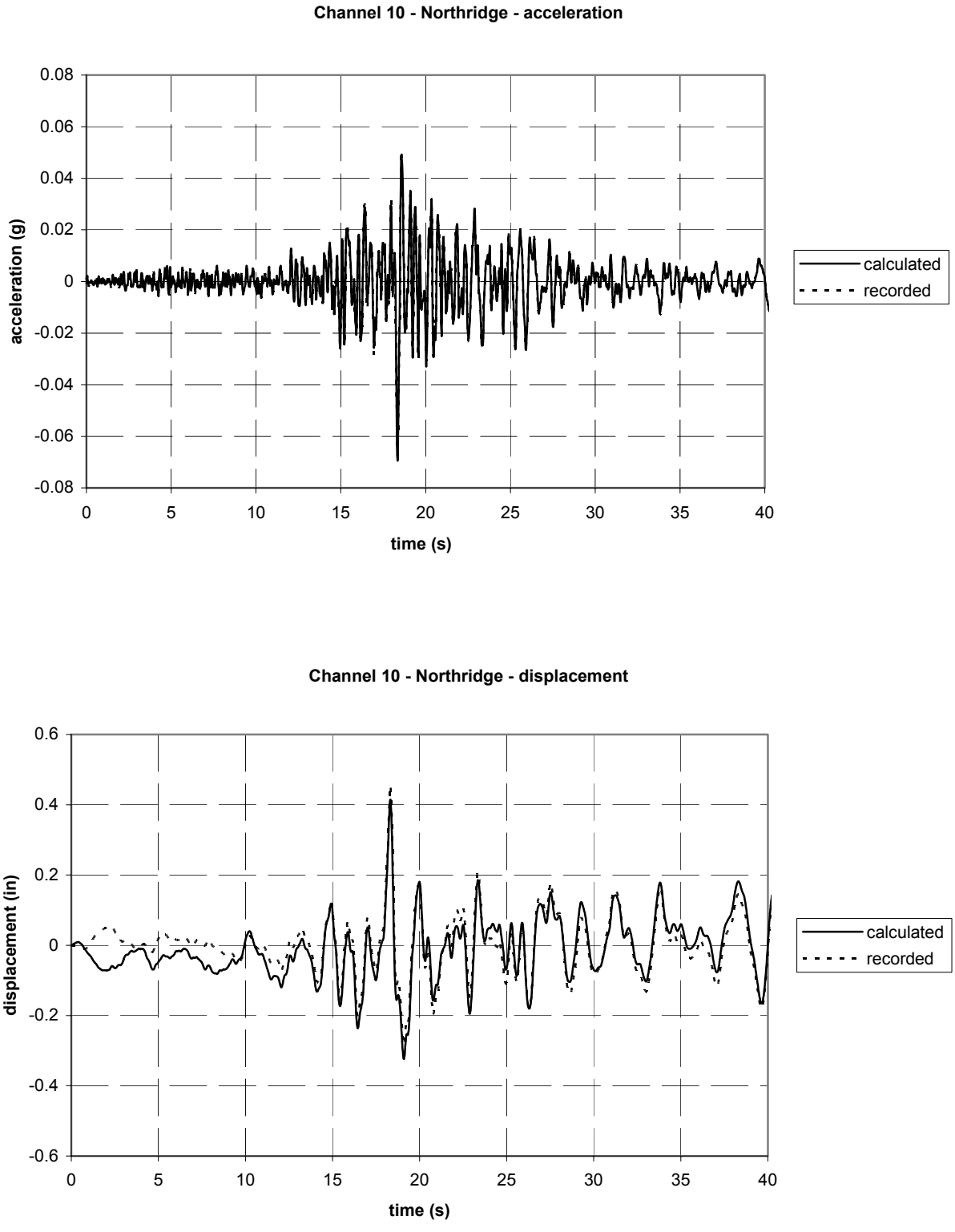

Fig. 6.27 Response comparisons, ch. 10, Northridge

6.1.3 Base Shear Demand versus Design Base Shear

The base shears developed by the recorded base motions of the four earthquakes are compared to the base shear design requirement of the 1997 UBC in Figures 6.28–6.31. Calculations for the code base shear are given in Appendix B. The base shear demand for the Palm Springs earthquake in the transverse (E-W) direction is compared to the code requirement in Figure 6.28a. It can be seen that the peak demand of 175 kips is well below the design capacity of 247 kips. In the longitudinal (N-S) direction (Fig. 6.28b), the demand is only 25 kips compared to the code design capacity of 247 kips.

For the Landers earthquake, the calculated base shear in the transverse (E-W) direction, shown in Figure 6.29a, reaches a maximum value of 450 kips and exceeds the code value of 247 kips on six excursions. Due to the limited number of excursions above the code value, any predicted damage to the structure will be limited and may not occur due to the inherent over-strength of the building. The maximum base shear in the longitudinal direction (N-S) (Fig. 6.29b) reaches 70 kips. which is much less than the minimum design requirement.

The time history of the calculated base shear for the Big Bear earthquake is shown in Figure 6.30. In the transverse direction (Fig. 6.30a), the calculated base shear reaches a maximum of 470 kips and exceeds the code requirement of 247 kips on nine excursions. This behavior implies that the effect of this earthquake is slightly greater than that of the Landers earthquake. As before, any damage to the building will be limited. In the longitudinal direction, the maximum base shear just exceeds 60 kips, as can be seen in Figure 6.30b.

The calculated time history of the base shear for the Northridge earthquake is shown in Figure 6.31. The base shear calculated in the transverse direction (Fig. 6.31a) reaches a maximum value of 120 kips on only one excursion. This response is similar to that discussed for the Palm Springs earthquake and implies that the behavior for this ground motion is primarily linear elastic. In the longitudinal direction (Fig. 6.31b), the maximum base shear reaches 40 kips, which is well below the code value.

It should be noted that in calculating the base shear, the acceleration is multiplied by the modal participation factor for the mass of the structure. For this structure, the results presented in Table 6.1 indicate that the mass participation in the transverse direction is three times that of the longitudinal direction. The effect of this difference is not currently considered in the static equivalent lateral load procedure commonly used for the design of these structures.

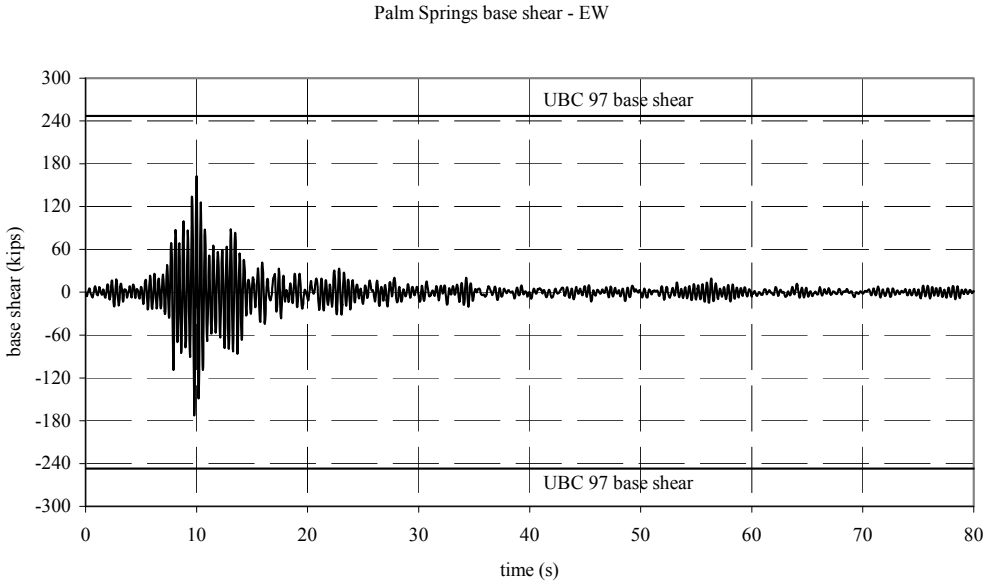

(a) E-W base shear

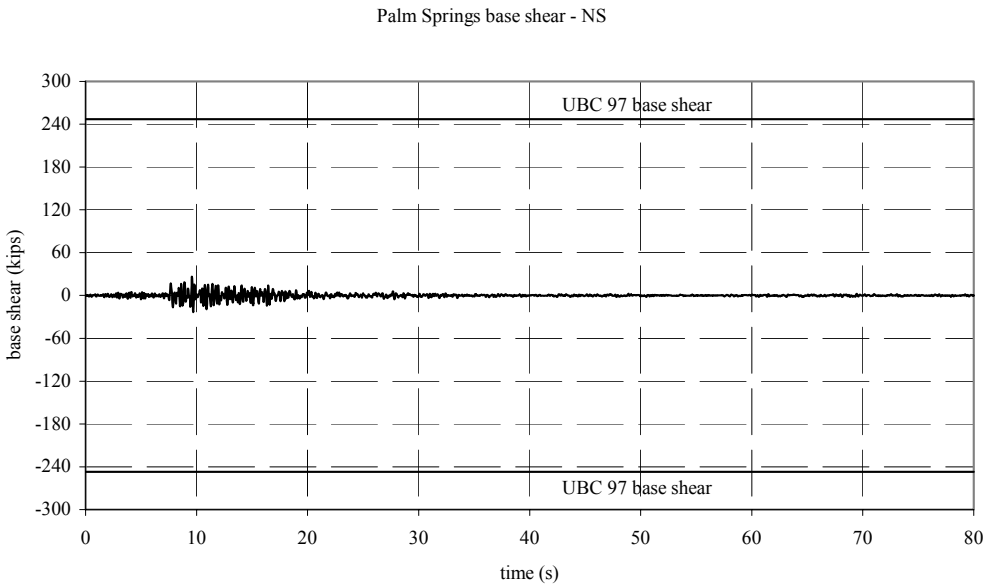

(b) N-S base shear

Fig. 6.28 Base shear, Palm Springs

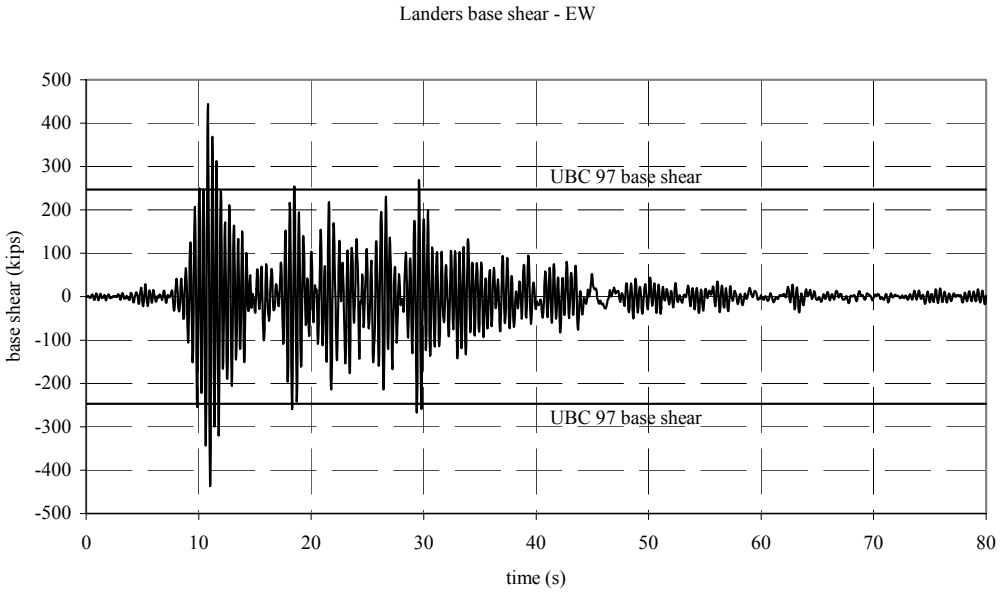

(a) base shear (E-W)

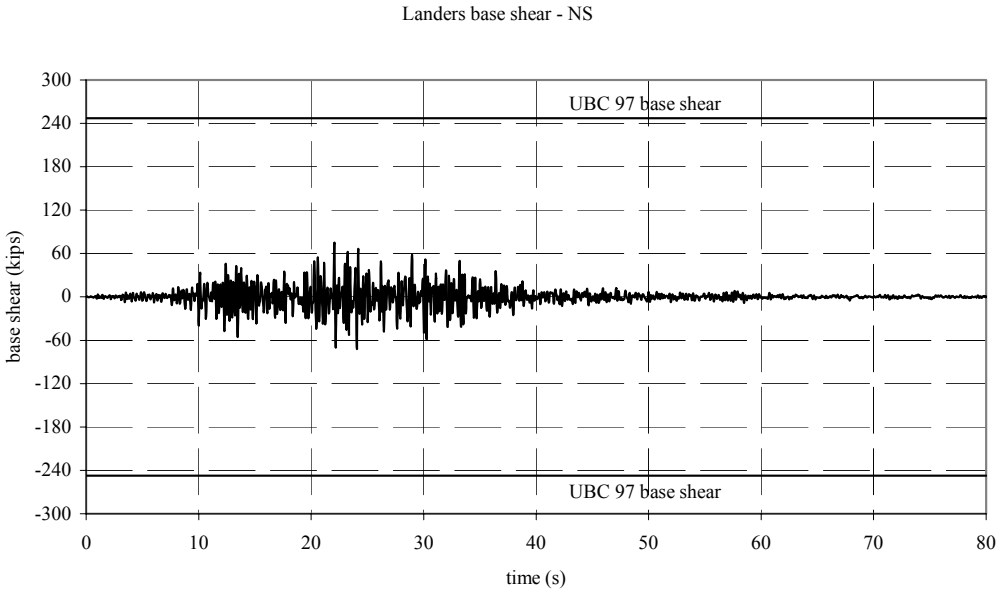

(b) base shear (N-S)

Fig. 6.29 Base shear, Landers

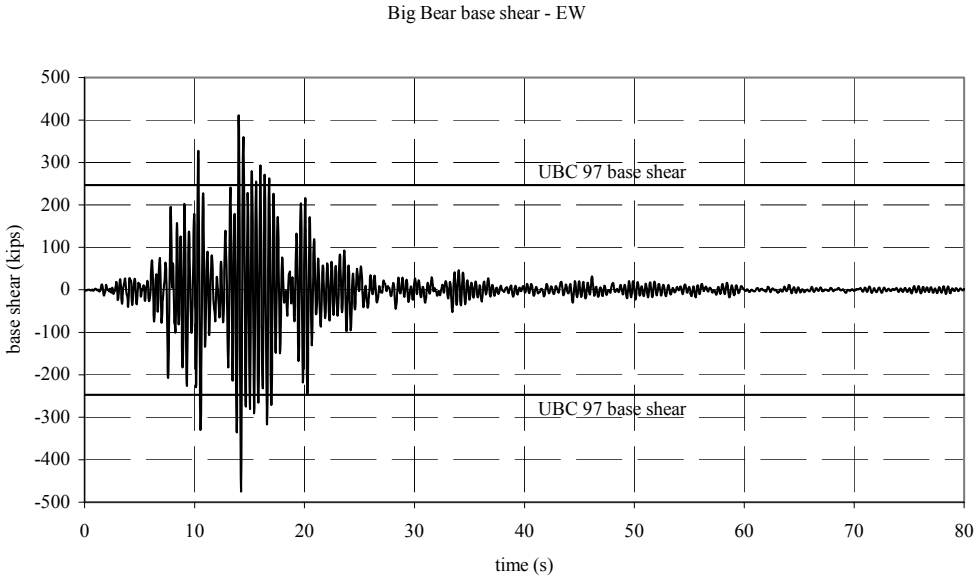

(a) base shear (E-W)

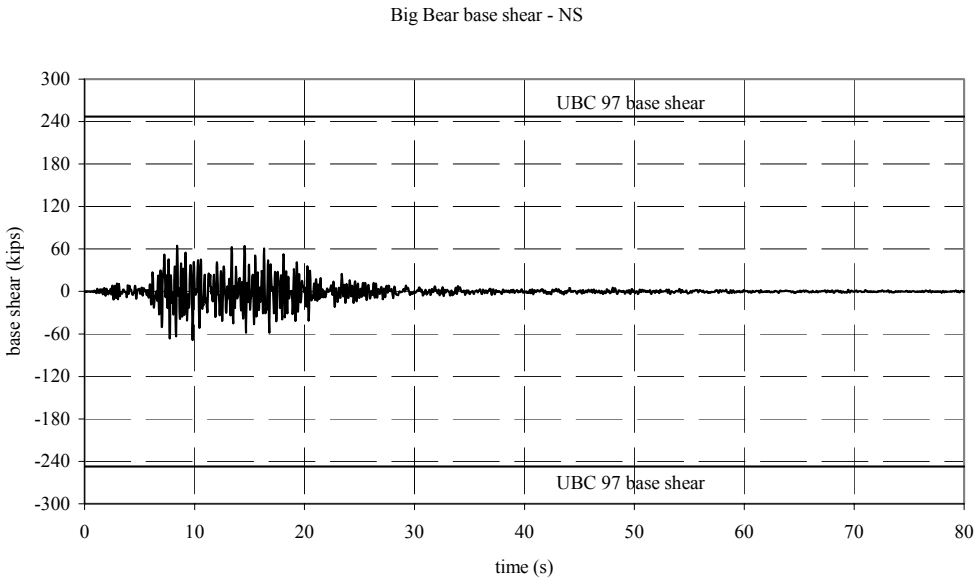

(b) base shear (N-S)

Fig. 6.30 Base shear, Big Bear

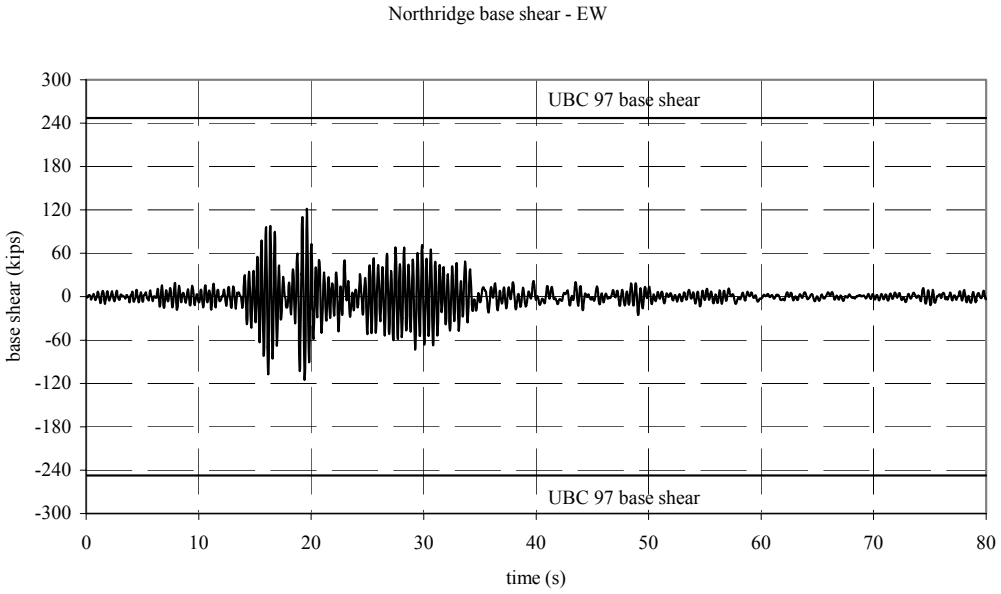

(a) base shear (E-W)

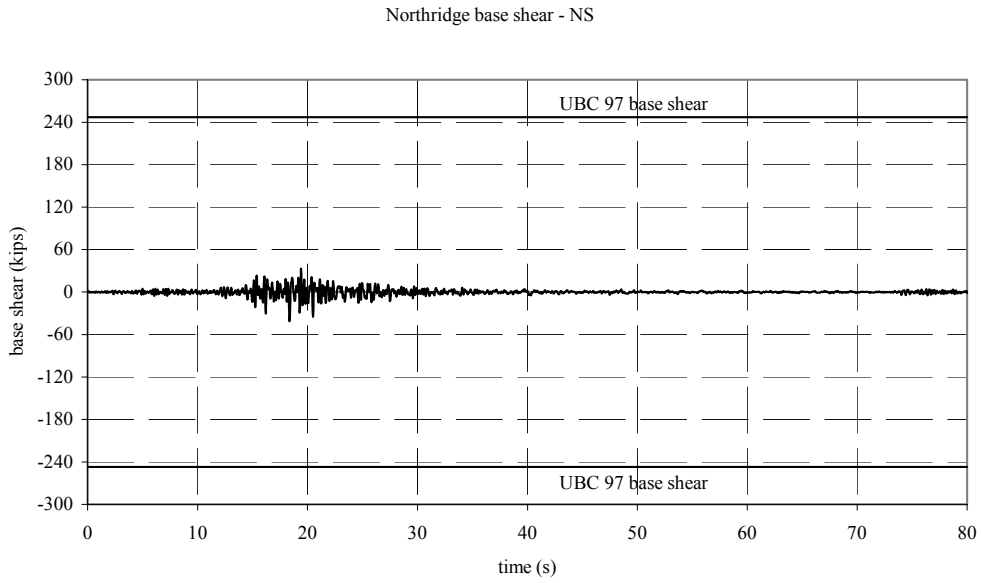

(b) base shear (N-S)

Fig. 6.31 Base shear, Northridge

6.1.4 Force Contours

Force contours for in-plane shear force and vertical out-of-plane moment are shown in Figures 6.32–6.36 for the Landers earthquake and in Figures 6.37–6.41 for the Big Bear earthquake. The in-plane shear strength of the tilt-up walls was estimated as

$$V_n = 2.0 \sqrt{f'_c} hd + A_{vh} f_y d/s_2$$

The concrete strength used in the building was not known and therefore was assumed to be 4,000 psi. Nominal reinforcing steel consisting of 1-#4 @ 14-inch spacing in both directions is used in the walls. Taking h = 7″ and d=1″ for a unit length of wall, the shear flow capacity becomes

$$q_n = 0.88 \text{ kips/in.} + 0.86 \text{ kips/in.} = 1.74 \text{ kips/in.}$$

The steel in the walls is assumed to be placed at the centerline of the wall resulting in a effective depth of h/2 = 3.5 inches. The nominal moment capacity becomes 3 in.-kips/in.

The roof sheathing is ½-inch plywood. The available plans do not indicate the plywood grade, so structural grade-one plywood is assumed. With ½-inch plywood, dense nailing and 2x blocking members, the UBC ’97 (Table 23-II-H) permits an allowable shear of 730 lbs/ft. Converting this value to the ultimate load in kips/in. results in 0.085 kips/in.

The in-plane shear force in the transverse walls at the north and south ends of the building are shown in Figure 6.32 for the Landers ground motions. It can be seen that the shear flow (kips/in.) in the wall is not uniform. If the limited regions of increased shear in the four lower corners of the wall are neglected, the largest shear flow (kips/in.) is on each side of the center of the wall and has a value of 0.15 kips/in., which is much less than the estimated strength of the wall (1.7 kips/in.). The in-plane shear contours for the longitudinal walls on the east and west sides of the building are shown in Figure 6.33. In the west wall (Fig. 6.33b) on the back side of the building, there are no openings for access to the interior and the shear flows are similar in magnitude to those for the end walls, reaching a maximum value of 0.15 kips/in. For the east wall (Fig. 6.33a) the openings in the wall cause the shear flows to be more irregular; however, the maximum value remains 0.15 kips/in.

The contours of the out-of-plane bending moments in the north and south walls are shown in Figure 6.34. These two plots are quite similar and the maximum moment has a value of 0.8 in.-kips/in. Similar plots for the east and west walls are shown in Figure 6.35. It can be seen that the maximum moment occurs near the middle of the wall and has a value of 1.4 in.-kips/in.

These demands for out-of-plane moment are both less than the estimated capacity of 3.0 in.-kips/in. It should be noted that these plots do not include the moments in the pilasters which are treated separately.

In-plane shear force contours in the north and south walls are shown in Figure 6.36 for the Big Bear ground motions. Neglecting areas of local shear concentration, the maximum shear flow is taken to be 0.18 kips/in. The contours of shear flow in the east and west walls are shown in Figure 6.37. It can be seen that the east wall (Fig. 6.37a), with its access openings, has a much more irregular shear flow pattern compared to that of the solid west wall (Fig. 6.37b). Neglecting small areas of shear concentration, the maximum shear flow value remains 0.18 kips/in.

Contours for the out-of-plane moments in the north and south walls are shown in Figure 6.38. As before, these patterns are very similar and have a maximum value of 0.8 in.-kips/in. For the north and south walls, shown in Figure 6.39, the contour patterns are symmetrical and have a maximum value of 1.4 in.-kips/in. The contours of in-plane shear for the roof diaphragms under the two recorded ground motions are shown in Figure 6.40. For the Big Bear ground motion, the diaphragm shear is shown in Figure 6.40a and has a maximum value of 0.175 kips/in. For the Landers ground motion (Fig. 6.40b), the maximum shear flow is also 0.175 kips/in. The earthquake demands for these two earthquakes are compared with the estimated capacities in Table 6.3. These results indicate that based on the response calculated from the recorded data, the in-plane shear in the roof diaphragm is the critical component of the system. Next most critical are the glulam to pilaster connections and the out-of-plane moments in the walls. The in-plane shear capacity of the walls have considerable overstrength due to the length of the walls and the use of minimum steel reinforcement.

Table 6.3 Linear model, recorded response demand

	Glulam to Pilaster (Axial) (kips)	In-Plane Shear (Wall) kips/in.	Out-of-Plane Moment (Wall) in.-kips/in.	In-Plane Shear (Diaphragm) kips/in.
Est. Capacity	26/34	1.74	3.0	0.085
Landers	13.6	0.15	1.4	0.175
Big Bear	14	0.18	1.4	0.175

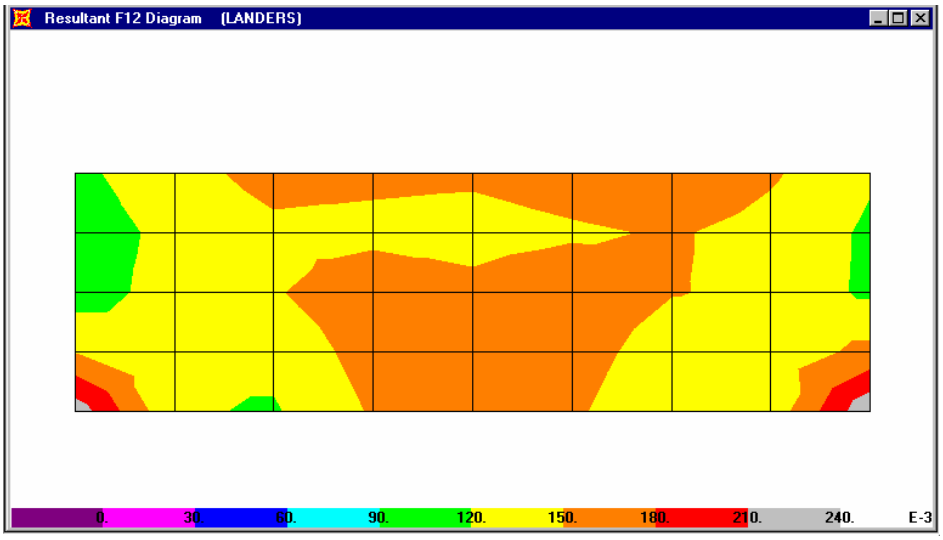

(a) north wall

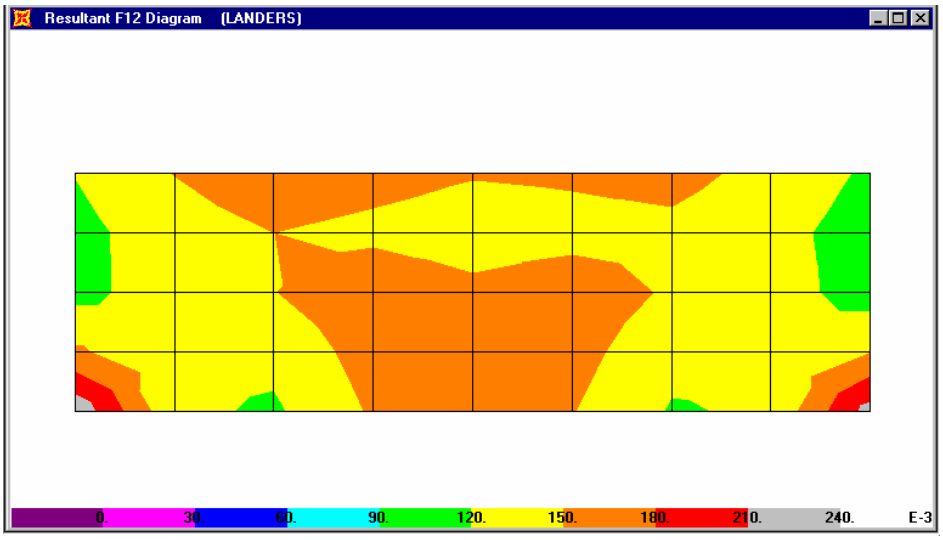

(b) south wall

Fig. 6.32 In-plane shear contours, north and south walls, Landers

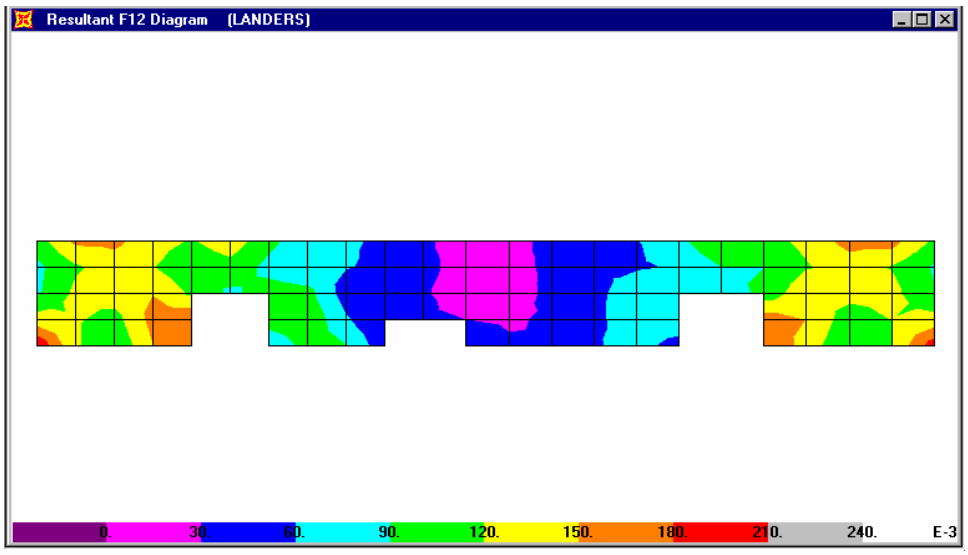

(a) east wall

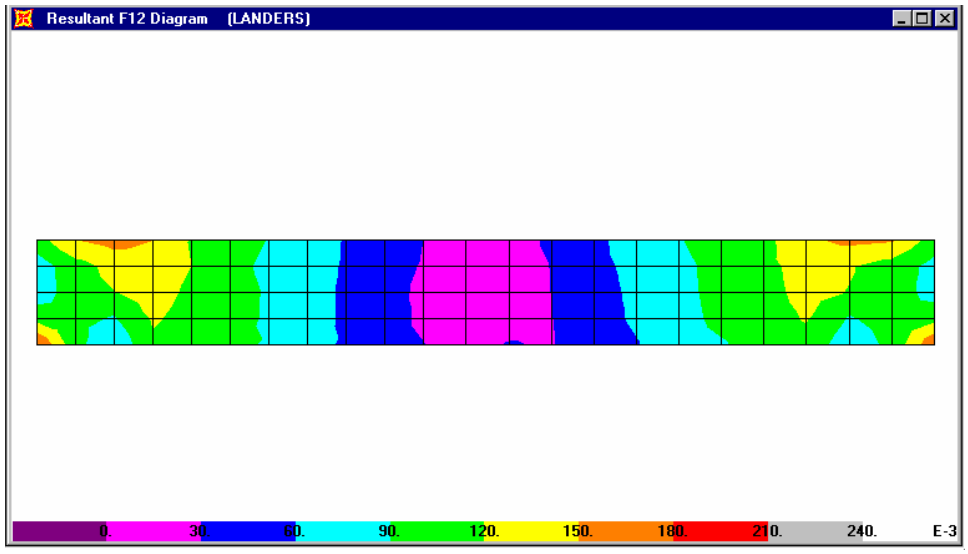

(b) west wall

Fig. 6.33 In-plane shear contours, east and west walls, Landers

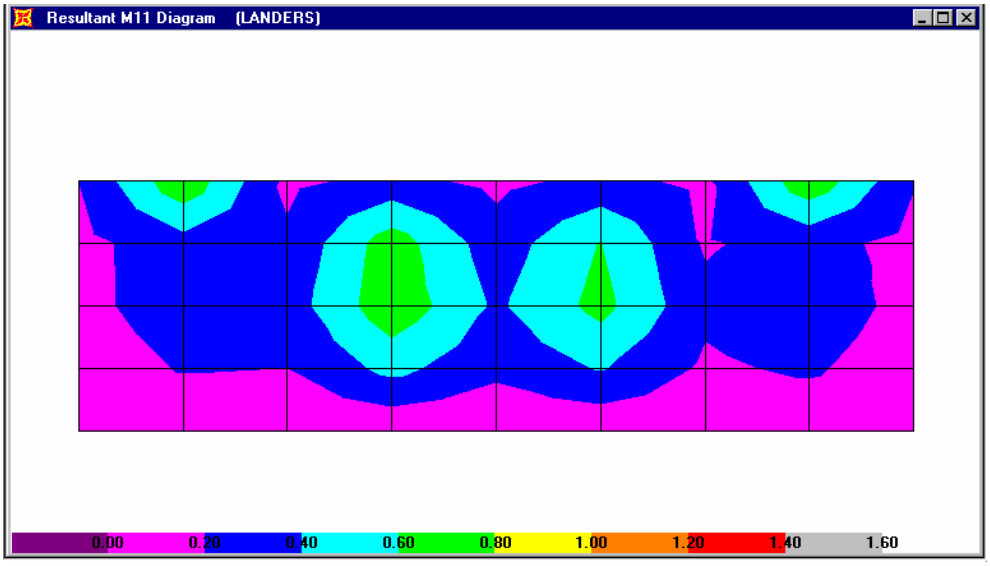

(a) north wall

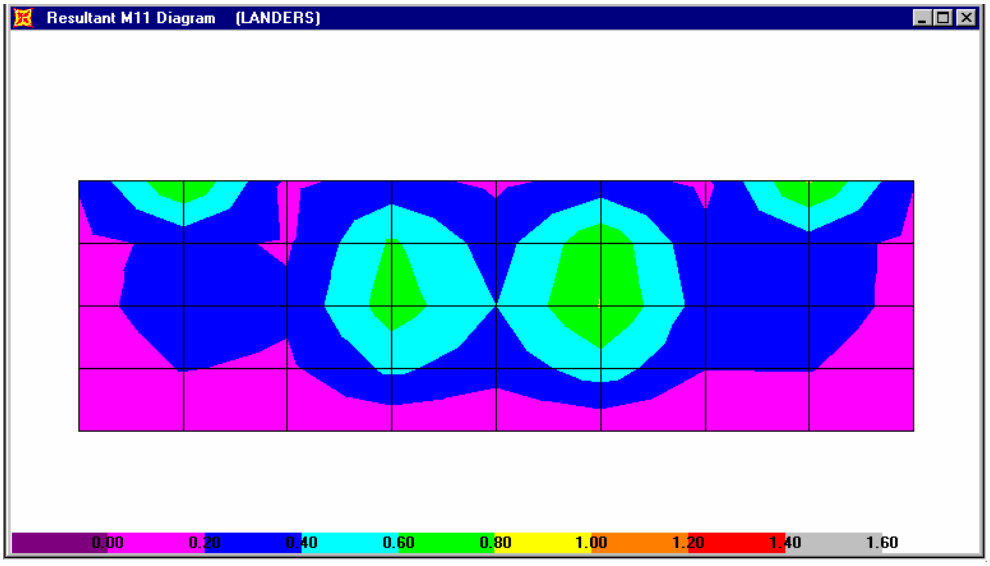

(b) south wall

Fig. 6.34 Out-of-plane moment contours, north and south walls, Landers

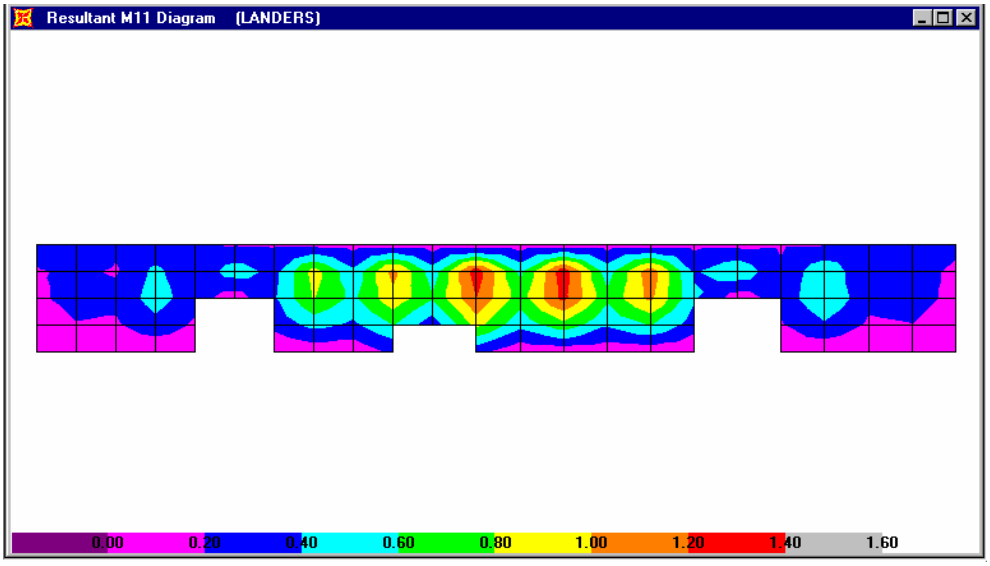

(a) east wall

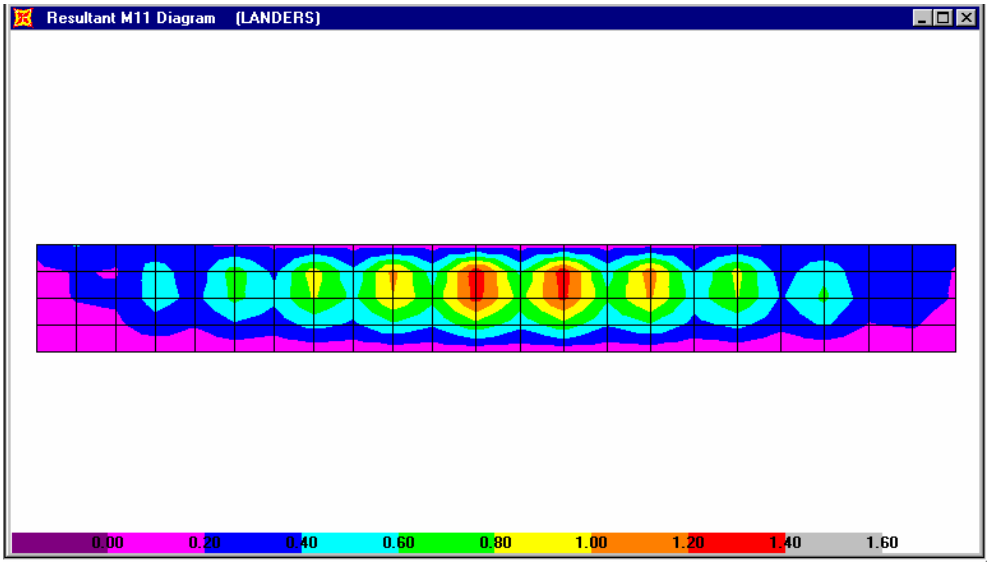

(b) west wall

Fig. 6.35 Out-of-plane moment contours, east and west walls, Landers

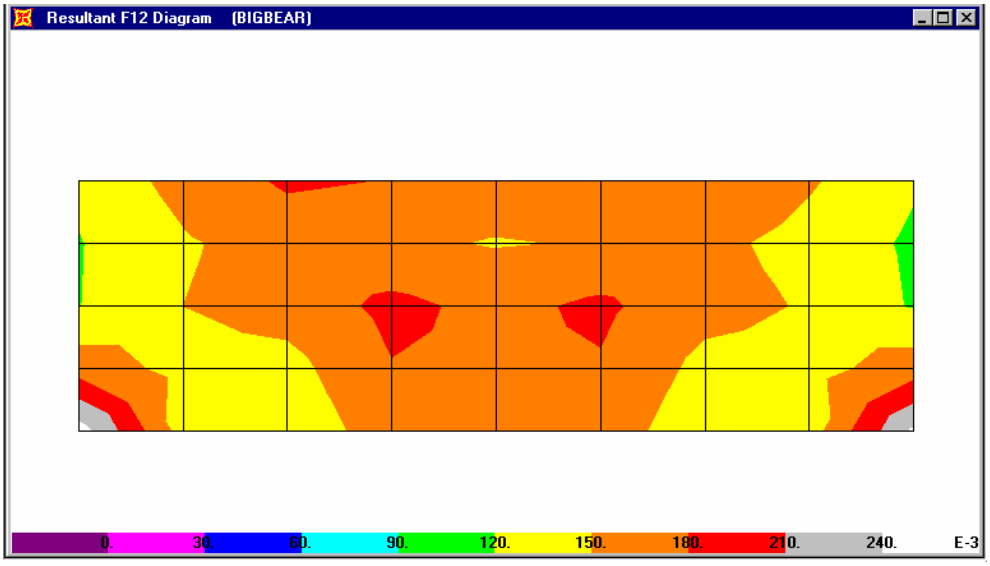

(a) north wall

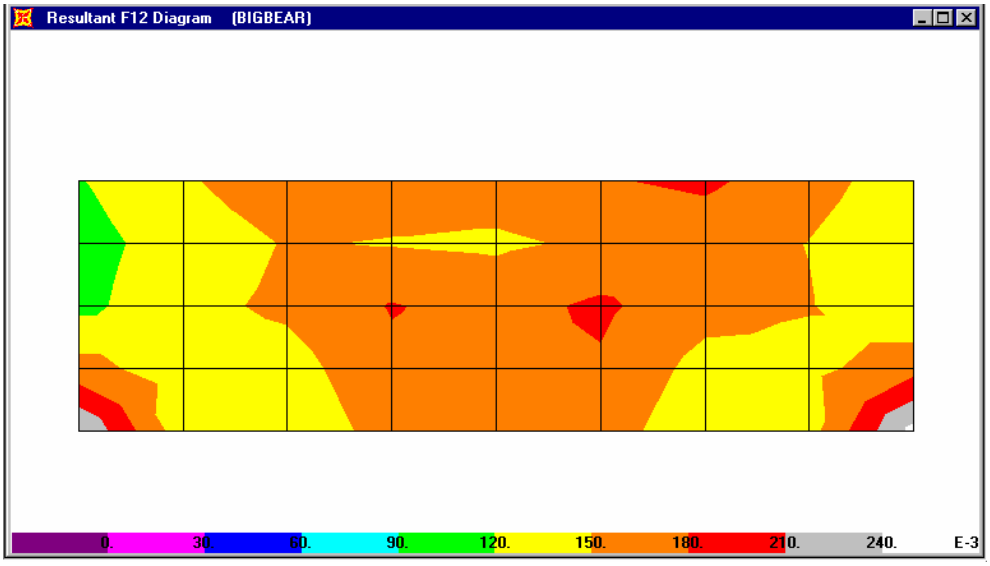

(b) south wall

Fig. 6.36 In-plane shear contours, north and south walls, Big Bear

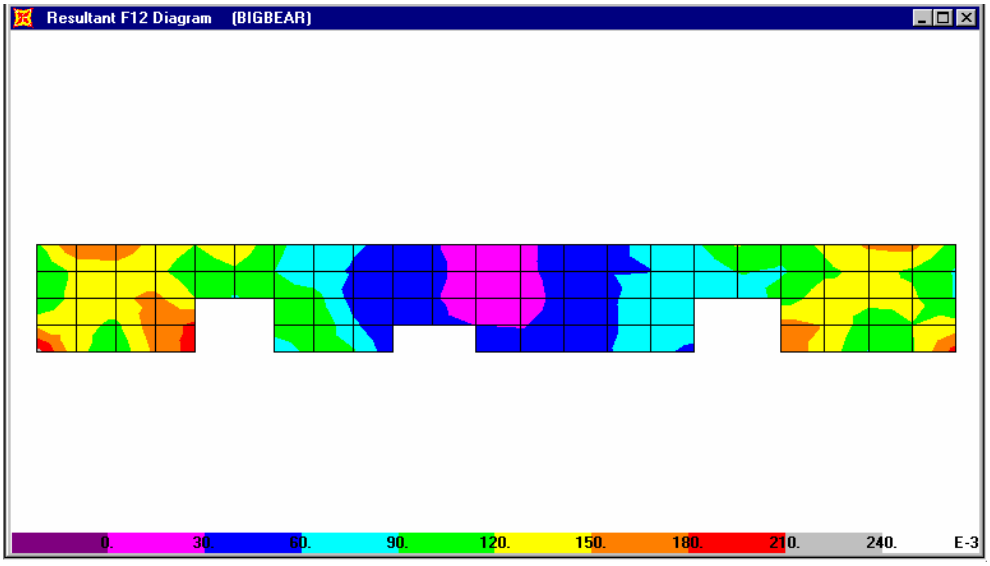

(a) east wall

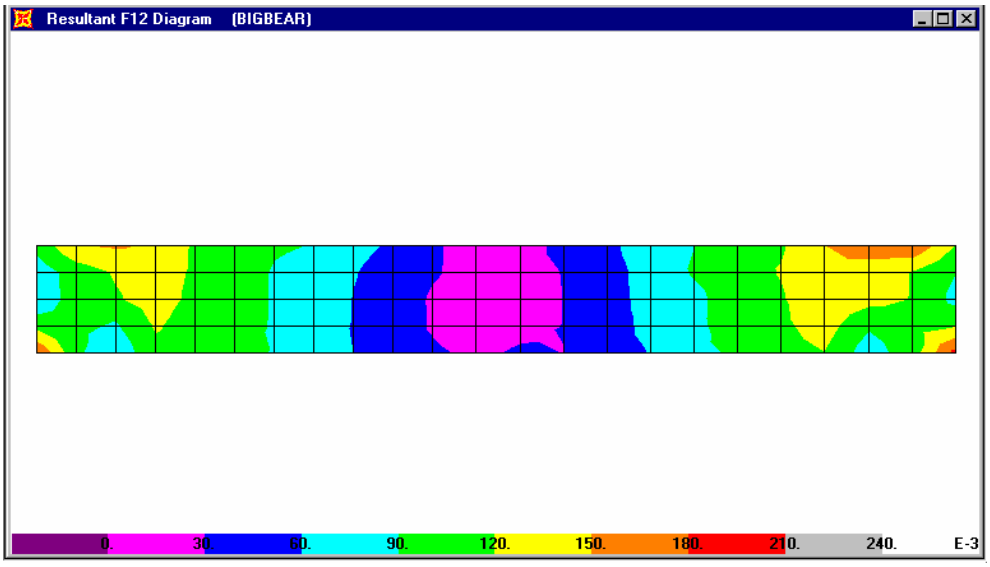

(b) west wall

Fig. 6.37 In-plane shear contours, east and west walls, Big Bear

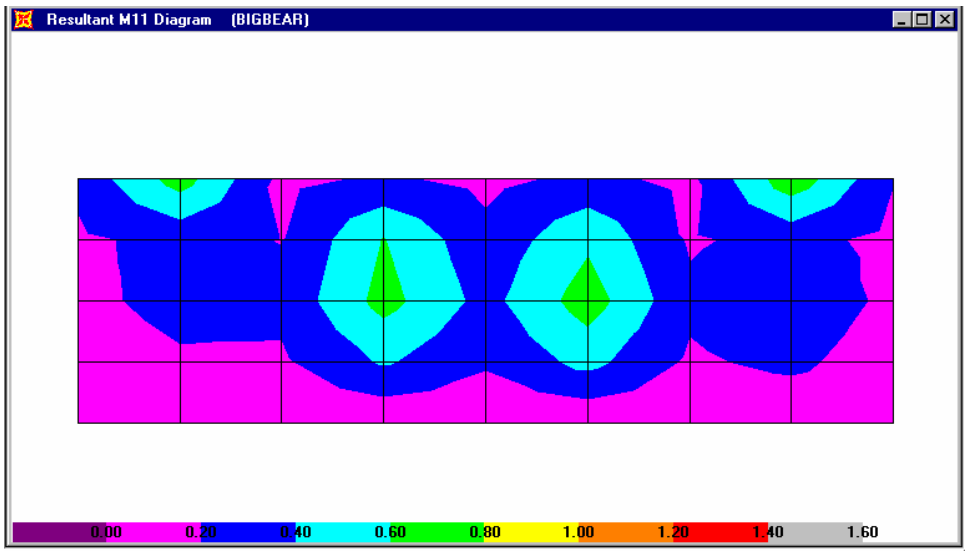

(a) north wall

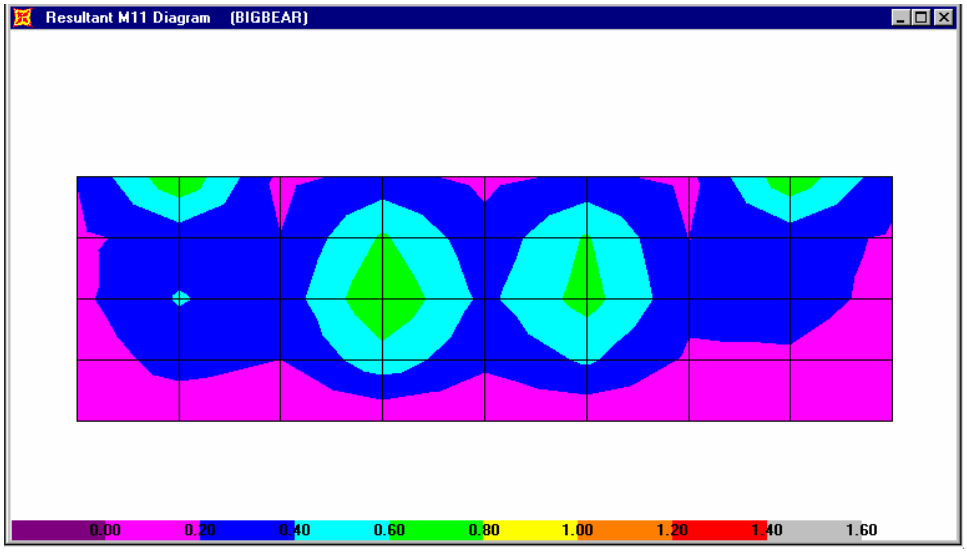

(b) south wall

Fig. 6.38 Out-of-plane moment contours, north and south walls, Big Bear

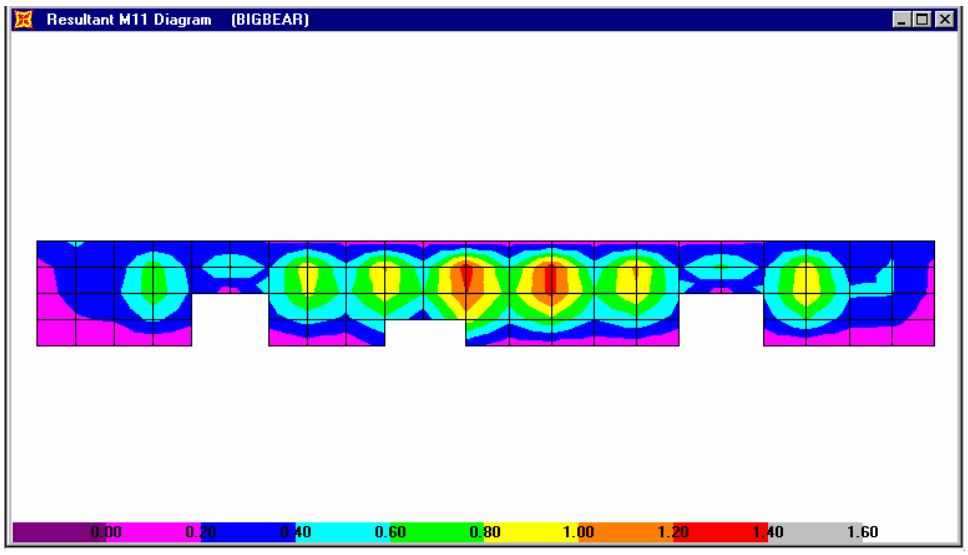

(a) east wall

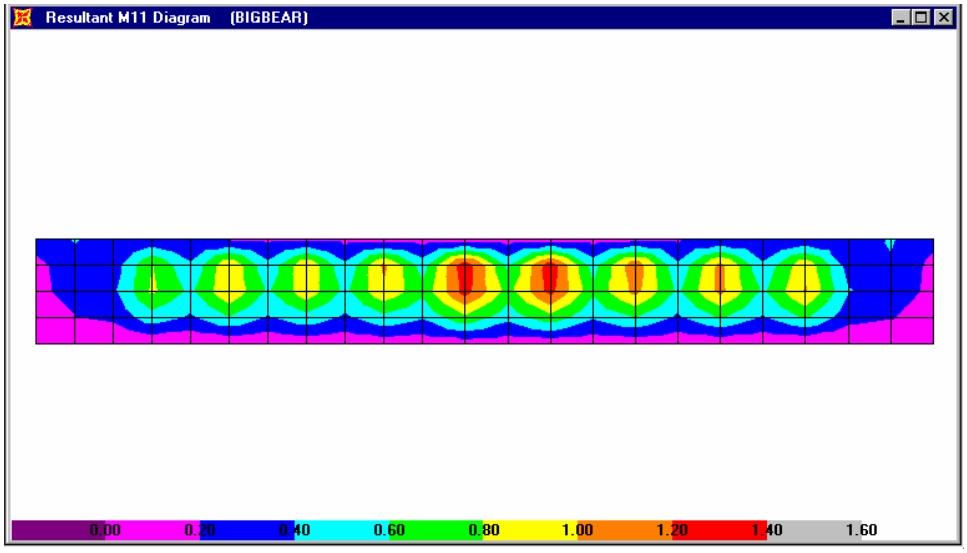

(b) west wall

Fig. 6.39 Out-of-plane moment contours, east and west walls, Big Bear

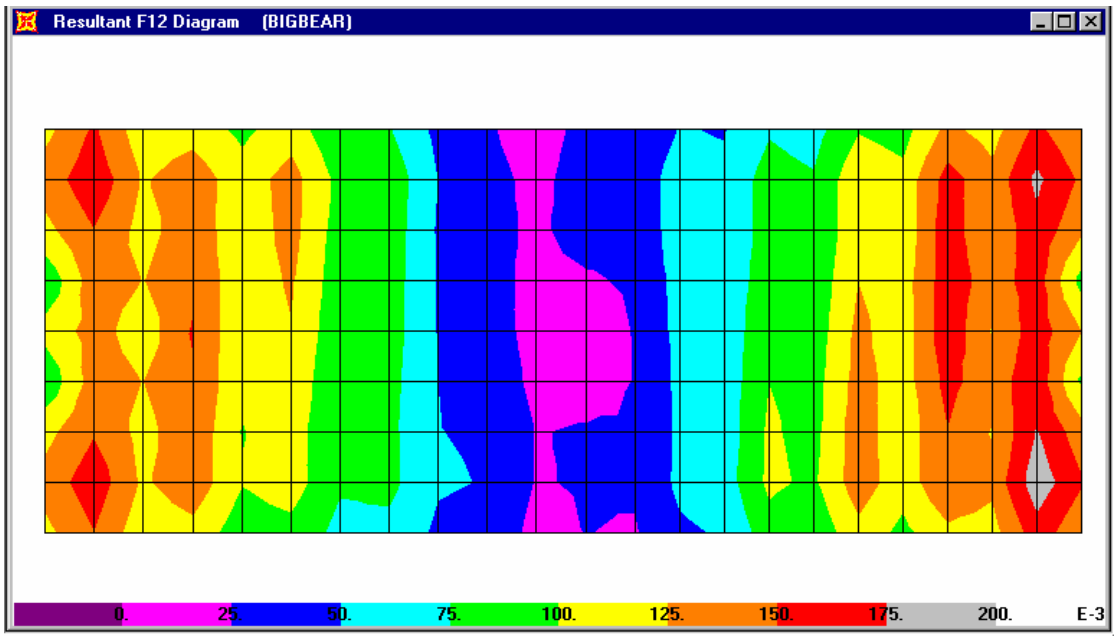

(a) Big Bear, roof

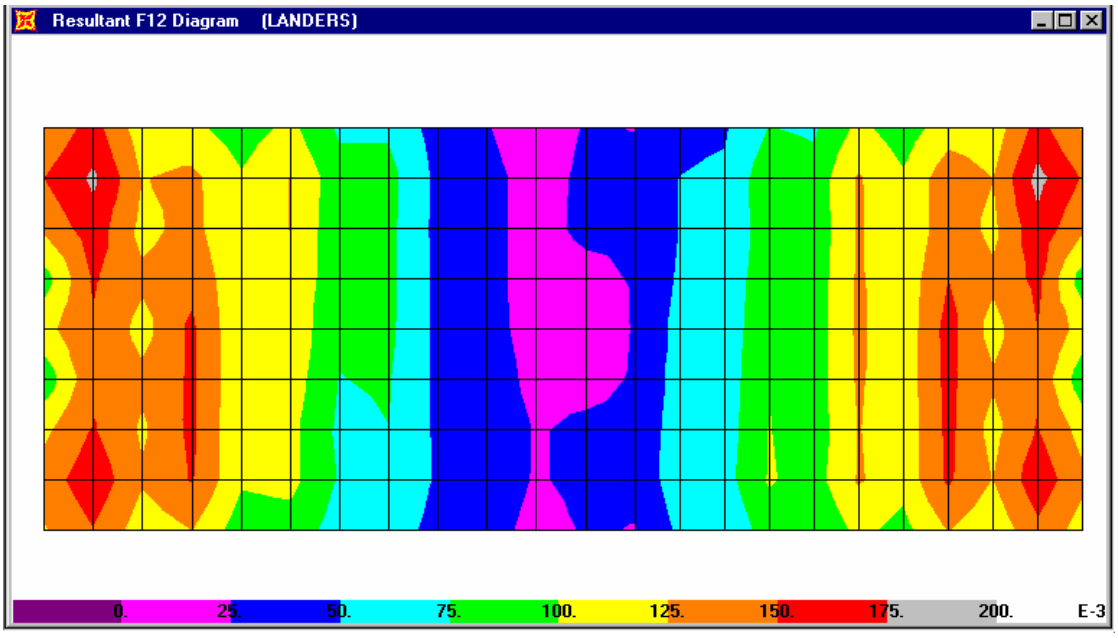

(b) Landers, roof

Fig. 6.40 In-plane shear contours

6.2 DISCONNECTED CORNERS

Although the limited drawings that were available for the building did not indicate the connectivity at the four corners, a field visit to the building indicated that the walls at these locations were not connected through the pilaster. Therefore, this condition was investigated by separating the walls throughout the height of the wall. However, at the corner of the roof both the roof node and the wall nodes remained constrained. The corner pilasters were removed and the dynamic response for the Big Bear ground motion was evaluated by comparing the response of this model with that of the original model.

Transverse acceleration time histories at channel 5, located at the roof level midway between the fire wall and the south wall are shown in Figure 6.41. Those calculated with the original model are shown in Figure 6.41a, and those calculated with the disconnected corners, in Figure 6.41b. The two responses were separated because superposition of the two results made it impossible to distinguish the two curves. It can be seen from the data presented that the acceleration results are virtually identical. The corresponding displacement data (Fig. 6.42) shows identical behavior.

Channel 9 measures out-of-plane acceleration at the roof level at midpoint of the south wall. Accelerations calculated at this location for the two models are compared in Figure 6.43. The values calculated from the original model are shown in Figure 6.43a and those from the model with disconnected corners, in Figure 6.43b. Careful examination of these two time histories indicates that there are some very minor differences in the magnitude and phasing of the peak values, but that overall the two acceleration records are the same. The displacement time histories shown in Figure 6.44 indicate that it is hard to distinguish any differences.

The calculated base shears in the transverse direction (E-W) for the Big Bear ground motions are shown in Figure 6.45. For the model with connected corners (Fig. 6.45a), the peak shear reaches a value of 480 kips, whereas the model with disconnected corners (Fig. 6.45b**)** has a peak shear value of 490 kips. The results in the longitudinal (N-S) direction (Fig. 6.46) indicate that the peak shear with corners connected reaches 70 kips, whereas with disconnected corners the peak shear reaches 83 kips.

In-plane shear contours are compared in Figure 6.47. In both cases, the maximum value in the main part of the wall is 0.15 kips/in. for all four walls. There are some limited locations near the doors and in the corners where the shear flow reaches 0.24 kips/in. These areas increase

slightly when the corners are disconnected. The contours of vertical out-of-plane moment for the two cases are compared in Figure 6.48. A significant increase in the moments can be seen at the four disconnected corners. Out-of-plane moments in the disconnected corners are above 2.0 in.-kips/in. The in-plane shear flows in the roof diaphragm are compared for the two cases in Figure 6.49. Comparing the results for the connected corners (Fig. 6.49a) and for the disconnected corners (Fig. 6.49b) indicates almost no difference between the two results, with both reaching a maximum shear flow of 0.175 kips/in.

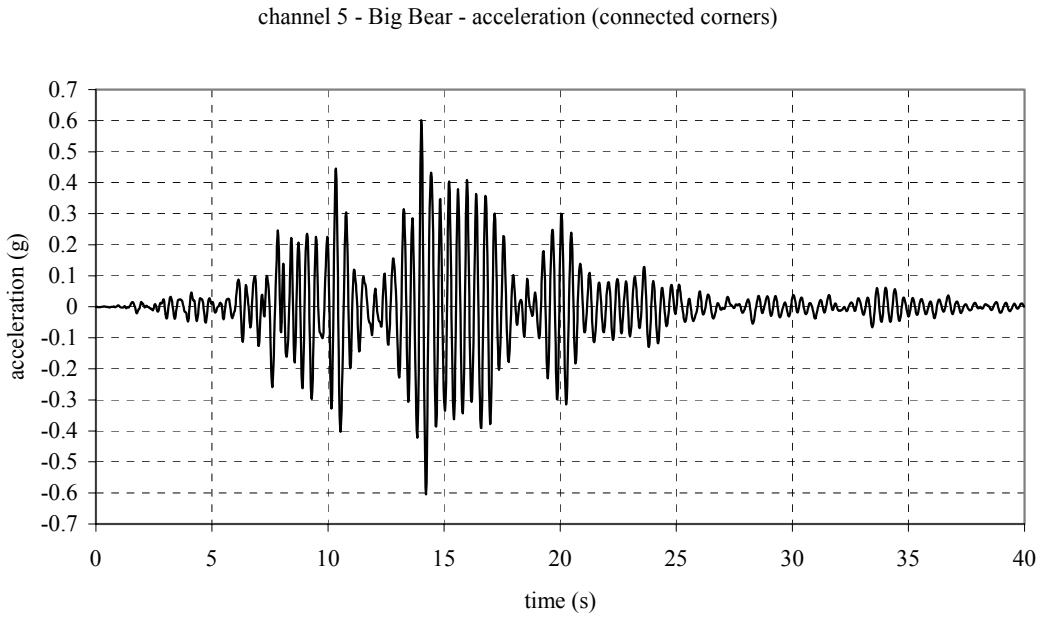

(a) connected corners

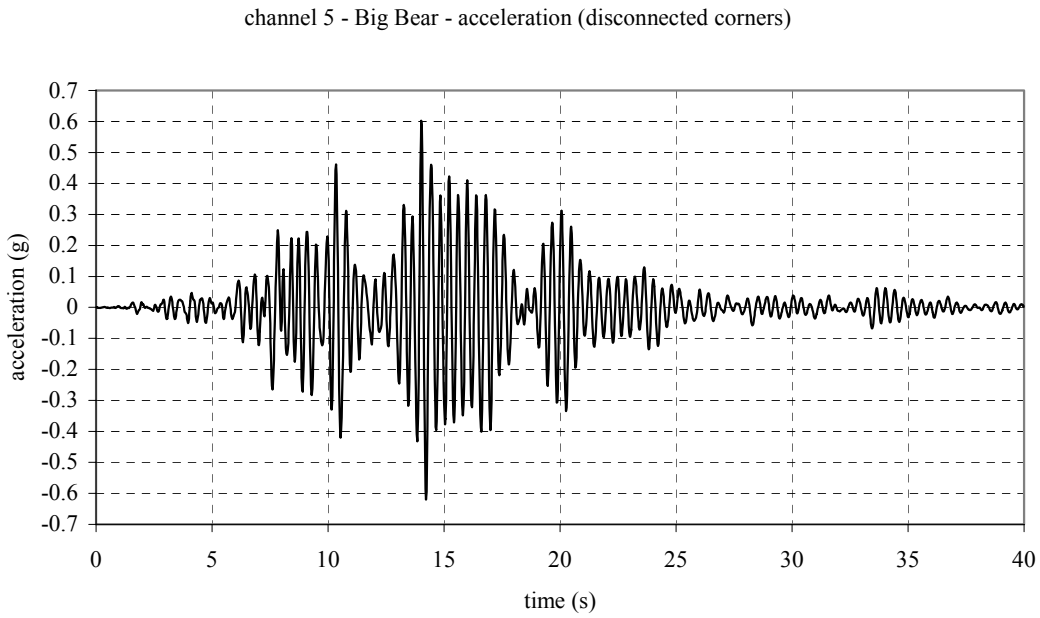

(b) disconnected corners

Fig. 6.41 Acceleration comparisons, disconnected corners, ch. 5

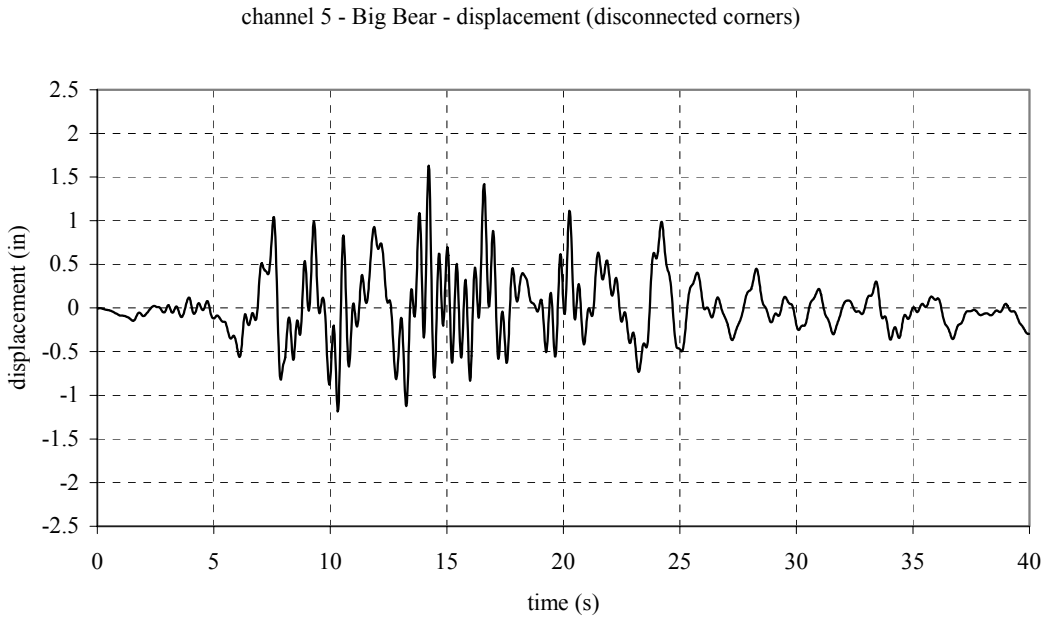

(a) connected corners

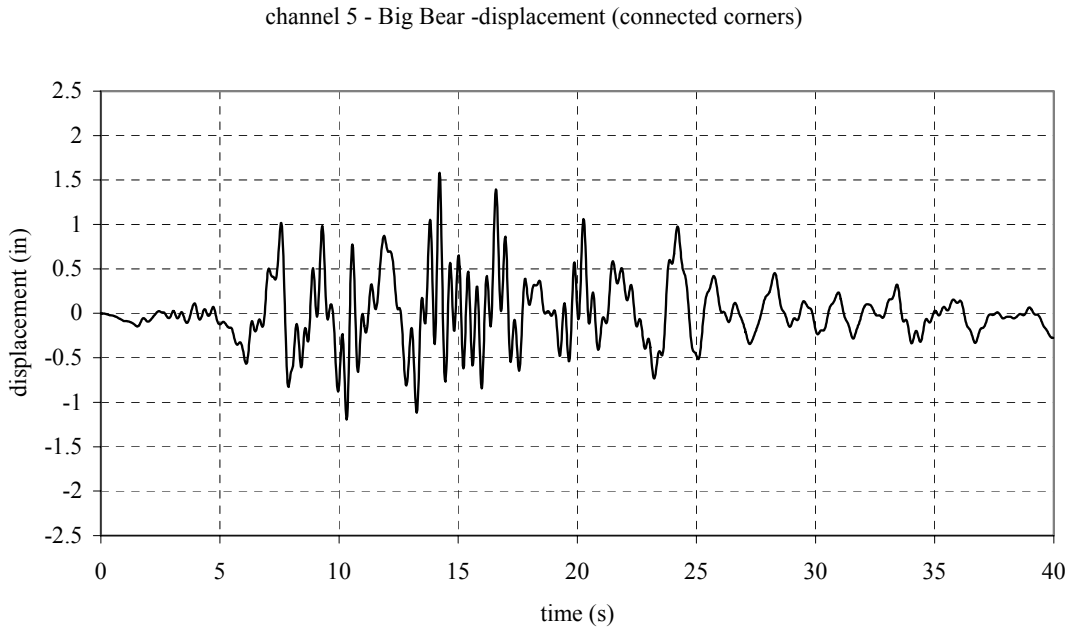

(b) disconnected corners

Fig. 6.42 Displacement comparisons, disconnected corners, ch. 5

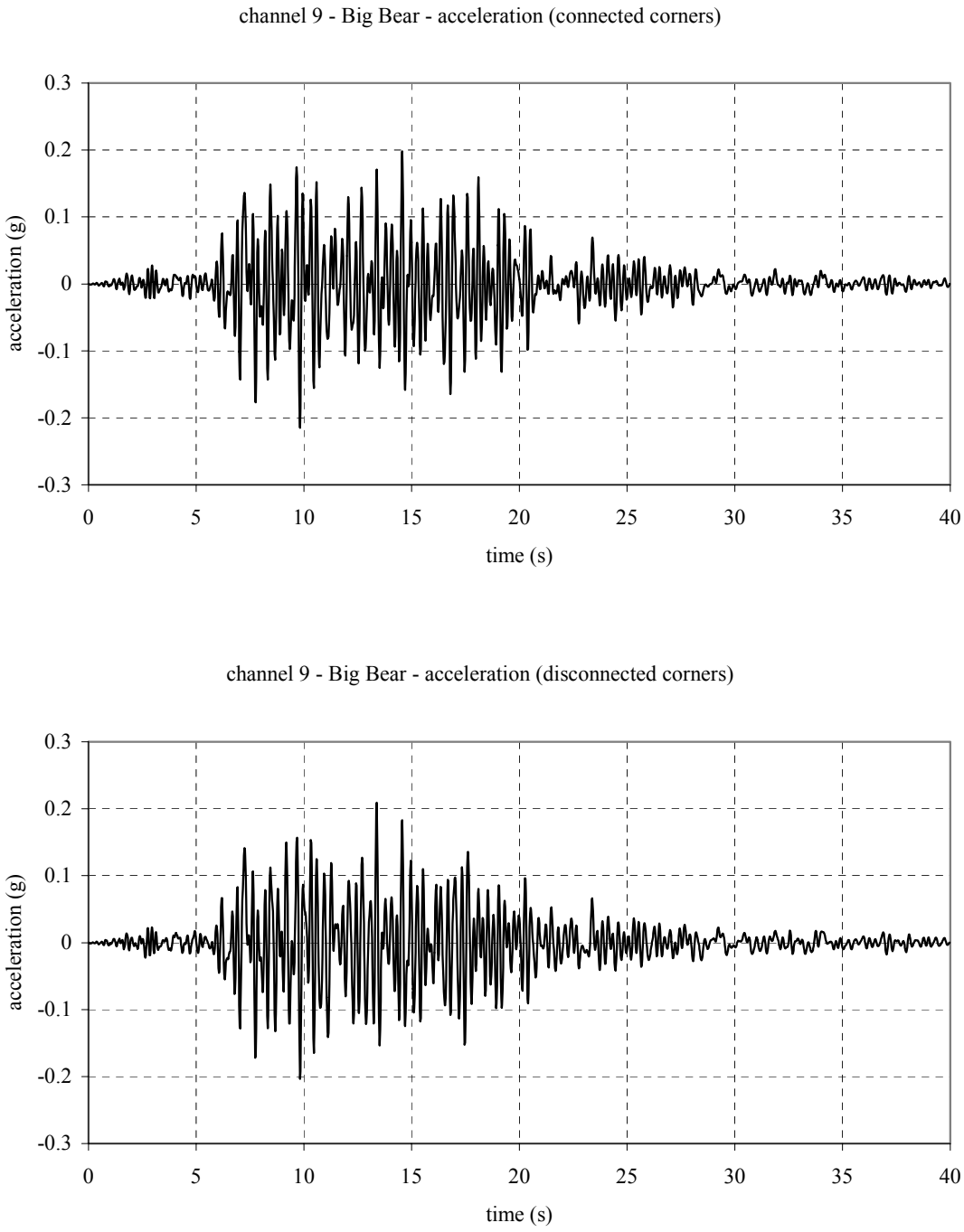

Fig. 6.43 Acceleration comparisons, disconnected corners, ch. 9

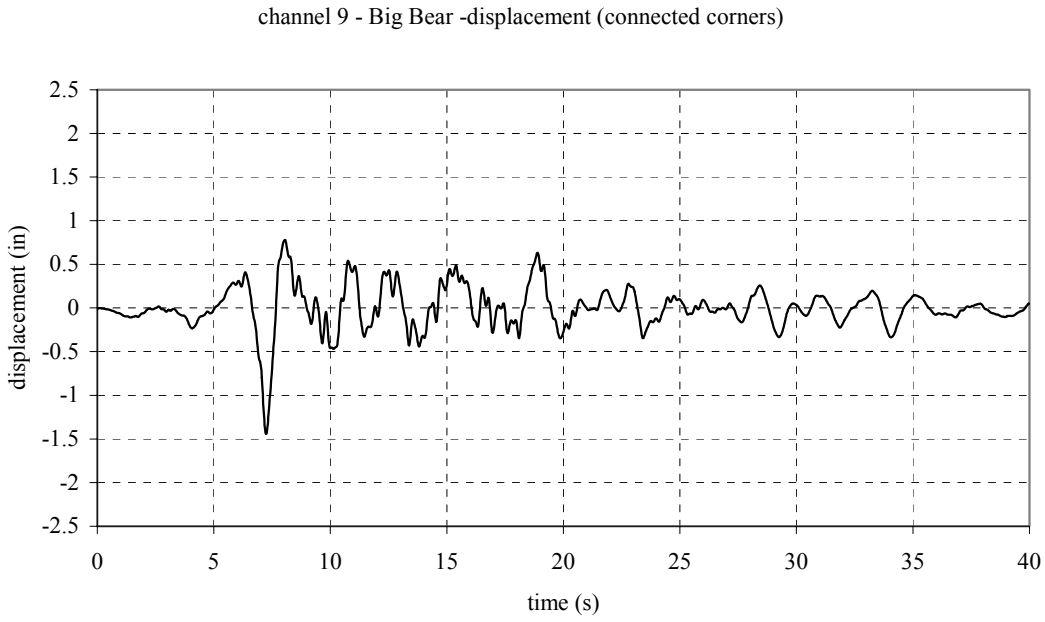

(a) connected corners

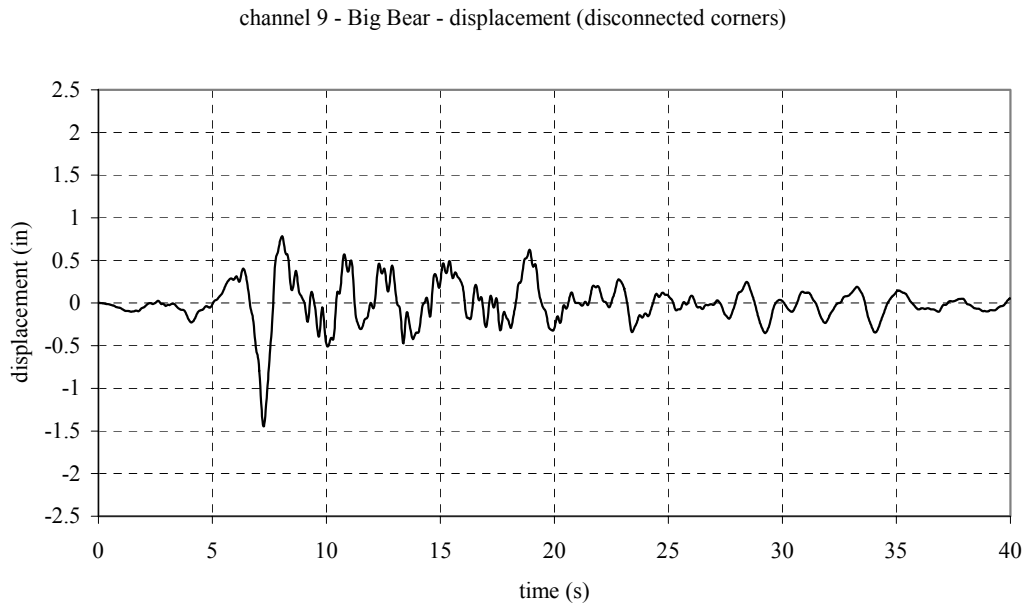

(b) disconnected corners

Fig. 6.44 Displacement comparisons, disconnected corners, ch. 9

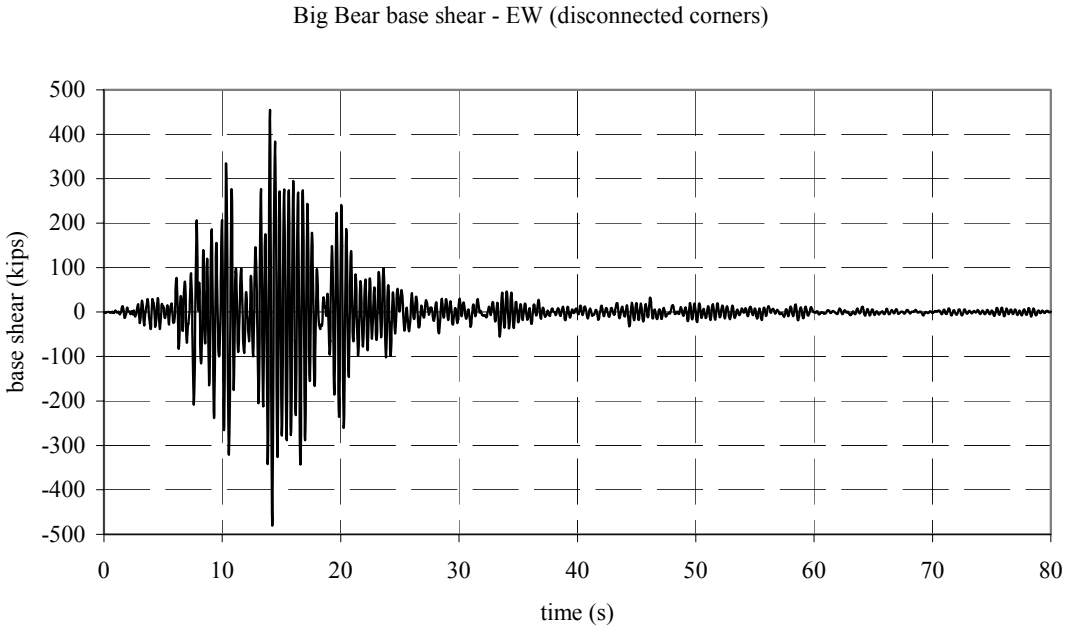

(a) connected corners

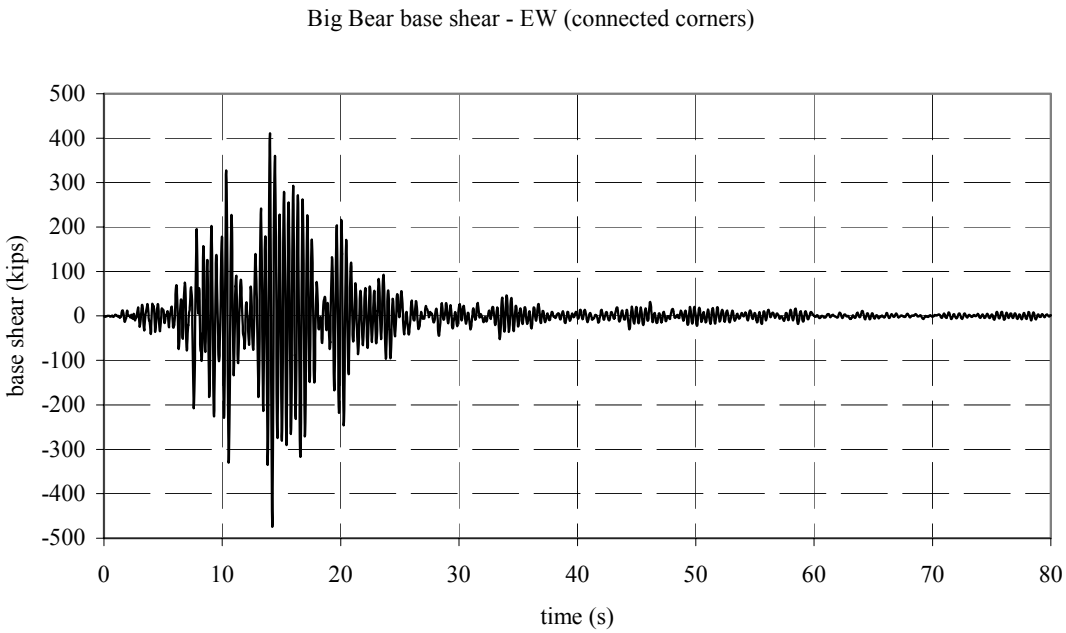

(b) disconnected corners

Fig. 6.45 Base shear comparisons, disconnected corners, E-W

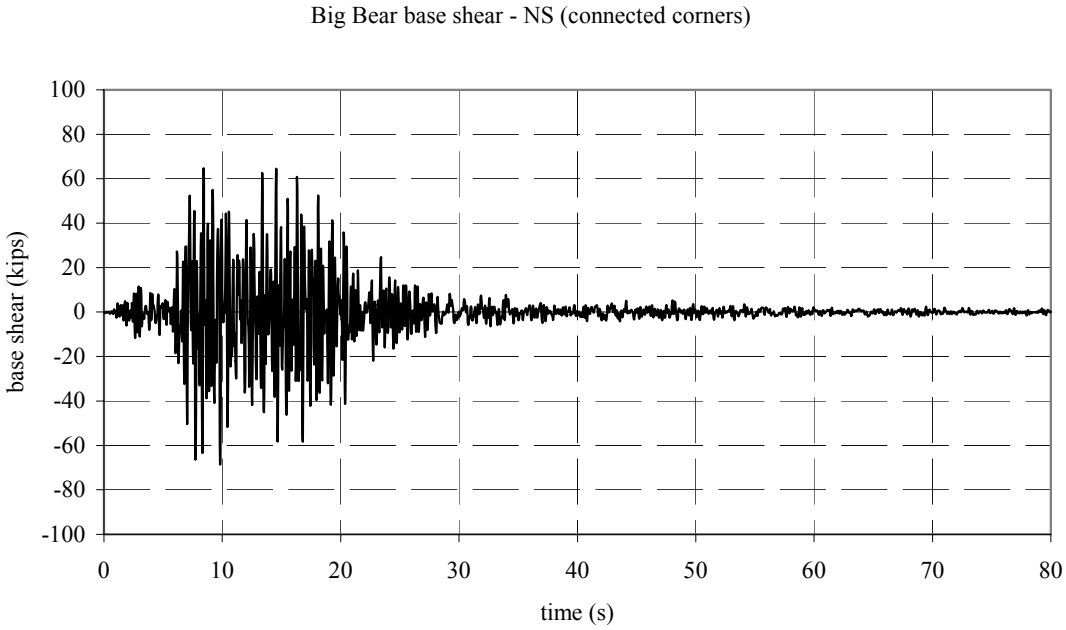

(a) connected corners

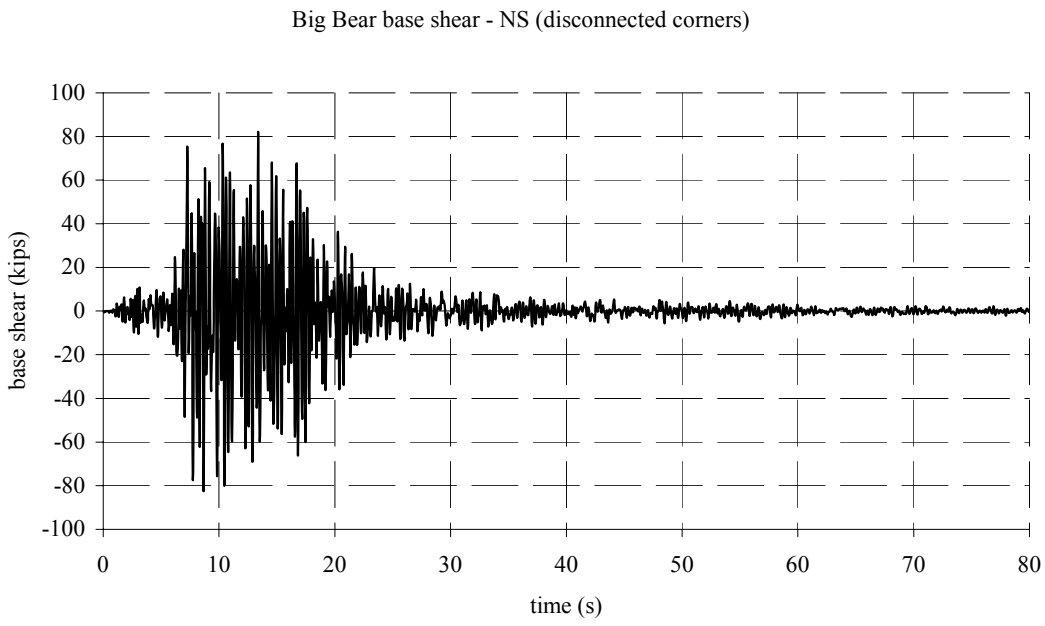

(b) disconnected corners

Fig. 6.46 Base shear comparisons, disconnected corners, N-S

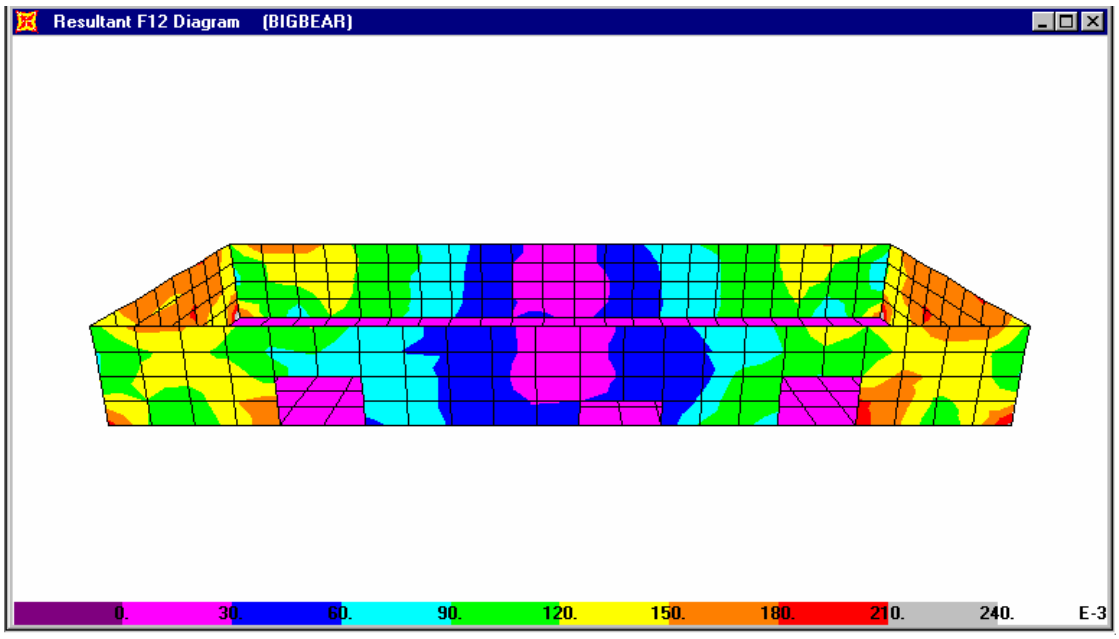

(a) Big Bear: in-plane shear — connected corners

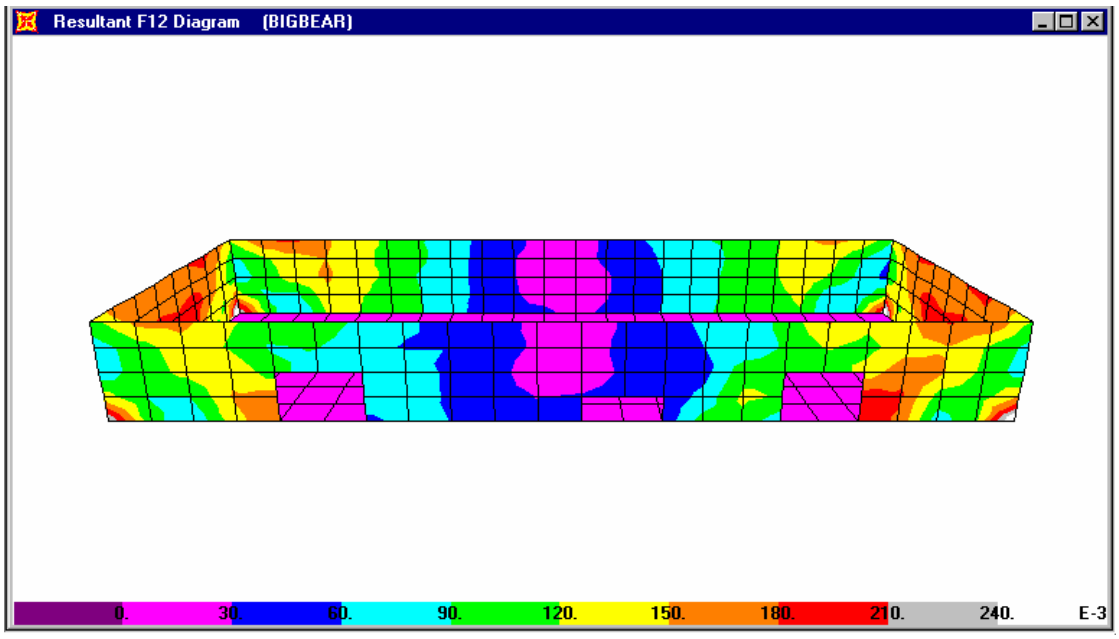

(b) Big Bear: in-plane shear — disconnected corners

Fig 6.47 In-plane shear comparisons, Big Bear

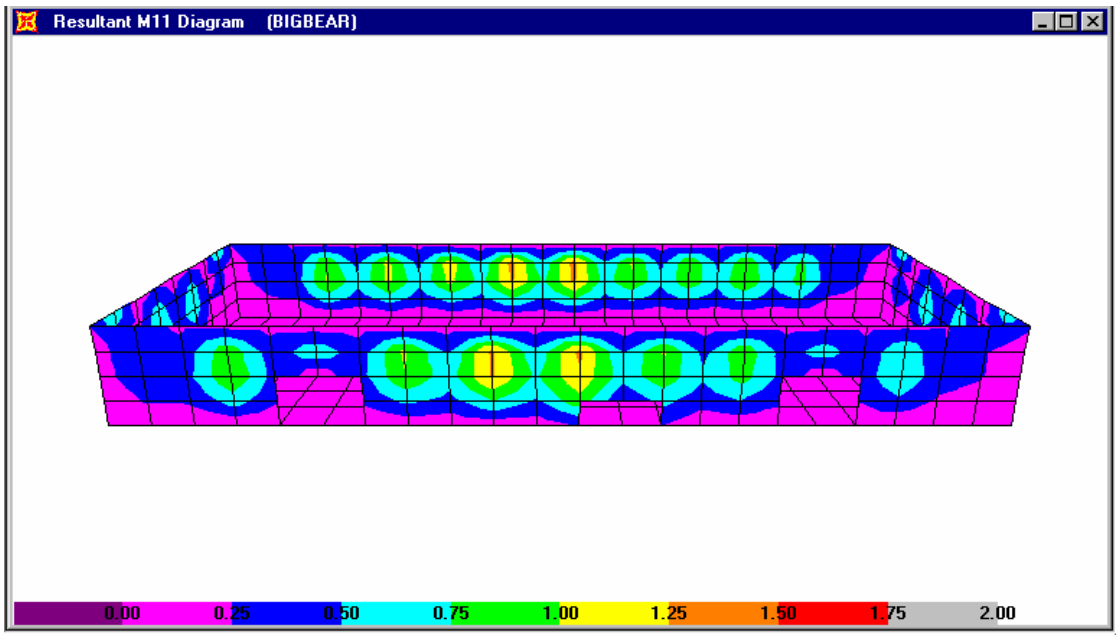

(a) Big Bear: vertical out-of-plane moment — connected corners

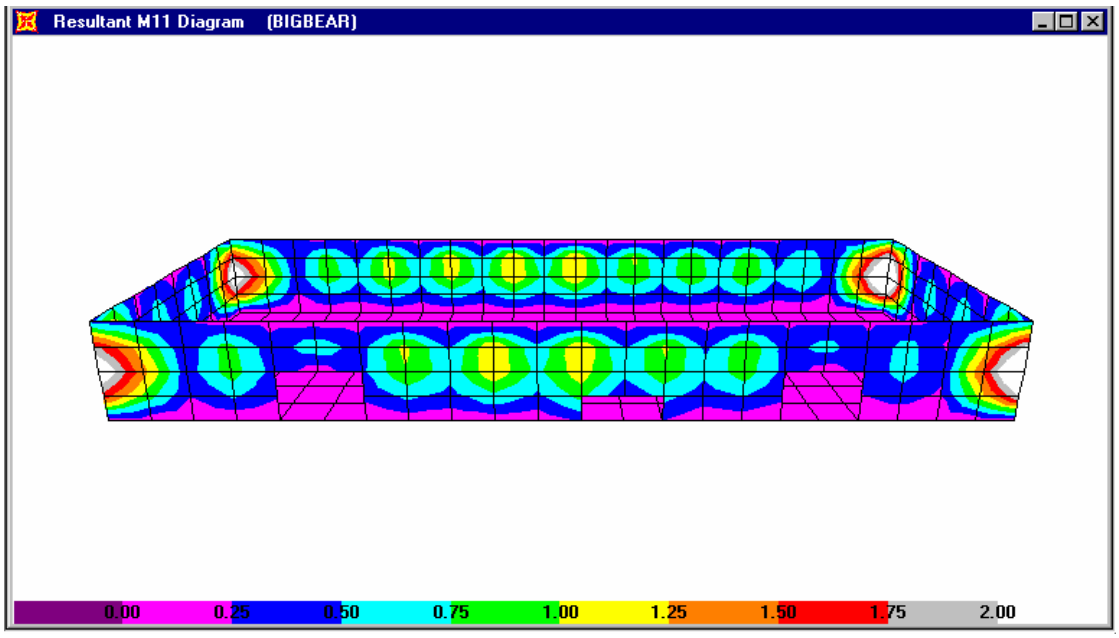

(b) Big Bear: vertical out-of-plane moment — disconnected corners

Fig 6.48 Vertical out-of-plane moment, Big Bear

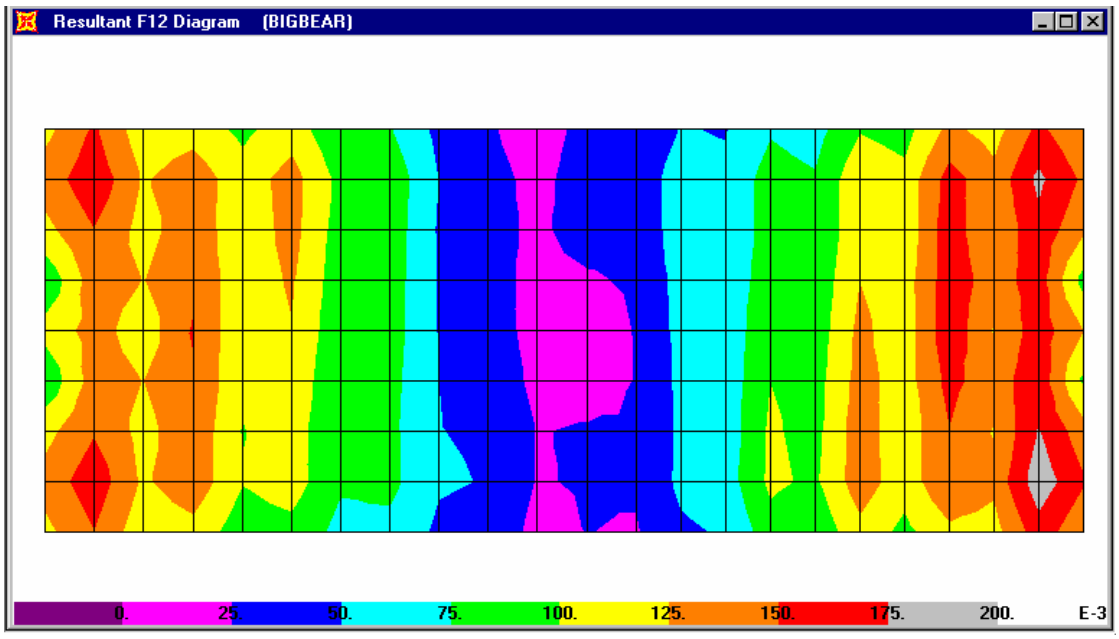

(a) Big Bear: roof in-plane shear — connected corners

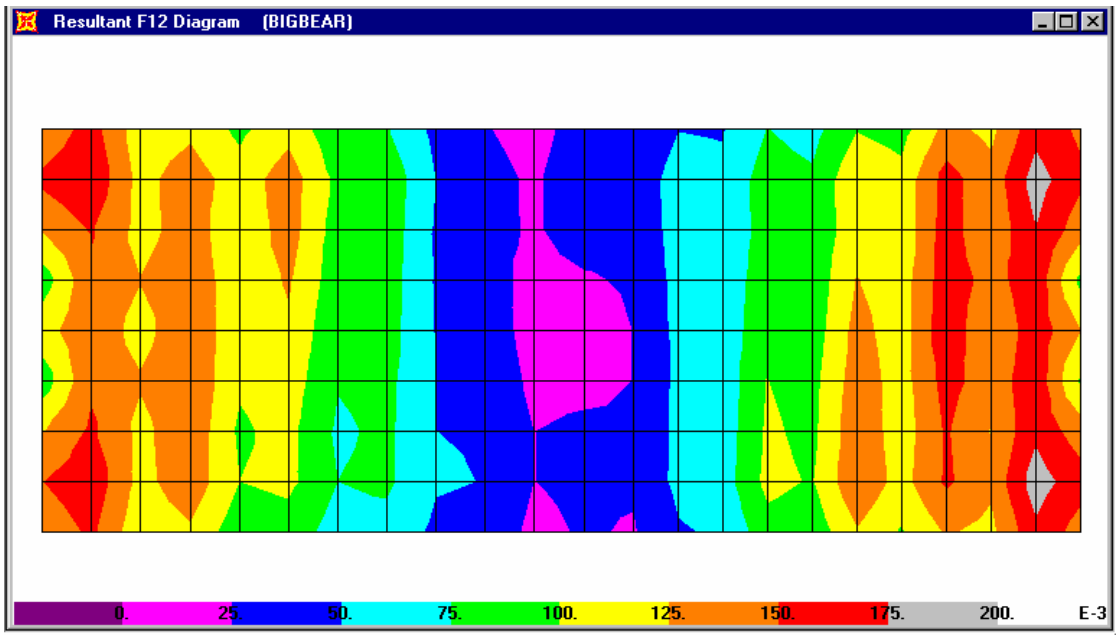

(b) Big Bear: roof in-plane shear — disconnected corners

Fig. 6.49 Roof in-plane shear, Big Bear

6.3 DISCONNECTED CORNERS, ELASTIC SPRING CONNECTIONS

For these investigations, the model just discussed with the disconnected corners was modified to introduce linear springs at the roof to pilaster connection to obtain an estimate of the forces in the connection elements. In order to limit the elastic deformation in the connection, a stiff linear spring (5800 kips/in.) was arbitrarily used in the three orthogonal directions. In all cases, the two horizontal components of the recorded ground motions due to the Landers and Big Bear earthquakes are applied in the two principal directions of the building.

The axial force distribution in the purlins and glulam beams under the Landers ground motion is shown in Figure 6.50a. Distribution of the axial force in the connection of the purlins to the pilasters in the transverse walls on the north and south ends of the building are shown in Figure 6.50b. The maximum connection demand occurs at midpoint of the wall and has a value of 6.1 kips. The axial force demand in the connections of the glulam beams to the pilasters is shown in Figure 6.50c. This figure indicates a maximum axial force of 13.6 kips that is less than the idealized yield strength of 26 kip for the older type of connection (Appendix A).

The vertical shear forces developed in the purlin to pilaster connections (Fig. 6.51b) reach a maximum value of 2.6 kips toward the ends of the walls. The maximum vertical shear forces in the glulam to pilaster connections (Fig. 6.51c) reach a maximum value of only 1.5 kips. The maximum horizontal shear forces developed parallel to the transverse end walls (Fig. 6.52b) have a maximum value of 21 kips, whereas a slightly smaller value of 17.5 kips is developed parallel to the longitudinal walls (Fig. 6.52c). In both cases these maximum values occur near the ends of the walls. Unfortunately, no experimental test data were available for this force component.

Under the Big Bear ground motion the maximum axial forces in the purlin to pilaster connections (Fig. 6.53b) reach a maximum value of 5.5 kips. The axial force demand in the connections of the glulam beams to the pilasters along the east and west walls are summarized in Figure 6.53c. This figure indicates a maximum axial force of 13.5 kips that is similar to the Landers demand just discussed.

The vertical shear forces developed in the purlin connections along the north and south walls (Fig. 6.54b) reach a maximum value of 2.9 kips toward the ends of the walls. The maximum vertical shear forces in the glulam connections along the east and west walls (Fig. 6.54c) reach a maximum value of only 1.65 kips. The horizontal shear forces developed in the

transverse end walls are shown in Figure 6.55b and have a maximum value of 20 kips, which is similar to the 19.5 kips obtained for the longitudinal walls (Fig. 6.55c). In both cases these maximum values occur near the ends of the walls. There is no record of any damage to these connections due to the Landers and Big Bear earthquakes. This appears to be consistent with the results obtained from the analytical solutions.

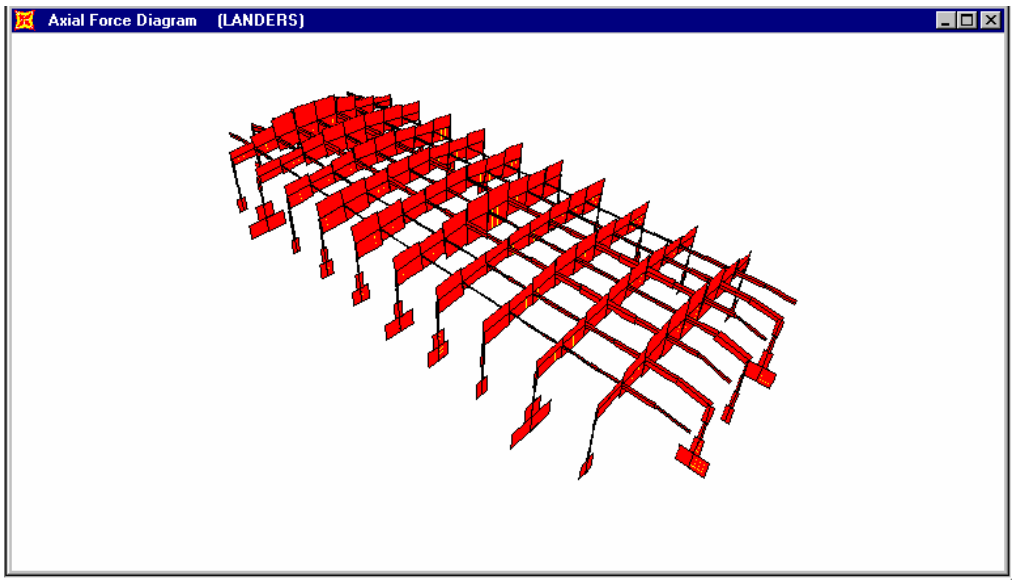

(a) Landers: axial force — disconnected corners, springs between roof elements and pilasters

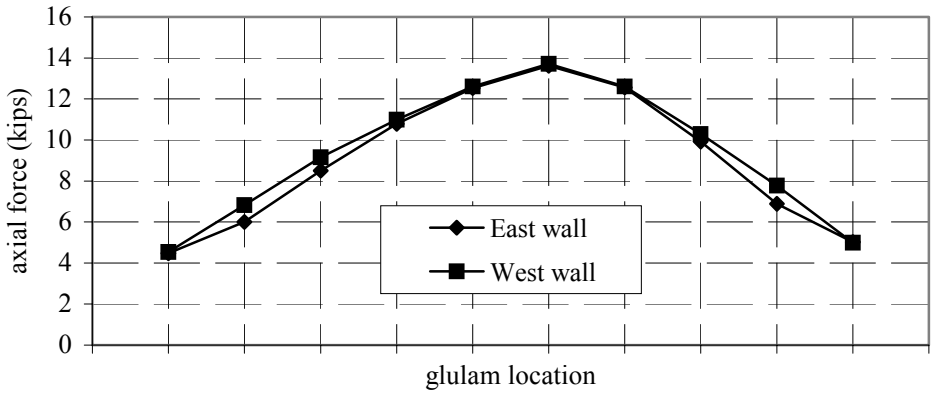

(b)

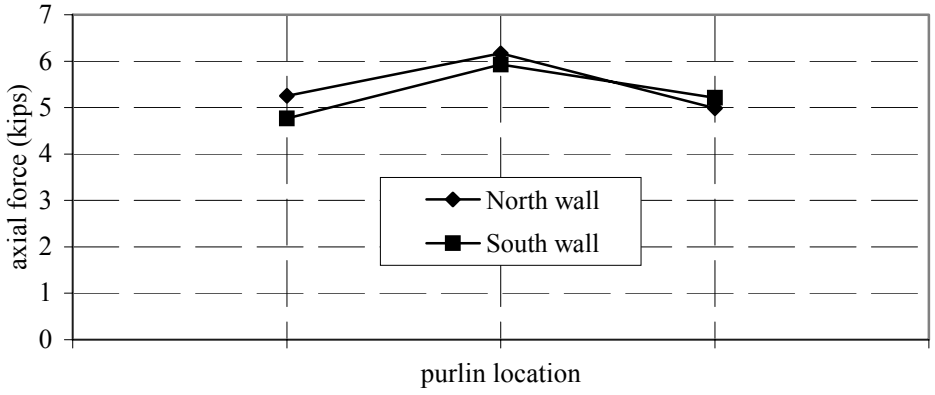

(c)

Fig. 6.50 Axial force in linear connection elements, Landers

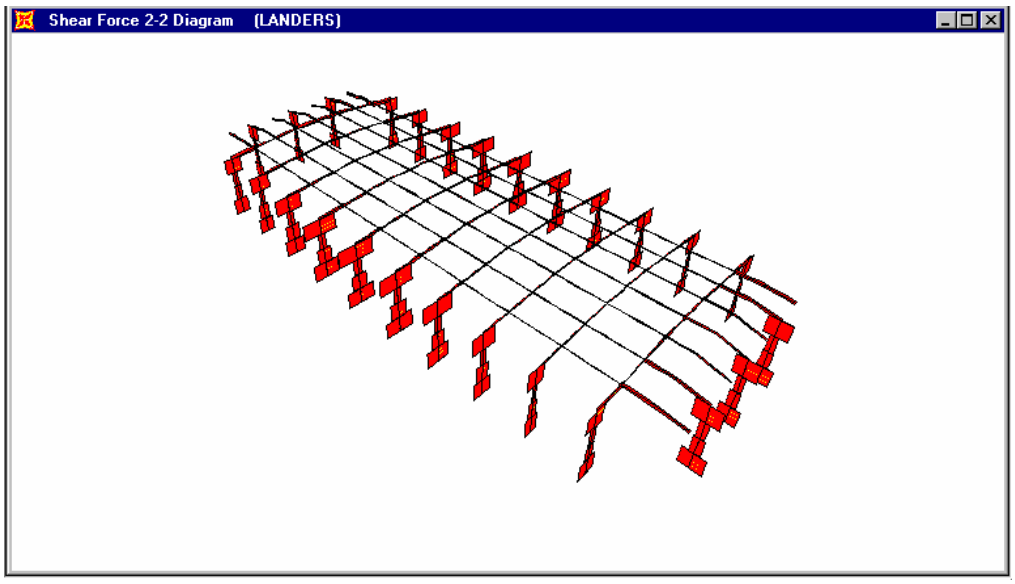

(a) Landers: 2-2 shear — disconnected corners, springs between roof elements and pilasters

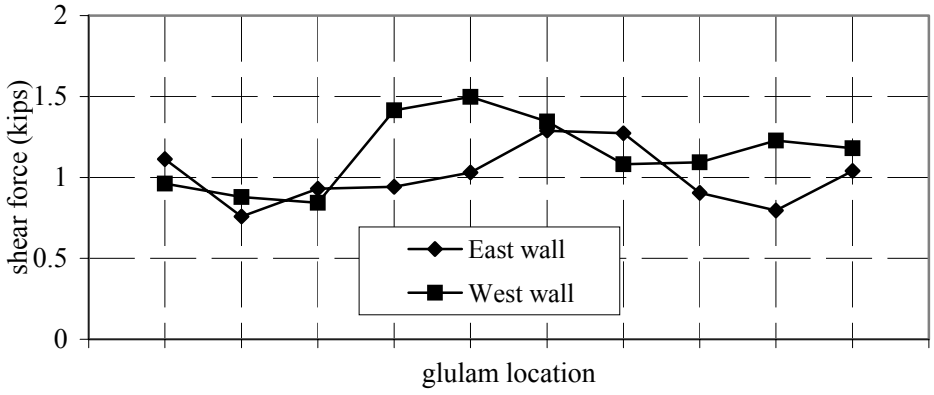

(b)

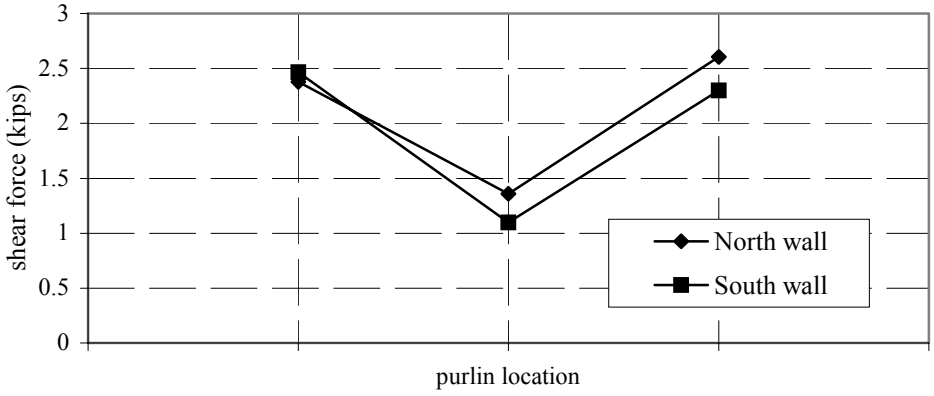

(c)

Fig. 6.51 Vertical shear force in linear connection elements, Landers

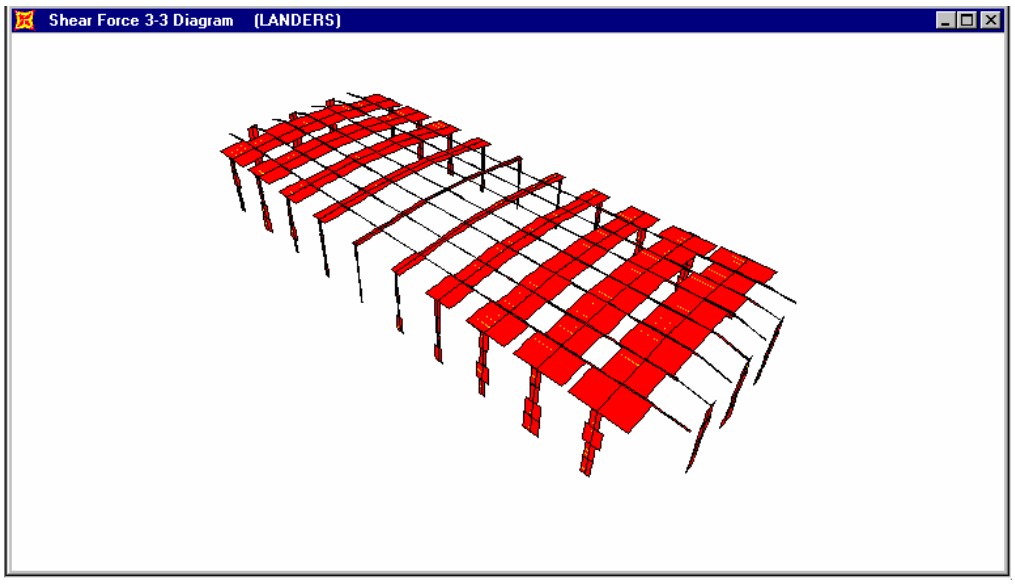

(a) Landers: 3-3 shear — disconnected corners, springs between roof elements and pilasters

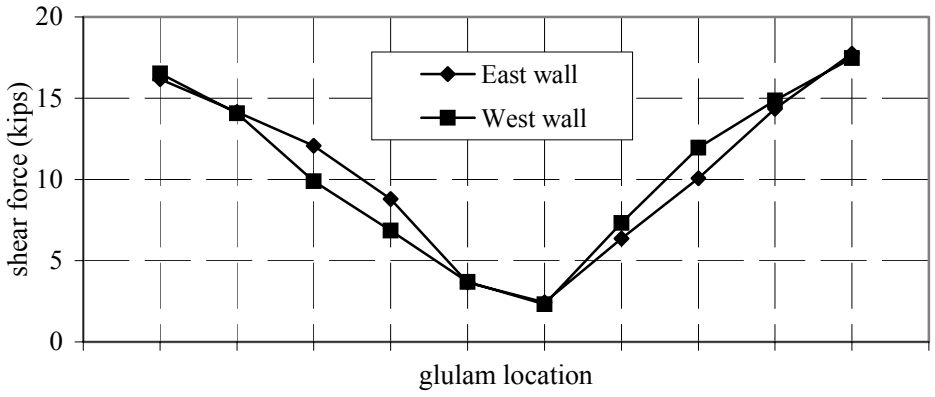

(b)

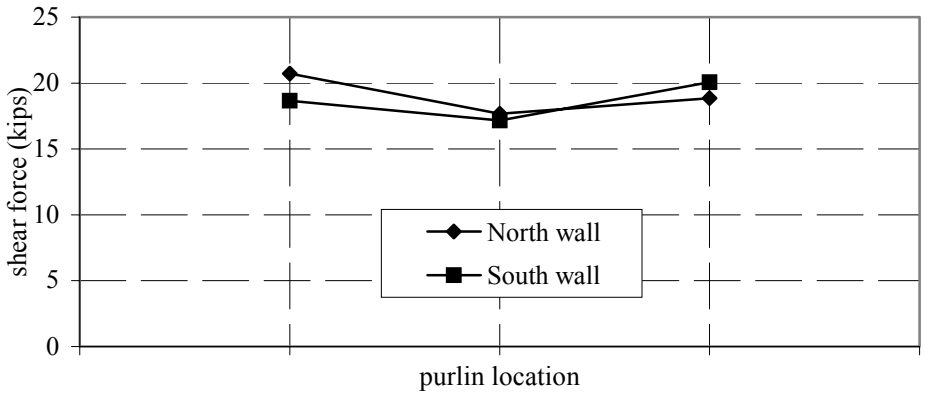

(c)

Fig. 6.52 Horizontal shear force in linear connection elements, Landers

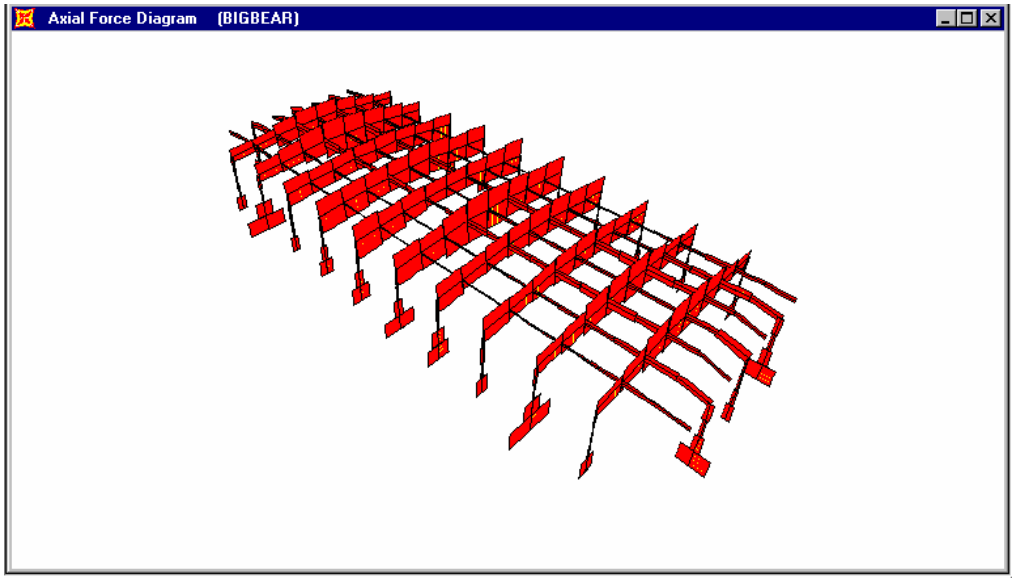

(a) Big Bear: axial force — disconnected corners, springs between roof elements and pilasters

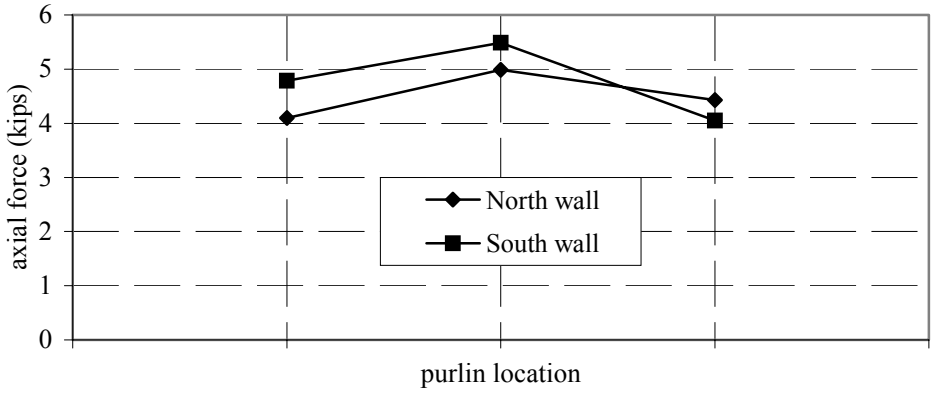

(b)

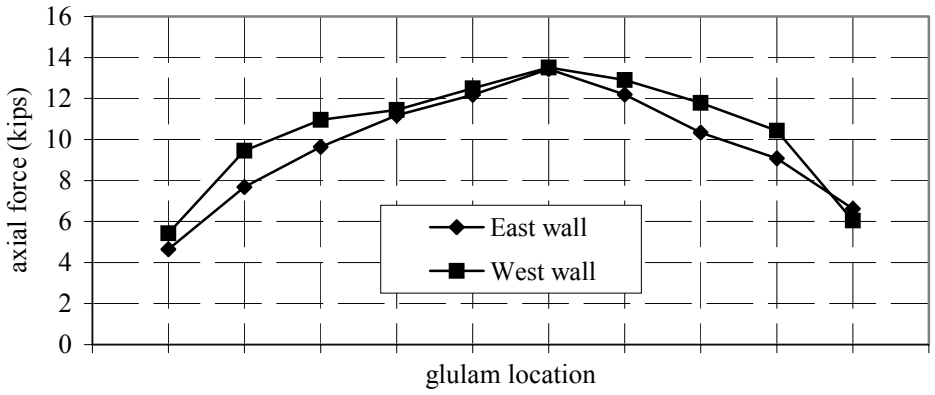

(c)

Fig. 6.53 Axial force in linear connection elements, Big Bear

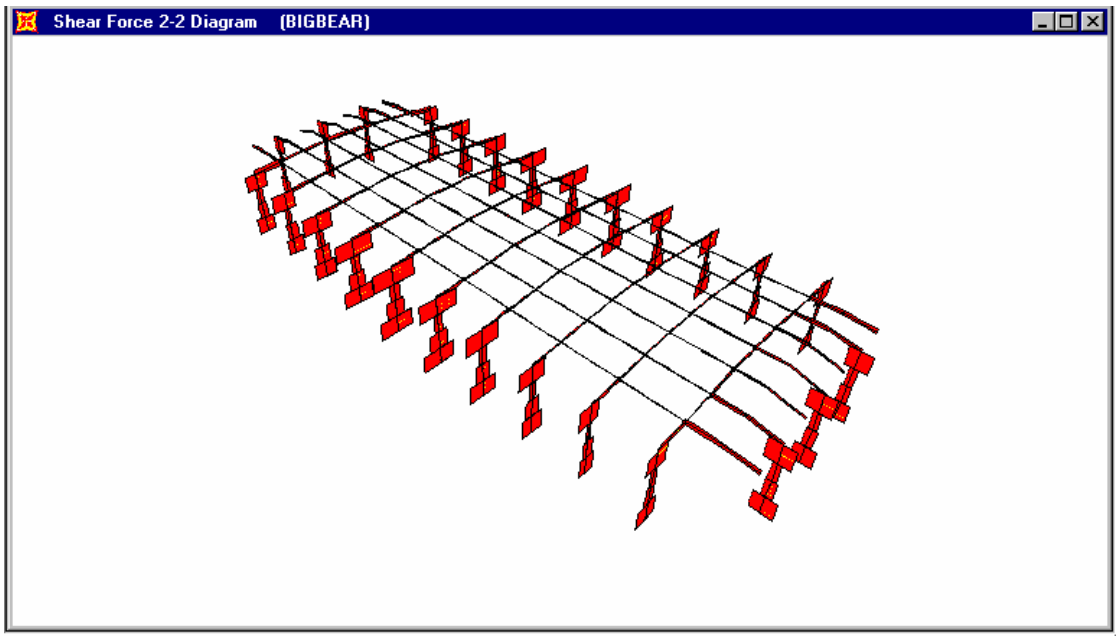

(a) Big Bear: 2-2 shear — disconnected corners, springs between roof elements and pilasters

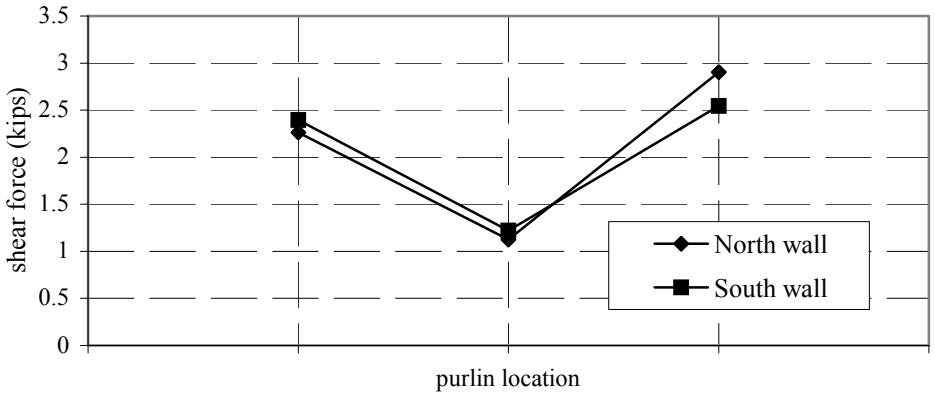

(b)

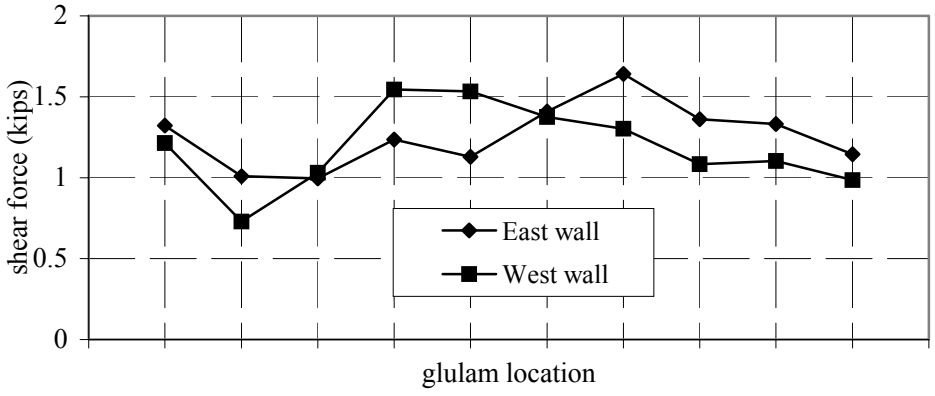

(c)

Fig. 6.54 Vertical shear force in linear connection elements, Big Bear

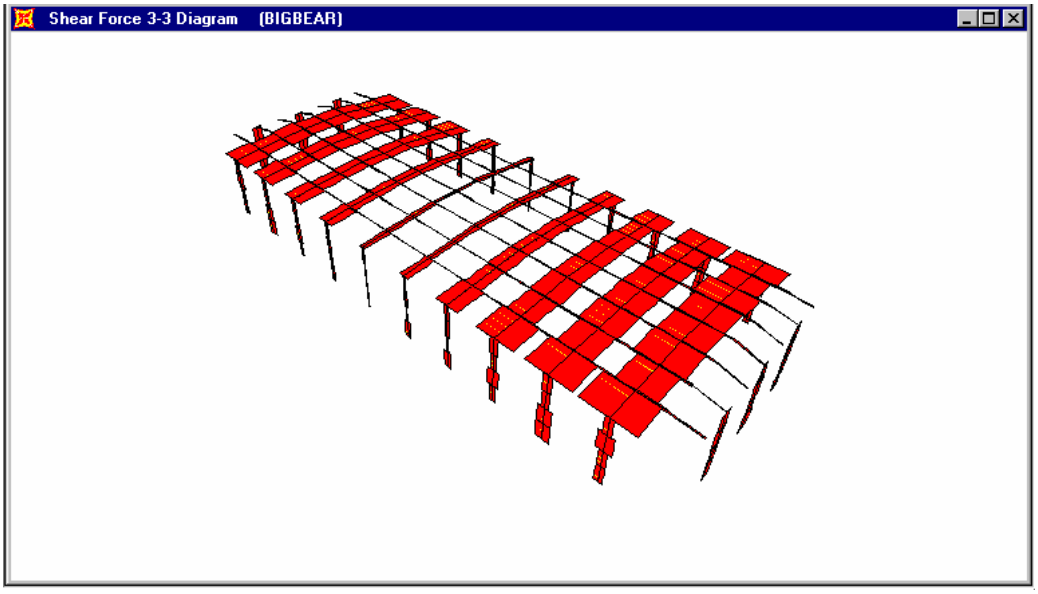

(a) Big Bear: 3-3 shear — disconnected corners, springs between roof elements and pilasters

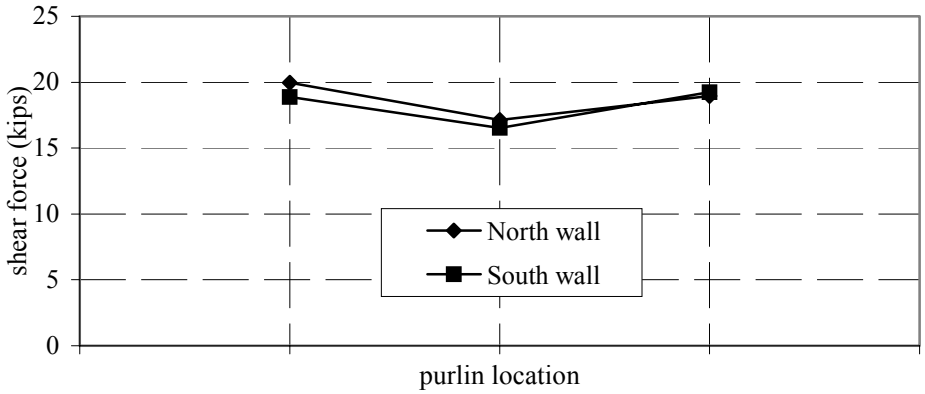

(b)

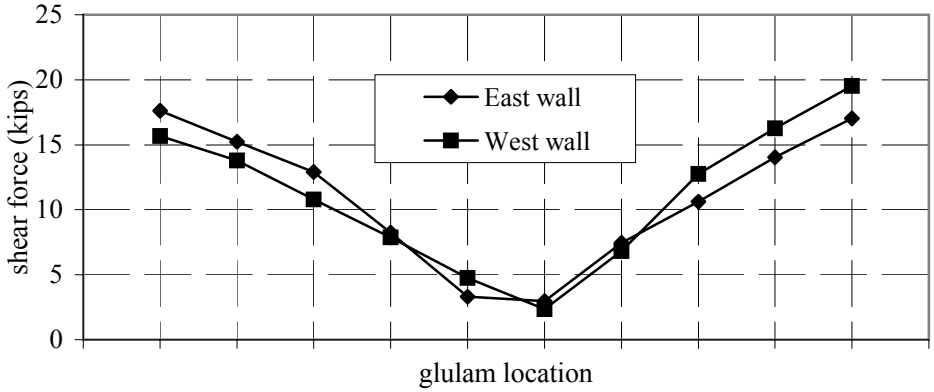

(c)

Fig. 6.55 Horizontal shear force in linear connection elements, Big Bear

6.4 RESPONSE TO PULSE-TYPE GROUND MOTIONS

6.4.1 Base Shear Demand versus Design Base Shear

In this section, the response of the tilt-up building is investigated for the effect of severe pulse-type ground motions recorded during recent earthquakes. Three recorded ground motions were selected as representative of generic types of pulse-type ground motions. The ground acceleration recorded at Lucerne during the Landers earthquake is representative of a one-sided displacement pulse, whereas the ground acceleration recorded at the Takatori Station during the Kobe earthquake represents a two-sided displacement pulse. The third ground motion record, obtained at the Los Gatos Presentation Center during the Loma Prieta earthquake, is representative of a multiple-sided displacement pulse.

Linear springs are included at the roof to pilaster connection in order to obtain an estimate of the forces in the connection elements. In all cases, the two horizontal components of the recorded ground motion are applied in the two principal directions of the building.

The calculated base shear is compared to the base shear design requirement of UBC ’97 in Figures 6.56–6.58 for the three ground motions. The time histories of the base shear demand in the transverse (E-W) direction for the Lucerne ground motion is shown in Figure 6.56a. It can be seen that the calculated base shear reaches a maximum value of 880 kips and that during the earthquake the base shear exceeds 400 kips on as many as 14 cycles in one direction and 10 cycles in the other. Both of these values are well above the design value of 247 kips. In the longitudinal direction (N-S) (Fig. 6.56b), the maximum calculated base shear is 340 kips and the design base shear is exceeded only two times in one direction and four times in the other.

The time histories of the calculated base shear for the ground motions at Takatori are shown in Figure 6.57. In the transverse direction (Fig. 6.57a), the maximum value reaches almost 2300 kips and there are more than 33 excursions above the design base shear value. The magnitude and duration of this base shear is an indication of the potential for significant inelastic behavior in the building in this direction. In the longitudinal direction (Fig. 6.57b), the base shear demand is much less severe, reaching a maximum value of 390 kips. It can also be seen that the number of excursions above the code design level are 4 in one direction and 6 in the other.

Time histories of the base shear demand for the Los Gatos ground motions are shown in Figure 6.58. The base shear for the transverse direction (Fig. 6.58a) indicates a maximum value of 1667 kips. The number of excursions of the base shear above the code design value is also

significant with 31 in both directions. Therefore, this ground motion may result in significant nonlinear behavior in this building with an increased damage potential. The calculated base shear in the longitudinal direction (Fig. 6.58b) indicates a much lower base shear demand. The maximum base shear reaches 425 kip with 6 excursions above the code design value in one direction and 7 in the other.

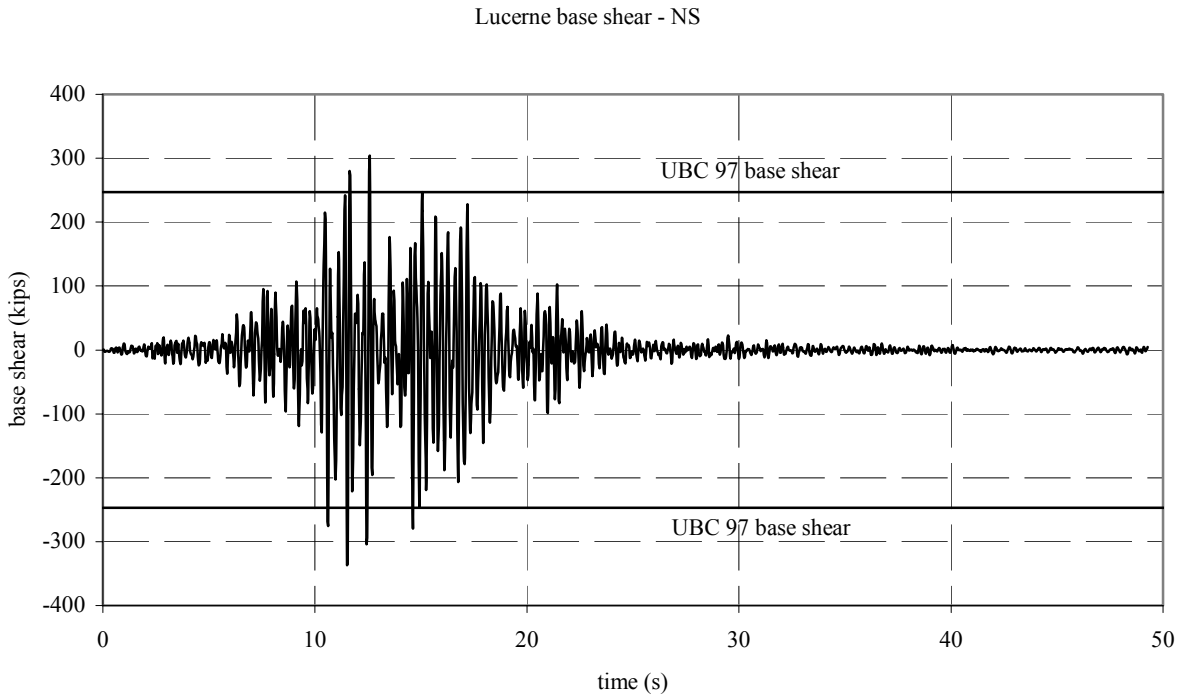

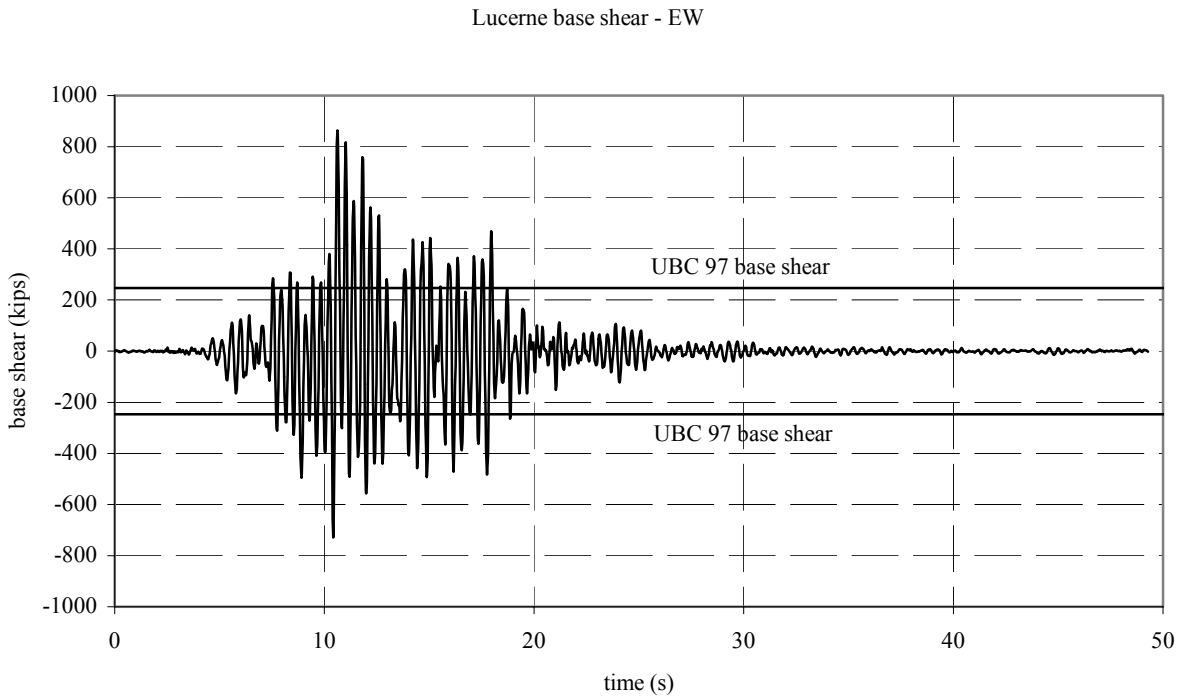

Fig. 6.56 Base shear, Lucerne

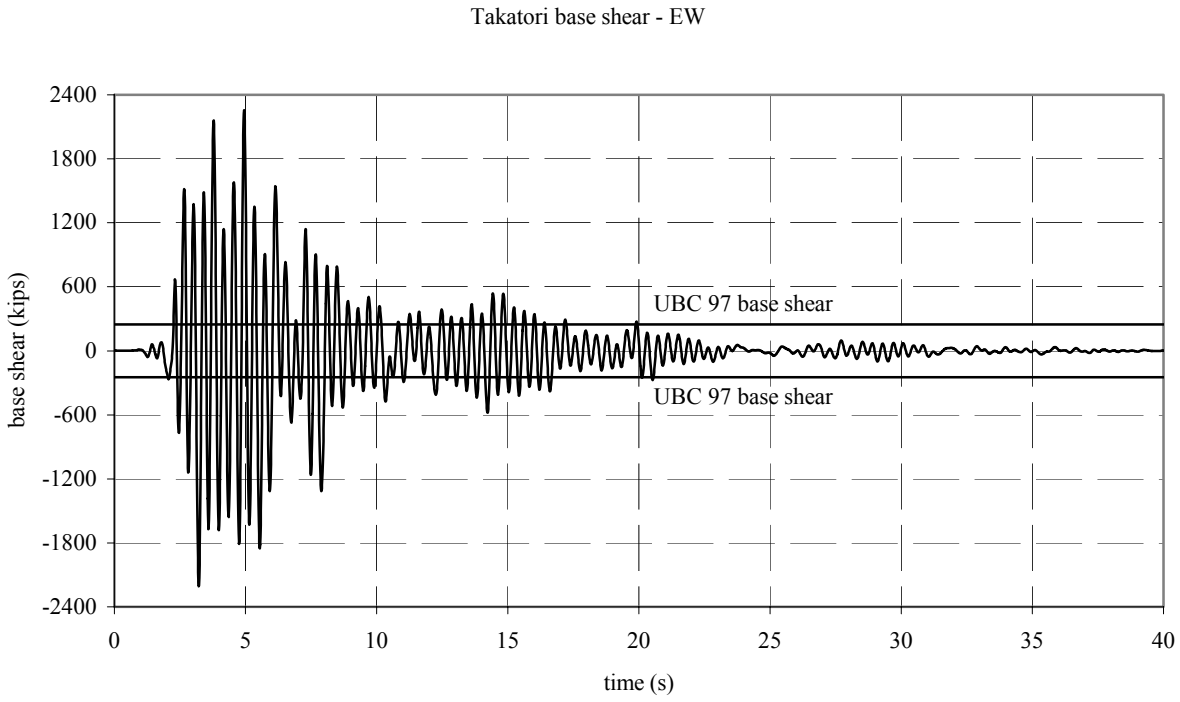

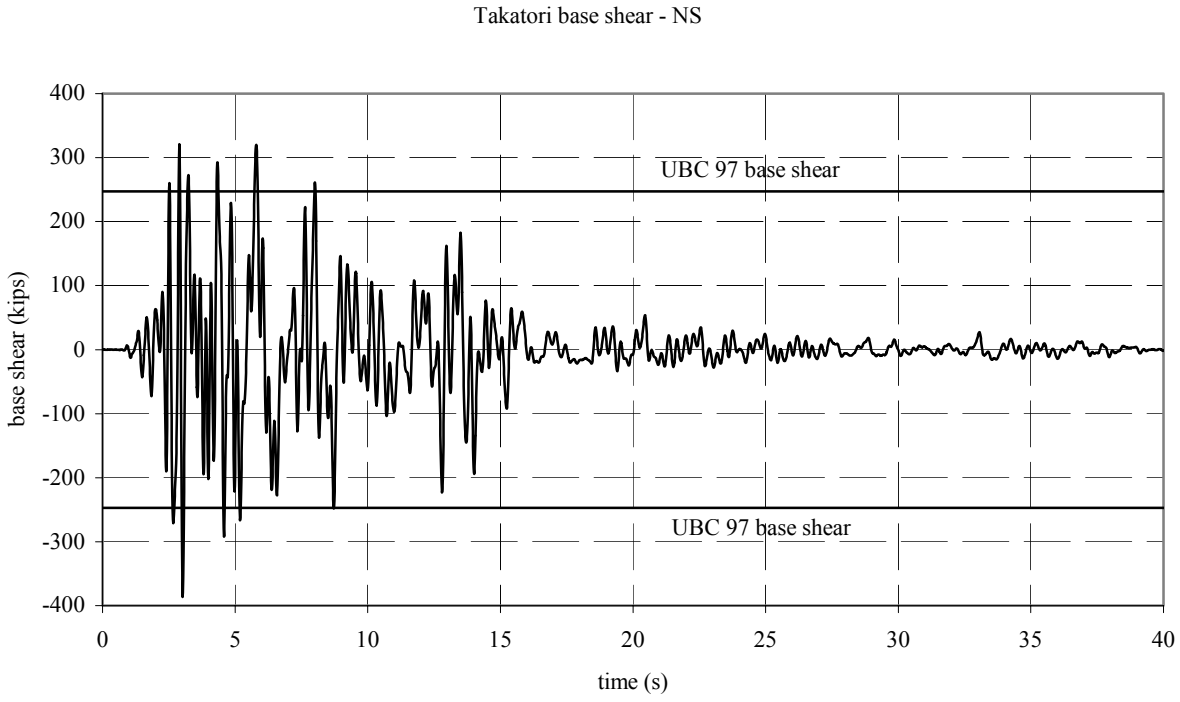

Fig. 6.57 Base shear, Takatori

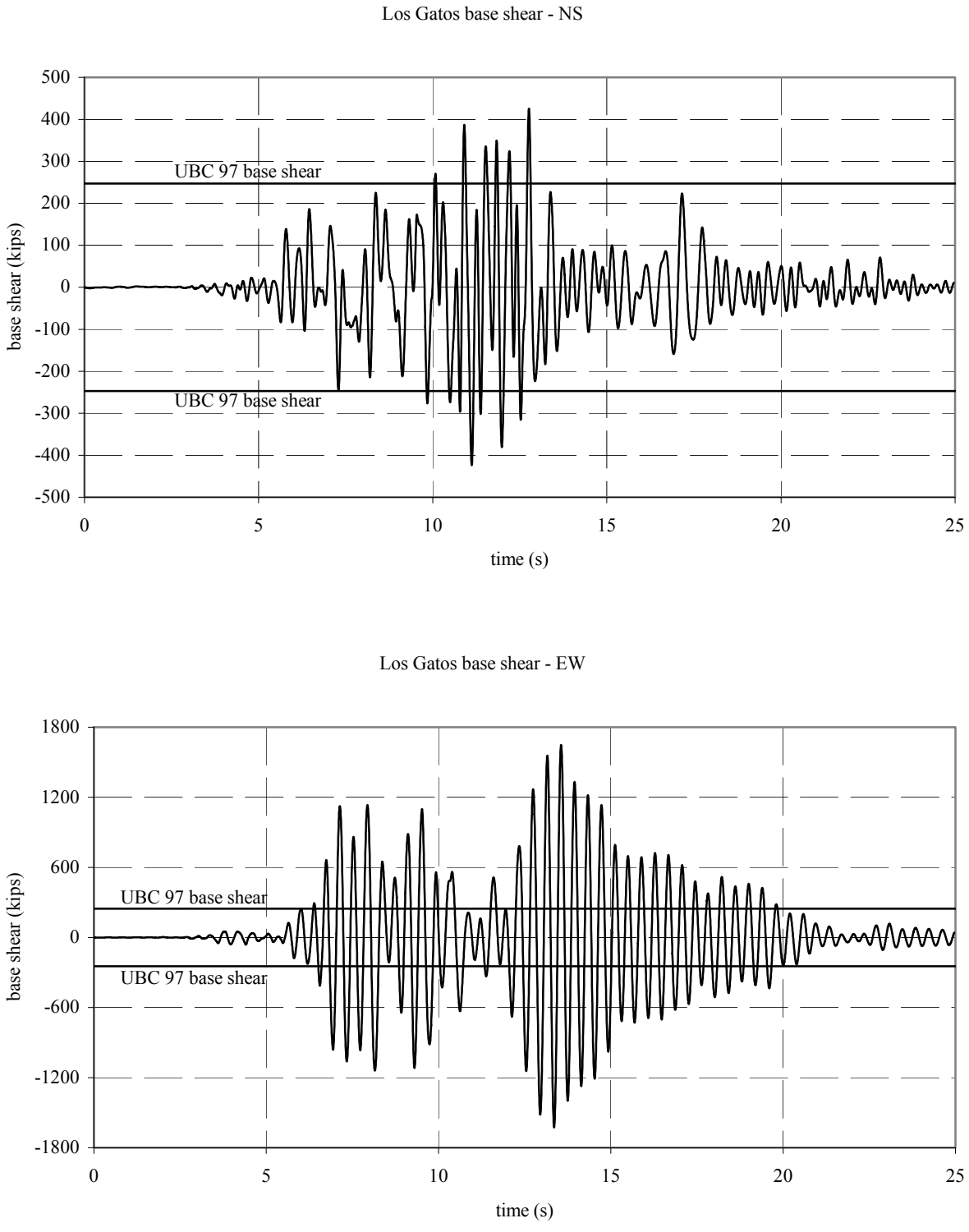

Fig. 6.58 Base shear, Los Gatos

6.4.2 Roof to Wall Connections

Forces in the connections of the glulam beams to the walls (transverse) and the purlins to the walls (longitudinal) are summarized in Figures 6.59–6.67. Force components are identified as axial force, vertical shear, and horizontal shear. Axial forces in the frame elements and connections under the Lucerne ground motion are shown in Figure 6.59. An isometric view of the axial forces in the frame elements is shown in Figure 6.59a. The axial forces in the three purlins that connect to pilasters (Fig. 6.59b) indicate that the maximum axial force occurs at the midwall position and has a value of 24 kips. The distribution of axial forces in the glulam to pilaster connections (Fig. 6.59c) indicates a maximum value of 26 kips near the center of the east and west walls. The results of tests on connections of this type, conducted by others, are summarized in Appendix A. The older type of connection is seen to have started yielding at about 13 kips, whereas the connection representative of current practice does not begin to yield until 26 kips. Therefore, the older connection would not be adequate for resisting in an elastic manner the axial force due to this earthquake, whereas the new connection would.

The distributions of vertical shear in the glulam to wall and purlin to wall connections are shown in Figure 6.60. The maximum value in the purlin connection is approximately 5.5 kips, and the maximum value in the glulam connection is just under 5 kips. With these relatively low demands, the connection in this direction is not considered to be critical and either the old or new connection will be adequate for this ground motion. However, it should be noted that this shear component will be sensitive to the vertical component of ground motion, which will be discussed in a later section. The distribution of the horizontal shear forces connecting the wall to the roof is shown in Figure 6.61. The shear forces in the purlins (Fig. 6.61b) indicate that maximum values occur at the ends of the wall and reach a value of 44 kips. The distribution for the horizontal shear in the connection of the glulam beams to the roof diaphragm (Fig. 6.61c) indicates a maximum value of 36 kips near the end wall.

Axial forces in the frame elements and connections under the Takatori ground motion are shown in Figure 6.62. An isometric view of the axial forces in the frame elements is shown in Figure 6.62a. The axial forces in the three purlins that connect to pilasters (Fig. 6.62b) indicate that the maximum axial force occurs at the midwall position and has a value of 23 kips. The distributions of axial forces in the glulam to pilaster connections (Fig. 6.62c) indicate a maximum value of 69 kips near the center of the east and west walls. Although the older type of

connection has an idealized yield of about 26 kips compared to the initial yield of about 13 kips, it is still well below the demanded connection capacity. For the current connection detail, the idealized yielding strength is about 34 kips, well below the demand. Therefore, either the old or the new connection will be loaded well into the inelastic range under this ground motion. This behavior will be investigated in Section 7 which follows.

The distributions of vertical shear in the glulam to wall and purlin to wall connections are shown in Figure 6.63. The maximum value in the purlin connection is approximately 14.0 kips and the maximum value in the glulam connection is about 7.5 kips. With these relatively low demands, the connection in this direction is not considered to be critical and either the old or new connection will be adequate for this ground motion depending on the effect of vertical ground accelerations. The distributions of the horizontal shear forces in the connections of the wall to the roof are shown in Figure 6.64. The shear forces in the purlins (Fig. 6.64b) indicate that maximum values occur at the ends of the wall and reach a value of 99 kips, which is well into the inelastic range. The distribution for the horizontal shear in the connection of the glulam beams to the pilasters is shown in Figure 6.64c. This figure indicates a maximum value of almost 90 kips near the end wall.

Axial forces in the frame elements and connections under the Los Gatos ground motion are shown in Figure 6.65. An isometric view of the axial forces in the frame elements is shown in Figure 6.65a. The axial forces in the three purlins that connect to pilasters (Fig. 6.65b**)** indicate that the maximum axial force occurs at the midwall position and has a value of just under 22 kips. The distribution of axial forces in the glulam to pilaster connections (Fig. 6.65c) indicates a maximum value of 46 kips near the center of the east and west walls. Although the older type of connection has an idealized yield of about 26 kips compared to the initial yield of about 13 kips (Appendix A), it is still well below the demanded connection capacity. For the current connection detail, the idealized yielding strength is about 34 kips, which is also below the demand. This will cause either the old or the new connection to be loaded into the inelastic range under this ground motion. This behavior will be investigated in Section 7.

The distribution of vertical shear in the glulam to wall and purlin to wall connections is shown in Figure 6.66. The maximum value at the purlin connection is just under 10.0 kips and the maximum value at the glulam connection is just over 6.0 kips. With these relatively low demands, the connection in this direction is not considered to be critical and either the old or new connection will be adequate for vertical shear, depending on the effects of vertical ground

motions. The distribution of the horizontal shear forces connecting the wall to the roof is shown in Figure 6.67. The shear forces in the purlins (Fig. 6.67b) indicate that maximum values occur at the ends of the wall and reach a value that is just under 72 kips, which will load the connection into the inelastic range. The distribution for the horizontal shear in the connection of the glulam beams to the roof diaphragm is shown in Figure 6.67c. This figure indicates a maximum value of almost 60.5 kips near the end wall.

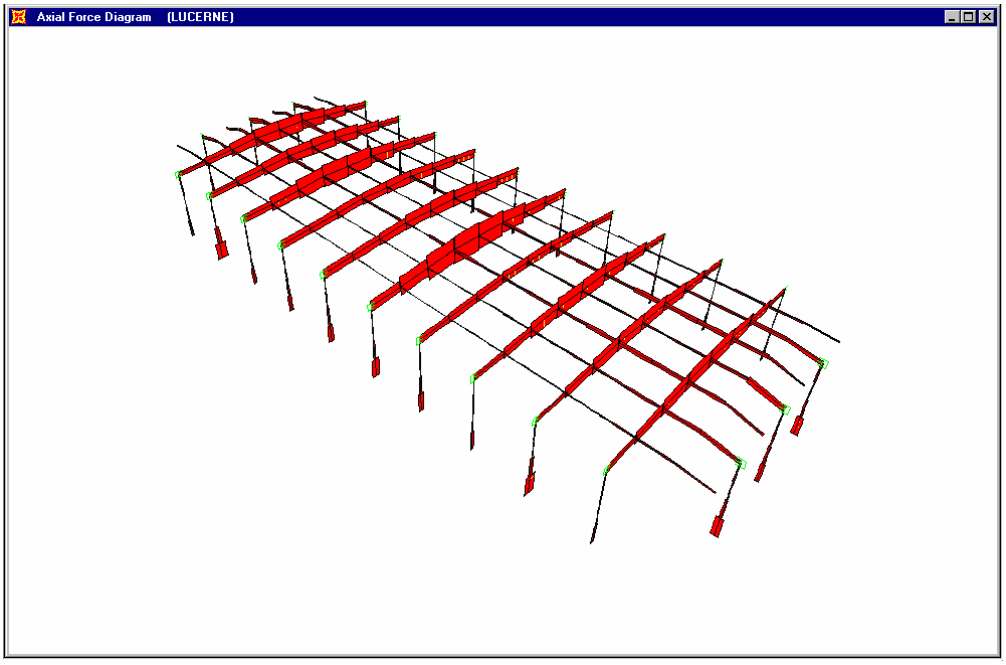

(a) Lucerne, 1-1 axial force

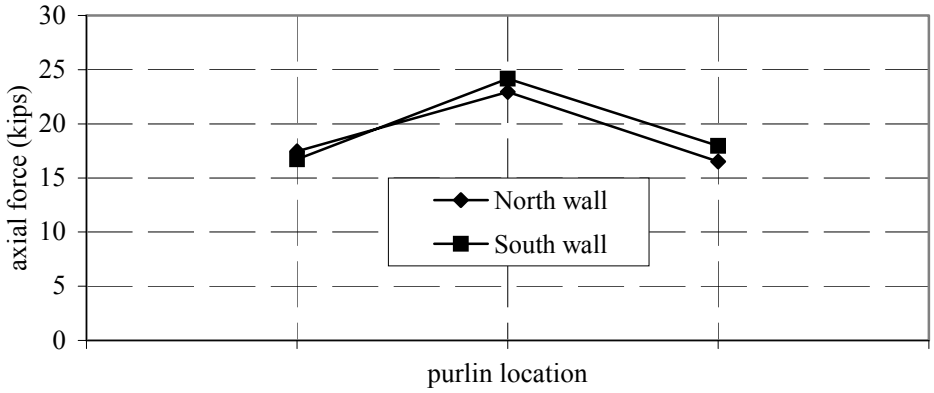

(b)

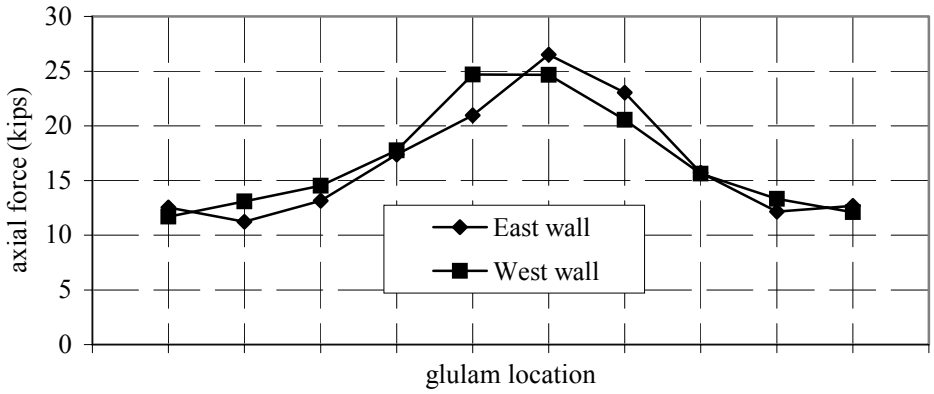

(c)

Fig. 6.59 Axial force in linear connection elements, Lucerne

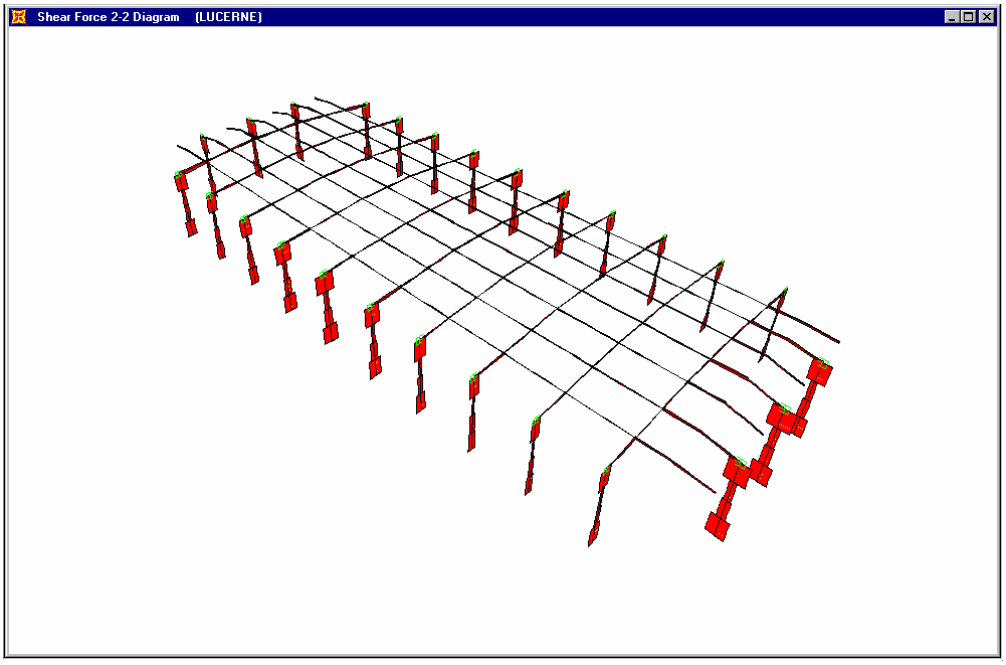

(a) Lucerne, 2-2 shear force

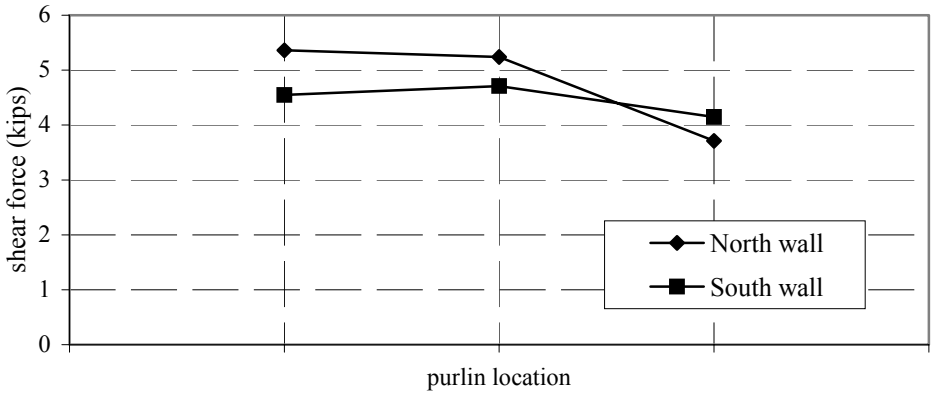

(b)

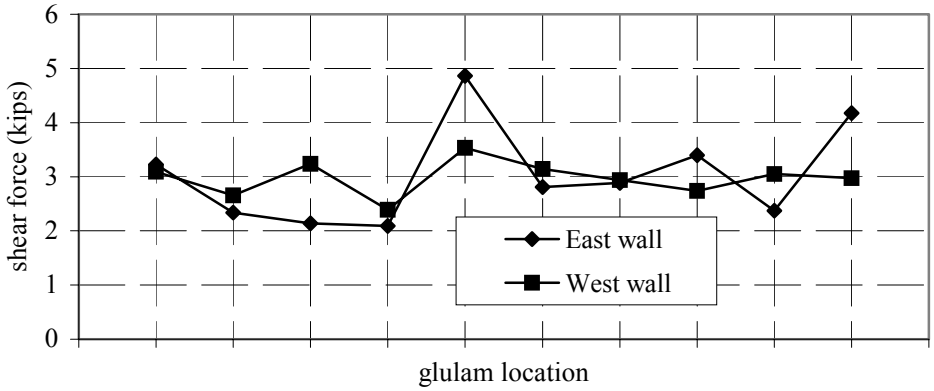

(c)

Fig. 6.60 Vertical shear force in linear connection elements, Lucerne

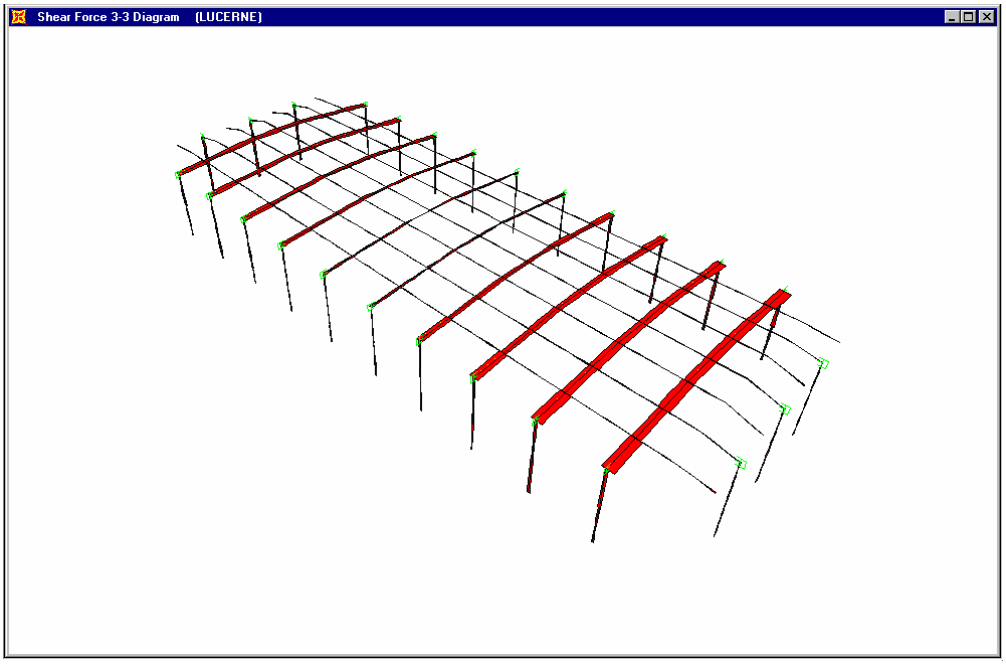

(a) Lucerne, 3-3 shear force

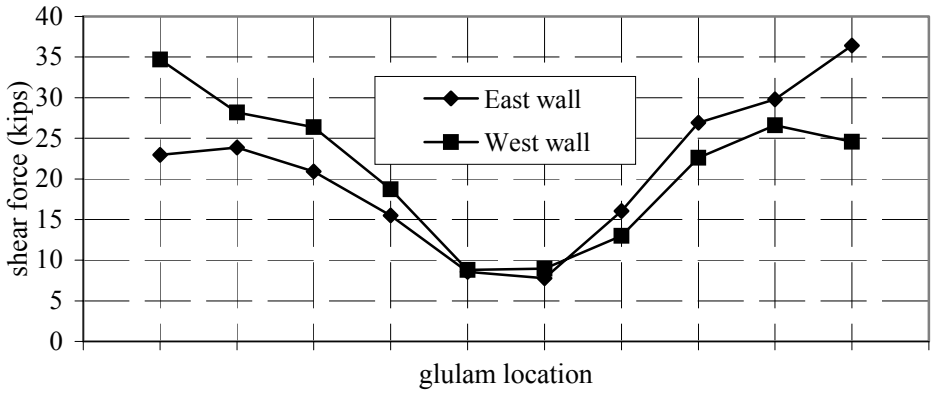

(b)

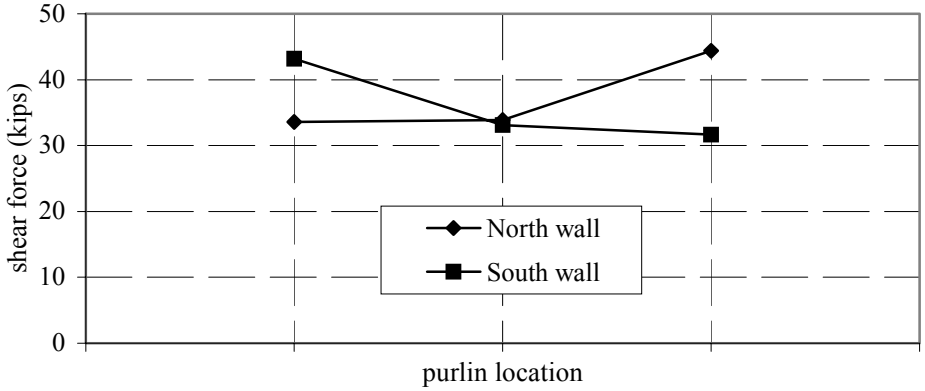

(c)

Fig. 6.61 Horizontal shear force in linear connection elements, Lucerne

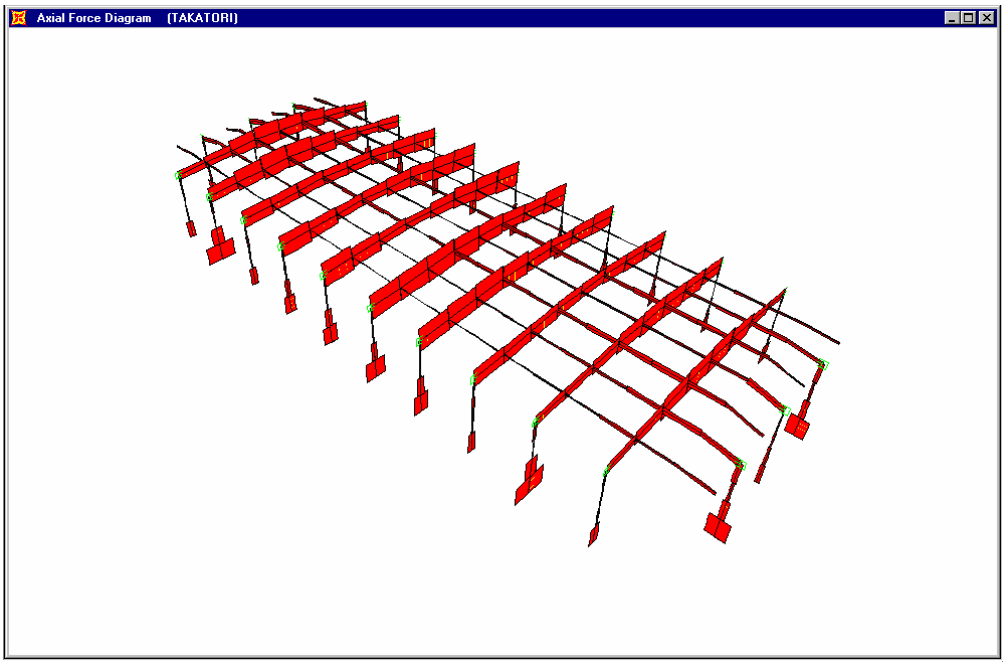

(a) Takatori, 1-1 axial force

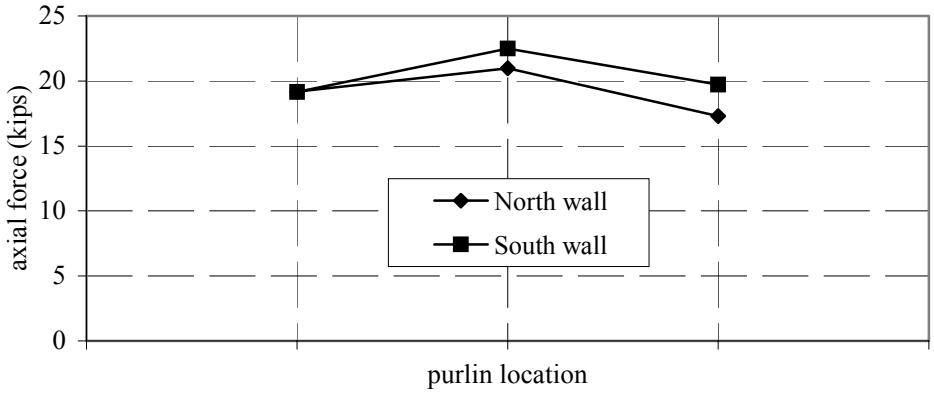

(b)

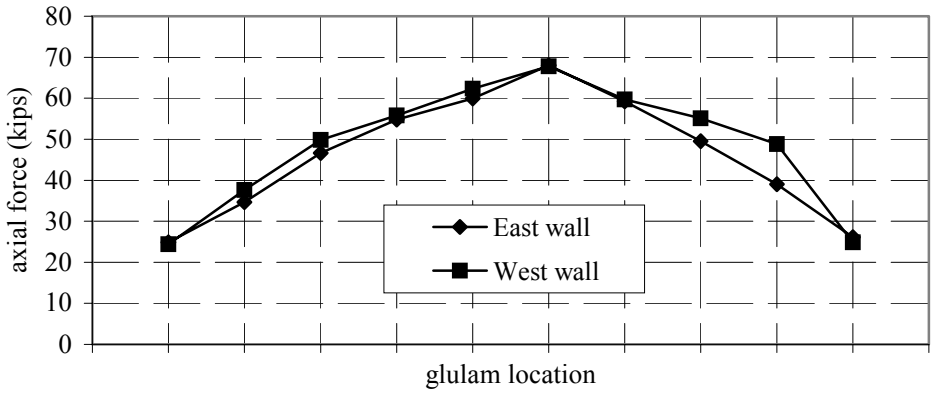

(c)

Fig. 6.62 Axial force in linear connection elements, Takatori

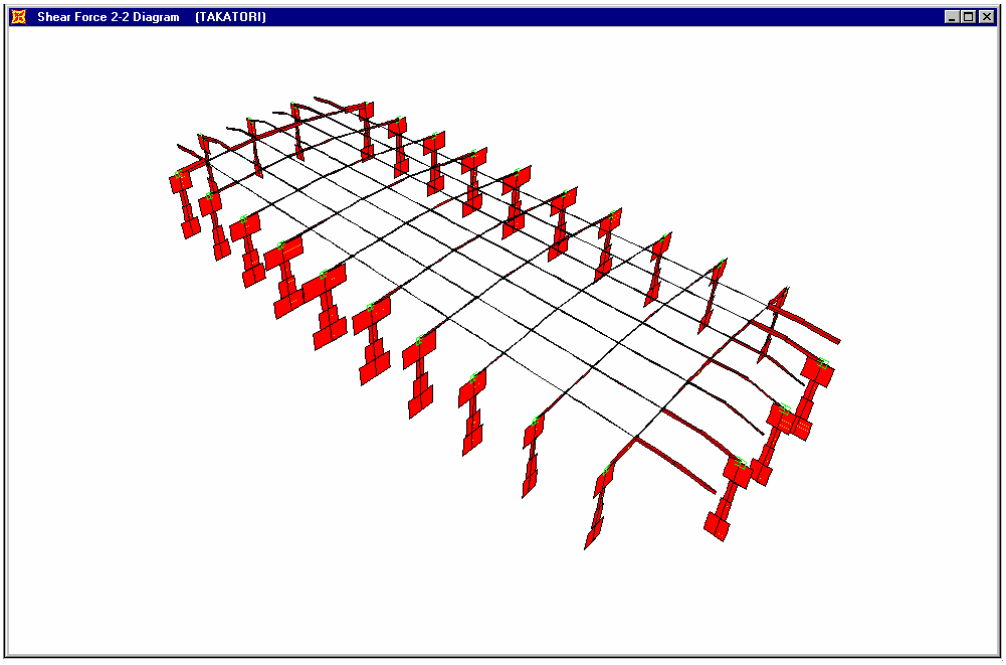

(a) Takatori, 2-2 shear force

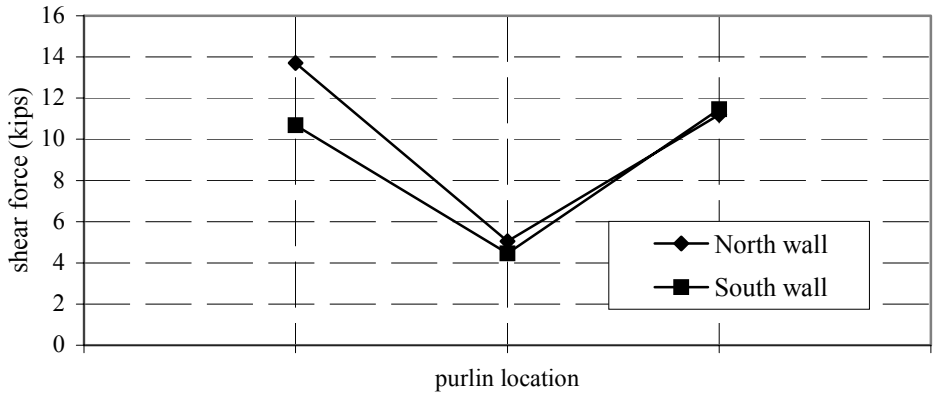

(b)

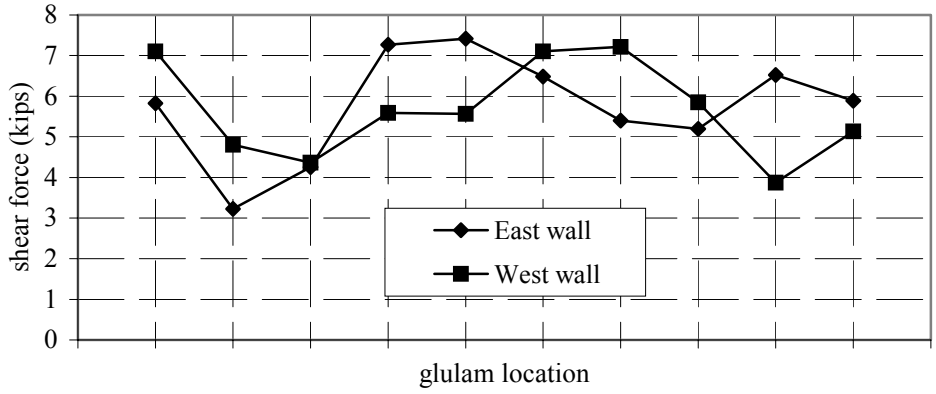

(c)

Fig. 6.63 Vertical shear force in linear connection elements, Takatori

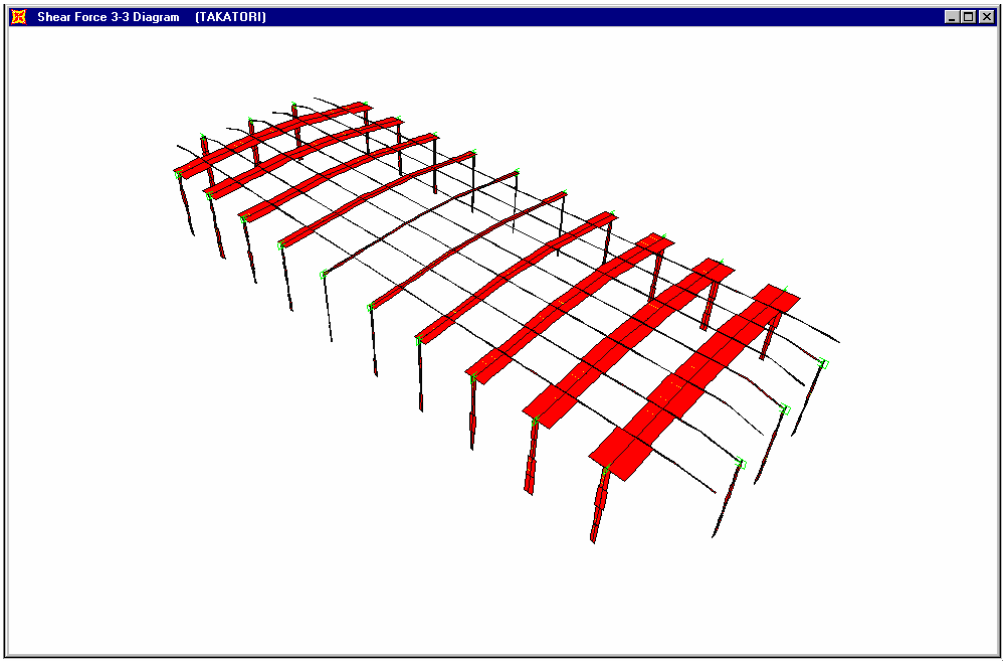

(a) Takatori, 3-3 shear force

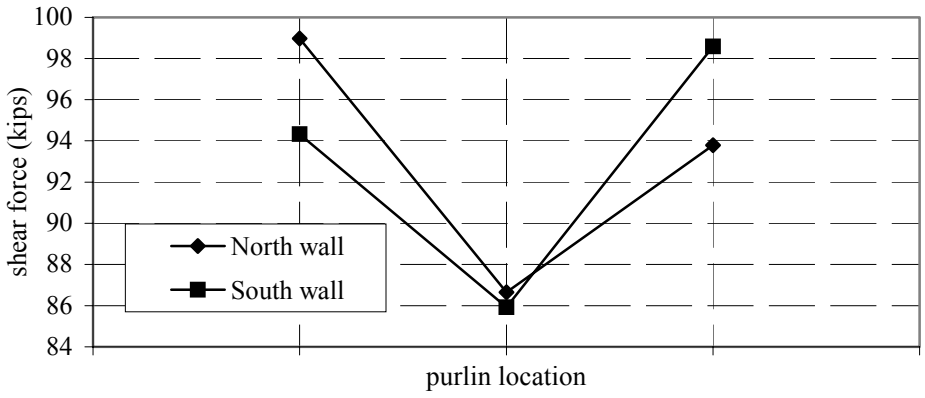

(b)

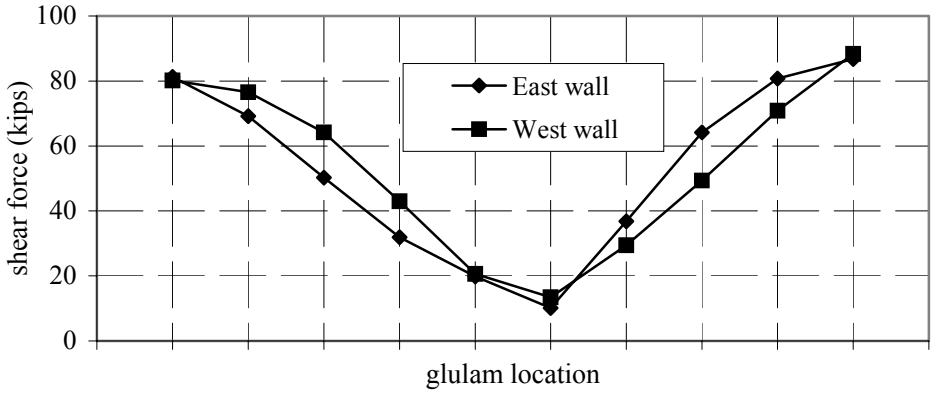

(c)

Fig. 6.64 Horizontal shear force in connection elements, Takatori

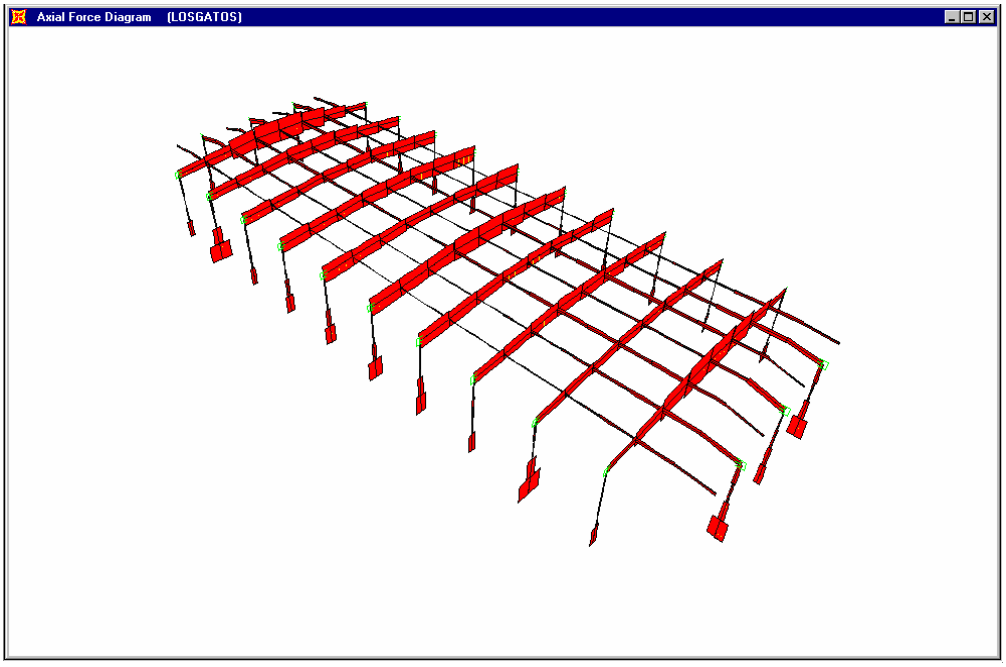

(a) Los Gatos, 1-1 axial force

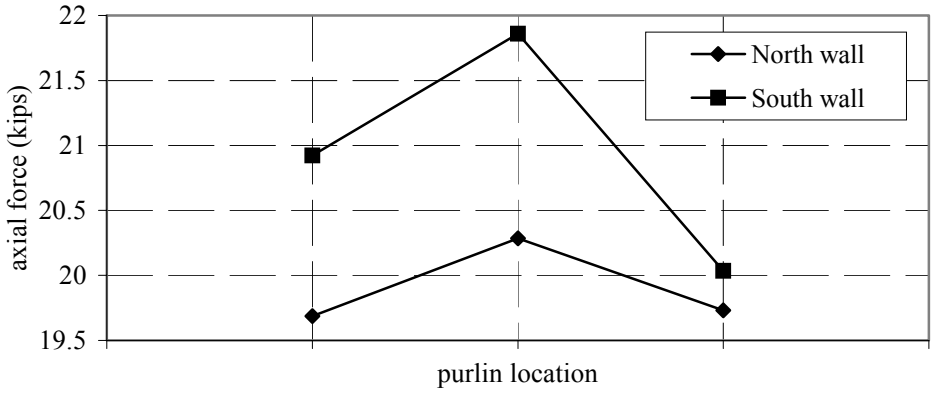

(b)

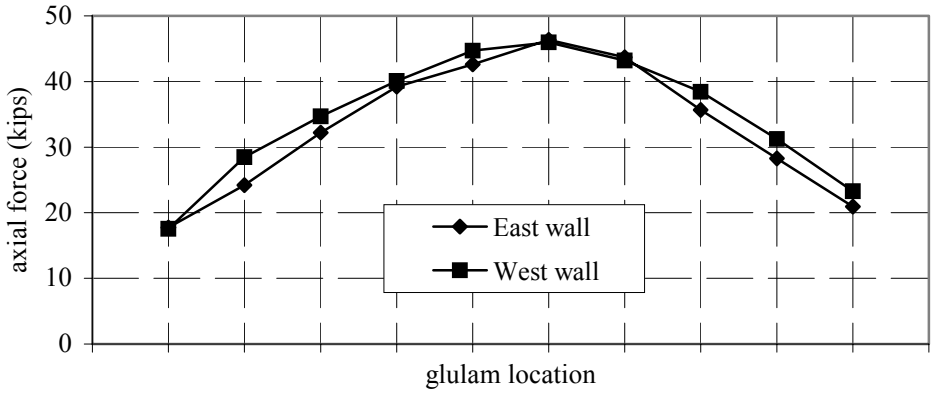

(c)

Fig. 6.65 Axial force in linear connection elements, Los Gatos

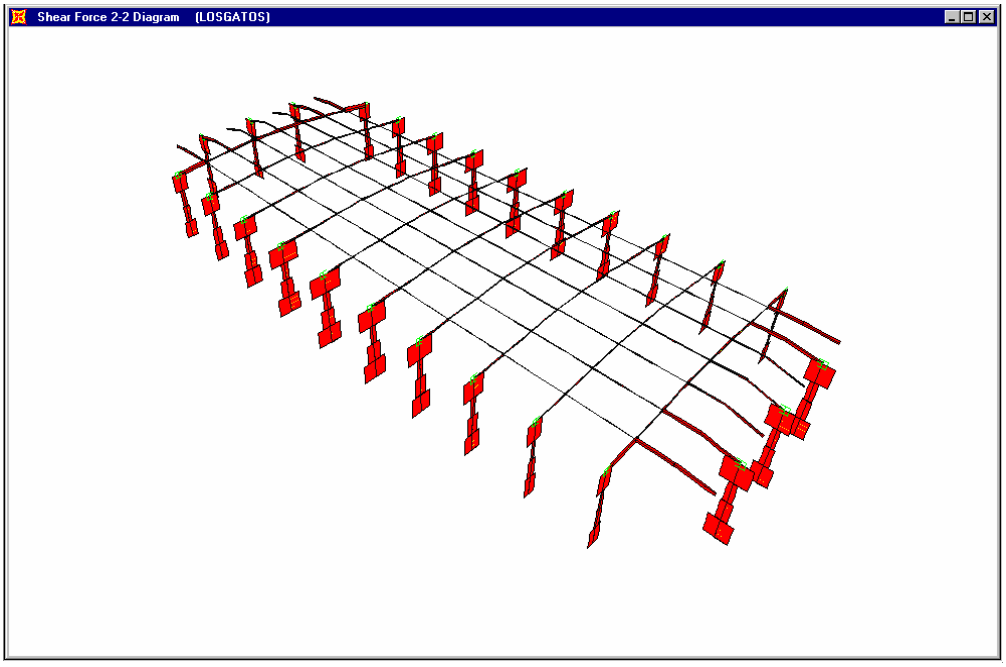

(a) Los Gatos, 2-2 shear force

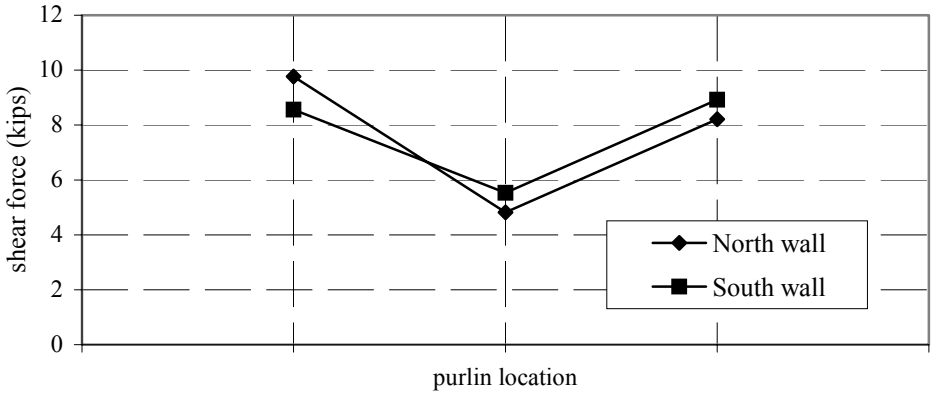

(b)

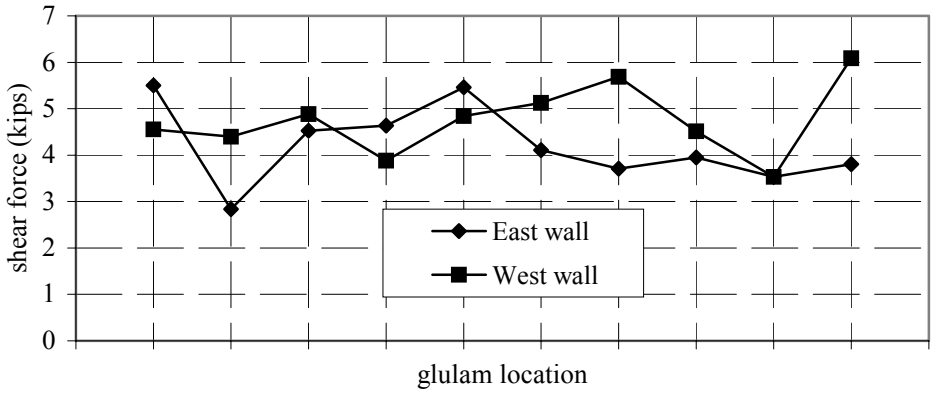

(c)

Fig. 6.66 Vertical shear force in linear connection elements, Los Gatos

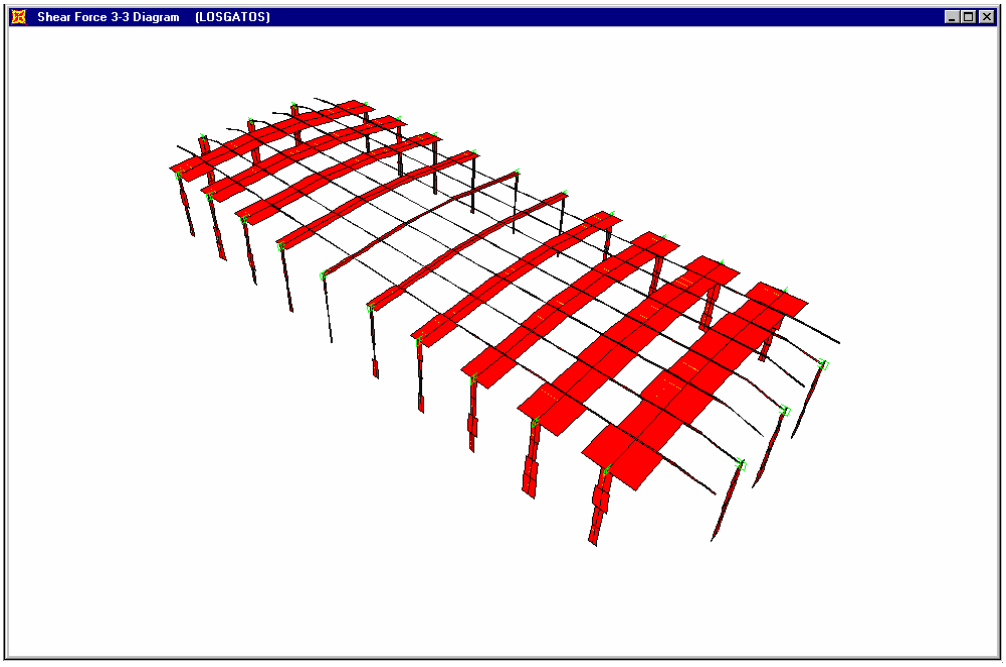

(a) Los Gatos, 3-3 shear force

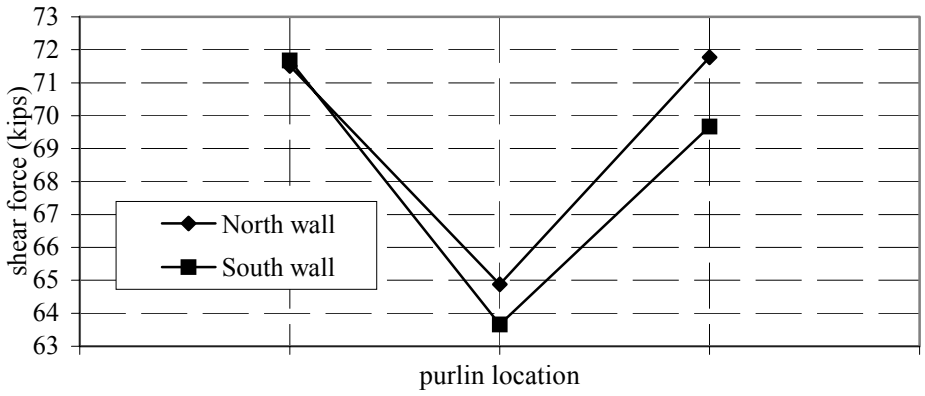

(b)

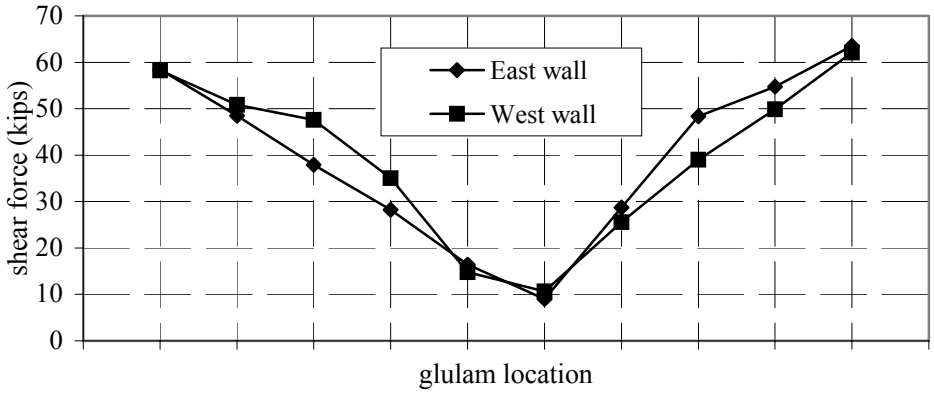

(c)

Fig. 6.67 Horizontal shear force in linear connection elements, Los Gatos

6.4.3 Force Contours under Pulse-Type Ground Motions

Contour plots of in-plane shear force and out-of-plane bending moment are presented for the three pulse-type ground motions in Figures 6.68–6.81. Contour plots of the in-plane shear forces in the north and south walls are shown in Figure 6.68 for the Lucerne ground motion. Neglecting localized areas of high shear, the maximum shear flow in both walls is 0.42 kips/in. Contours for the east and west walls (Fig. 6.69) indicate that there are local areas in both walls where the shear flow reaches 0.36 kips/in. Contours for the out-of-plane moments in the north and south walls are shown in Figure 6.70. This set of figures indicates that the maximum moment reaches a value of 8.1 in.-kips/in. The out-of-plane moments for the east and west walls, shown in Figure 6.71 indicate a maximum moment of 7.20 in.-kips/in.

The in-plane shear force in the transverse walls at the north and south ends of the building are shown in Figure 6.72 for the Takatori ground motions. It can be seen that the shear flow in the wall is far from uniform. If the limited regions of high shear (1.35 kips/in.) located in the four lower corners of the wall are neglected, the largest shear flow (kips/in.) is in the center of the wall and has a value of 0.9 kips/in., which is less than the estimated strength of the wall (1.7 kips/in.). The in-plane shear contours for the longitudinal walls on the east and west side of the building are shown in Figure 6.73. In the west wall (Fig. 6.73b) on the back side of the building, there are no openings for access to the interior, and the shear flows are less than for the end wall, reaching a value of 0.6 kips/in., although a shear flow of 0.90 kips/in. is obtained at the bottom corner. For the east wall (Fig. 6.73a) the openings in the wall cause the shear flows to be more irregular, and there are two regions adjacent to the large doors where the shear flow increases to 0.9 kips/in. and 1.05 kips/in. at the bottom corner.

Contours of the out-of-plane bending moment in the north and south walls are shown in Figure 6.74. The maximum bending moment occurs near the corner and has a value of 11.7 in.-kips/in. A similar value is obtained for the east and west walls, shown in Figure 6.75 at the corners where they connect with the south and north walls.

In-plane shear contours for the north and south walls under the Los Gatos ground motion are shown in Figure 6.76. Neglecting the effects at the bottom corners, the maximum shear flow in these walls can be seen to be 0.60 kips/in. Although the distributions in the east and west walls are more irregular (Fig. 6.77), the maximum value is the same. The contours of out-of-plane moment, shown in Figure 6.78, indicate a maximum value of 12.6 in-kips/in. at the ends of the

north and south walls. For the east and west walls, shown in Figure 6.79, the maximum moment reaches only 7.0 in.-kips/in.

Contours of the in-plane shear in the roof diaphragm are shown in Figure 6.80 for the Lucerne and Takatori ground motions. For the Lucerne ground motions (Fig. 6.80a), the maximum shear flow has a value of 0.36 kips/in. A maximum value of 0.9 kips/in. is obtained for the Takatori ground motion contours (Fig. 6.80b). The in-plane shear contours for the roof diaphragm under the Los Gatos ground motions are shown in Figure 6.81. In this case the maximum shear flow has a value of 0.6 kips/in.

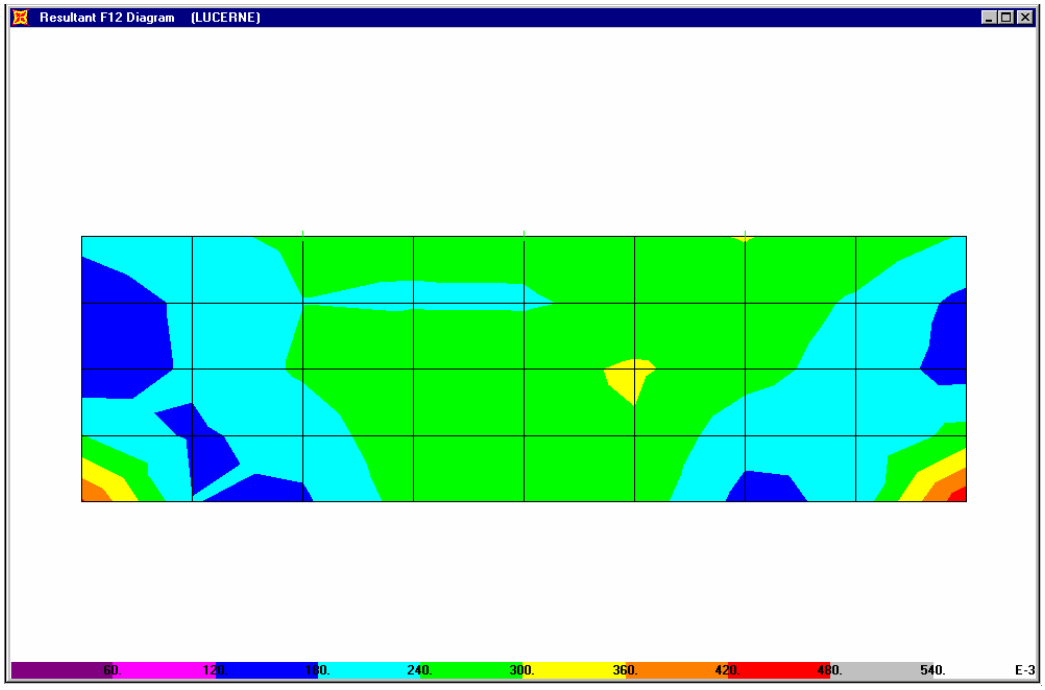

(a) In-plane shear contour, Lucerne, north wall (kips/in.)

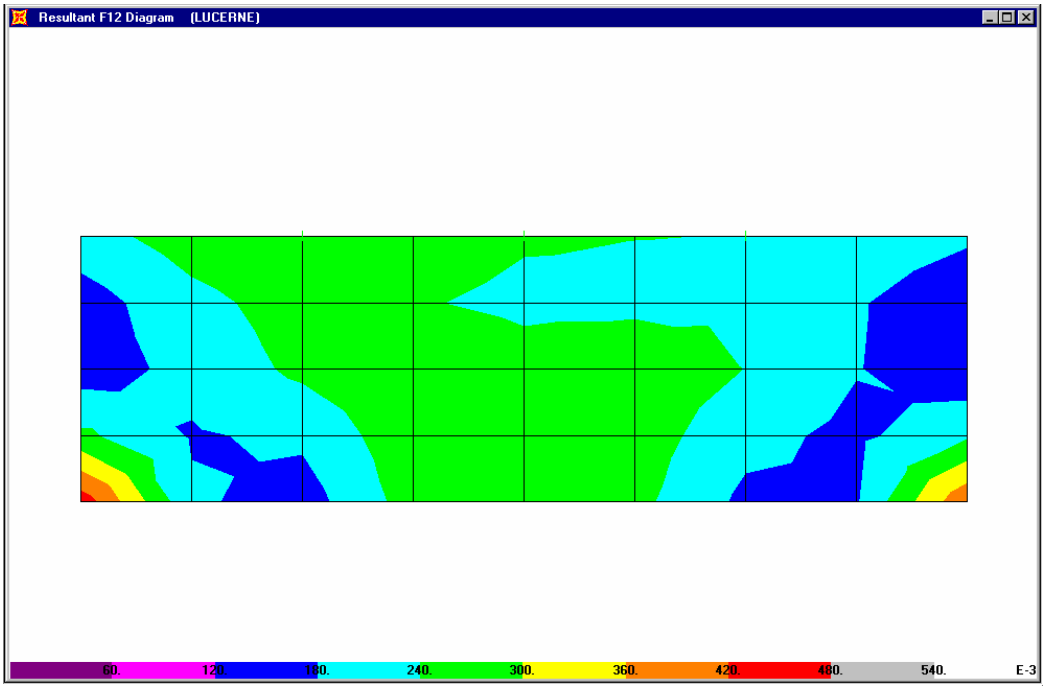

(b) In-plane shear contour, Lucerne, south wall (kips/in.)

Fig. 6.68 In-plane shear contours, north and south walls, Lucerne

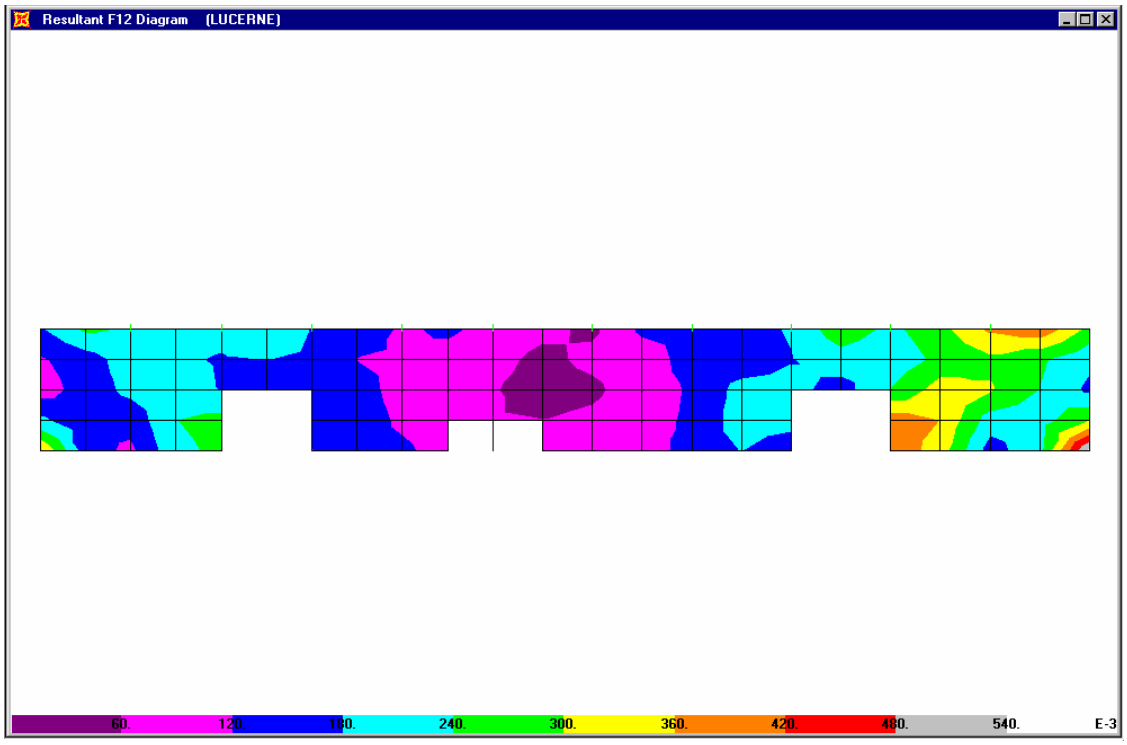

(a) In-plane shear contour, Lucerne, east wall (kips/in.)

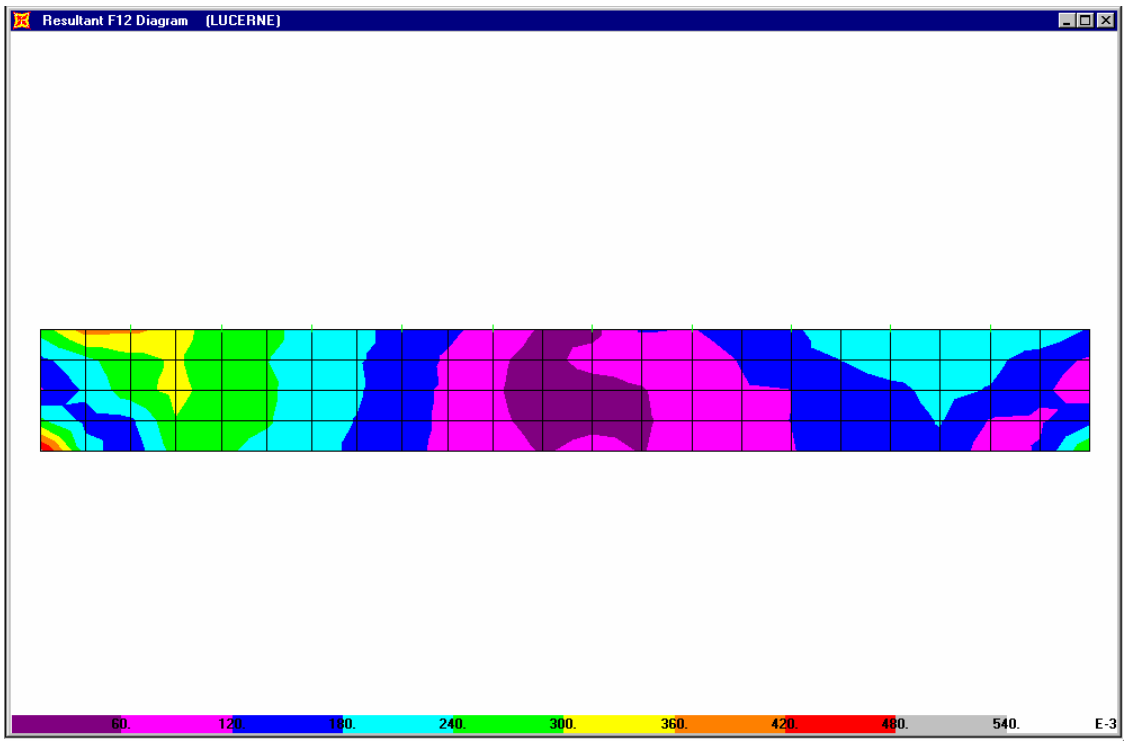

(b) In-plane shear contour, Lucerne, west wall (kips/in.)

Fig. 6.69 In-plane shear contours, east and west walls, Lucerne

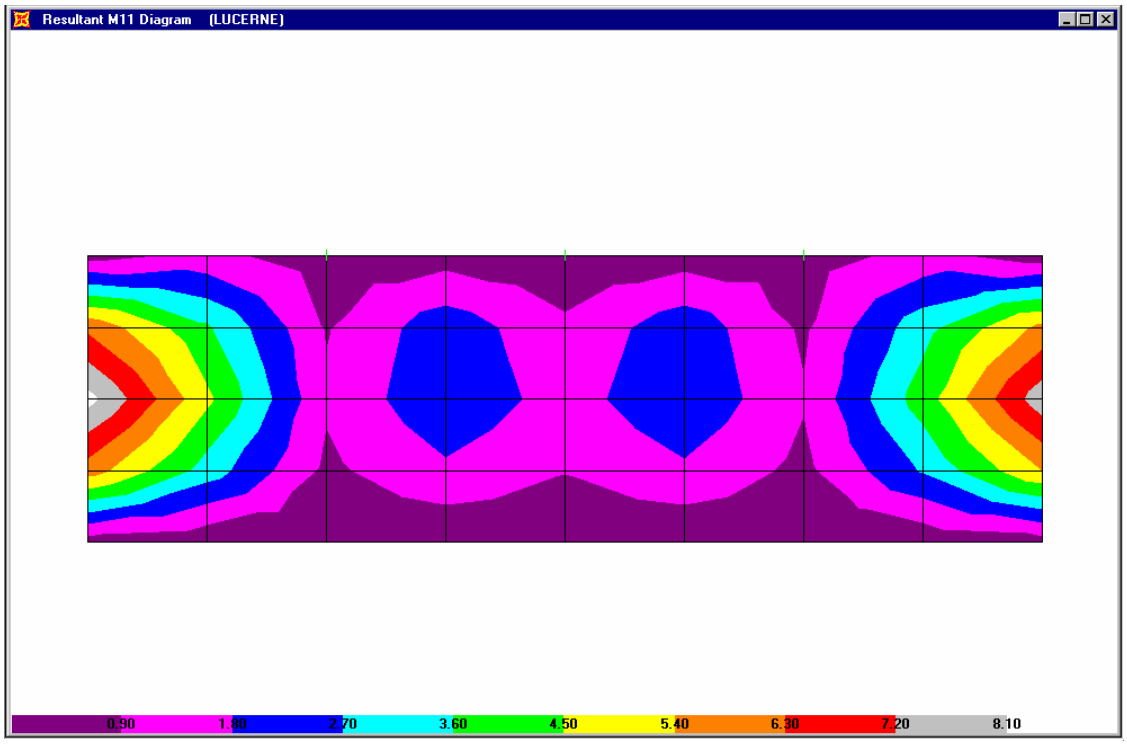

(a) Vertical out-of-plane moment contour, Lucerne, north wall (kips/in.)

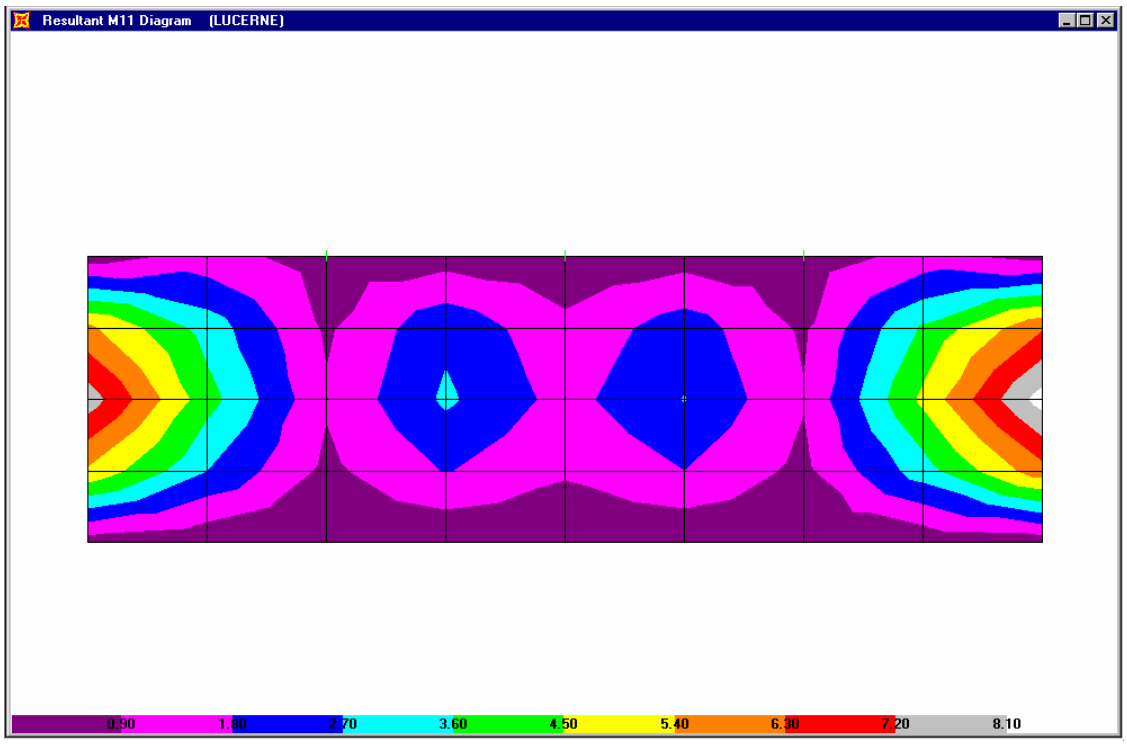

(b) Vertical out-of-plane moment contour, Lucerne, south wall (kips/in.)

Fig. 6.70 Out-of-plane moment contours, north and south walls, Lucerne

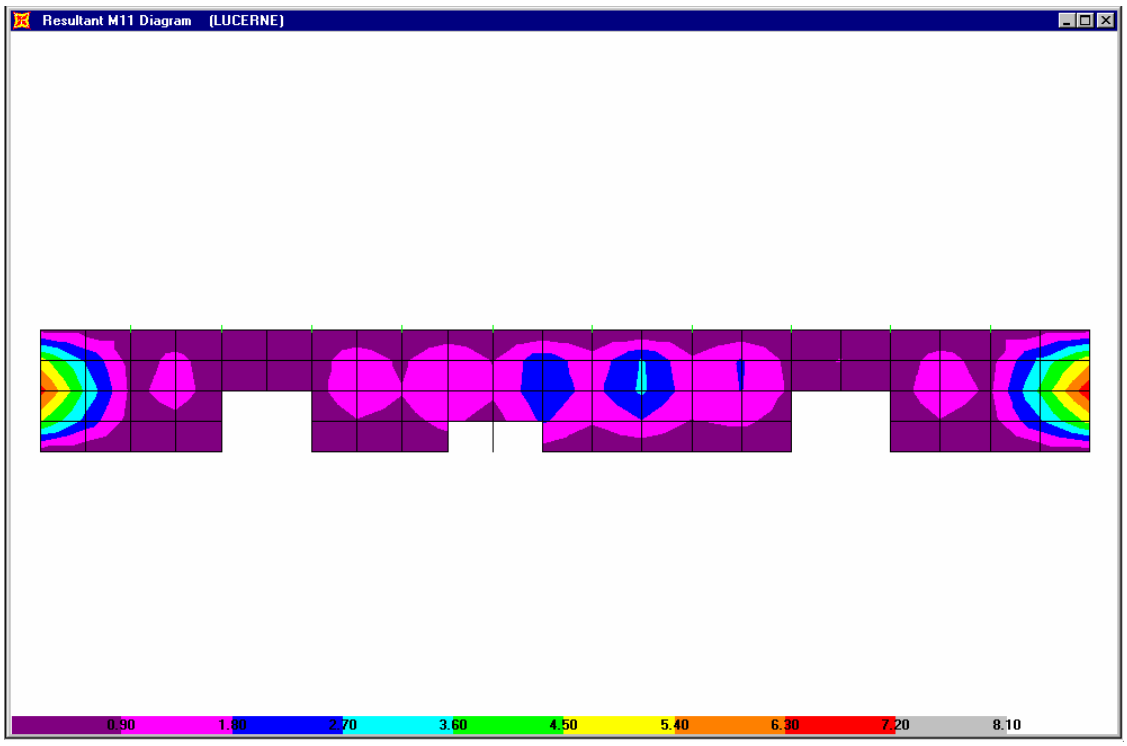

(a) Vertical out-of-plane moment contour, Lucerne, east wall (kips/in.)

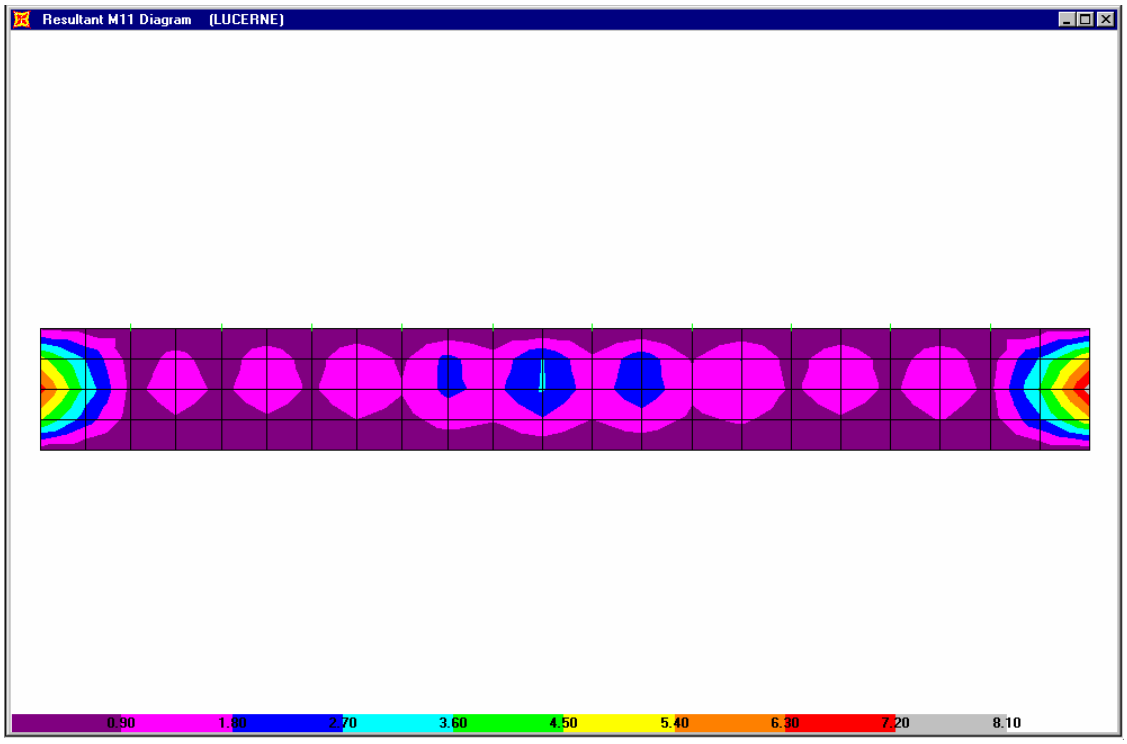

(b) Vertical out-of-plane moment contour, Lucerne, west wall (kips/in.)

Fig. 6.71 Out-of-plane moment contours, east and west walls, Lucerne

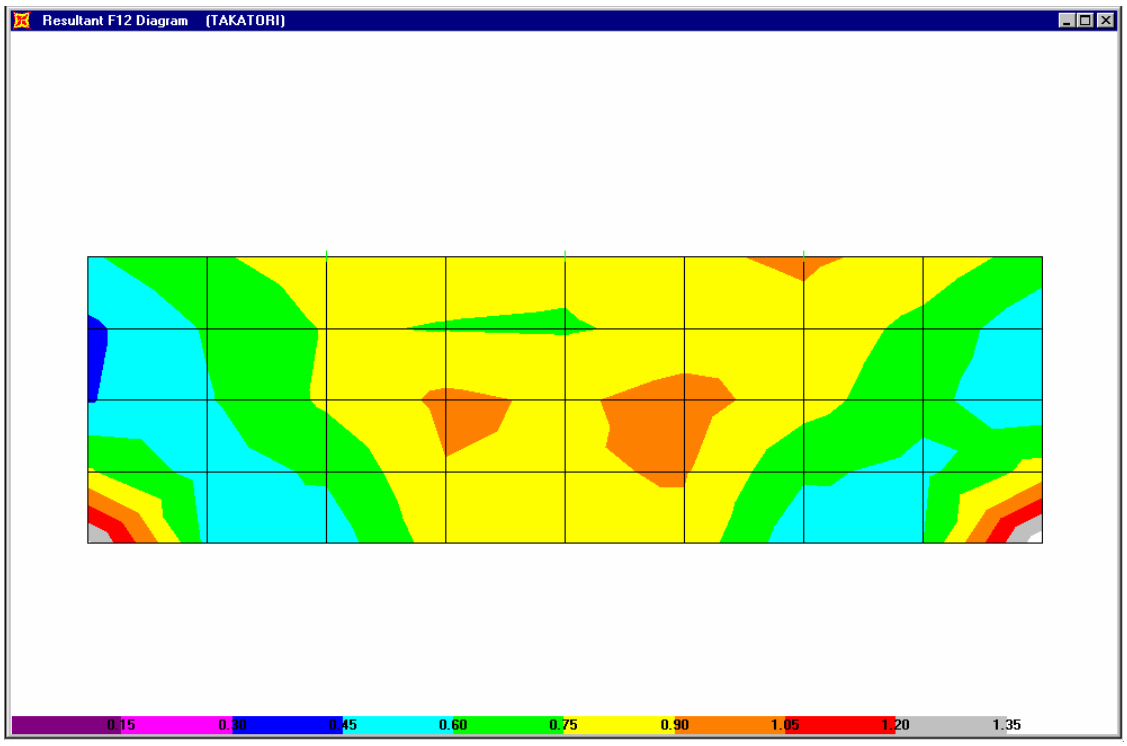

(a) In-plane shear contour, Takatori, north wall (kips/in.)

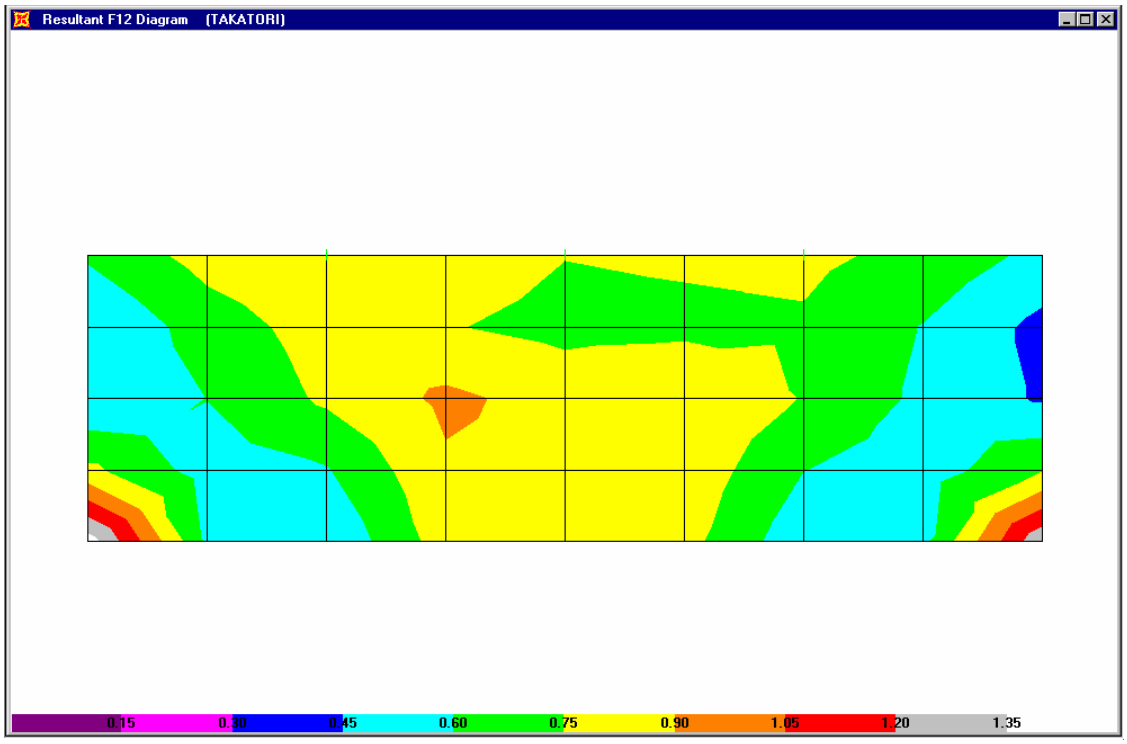

(b) In-plane shear contour, Takatori, south wall (kips/in.)

Fig. 6.72 In-plane shear contours, north and south walls, Takatori

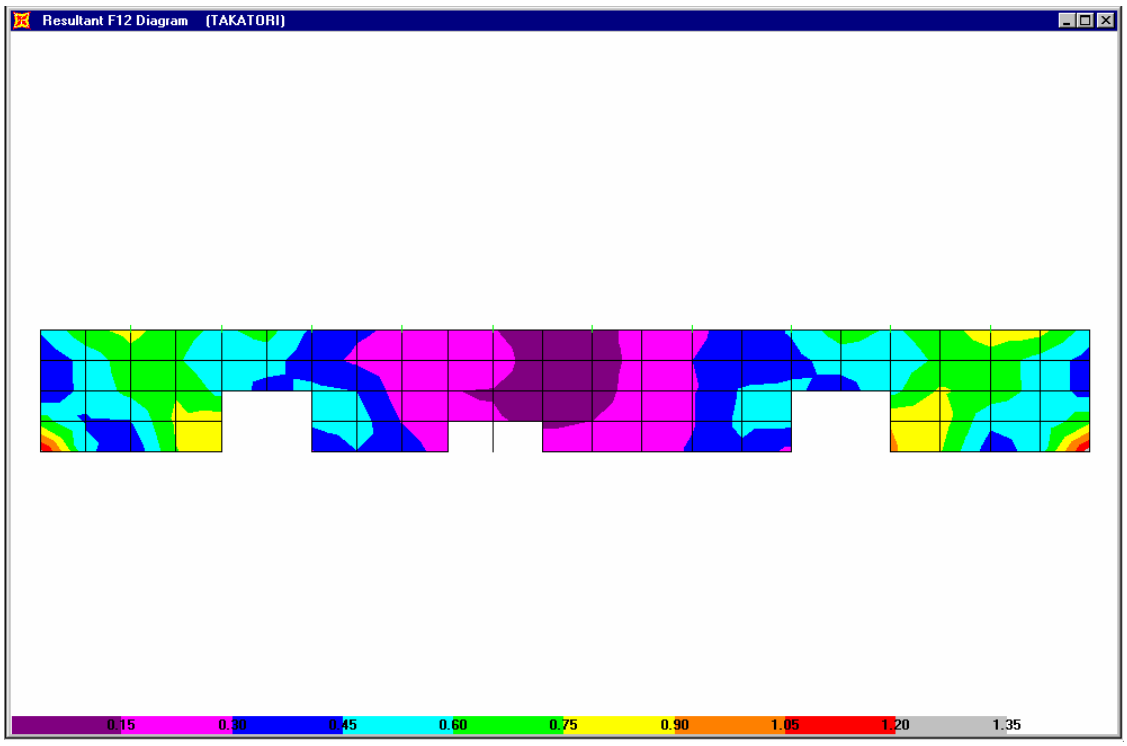

(a) In-plane shear contour, Takatori, east wall (kips/in.)

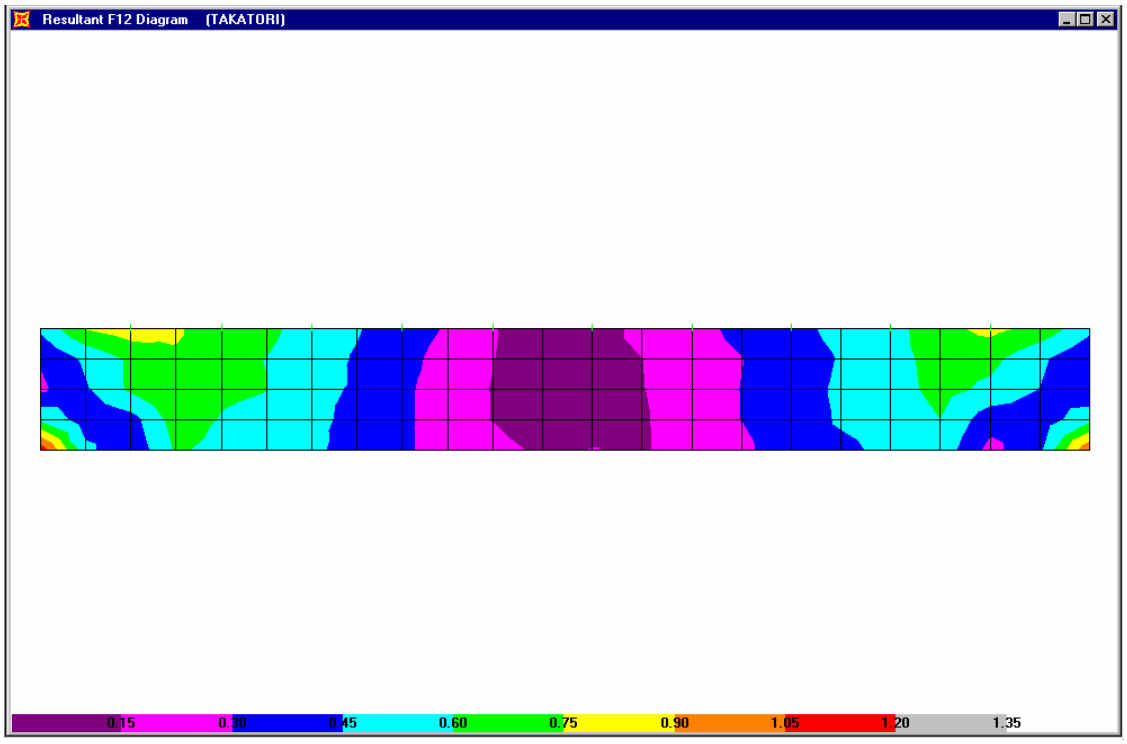

(b) In-plane shear contour, Takatori, west wall (kips/in.)

Fig. 6.73 In-plane shear contours, east and west walls, Takatori

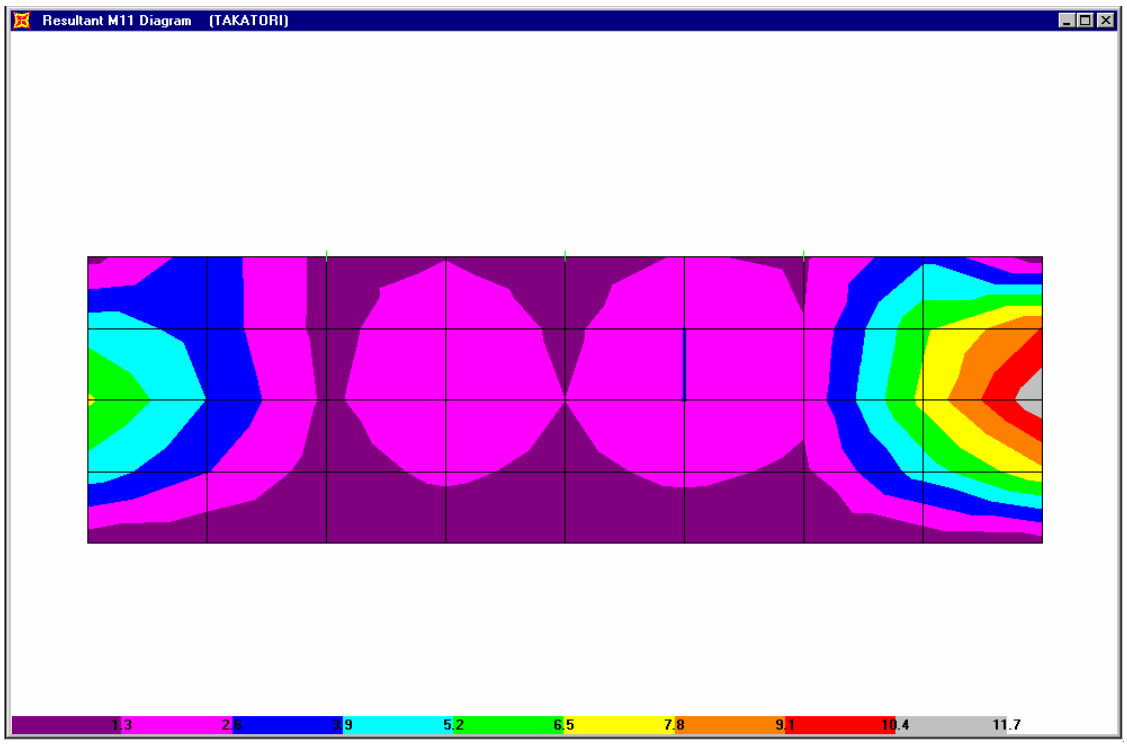

(a) Vertical out-of-plane moment contour, Takatori, north wall (kips/in.)

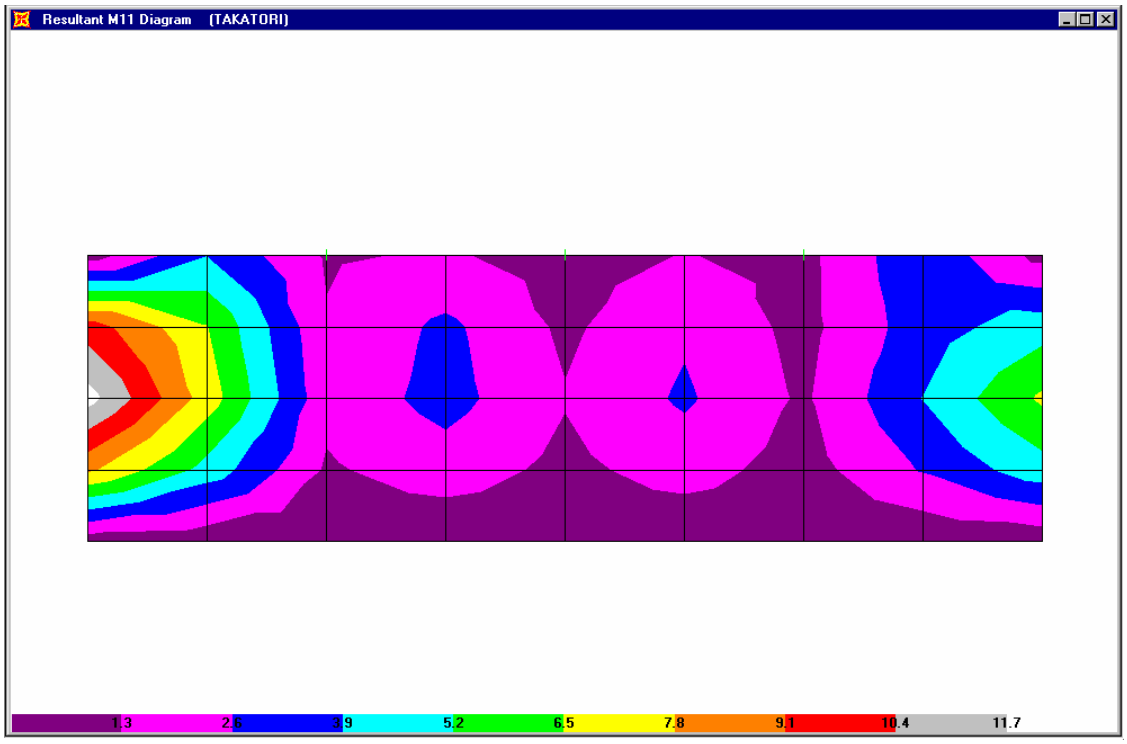

(b) Vertical out-of-plane moment contour, Takatori, south wall (kips/in.)

Fig. 6.74 Out-of-plane moment contours, north and south walls, Takatori

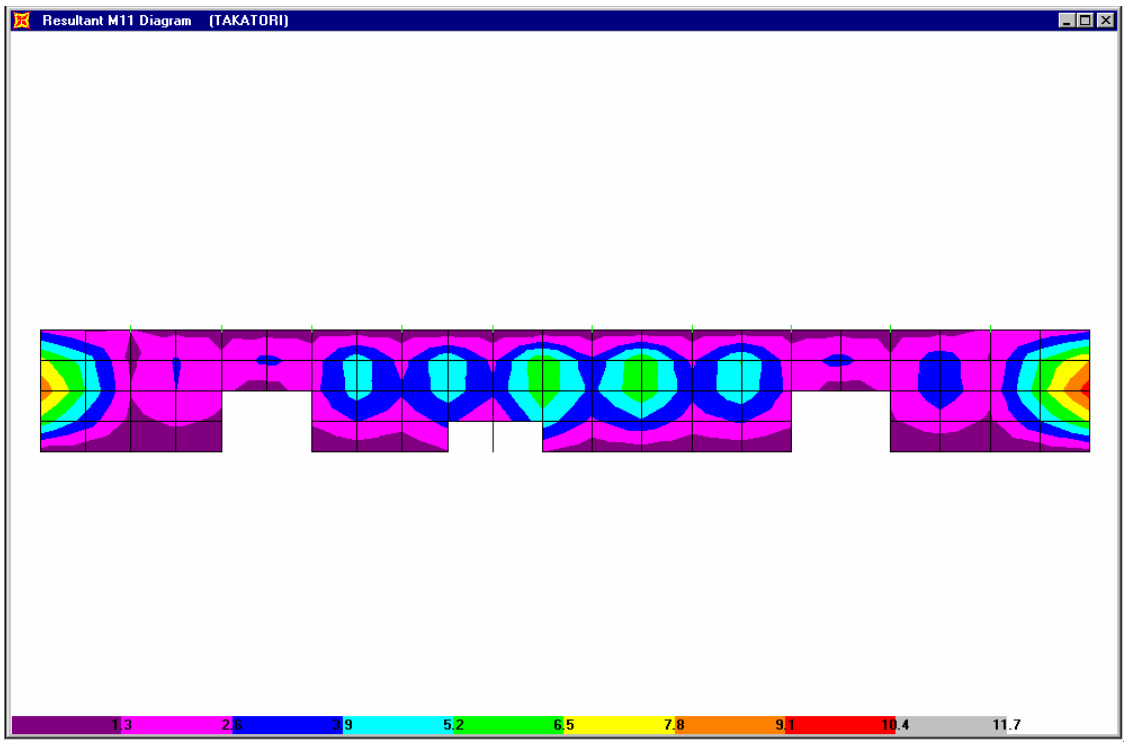

(a) Vertical out-of-plane moment contour, Takatori, east wall (kips/in.)

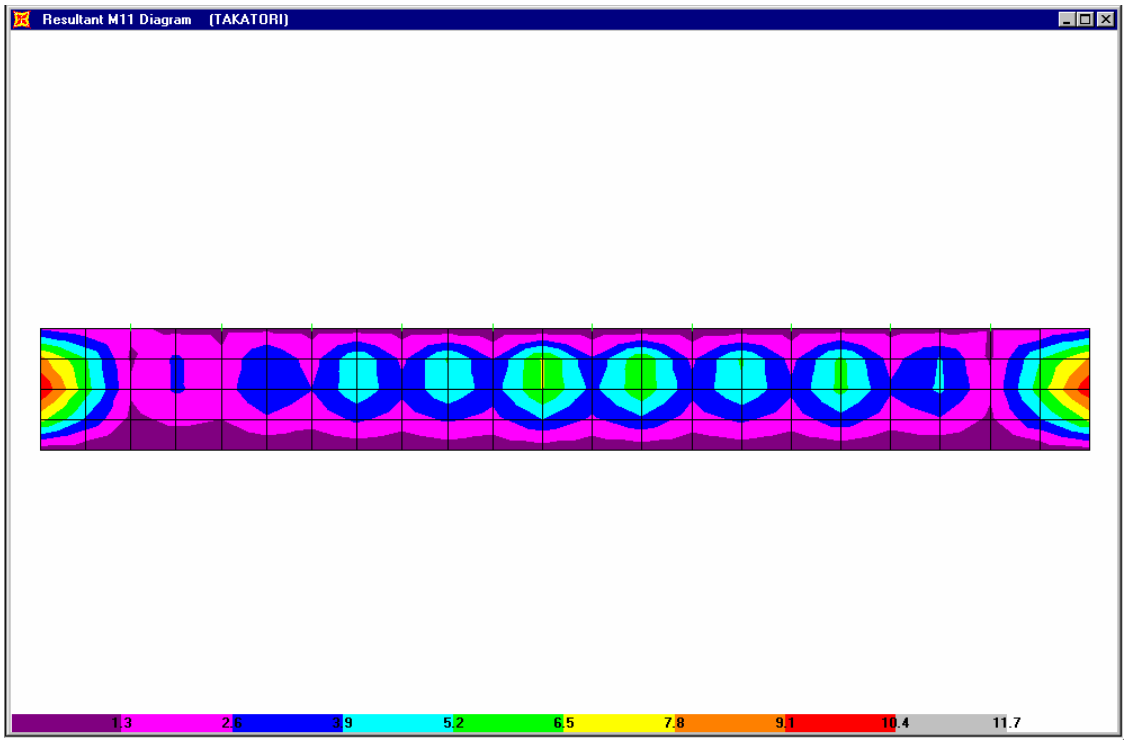

(b) Vertical out-of-plane moment contour, Takatori, west wall (kips/in.)

Fig. 6.75 Out-of-plane moment contours, east and west walls, Takatori

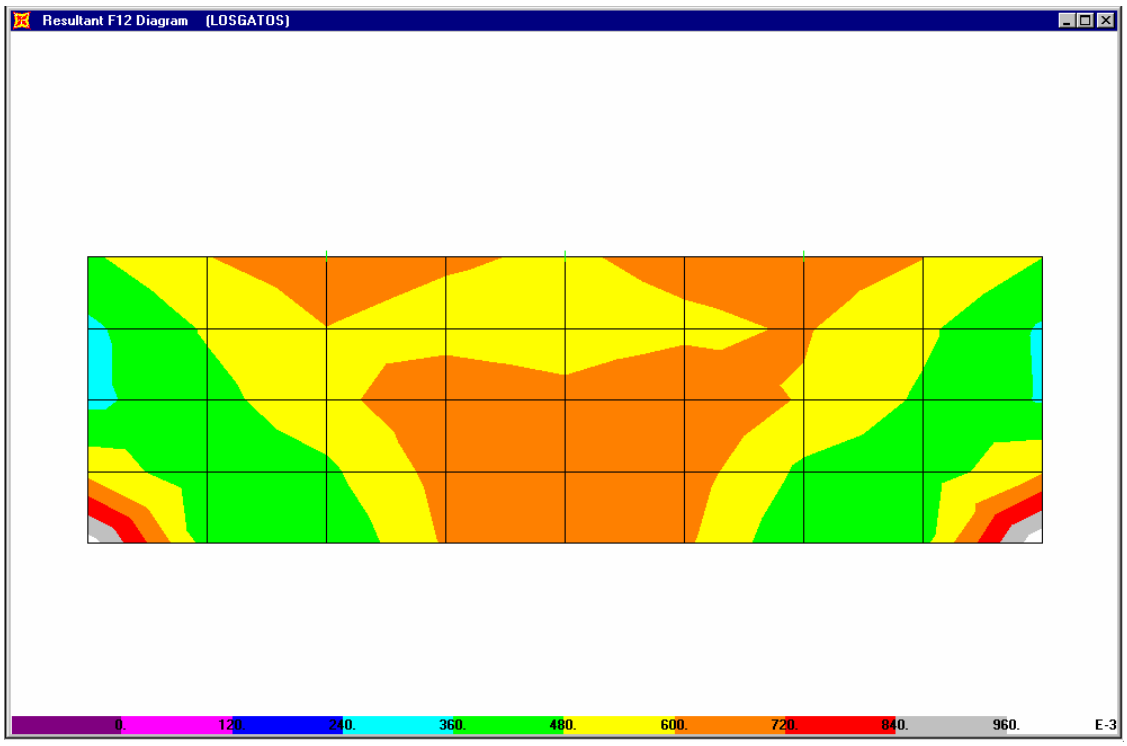

(a) In-plane shear contour, Los Gatos, north wall (kips/in.)

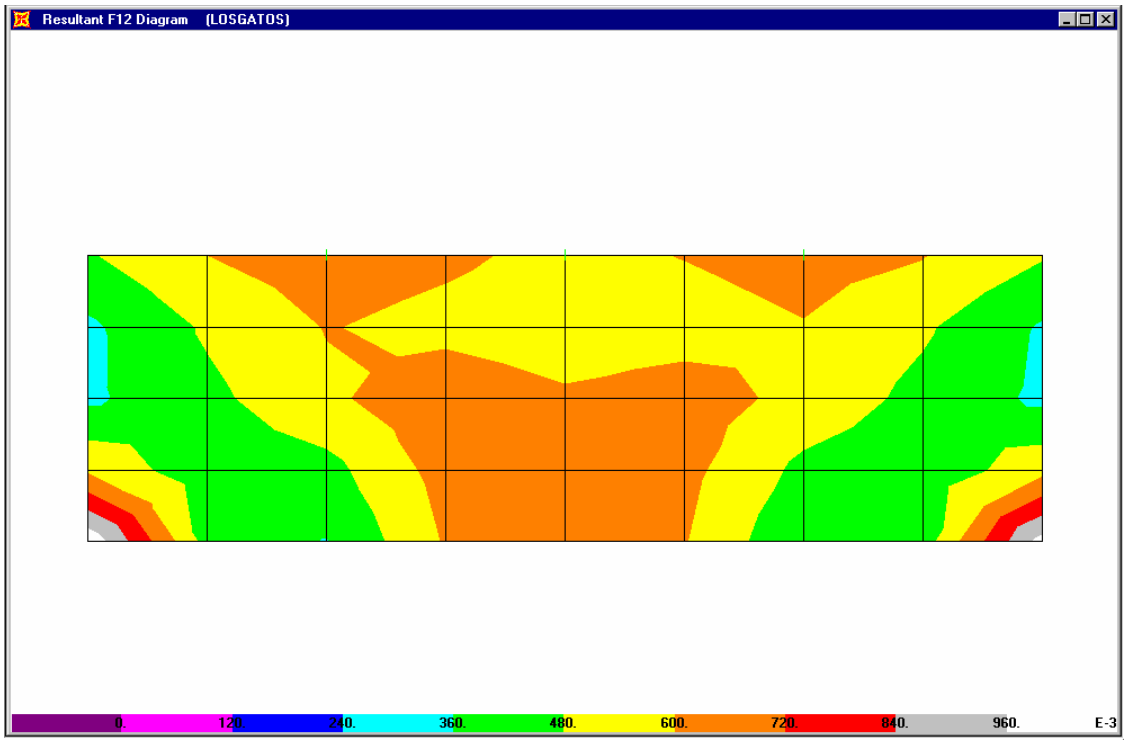

(b) In-plane shear contour, Los Gatos, south wall (kips/in.)

Fig. 6.76 In-plane shear contours, north and south walls, Los Gatos

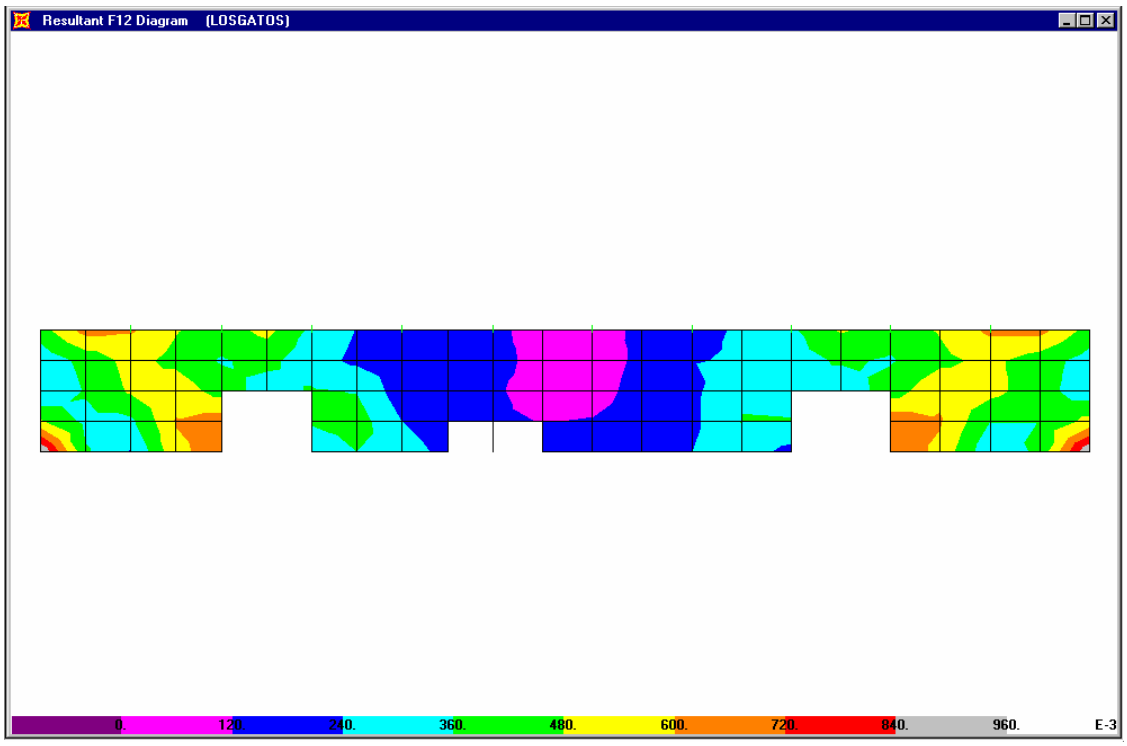

(a) In-plane shear contour, Los Gatos, east wall (kips/in.)

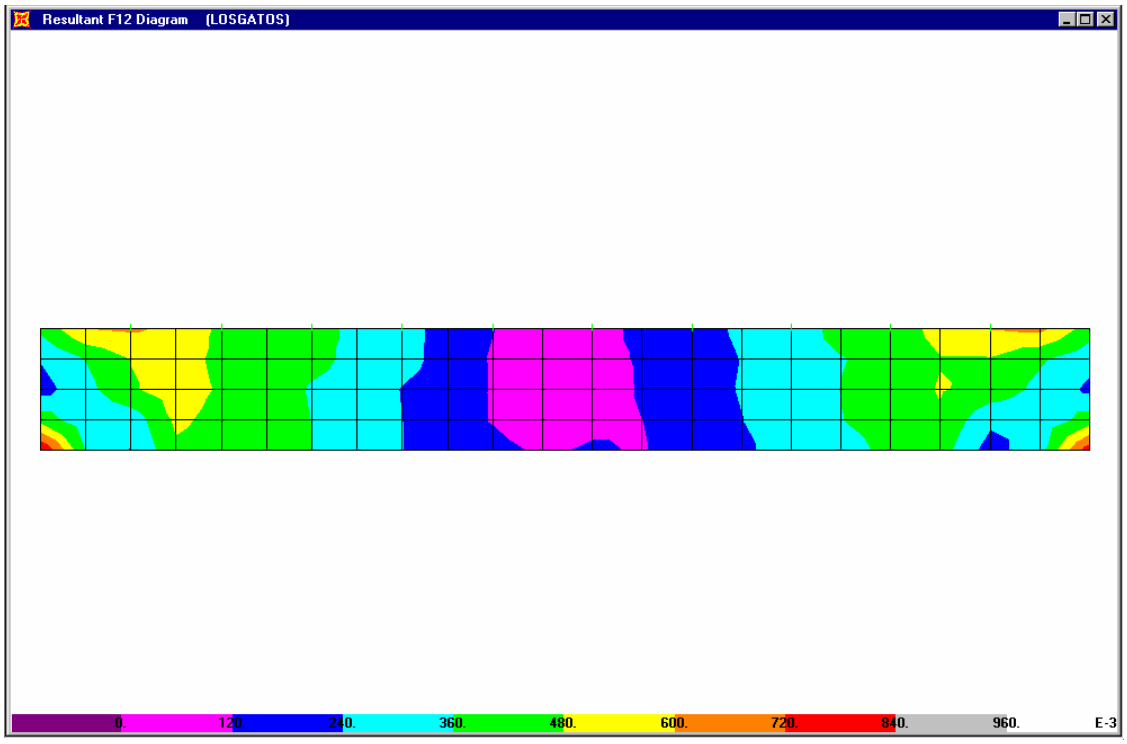

(b) In-plane shear contour, Los Gatos, west wall (kips/in.)

Fig. 6.77 In-plane shear contours, east and west walls, Los Gatos

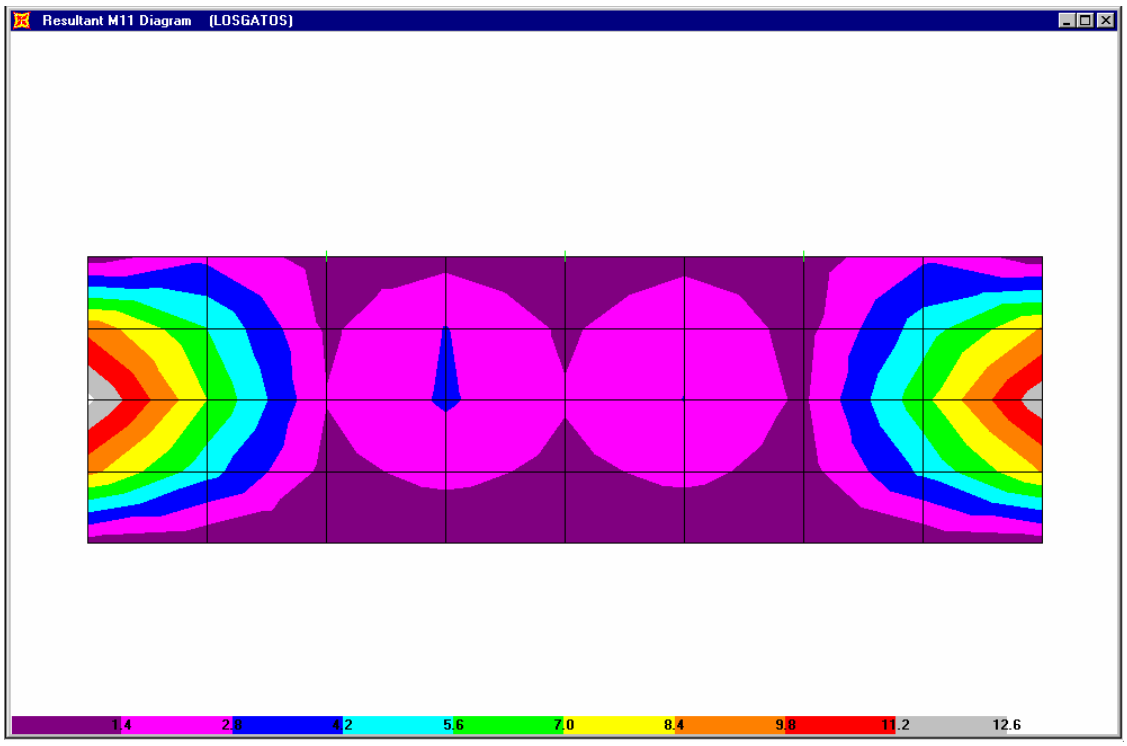

(a) Vertical out-of-plane moment contour, Los Gatos, north wall (kips/in.)

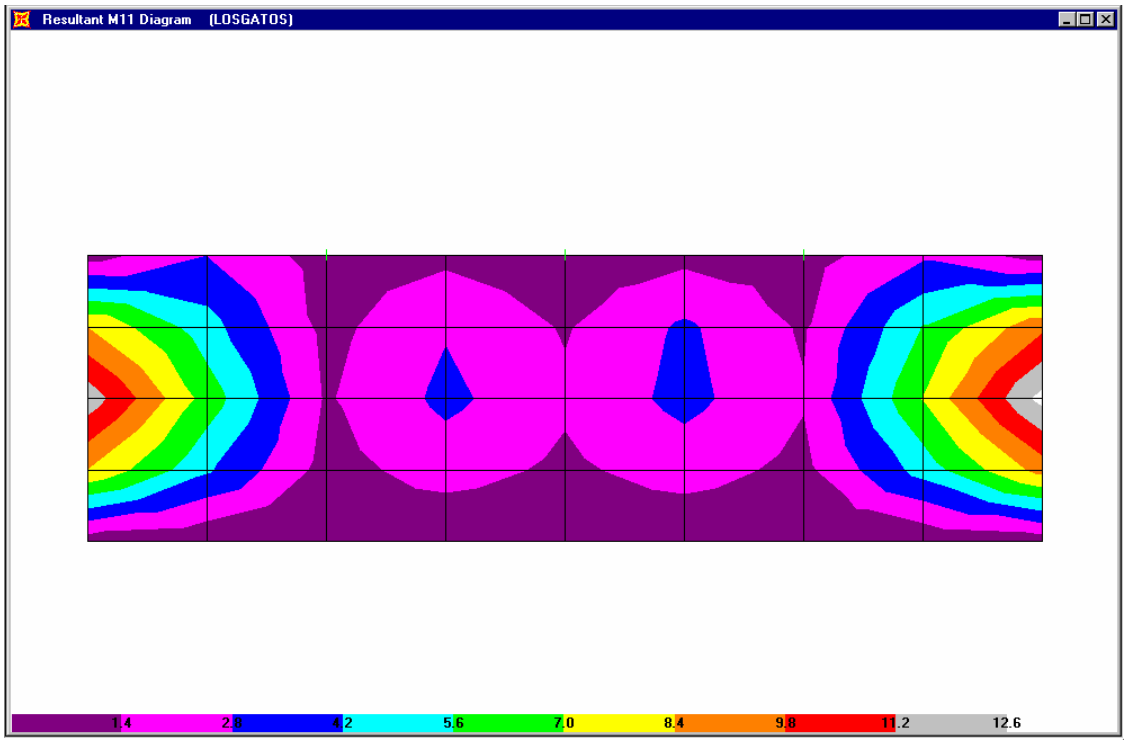

(b) Vertical out-of-plane moment contour, Los Gatos, south wall (kips/in.)

Fig. 6.78 Out-of-plane moment contours, north and south walls, Los Gatos

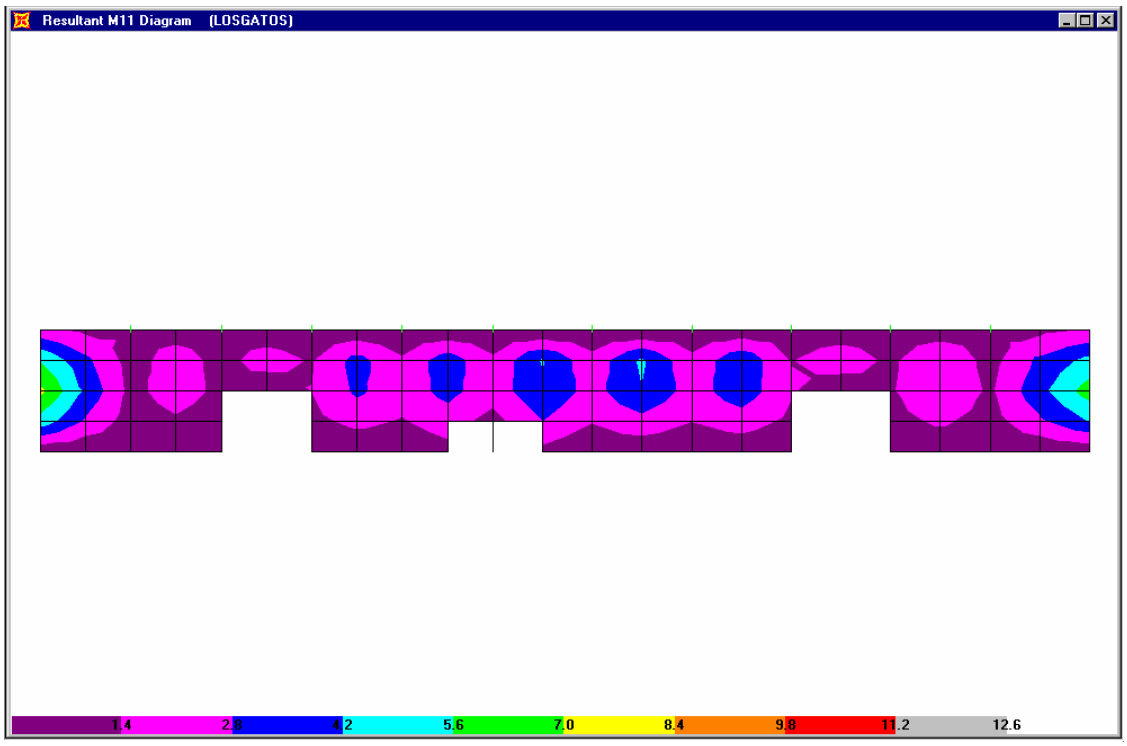

(a) Vertical out-of-plane moment contour, Los Gatos, east wall (kips/in.)

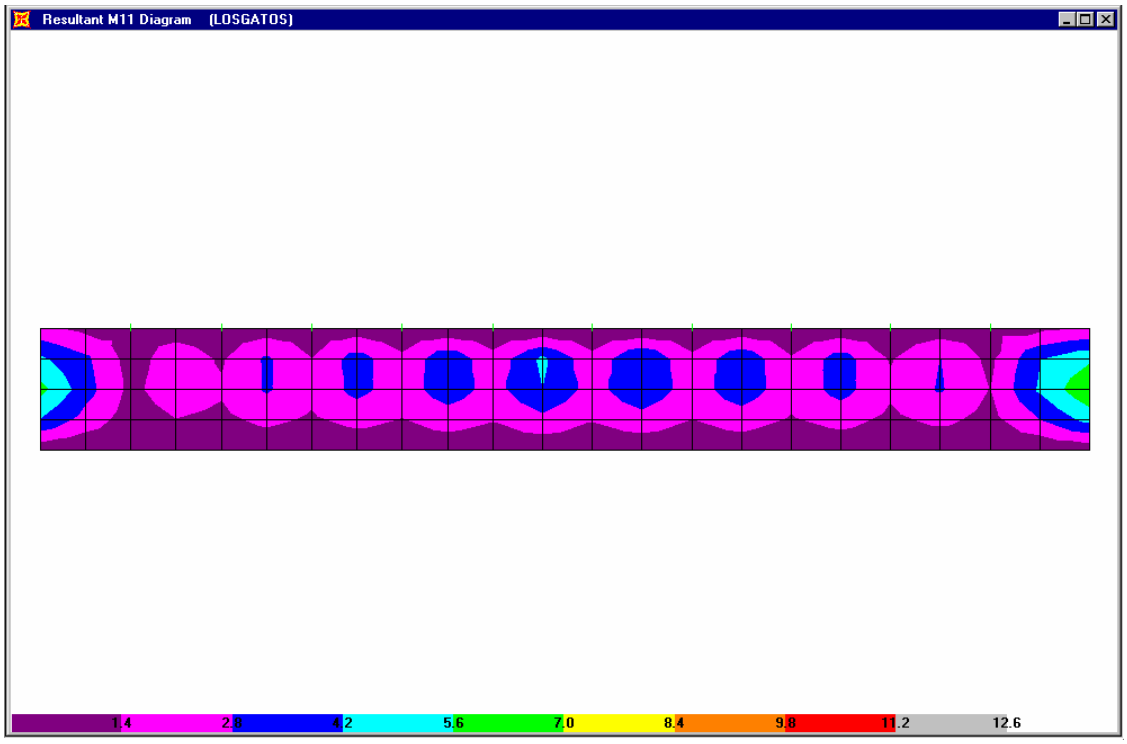

(b) Vertical out-of-plane moment contour, Los Gatos, west wall (kips/in.)

Fig. 6.79 Out-of-plane moment contours, east and west walls, Los Gatos

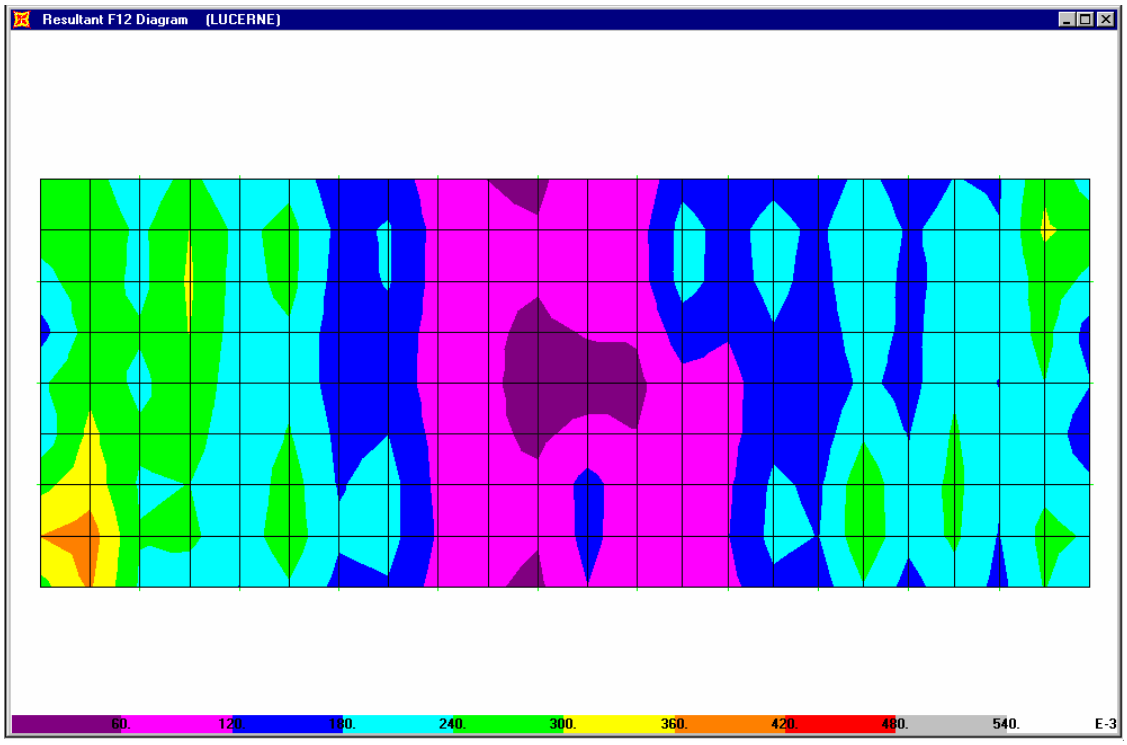

(a) In-plane shear, Lucerne, roof (kips/in.)

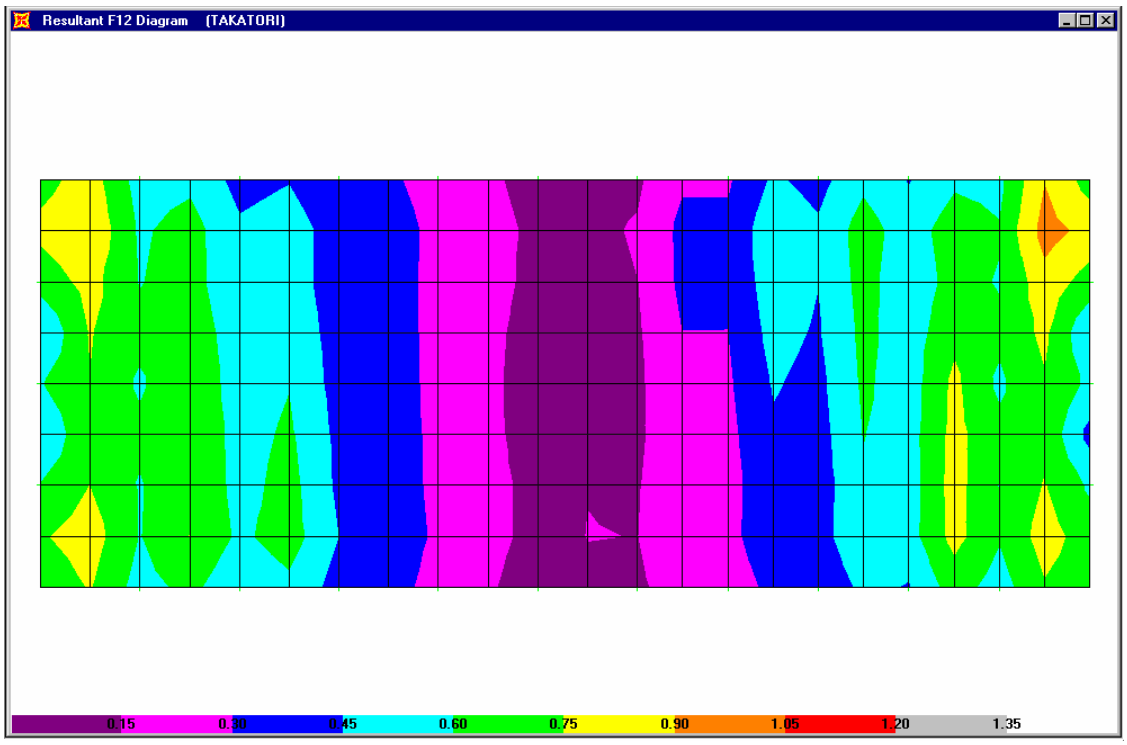

(b) In-plane shear, Takatori, roof (kips/in.)

Fig. 6.80 In-plane shear contours, roof, Takatori and Lucerne

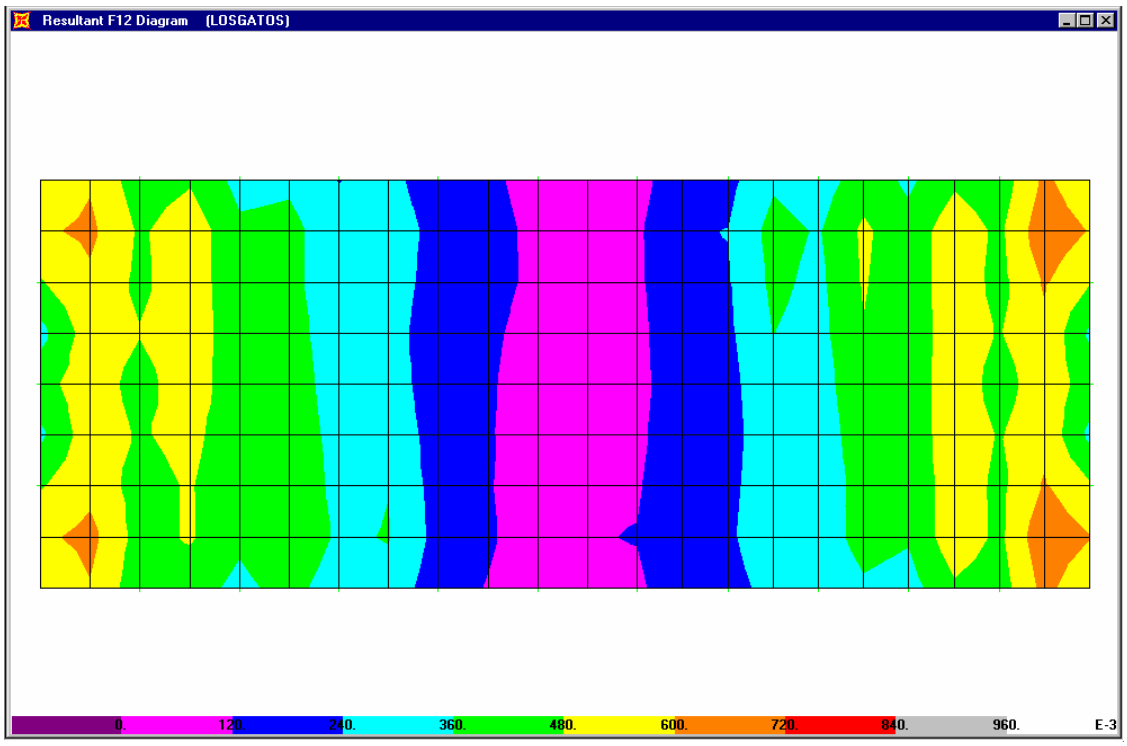

In-plane shear, Los Gatos, roof (kips/in.)

Fig. 6.81 In-plane shear contours, roof, Los Gatos

The force demands under the pulse-type ground motions are summarized in Table 6.4 below. The in-plane shear capacity of the roof diaphragm is exceeded by the in-plane shear demand of all three pulse type ground motions. The amount by which the demand exceeds the capacity indicates that this is a critical component. The out-of-plane moment capacity of the walls is also exceeded by the corresponding demand of all three ground motions. The in-plane shear capacity of the walls is adequate for all ground motions. The capacity of the glulam to pilaster connection in the axial direction is adequate for the force demanded by the Lucerne ground motion but does not meet the demand of the other two ground motions.

Table 6.4 Elastic model, pulse-type demand

	Glulam to Pilaster (Axial) kips	In-Plane Shear (Wall) kips/in.	Out-of-Plane Moment (Wall) in.-kips/in.	In-Plane Shear (diaphragm) kips/in.
Est. Capacity	26/34	1.74	3.0	0.085
Lucerne	26	0.42	8.1	0.360
Takatori	69	0.90	10.4	0.900
Los Gatos	46	0.60	12.6	0.600

6.5 SEGMENTAL WALLS

Once the tilt-up panels are in place the adjacent panels are connected. Before the early 1970s this was accomplished by using cast-in-place pilasters or cast-in-place segments of the wall (stitch columns) that are flush with the interior and exterior surfaces of the walls. More recently, the trend has been to minimize the connection between panels through the use of welded or bolted steel plates or splicing of the chord steel at the roof level. Current trends in TUW construction tend to exclude the use of pilasters.

The following section considers the effect of separated walls on the overall seismic response of a TUW building. In order to simulate this behavior, the existing model with the disconnected corners was modified to separate the existing wall panels. The panels around the openings in the east wall were left connected to provide stability. All pilasters in the previous model were removed. The segments of the transverse walls at the north and south ends of the building are shown in Figure 6.82. Each wall is divided into 4 wall segments consisting of 8 elements. The segmentation of the east wall is shown in Figure 6.83a. In this case the segments are irregular due to the openings in the original wall. The current arrangement was constructed to keep the segments symmetrical about an opening and to avoid joints through an opening. It was also necessary to relocate the connections of the glulam beams and purlins to the center of the wall panels. The segmentation of the west wall was uniform as shown in Figure 6.83b. The revised model was then subjected to the recorded Big Bear acceleration time history and the response compared to that of the original model with pilasters.

The acceleration time histories computed near channel 5 located on the west wall midway between the south wall and the fire wall are shown in Figure 6.84. The acceleration record obtained from the original model is shown in Figure 6.84a and the acceleration record obtained from the model with the separated wall segments, in Figure 6.84b. It can be seen that the accelerations from the connected segments model reach a peak of 0.6g compared with 0.25g with the separated segments. It can also be seen that the frequency of the separated segments is slightly lower than for the connected segments. The corresponding displacements are shown in Figure 6.85. Displacements with the connected segments (Fig. 6.85a) indicate a maximum value of 1.6 inches, which compares with a value of 1.15 inches for the separated segments (Fig. 6.85b).

The out-of-plane accelerations calculated near channel 9 at the midpoint on the south wall are shown in Figure 6.86. The accelerations for the original connected wall segment model are shown in Figure 6.86a and the accelerations for the separated wall segments, in Figure 6.86b. With the connected wall segments, the peak acceleration at the top of the wall reaches 0.2g, whereas for the separated wall segments, the peak acceleration reaches only 0.13g. It can also be seen that there is a slight lengthening of the period of vibration for the separated wall segments. The corresponding displacements at this location are shown in Figure 6.87. These are very similar in both amplitude and frequency, with the maximum displacement reaching 1.5 inches for connected walls and 1.4 inches for separated walls.

The time histories of the base shear calculated by the two models are shown in Figure 6.88 for the longitudinal (N-S) direction. It can be seen that the maximum base shear for the connected walls model reaches 80 kips (Fig. 6.88a). With the separated wall segments (Fig. 6.88b), the maximum base shears reach 100 kips. Both of these are well below the code design capacity of 247 kips. Time histories for the base shear in the transverse (E-W) direction are shown in Figure 6.89. With the connected wall segments (Fig. 6.89a), one cycle reaches a maximum of 475 kips, while multiple cycles exceed 250 kips. The base shear for the separated walls (Fig. 6.89b) indicates one cycle at a maximum value of 310 kips, with multiple cycles at 250 kips or less.

Contours of in-plane shear in the four walls are shown in Figure 6.90. For the connected segments (Fig. 6.90a), the shear reaches a maximum value of 0.210 kips/in. in the shorter, transverse walls. For the separated walls (Fig. 6.90b), the shear reaches a maximum value of 0.105 kips/in. in the same locations. Both of these compare to an estimated shear capacity of 1.74 kips/in.

Contours of the out-of-plane moment in the vertical direction are shown in Figure 6.91. The connected walls (Fig. 6.91a) have a maximum moment demand at the corners where the moments exceed 2.0 in.-kips/in. As might be expected, the moments in the separated walls are significantly higher as seen in Figure 6.91b. Maximum out-of-plane moments reach 5.0 in.-kips/in. near the center opening in the east wall and 4.2–4.8 in.-kips/in. near midheight of the east wall in the area of the openings. At both of these locations the flexural demands are considerably above the estimated flexural capacity of 3.0 in.-kips/in.

Contours of in-plane shear in the roof diaphragm are shown in Figure 6.92. For the connected walls, the maximum in-plane shear reaches 0.175 kips/in. (Fig. 6.92a). The shear in

the roof diaphragm with the separated walls (Fig. 6.92b) reaches a maximum of 0.125 kips/in. in the corners.

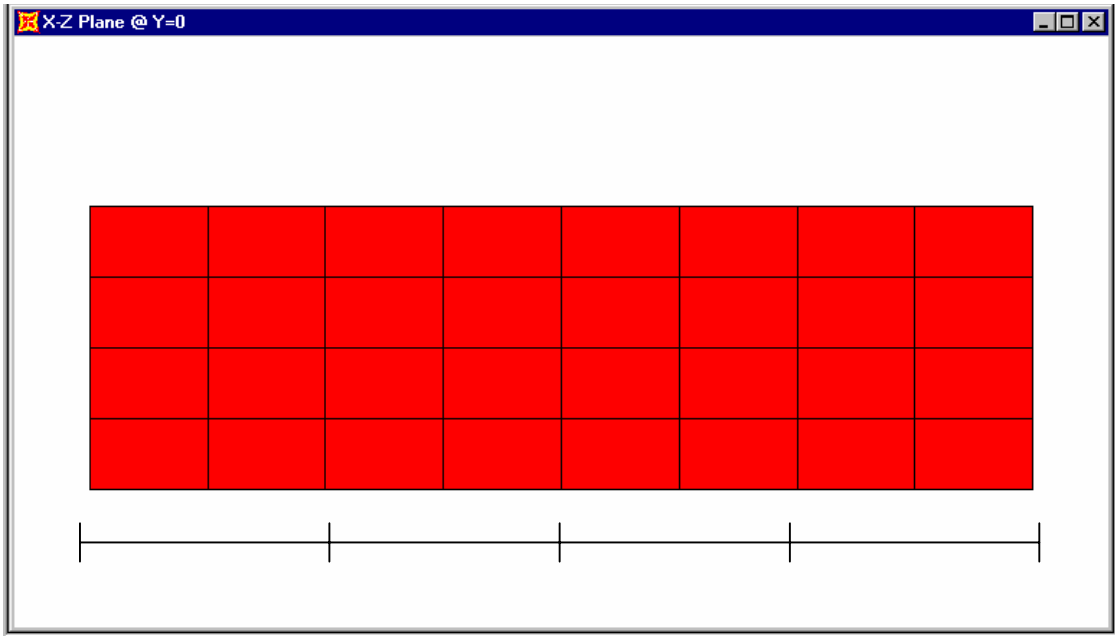

(a) north wall segments

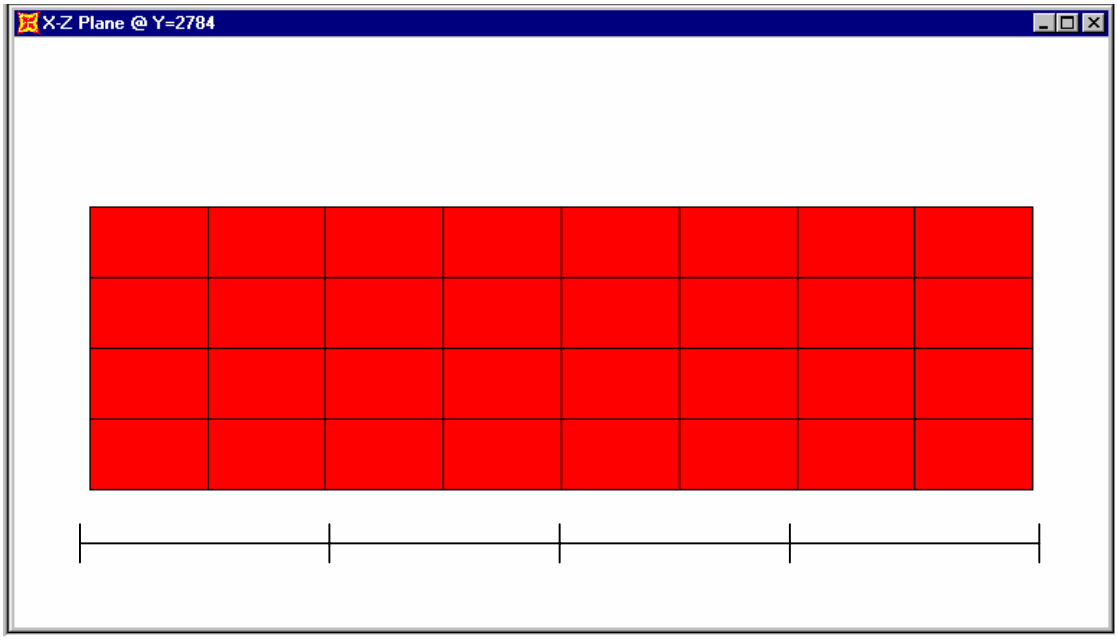

(b) south wall segments

Fig. 6.82 Wall segments, north and south walls

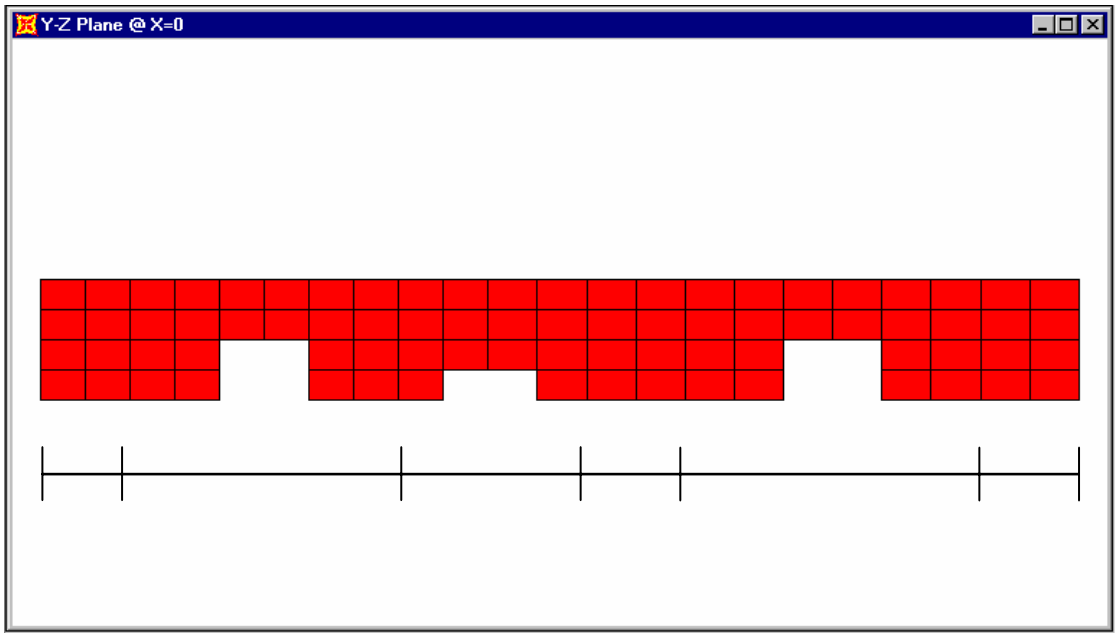

(a) east wall segments

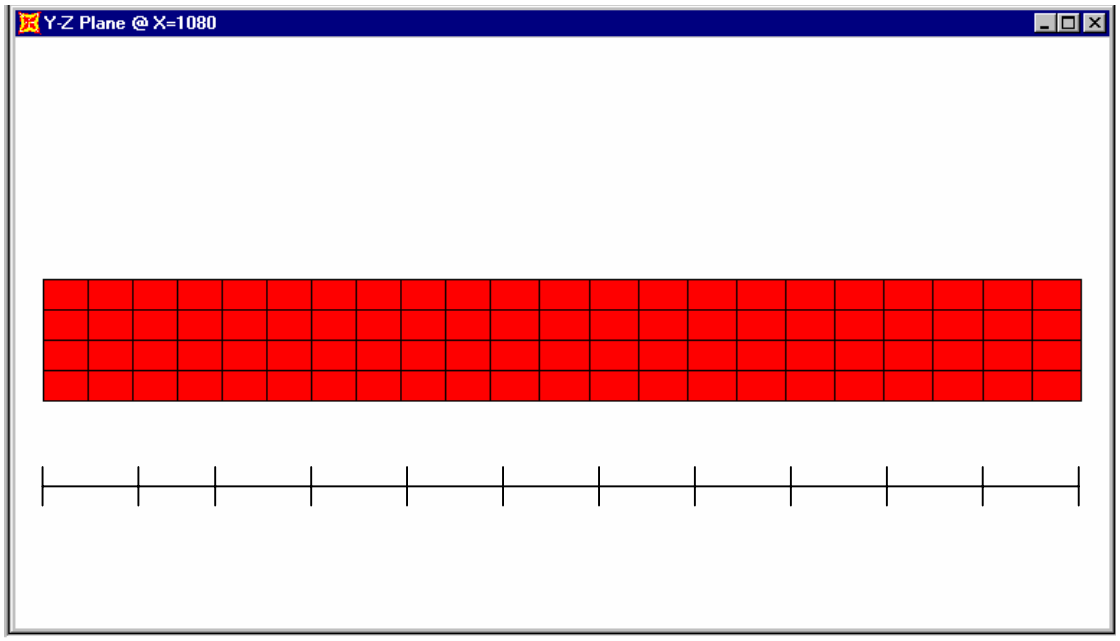

(b) west wall segments

Fig. 6.83 Wall segments, east and west walls

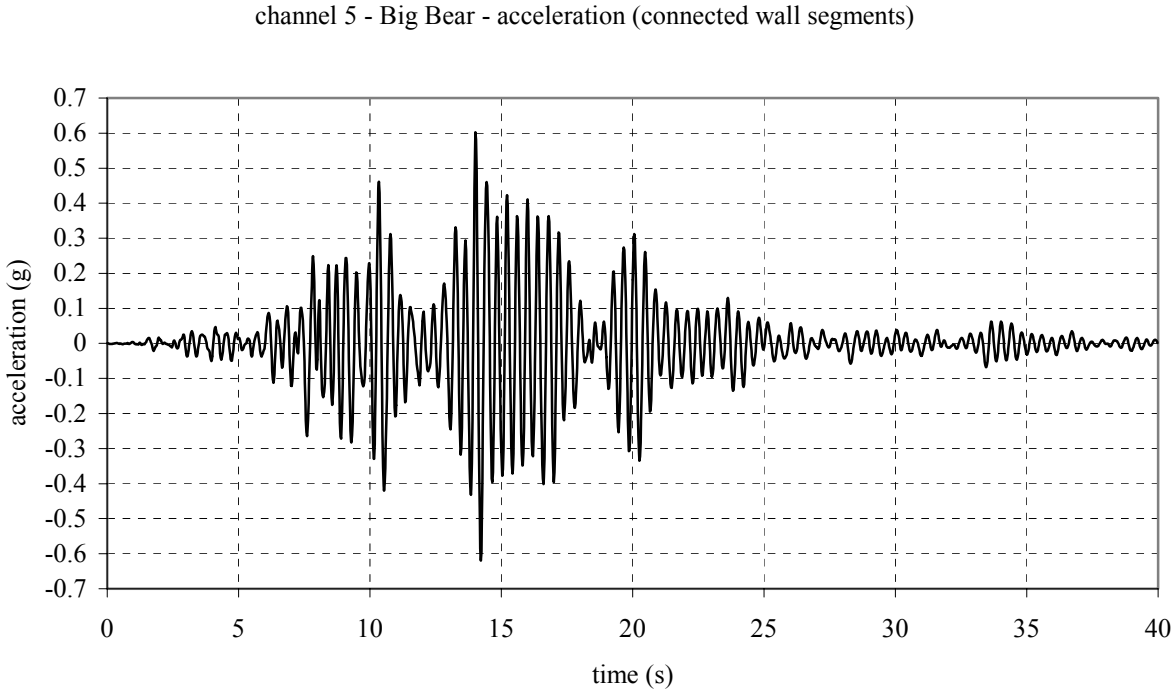

(a) connected wall segments

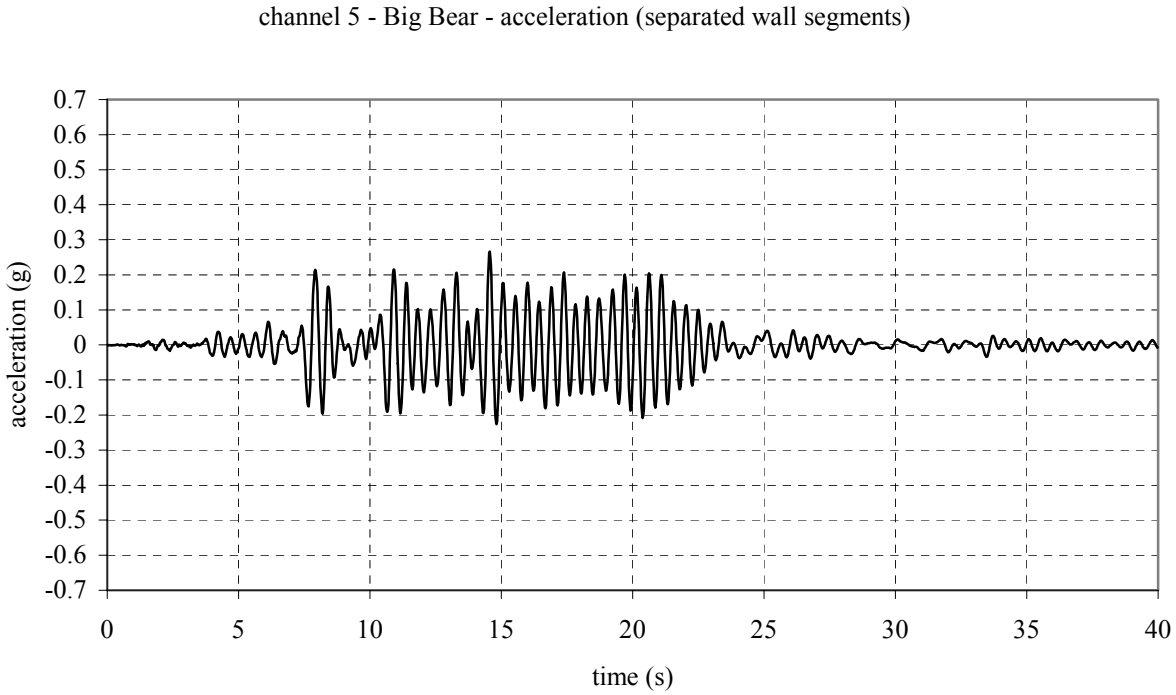

(b) separated wall segments

Fig. 6.84 Acceleration comparisons, segmental walls, ch. 5

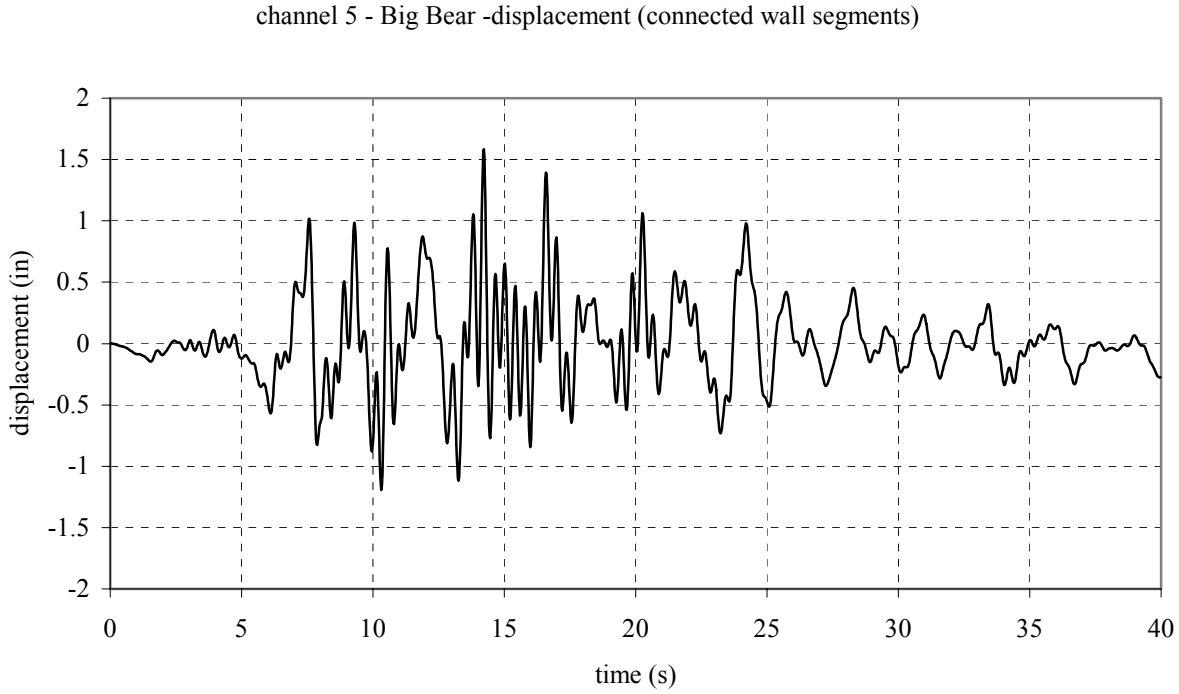

(a) connected wall segments

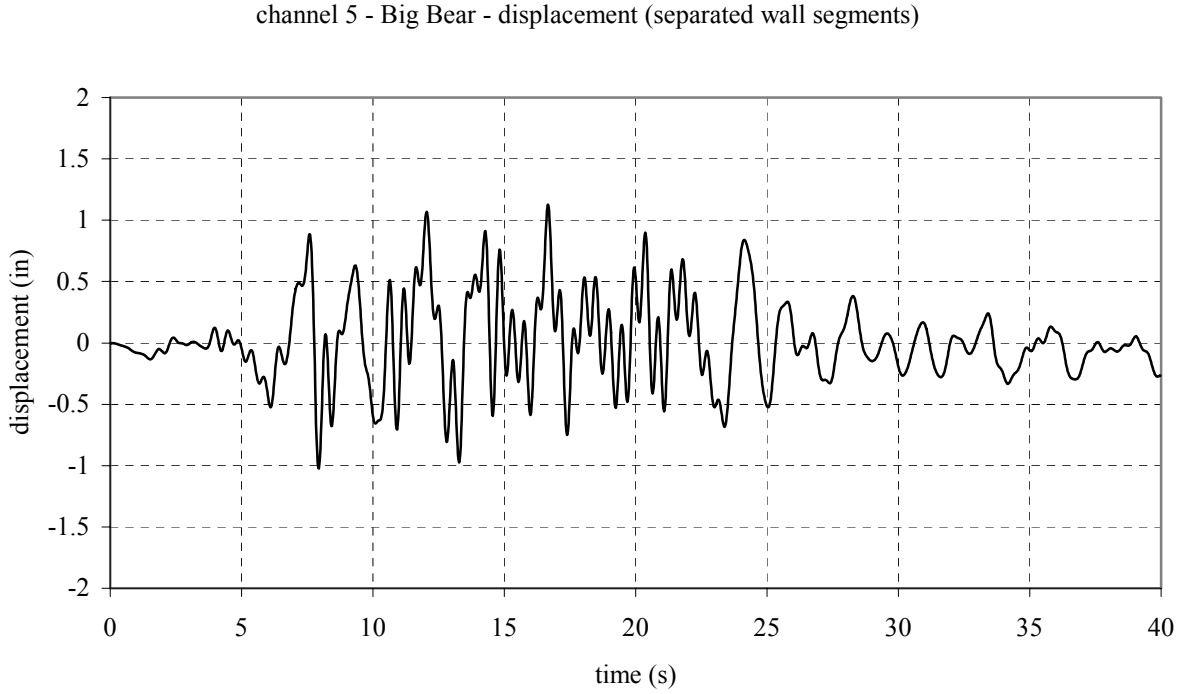

(b) separated wall segments

Fig. 6.85 Displacement comparisons, segmental walls, ch. 5

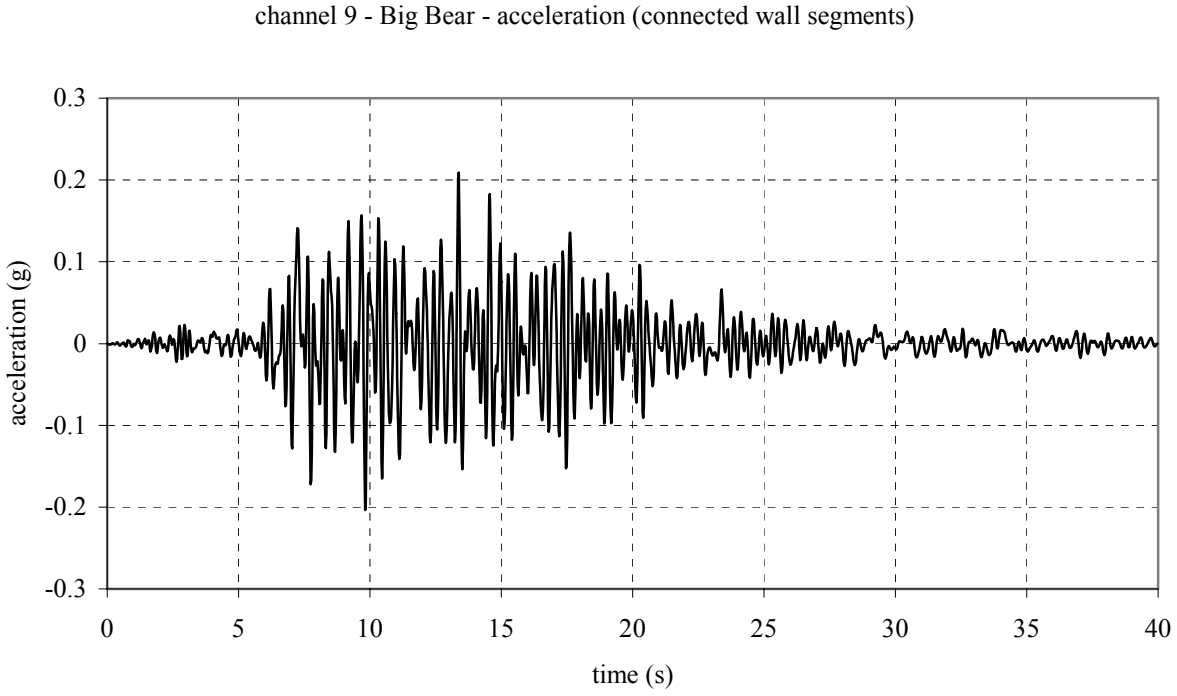

(a) connected wall segments

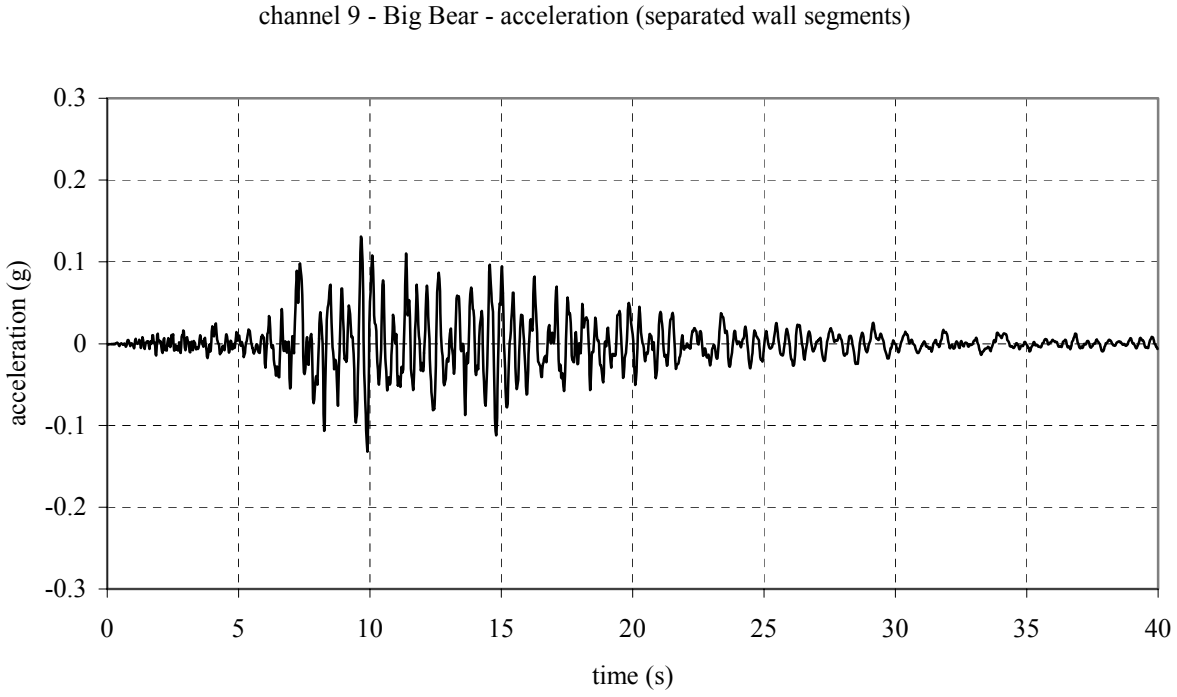

(b) separated wall segments

Fig. 6.86 Acceleration comparisons, segmental walls, ch. 9

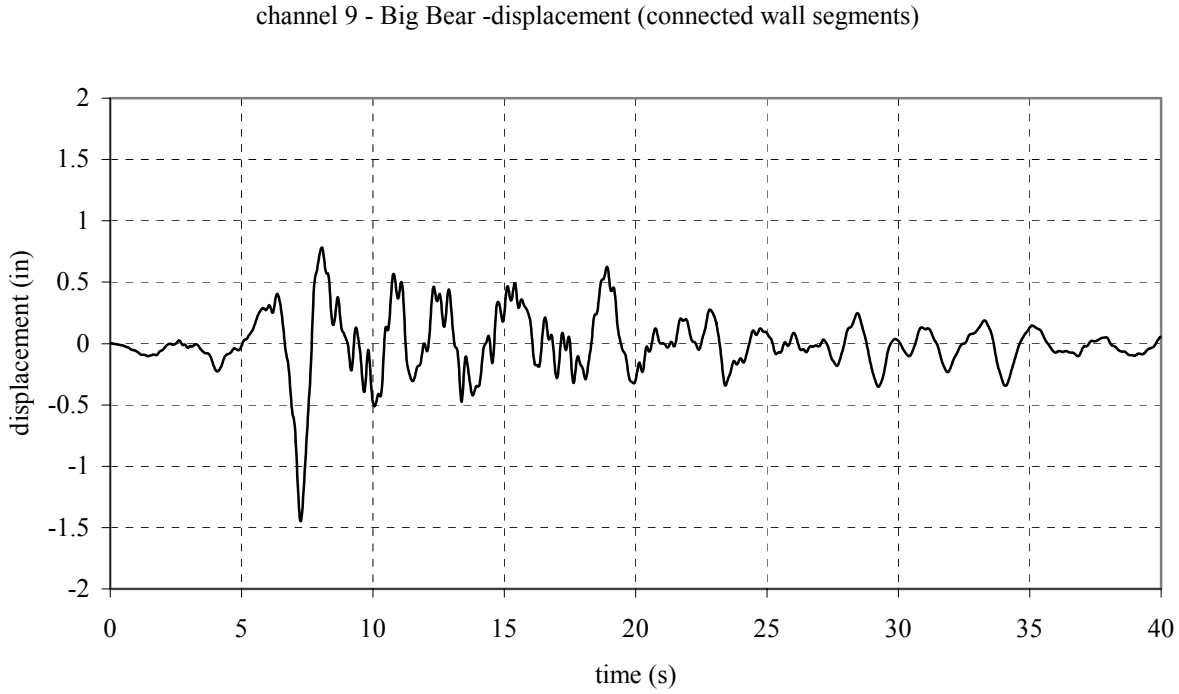

(a) connected wall segments

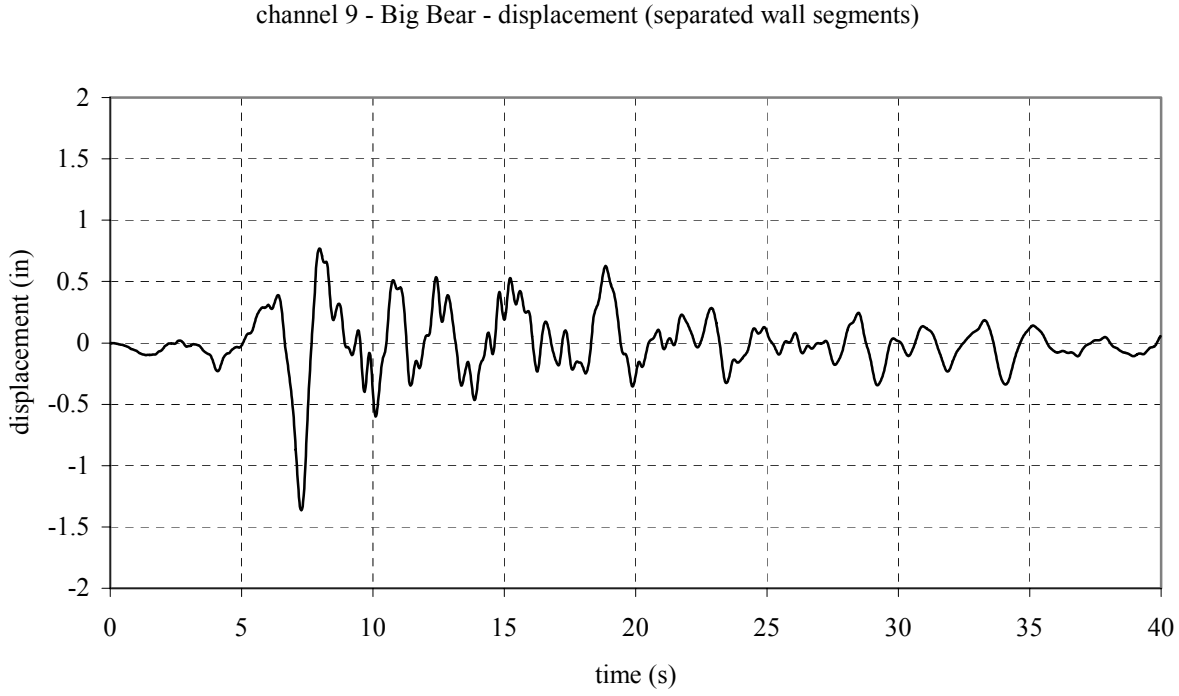

(b) separated wall segments

Fig. 6.87 Displacement comparisons, segmental walls, ch. 9

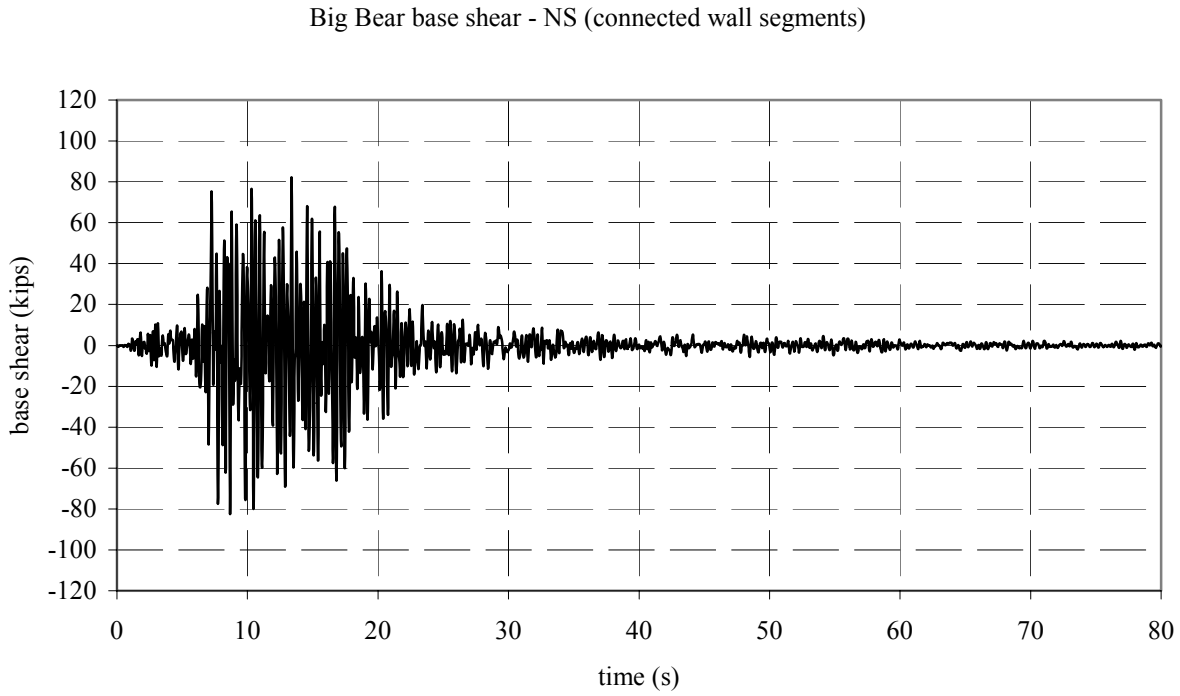

(a)

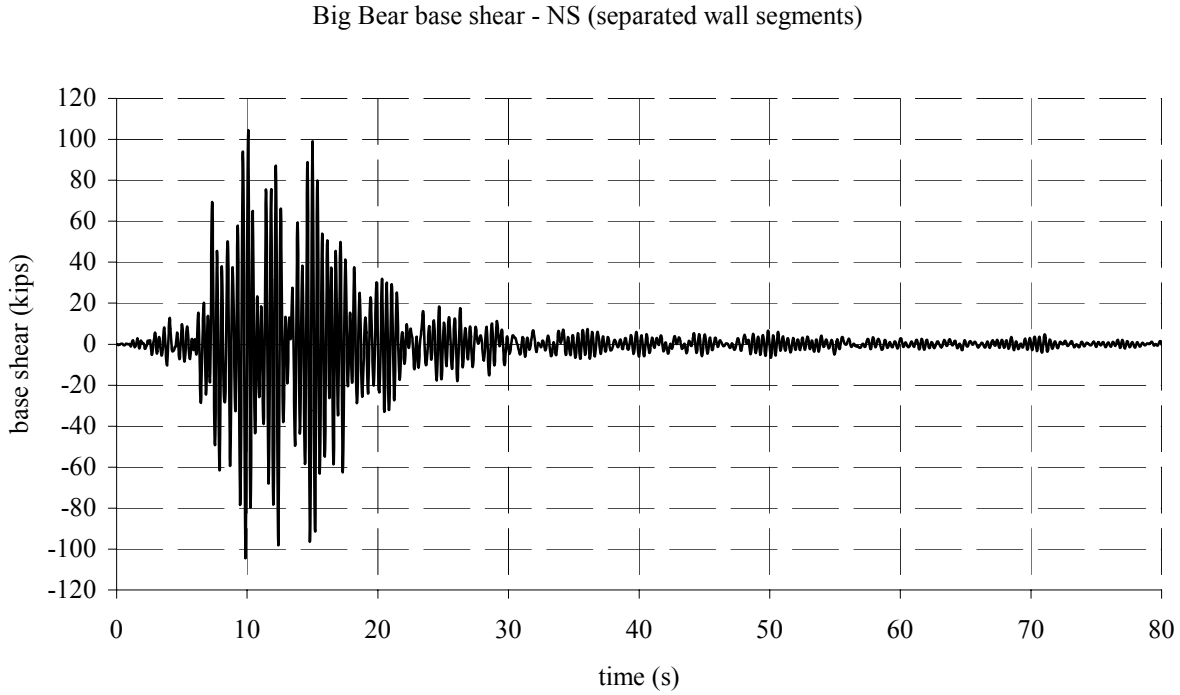

(b)

Fig. 6.88 Base shear comparisons, segmental walls, N-S

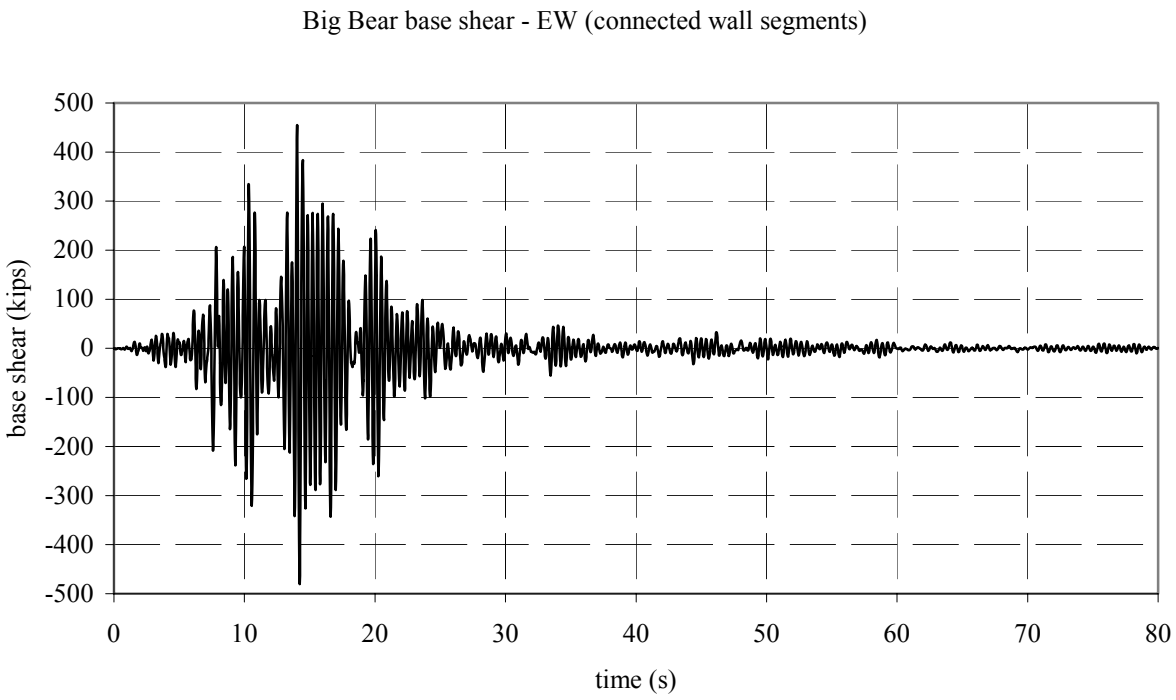

(a)

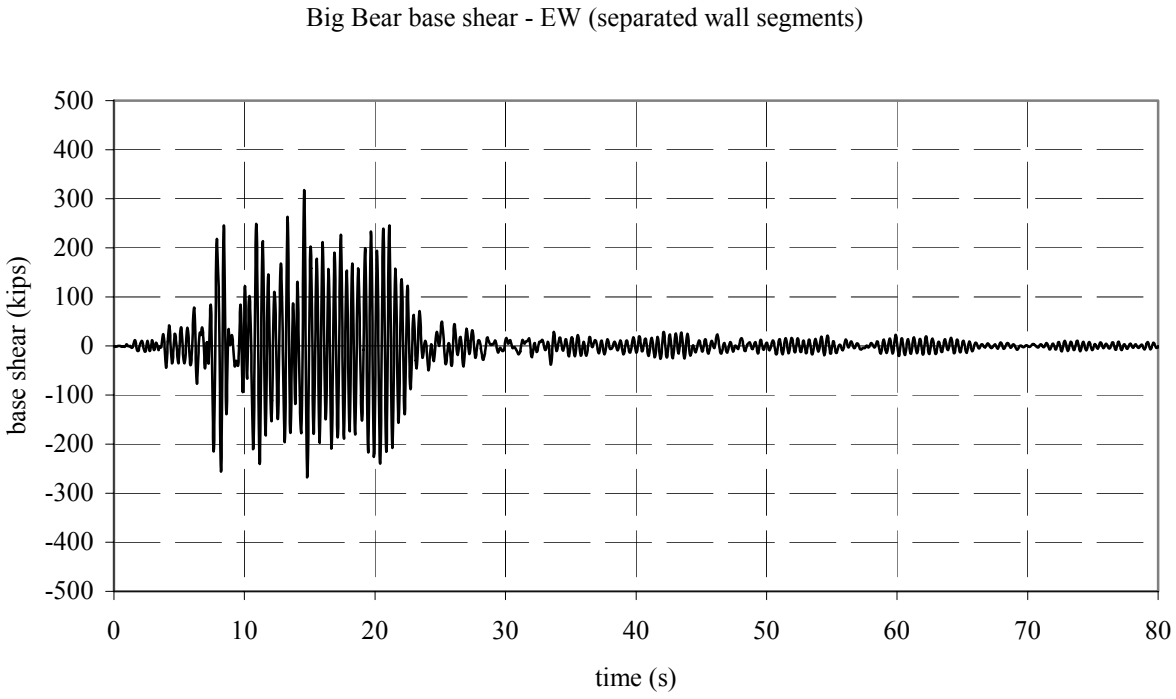

(b)

Fig. 6.89 Base shear comparisons, segmental walls, E-W

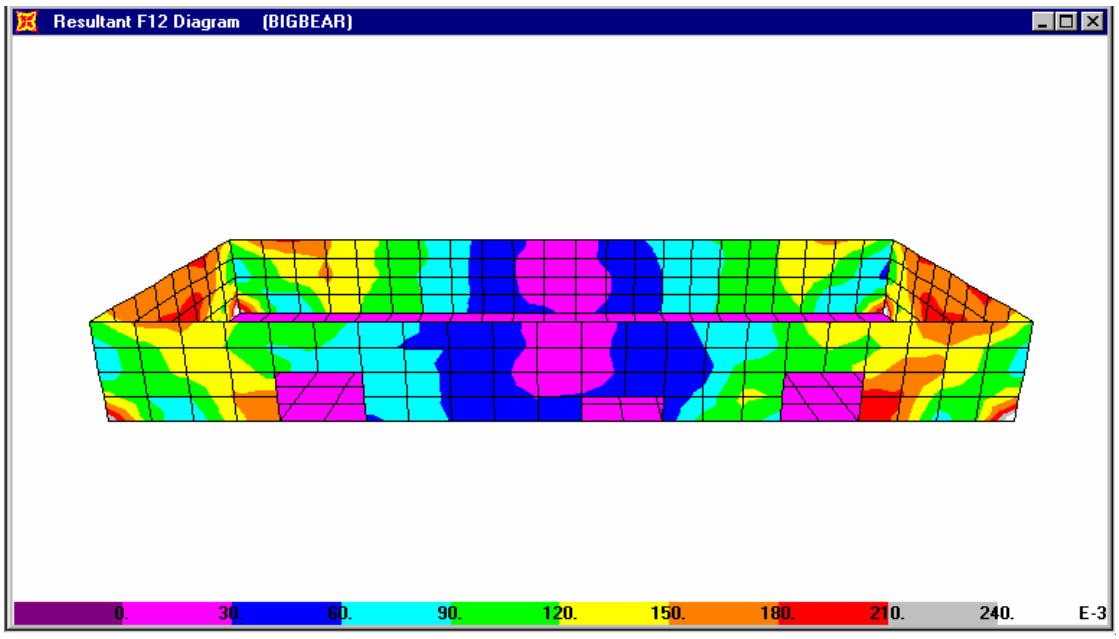

(a) Big Bear: in-plane shear — connected wall segments (kips/in.)

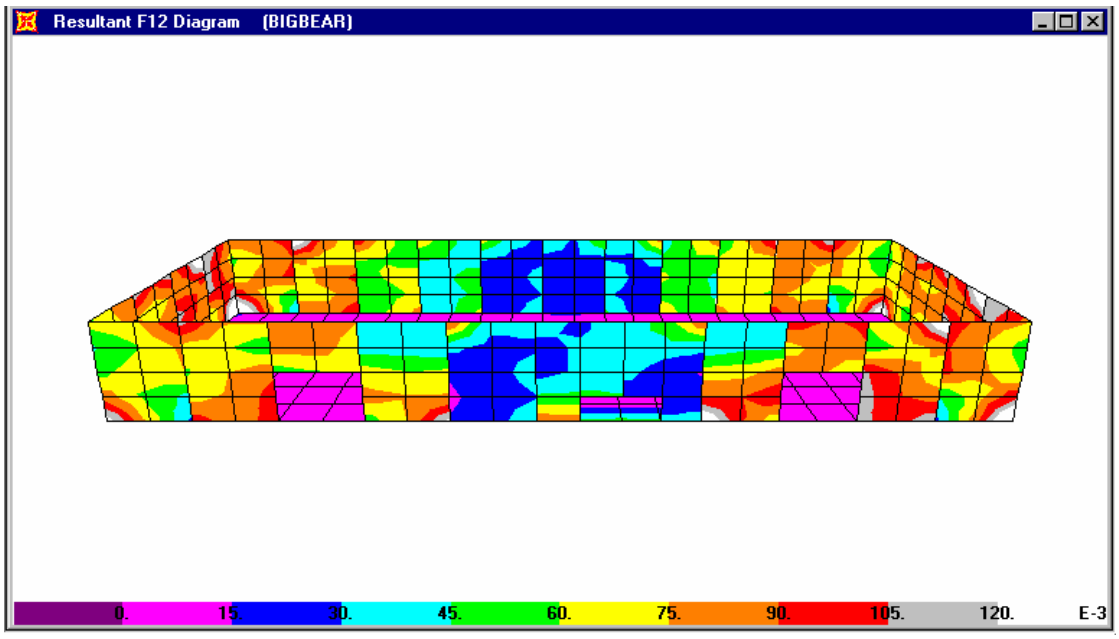

(b) Big Bear: in-plane shear — separated wall segments (kips/in.)

Fig. 6.90 In-plane shear comparisons, segmental walls

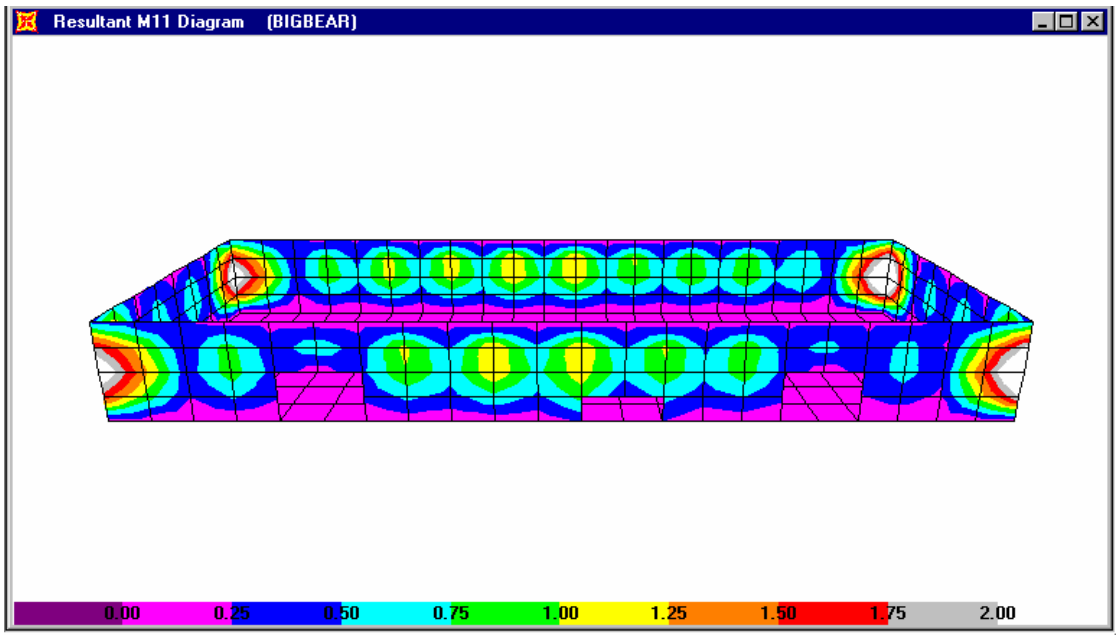

(a) Big Bear: vertical out-of-plane moment — connected wall segments (kips/in.)

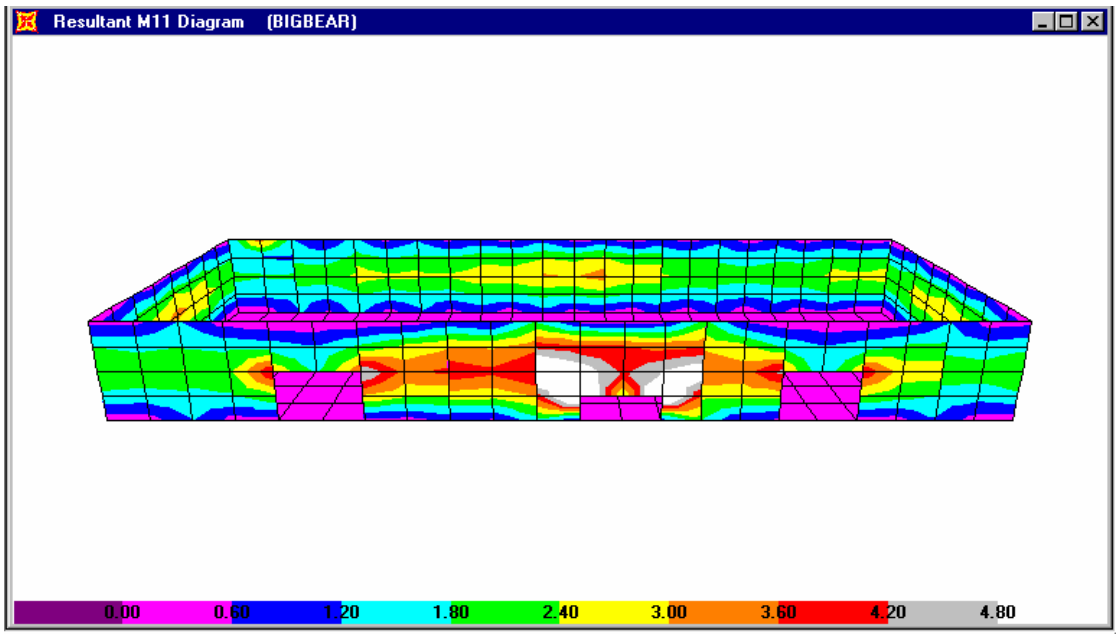

(b) Big Bear: vertical out-of-plane moment — separated wall segments (kips/in.)

Fig. 6.91 Out-of-plane moment comparisons, segmental walls

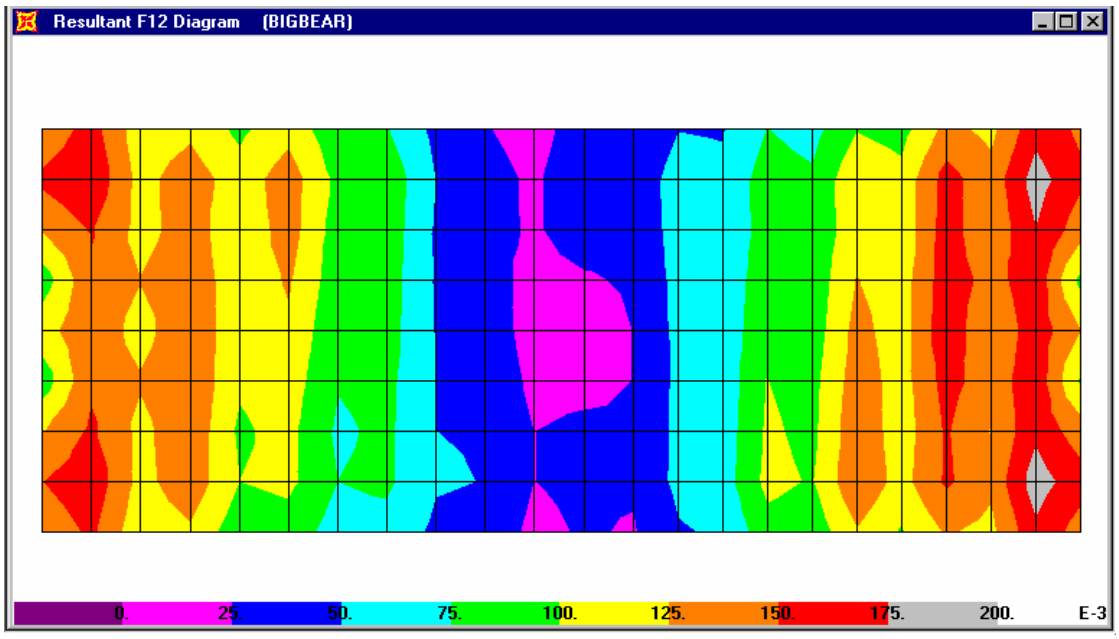

(a) Big Bear: roof in-plane shear — connected wall segments (kips/in.)

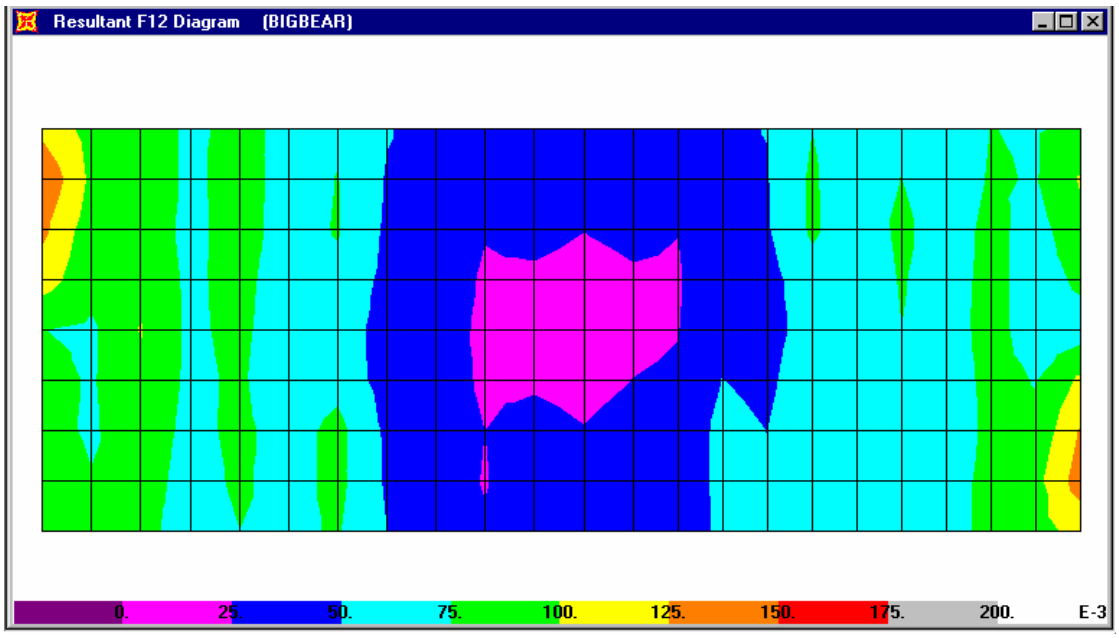

(b) Big Bear: roof in-plane shear — separated wall segments (kips/in.)

Fig. 6.92 In-plane shear comparisons, roof, segmental walls

7 Nonlinear Analyses

The linear elastic analyses discussed in the previous sections have indicated that at least two of the critical components of the TUW building may experience nonlinear behavior during moderate or strong earthquakes. The more critical systems were identified as the timber roof diaphragm and the connections of this diaphragm to the tilt-up walls. Using the nonlinear elements currently available in the SAP2000 computer program, the structure was discretized to make use of these elements.

7.1 NONLINEAR SPRING CONNECTIONS

Initial studies of the nonlinear response were conducted using nonlinear "Nlink" (spring) elements in SAP2000. The force versus displacement relationships for these elements were assumed to be bilinear. Using the building model with the disconnected corners, the constraint connections between the glulam beams and purlins of the roof diaphragm and the pilasters were replaced with nonlinear translation springs in the three principal directions. The nonlinear properties of these springs were derived from the experimental results of the tests conducted at UC Irvine [Pardoen, et al. (2001)] that are summarized in Appendix A. The idealized properties that are representative of "older" connection details are summarized in Table 7.1. The horizontal shear component was taken as linear-elastic, since no experimental data were readily available for loading the connection in this direction. The responses of these elements were evaluated for the recorded Big Bear ground motion and for the Los Gatos ground motion, which is representative of a pulse-type ground motion. Hysteretic force-displacement curves are shown for connections at various locations around the diaphragm perimeter.

Table 7.1 Idealized connection properties (old type)

Glulam Beam to Pilaster: P_y = 13 kips

	Elastic Stiffness, K_1	Inelastic Stiffness, K_2
Axial	60 kips/in.	0.134 K_1
Vertical Shear	60 kips/in.	0.134 K_1
Horizontal Shear	30 kips/in.	1.0 K1(linear)

Purlin to Pilaster or Wall Connection: P_y = 3 kips

	Elastic Stiffness, K_1	Inelastic Stiffness, K_2
Axial	33 kips/in.	0.035 K_1
Vertical Shear	33 kips/in.	0.035 K_1
Horizontal Shear	30 kips/in.	1.0 K_1(linear)

7.1.1 Big Bear, Old Connections

The axial forces in the connections of the purlins and glulams to the pilasters are shown in Figure 7.1 for the Big Bear ground motion. It can be seen that the maximum axial load in the purlin to pilaster connection is 3.05 kips (Fig. 7.1b) compared to 5.5 kips for the elastic springs. For the glulam to pilaster connection (Fig. 7.1c), the maximum value reaches 12 kips compared to 13.5 kips for the elastic springs. The distribution of the vertical shear forces for this ground motion is shown in Figure 7.2. For the purlins located along the north and south walls (Fig. 7.2b), the maximum connection force occurs near the end of the wall and has a value of 2.0 kips, as compared to almost 3.0 kips for the elastic springs. The vertical shear forces for the glulam beams along the east and west walls (Fig. 7.2c) have a maximum value of 1.75 kips that is similar to that of the elastic springs. The horizontal shear forces in the connection of the purlins to the end walls are shown in Figure 7.3. Here it can be seen that the maximum value occurs near the center of the wall and has a value of just over 12.1 kips (Fig. 7.3b). This compares to a maximum value of 20 kips for the elastic connection springs. The horizontal shear forces in the glulam connections to the east and west walls (shown in Fig. 7.3c) reach a maximum value of only 2.1 kips compared to 20 kips for the elastic connection springs.

Hysteretic force versus displacement plots for the three force components at the connection of the glulam to pilaster at the middle of the longitudinal wall are shown in Figure 7.4. The axial force (Fig. 7.4a) indicates a weakly nonlinear behavior, with a displacement demand of 0.26 inches and a displacement ductility demand of 1.5. The other two components ((Figs. 7.4b–c) indicate linear behavior. Similar data for a glulam to pilaster connection near the

corner of the longitudinal wall are shown in Figure 7.5. The plots are very similar to the previous case, with the axial force (Fig. 7.5a) indicating weakly nonlinear behavior and the two shear components remaining elastic. Note that the inelastic displacement and the corresponding force are less than the previous case.

The hysteretic behavior of the three force components of a purlin to pilaster connection at the middle of a transverse wall is shown in Figure 7.6. The overall behavior is also similar to that of the glulam to pilaster connections. The axial force (Fig. 7.6a) has a nonlinear behavior with a maximum displacement demand of 0.17 inches and a displacement ductility demand of 1.9. The two shear components (Figs. 7.6b–c) respond in an elastic manner. Note the low yield force of the older type of purlin to pilaster connection. The hysteretic behavior of the purlin to pilaster connection at the end of the transverse wall is shown in Figure 7.7. The axial load (Fig. 7.7a) indicates increased inelastic behavior, although the yield force of these older connections is low at 3.0 kips. At this location, the vertical shear force also indicates weakly nonlinear behavior as shown in Figure 7.7b. However, the horizontal shear (Fig. 7.7c) remains elastic.

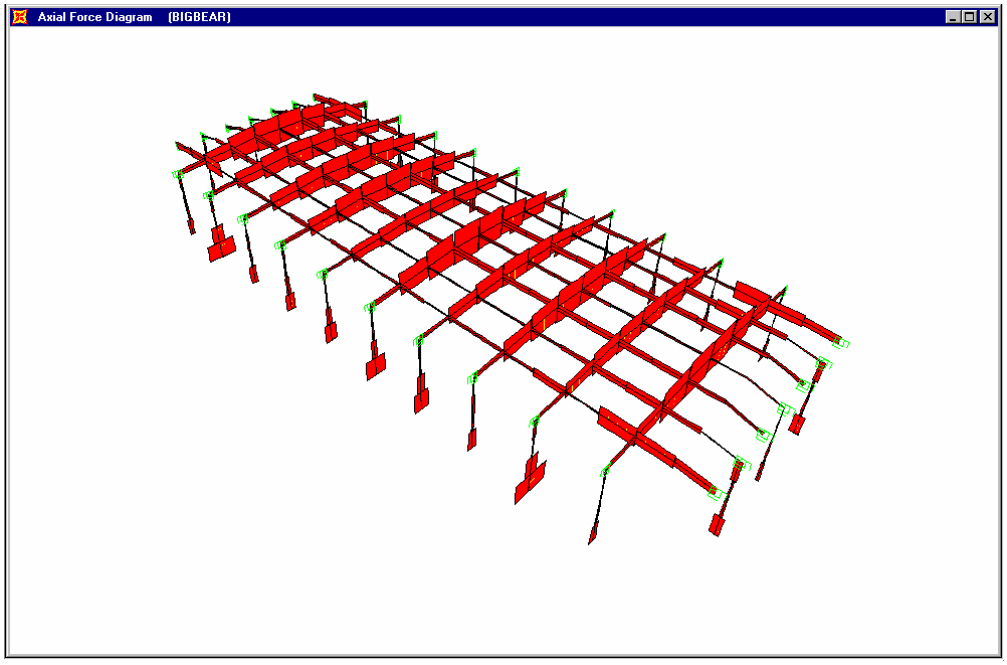

(a) Big Bear, axial force

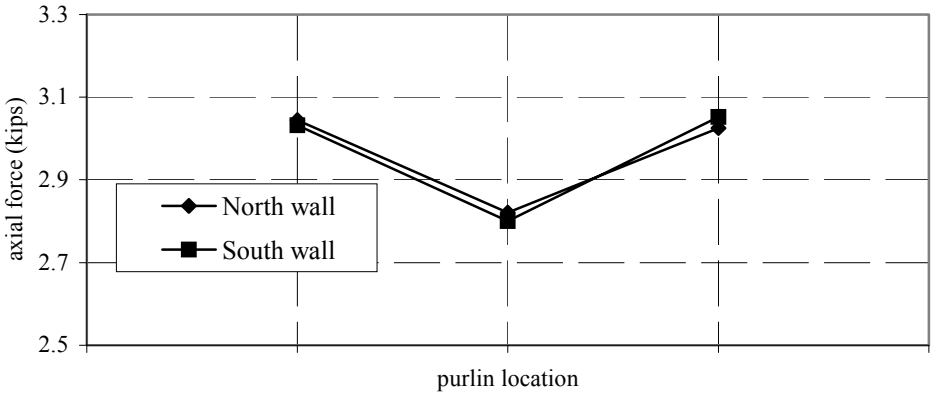

(b)

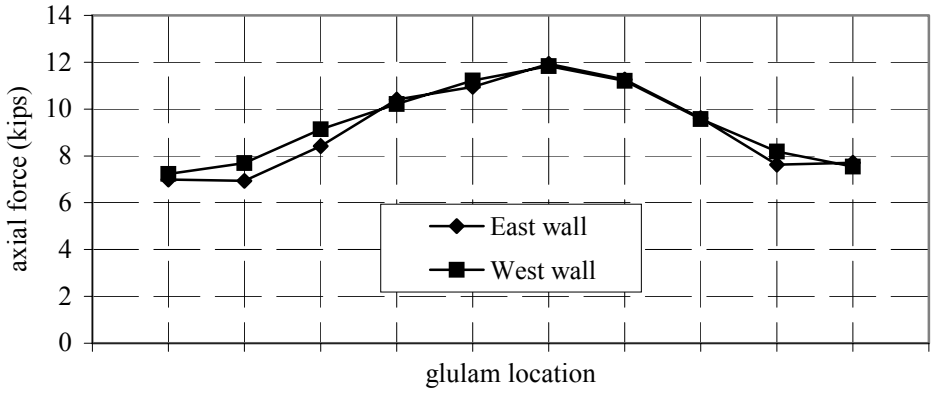

(c)

Fig. 7.1 Axial force, nonlinear old connections, Big Bear

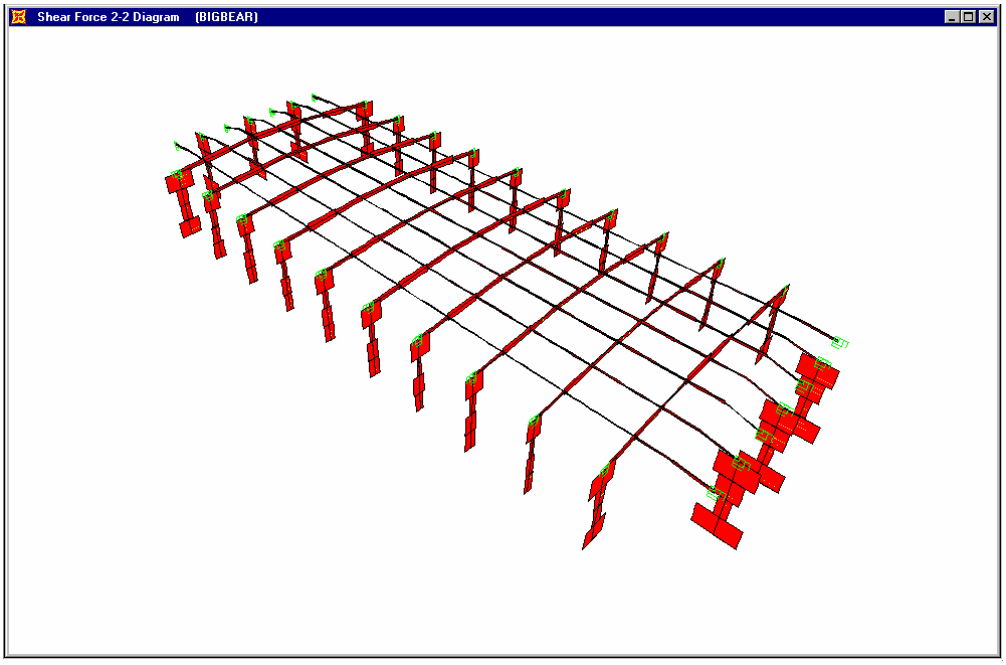

(a) Big Bear, vertical shear force

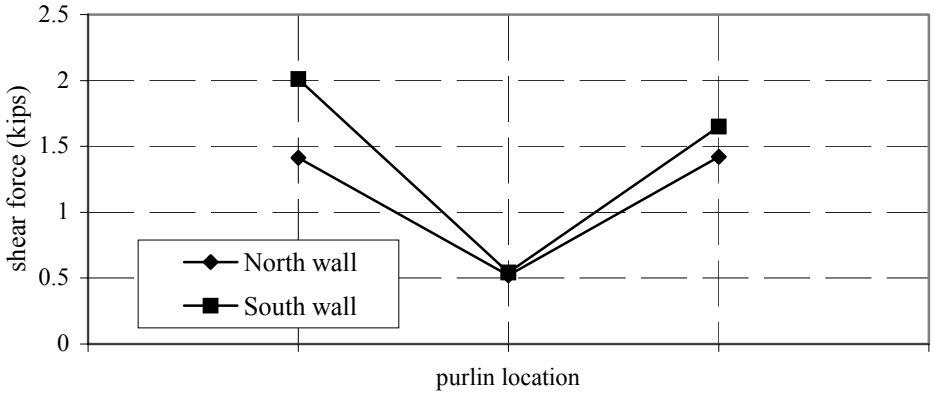

(b)

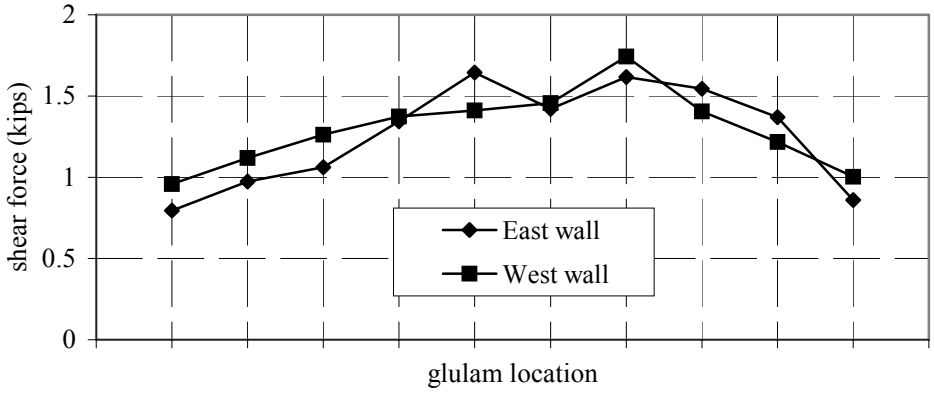

(c)

Fig. 7.2 Vertical shear force, nonlinear old connections, Big Bear

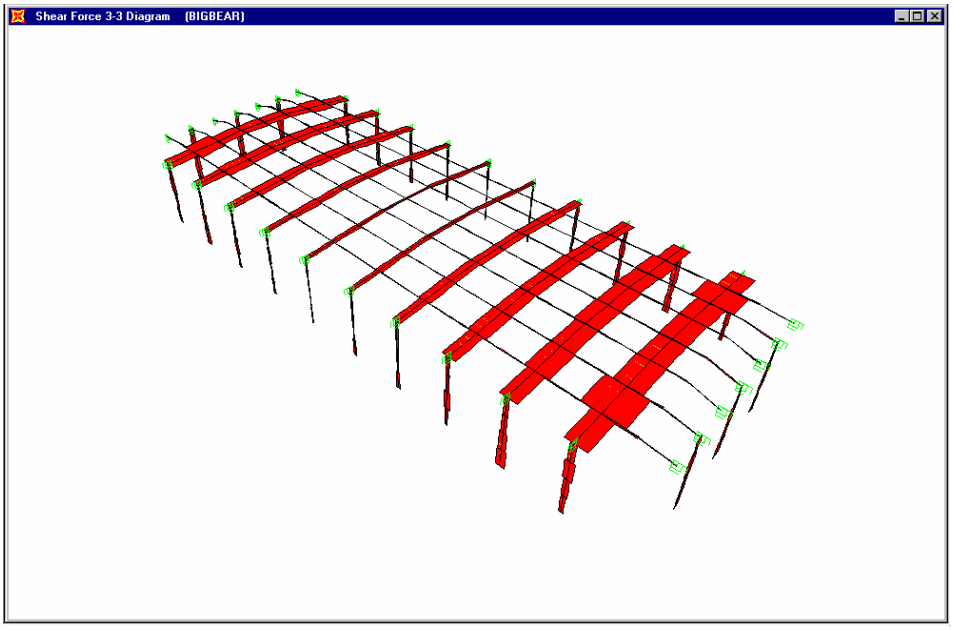

(a) Big Bear: horizontal shear force

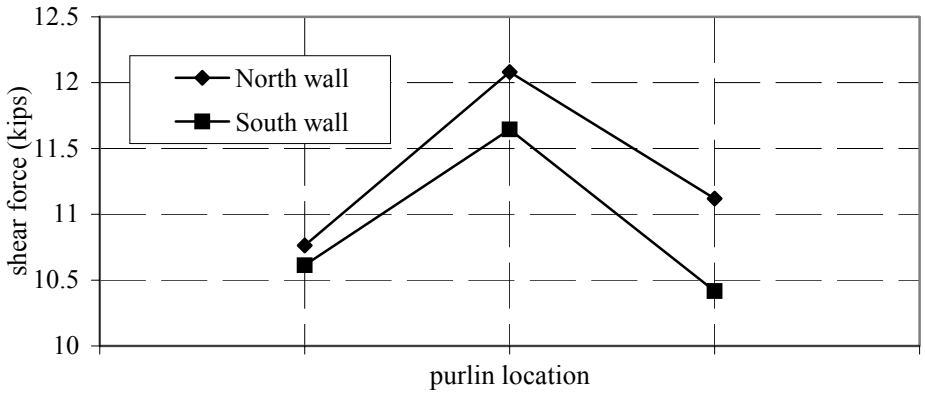

(b)

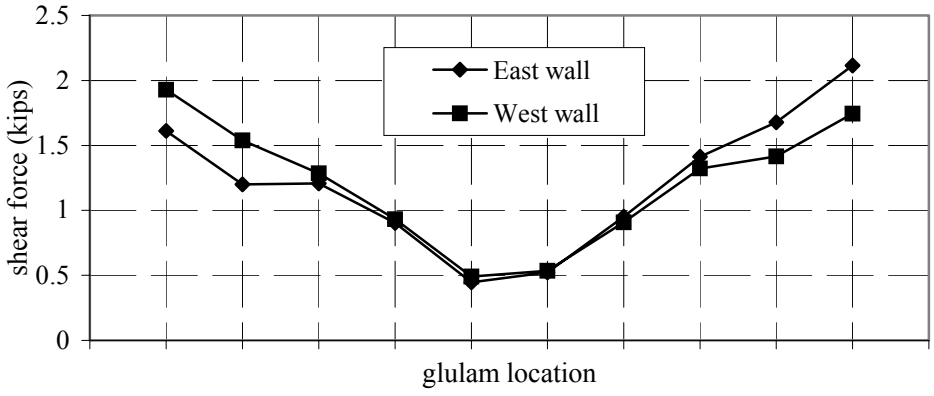

(c)

Fig. 7.3 Horizontal shear force, nonlinear old connections, Big Bear

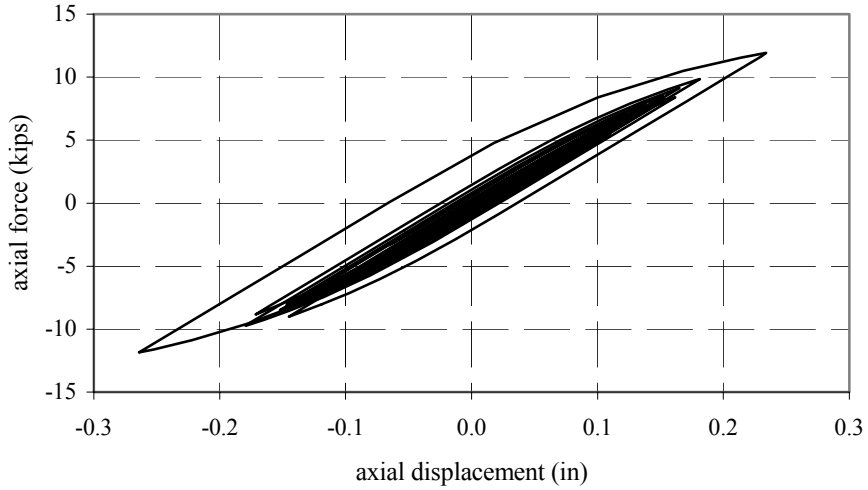

(a)

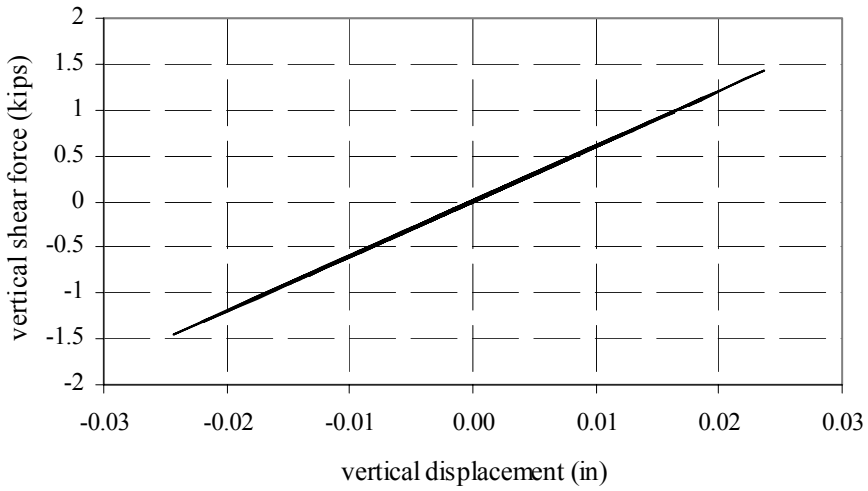

(b)

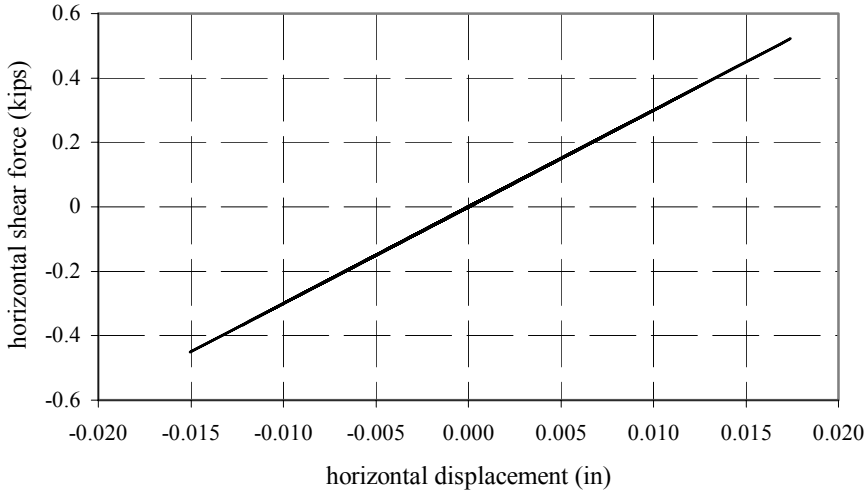

(c)

Fig. 7.4 Old glulam to pilaster connection, middle of wall, Big Bear

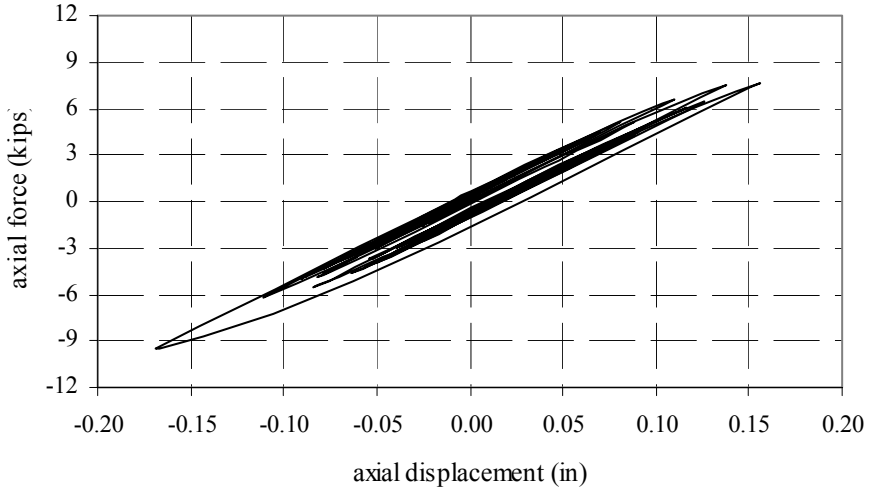

(a)

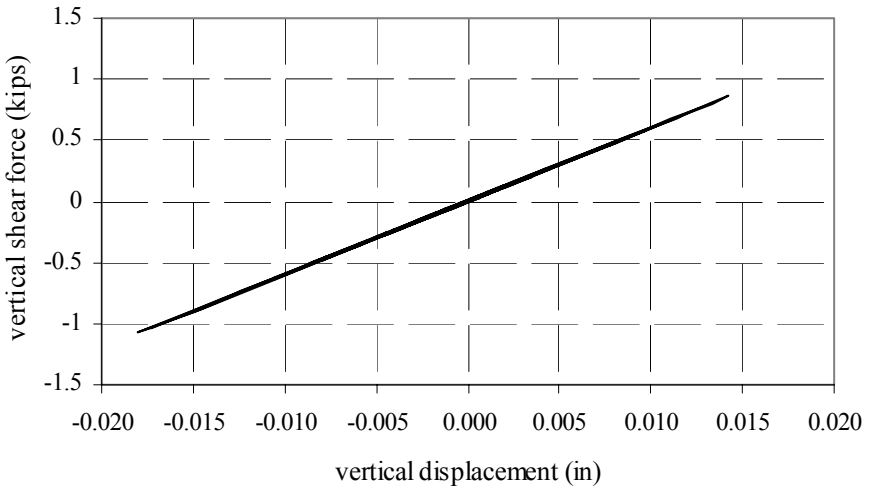

(b)

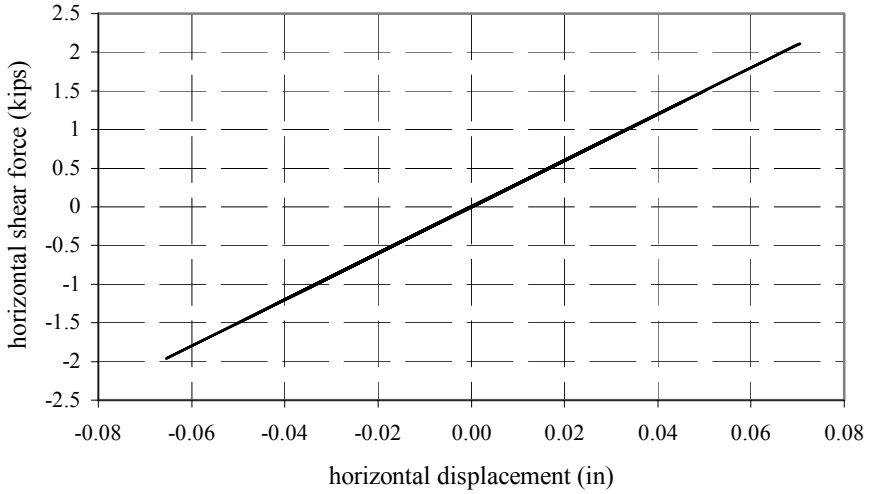

(c)

Fig. 7.5 Old glulam to pilaster connection, near corner, Big Bear

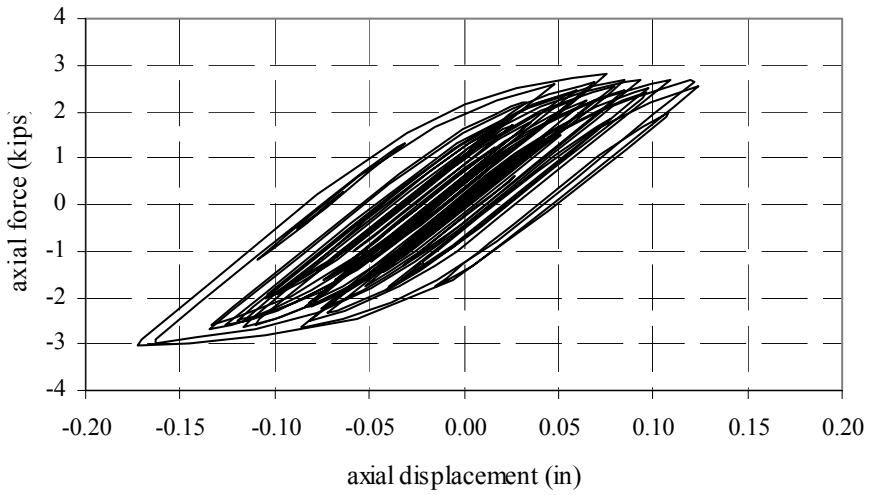

(a)

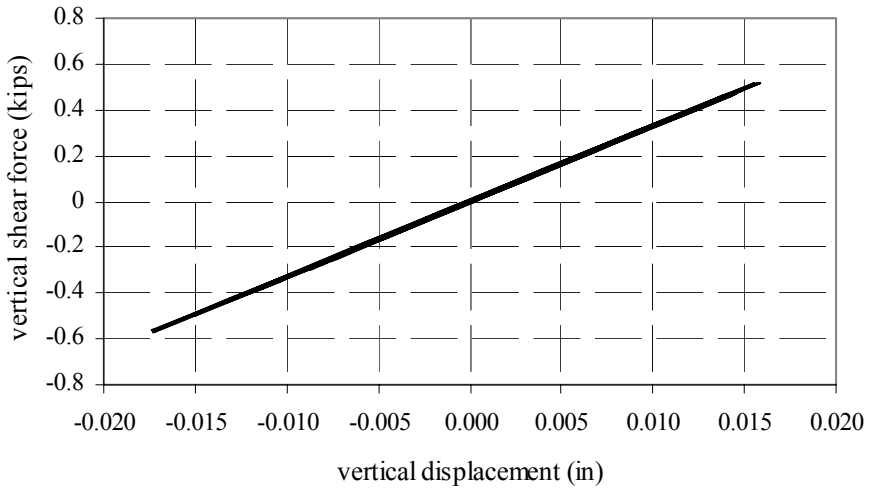

(b)

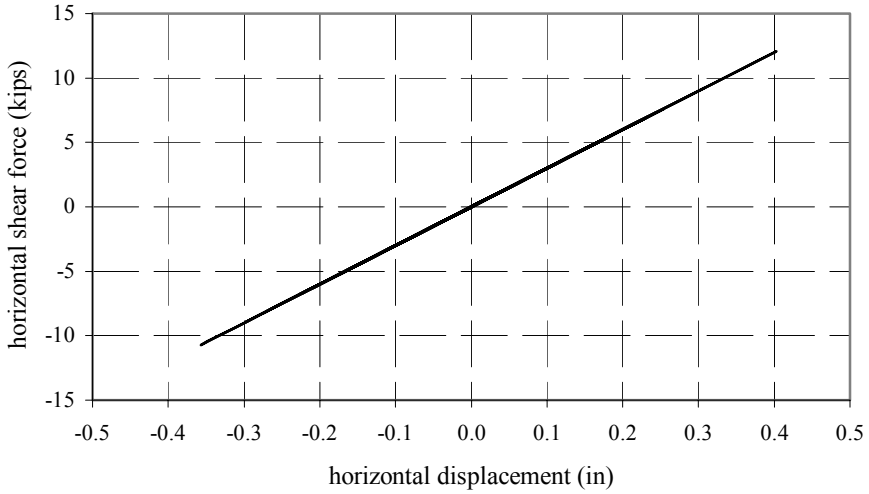

(c)

Fig. 7.6 Old purlin to pilaster connection, middle of wall, Big Bear

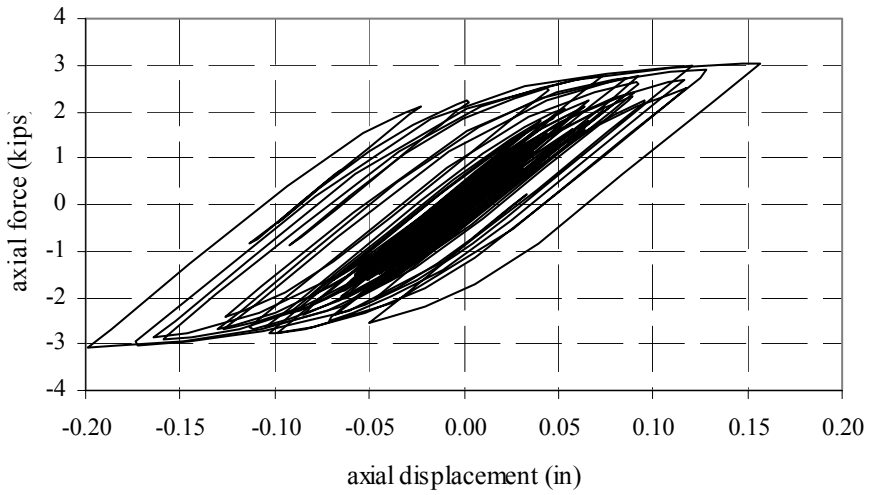

(a)

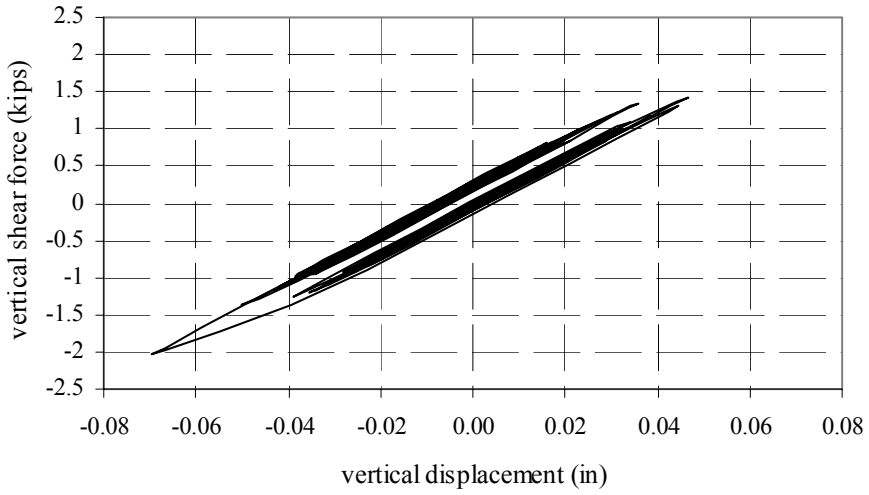

(b)

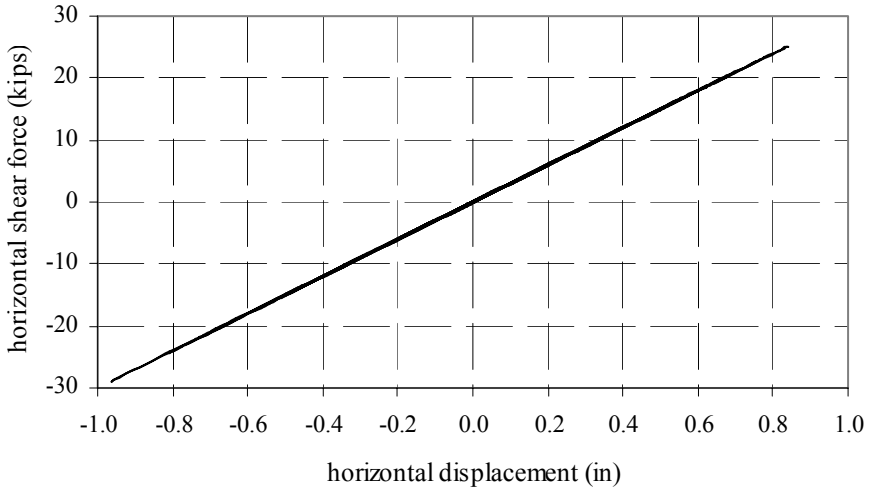

(c)

Fig. 7.7 Old purlin to pilaster connection, near corner, Big Bear

7.1.2 Los Gatos Ground Motion (Old Connections)

The ground motion recorded at Santa Cruz (Los Gatos Presentation Center) during the Loma Prieta earthquake is representative of a strong pulse-type ground motion. In the figures that follow it will be shown that this type of ground motion can have a serious effect on the performance of this type of structure. The maximum axial loads in the purlin and glulam connections to the pilasters on the perimeter of the building are shown in Figure 7.8. The axial force in the purlin to pilaster connections (Fig. 7.8b) reaches a maximum value of 13.2 kips at the center of the end wall. This compares to a force of almost 22 kips for the elastic connection model. The maximum axial force in the glulam connection (Fig. 7.8c) reaches 19 kips near the center of the wall. This is also considerably less than the axial force demand of 46 kips indicated by the elastic connection.

The distribution of vertical shear force in the purlin to pilaster connections is shown in Figure 7.9b and indicates a maximum value of 5 kips near the end of the transverse wall. This is 50% of the value indicated by the elastic connections. For the glulam to pilaster connection (Fig. 7.9c) the vertical shear reaches a value of 4.7 kips, compared to 6.1 kips for the elastic connection model. The maximum horizontal shear forces parallel to the face of the wall are shown in Figure 7.10. The maximum horizontal shear force in the purlin to pilaster connections (Fig. 7.10b) reaches a value of 29 kips, which is considerably less than the 72 kips obtained from the elastic connection model. The maximum horizontal shear force in the glulam connections (Fig. 7.10c) has a maximum value of 5.5 kips, much less than the 62 kips of the elastic model.

Whereas the inclusion of inelastic behavior has resulted in a significant reduction in the force demand, the figures that follow show that the displacement demand has increased to a value that will not be sustainable. It should be reiterated that these connections are representative of older connections in existing buildings and were typical of building practice during the 1970s.

The hysteretic behavior of the glulam to pilaster connection near the middle of a longitudinal wall is shown in Figure 7.11. From the axial component in Figure 7.11a, it can be seen that there is substantial inelastic behavior in this component, including many inelastic cycles. The maximum displacement demand is one inch and the displacement ductility demand is estimated to be near four. The other two shear components (Figures 7.11b–7.11c) remain elastic for this connection. The forces in a similar connection located near the end of the longitudinal wall are shown in Figure 7.12. The axial force, although still exhibiting inelastic behavior (Fig.

7.12a) has a reduced demand as compared to the previous case. The displacement ductility demand at this location is estimated to be a more modest two. The two shear components of Figures 7.12b–c remain elastic as in the previous case.

The hysteretic behavior of the purlin to pilaster connections at the transverse walls is shown in the two figures that follow. The hysteretic behavior of a connection near the middle of the wall is shown in Figure 7.13. The hysteretic behavior of the axial component is shown in Figure 7.13a. This figure indicates an extreme displacement demand for the connection of 10 inches in the axial direction and a displacement ductility demand of more than 100. The old type of connection will not be able to develop this amount of displacement and failure of the connection is likely. The vertical shear behavior (Fig. 7.13b) indicates weakly nonlinear behavior. The horizontal shear acts concurrently with the axial force and develops a force of 30 kips as shown in Figure 7.13c. Similar data for a connection near the end of the transverse wall are shown in Figure 7.14. The axial force has a hysteretic behavior that is similar to the previous connection (Fig. 7.14a), and the vertical shear force at this location has a strongly nonlinear behavior (Fig. 7.14b). The horizontal shear force (Fig. 7.14c) remains elastic, since there is no information on the inelastic behavior of this component.

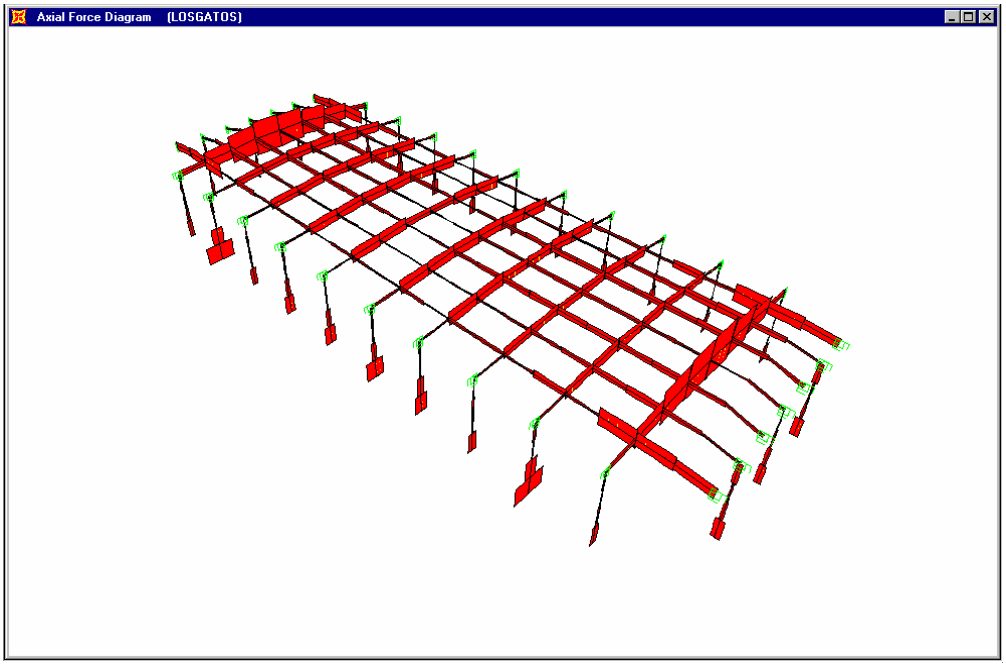

(a) Los Gatos, axial force

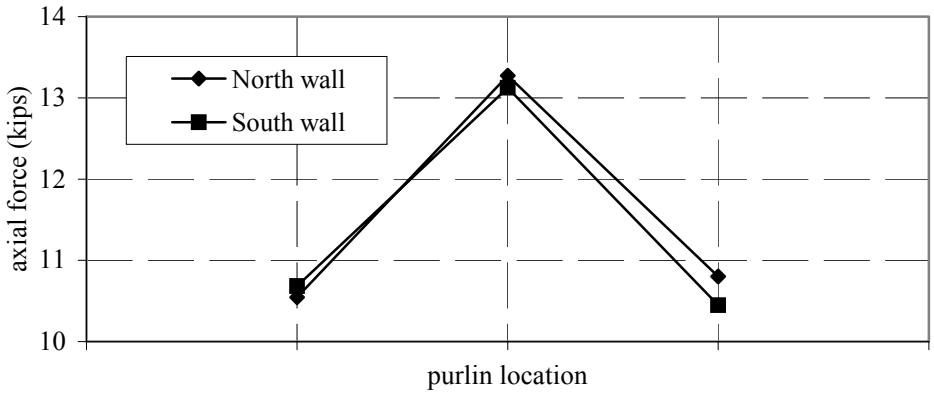

(b)

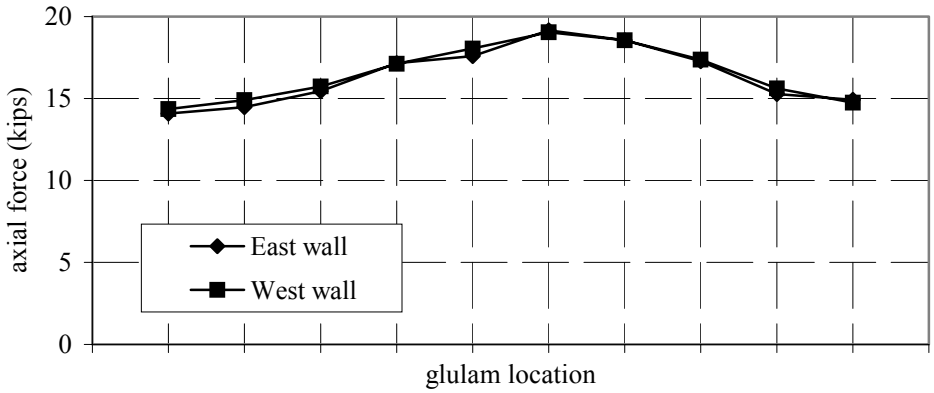

(c)

Fig. 7.8 Axial force, nonlinear old connections, Los Gatos

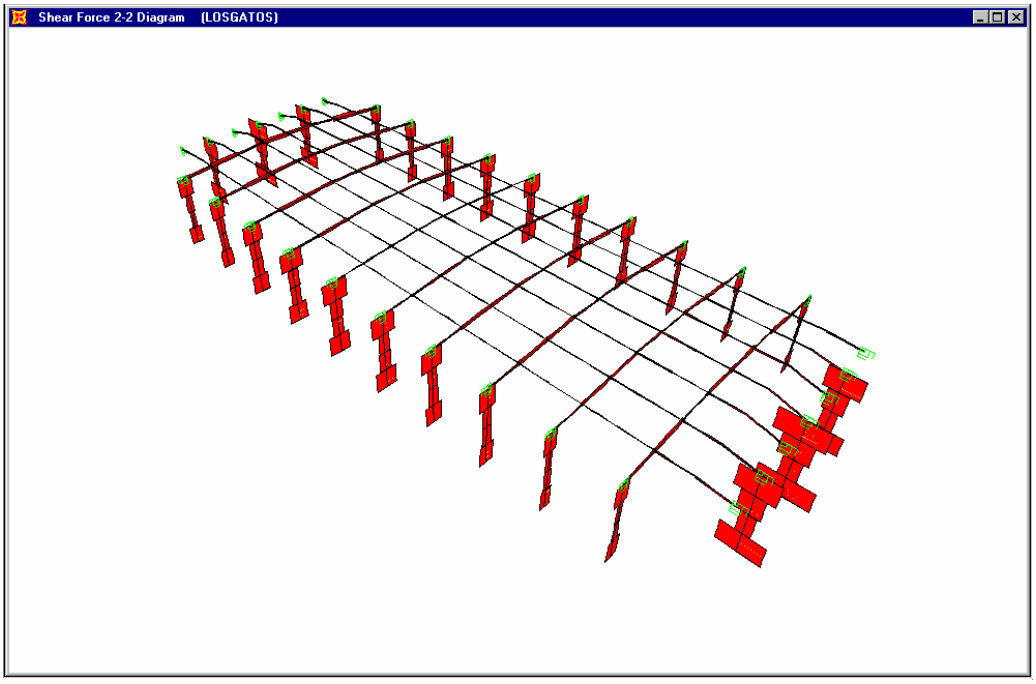

(a) Los Gatos, vertical shear force

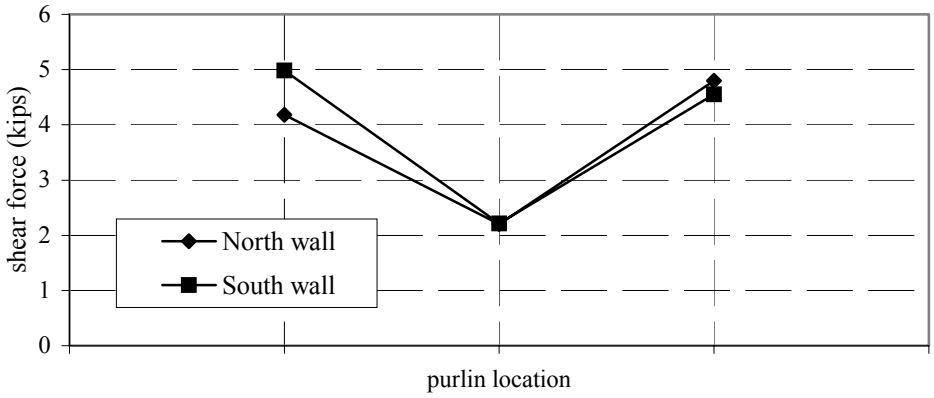

(b)

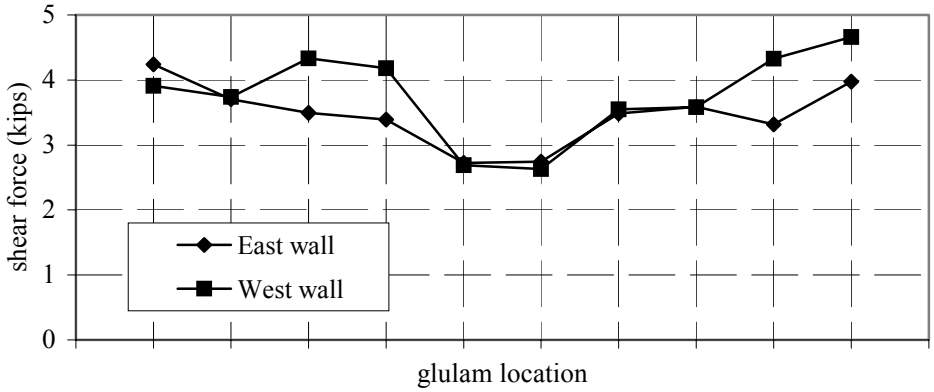

(c)

Fig. 7.9 Vertical shear force, nonlinear old connections, Los Gatos

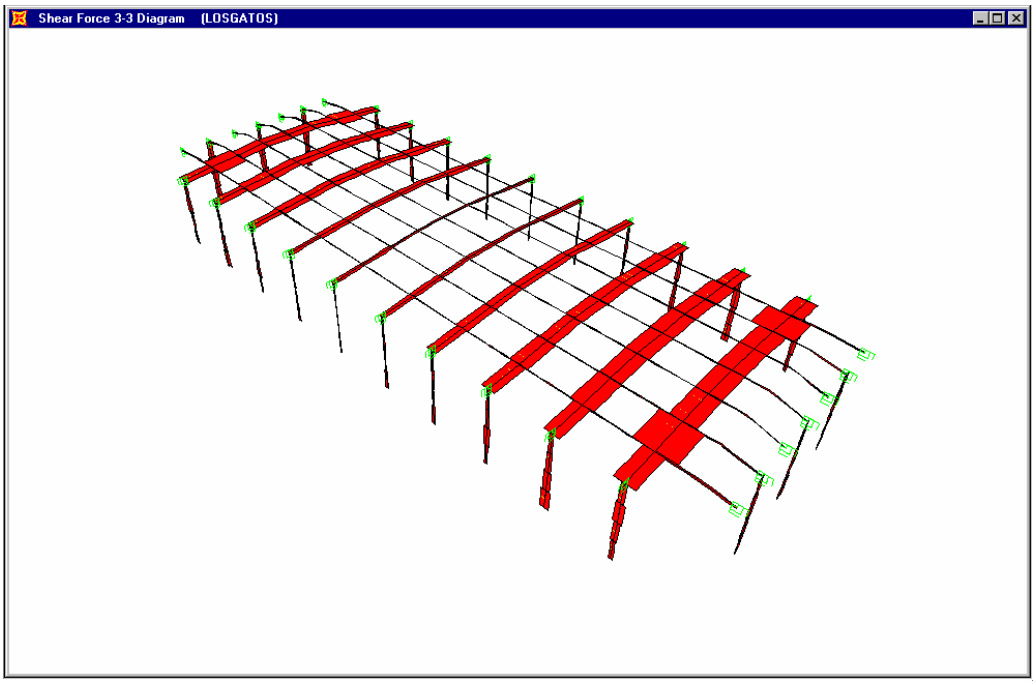

(a) Los Gatos, horizontal shear force

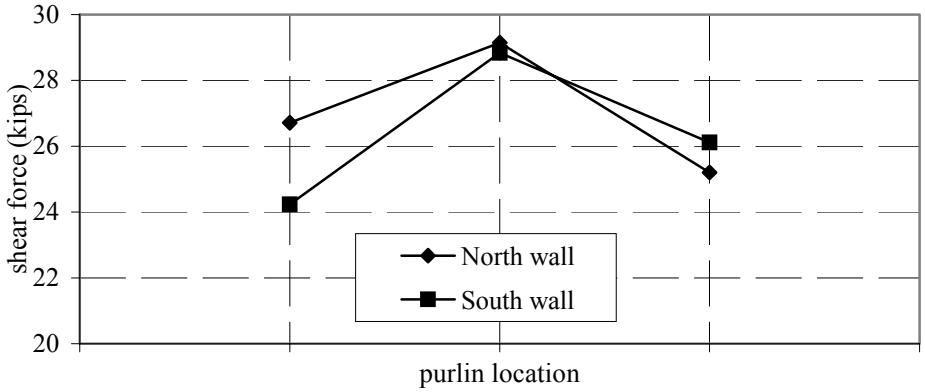

(b)

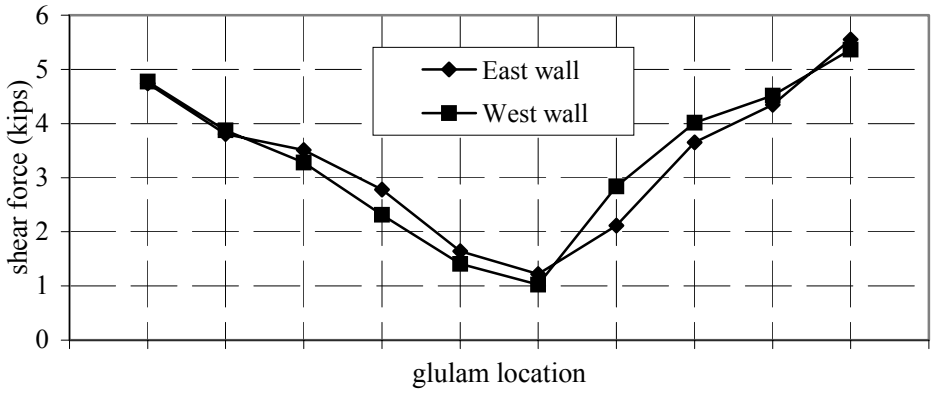

(c)

Fig. 7.10 Horizontal shear force, nonlinear old connections, Los Gatos

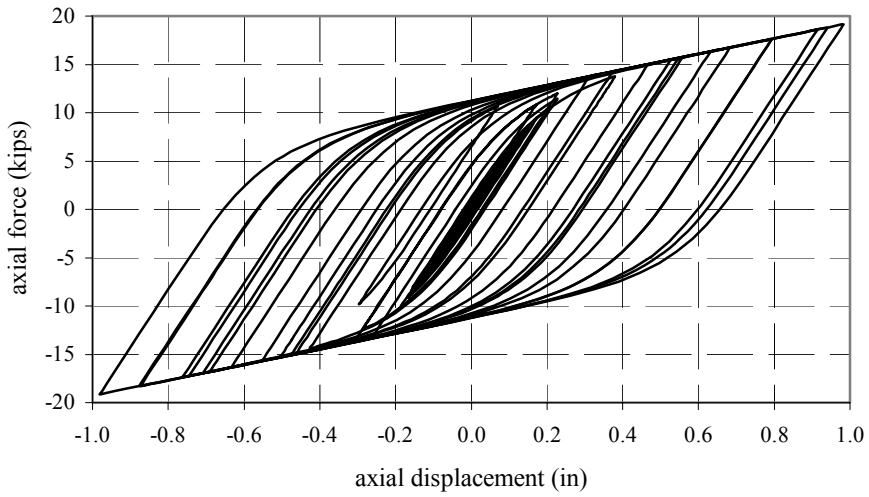

(a)

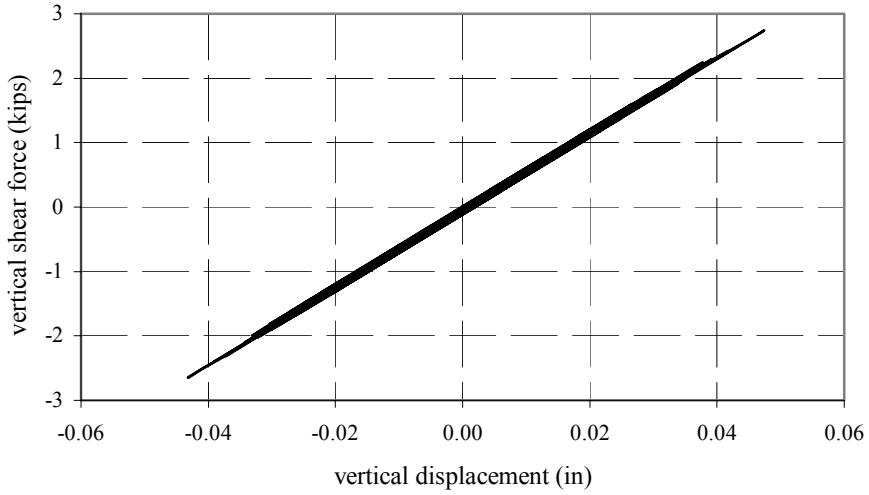

(b)

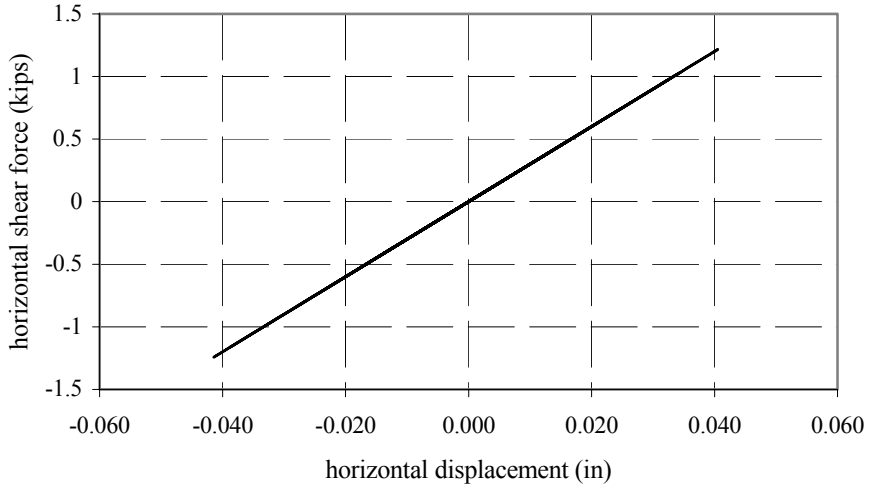

(c)

Fig. 7.11 Old glulam to pilaster connection, middle of wall, Los Gatos

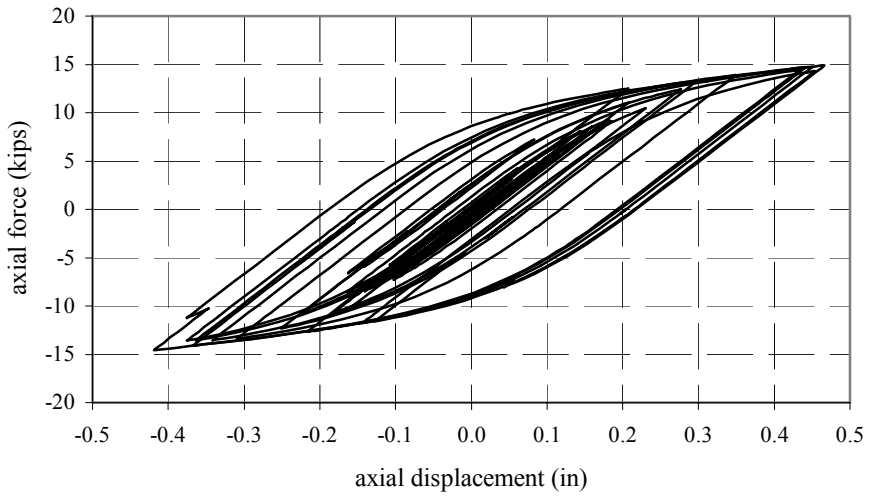

(a)

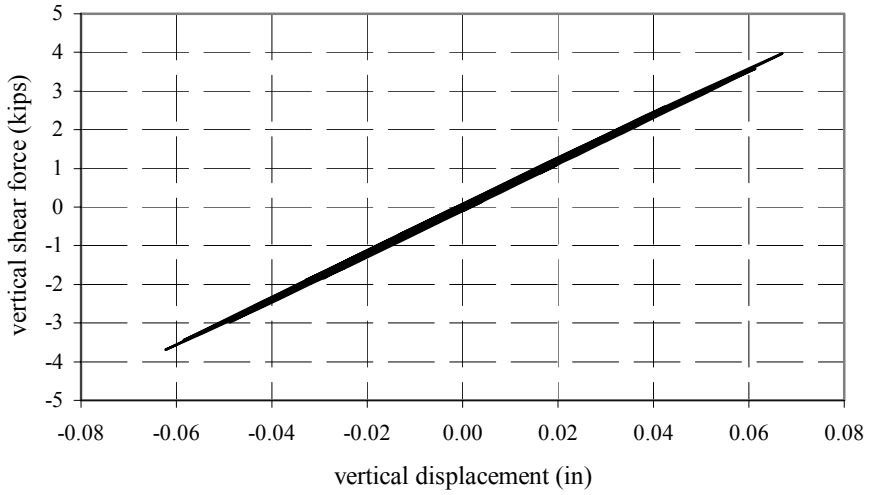

(b)

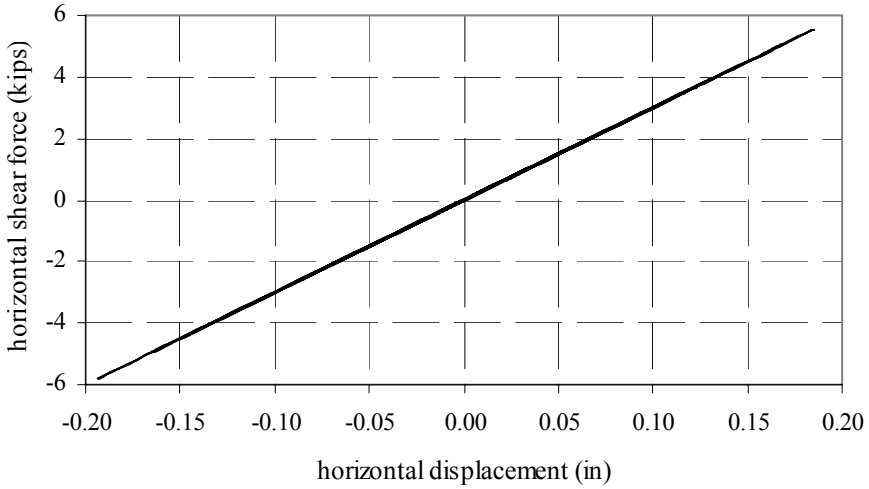

(c)

Fig 7.12 Old glulam to pilaster connection, near corner, Los Gatos

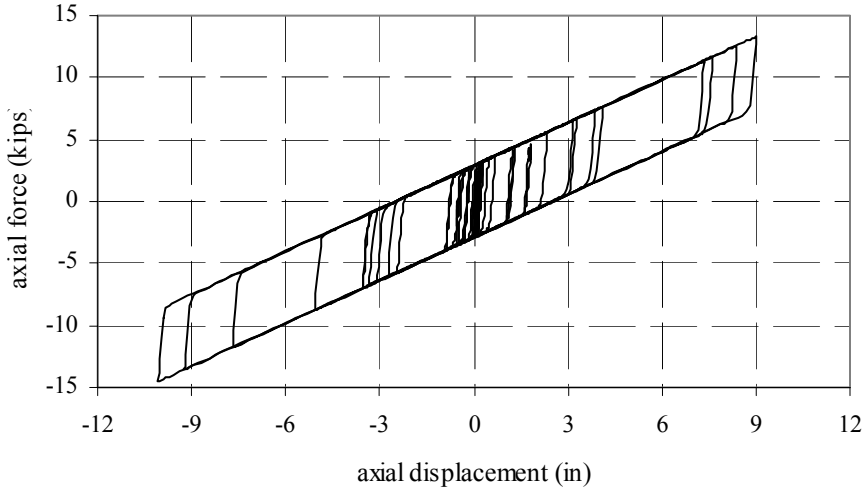

(a)

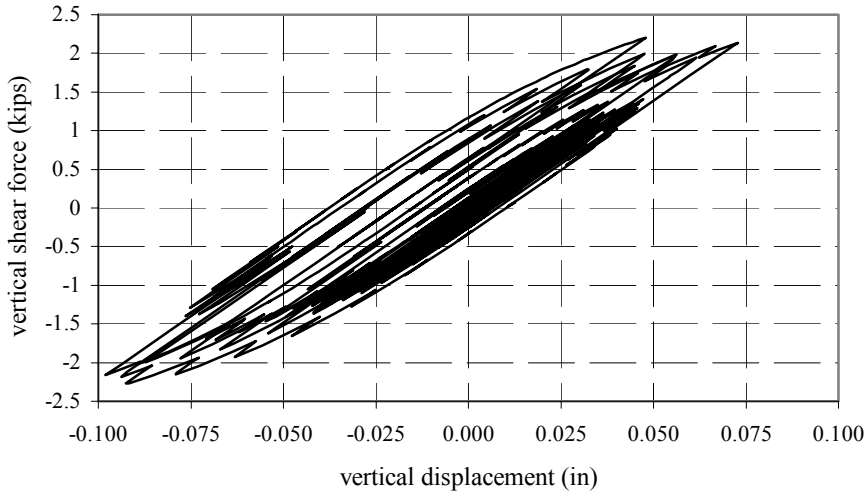

(b)

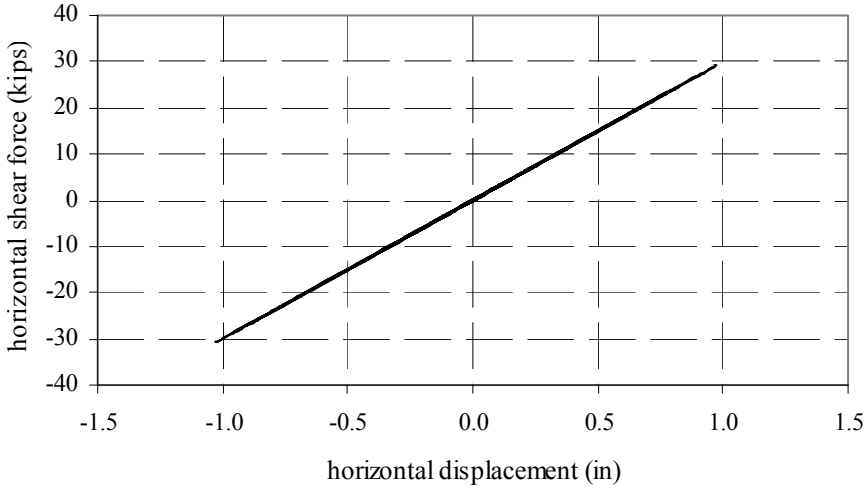

(c)

Fig. 7.13 Old purlin to pilaster connection, middle of wall, Los Gatos

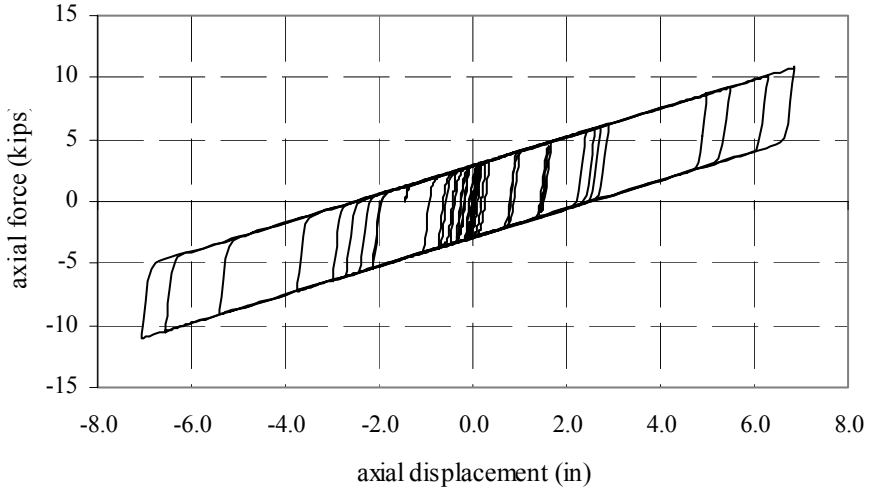

(a)

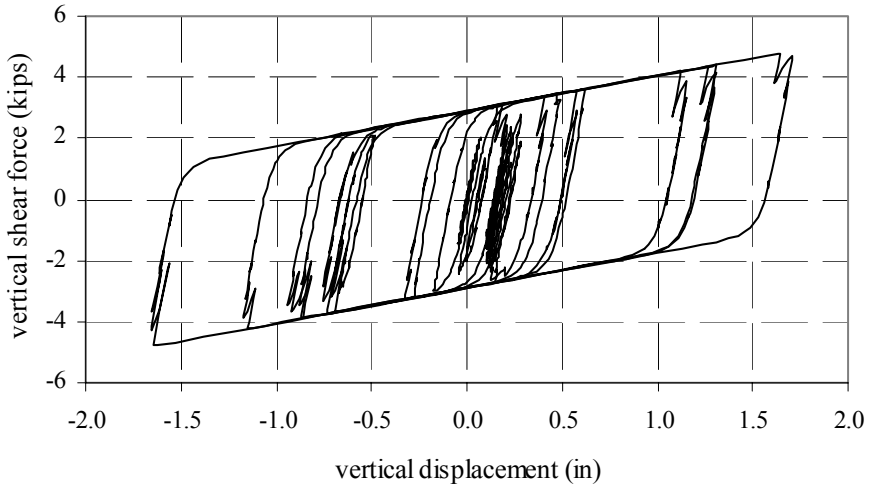

(b)

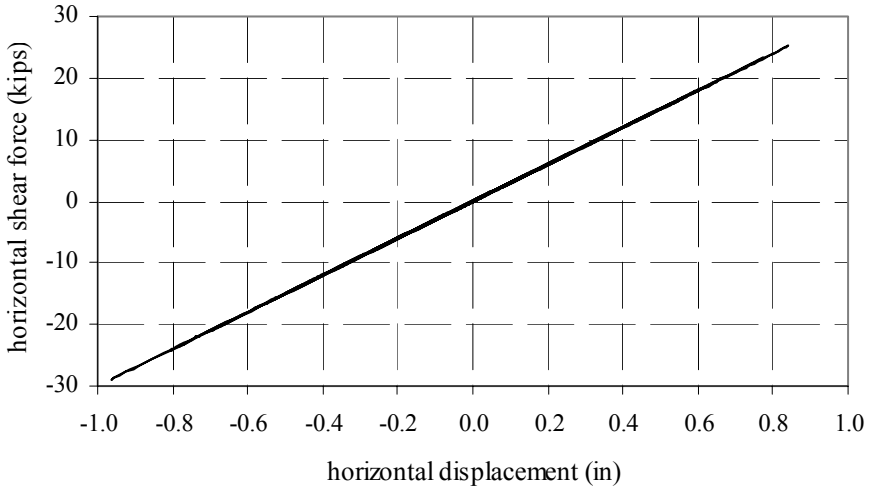

(c)

Fig. 7.14 Old purlin to pilaster connection, near corner, Los Gatos

7.1.3 Los Gatos Ground Motion (New Connections)

Connection details that were used in TUW construction in the late 1970s and 1980s are referred to as "new" connections. Samples of these connections were also tested [Pardoen et al., 1999] and the results are summarized in Appendix A. The idealized bilinear properties of these connections are summarized in Table 7.2.

Table 7.2 Idealized connection properties (new type)

Glulam Beam to Pilaster: P_y = 34 kips

	Elastic Stiffness, K_1	Inelastic Stiffness, K_2
Axial	44 kips/in.	0.030 K_1
Vertical Shear	44 kips/in.	0.030 K_1
Horizontal Shear	30 kips/in.	1.0 K_1(linear)

Purlin to Pilaster or Wall Connection: P_y = 18 kips

	Elastic Stiffness, K_1	Inelastic Stiffness, K_2
Axial	120 kips/in.	0.021 K_1
Vertical Shear	120 kips/in.	0.021K_1
Horizontal Shear	30 kips/in.	1.0 K_1(linear)

The maximum axial loads in the purlin and glulam connections to the pilasters on the perimeter of the building are shown in Figure 7.15. The axial force in the purlin to pilaster connections (Fig. 7.15b) reaches a maximum value of 18.3 kips at the center of the end wall. This compares to a force of 13.2 kips for the old connection and almost 22 kips for the elastic connection model. The maximum axial force in the glulam to pilaster connection (Fig. 7.15c) reaches 33 kips near the center of the longitudinal wall. This value is larger than the 19 kips for the old connection but considerably less than the axial force demand of 46 kips indicated by the elastic connection.

The distribution of the vertical shear forces is shown in Figure 7.16. The distribution of vertical shear force in the purlin to pilaster connections (Fig. 7.16b) indicates a maximum value of 7 kips near the end of the transverse wall. This compares with a value of 5 kips for the old connections and 10 kips as indicated by the elastic connections. For the glulam to pilaster connection (Fig. 7.16c), the vertical shear reaches a value of 5.0 kips, which compares to 4.7 kips for the old connection and 6.1 kips for the elastic connection model. The maximum horizontal shear forces parallel to the face of the wall are shown in Figure 7.17. The maximum horizontal shear force in the purlin to pilaster connections (Fig. 7.17b) reaches a value of 39 kips for the

new connection compared to 29 kips for the old connection and 72 kips obtained from the elastic connection model. The maximum horizontal shear force in the glulam to pilaster connections (Fig. 7.17c) has a maximum value of 7.5 kips, which is not too different from the 5.5 kips for the old connection but which is much less than the 62 kips of the elastic model.

The hysteretic behavior of the glulam to pilaster connection near the middle of a longitudinal wall is shown in Figure 7.18. The behavior of the axial component is shown in Figure 7.18a. Here it can be seen that the total displacement demand is approximately the same (1.0 in.). This is largely due to the reduction in stiffness of the new connections. However, the amount of inelastic deformation has been substantially reduced to an estimated displacement ductility of 2.0 compared to 4.0. The other two shear components (Figs. 7.18b–c) both remain elastic for this connection. The forces in a similar connection located near the end of the longitudinal wall are shown in Figure 7.19. For the new connections, the axial force is only weakly nonlinear with a maximum displacement demand of 0.7 inches, as shown in Figure 7.19a**.** The displacement ductility demand at this location is estimated to be just over unity. The two shear components (Figs. 7.19b–c) remain elastic as in the previous case.

In the two figures that follow, it can be seen that the increased stiffness (4x) and strength (6x) of the new connections of the purlin to pilaster connections at the transverse walls have a significant effect on the inelastic behavior of these connections. The hysteretic behavior of the axial force component for a connection near the middle of the wall is shown in Figure 7.20a. This figure indicates a displacement demand of only 0.5 inches compared to an extreme displacement demand of 10 inches in the axial direction for the old type of connection. A displacement ductility demand of only 3.3 is indicated. The vertical shear behavior (Fig. 7.20b**)** and the horizontal shear (Fig. 7.20c) both indicate linear elastic behavior. Similar data for a connection near the end of the transverse wall are shown in Figure 7.21. The axial force has a similar weakly nonlinear behavior but with a reduced displacement demand (0.3 in.), and the vertical shear force at this location is now linear Figure 7.21b. The horizontal shear force (Fig. 7.21c) remains elastic, since there is no information on the inelastic behavior of this component.

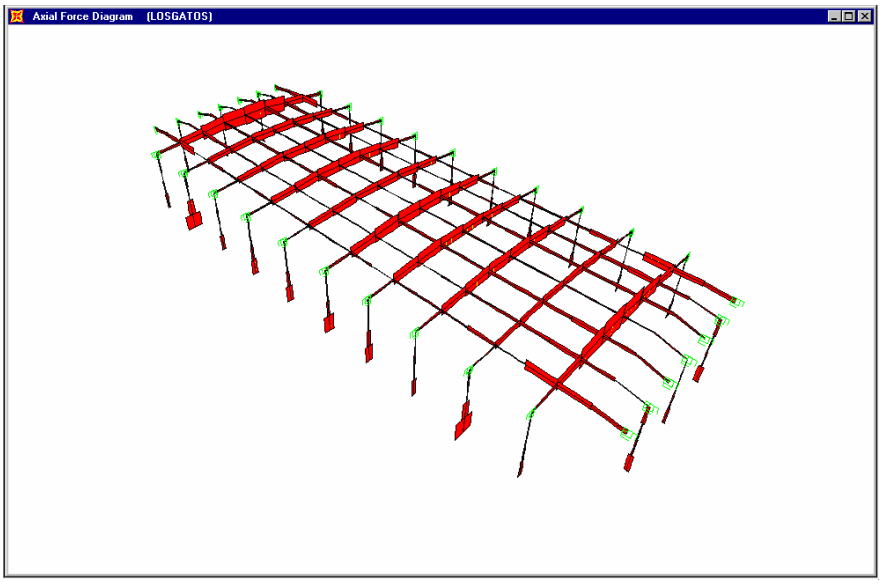

(a) Los Gatos, axial force

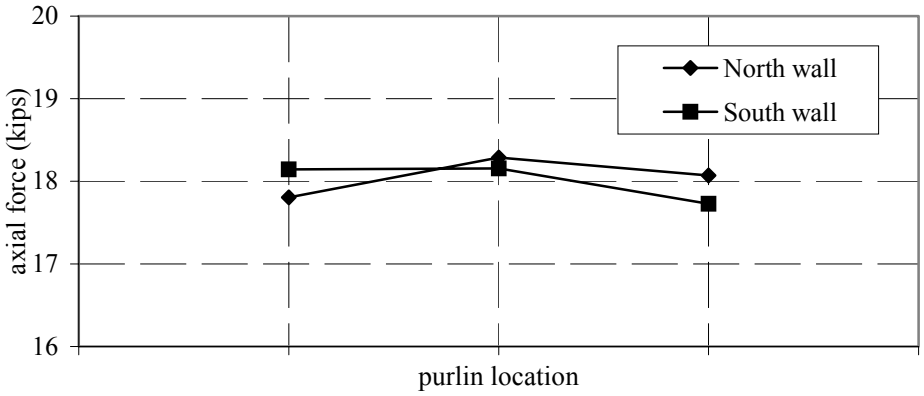

(b)

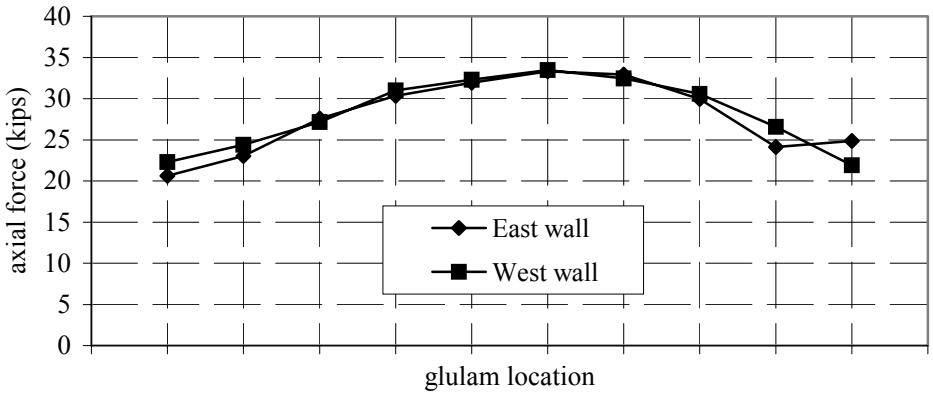

(c)

Fig. 7.15 Axial force, nonlinear new connections, Los Gatos

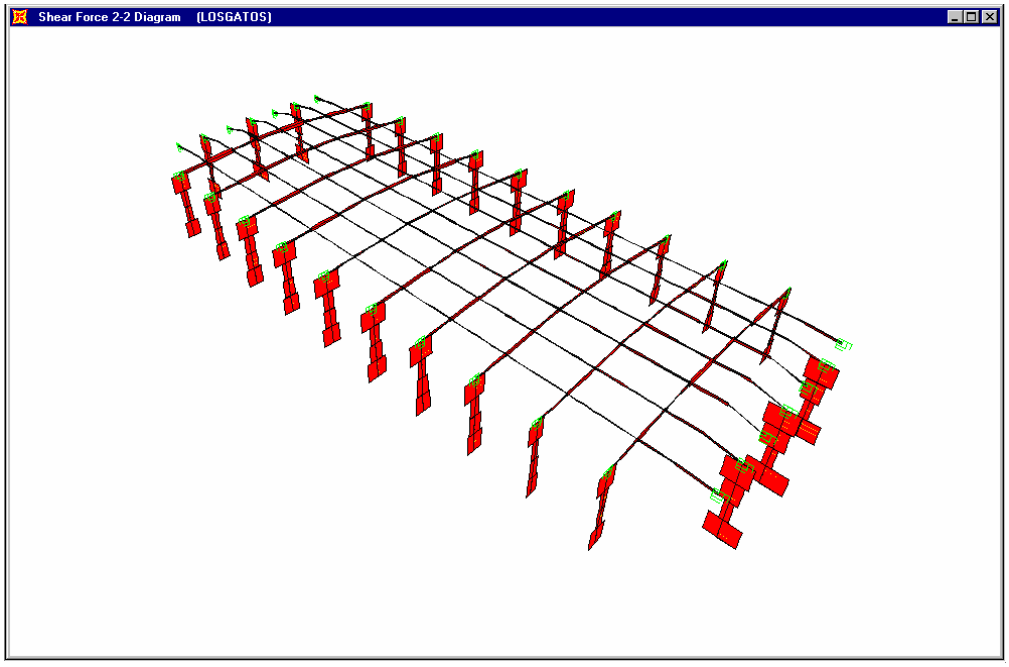

(a) Los Gatos, vertical shear force

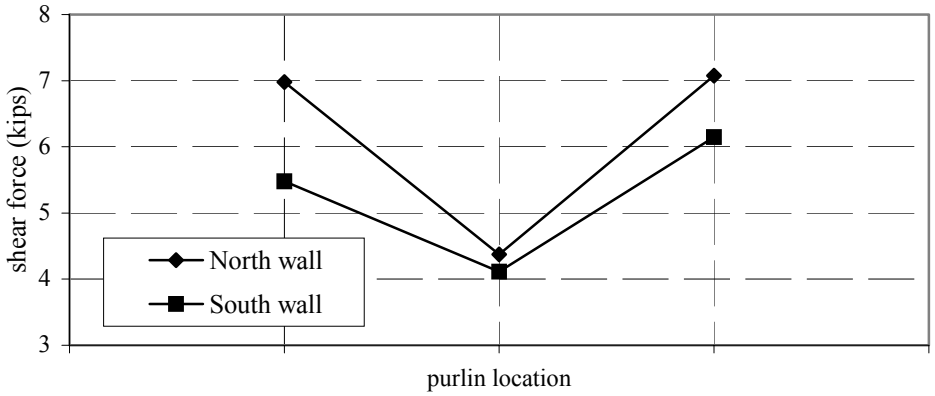

(b)

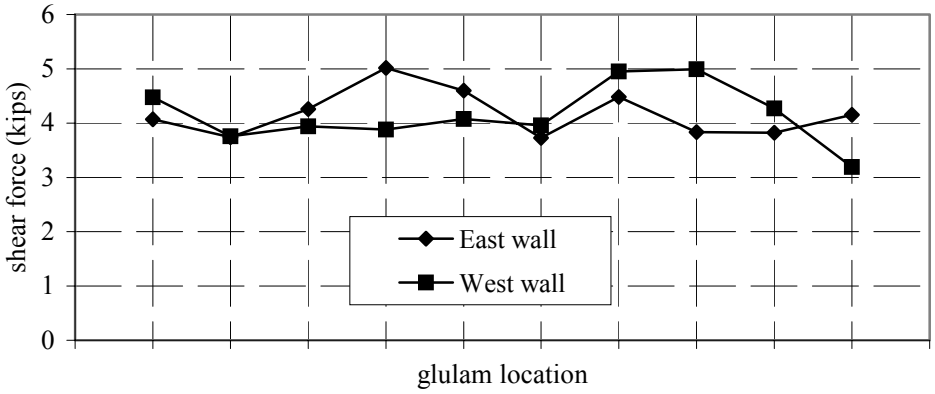

(c)

Fig. 7.16 Vertical shear force, nonlinear new connections, Los Gatos

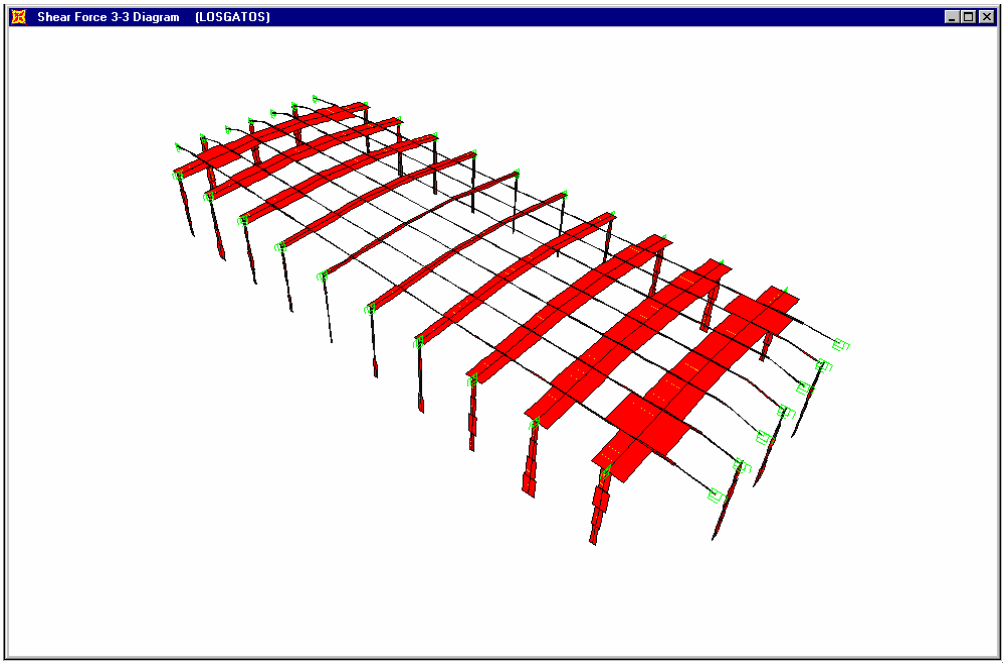

(a) Los Gatos, horizontal shear force

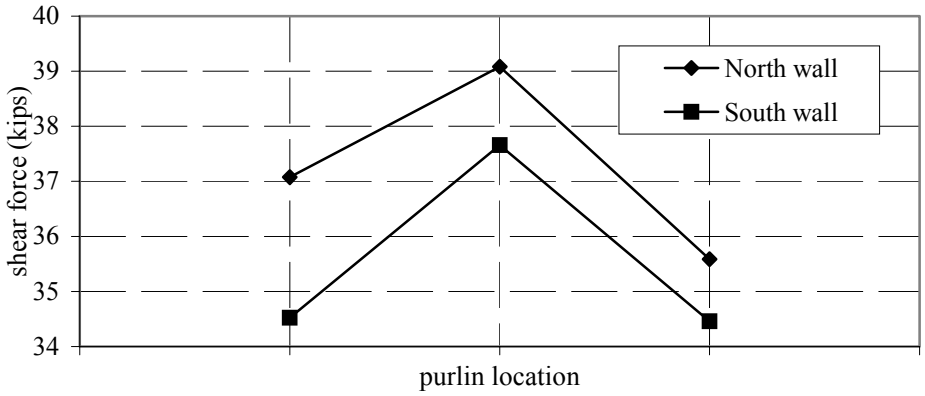

(b)

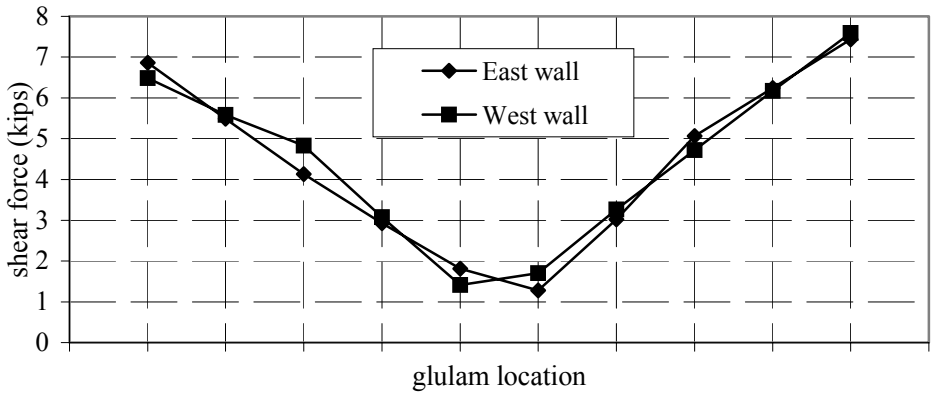

(c)

Fig. 7.17 Horizontal shear force, nonlinear new connections, Los Gatos

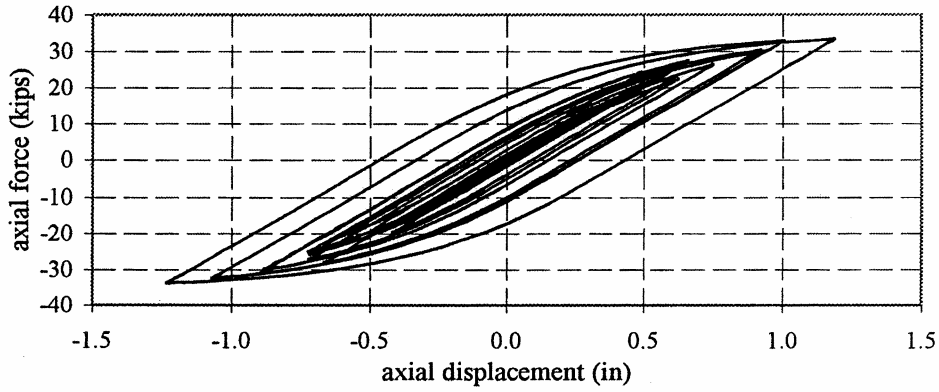

(a)

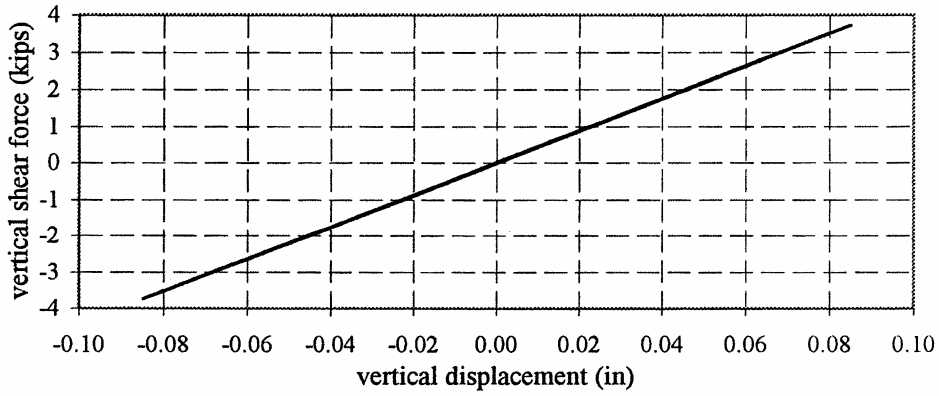

(b)

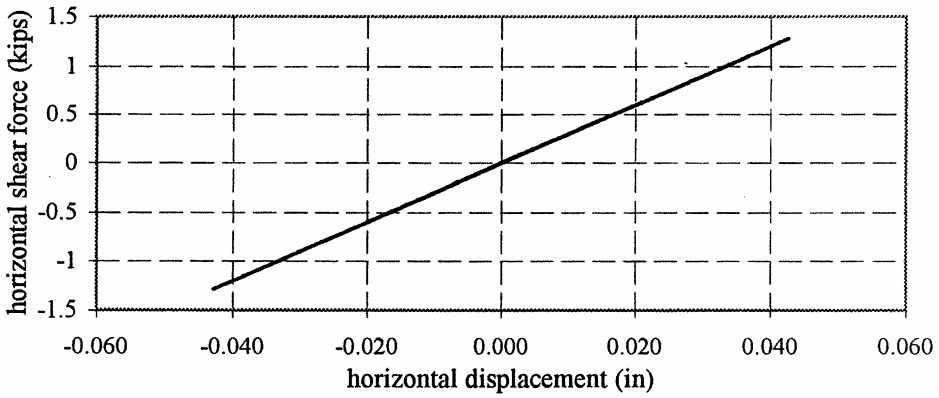

(c)

Fig. 7.18 New glulam to pilaster connection, middle of wall, Los Gatos

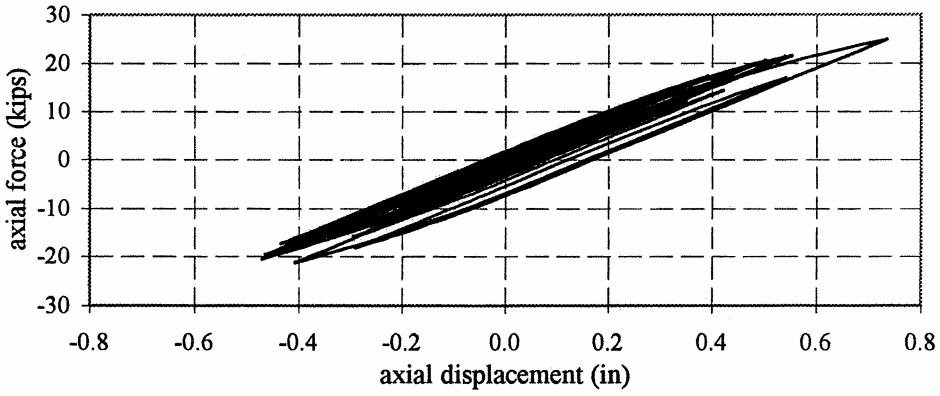

(a)

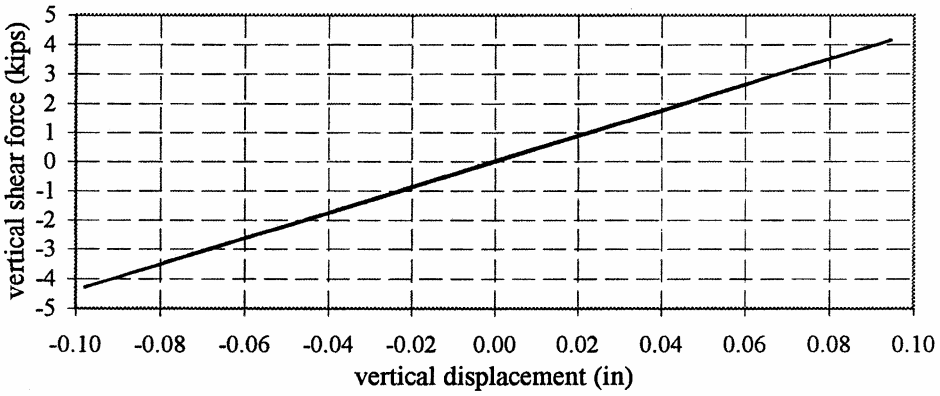

(b)

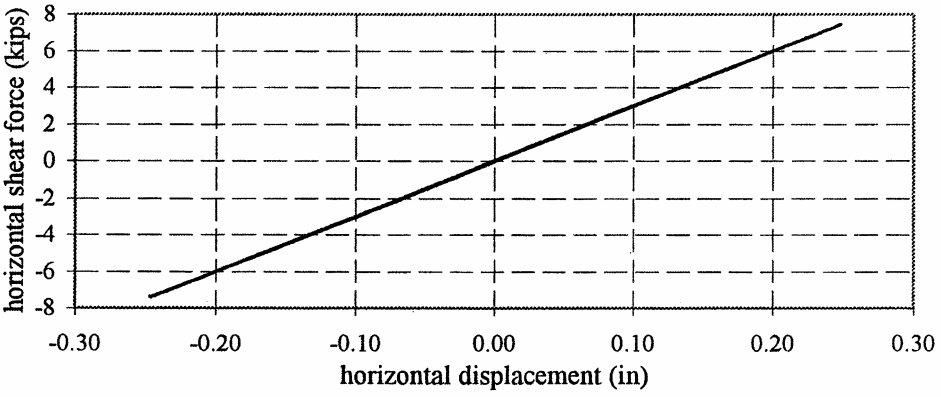

(c)

Fig. 7.19 New glulam to pilaster connection, near corner, Los Gatos

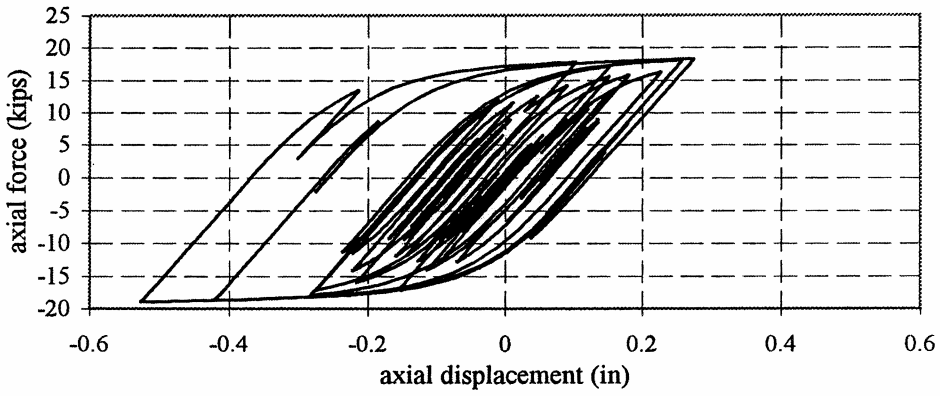

(a)

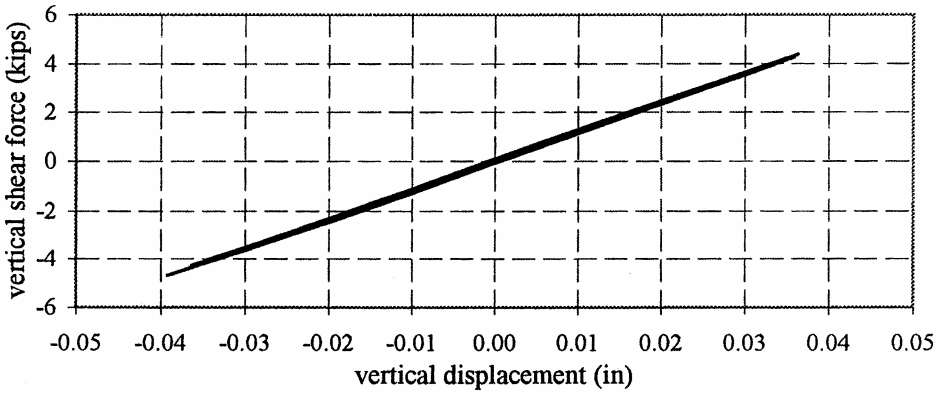

(b)

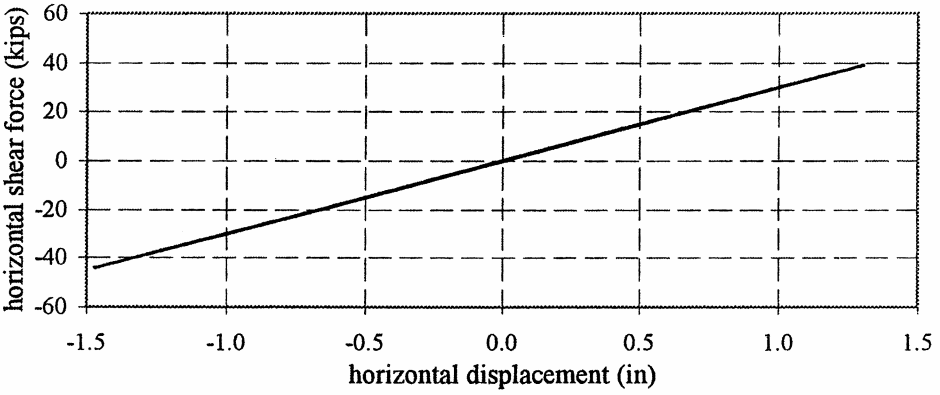

(c)

Fig. 7.20 New purlin to pilaster connection, middle of wall, Los Gatos

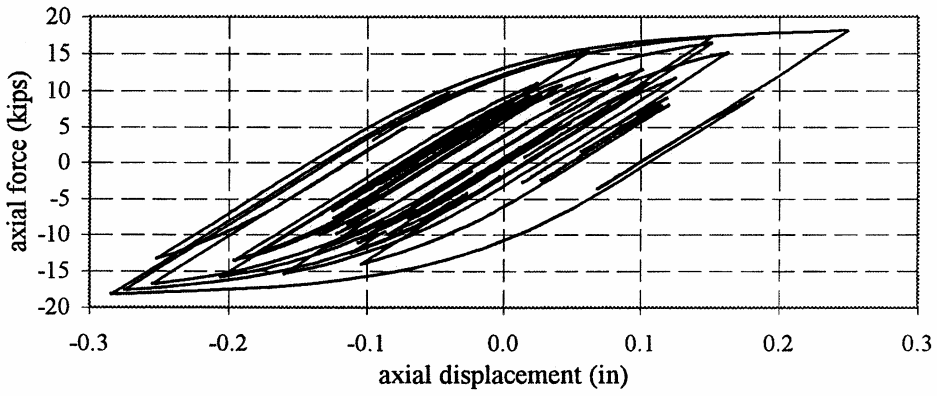

(a)

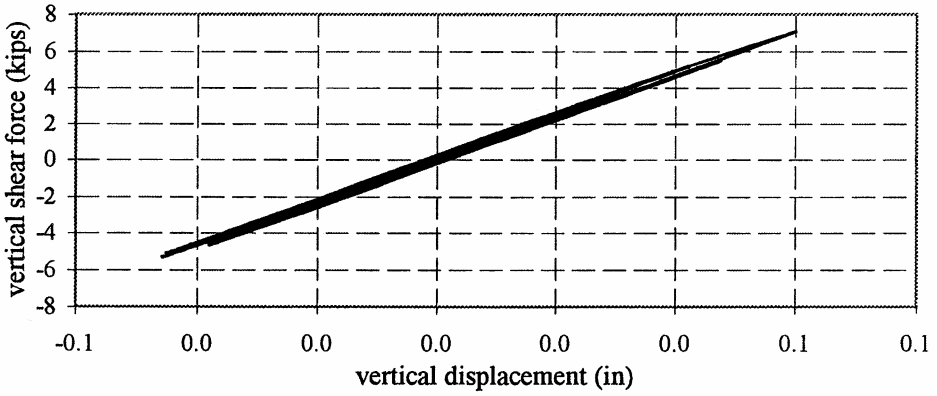

(b)

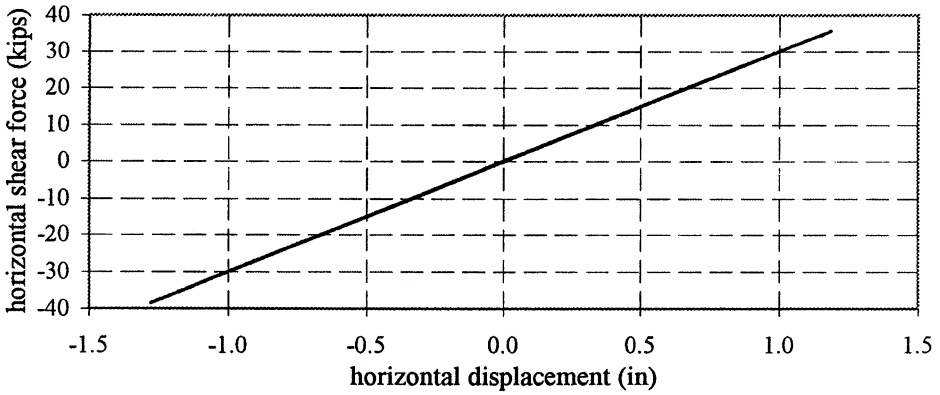

(c)

Fig. 7.21 New purlin to pilaster connection, near corner, Los Gatos

7.2 NONLINEAR DIAPHRAGM

The roof diaphragm was also identified as being a critical system under strong ground motion. Therefore, it was decided to attempt to model the nonlinear behavior using the SAP2000 program. As mentioned previously, the NLINK element can be used either alone or in combination with the FRAME element to model nonlinear behavior. It was necessary to develop an analytical model of the diaphragm using this capability. A procedure for representing a two-dimensional continua by an assemblage of beam and truss elements was suggested by Hrennikoff [Hrennikoff, 1941] more than 60 years ago for the analysis of elastic systems. The application of this procedure for determining the nonlinear response of the roof diaphragm will be evaluated.

7.2.1 Hrennikoff Model

Hrennikoff suggested a procedure for using the familiar concepts of frame analysis to approximate the behavior of two-dimensional continua. Arranging an assemblage of bars and beams with certain elastic properties in definite patterns accomplished this. In this manner, the framework method replaced the continuous structure with an idealized discrete system with the elements interconnected only at nodal points. Hence, the behavior of the continuous system is approximated by an equivalent truss or grid. Although the finite idealization cannot be completely equivalent to the continuum, it is possible that sufficient accuracy for most practical purposes can be achieved. A square framework pattern having vertical, horizontal, and diagonal truss members is suggested for the solution of two-dimensional stress problems. The horizontal and vertical members are assigned an equivalent cross-sectional area of $A_1 = 0.75ah$ and the diagonal members are assigned an area of $A_2 = A_1/\sqrt{2}$. In these relationships, "a" is the framework dimension and "h" is the diaphragm thickness. It is also suggested that at the boundaries, the area A_1 should be reduced by one half. Details of this procedure are summarized elsewhere [R. Szilard, 1974].

7.2.2 UCI Test Comparisons

Full-scale tests were conducted at the University of California, Irvine, to evaluate the strength and stiffness properties of six panels (20 ft x 16 ft) that are representative of timber roof diaphragms. Data from these tests, summarized in Appendix A, were used to calibrate and

evaluate the analytical models. Two models were considered, one with standard nail spacing (6 in. o.c.) and one with dense nail spacing (3 in. o.c.). The lower edge of a panel was fixed to the laboratory floor and a steel channel was fixed to the top edge to prevent any out-of-plane motion. A hydraulic actuator applied a horizontal load at the top of a panel and a string potentiometer at this level was used to measure displacement.

The initial model of the test panel, shown in Figure 7.22a, used shell elements to represent the elastic behavior of the panel. Since material properties were not given in the test report, a value of E=1400 ksi was used for the glulam (4x12). The plywood panels were modeled as orthotropic plate elements with E=950 ksi and G=59 ksi. The goal of this initial model was to calculate the initial stiffness of the test specimen. At a horizontal load of 15 kips, a calculated displacement of 1.04 inches was obtained compared to 1.0 inches measured.

In the second model (Fig. 7.22b), the shell elements are replaced by the Hrennikoff truss model. The use of dense nailing results in a system that is more representative of the continuous analytical model. Therefore, the discrete (Hrennikoff) model was proportioned to be representative of dense nailing. Properties of the glulam beam (4 x 12) are the same as those of the previous model. Areas of the Hrennikoff truss elements are determined, as described above, resulting in three different size elements. A pipe section was used with the following diameters: D=3.0 inches for interior, D=2.14 inches for exterior, and D=1.29 inches for the diagonal. The modulus of elasticity was E=950 ksi with Poisson's ratio of 0.3. Using this model, the displacement under the 15 kip load was calculated to be 1.05 inches, which compares very well with the 1.04 inches calculated from the model with shell elements and the 1.00 inches measured from the test.

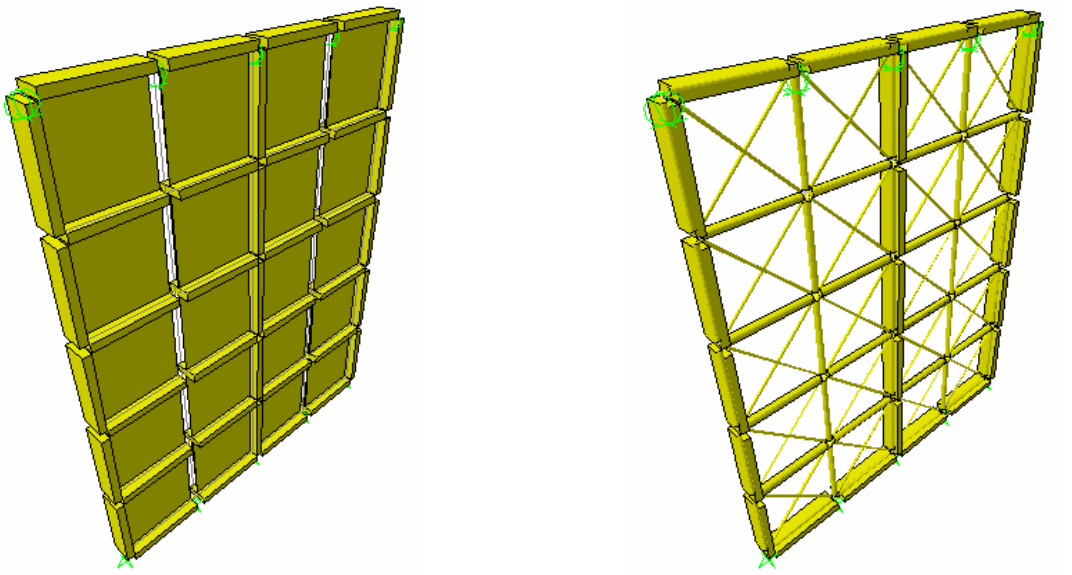

(a) shell element model (b) Hrennikoff truss element model

Fig. 7.22 Analytical models of test panels

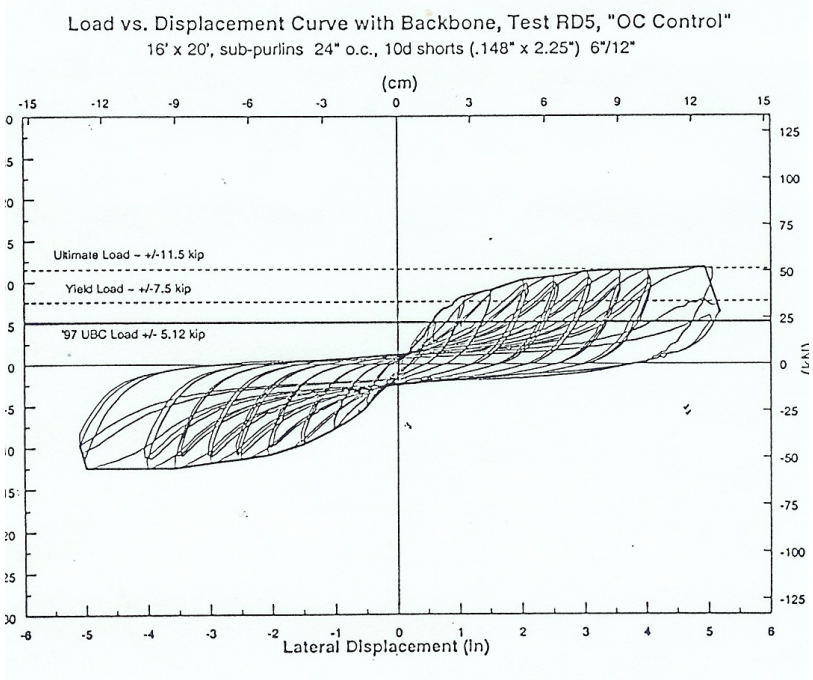

(a) sparse nailing

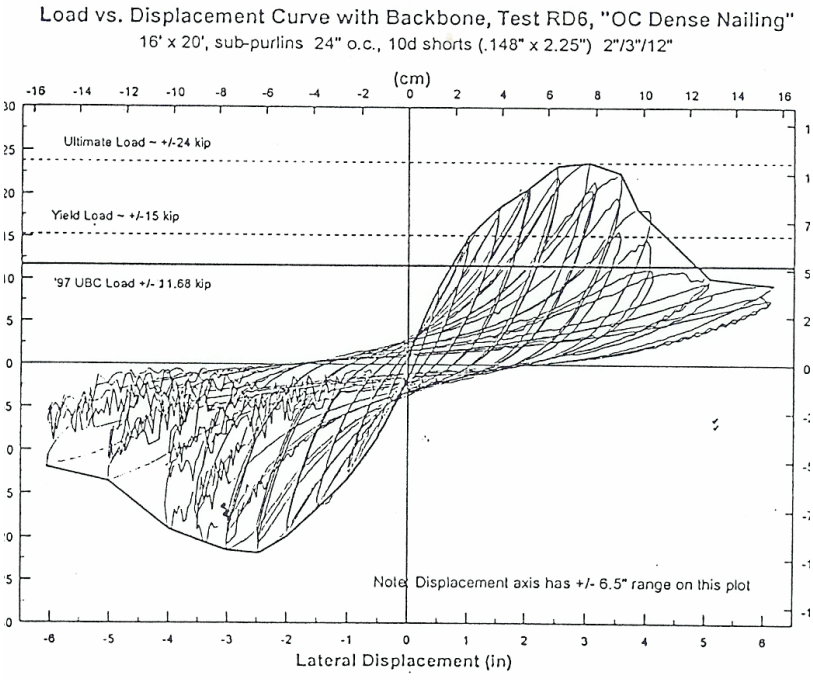

(b) dense nailing

Fig. 7.23 Load versus displacement curves, panel tests

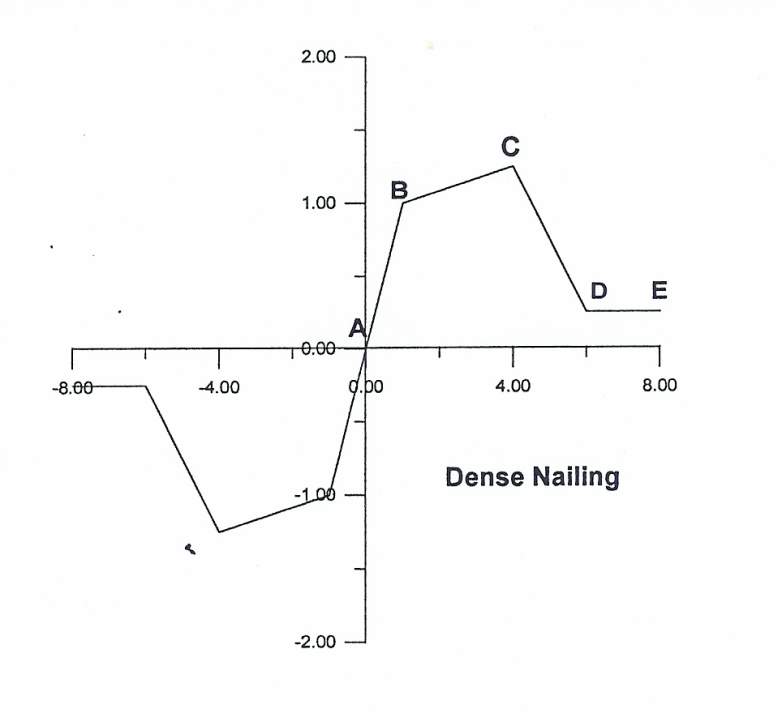

(a)

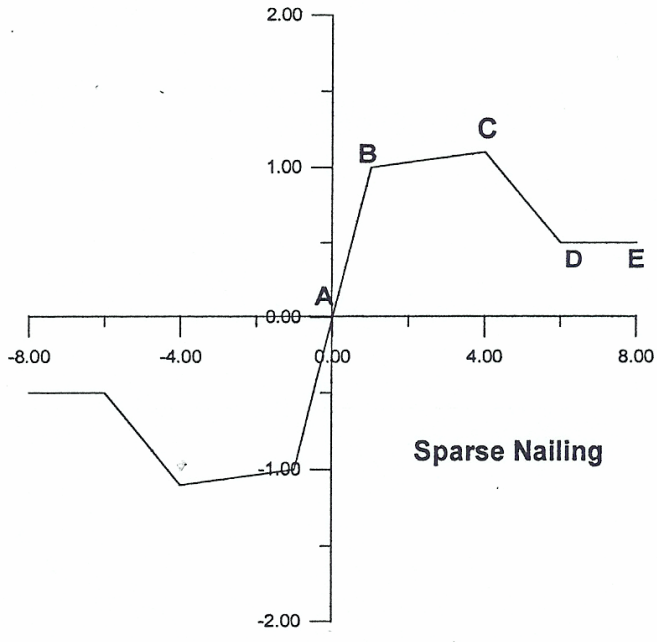

(b)

Fig. 7.24 SAP2000 pushover idealization, panel tests

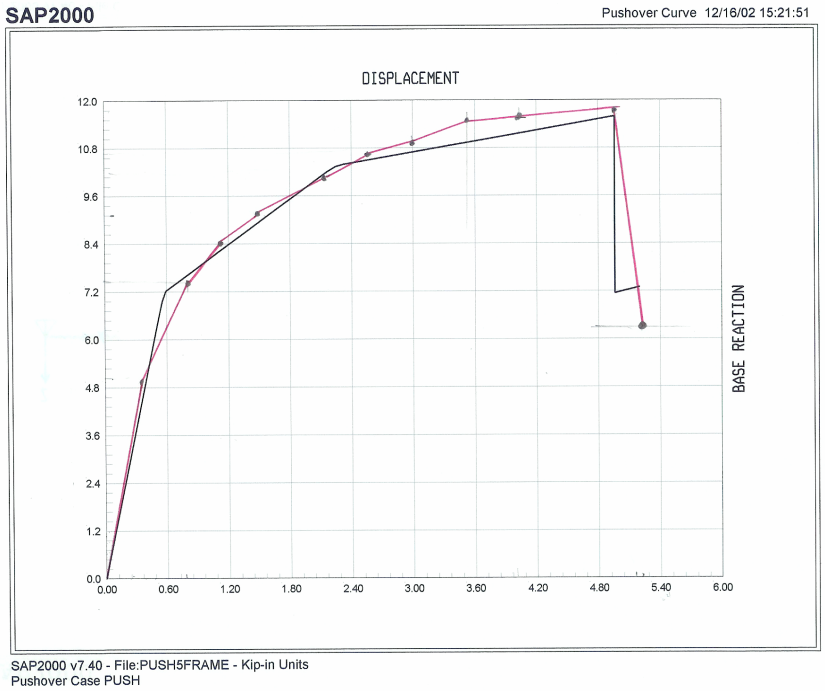

(a)

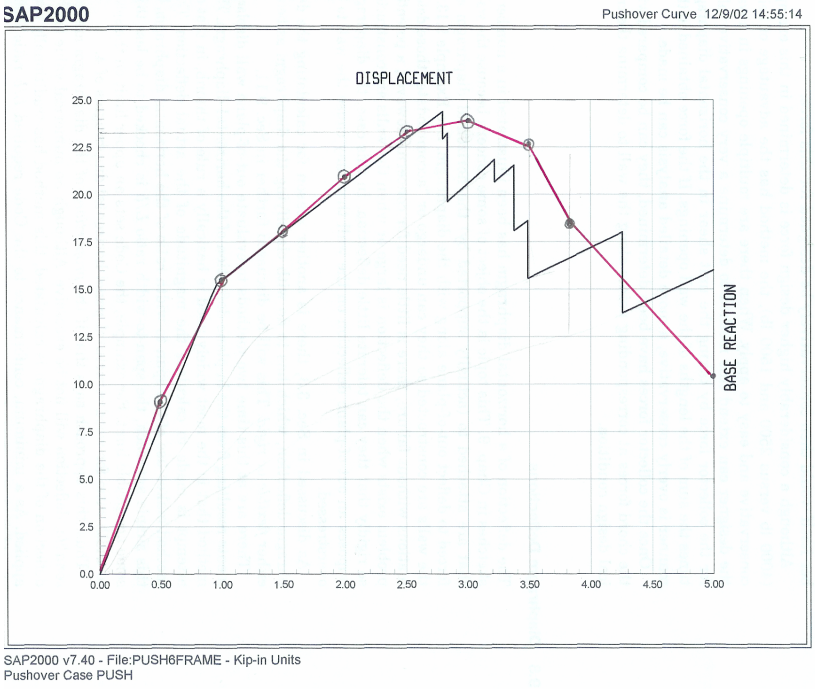

(b)

Fig. 7.25 Pushover comparisons, analytical vs. experimental, panel tests

The third model considered standard (sparse) nailing. The test data indicate that this condition results in a reduced initial stiffness. In order to account for this in the Hrennikoff model, the modulus of elasticity was reduced to 600 ksi. Other than this modification, all other properties were the same as for the second model just discussed. The calculated displacement of 1.65 inches compared well to 1.60 inches measured in the test.

As an additional test of the Hrennikoff model, pushover analyses simulating the lateral force versus displacement envelope obtained from the panel testing were conducted using SAP2000. The experimental force versus displacement curves for the two test panels are shown in Figure 7.23. The cyclic behavior of Figure 7.23a is representative of the panel with the sparse nailing and the cyclic behavior of Figure 7.23b is representative of the panel with dense nailing. The idealized envelope curves used as input to SAP2000 are shown in Figure 7.24. Sparse nailing is represented in Figure 7.24a and dense nailing in Figure 7.24b. The calculated pushover curve for the test specimen with the standard (sparse) nailing is compared with the experimental envelope in Figure 7.25a, and the pushover curve for the test specimen with dense nailing is compared with the corresponding experimental envelope in Figure 7.25b.

7.3 NONLINEAR 3D BUILDING MODEL

Following the evaluation of the panel tests, just discussed, a nonlinear model of the 3D TUW building was developed by replacing the subpurlins and the plywood diaphragm with the Hrennikoff truss model. The properties of these elements are similar to those used in the panel tests with adjustment made for panel dimensions. The glulam beams and main purlins remain as elastic frame elements. The modified SAP2000 model with the plywood diaphragm with the Hrennikoff elements representing the diaphragm is shown in Figure 7.26. For the dynamic analysis, the diagonal members of the Hrennikoff truss model are nonlinear spring elements (NLINK) that are available in SAP2000. In the static pushover analysis, the diagonal members are modified frame elements having an axial load hinge. The other truss elements making up the Hrennikoff panel are elastic. The modal periods and participation factors for the building model with the Hrennikoff elements are summarized in Table 7.3. Comparing these values with those shown in Table 6.1 for the elastic model indicates that the fundamental period in the N-S direction has increased from 0.39 seconds to 0.46 seconds and in the E-W direction from 0.29

seconds to 0.42 seconds. This is due to the use of flexible connections representative of the UCI tests in the nonlinear model and pinned connections in the elastic model.

Table 7.3 Modal periods and mass participation, nonlinear model

MODE	PERIOD	INDIVIDUAL MODE (PERCENT)			CUMULATIVE MODE (PERCENT)		
		UX	UY	UZ	UX	UY	UZ
1	4.272011	0.0044	0	0	0.0044	0	0
2	3.676708	0.0002	0	8.9807	0.0046	0	8.9807
3	2.090801	0	0	0	0.0046	0	8.9807
4	1.58491	0	0.0454	0	0.0046	0.0454	8.9807
5	1.336754	0.035	0	0	0.0396	0.0454	8.9807
6	1.025605	0.0002	0	0.9303	0.0398	0.0454	9.9109
7	0.982591	0	0	0	0.0398	0.0454	9.9109
8	0.782063	0	0.2983	0.0002	0.0398	0.3437	9.9111
9	0.76294	0.2611	0	0	0.301	0.3437	9.9111
10	0.631591	0	0.0001	0.2042	0.301	0.3438	10.1153
11	0.624766	0.001	0	0	0.302	0.3438	10.1153
12	0.535936	0.0001	0.7333	0.0003	0.302	1.0771	10.1156
13	0.534104	2.4863	0	0	2.7883	1.0771	10.1156
14	0.466031	0.0318	0.0002	0.0353	2.8201	1.0773	10.1509
15	0.464473	30.2119	0	0	33.032	1.0773	10.1509
16	0.461498	8.6338	0	0	41.6658	1.0773	10.1509
17	0.427256	0.0003	0.0031	0.0012	41.6661	1.0804	10.1521
18	0.425479	2.0475	0	0	43.7136	1.0804	10.1521
19	0.417633	0	1.4084	0	43.7137	2.4888	10.1522
20	0.410533	0	0.1454	0.0001	43.7137	2.6342	10.1522
21	0.392695	0.0001	0.0054	0.0042	43.7138	2.6395	10.1565
22	0.382468	0	0.0053	0.0001	43.7138	2.6448	10.1566
23	0.37958	0.0998	0	0	43.8137	2.6448	10.1566
24	0.370629	0	1.9118	0	43.8137	4.5566	10.1566
25	0.358312	0	0.0005	0.0004	43.8137	4.5571	10.157
26	0.350053	0	2.1585	0	43.8137	6.7156	10.157
27	0.338946	0	1.6286	0.0005	43.8137	8.3442	10.1575
28	0.323809	0.0005	0.0809	0.011	43.8142	8.4251	10.1685
29	0.319937	0.8878	0.001	0	44.702	8.4261	10.1686
30	0.316252	0.3393	0.0002	0	45.0413	8.4263	10.1686
31	0.315729	0.1917	0.0001	0	45.233	8.4265	10.1686
32	0.312015	0.0007	4.5066	0.0009	45.2337	12.933	10.1694
33	0.309706	0.0002	0.3614	0.0094	45.2339	13.2945	10.1788
34	0.308827	0	0.8685	0.0001	45.2339	14.1629	10.1789
35	0.300228	1.5116	0.0001	0	46.7455	14.163	10.1789

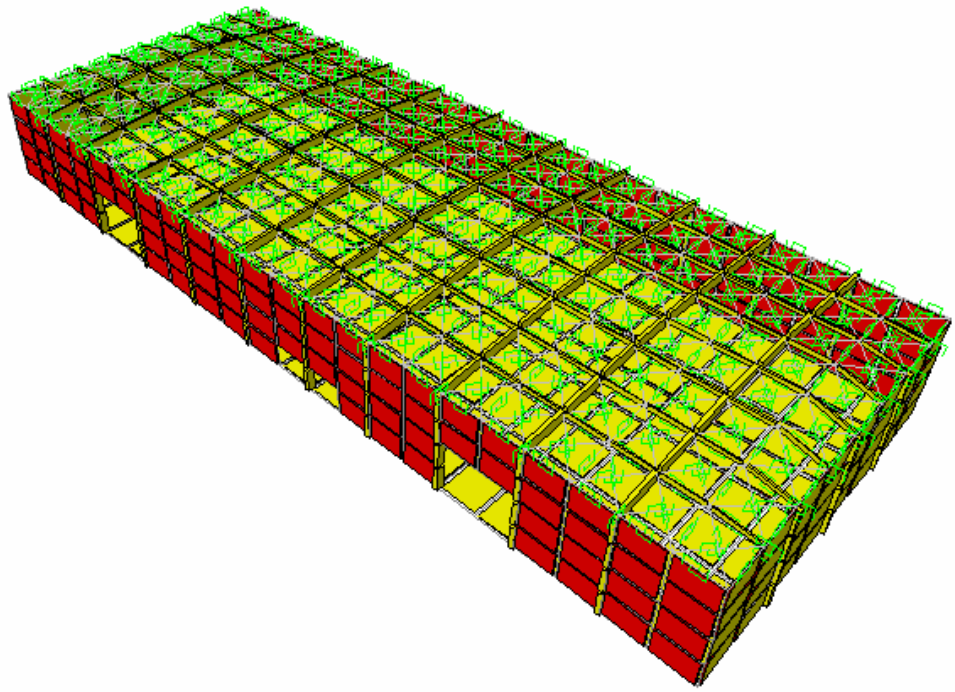

Fig. 7.26 Nonlinear 3D building model

7.4 NONLINEAR STATIC 3D PUSHOVER ANALYSIS

In an effort to gain additional insight into the lateral force capacity of the TUW building, a 3D pushover analysis was conducted within the limitations of the SAP2000 program and the 3D model of the building developed for previous elastic response studies. The critical building component for the TUW system has been identified as the roof diaphragm, followed closely by the connections of the diaphragm to the pilasters. The program allows only the use of frame elements for the pushover analysis. In order to model the nonlinear behavior, the diagonal members used to model the roof diaphragm were idealized as truss members and given user-defined axial load hinge properties. The axial hinge properties are those determined from the comparison with the sub-diaphragm pushover test results discussed previously, with the hinge located at midlength of the element. The pushover of the 3D model was conducted in the transverse direction; a typical deformed shape is shown in Figure 7.27. The capacity curve depends upon the assumed lateral force distribution. The mass of the entire building is considered as being distributed based on the element sizes and the material properties, and is then concentrated (lumped) at the nodal points by the program. Due to the many nodal points, the

approximation to the actual distribution is thought to be very good. The loading for the pushover analysis was obtained by multiplying the distributed masses by a 0.1g acceleration.

The following two figures compare the effects of sparse and dense nailing in the diaphragm on the two connection types. The pushover strengths obtained using sparse nailing in the diaphragm with the old and new connection types are compared in Figure 7.28. These curves indicate that there is little difference between the two connection types when used with the sparse nailing. It can be seen that nonlinear behavior begins at a relatively low base shear of 50 kips and that neither configuration is capable of developing the necessary strength design force capacity of the building (247 kips) within a roof displacement of 16 inches. The pushover strengths obtained using the old and new connections with dense nailing in the diaphragm are shown in Figure 7.29. This figure indicates that the new connection reaches the design strength level (247 kips) in 8 inches of roof displacement and actually continues to a lateral force of 325 kips before the loading was stopped at a displacement of 12 inches. The initial yield level is also increased to almost 150 kips. This clearly shows a significant improvement in performance due to the dense nailing.

The next two figures compare the effects of the old and new connection types on the nailing used in the diaphragm. The strengths obtained with the old connections are shown in Figure 7.30. This figure shows that the dense nailing allows the old connection to reach the strength design level; however, the model then unloads and the strength falls back to near the sparse nailing level. The effects of using the new connections in combination with the nailing density in the diaphragm are shown in Figure 7.31. Here, the improved performance of the new connections in combination with the dense nailing in the diaphragm is apparent as discussed above.

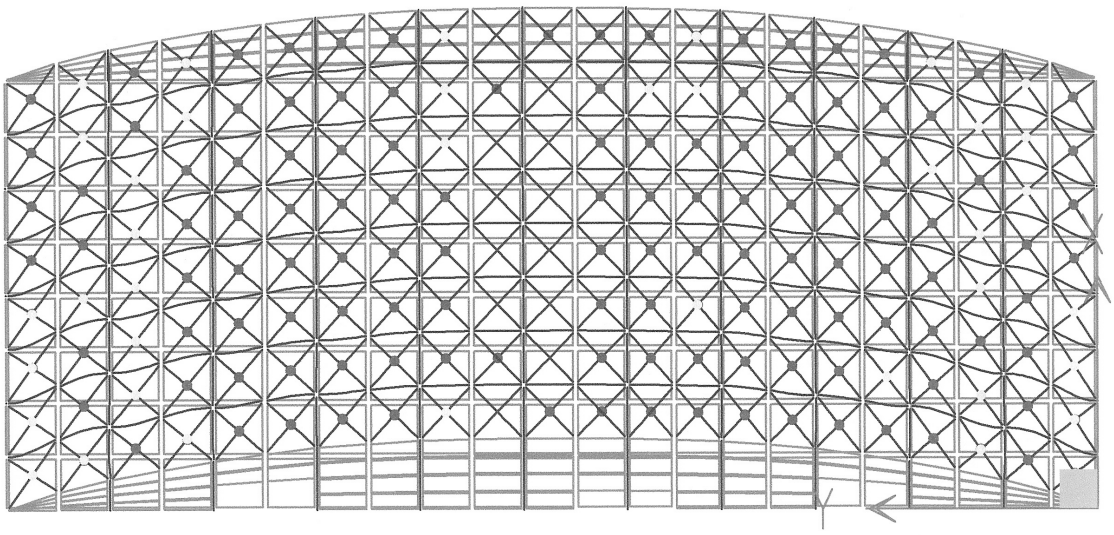

Fig. 7.27 Deformed shape, static pushover

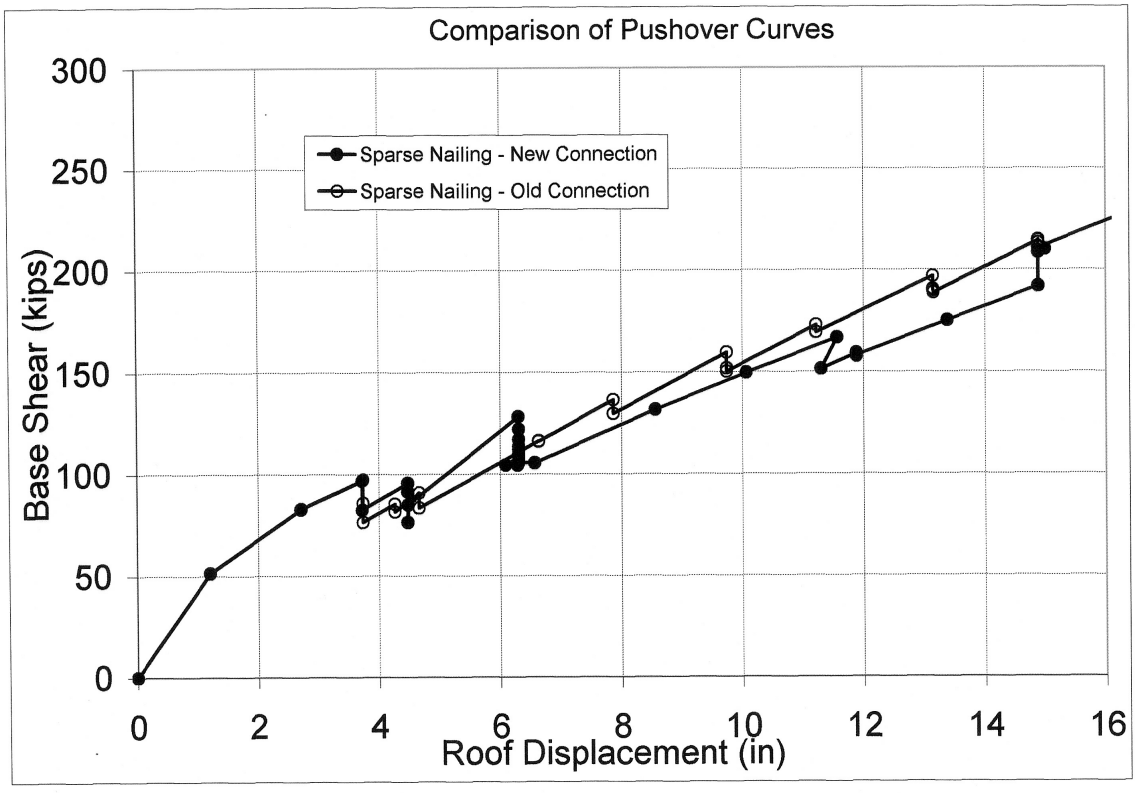

Fig. 7.28 Pushover behavior, sparse nailing

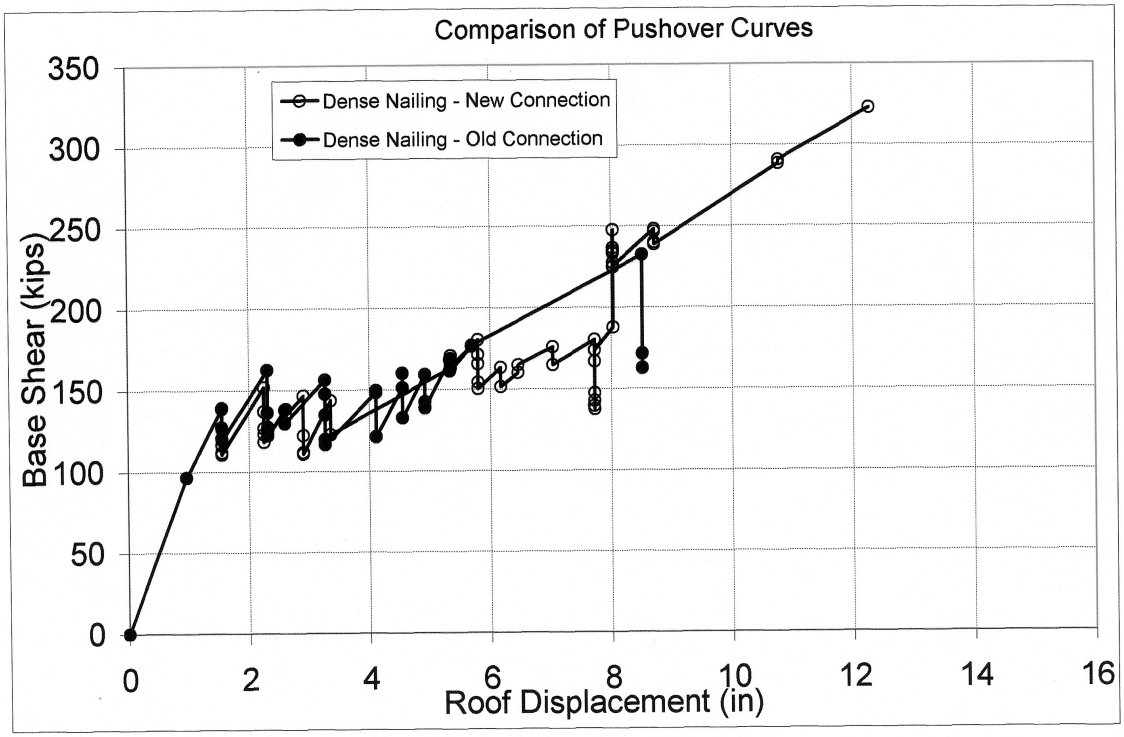

Fig. 7.29 Pushover behavior, dense nailing

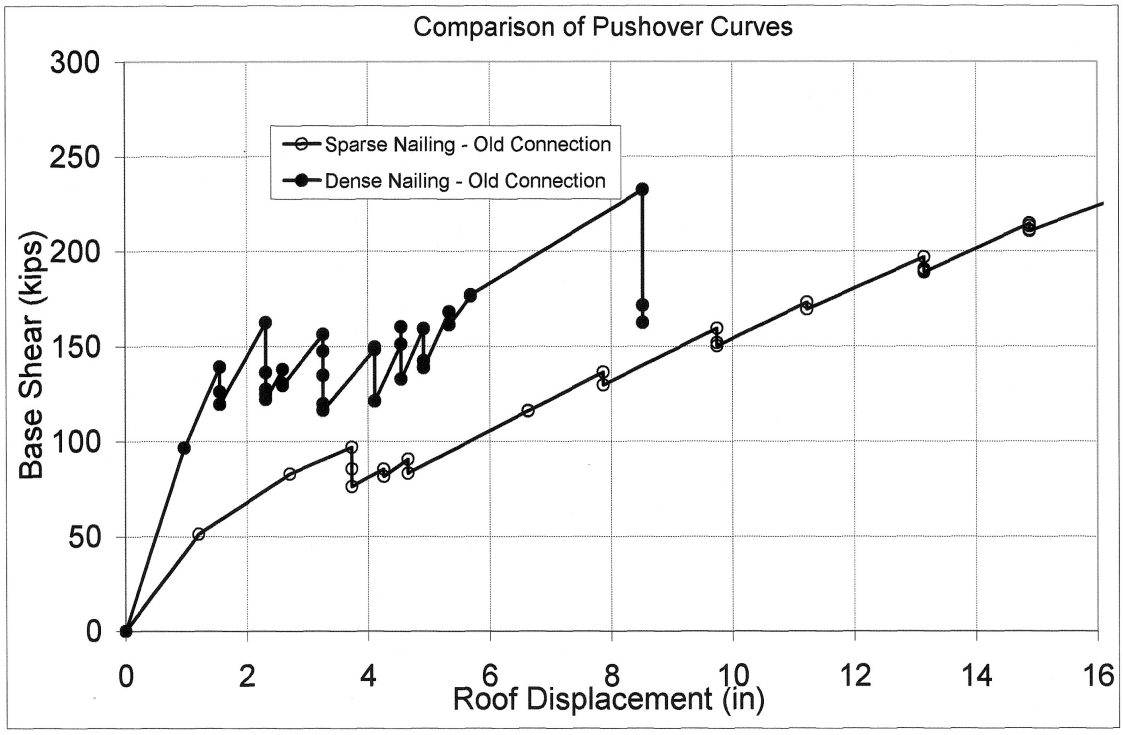

Fig. 7.30 Pushover comparisons, old connections

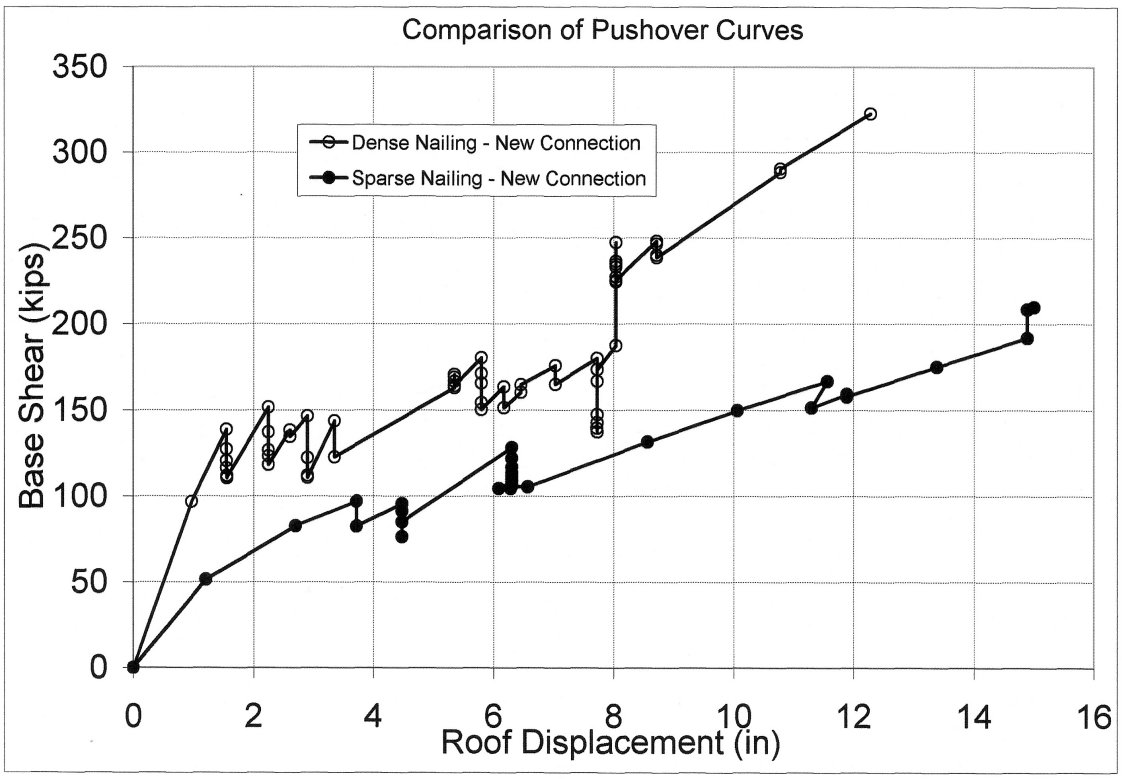

Fig. 7.31 Pushover comparisons, new connections

7.5 NONLINEAR DYNAMIC 3D TIME-HISTORY ANALYSIS

Displacements in the transverse (E-W) and longitudinal (N-S) directions under the Landers earthquake ground motion are shown in Figure 7.32. The calculated values in the transverse direction are compared with the recorded values in Figure 7.32a. It can be seen that the comparison is very good, with a maximum calculated displacement of 2.0 inches compared with a recorded value of 2.25 inches. Data for the longitudinal direction (Fig. 7.32b) indicate a similar result with a calculated displacement of 2.2 inches and a recorded value of 1.9 inches.

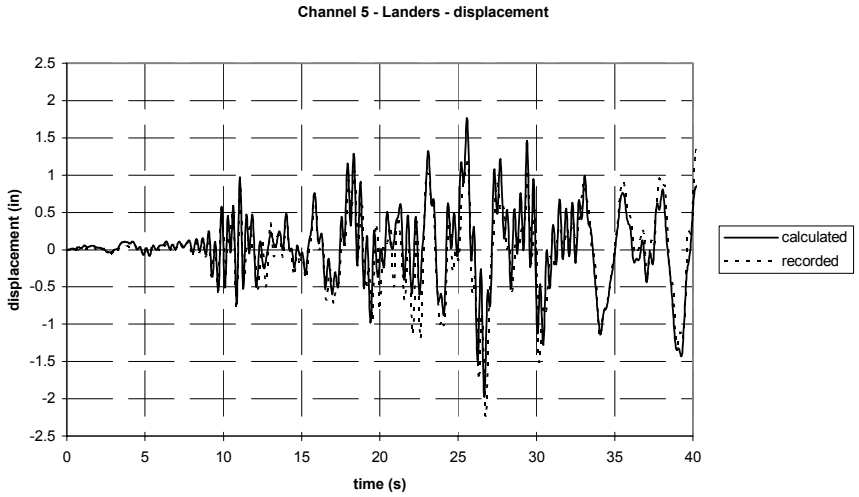

(a) channel 5

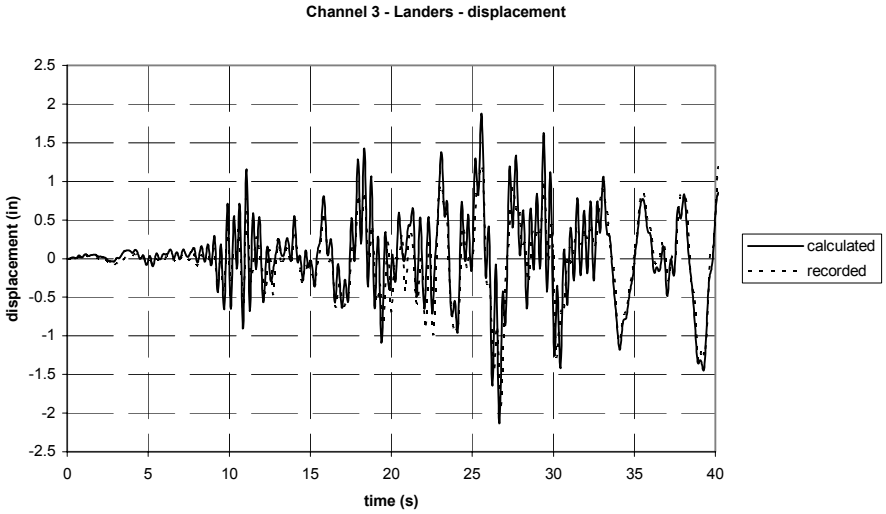

(b) channel 3

Fig. 7.32 Calculated vs. measured displacements, nonlinear model, Landers

The contour plots of the elastic shear stresses in the roof diaphragm under the base motion recorded during the Big Bear earthquake were shown in Figure 6.49. These contours indicate that the maximum stresses occur in the upper and lower corners of the diaphragm on the north end of the building. An expanded view of this region of the finite element model is shown in Figure 7.33. The hysteretic behavior of the three selected panels represented by the nonlinear Hrennikoff elements (a), (b), and (c) as shown in the figure are monitored in the nonlinear response analyses that follow.

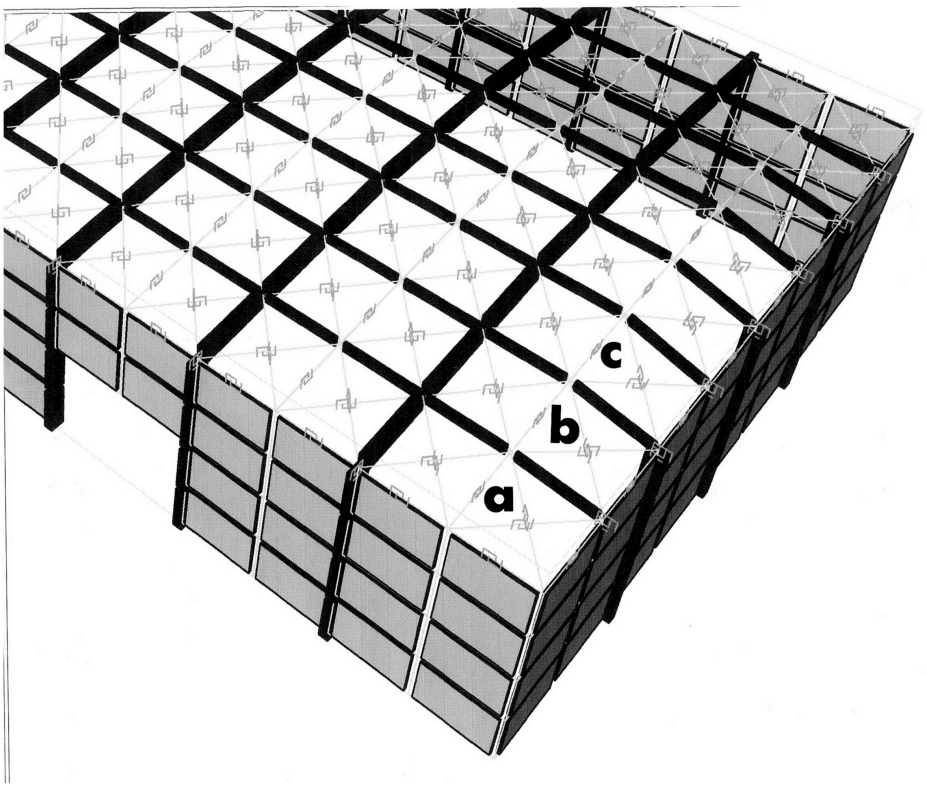

Fig. 7.33 Selected nonlinear Hrennikoff element locations

7.5.1 Big Bear, Dense Nailing, Old Connections

The responses of the nonlinear model under the recorded Big Bear base motions are presented in Figures 7.34–7.42. The time history of the calculated base shear in the transverse direction is shown in Figure 7.34a. With the nonlinear response, the base shear is less than the code design requirement of 247 kips, reaching a maximum of 220 kips on one cycle. In the longitudinal direction (Fig. 7.34b), the maximum base shear reaches only 60 kips. Similar values obtained with the elastic model, shown in Figure 6.30, indicate a maximum base shear in the transverse direction of 480 kips for a reduction of 55% due to nonlinear behavior. The maximum axial forces in the connection of the glulam beams and purlins to the pilasters are shown in Figure 7.35. The maximum axial force in the purlin connection (Fig. 7.35b) reaches a value of 3.25 kips compared with 5.5 kips in the elastic model. The maximum axial force in the glulam beam connection reaches a value of 9 kips (Fig. 7.35c). This value compares with 13.5 kips in the elastic model.

Vertical shear forces in the connections for this ground motion are shown in Figure 7.36. Vertical shear in the purlins are shown in Figure 7.36b and reach a maximum value of 4.25 kips compared to 2.8 kips for the elastic connections. The vertical shear in the glulam beams is shown in Figure 7.36c. These forces reach a maximum of 2.4 kips compared to 1.6 kips for the elastic condition. The horizontal shear force in the connections is shown in Figure 7.37. The horizontal shear in the purlin connections reaches a maximum value of 0.6 kips (Fig. 7.37b). This compares to 20 kips in the elastic case. For the glulam beams (Fig. 7.37c), a maximum value of 0.49 kips is obtained compared with 19 kips for the elastic case.

The hysteretic behavior of the axial force in the glulam beam connection near the middle of a longitudinal wall is shown in Figure 7.38a. Here it can be seen that the total displacement demand is approximately 0.18 inches. The amount of inelastic behavior is small and the behavior can be characterized as weakly nonlinear. The other two shear components (Figs. 7.38b–c) both remain elastic for this connection. The forces in a similar connection located near the end of the longitudinal wall are shown in Figure 7.39. The behavior of this connection is very similar to the connection at the middle of the wall with the axial force only weakly nonlinear with a maximum displacement demand of 0.17 inches (Fig. 7.39a). The two shear components (Figs. 7.39b–c) remain elastic as in the previous case.

The hysteretic behavior of the axial force for a purlin connection near the middle of the transverse wall is shown in Figure 7.40a. This figure indicates a displacement demand of just under 0.1 inches with weakly nonlinear behavior. The vertical shear behavior at this location (Fig. 7.40b) has a displacement of 0.12 inches and an estimated ductility demand of 1.7. The horizontal shear (Fig. 7.40c) remains linear elastic. Similar data for a connection near the end of the transverse wall are shown in Figure 7.41. At this location the axial force has a distinctly nonlinear behavior with a displacement demand of 0.26 inches and an estimated displacement ductility of 2.2 (Fig. 7.41a). The vertical shear force at this location (Fig. 7.41b) also exhibits a distinctly nonlinear behavior. The maximum displacement demand is 1 inch and the estimated displacement ductility is approximately 7.6. The horizontal shear force (Fig. 7.41c) remains elastic, since there is no information on the inelastic behavior of this component.

The axial forces in three consecutive diagonal components of the Hrennikoff diaphragm model are shown in Figure 7.42. The three components are located at the end of the longitudinal wall, adjacent to the transverse wall. This is the area of highest diaphragm shear as indicated by the shear force contours from the elastic model. The components shown in Figure 7.42 from top

to bottom start near the corner of the transverse wall and end near the center. The hysteretic behavior of the component nearest the longitudinal wall, (a), is shown in Figure 7.42a. At this location, the displacement demand is approximately 0.055 inches with a displacement ductility demand of approximately 3. The hysteretic behavior at the middle location, (b), is shown in Figure 7.42b. The model also exhibits nonlinear behavior at this location with a maximum displacement demand of 0.078 inches. The corresponding displacement ductility demand is estimated to be near 4.5. At the location near the center of the span, (c), (Fig. 7.42c) the behavior is linear elastic.

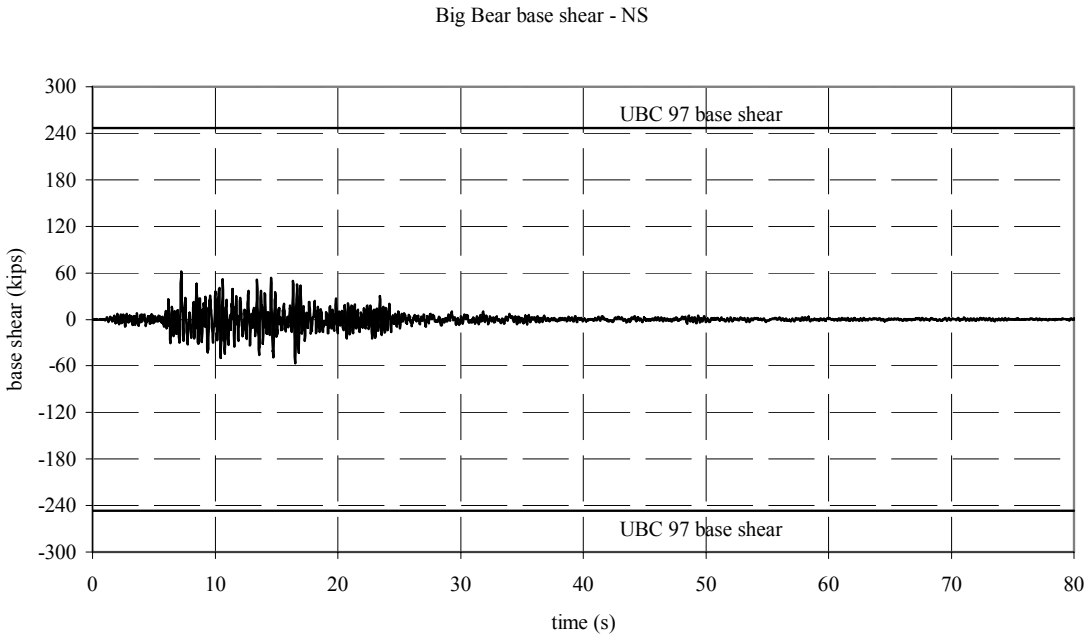

(a)

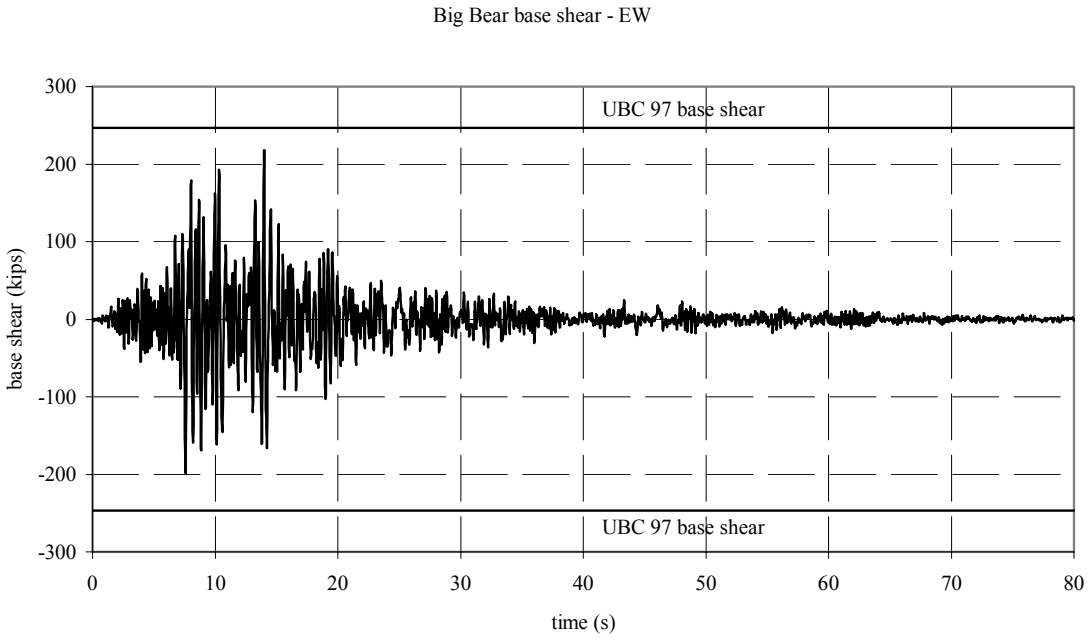

(b)

Fig. 7.34 Base shear, nonlinear old connection, dense nailing, Big Bear

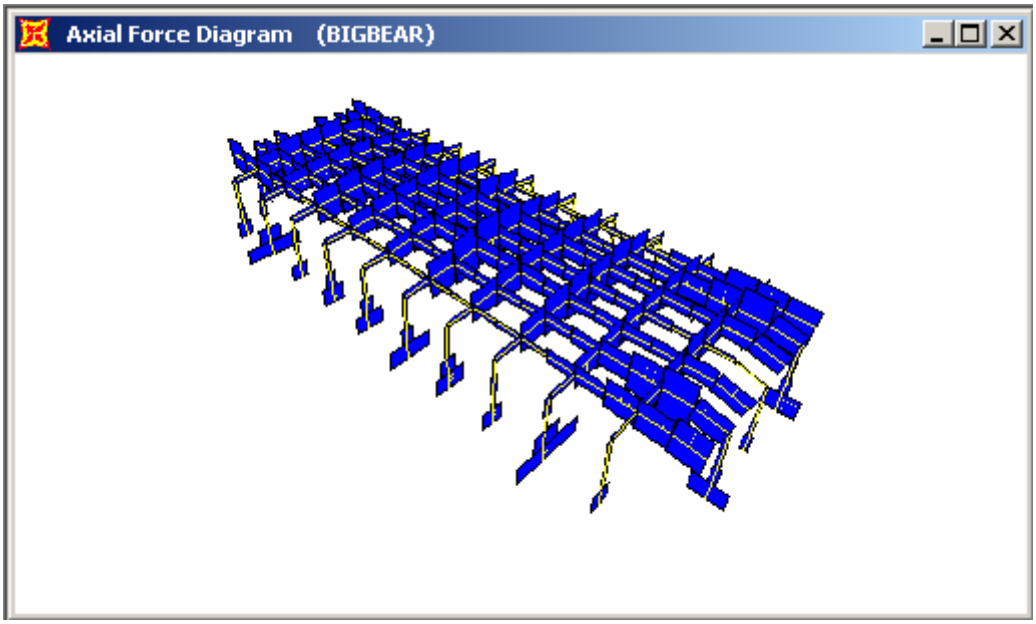

(a)

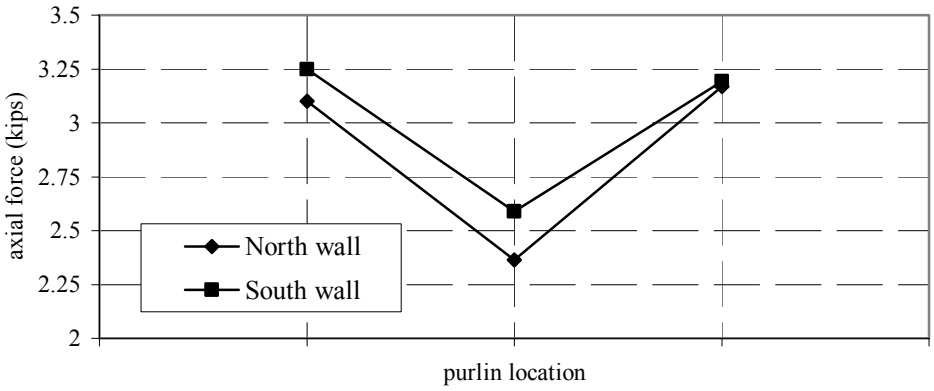

(b)

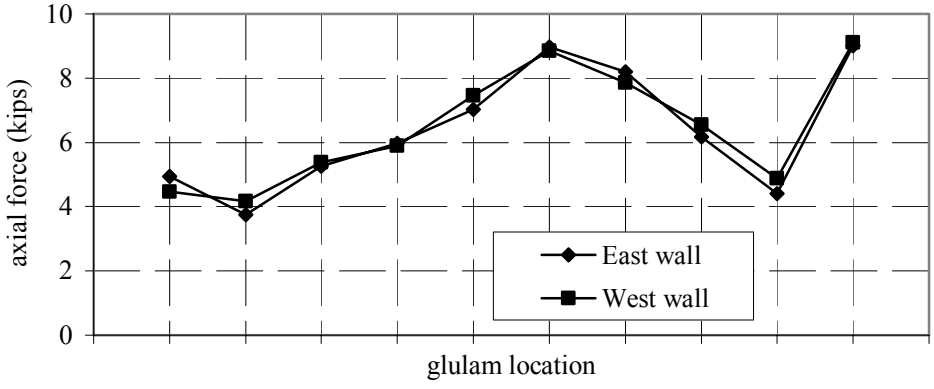

(c)

Fig. 7.35 Axial force, nonlinear old connections, dense nailing, Big Bear

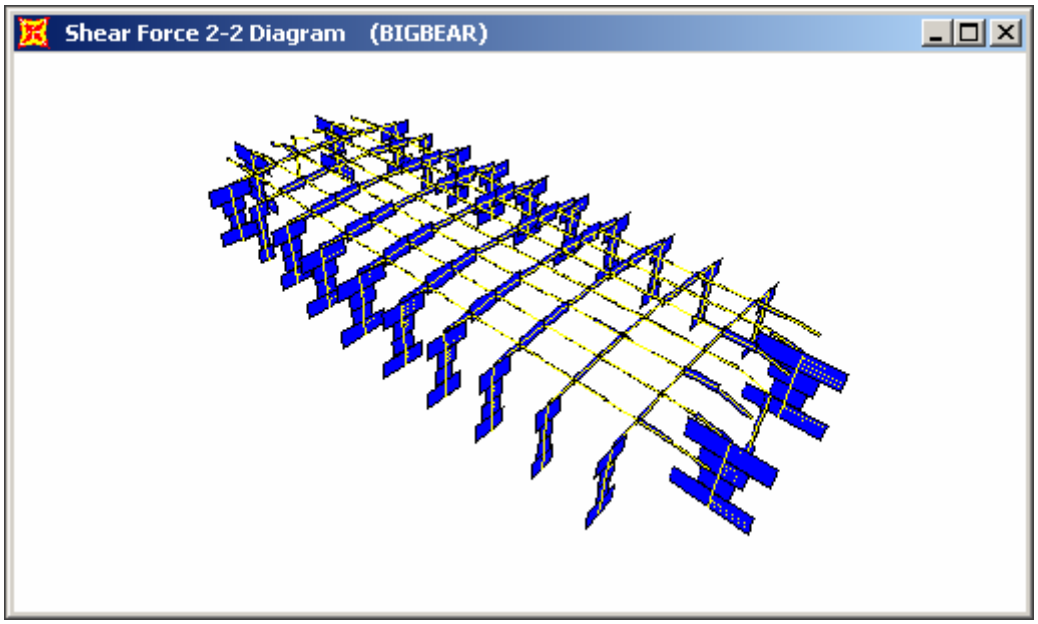

(a)

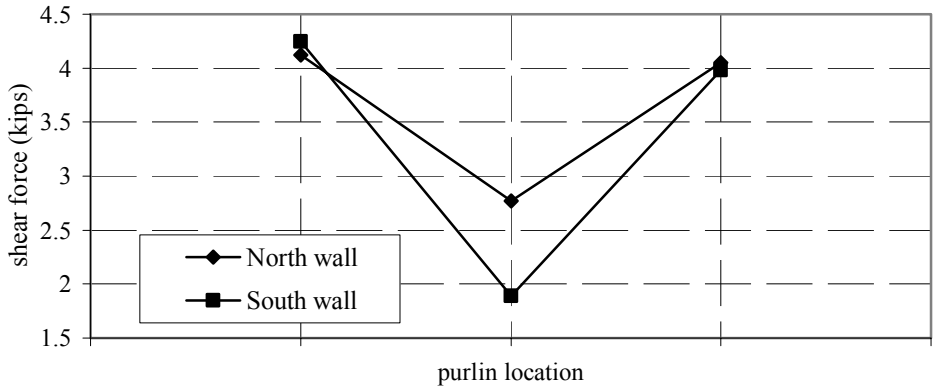

(b)

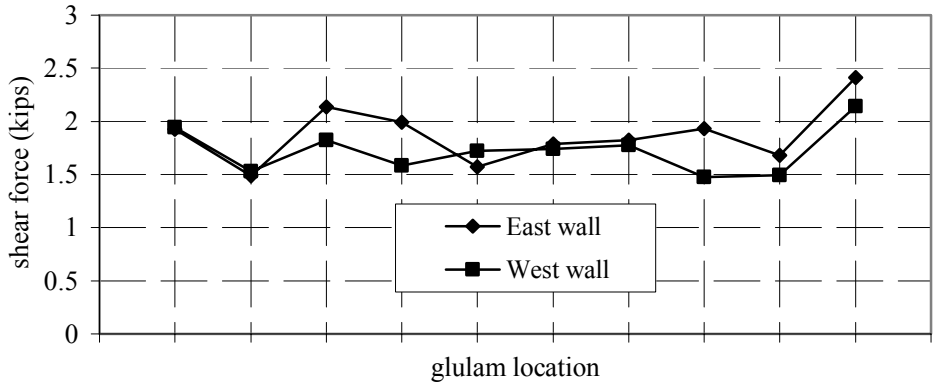

(c)

Fig. 7.36 Vertical shear, nonlinear old connection, dense nailing, Big Bear

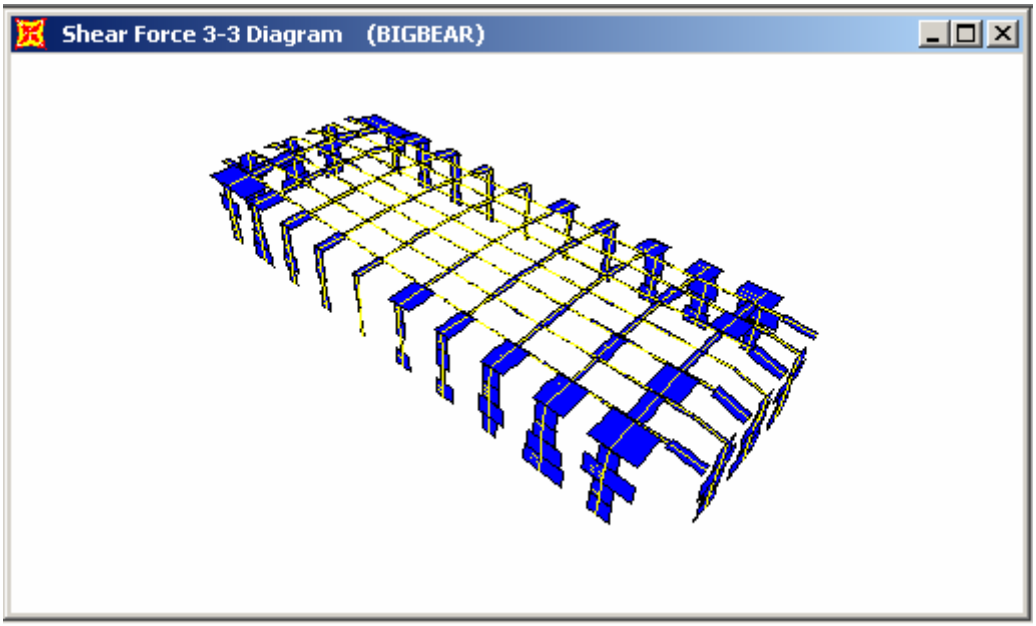

(a)

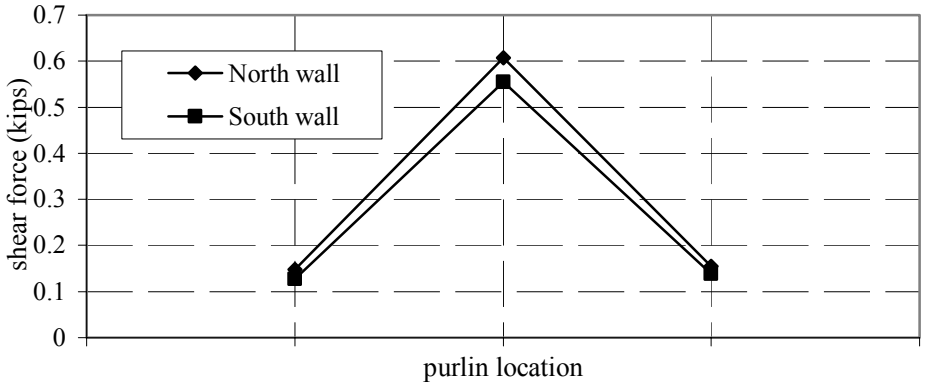

(b)

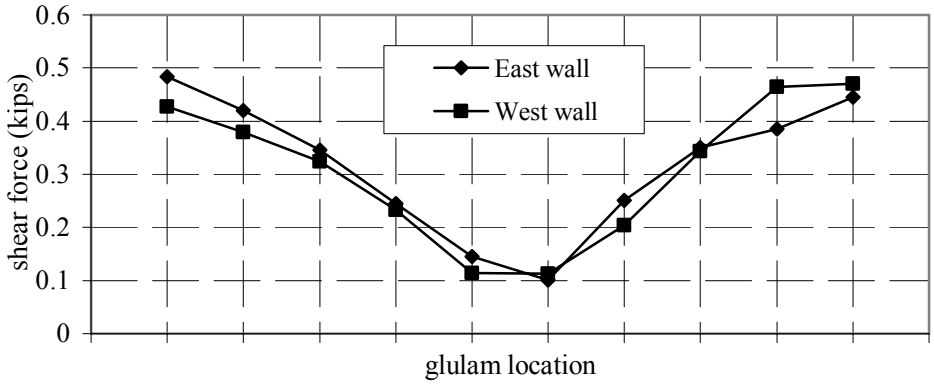

(c)

Fig. 7.37 Horizontal shear, nonlinear old connections, dense nailing, Big Bear

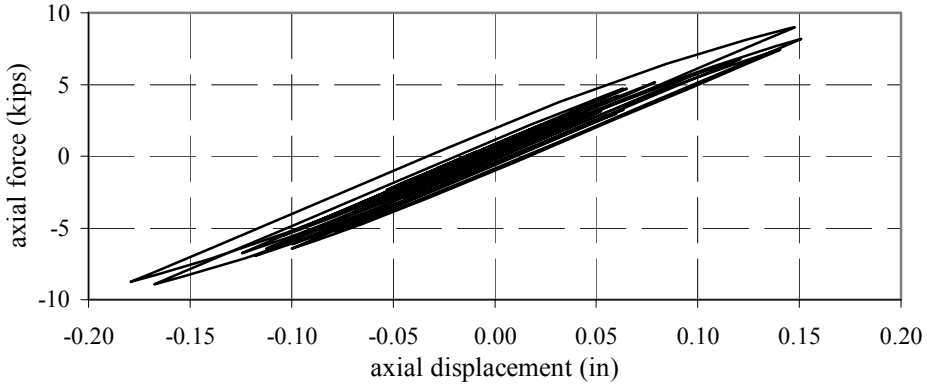

(a)

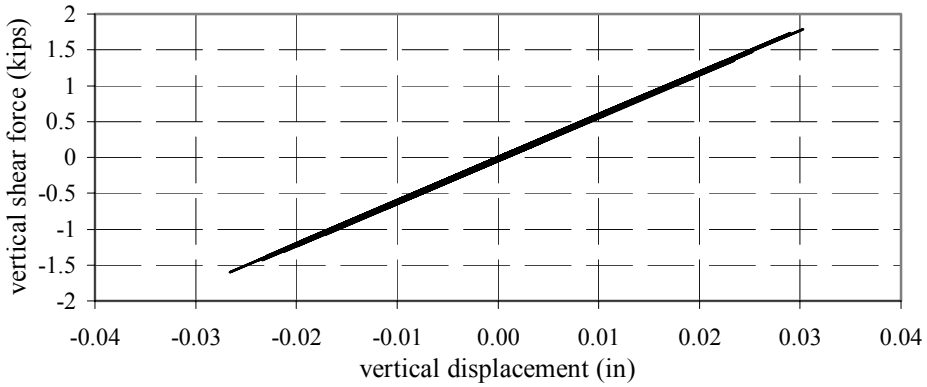

(b)

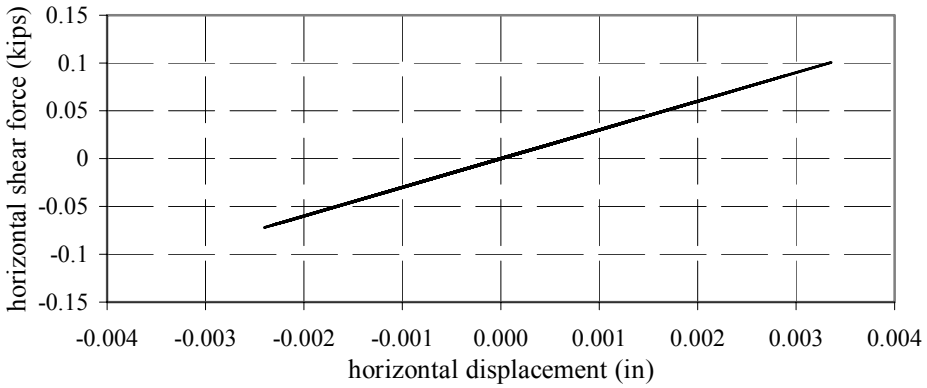

(c)

Fig. 7.38 Hysteretic behavior, glulam to pilaster, old connection, dense nailing, middle of wall, Big Bear

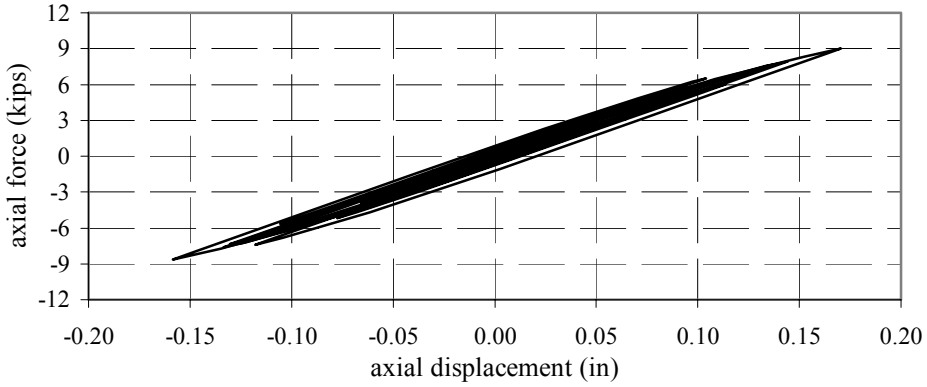

(a)

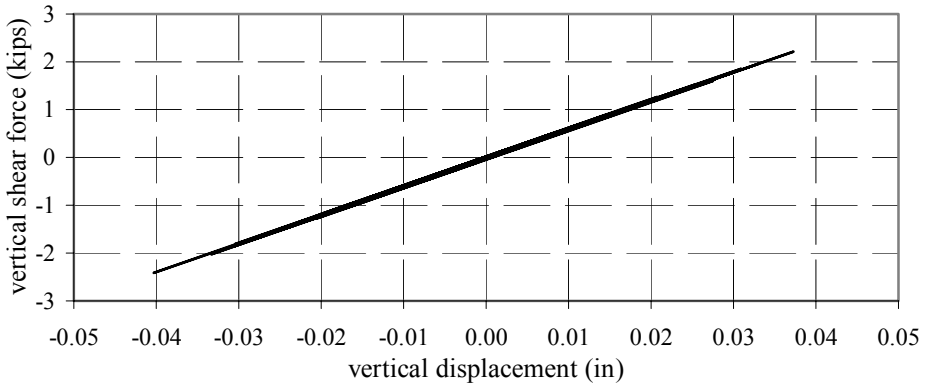

(b)

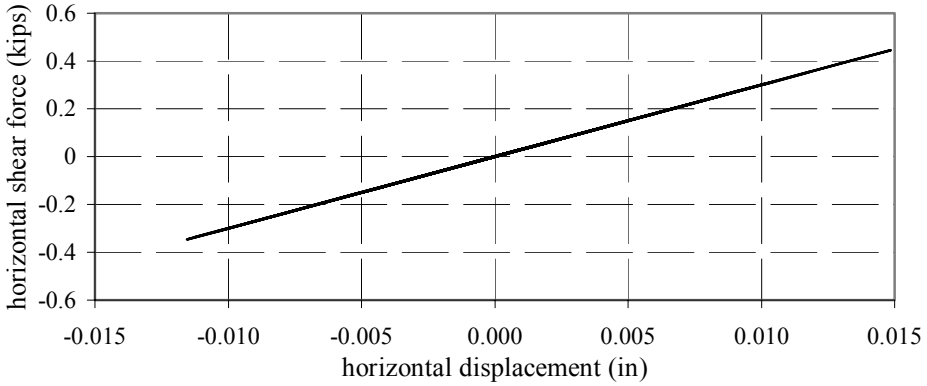

(c)

Fig. 7.39 Hysteretic behavior, glulam to pilaster, old connection, dense nailing, near corner, Big Bear

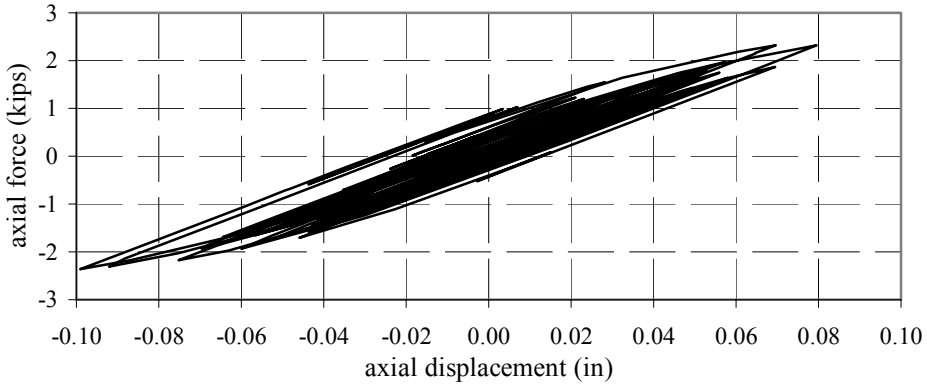

(a)

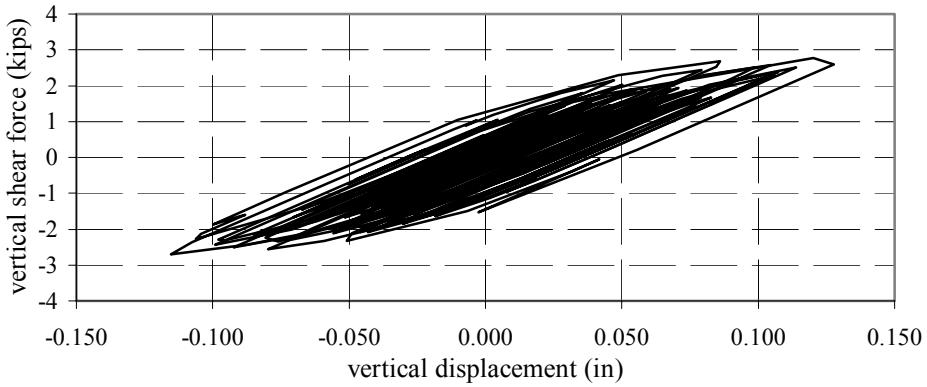

(b)

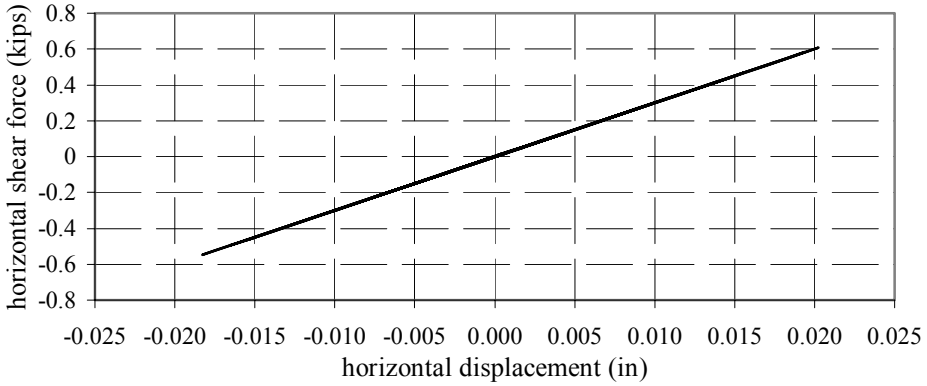

(c)

Fig. 7.40 Hysteretic behavior, purlin to pilaster, old connection, dense nailing, middle of wall, Big Bear

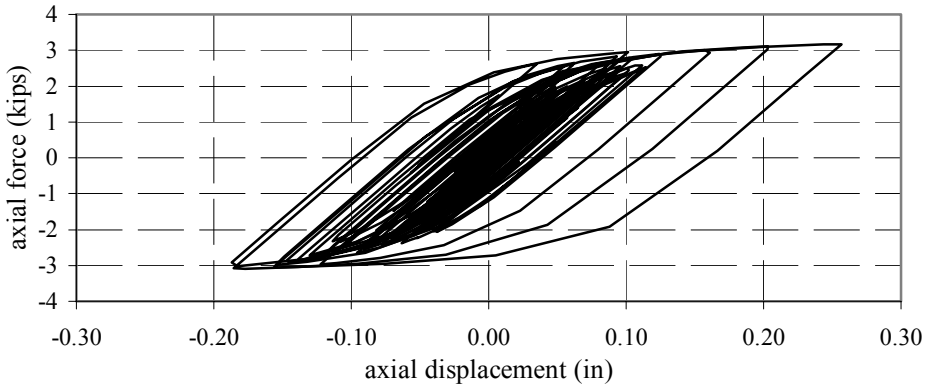

(a)

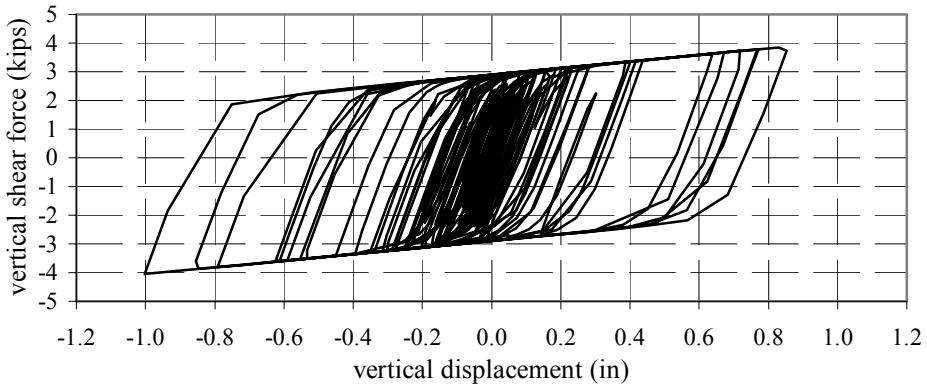

(b)

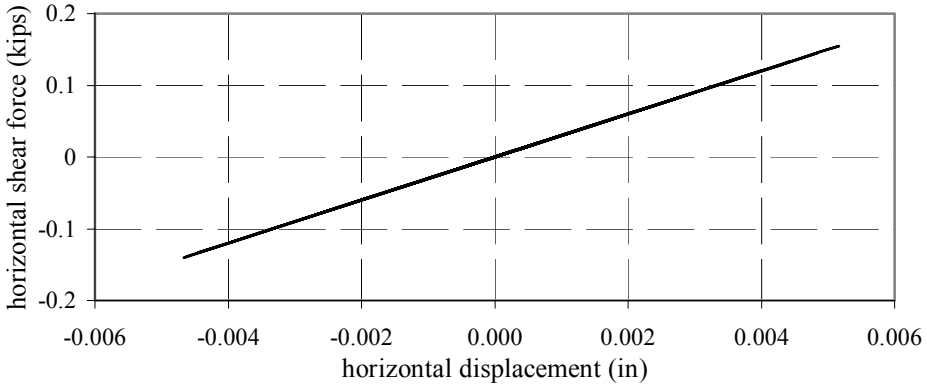

(c)

Fig. 7.41 Hysteretic behavior, purlin to pilaster, old connection, dense nailing, near corner, Big Bear

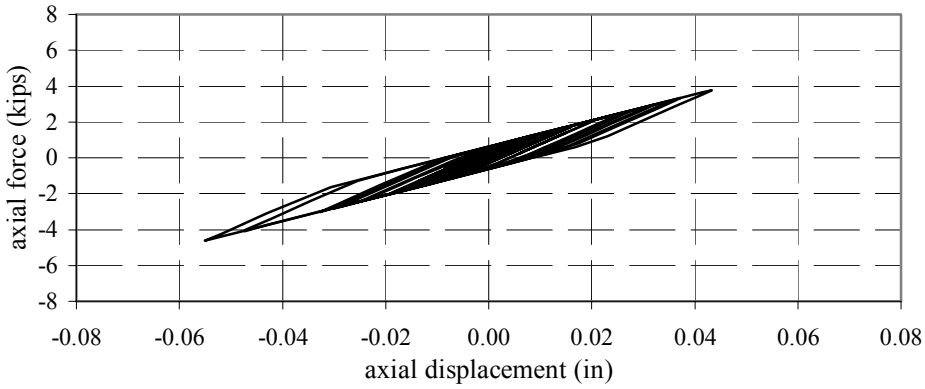

(a) element location

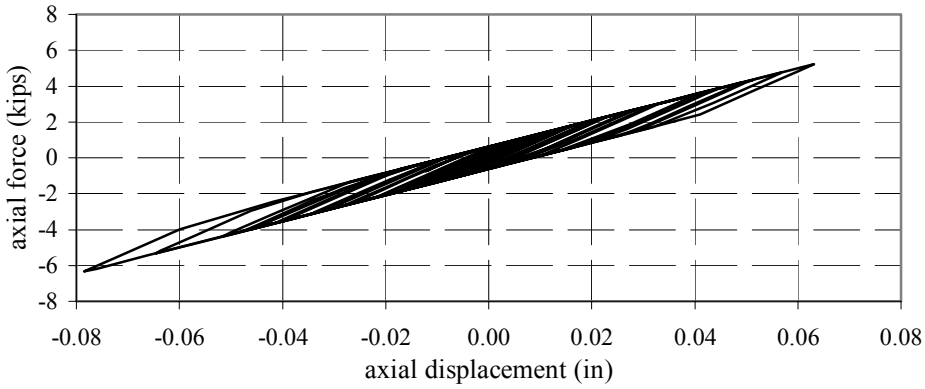

(b) element location

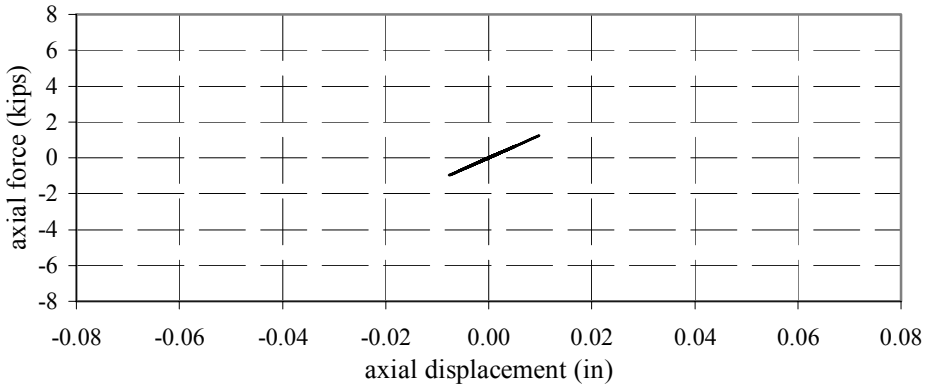

(c) element location

Fig. 7.42 Hysteretic behavior, roof diaphragm, old connections, dense nailing, Big Bear

7.5.2 Los Gatos, Dense Nailing, Old Connections

The responses of the nonlinear model having dense nailing and old connections under the Los Gatos ground motion are presented in Figures 7.43–7.51. The time history of the calculated base shear in the longitudinal (N-S) direction is shown in Figure 7.43a. In this direction the maximum base shear of 350 kips occurs on one excursion. Otherwise, the base shear is very close to the code design requirement. The results of the elastic analysis indicated a maximum base shear of 430 kips as shown in Figure 6.58. The time history of the base shear in the transverse (E-W) direction is shown in Figure 7.43b. In this direction, the maximum reaches 800 kips which is considerably larger than the code design value (240 kips) but is much lower than the result of the elastic dynamic analysis that indicated a maximum shear of 1,630 kips (Fig. 6.58). The maximum axial forces in the connections of the glulam beams and purlins to the pilasters are shown in Figure 7.44. The maximum axial force in the purlins (Fig. 7.44b) reaches a value of 4.85 kips, which is significantly less than the value of 13.2 kips obtained with nonlinear connections alone and much less than the almost 22 kips obtained from the elastic analysis. The distribution of axial forces in the glulam beams is shown in Figure 7.44c. In this case, the maximum value reaches 19 kips, which is near the 18 kips obtained with the nonlinear connections alone.

The distribution of vertical shear in the glulam and purlin connections is shown in Figure 7.45. The purlin connections (Fig. 7.45b) indicate a maximum value of 11 kips and the glulam connections (Fig. 7.45c) indicate a maximum value of 8.5 kips. Both of these are higher than the elastic analysis and may be due to an increase in the vertical response of the roof following yield. The maximum values of the horizontal, in-plane shear forces along the walls are shown in Figure 7.46. The maximum horizontal shear in the purlin connection has a value of 2.8 kips (Fig. 7.46b). This represents a significant reduction from the 29 kips obtained with the nonlinear connections alone. For the glulam connections (Fig. 7.46c), the maximum value reaches a similar value (2.8 kips); however, this compares with 5.5 kips for the nonlinear connections alone.

The hysteretic behavior of the glulam to pilaster connection near the middle of the longitudinal wall is shown in Figure 7.47. The axial force (Fig. 7.47a) has a distinct nonlinear hysteresis with a maximum displacement of 0.89 inches and an estimated displacement ductility of 3.6. The other two force components (Figs. 7.47b–c) are primarily linear elastic. A group of plots showing the behavior of a connection of the glulam to a pilaster near the corner of the

longitudinal wall is shown in Figure 7.48. It can be seen that there is reduced inelastic behavior in the axial direction with the maximum displacement reaching 0.53 inches. Primarily linear elastic behavior occurs in the other two directions.

The hysteretic behavior of the purlin to pilaster connection located near the middle of the transverse wall is shown in Figure 7.49. Both the axial force and the vertical shear exhibit a strong nonlinear behavior (Figs. 7.49a–b). The maximum axial displacement reaches 0.8 inches with an estimated displacement ductility of 8. The maximum vertical displacement reaches 2.2 inches with an estimated ductility of 12.1. The horizontal shear (Fig. 7.49c) is constrained to be linear elastic due to lack of applicable data on its inelastic behavior. The hysteretic behavior of a purlin to pilaster connection near the corner of the transverse wall is shown in Figure 7.50. It can be seen that there is hysteretic behavior in the axial force (Fig. 7.50a) with a displacement demand of 1.2 inches and an estimated ductility demand of 5.2. In the vertical direction (Fig. 7.50b), displacement reaches 5 inches with a ductility demand of 56.7. It is doubtful that these high ductility demands can be accommodated by these older connections. As done previously, the horizontal shear force is constrained to remain linear elastic (Fig. 7.50c).

The hysteretic behavior in the panels of the roof diaphragm as represented by the axial forces in the diagonal components of the Hrennikoff elements near the transverse wall is shown in Figure 7.51. The three components are located at the end of the longitudinal wall, adjacent to the transverse wall. The hysteretic behavior of the component nearest the longitudinal wall is shown in Figure 7.51a. At this location, the maximum displacement demand is 0.32 inches with an estimated ductility demand of 13.5. The hysteretic behavior at the middle location (Fig. 7.51b) indicates a displacement demand of 0.438 inches and a ductility demand of 18.3. At the location near the center of the transverse span (Fig. 7.51c) the displacement demand is only 0.058 inches and the ductility demand is 2.4.

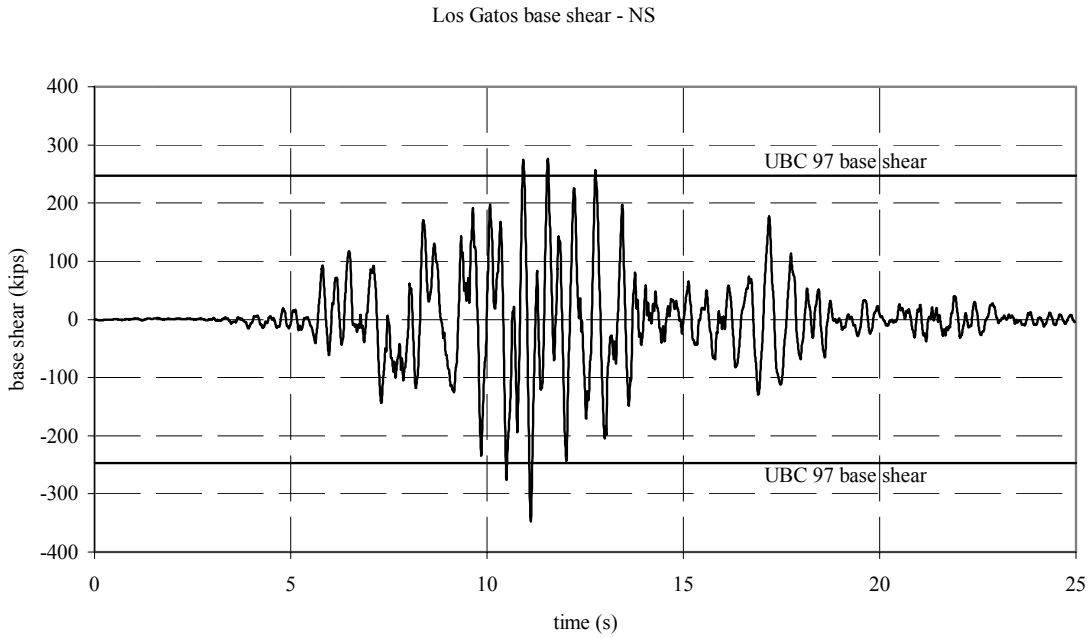

(a)

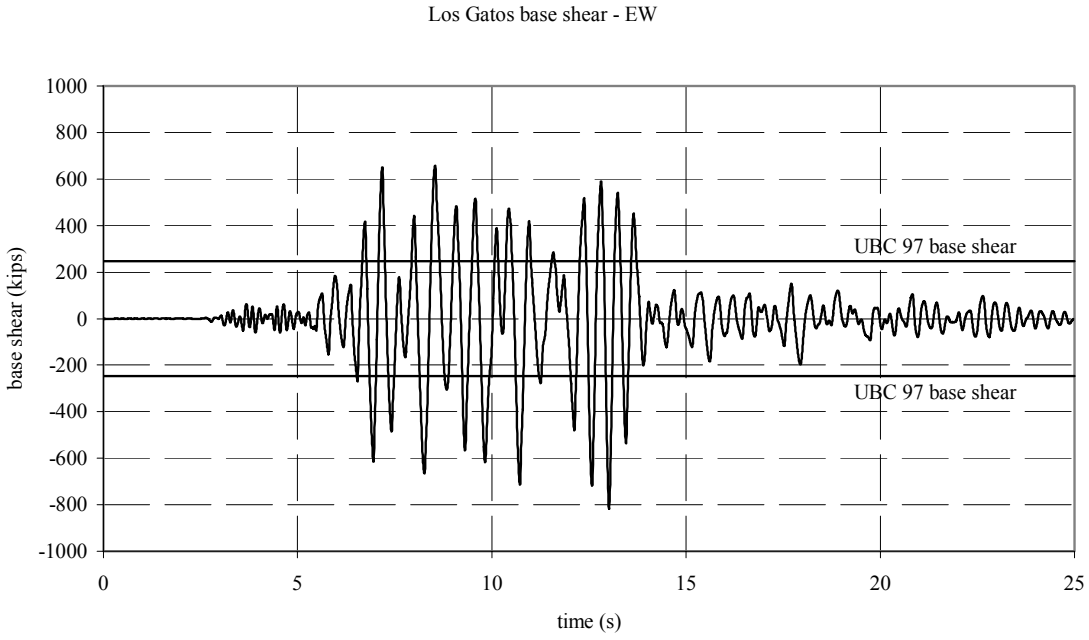

(b)

Fig. 7.43 Nonlinear base shear, old connections, dense nailing, Los Gatos

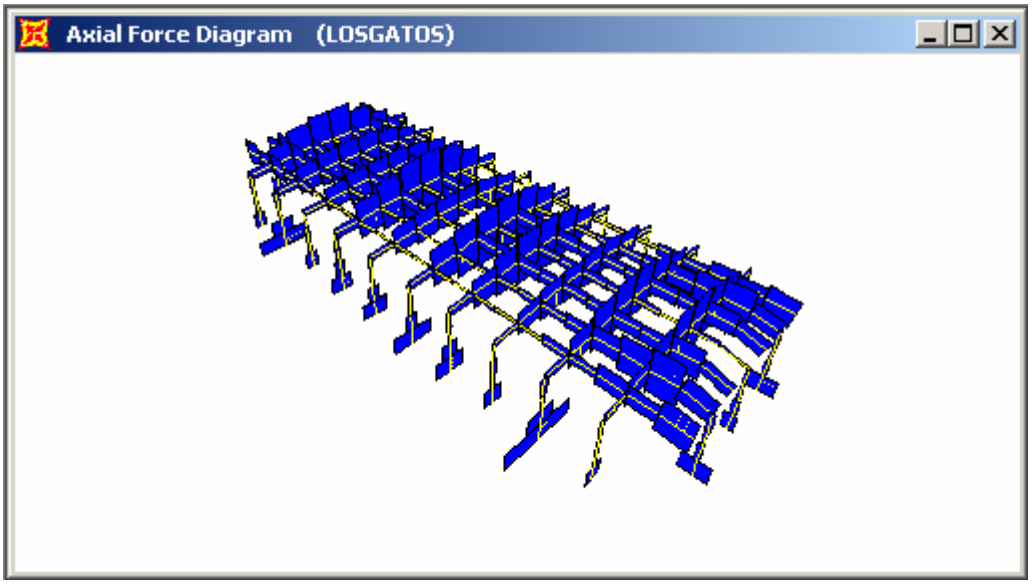

(a)

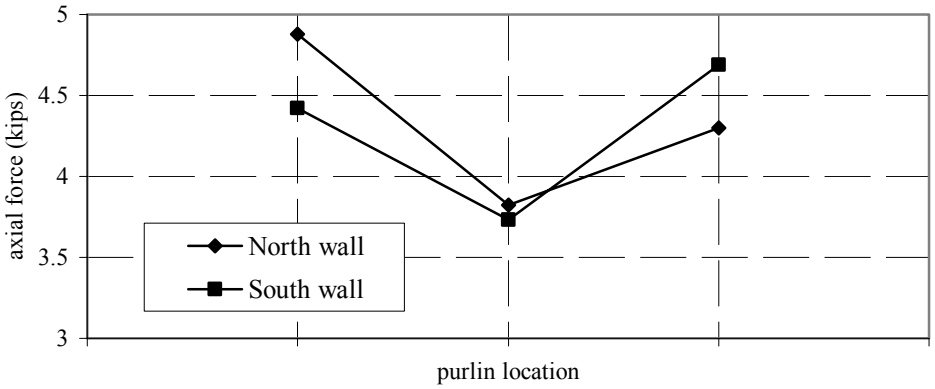

(b)

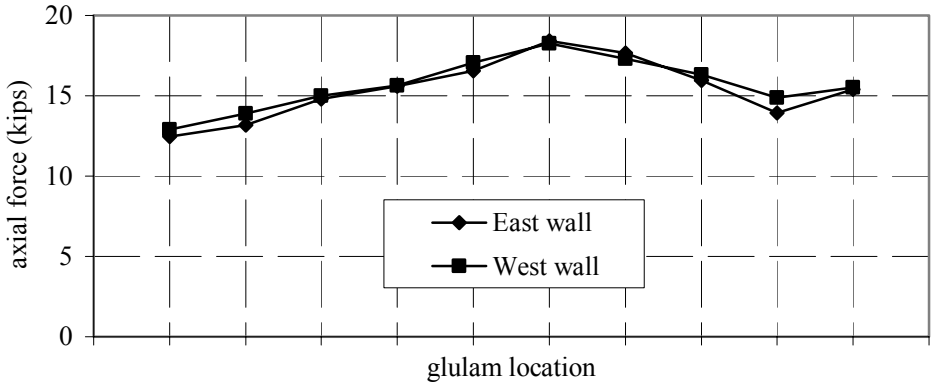

(c)

Fig. 7.44 Axial force, nonlinear old connections, dense nailing, Los Gatos

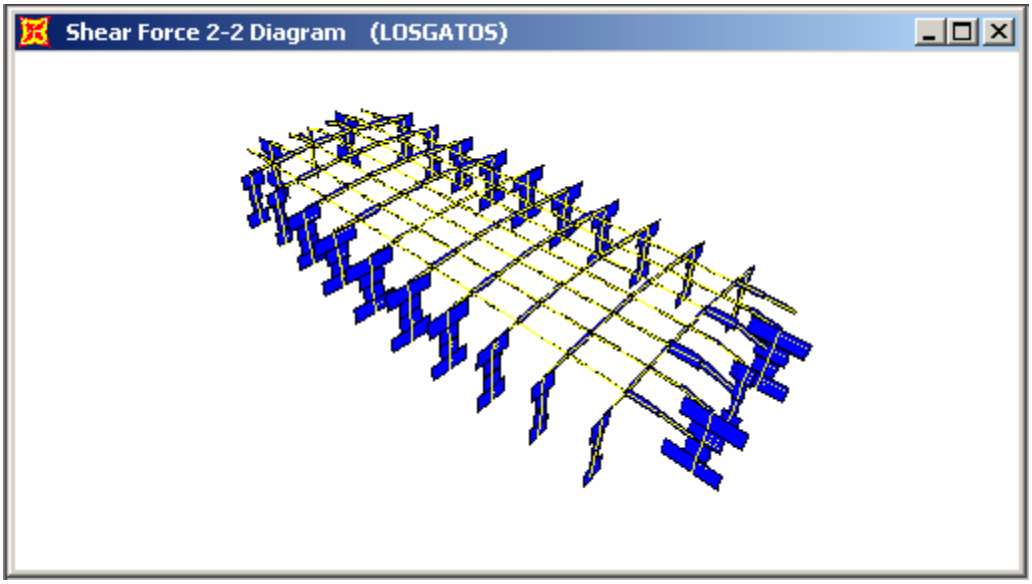

(a)

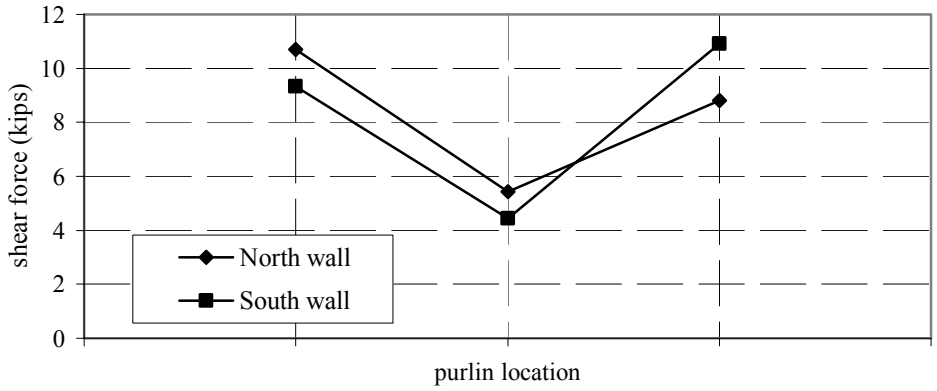

(b)

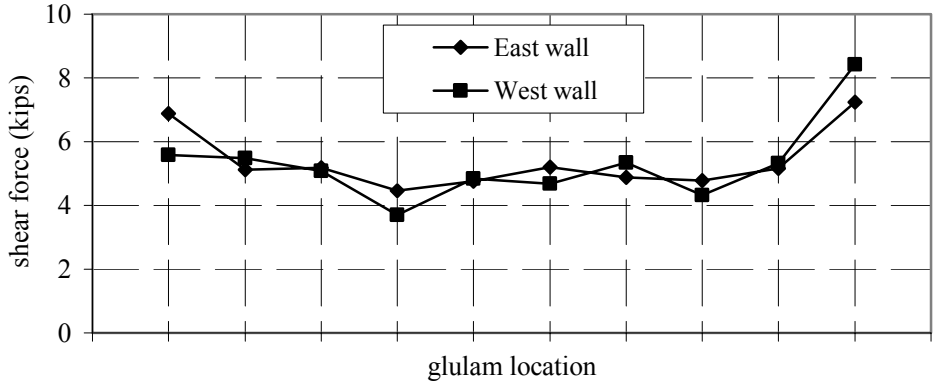

(c)

Fig. 7.45 Vertical shear, nonlinear old connections, dense nailing, Los Gatos

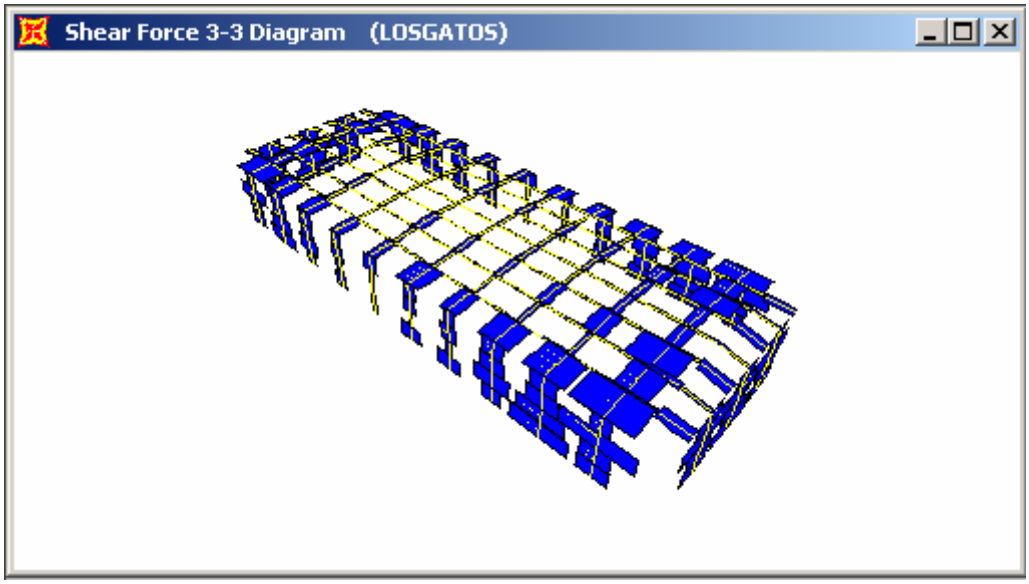

(a)

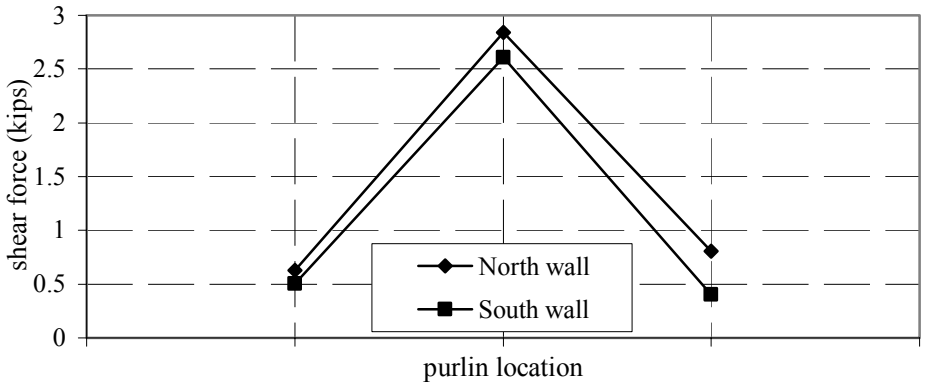

(b)

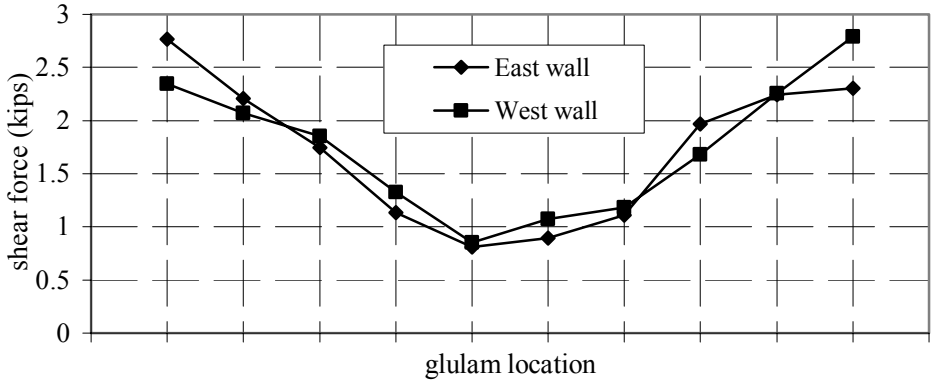

(c)

Fig. 7.46 Horizontal shear, nonlinear old connections, dense nailing, Los Gatos

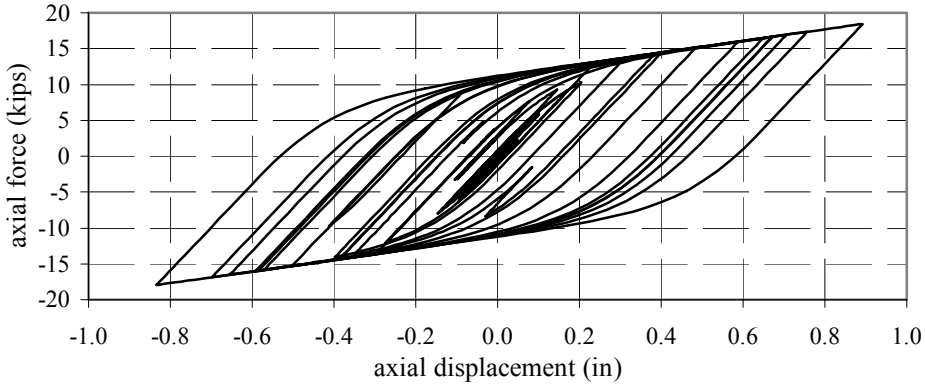

(a)

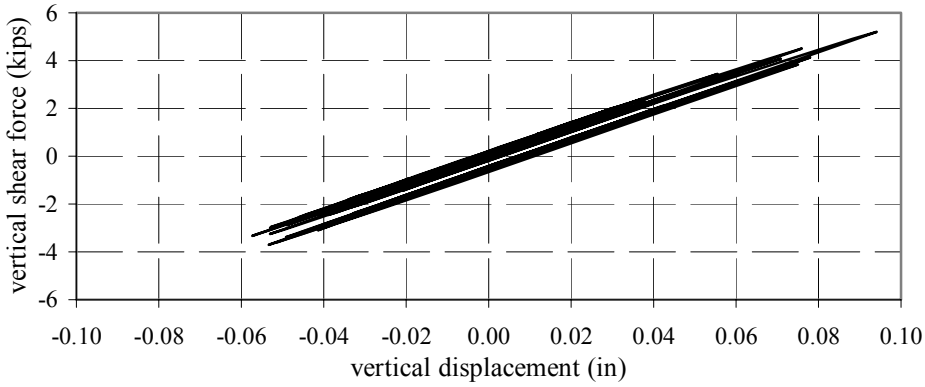

(b)

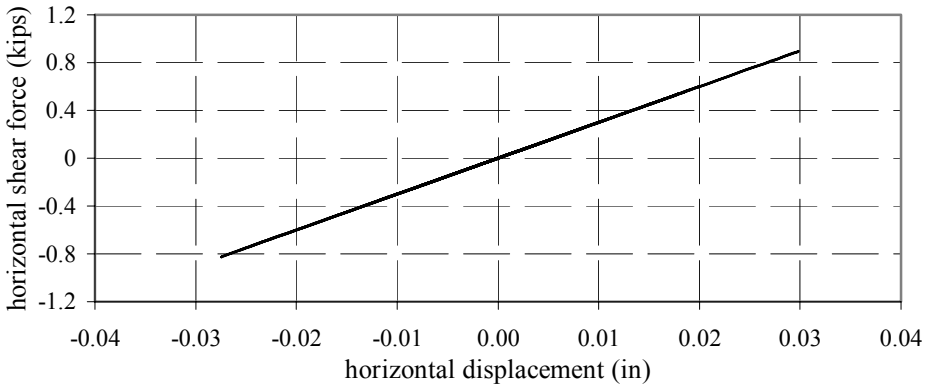

(c)

Fig. 7.47 Hysteretic behavior, glulam to pilaster, old connection, dense nailing, middle of wall, Los Gatos

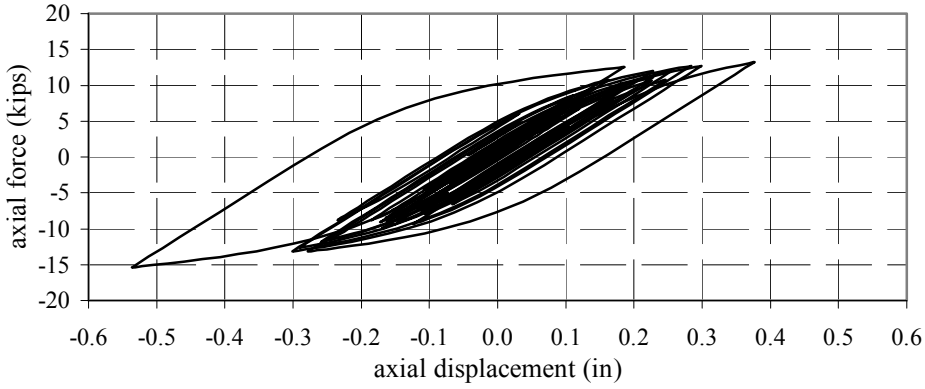

(a)

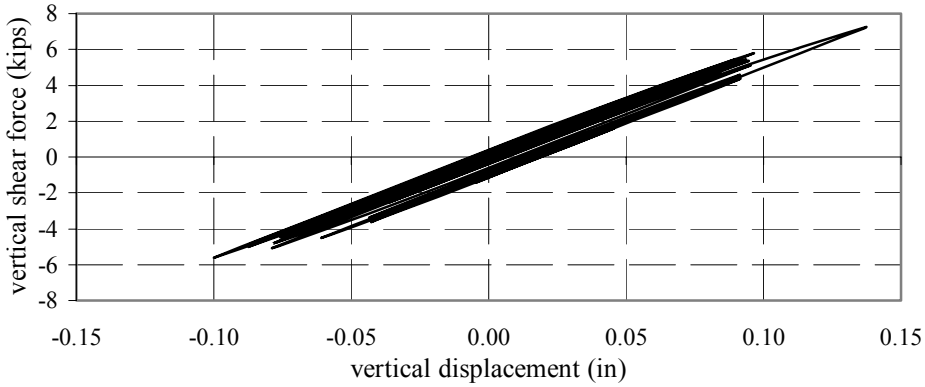

(b)

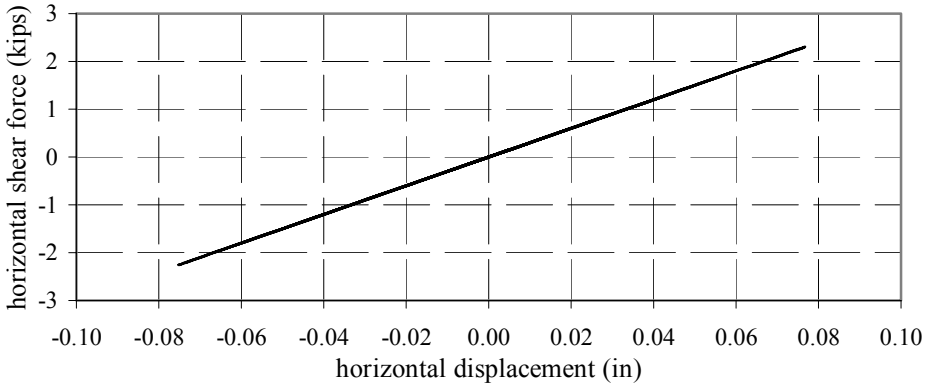

(c)

Fig. 7.48 Hysteretic behavior, glulam to pilaster, old connection, dense nailing, near corner, Los Gatos

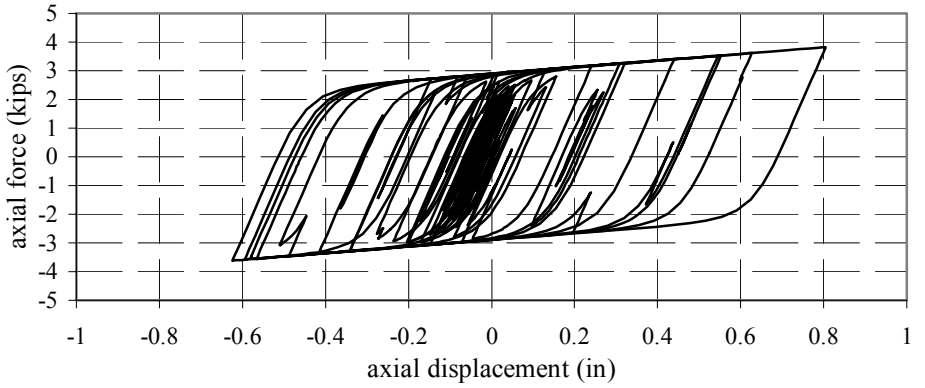

(a)

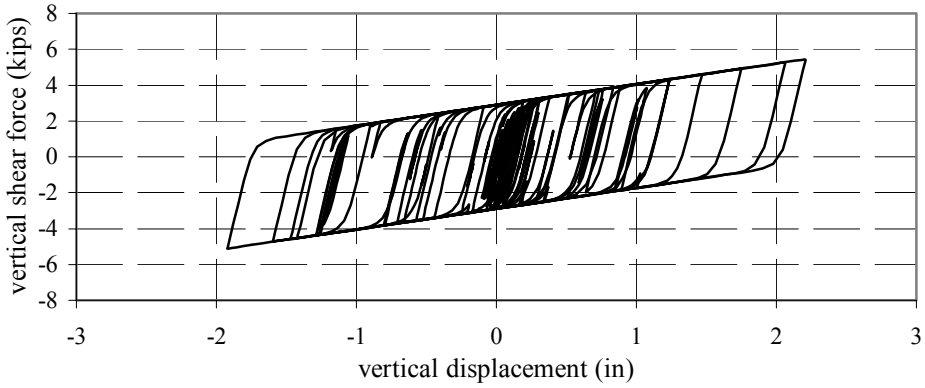

(b)

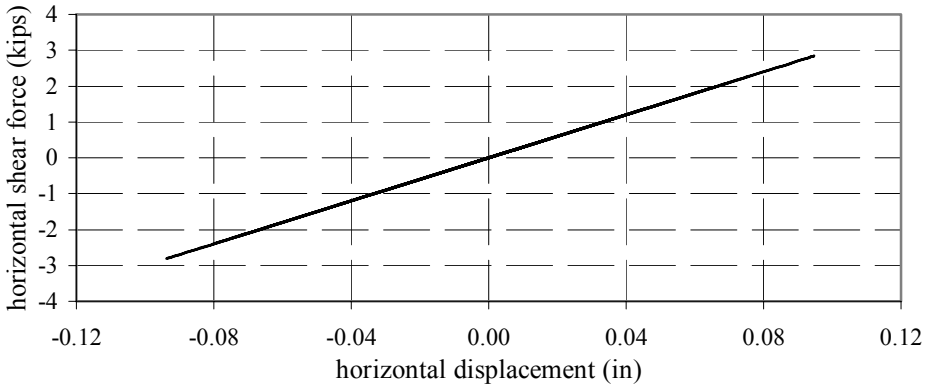

(c)

Fig. 7.49 Hysteretic behavior, purlin to pilaster, old connection, dense nailing, middle of wall, Los Gatos

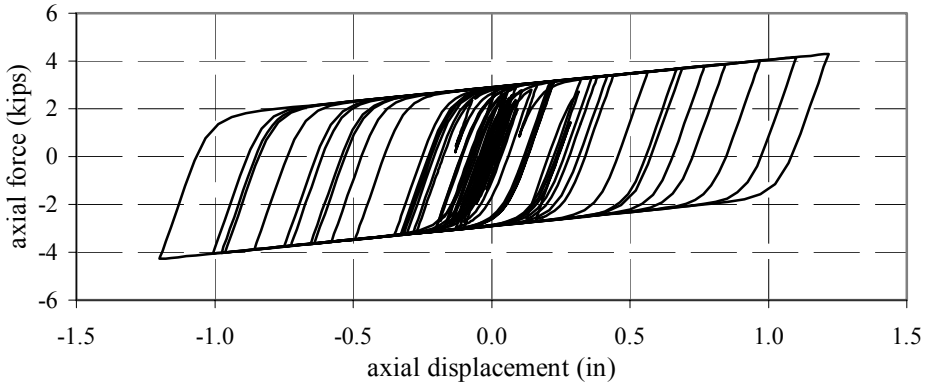

(a)

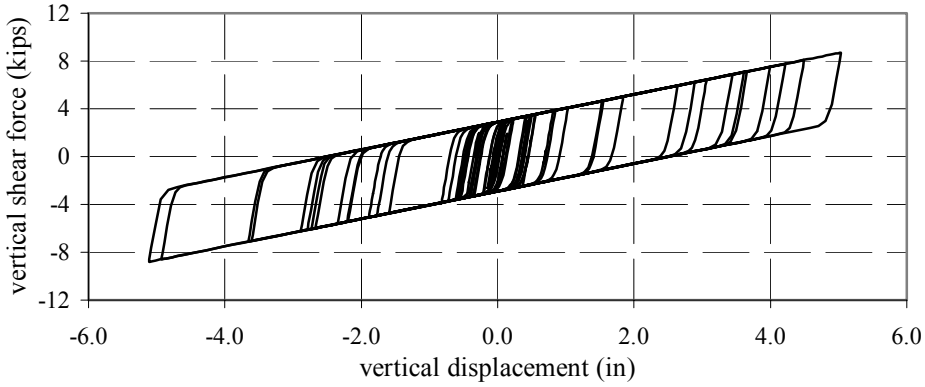

(b)

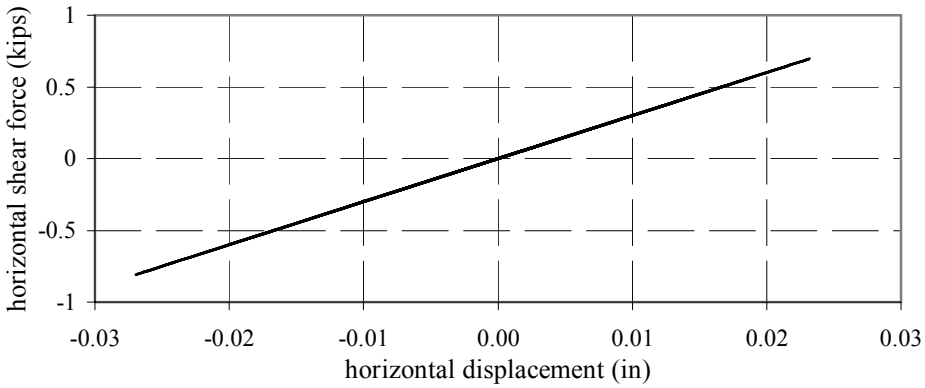

(c)

Fig. 7.50 Hysteretic behavior, purlin to pilaster, old connection, dense nailing, near corner, Los Gatos

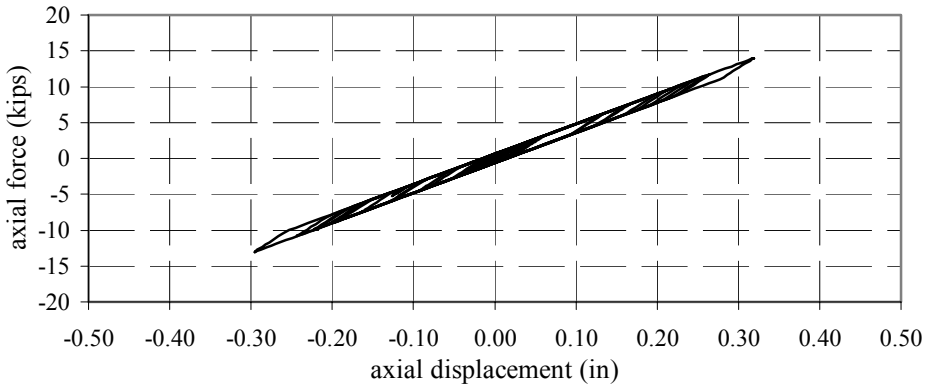

(a) element location

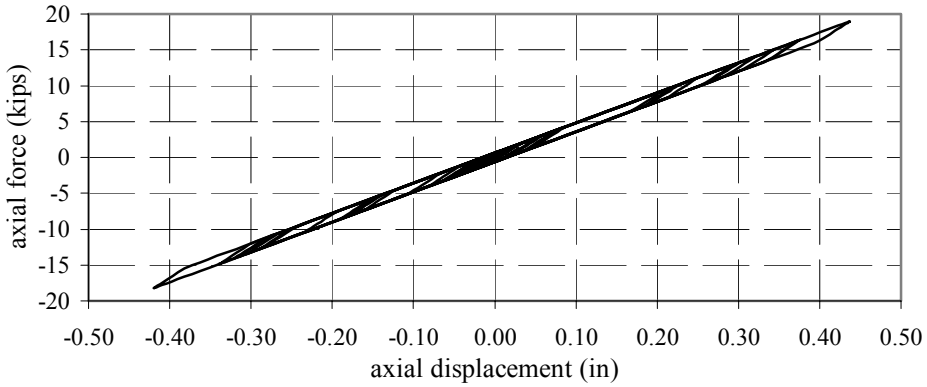

(b) element location

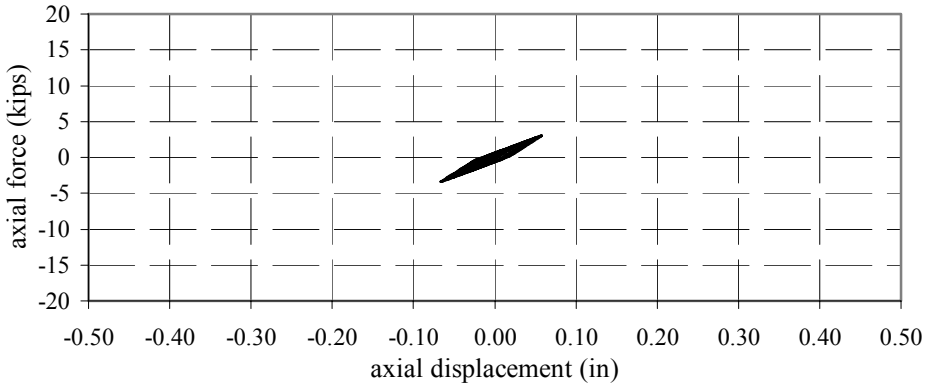

(c) element location

Fig. 7.51 Hysteretic behavior, roof diaphragm, old connections, dense nailing, Los Gatos

7.5.3 Los Gatos, Dense Nailing, New Connections

The responses of the nonlinear model having dense nailing and new connections under the Los Gatos ground motion are presented in Figures 7.52–7.64. The time history of the calculated base shear in the longitudinal (N-S) direction is shown in Figure 7.52a. In this direction the base shear reaches a maximum of 225 kips, which is less than the code design value of 240 kips. The results of the elastic analysis indicated a maximum base shear of 430 kips. The time history of the base shear in the transverse (E-W) direction is shown in Figure 7.52b. In this direction, the maximum reaches 533 kips, which is more than double the code design value (240 kips) but is lower than the previous result (800 kips) with the old connections and much lower than the result of the elastic dynamic analysis that indicated a maximum shear of 1,630 kips.

The maximum axial forces in the connections of the glulam beams and purlins to the pilasters are shown in Figure 7.53. The maximum axial force in the purlin connection (Fig. 7.53b) reaches a value of 21 kips, which is more than the value of 18.3 kips obtained with the new nonlinear connections alone and less than the 21.8 kips (Fig. 6.65) obtained for the connections using elastic analysis. The distribution of axial forces in the glulam beams is shown in Figure 7.53c. In this case, the maximum value is 35 kips, which is approximately the same as the 33 kips obtained with the new nonlinear connections alone, and both are about 25% less than the value obtained using elastic analysis.

The distribution of vertical shear in the glulam beam and purlin connections to the pilasters is shown in Figure 7.54. The purlin connections (Fig. 7.54b) indicate a maximum value of 26 kips compared with a value of 7.1 kips for the new nonlinear connections alone. The increase in the vertical response in this region may be due to the partial yielding of the roof diaphragm that occurs at this location near the ends of the transverse walls. The glulam beam connections (Fig. 7.54c) indicate a maximum value of 7 kips, which is only slightly above the 5 kips obtained with the new nonlinear connections alone. The maximum values of the horizontal, in-plane shear force along the walls is shown in Figure 7.55. The maximum horizontal shear in the purlin connections has a value of just over 7 kips (Fig. 7.55b). This is significantly less than the 39.1 kips obtained with the new nonlinear connections alone. For the glulam beam connections (Fig. 7.55c), the maximum value reaches 6.7 kips compared to 7.5 kips for the new nonlinear connections alone.

The hysteretic behavior of the glulam beam to pilaster connection near the middle of the longitudinal wall is shown in Figure 7.56. This figure indicates that the use of the new connections has permitted all three of the force components to remain in the elastic range. A plot showing the behavior of a similar glulam beam to pilaster connection near the corner of the longitudinal wall is shown in Figure 7.57. It can be seen that there is only weakly nonlinear behavior for the axial force (Fig. 7.57a). The behavior of the vertical shear in the connection (Fig. 7.57b) is judged to be elastic and the behavior of the horizontal shear (Fig. 7.57c) is constrained to be linear elastic.

The hysteretic behavior of the purlin to pilaster connection located near the middle of the transverse wall is shown in Figure 7.58. The axial force (Fig. 7.58a**)** now exhibits only a weakly nonlinear behavior with a significant reduction in the axial displacement demand. An even more significant reduction in inelastic behavior also occurs in the vertical shear (Fig. 7.58b). The deformation demand has been reduced to 0.18 inches from 2.2 inches. The horizontal shear (Fig. 7.58c) is constrained to be linear elastic due to lack of applicable data on its inelastic behavior. The hysteretic behavior of a purlin to pilaster connection near the corner of the transverse wall is shown in Figure 7.59. The hysteretic behavior of the axial force component is shown in Figure 7.59a. Although there is still inelastic deformation in this force component, the displacement demand is reduced to 0.58 inches, compared to 1.2 inches for the old connections. The estimated displacement ductility demand is a more manageable 3.5. An even more significant reduction in the displacement demand for the vertical direction can be seen in Figure 7.59b. Although the response is still inelastic, the required displacement in this direction is now a more reasonable 1.26 inches compared to 5 inches for the old connections, and the displacement ductility is estimated at 7.4. As described previously, the horizontal shear force is constrained to remain linear elastic (Fig. 7.59c).

The hysteretic behavior in the panels of the roof diaphragm as represented by the axial forces in the diagonal components of the Hrennikoff elements near the transverse wall is shown in Figure 7.60. The three components are located at the end of the longitudinal wall, adjacent to the transverse wall. The hysteretic behavior of the component nearest the longitudinal wall is shown in Figure 7.60a. At this location, the maximum displacement demand is 0.083 inches, which is one-fourth the demand with the old connections. The estimated ductility demand is reduced to a much lower value of 3.2. The hysteretic behavior at the middle location (Fig. 7.60b) indicates a displacement demand of 0.134 inches, which is about one third the comparable

displacement for the old connection, and a ductility demand of 4.3. At the location near the center of the transverse span (Fig. 7.60c), the displacement demand is only 0.015 inches and the behavior is elastic.

Although the roof diaphragm and connections are modeled using nonlinear elements, the tilt-up walls are still considered as behaving in a primarily elastic condition. The validity of this assumption can be evaluated by a review of the stress contours shown in Figures 7.61–7.64. The in-plane shear contours in the north and south walls are shown in Figure 7.61. Neglecting the lower corners in the north wall, the shear force in the main part of both walls is less than 78 lbs/in. This compares with more than 600 lbs/in. under the same ground motion in the elastic model (Fig. 6.76). Similar results are shown for the in-plane shear in the east and west walls shown in Figure 7.62. However, these values are well below the capacity of 1.74 kips/in. Contours of vertical out-of-plane moment in the north and south walls are shown in Figure 7.63. Maximum moments occur near the disconnected ends of the wall and reach a value of more than 5.4 in.-kips./in., which is greater than the calculated capacity of 3.0 in.-kips/in. However, it should be noted that this high value occurs in only one location and may cause some local cracking. The corresponding value for the elastic model was more than 11.2 in.-kips/in. (Fig. 6.78). Similar contours for the longitudinal, east, and west walls are shown in Figure 7.64. In this direction the maximum moment at the corner of the wall is just above 3.0 in.-kips/in. in a very localized position. Hence it can be concluded that the behavior of these walls is almost entirely linearly elastic. In the elastic model (Fig. 6.79), the corresponding value is more than 5.6 in.-kips/in.

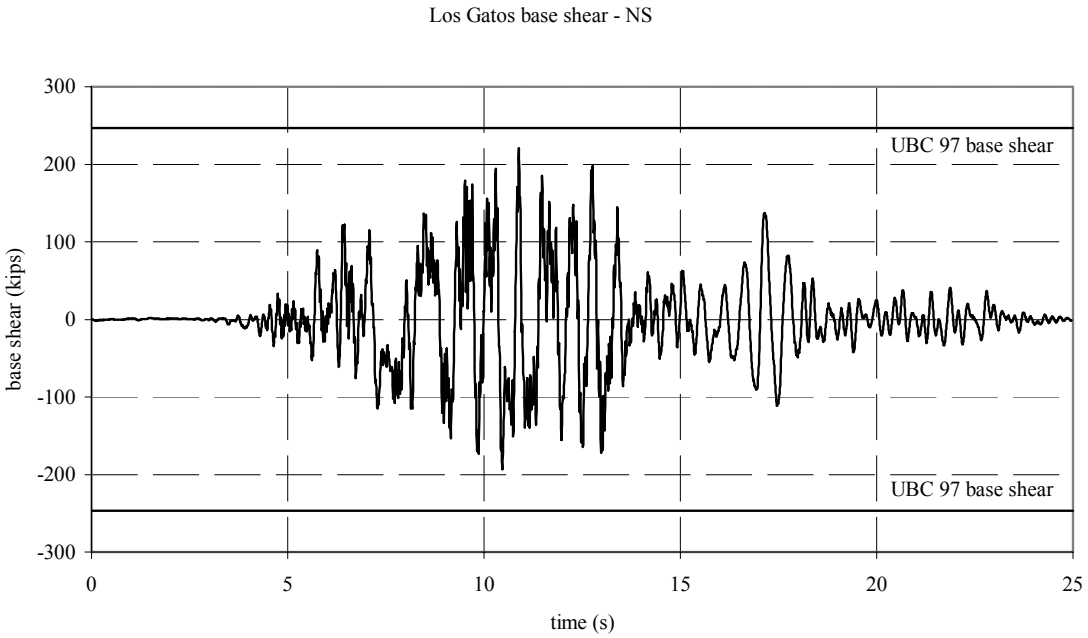

(a)

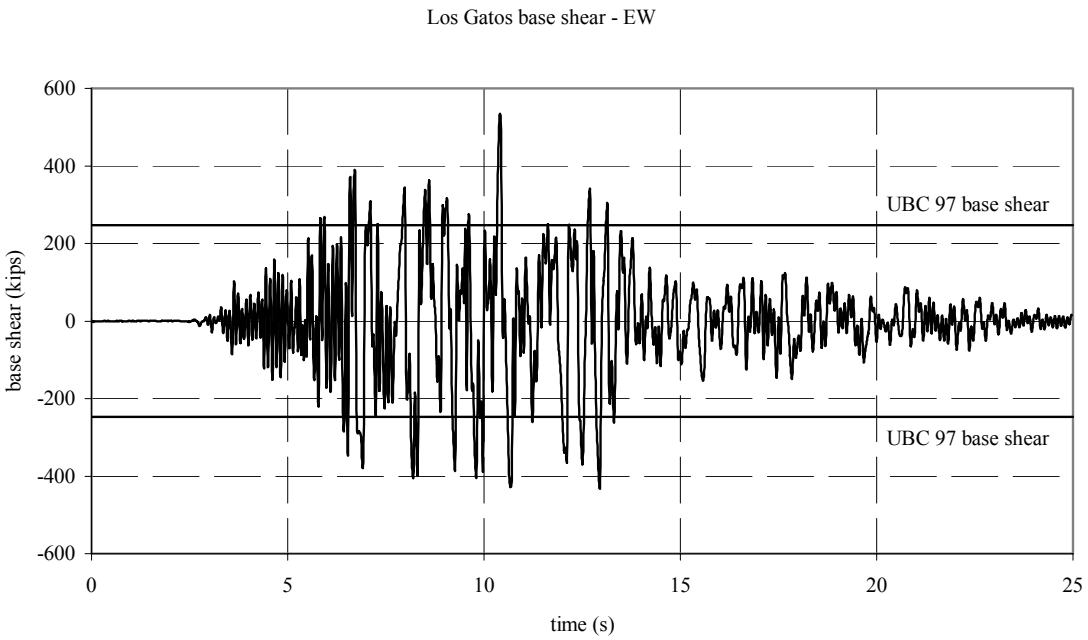

(b)

Fig. 7.52 Base shear, nonlinear new connections, dense nailing, Los Gatos

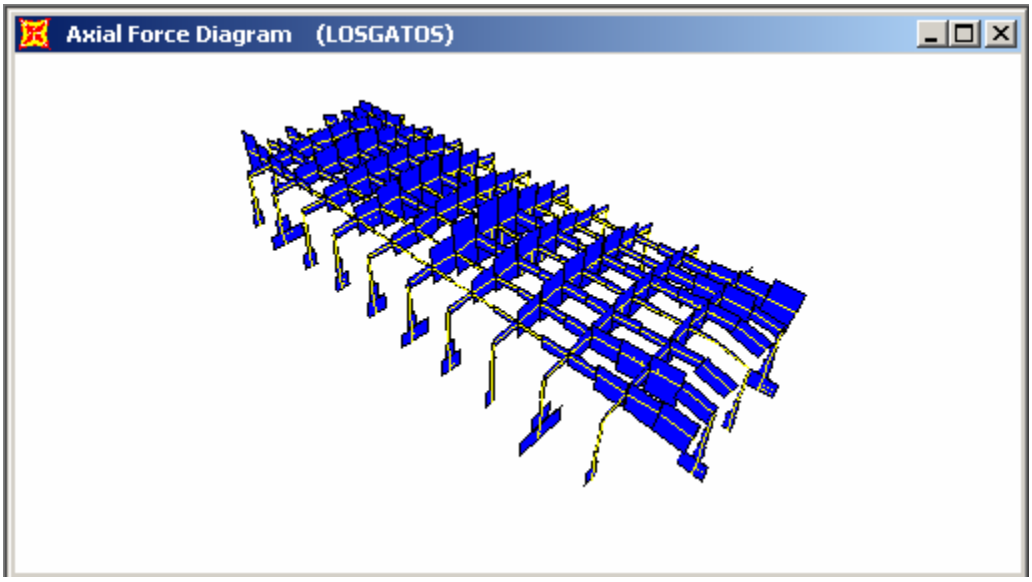

(a)

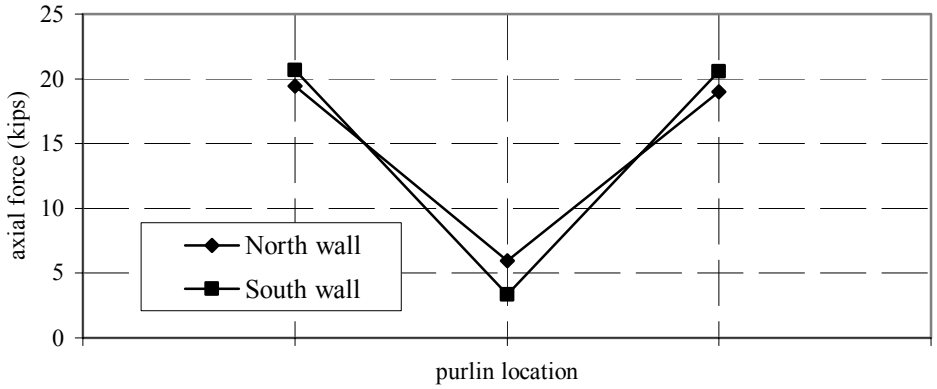

(b)

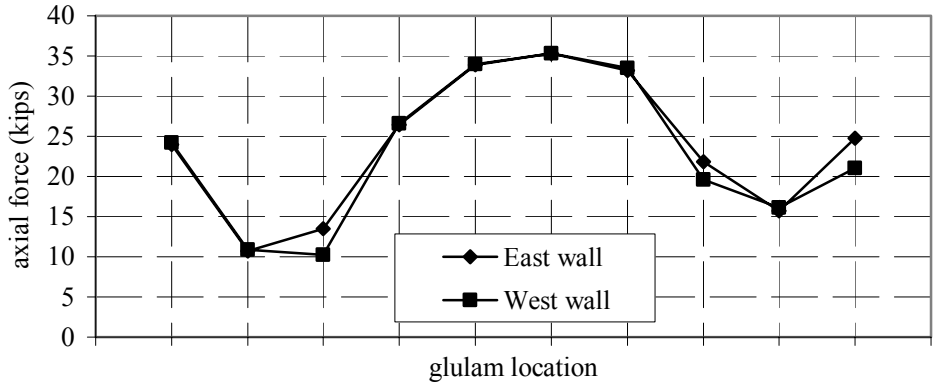

(c)

Fig. 7.53 Axial force, nonlinear new connections, dense nailing, Los Gatos

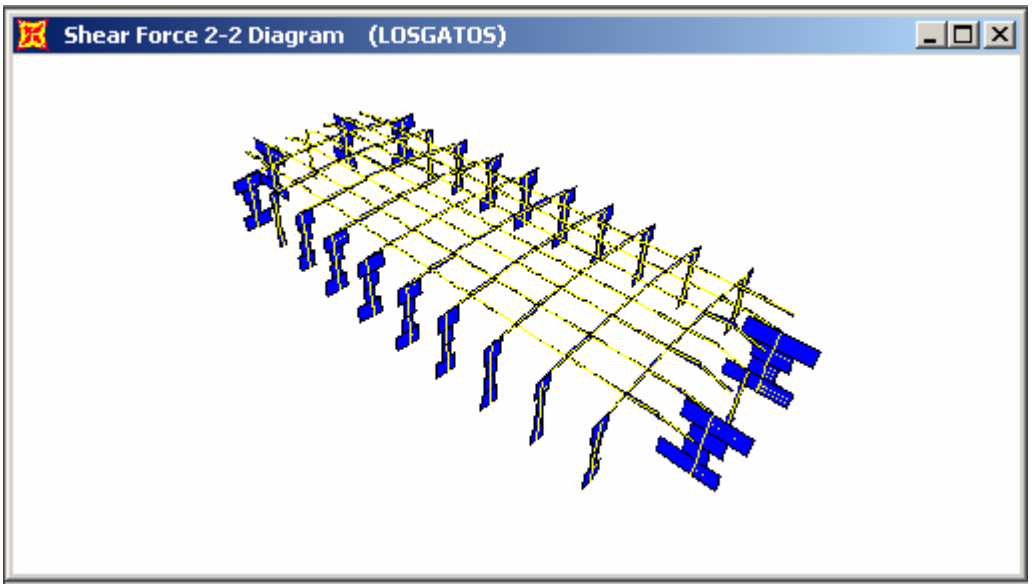

(a)

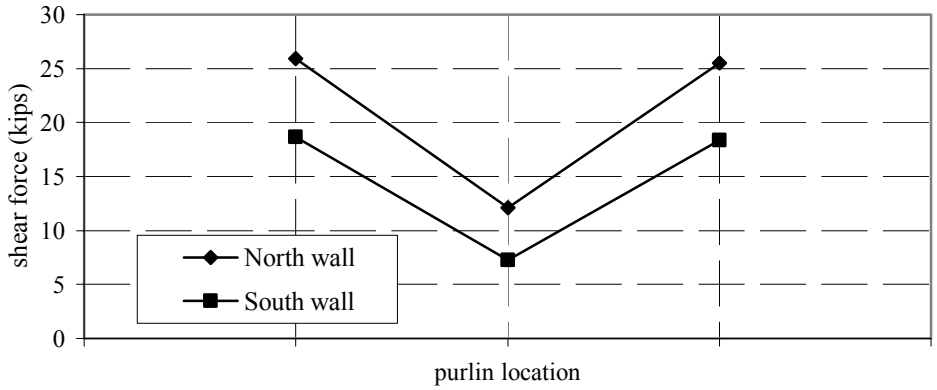

(b)

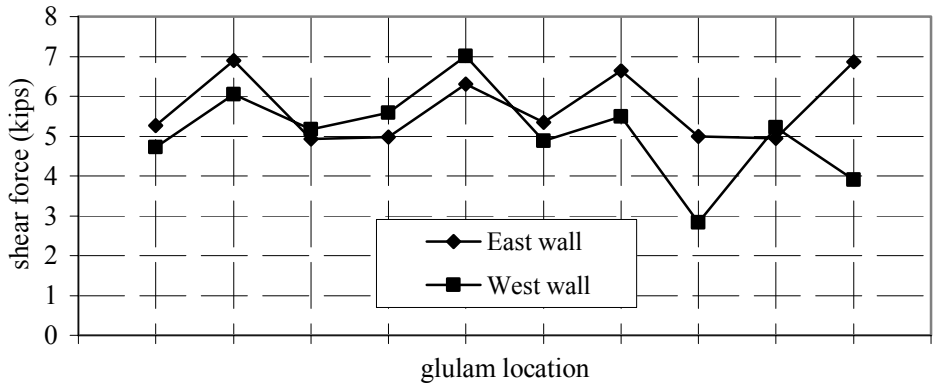

(c)

Fig. 7.54 Vertical shear force, nonlinear new connections, dense nailing, Los Gatos

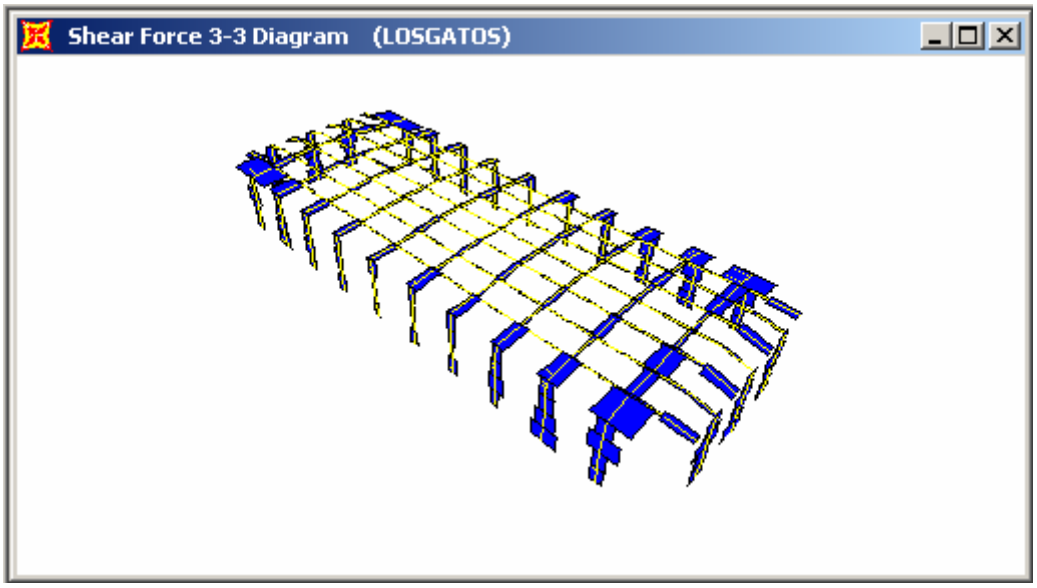

(a)

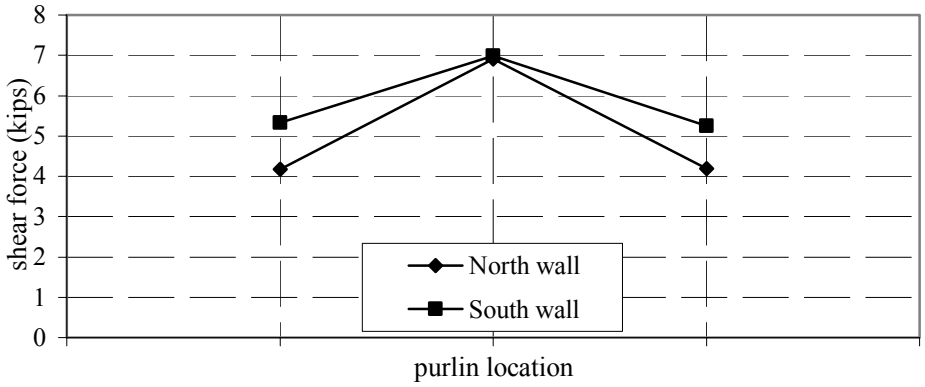

(b)

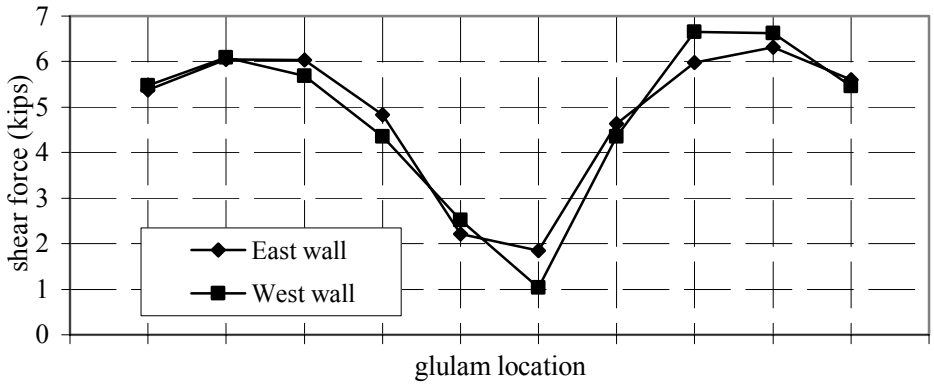

(c)

Fig. 7.55 Horizontal shear force, nonlinear new connections, dense nailing, Los Gatos

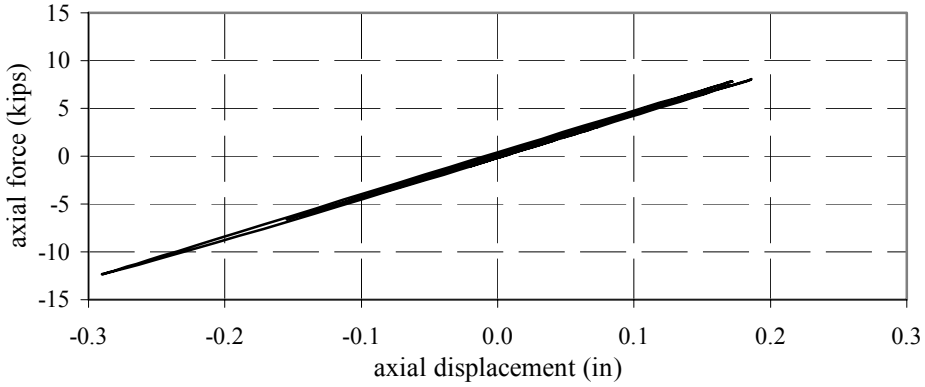

(a)

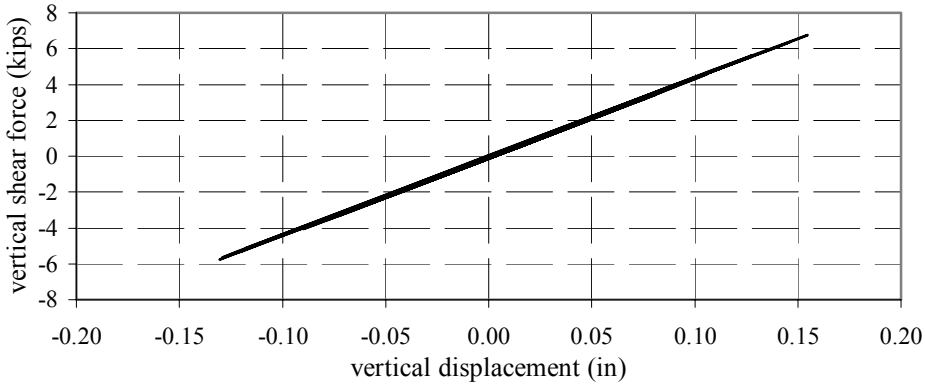

(b)

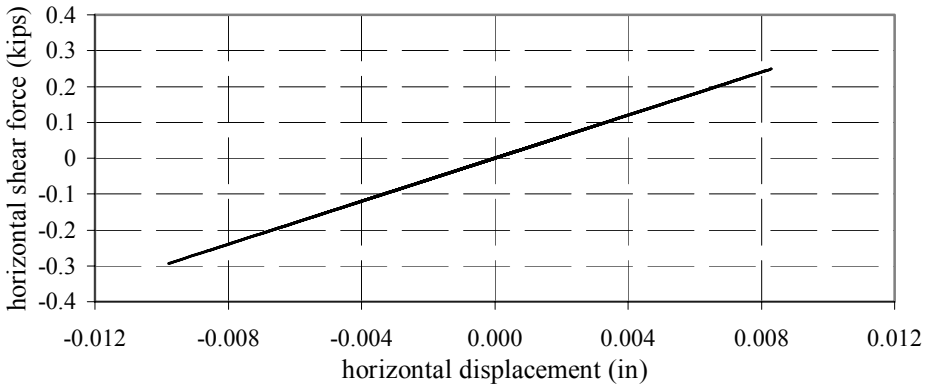

(c)

Fig. 7.56 Hysteretic behavior, glulam to pilaster, new connection, dense nailing, middle of wall, Los Gatos

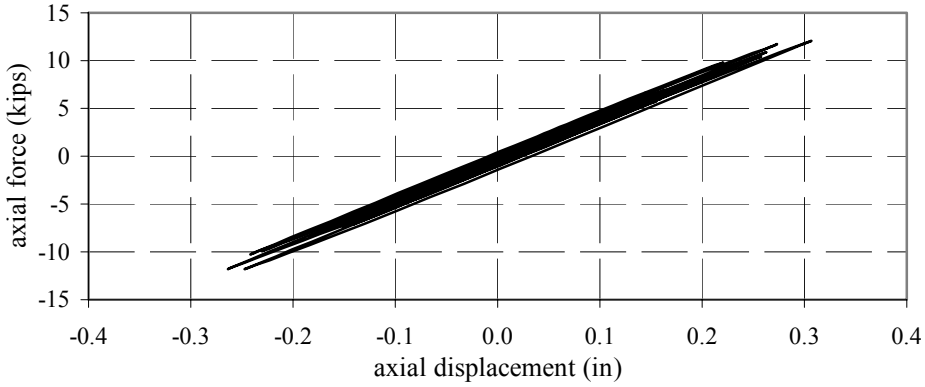

(a)

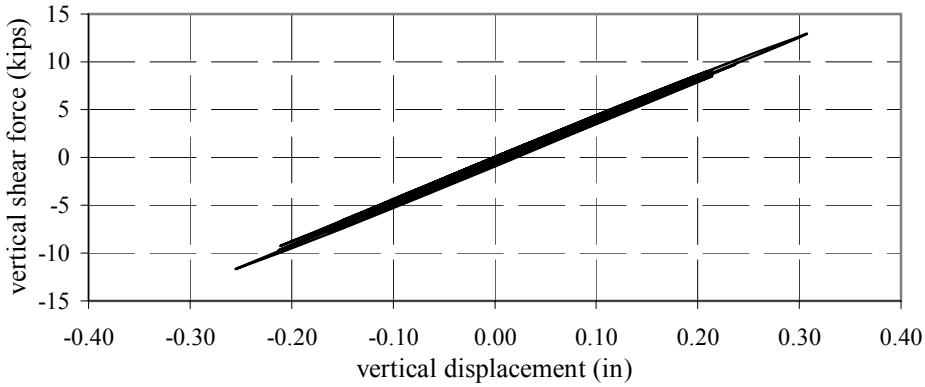

(b)

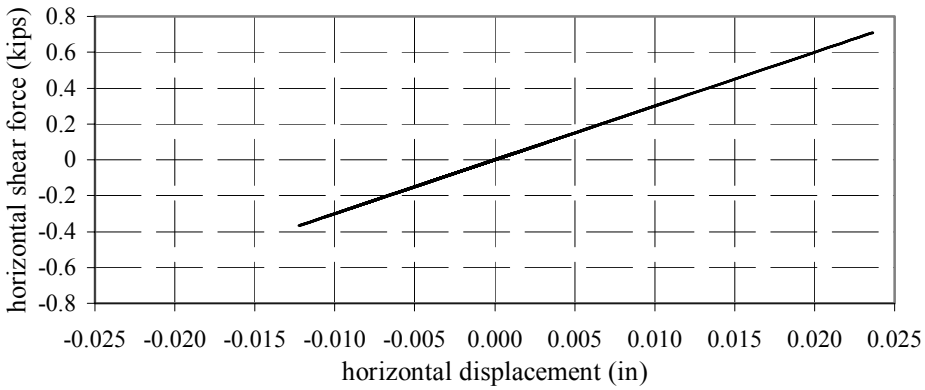

(c)

Fig. 7.57 Hysteretic behavior, glulam to pilaster, new connection, dense nailing, near corner, Los Gatos

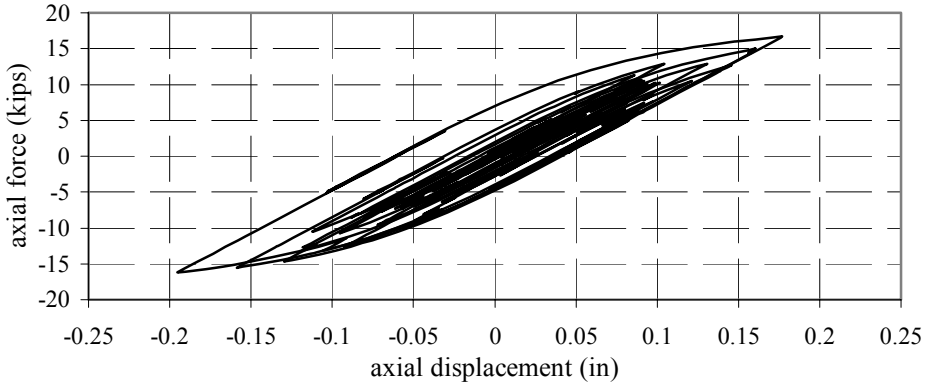

(a)

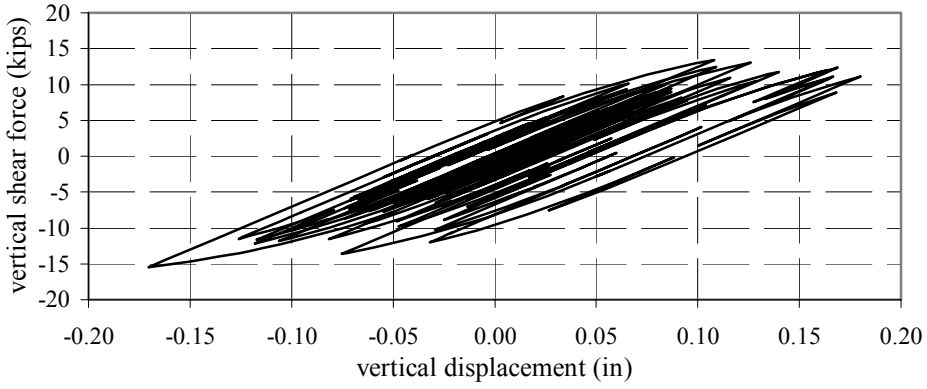

(b)

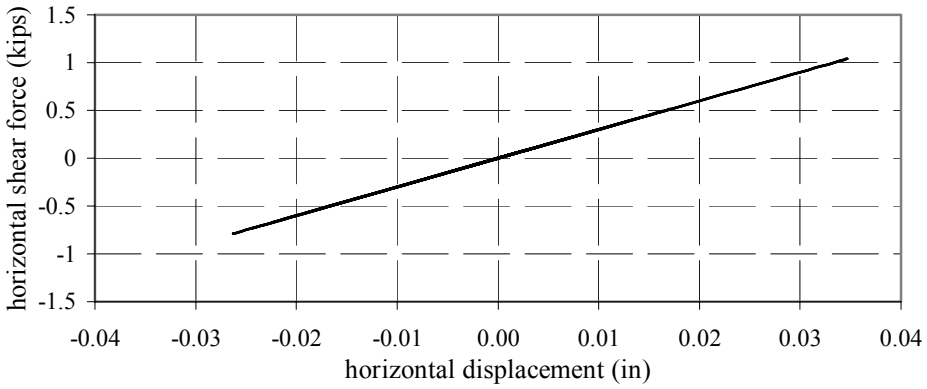

(c)

Fig. 7.58 Hysteretic behavior, purlin to pilaster, new connection, dense nailing, middle of wall, Los Gatos

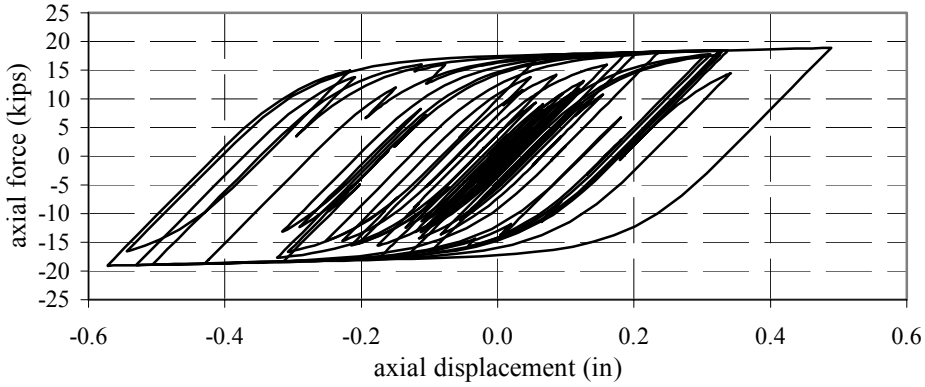

(a)

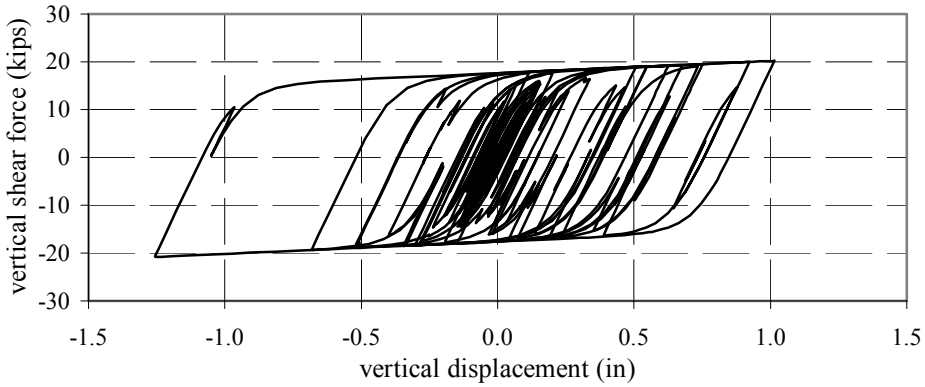

(b)

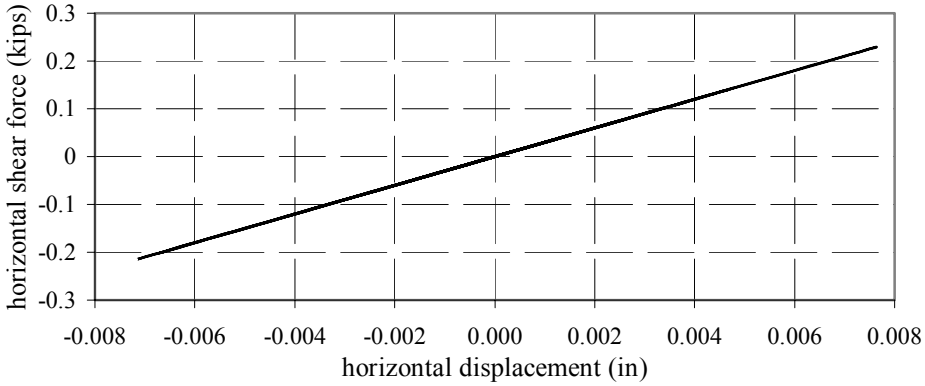

(c)

Fig. 7.59 Hysteretic behavior, purlin to pilaster, new connection, dense nailing, near corner, Los Gatos

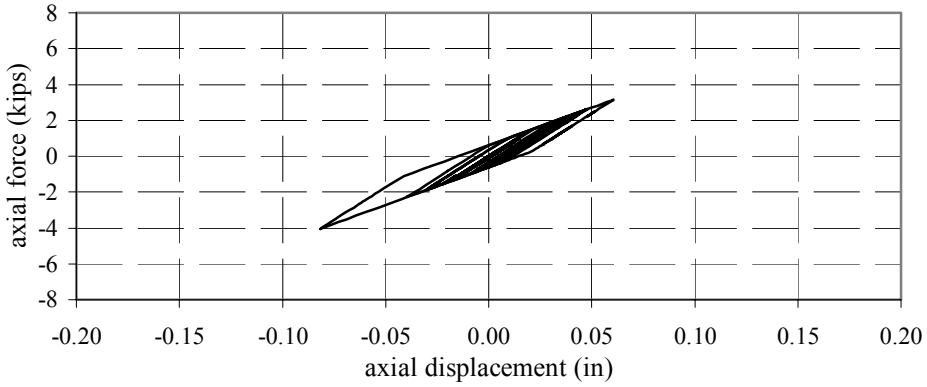

(a) element location

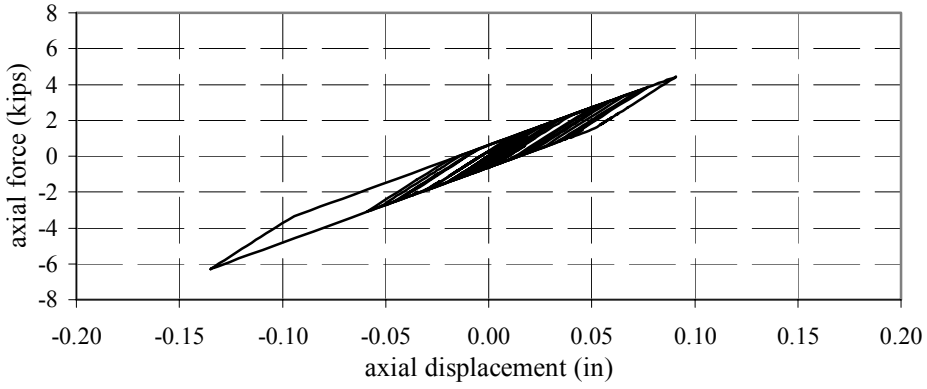

(b) element location

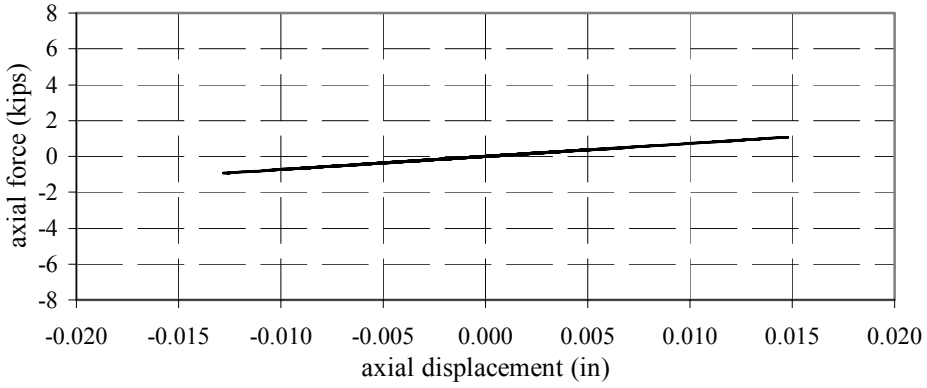

(c) element location

Fig. 7.60 Hysteretic behavior, roof diaphragm, new connections, dense nailing, Los Gatos

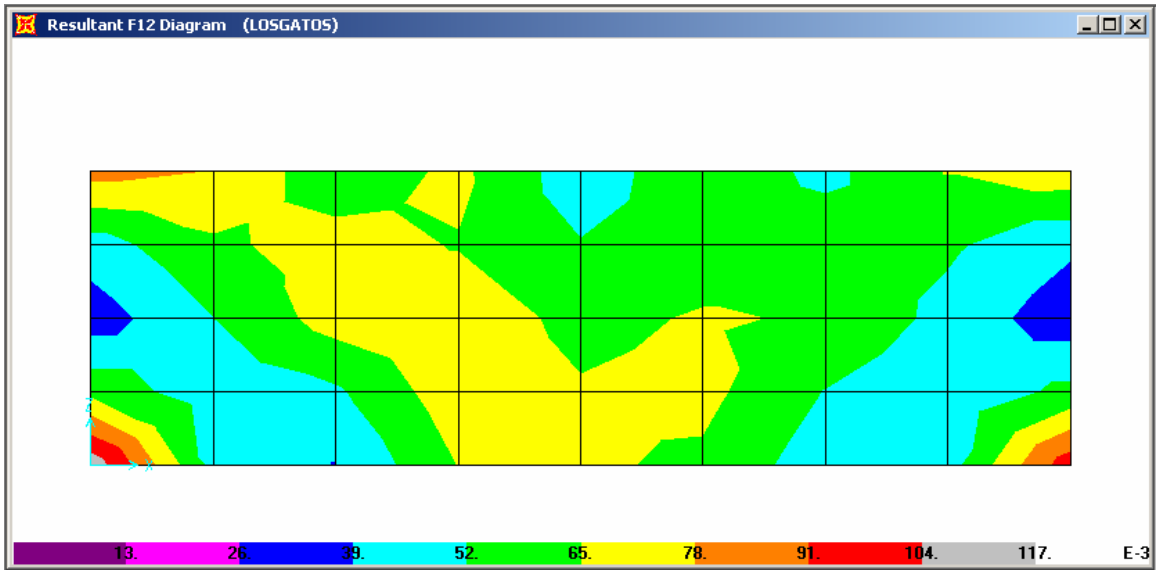

(a) Los Gatos, in-plane shear contour, north wall

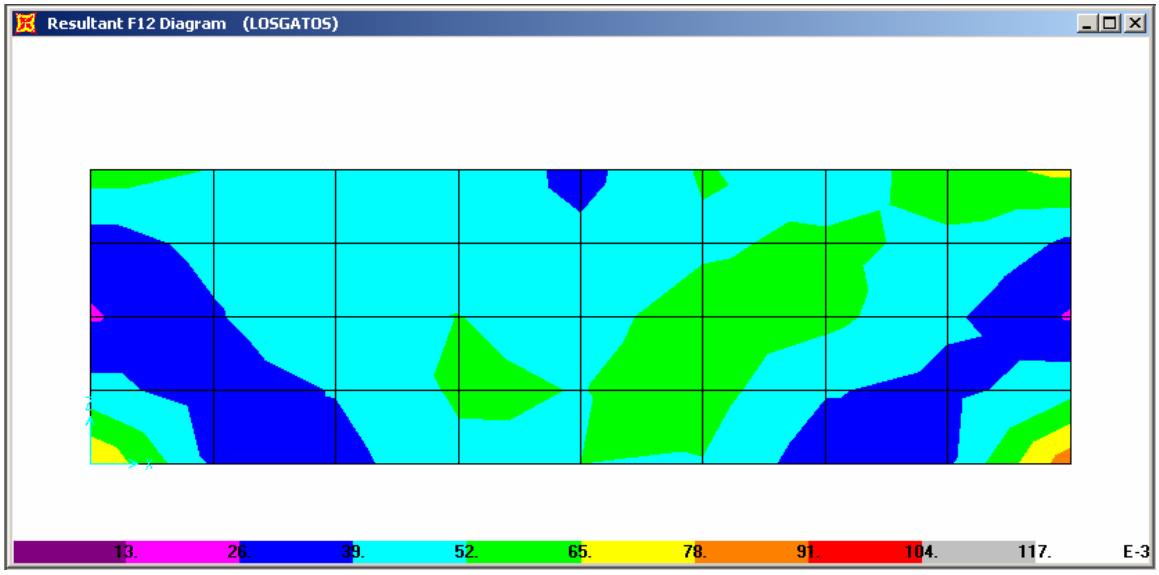

(b) Los Gatos, in-plane shear contour, south wall

Fig. 7.61 In-plane shear contours, north and south walls, new connection, dense nailing, Los Gatos

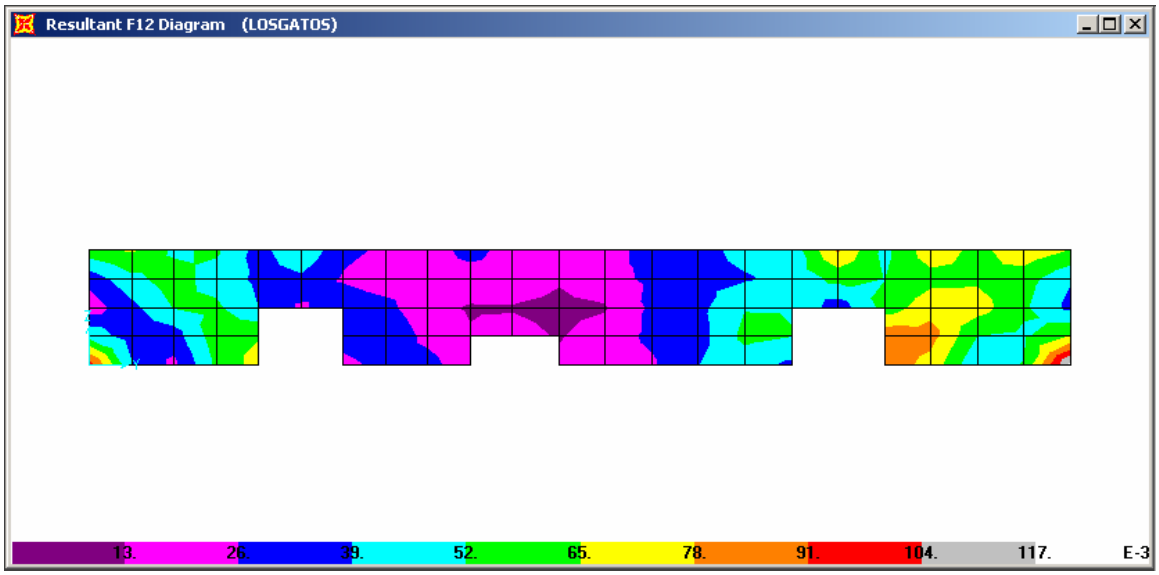

(a) Los Gatos, in-plane shear contour, east wall

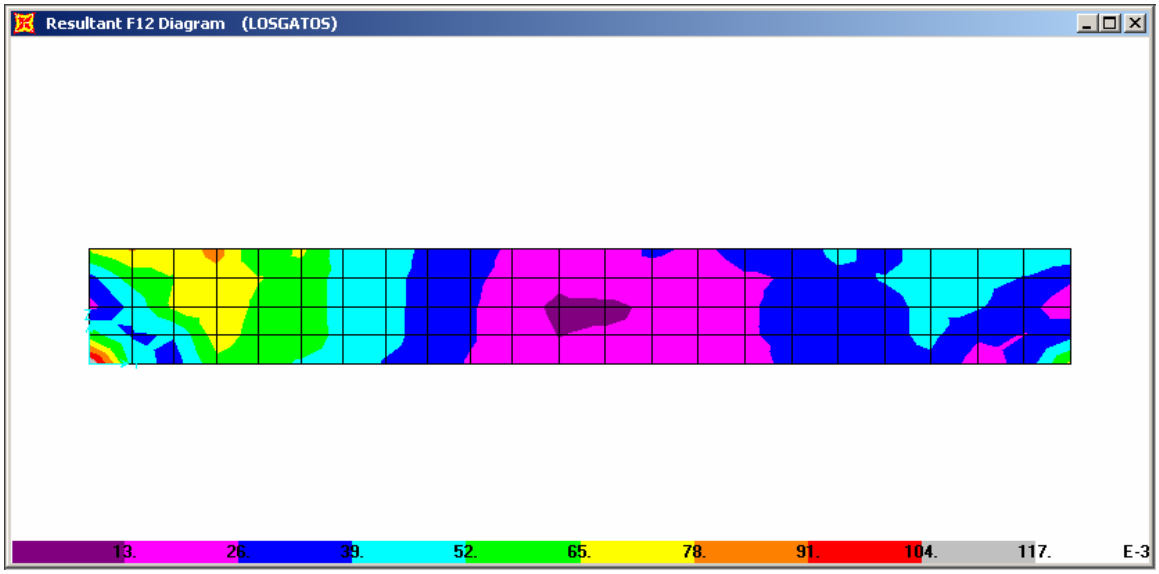

(b) Los Gatos, in-plane shear contour, west wall

Fig. 7.62 In-plane shear contours, east and west walls, new connection, dense nailing, Los Gatos

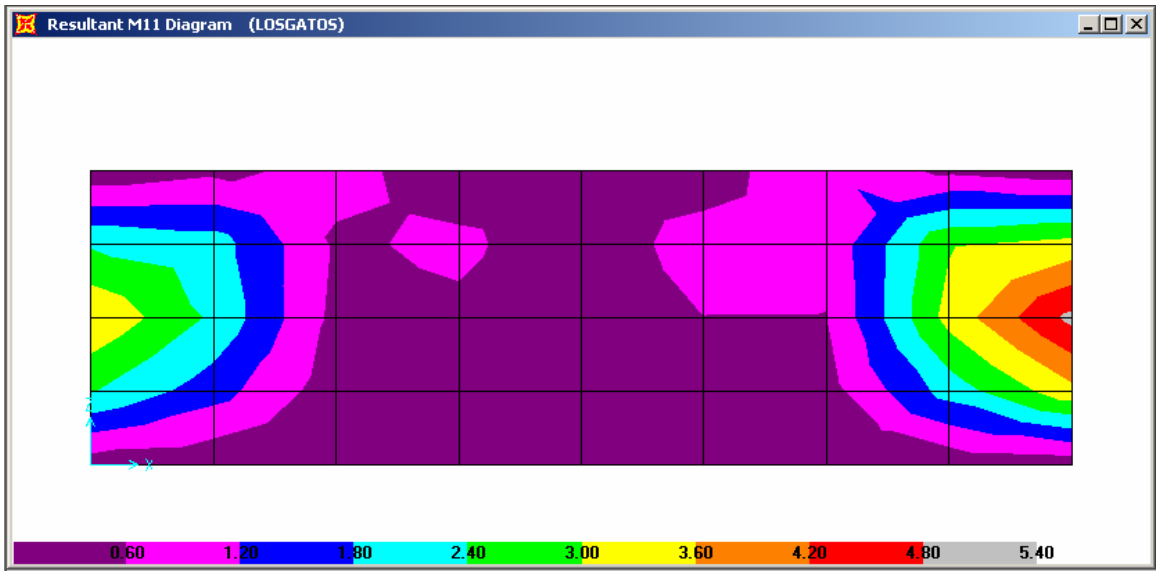

(a) Los Gatos, vertical out-of-plane moment contour, north wall

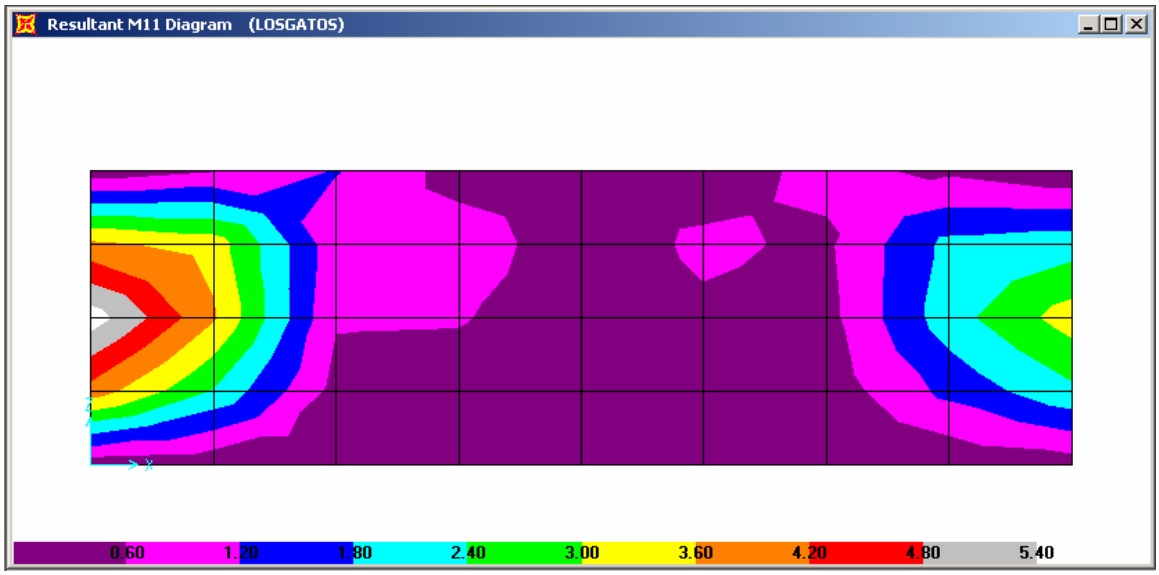

(b) Los Gatos, vertical out-of-plane moment contour, south wall

Fig. 7.63 Vertical out-of-plane moment, north and south walls, new connection, dense nailing, Los Gatos

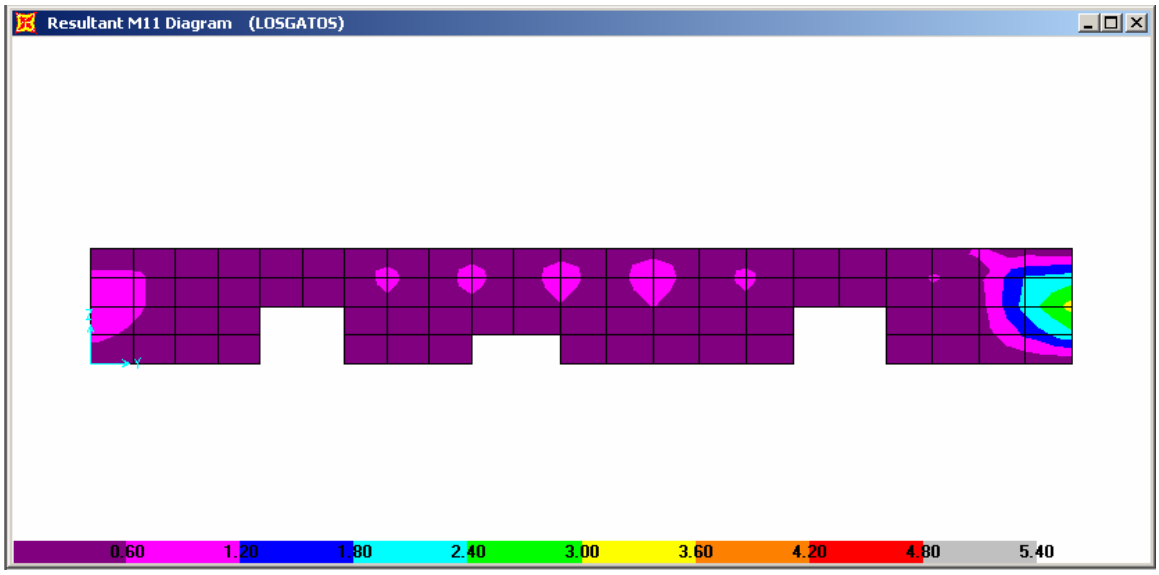

(a) Los Gatos, vertical out-of-plane moment contour, east wall

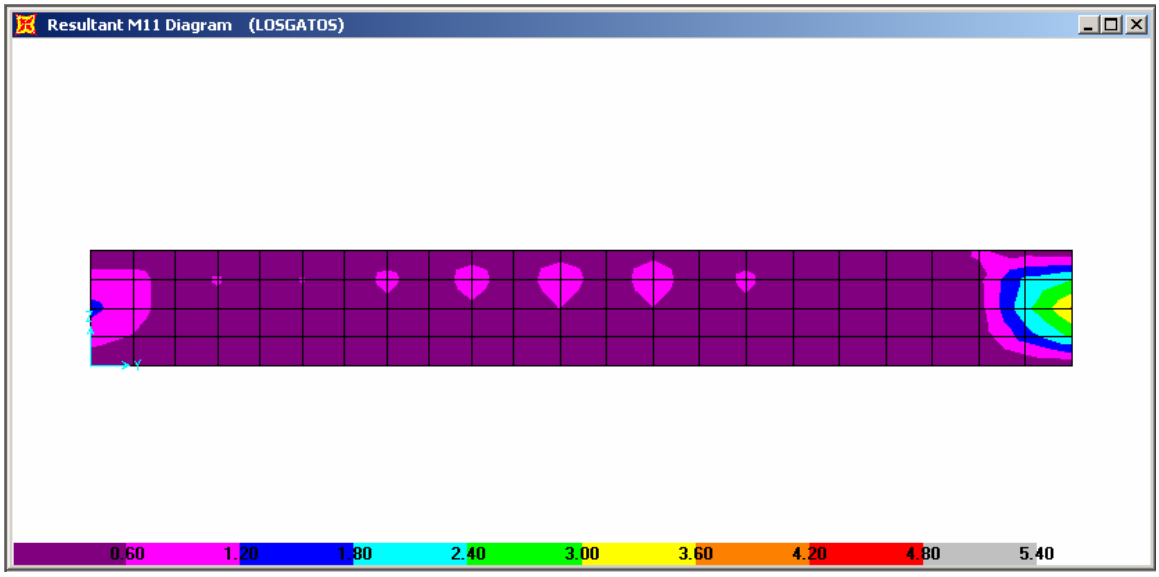

(b) Los Gatos, vertical out-of-plane moment contour, west wall

Fig. 7.64 Vertical out-of-plane moments, east and west walls, new connection, dense nailing, Los Gatos

7.5.4 Los Gatos, Sparse Nailing, Old Connections

All of the analytical models discussed up to this point considered plywood panels with dense nailing. The dense nailing gives a continuity to the panels that makes them more representative of the finite element model. With the use of the sparse nailing, some of the continuity between panels is lost, resulting in a reduction in the elastic stiffness. This effect is represented in a revised analytical model by a reduction in the modulus of elasticity of the Hrennikoff elements. The reduction is adjusted so that the results from the analytical model agree with the results from the test panels discussed earlier.

The responses of the revised nonlinear model having sparse nailing and old connections are presented in Figures 7.65–7.73 for the Los Gatos ground motion. The time history of the calculated base shear in the longitudinal (N-S) direction is shown in Figure 7.65a. In this direction the base shear reaches a maximum of 150 kips, which is less than the code design value of 240 kips, smaller than the 350 kips demanded by the old connections with dense nailing, and also less than the 220 kips demanded by the new connections with dense nailing. The reduction from the base shear demand (430 kips) obtained from the elastic analysis is substantial but may not be able to be developed due to the displacement demands. The time history of the base shear in the transverse (E-W) direction is shown in Figure 7.65b. In this direction, the maximum demand reaches 320 kips, which is above the code design value (240 kips) but is much lower than the result of the elastic dynamic analysis that indicated a maximum shear of 1,630 kips. It is also smaller than the 810 kips demanded by the old connections with dense nailing and the 530 kips demand of the new connections with dense nailing.

The maximum axial forces in the connections of the glulam beams and purlins to the pilasters are shown in Figure 7.66. The maximum axial force in the purlin to pilaster connections (Fig. 7.66b) reaches a value of only 4 kips, which is considerably less than the almost 22 kips obtained from the elastic analysis with dense nailing. The distribution of axial forces in the connection of the glulam beams to pilasters is shown in Figure 7.66c. In this case, the maximum value reaches just under 25 kips.

The distribution of vertical shear in the glulam and purlin connections is shown in Figure 7.67. The purlin to pilaster connections (Fig. 7.67b) indicate a maximum value of just over 10 kips, whereas the glulam beam to pilaster connections (Fig. 7.67c) indicate a maximum value of just under 7 kips. The maximum values of the horizontal connection force parallel to the walls

are shown in Figure 7.68 for the purlin and glulam beam. The maximum horizontal shear in the purlin connection has a value of 7 kips (Fig. 7.68b). For the glulam beam connections (Fig. 7.68c), the maximum value reaches 6.5 kip.

The hysteretic behavior of the glulam to pilaster connection near the middle of the longitudinal wall is shown in Figure 7.69. The axial force (Fig. 7.69a) indicates that the combination of sparse nailing and old connection places a displacement demand of 1.7 inches on the old connection and a corresponding displacement ductility of approximately 5.7. It is doubtful that the connection can develop this amount of ductility. The vertical shear force at the connection (Fig. 7.69b) indicates that the behavior of this component is only weakly nonlinear, with a displacement demand of 0.086 inches. The behavior of the horizontal shear (Fig. 7.69c) is constrained to be linearly elastic and indicates a displacement demand of 0.05 inches. A plot showing the behavior of a similar glulam beam connection near the corner of the longitudinal wall is shown in Figure 7.70. For the axial component Figure 7.70a indicates that the inelastic behavior is much less at this location. The displacement demand is a more manageable 0.46 inches and a displacement ductility of approximately 1.5. It can be seen in Figure 7.70b that the vertical shear component is only weakly nonlinear with a displacement demand of 0.11 inches. The horizontal shear (Fig. 7.70c) that is constrained to be linear elastic has a displacement demand of 0.20 inches.

The hysteretic behavior of the purlin to pilaster connection located near the middle of the transverse wall is shown in Figure 7.71. The axial force (Fig. 7.71a**)** exhibits a strongly nonlinear behavior with a displacement demand of 0.92 inches and a ductility demand of approximately 9. An even stronger nonlinear response is shown for the vertical shear force component in the connection (Fig. 7.71b). A displacement demand of 2.6 inches is required in this direction along with a displacement ductility demand of 18.6. The horizontal shear (Fig. 7.71c**)** is constrained to be linear elastic but has a displacement demand of .24 inches. The hysteretic behavior of a purlin to pilaster connection near the corner of the transverse wall is shown in Figure 7.72. The hysteretic behavior of the axial force component (Fig. 7.72a) indicates inelastic behavior similar to that at the middle of the transverse wall with the axial displacement reaching 0.85 inches. The displacement ductility demand is approximately 8.5. For the vertical shear force component, the displacement demand reaches 6.5 inches (Fig. 7.72b), and the displacement ductility demand reaches the extreme value of 48. The horizontal shear force, constrained to remain linear elastic, has a displacement demand of 0.13 inches (Fig. 7.72c).

The combination of old connections and sparse nailing places severe inelastic response demands on the roof diaphragm under the Los Gatos ground motion. The hysteretic behavior in the panels of the roof diaphragm as represented by the axial forces in the diagonal components of the Hrennikoff elements near the transverse wall is shown in Figure 7.73. The three components are located at the end of the longitudinal wall, adjacent to the transverse wall. The hysteretic behavior of the component nearest the longitudinal wall is shown in Figure 7.73a. At this location, the maximum displacement demand is 0.55 inches and the estimated displacement ductility demand is 28.9. The hysteretic behavior at the middle location (Fig. 7.73b) indicates a displacement demand of 0.70 inches and a ductility demand of 36.8. At the location near the center of the transverse span (Fig. 7.73c), the displacement demand is only 0.18 inches and the ductility demand is 9.6.

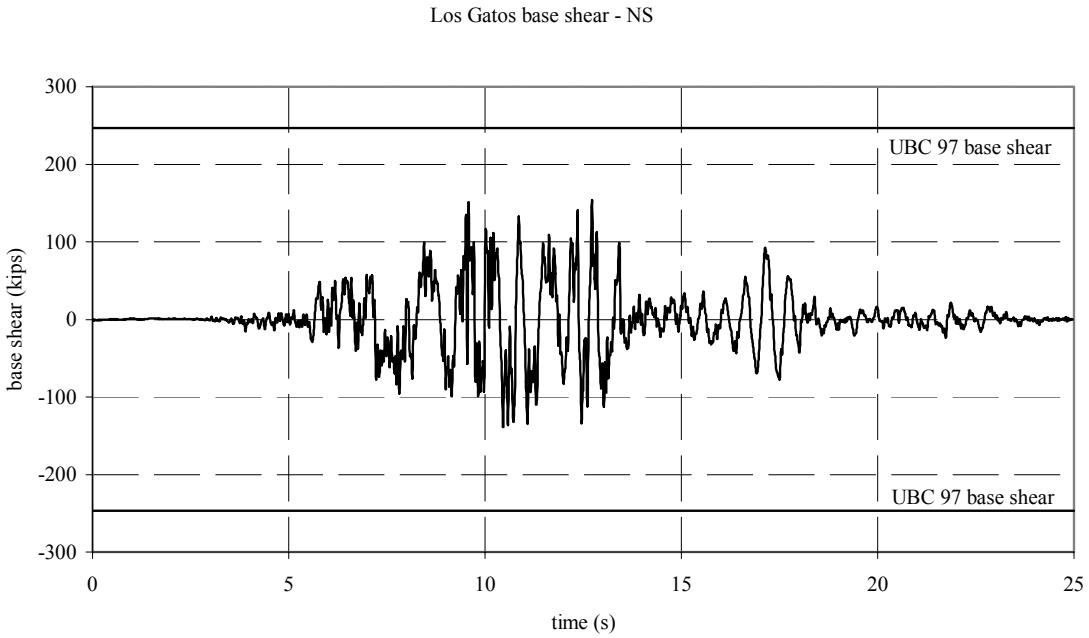

(a)

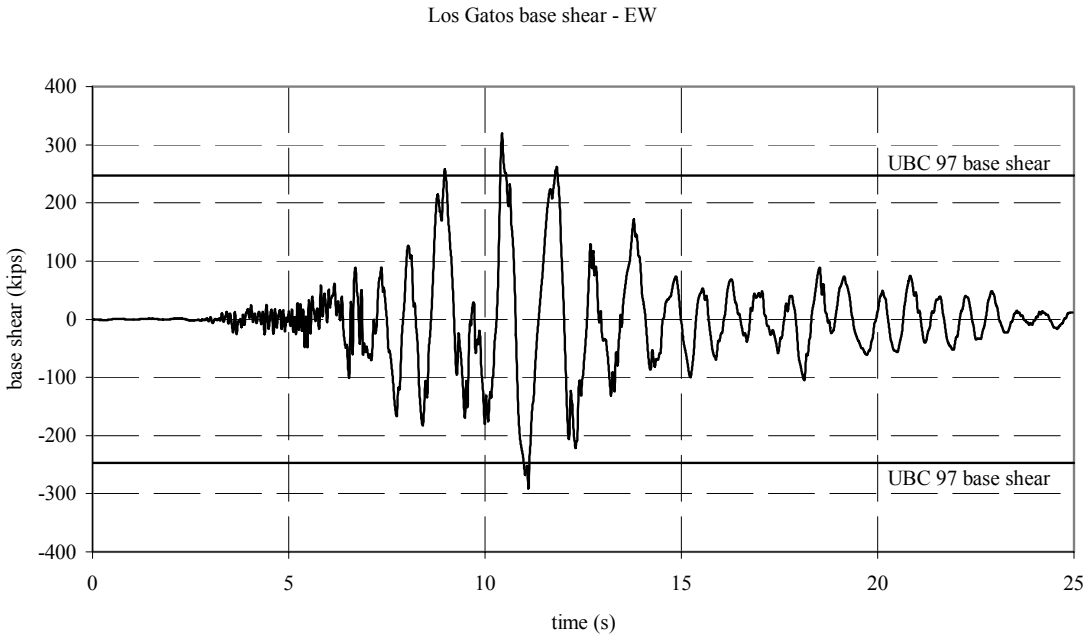

(b)

Fig. 7.65 Base shear, nonlinear old connections, sparse nailing, Los Gatos

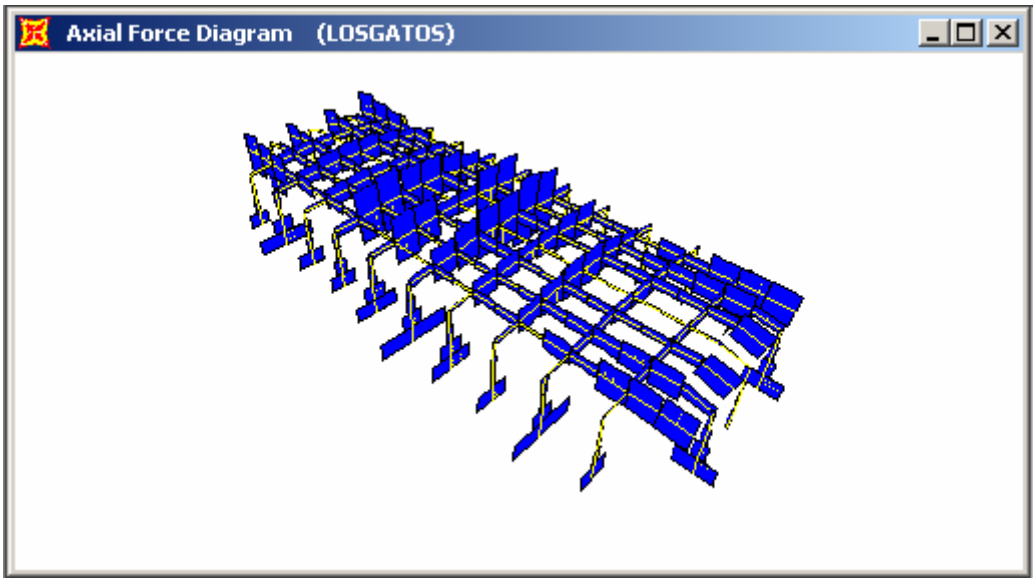

(a)

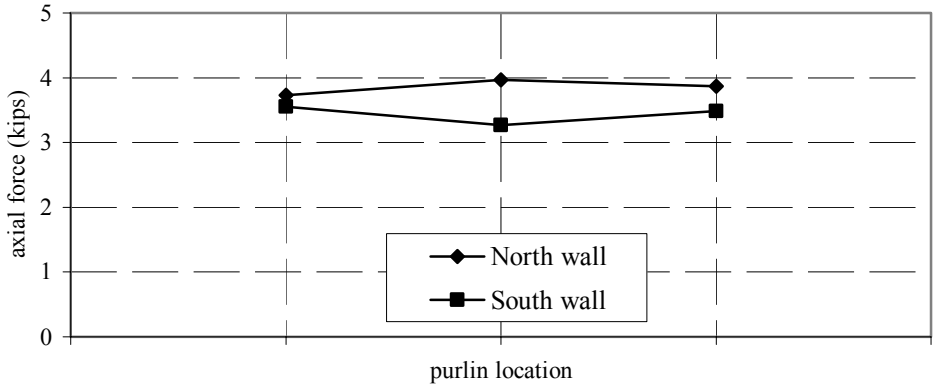

(b)

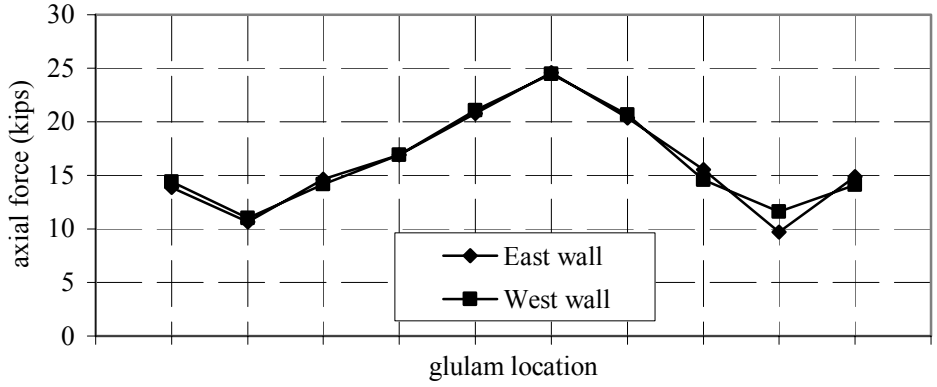

(c)

Fig. 7.66 Axial force, nonlinear old connections, sparse nailing, Los Gatos

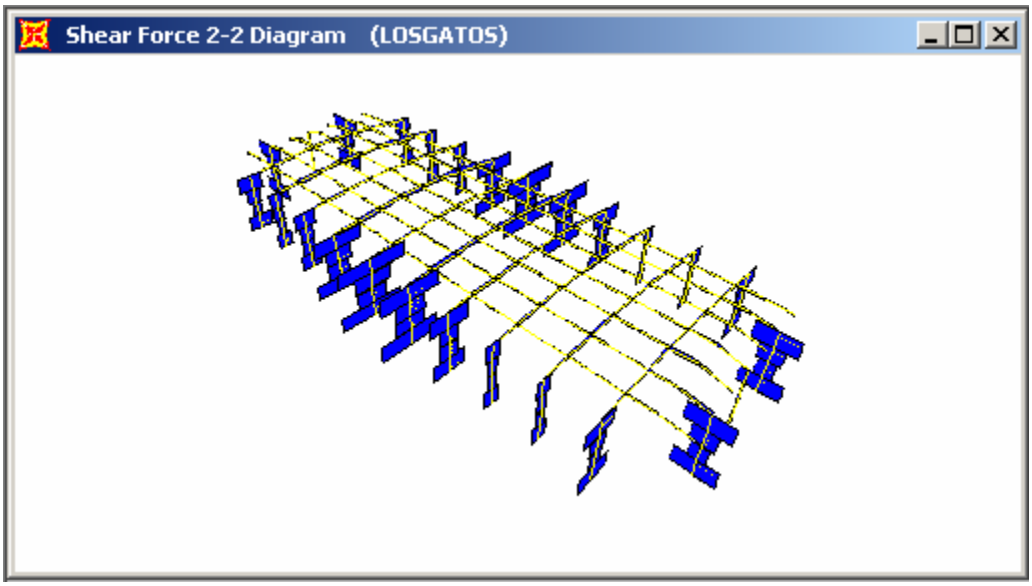

(a)

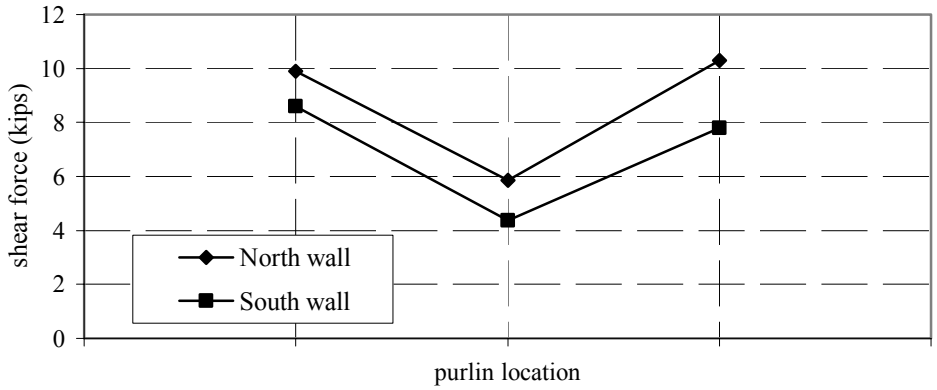

(b)

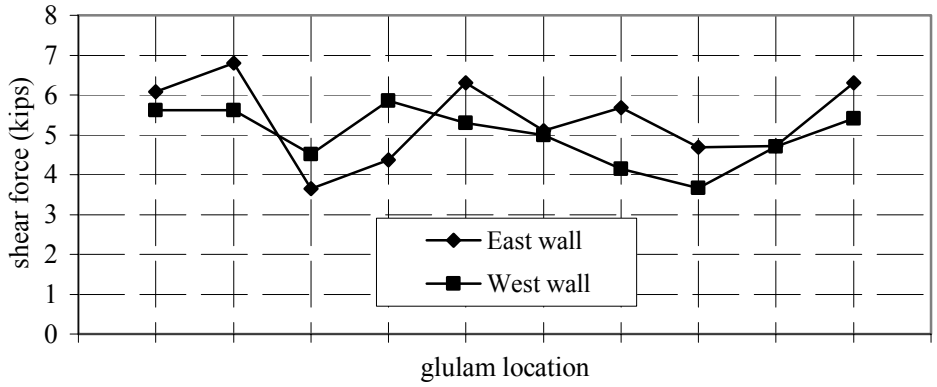

(c)

Fig. 7.67 Vertical shear force, nonlinear old connections, sparse nailing, Los Gatos

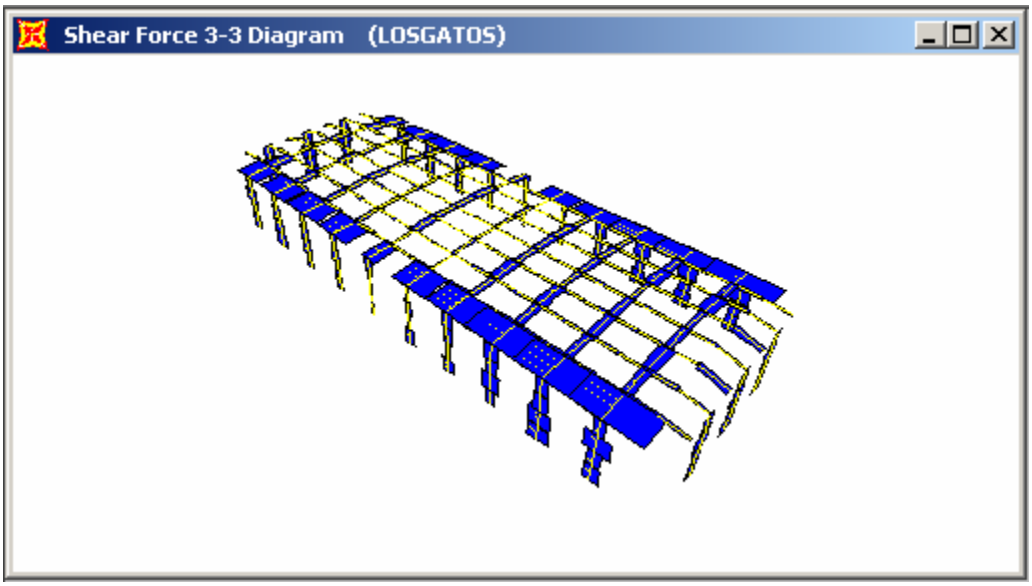

(a)

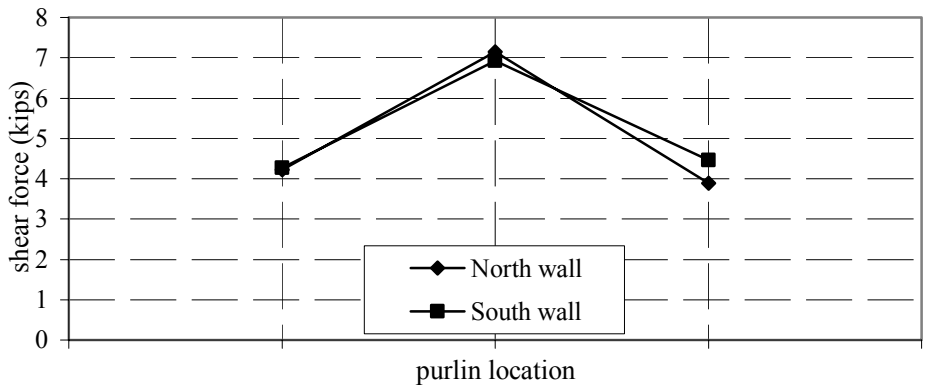

(b)

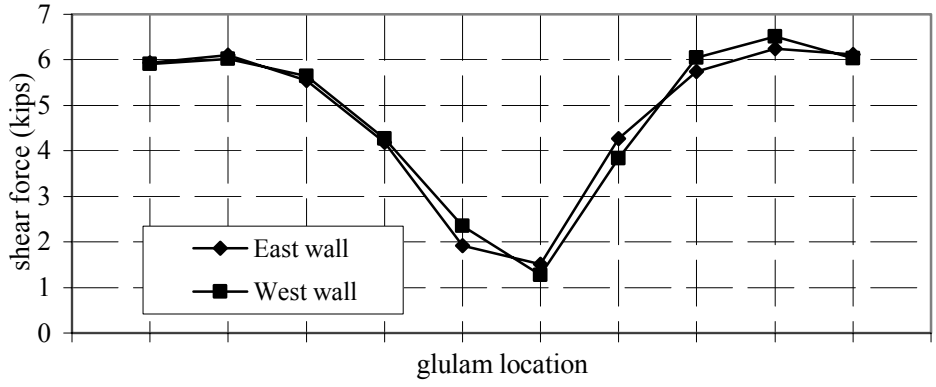

(c)

Fig. 7.68 Horizontal shear, nonlinear old connections, sparse nailing, Los Gatos

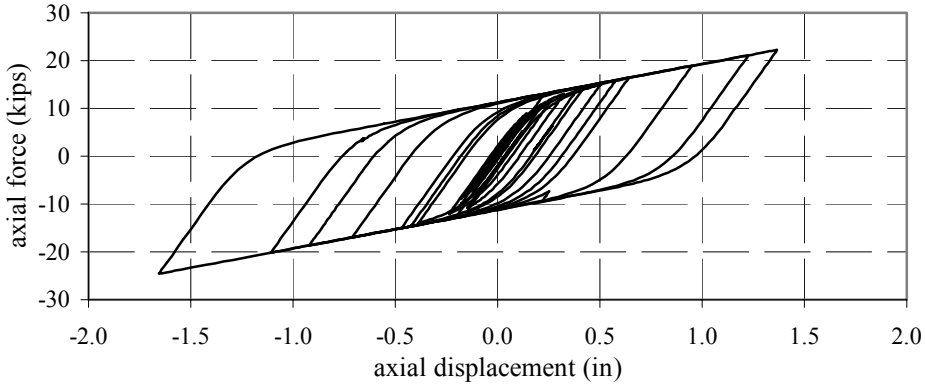

(a)

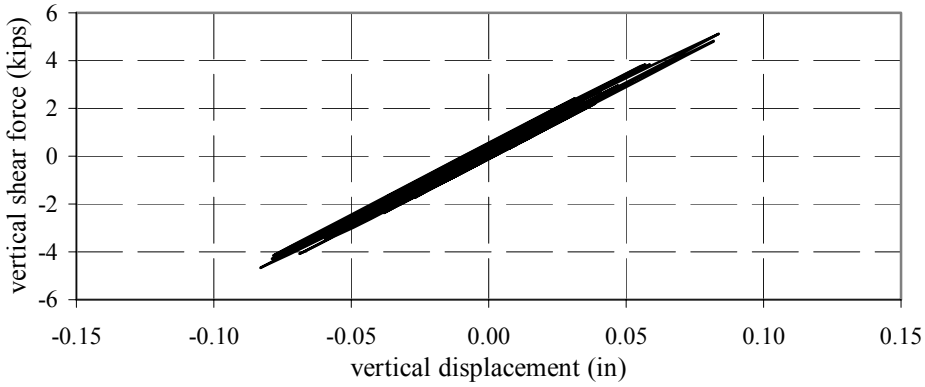

(b)

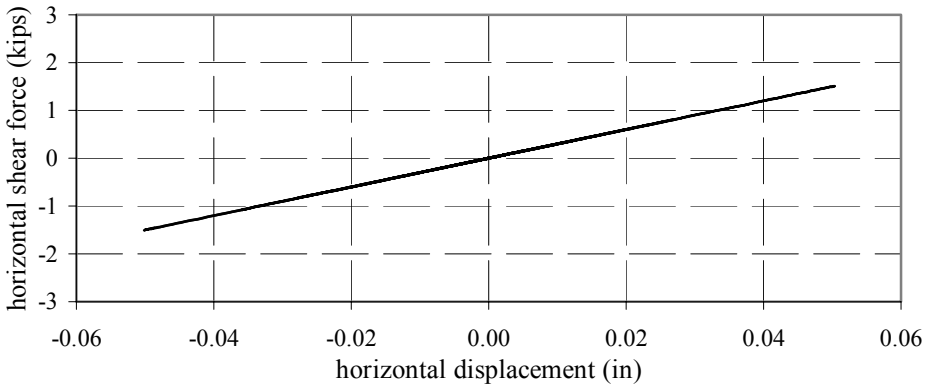

(c)

Fig. 7.69 Hysteretic behavior, glulam to pilaster, old connection, sparse nailing, middle of wall, Los Gatos

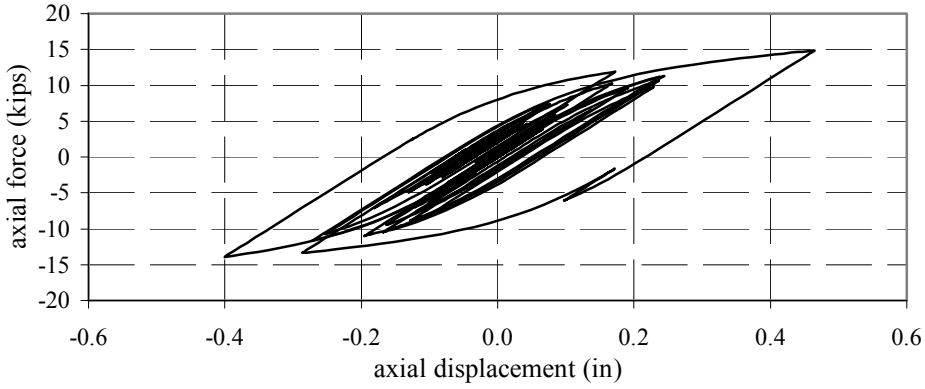

(a)

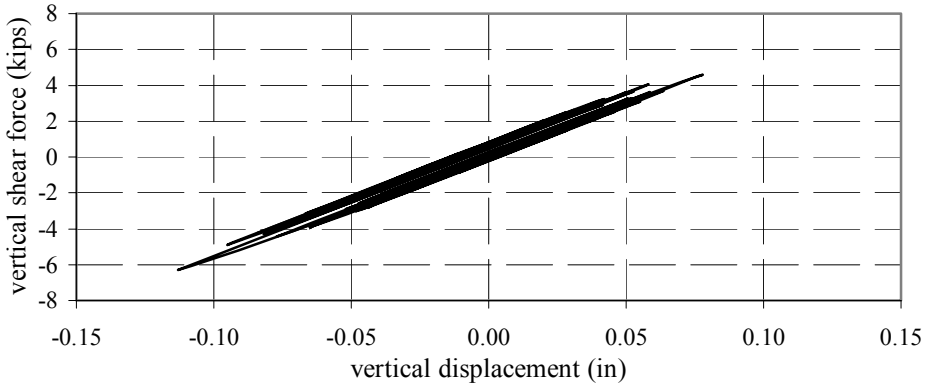

(b)

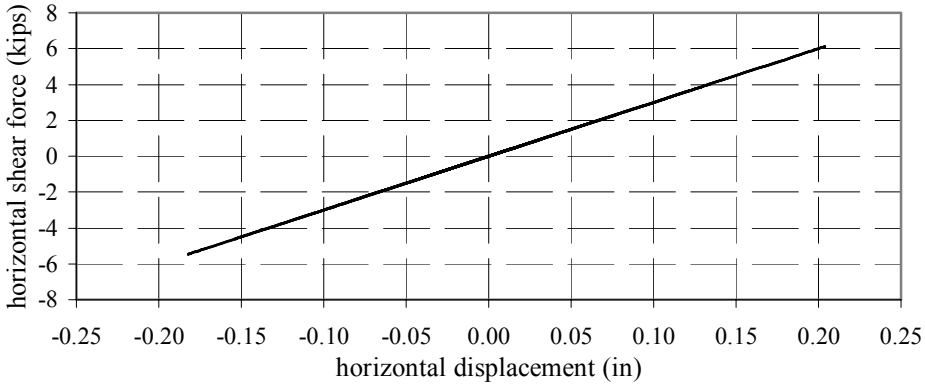

(c)

Fig. 7.70 Hysteretic behavior, glulam to pilaster, old connections, sparse nailing, near corner, Los Gatos

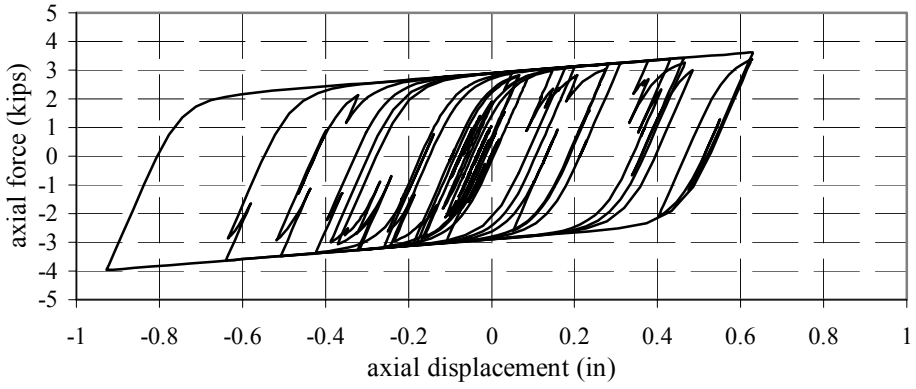

(a)

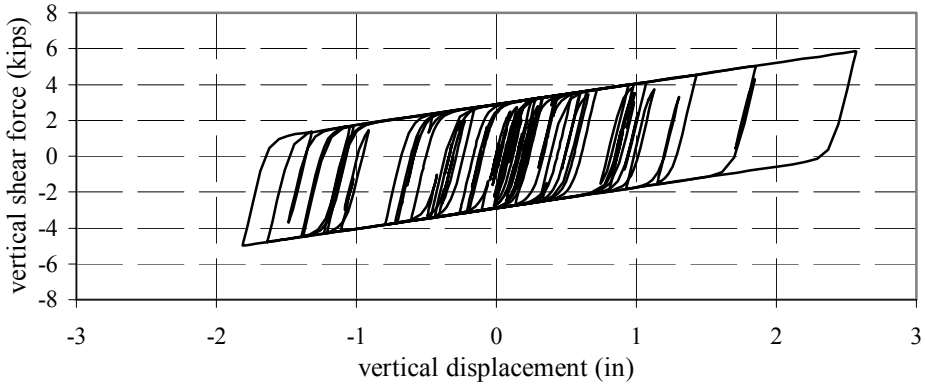

(b)

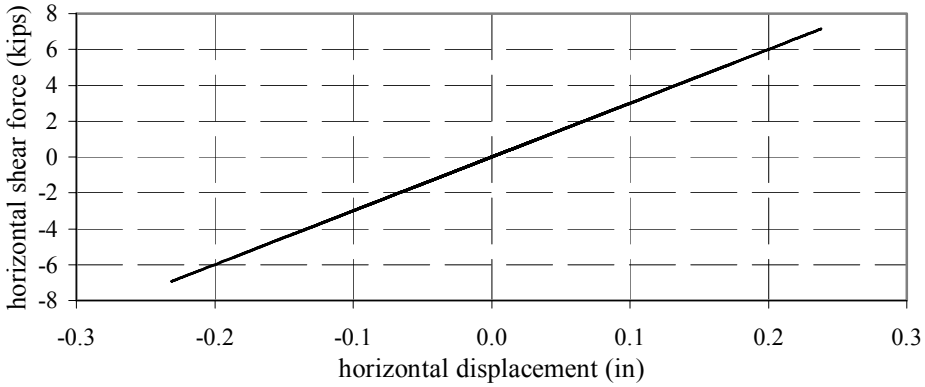

(c)

Fig. 7.71 Hysteretic behavior, purlin to pilaster, old connection, sparse nailing, middle of wall, Los Gatos

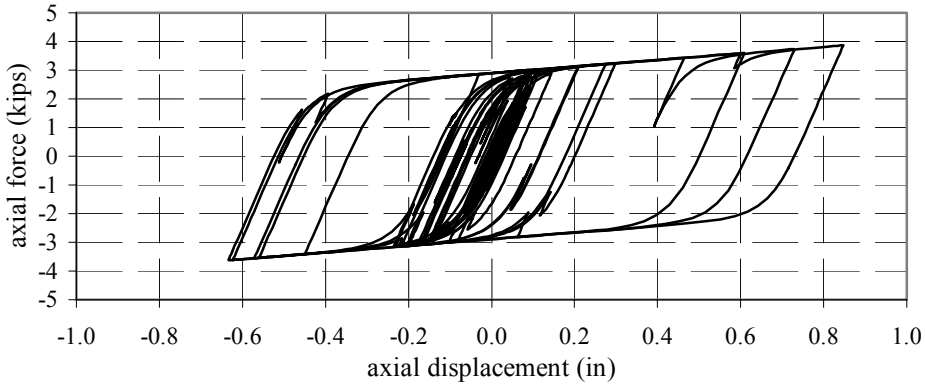

(a)

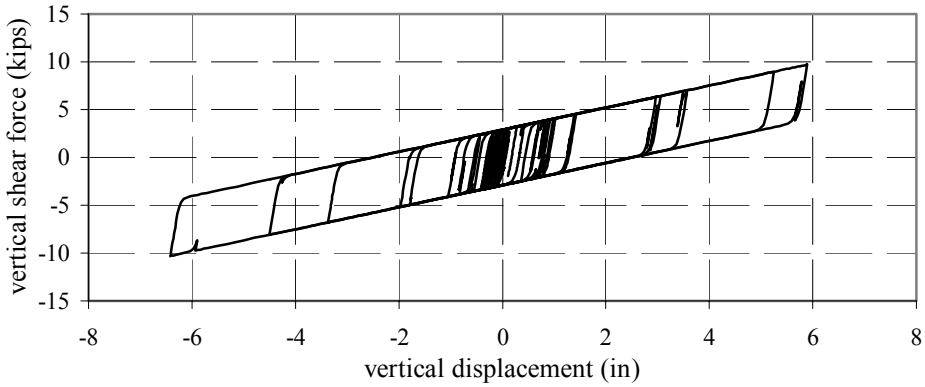

(b)

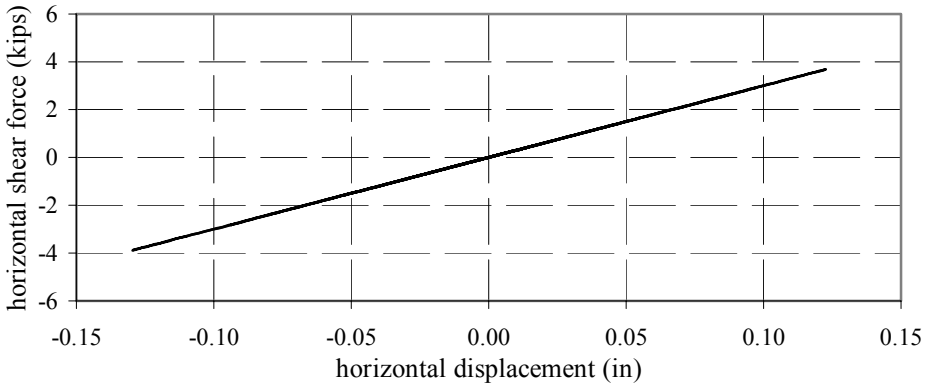

(c)

Fig. 7.72 Hysteretic behavior, purlin to pilaster, old connection,sparse nailing, near corner, Los Gatos

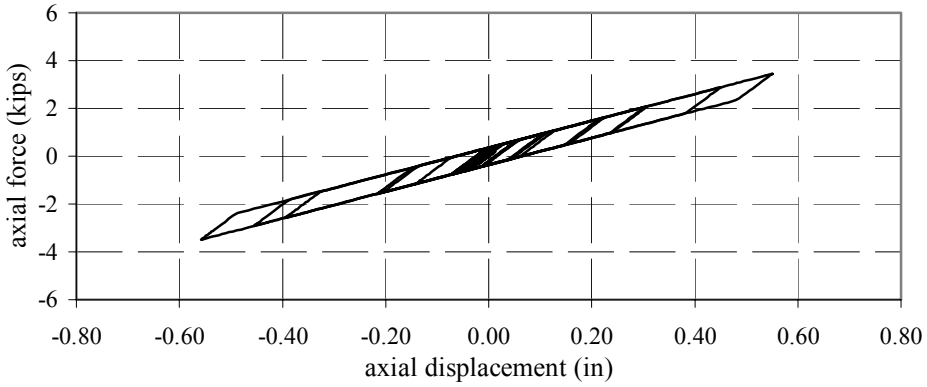

(a) element location

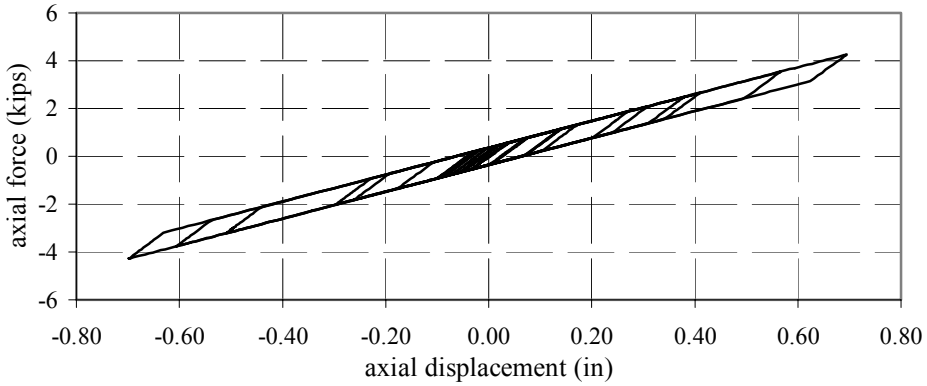

(b) element location

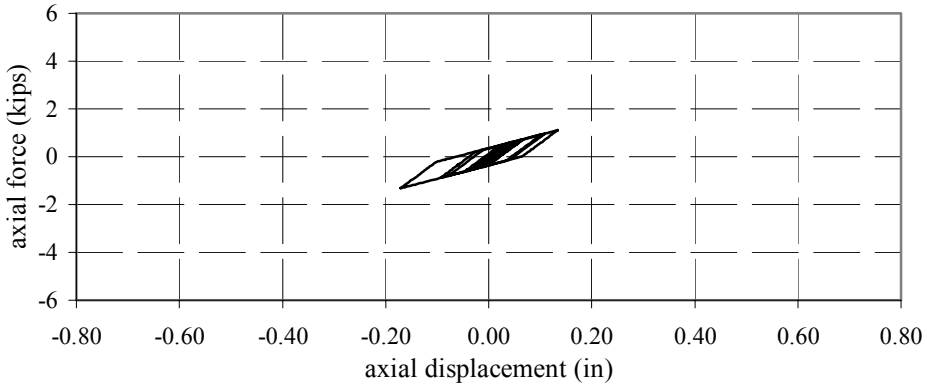

(c) element location

Fig. 7.73 Hysteretic behavior, roof diaphragm, old connections, sparse nailing, Los Gatos

7.5.5 Los Gatos, Sparse Nailing, New Connections

The responses of the revised nonlinear model having sparse nailing combined with the new connection details are presented in Figures 7.74–7.82 for the Los Gatos ground motion. The time history of the calculated base shear in the longitudinal (N-S) direction is shown in Figure 7.74a. In this direction the base shear is well below the code design value of 240 kips, reaching a maximum value of 150 kips, which is equal to the value obtained with the sparse nailing and old connections. The time history of the base shear in the transverse (E-W) direction is shown in Figure 7.74b. In this direction, the maximum base shear reaches 460 kips. This value is well above the code design value (240 kips) but is much lower than the result of the elastic dynamic analysis that indicated a maximum shear of 1,630 kips. However, it is 44% higher than the base shear demand using the old connections with sparse nailing.

The maximum axial forces in the connections of the glulam beams and purlins to the pilasters are shown in Figure 7.75. The maximum axial force in the purlins (Fig. 7.75b) reaches a value of 21 kips, which is approximately equal to the value of 22 kips obtained from the elastic analysis with dense nailing. The distribution of axial forces in the glulam beams is shown in Figure 7.75c. In this case, the maximum value of 35 kips is 11 kips less than the maximum value obtained from the elastic analysis with dense nailing and 28 kips more than the 7 kips demanded by the old connections with sparse nailing.

The distribution of vertical shear in the glulam beam and purlin connections is shown in Figure 7.76. The purlin connections (Fig. 7.76b) indicate a maximum value of 26 kips and the glulam connections (Fig. 7.76c) indicate a maximum value of 6.6 kips. The maximum values of the horizontal shear force parallel to the wall are shown in Figure 7.77 for the purlins and glulam beams. The maximum horizontal shear in the purlin connection has a value of 7 kips as shown in Figure 7.77b. For the glulam beam connections (Fig. 7.77c), the horizontal shear has a maximum value of 6.4 kips.

The hysteretic behavior of the glulam beam to pilaster connection near the middle of the longitudinal wall is shown in Figure 7.78. It can also be seen that the displacement demand for the connection is 1.9 inches with a corresponding displacement ductility demand of 2.4. The other two shear force components in the connection are in the elastic range (Figs. 7.78b–c). A plot showing the behavior of a similar glulam beam connection near the corner of the longitudinal wall is shown in Figure 7.79. For the axial component (Fig. 7.79a), a very weakly

nonlinear behavior is indicated with a displacement ductility demand of 1.6. As mentioned previously for the midwall connection, the other two shear force components are in the elastic range, as shown in Figure 7.79b for the vertical shear and Figure 7.79c for the horizontal shear.

The hysteretic behavior of the purlin to pilaster connection located near the middle of the transverse wall is shown in Figure 7.80. The axial force (Fig. 7.80a) exhibits a weakly nonlinear behavior with a displacement demand of 0.06 inches and a displacement ductility demand of approximately 1.25. A similar type of nonlinear response is shown for the vertical shear force component in Figure 7.80b. For this component a displacement demand of 0.13 inches is required and a displacement ductility of 1.6. The horizontal shear (Fig. 7.80c) is constrained to be linear elastic due to lack of applicable data on its inelastic behavior. The hysteretic behavior of a purlin to pilaster connection near the corner of the transverse wall is shown in Figure 7.81. The hysteretic behavior of the axial force component (Fig. 7.81a) indicates a more inelastic behavior than at the middle of the transverse wall, with the axial displacement reaching 0.54 inches and a displacement ductility demand of 3.8. For the vertical shear force component, the displacement demand is 3.1 inches (Fig. 7.81b) with a displacement ductility demand of 13. The horizontal shear force is constrained to remain linear elastic (Fig. 7.81c). However, it can also be seen that the force levels for this component are very low (0.2 kips).

The combination of old connections and dense nailing also places severe inelastic response demands on the roof diaphragm under the Los Gatos ground motion. The hysteretic behavior in the panels of the roof diaphragm as represented by the axial forces in the diagonal components of the Hrennikoff elements near the transverse wall is shown in Figure 7.82. The three components are located at the end of the longitudinal wall, adjacent to the transverse wall. The hysteretic behavior of the component nearest the longitudinal wall is shown in Figure 7.82a. At this location, the maximum displacement demand is 0.47 inches and the estimated displacement ductility demand is 9.4. The hysteretic behavior at the middle location (Fig. 7.82b) indicates a displacement demand of 0.60 inches and a ductility demand of 13.2. At the location near the center of the transverse span (Fig. 7.82c) the displacement demand is only 0.20 inches and the ductility demand is 4.0. The advantage of the dense nailing can be seen in the reduced displacement and ductility demands for this ground motion.

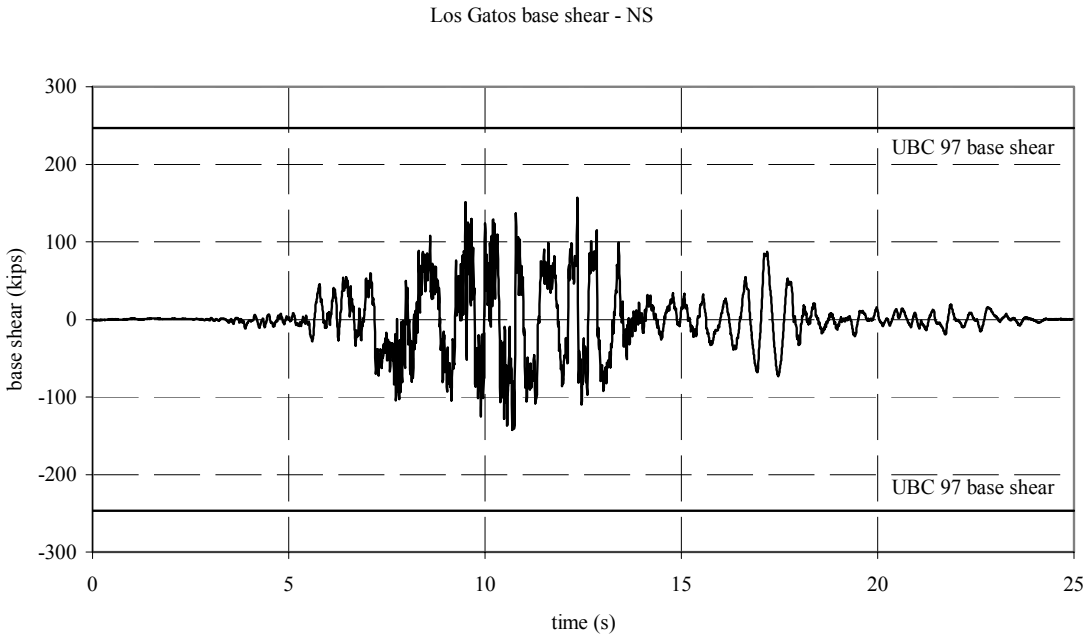

(a)

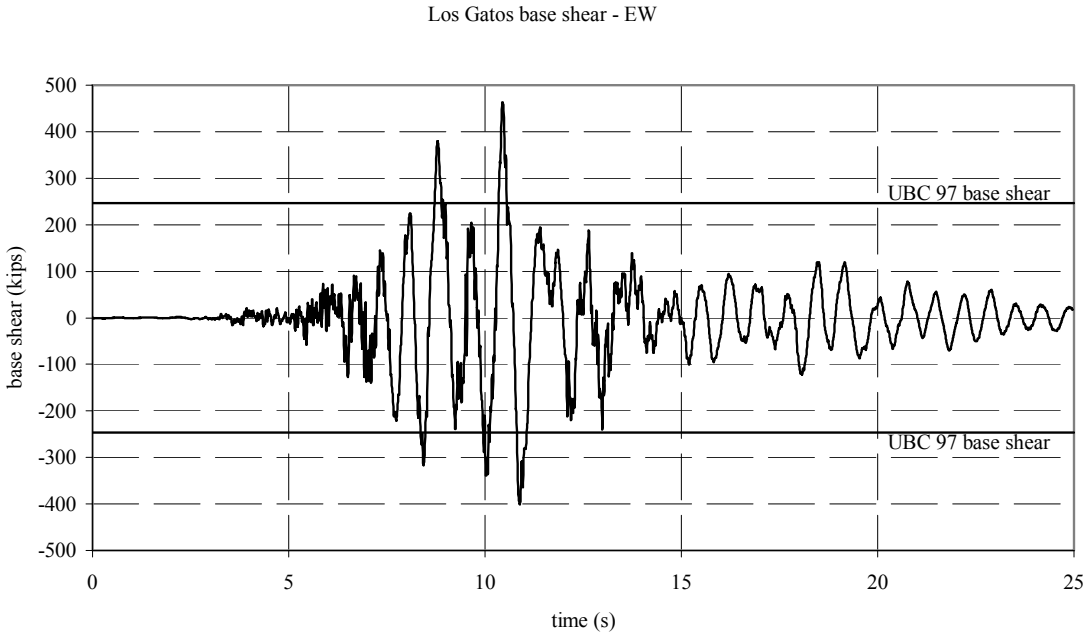

(b)

Fig. 7.74 Base shear, nonlinear new connections, sparse nailing, Los Gatos

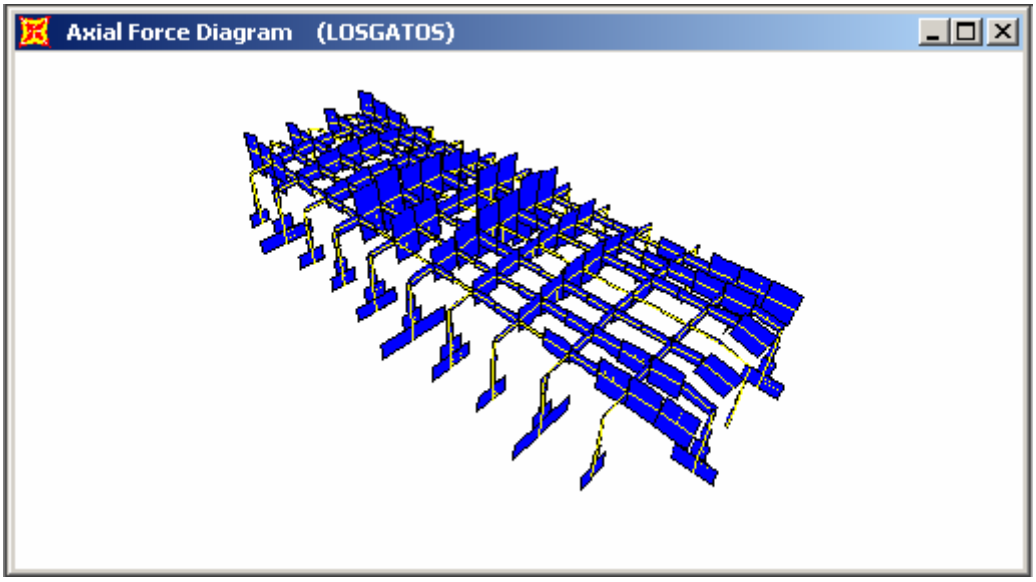

(a)

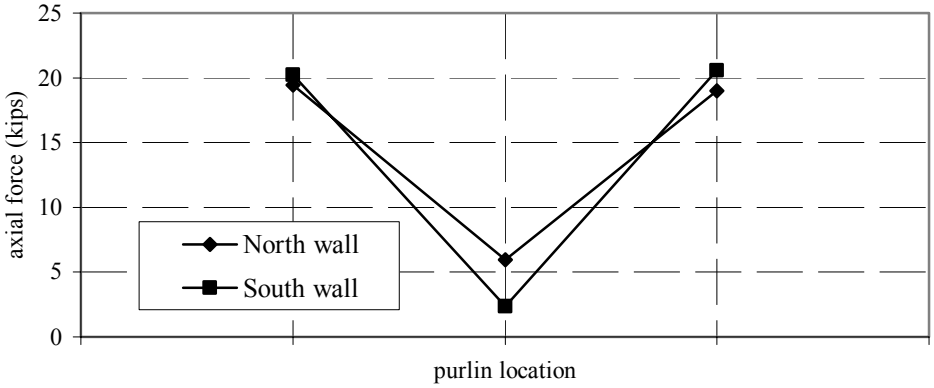

(b)

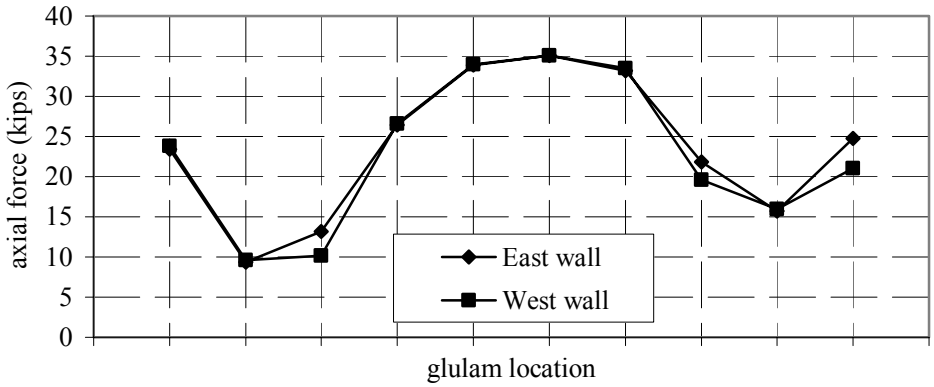

(c)

Fig. 7.75 Axial force, nonlinear new connections, sparse nailing, Los Gatos

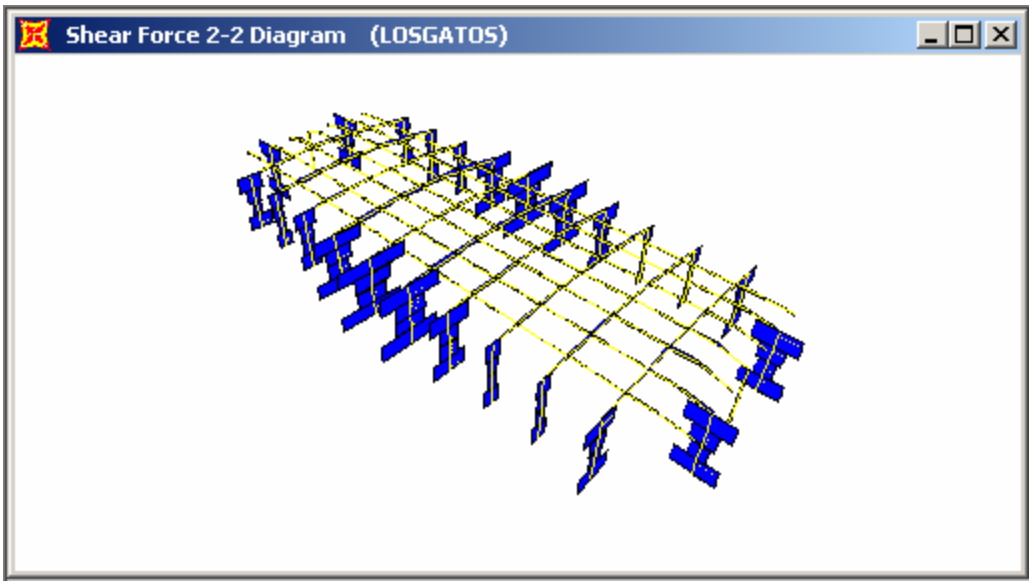

(a)

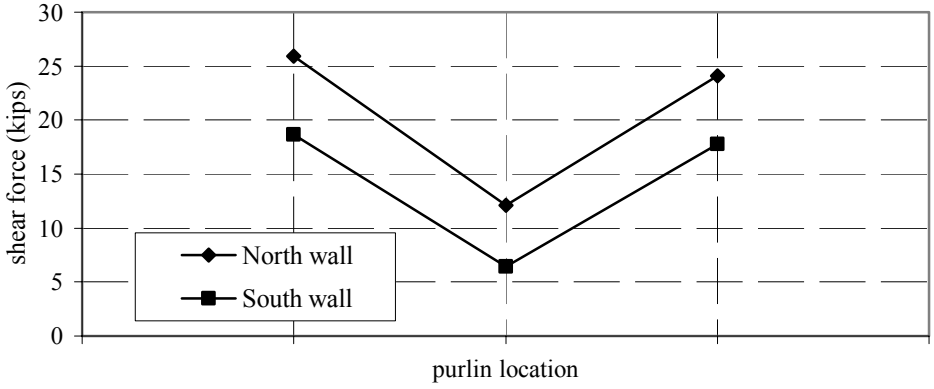

(b)

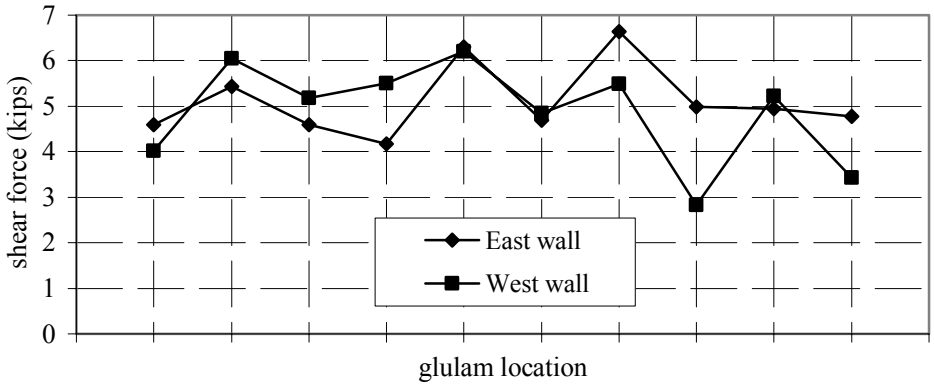

(c)

Fig. 7.76 Vertical shear force, nonlinear new connections, sparse nailing, Los Gatos

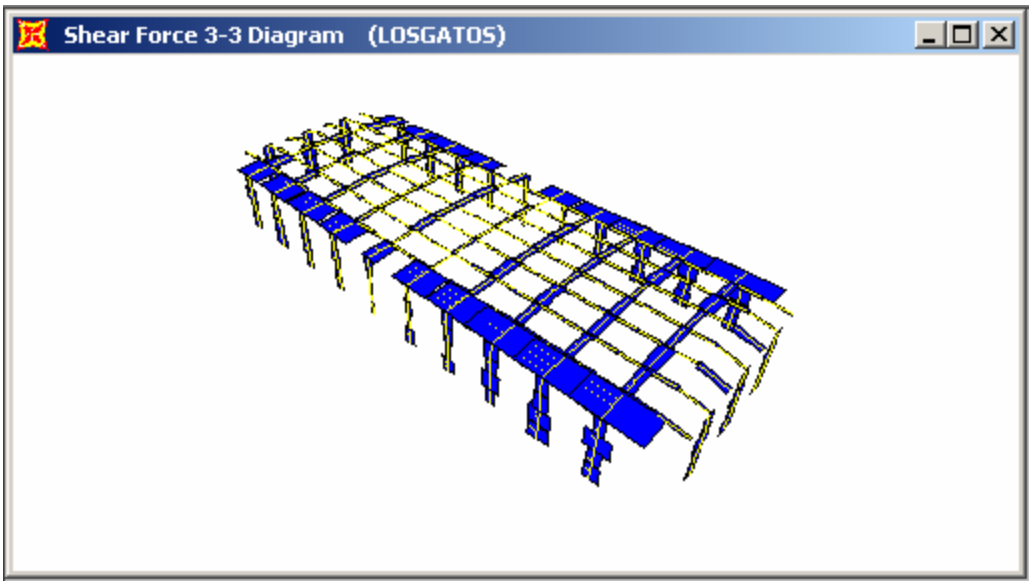

(a)

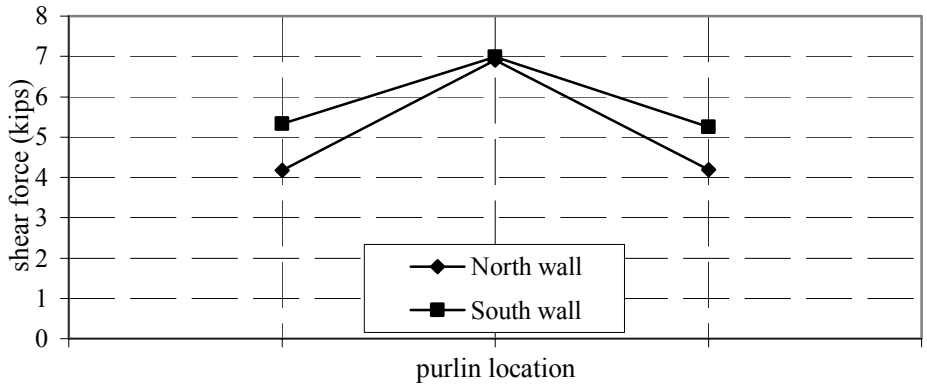

(b)

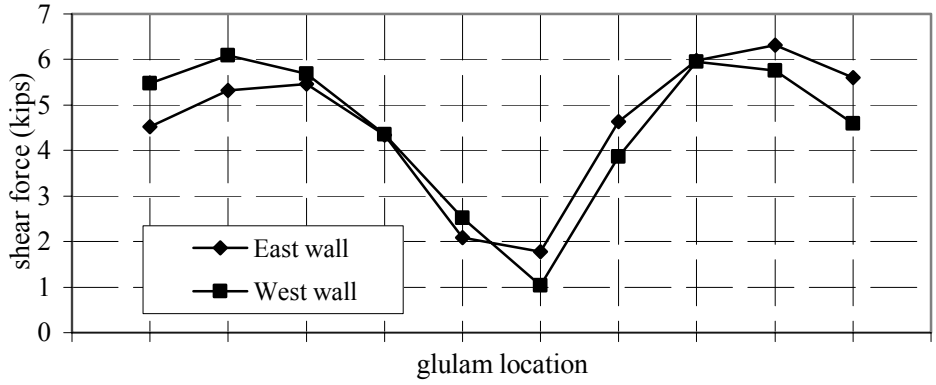

(c)

Fig. 7.77 Horizontal shear force, nonlinear new connections, sparse nailing, Los Gatos

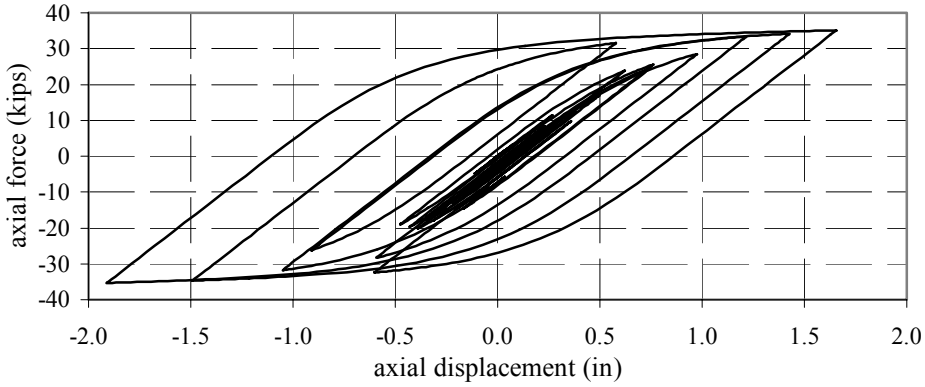

(a)

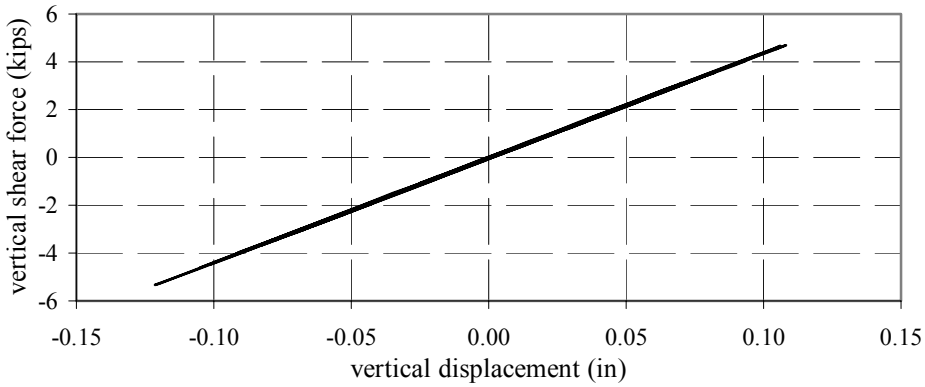

(b)

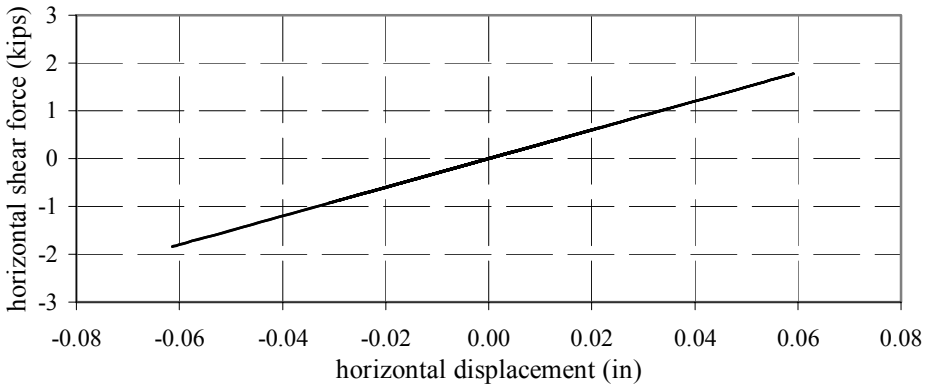

(c)

Fig. 7.78 Hysteretic behavior, glulam to pilaster, new connection, sparse nailing, middle of wall, Los Gatos

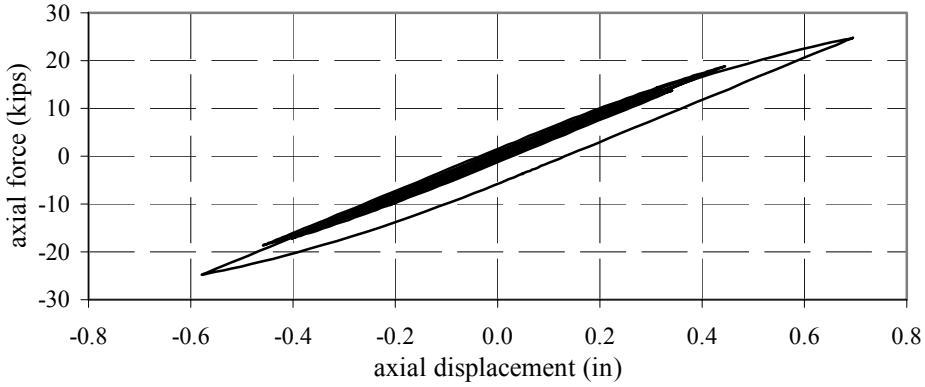

(a)

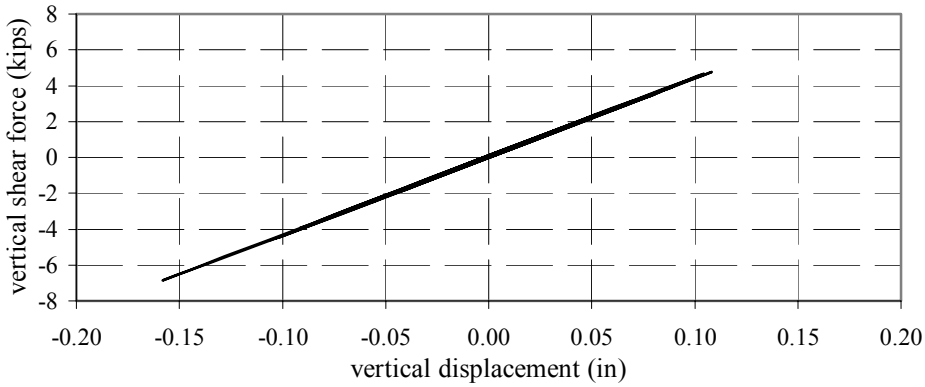

(b)

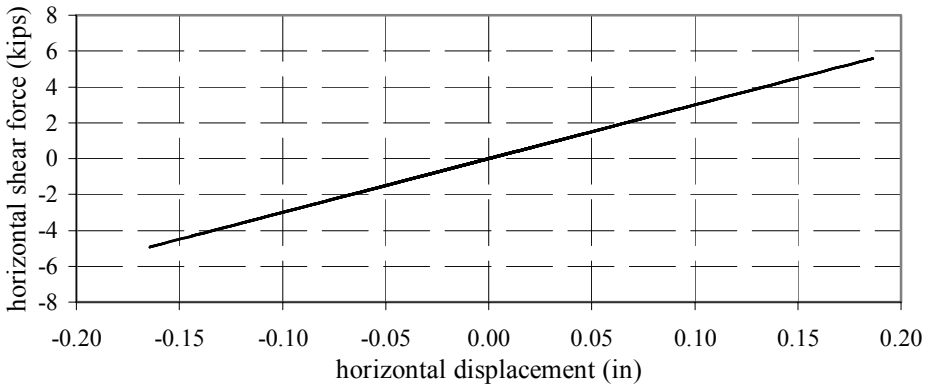

(c)

Fig. 7.79 Hysteretic behavior, glulam to pilaster, new connection, sparse nailing, near corner, Los Gatos

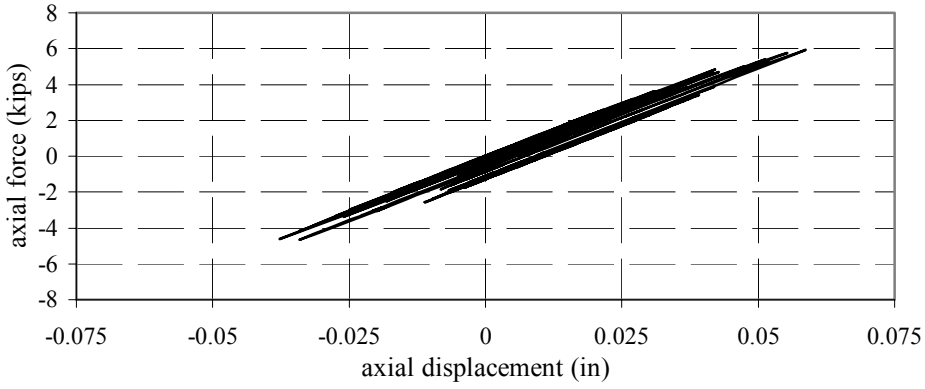

(a)

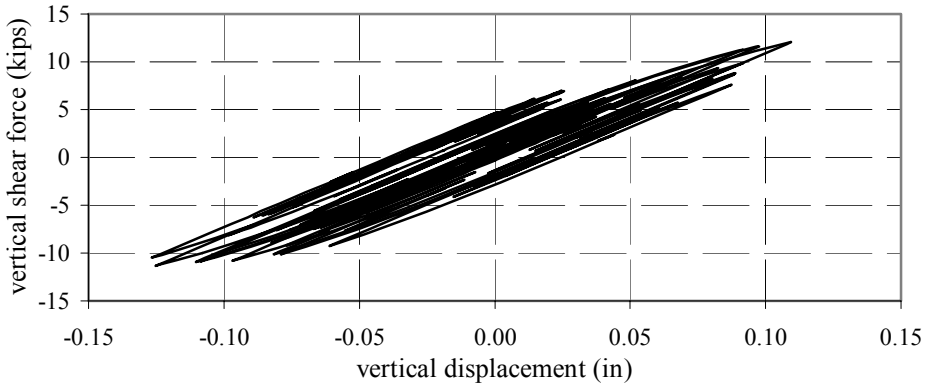

(b)

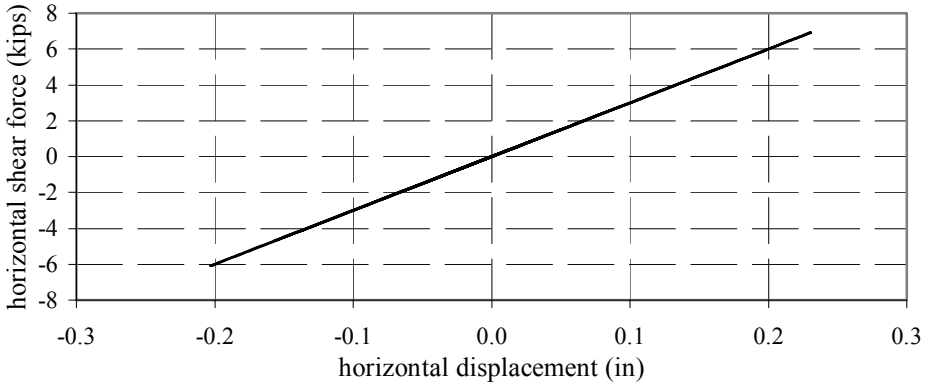

(c)

Fig. 7.80 Hysteretic behavior, purlin to pilaster, new connection, sparse nailing, middle of wall, Los Gatos

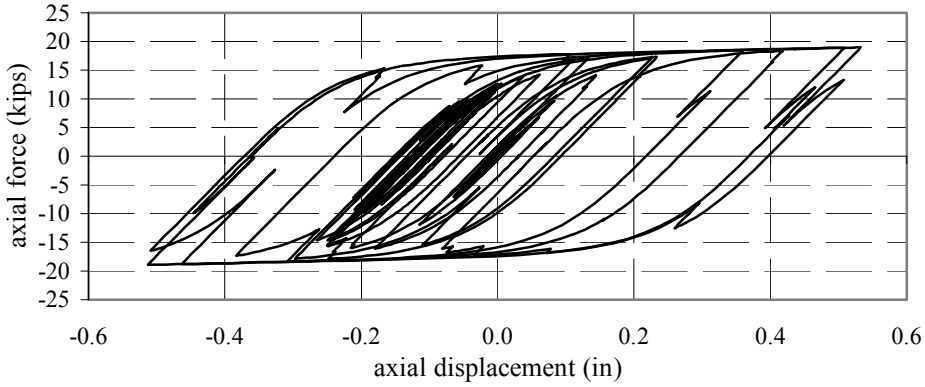

(a)

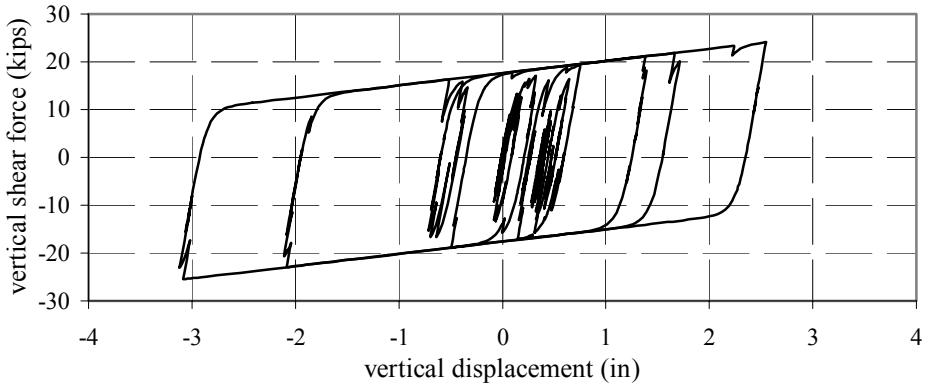

(b)

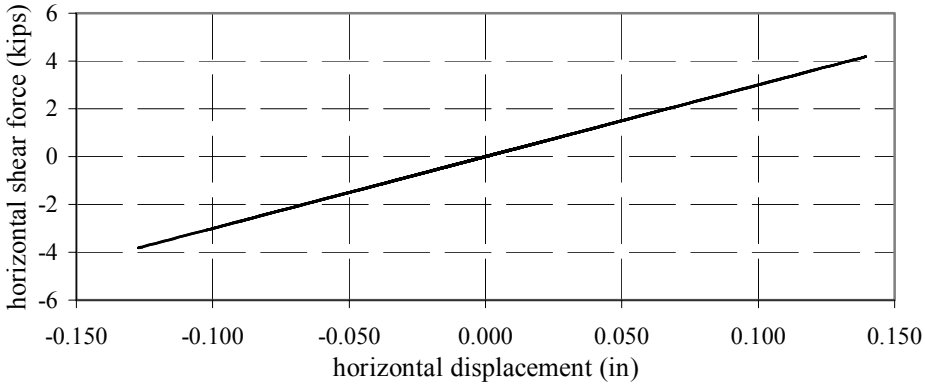

(c)

Fig. 7.81 Hysteretic behavior, purlin to pilaster, new connection, sparse nailing, near corner, Los Gatos

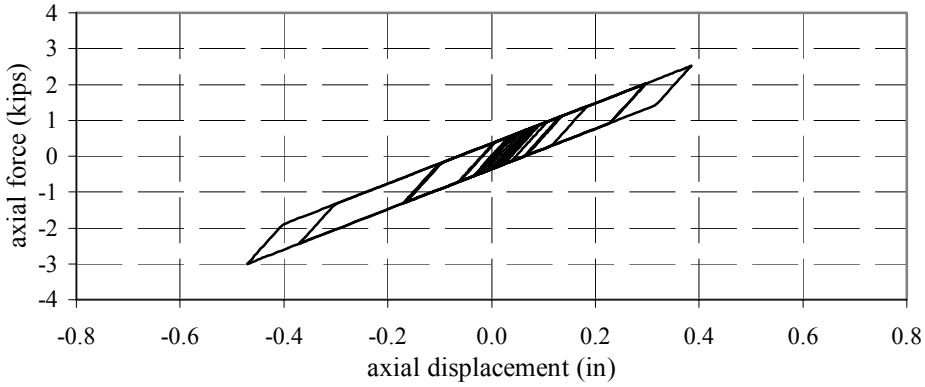

(a) element location

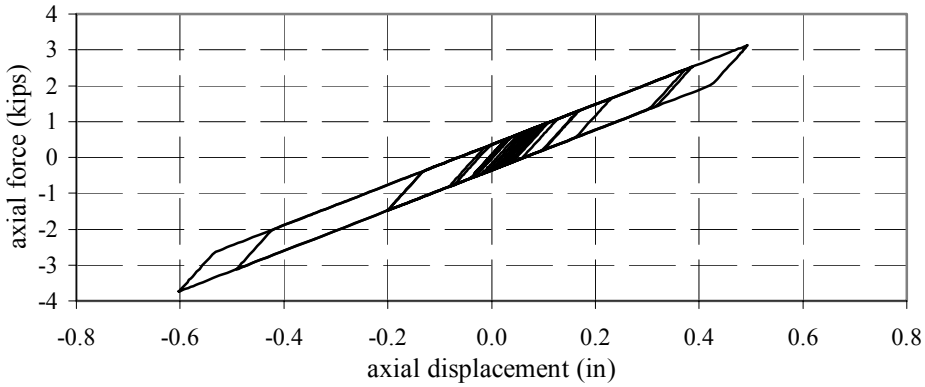

(b) element location

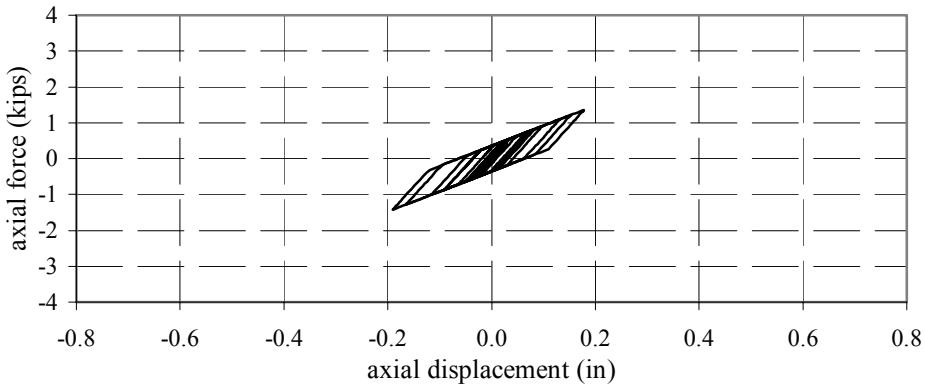

(c) element location

Fig. 7.82 Hysteretic behavior (Hrennikoff elements), roof diaphragm, new connections, sparse nailing, Los Gatos

8 Vertical Ground Motions

Long-span roofs, such as the one on the building considered in this study (90 ft), may experience an increased response when subjected to strong vertical ground motions. As shown in Table 6.1, the mode shape with the longest period (0.72 sec) is the primary vertical mode of vibration. This compares with a period of 0.39 seconds for the first significant horizontal mode in the transverse direction. In order to investigate the effect of vertical ground motions, dynamic analyses were conducted using the elastic building model subjected to three simultaneous ground motion components. The results are presented in terms of the reactive force components at the connections of the roof beams, glulams and purlins, to the pilasters. Also shown in these figures are the similar force components under the action of only the two horizontal earthquake acceleration components shown previously.

Three recorded ground motions were considered in this phase of the investigation. The initial ground motion was recorded at the base of the building during the Big Bear earthquake. Referring to Table 3.1, it can be seen that this earthquake produced the highest vertical acceleration at the site, although it was only 0.062g. The acceleration time history for this component is shown in Figure 8.1a. The second ground motion, recorded at the Newhall Fire Station during the Northridge earthquake, had a peak vertical acceleration of 0.54g (Fig. 8.1b). The third ground motion was recorded at the Los Gatos Presentation Center during the Loma Prieta earthquake and had a peak vertical acceleration of almost 0.9g (Fig. 8.1c).

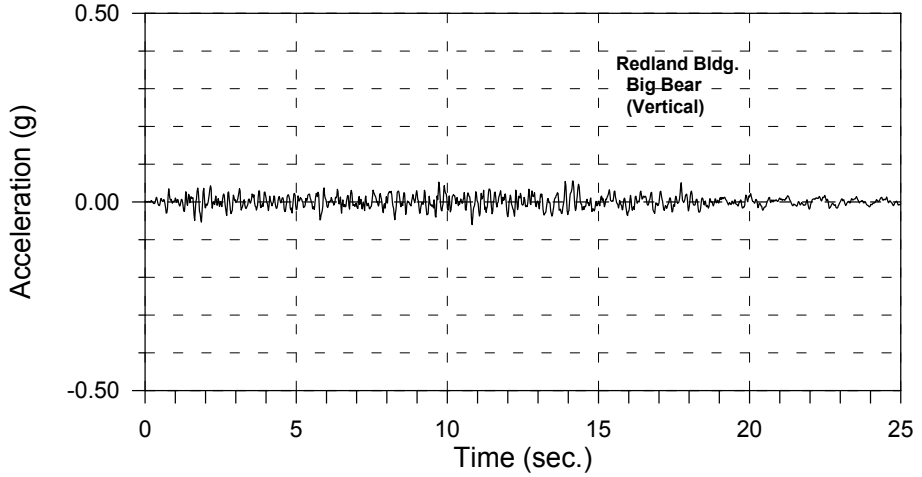

(a) Big Bear, Redland site

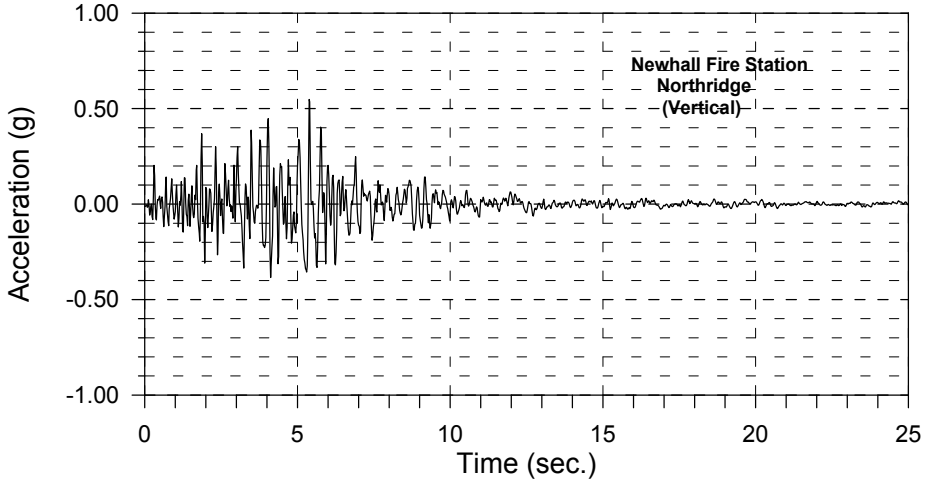

(b) Newhall fire station

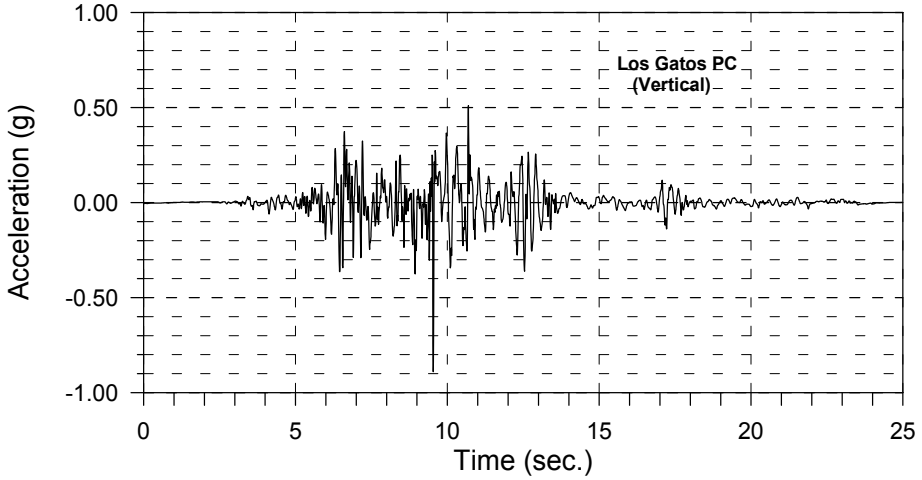

(c) Los Gatos

Fig. 8.1 Vertical ground motion acceleration components

8.1 RECORDED SITE MOTION, BIG BEAR

The axial force distribution in the purlins and glulam beams under the Big Bear ground motion is shown in Figure 8.2a. Distributions of the axial force in the connection of the purlins to the pilasters in the transverse walls on the north and south ends of the building are shown in Figures 8.2b and 8.2c, respectively. Here it can be seen that there is no significant effect on this force component due to the vertical acceleration. The axial force demand in the connections of the glulam beams to the pilasters is shown in Figures 8.3b–c for the east and west walls, respectively. These figures also indicate that the vertical acceleration has no significant effect on the axial force component of these members.

The distribution of the vertical shear forces in the purlins and glulam beams is shown in Figure 8.4a. The effects of the vertical accelerations on the vertical shear force component in the purlin to pilaster connections are not significant as can be seen in Figures 8.4b–c. The vertical shear force components in the glulam to pilaster connections (Figs. 8.5b–c**)** indicate that due to the vertical accelerations, there is a 24% increase in the vertical component of the connection force on the east wall and a 17% increase on the west wall. The distribution of horizontal shear forces in the glulam beams and purlins is shown in Figure 8.6a. The horizontal shears in the purlin to pilaster connections at the north and south walls are shown in Figures 8.6b and 8.6c, respectively. These figures indicate that there is only a small change in this force component due to the vertical accelerations. Horizontal shears in the glulam to pilaster connections along the east and west walls are shown in Figure 8.7b and 8.7c, respectively. The results shown in Figure 8.7b indicate an increase of approximately 21% in the horizontal shear forces in two glulam connections along the east wall near both ends of the building. However, the results shown in Figure 8.7c indicate that there is no change in the glulam connection forces along the west wall.

Based on these results, it could be concluded that there was no significant effect on the connections of the roof beams to the vertical pilasters due to the vertical accelerations under this ground motion. However, the vertical accelerations at the site due to the Big Bear earthquake were not very significant, as can be seen in Figure 8.1a, having a peak acceleration of only 6.2% of gravity.

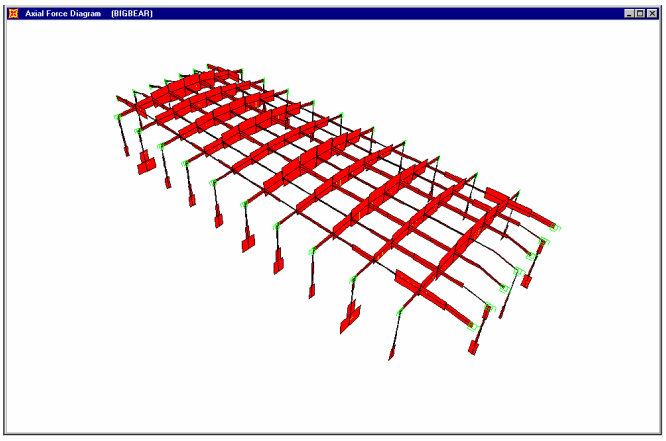

(a) Big Bear ground motion — axial force

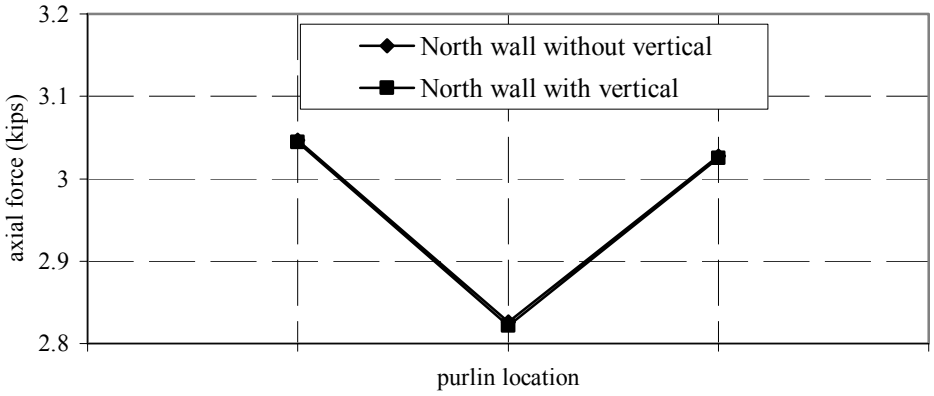

(b)

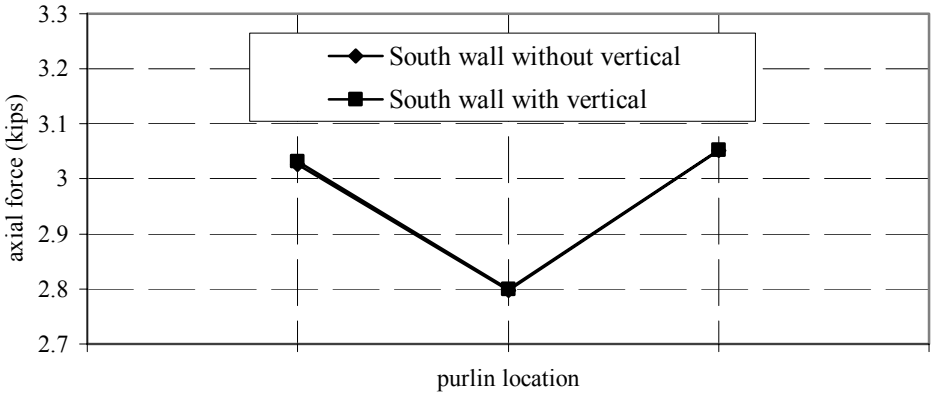

(c)

Fig. 8.2 Axial force component, end walls, Big Bear

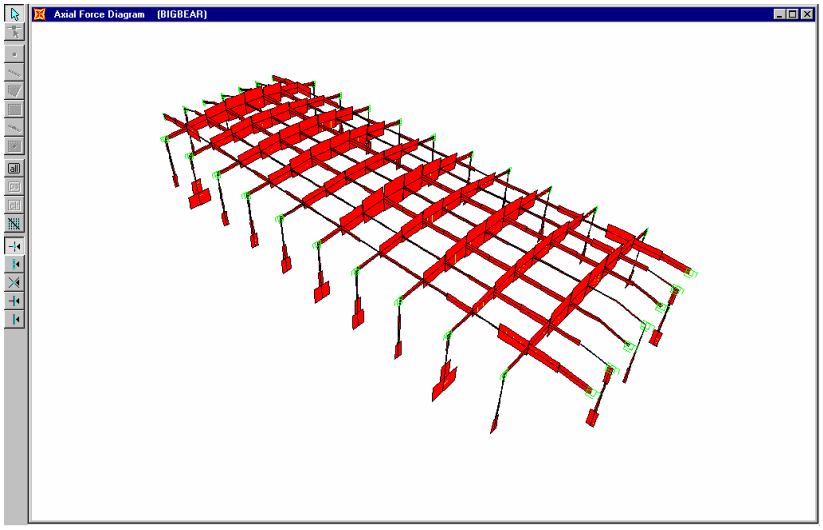

(a) Big Bear ground motion — axial force

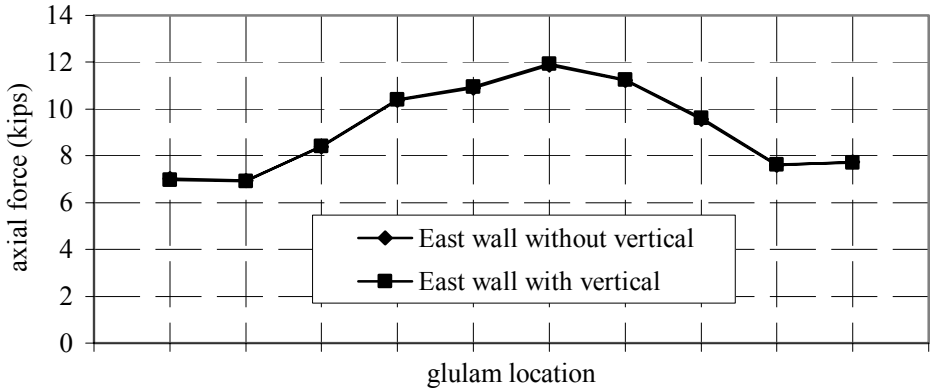

(b)

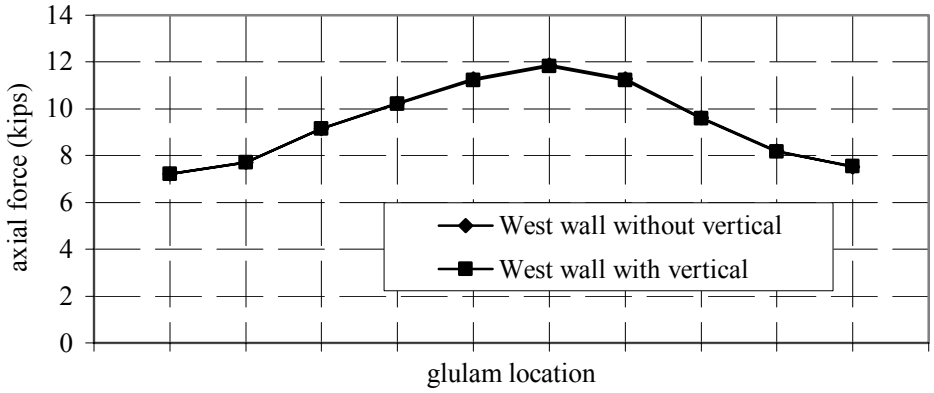

(c)

Fig. 8.3 Axial force component, longitudinal walls, Big Bear

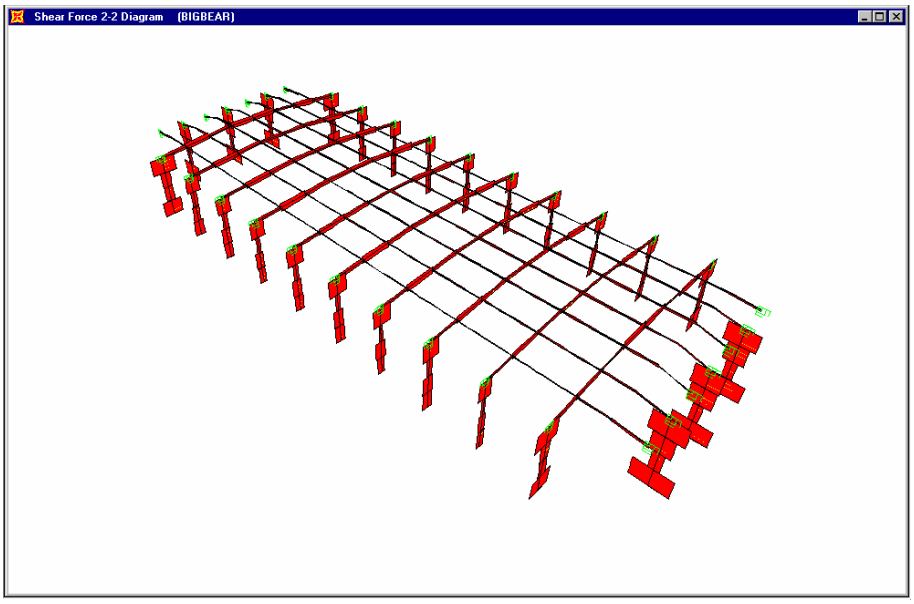

(a) Big Bear ground motion, 2-2 shear

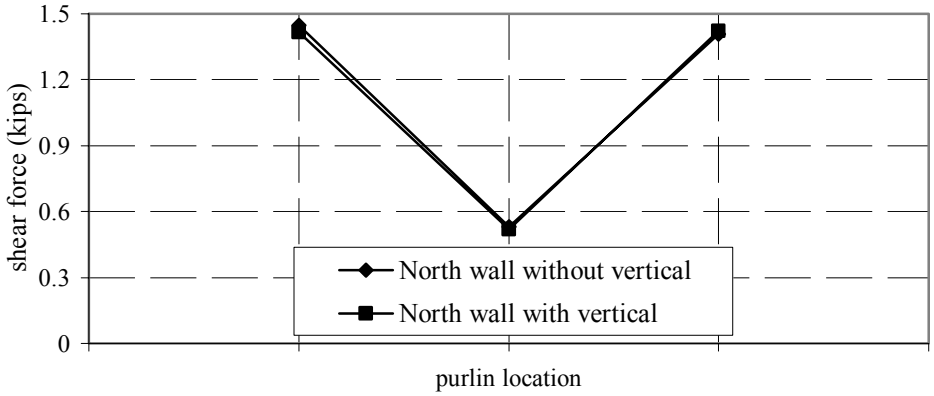

(b)

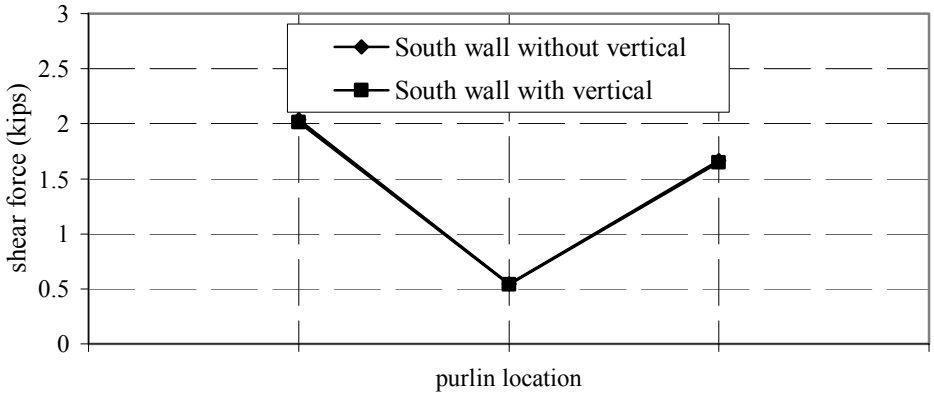

(c)

Fig. 8.4 Vertical shear force component, end walls, Big Bear

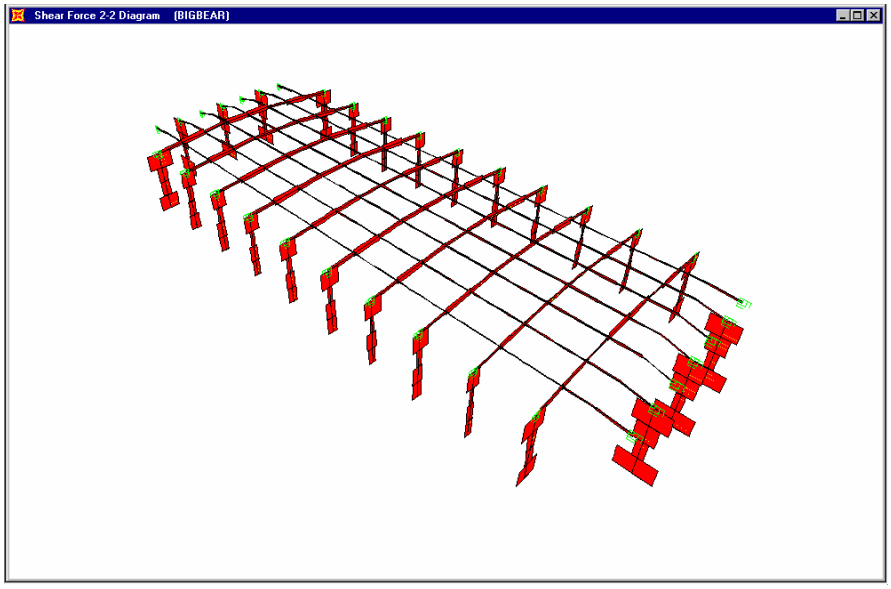

(a) Big Bear ground motion, 2-2 shear

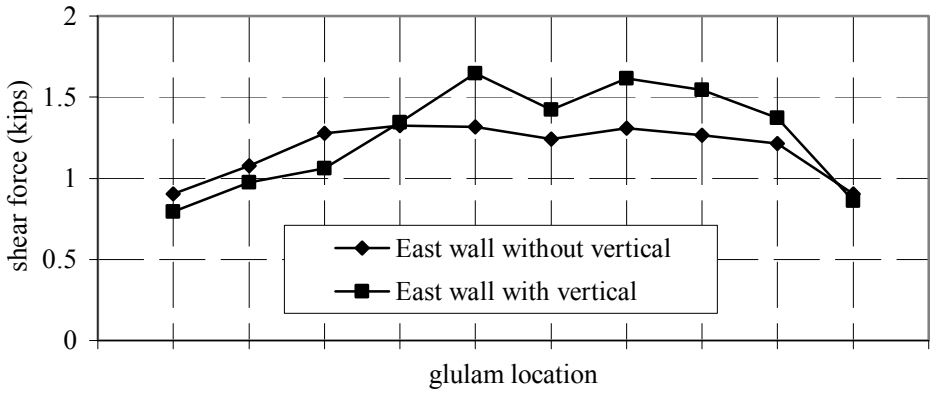

(b)

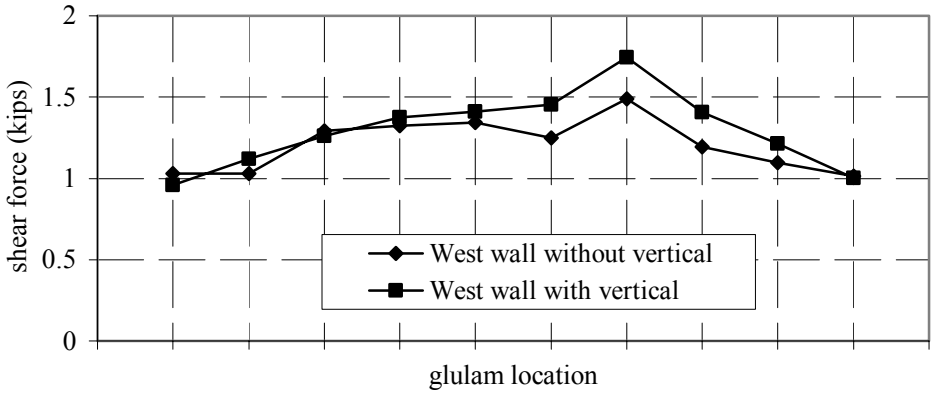

(c)

Fig. 8.5 Vertical shear force component, longitudinal walls, Big Bear

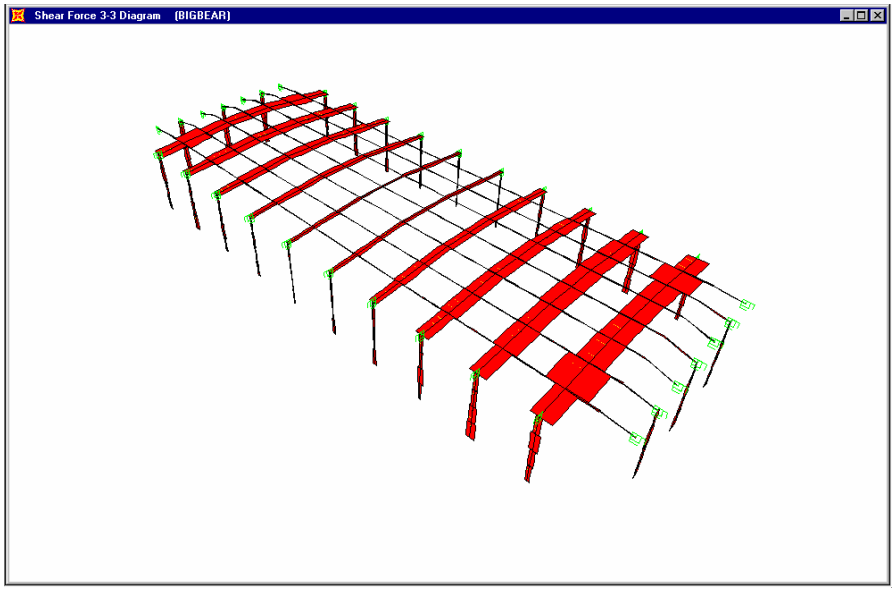

(a) Big Bear ground motion, 3-3 shear

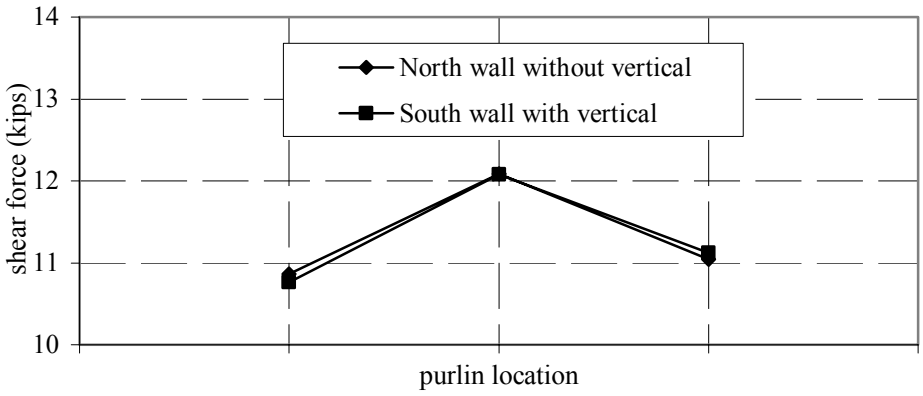

(b)

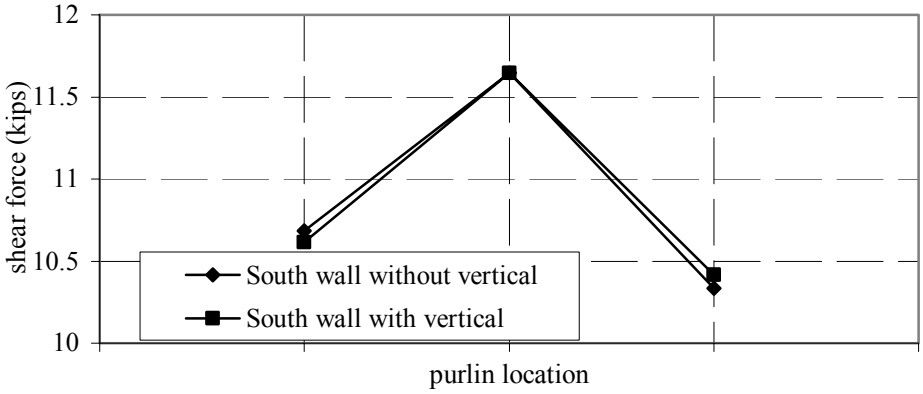

(c)

Fig. 8.6 Horizontal shear force component, end walls, Big Bear

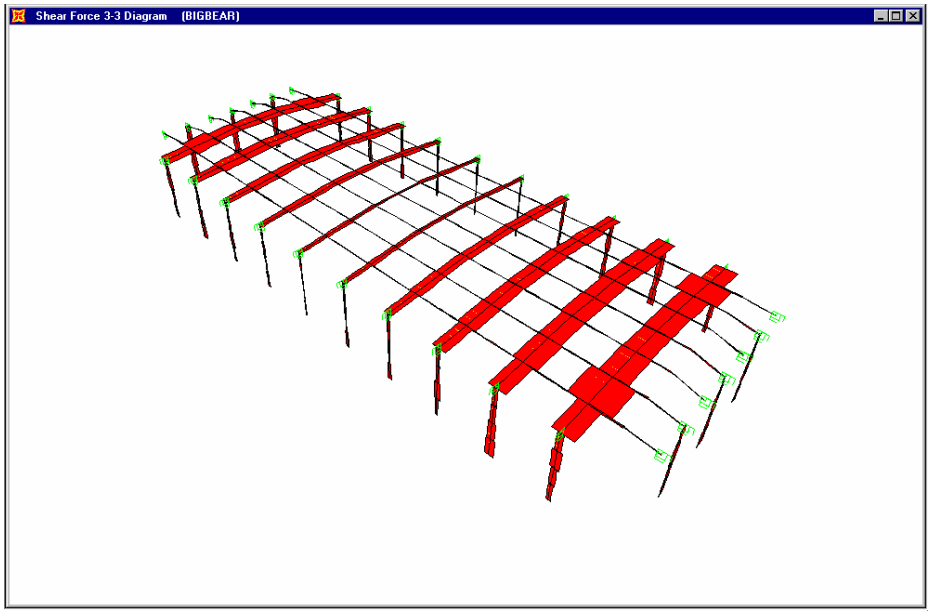

(a) Big Bear ground motion, 3-3 shear

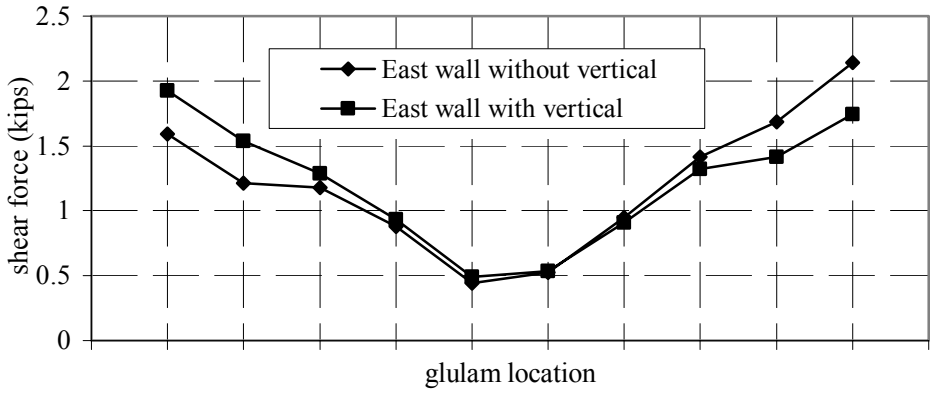

(b)

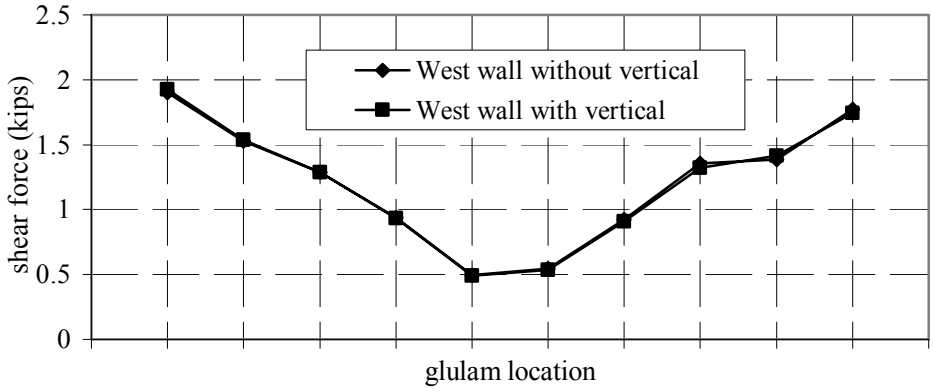

(c)

Fig. 8.7 Horizontal shear force component, longitudinal walls, Big Bear

8.2 NEWHALL FIRE STATION

The ground motions recorded at the Newhall Fire Station during the Northridge earthquake are much stronger and, in particular, have a significantly higher vertical component, as shown in Figure 8.1b. As mentioned previously, this component has a peak acceleration of 54% of gravity.

The axial force distribution in the purlins and glulam beams under the Newhall ground motion is shown in Figure 8.8a. Distributions of the axial force components in the connections of the purlins to the pilasters in the north and south walls are shown in Figures 8.8b–c, where it can be seen that there is no significant effect due to the vertical accelerations. The axial force demands in the connections of the glulam beams to the pilasters along the east and west walls are shown in Figures 8.9b–c. These figures also indicate no significant effect of the vertical accelerations on the axial force components of these members.

The distribution of the vertical shear forces in the purlins and glulam beams is shown in Figure 8.10a. The effects of the vertical accelerations on the vertical shear force component in the purlin to pilaster connections result in a maximum increase of 4% in the shear force (Figs. 8.10b–c). The vertical shear force components in the glulam to pilaster connections (Figs. 8.11b–c) indicate that the increase in force due to the vertical accelerations is substantial. The maximum increase occurs near the center of the longitudinal walls, increasing the vertical shear force in the connection by 114% in the east wall and by 95% in the west wall. The distribution of horizontal shear forces in the glulam beams and purlins is shown in Figure 8.12a. The horizontal shears in the purlin to pilaster connections at the north and south walls are shown in Figures 8.12b–c**,** respectively. Here it can be seen that the maximum increase in this component occurs in the south wall, where the horizontal shear increases from 23.5 kips to 24.4 kips (3.8%). The horizontal shear forces in the glulam to pilaster connections, shown in Figures 8.13b–c, indicate that the maximum increase in this force component due to vertical accelerations occurs at the ends of these walls and has a value of 15%.

.

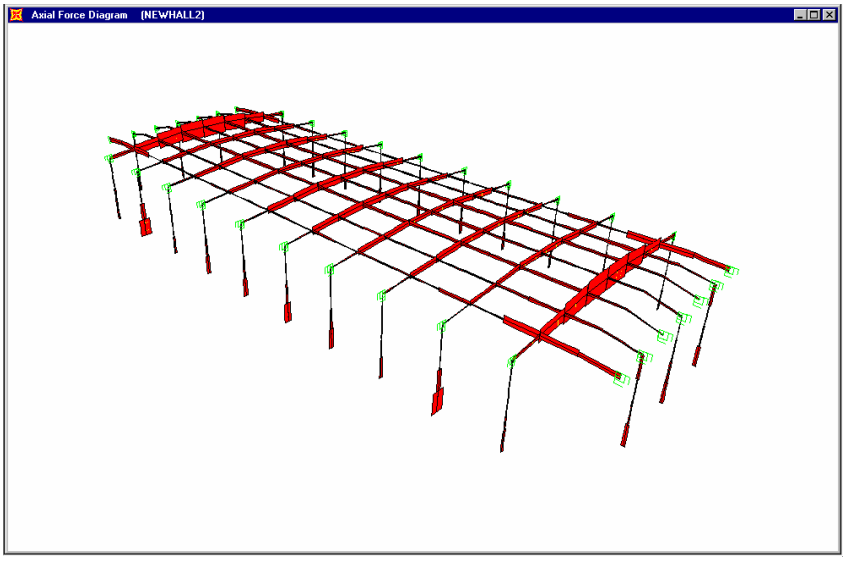

(a) Newhall ground motion — axial force

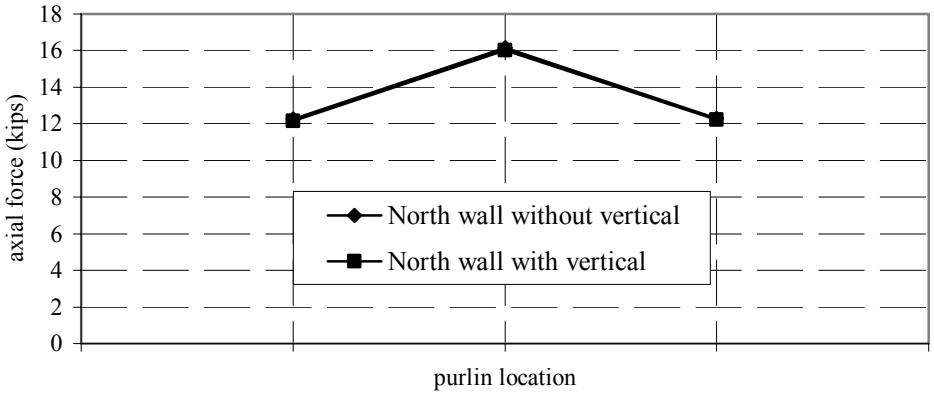

(b)

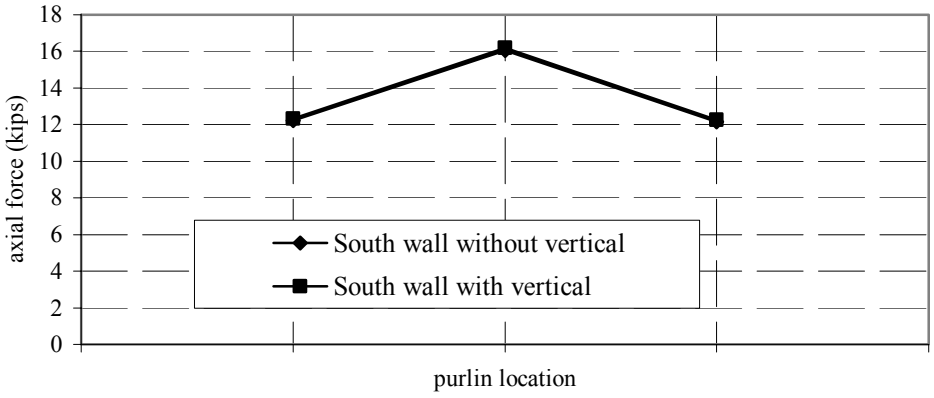

(c)

Fig. 8.8 Axial force component, end walls, Newhall

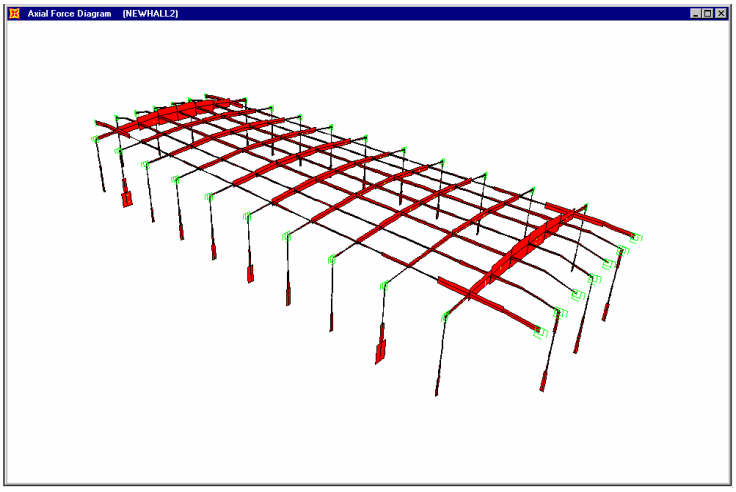

(a) Newhall ground motion — axial force

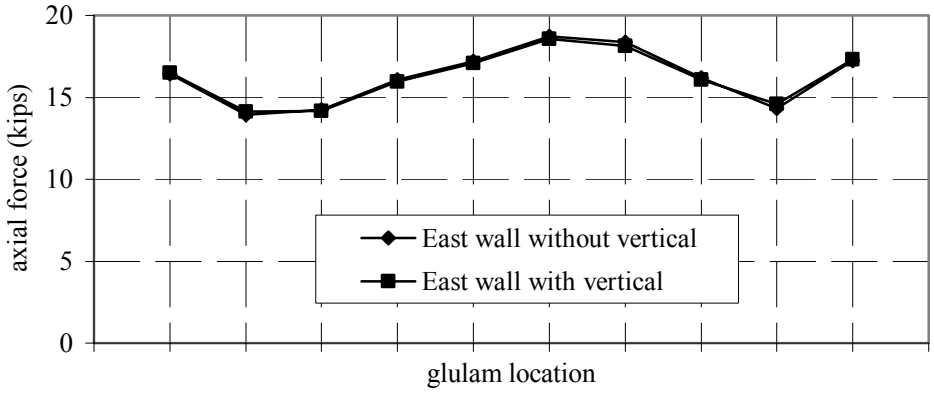

(b)

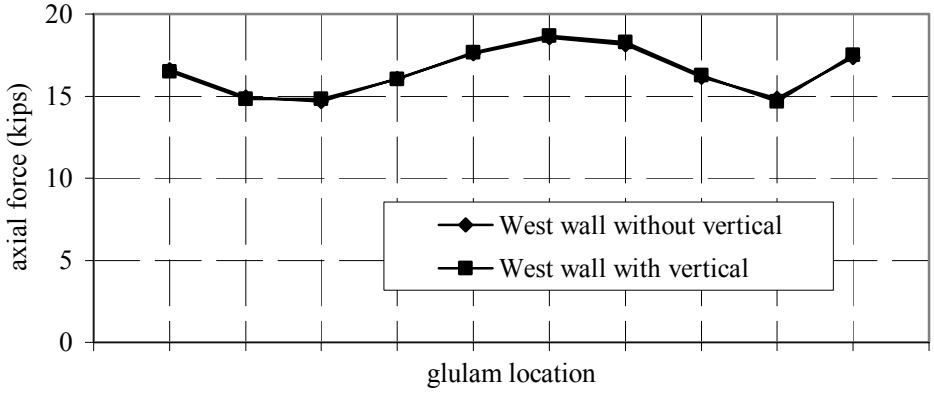

(c)

Fig. 8.9 Axial force component, longitudinal walls, Newhall

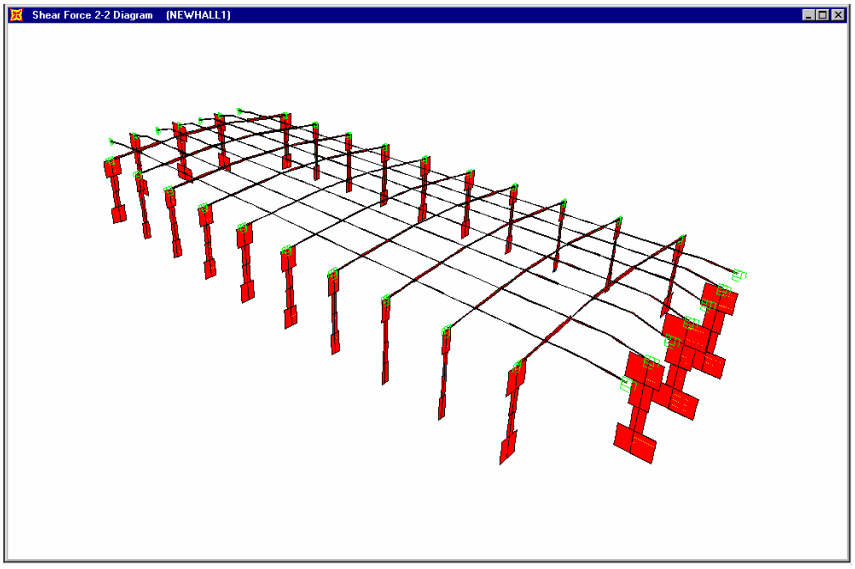

(a) Newhall ground motion, 2-2 shear

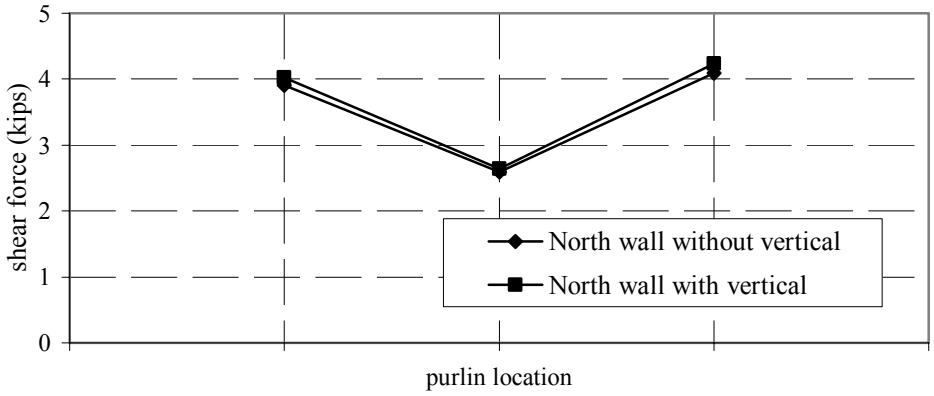

(b)

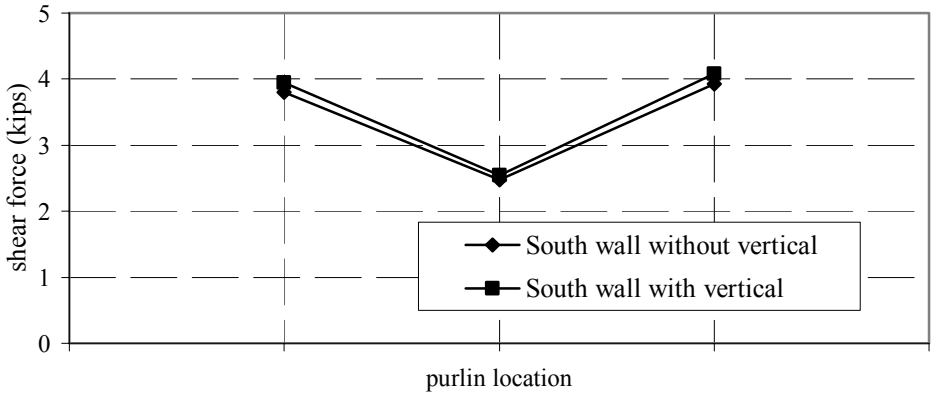

(c)

Fig. 8.10 Vertical shear force component, end walls, Newhall

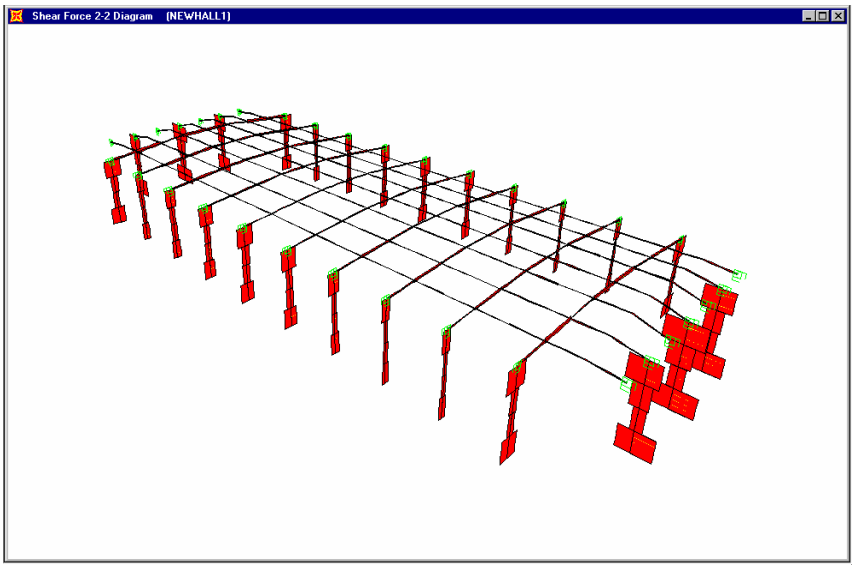

(a) Newhall ground motion, 2-2 shear

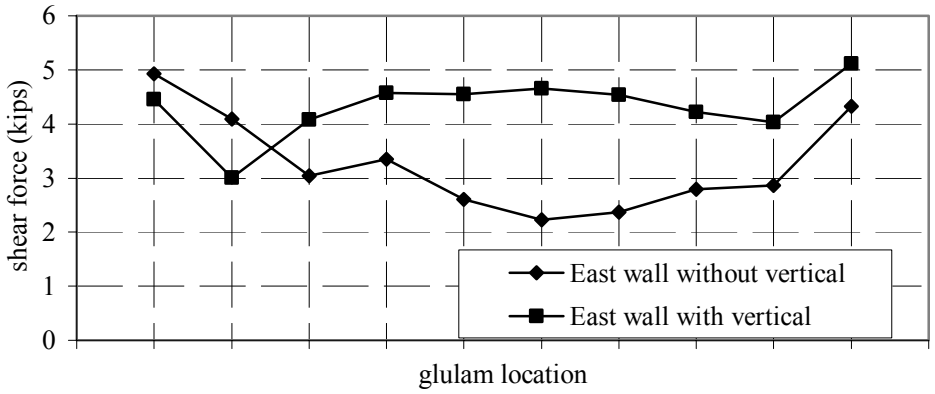

(b)

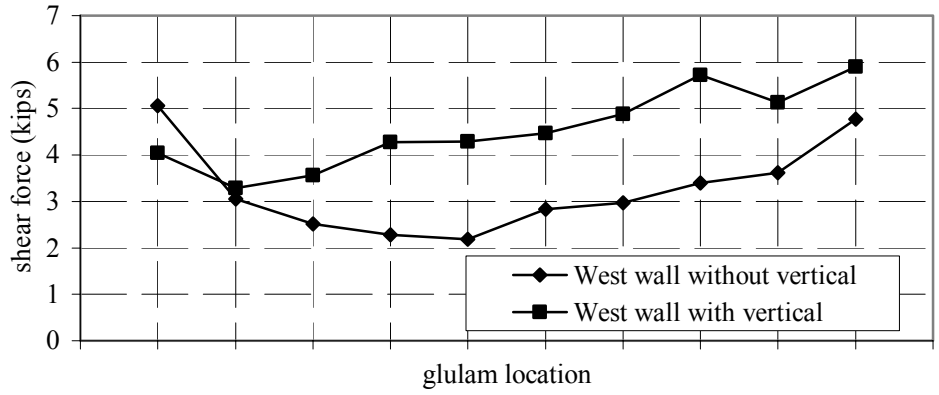

(c)

Fig. 8.11 Vertical shear force component, longitudinal walls, Newhall

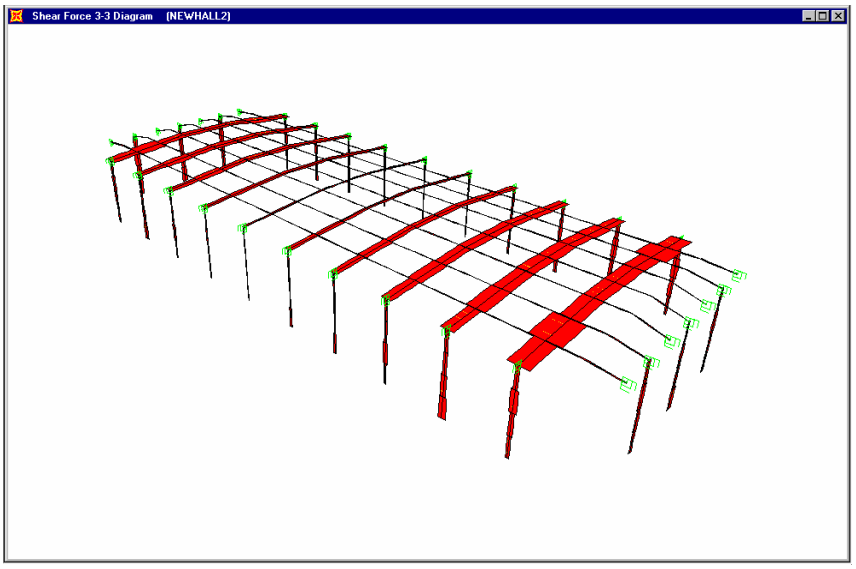

(a) Newhall ground motion, 3-3 shear

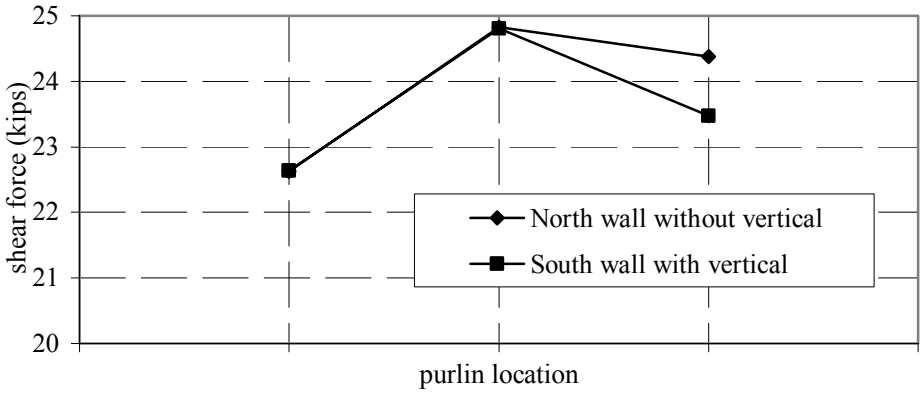

(b)

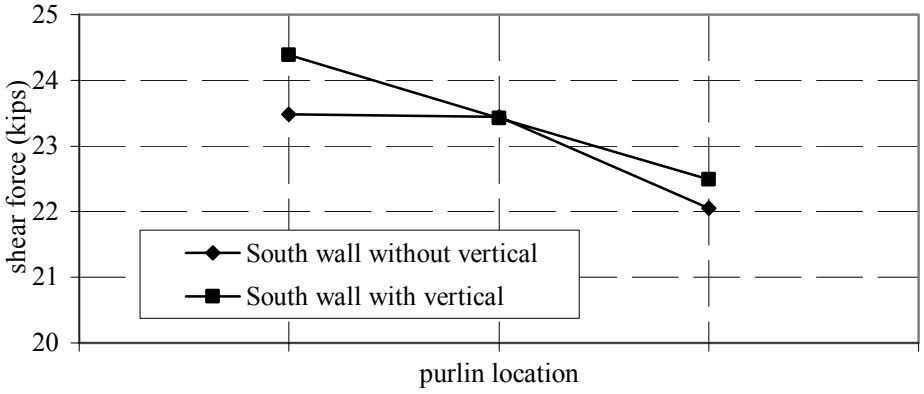

(c)

Fig. 8.12 Horizontal shear force component, end walls, Newhall

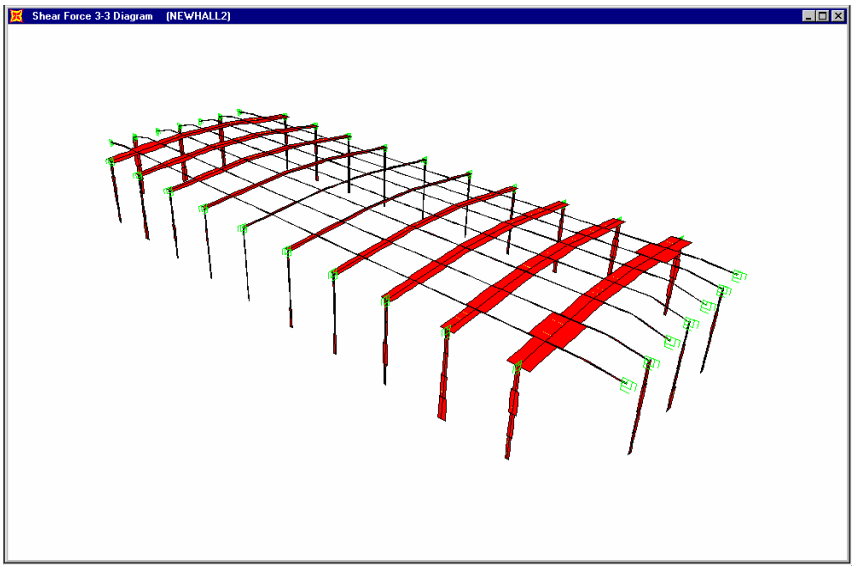

(a) Newhall ground motion, 3-3 shear

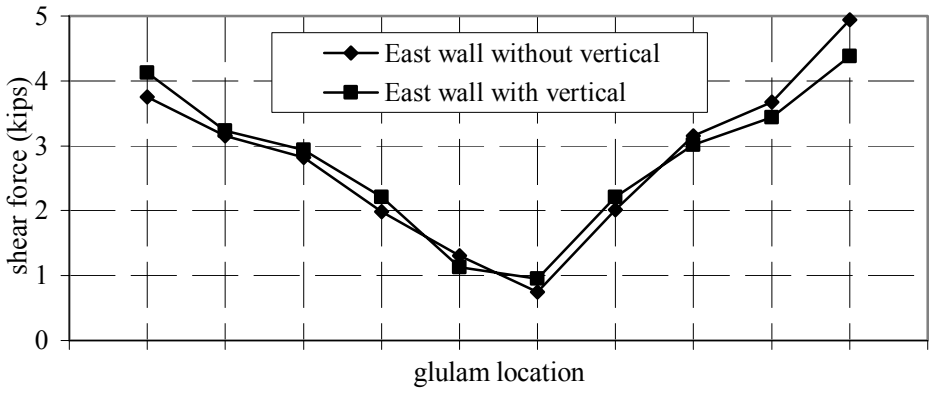

(b)

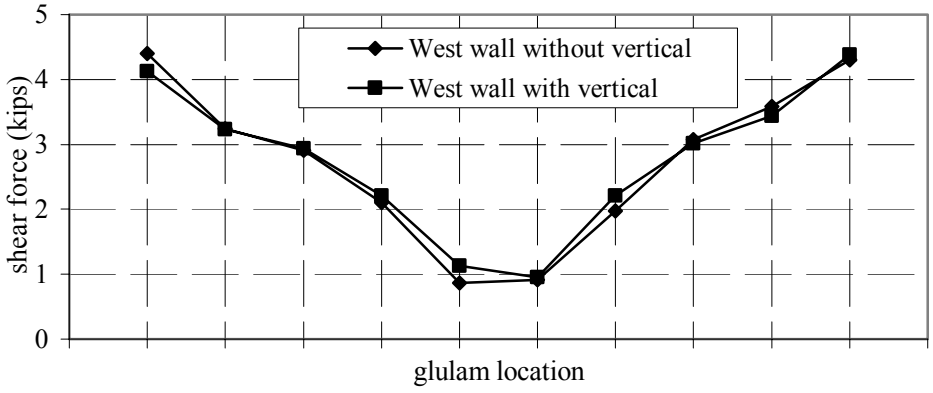

(c)

Fig. 8.13 Horizontal shear force component, longitudinal walls, Newhall

8.3 LOS GATOS PRESENTATION CENTER

The ground motions recorded at the Los Gatos Presentation Center during the Loma Prieta earthquake also have a strong vertical component, as can be seen in Figure 8.1c. Here it can be seen that an acceleration spike has a peak acceleration of 90% of gravity.

The axial force distributions in the purlins and glulam beams under the Los Gatos ground motion are shown in Figure 8.14a. The distribution of the axial force components in the connections of the purlins to the pilasters in the transverse walls is shown in Figures 8.14b–c. Here it can be seen that there is no significant change in this force component due to the vertical accelerations. The axial force demand in the connections of the glulam beams to the pilasters is shown in Figures 8.15b–c. These figures indicate a small increase in this force component, which has a maximum value of 2%.

The distribution of the vertical shear forces in the purlins and glulam beams is shown in Figure 8.16a. The effects of the vertical accelerations on the vertical shear force component in the purlin to pilaster connections result in a maximum increase of 6% (Figs. 8.16b–c). The vertical shear force components in the glulam to pilaster connections are shown in Figures 8.17b–c. Here the increase due to the vertical accelerations is substantial, increasing by 136% near the center of the east wall where the shear force increases from 2.75 kips to 6.5 kips. A similar increase can be seen in the west wall (Fig. 8.17c). The distribution of horizontal shear forces in the glulam beams and purlins is shown in Figure 8.18a. The horizontal shears in the purlin to pilaster connections at the north and south walls are shown in Figures 8.18b and 8.18c, respectively. Here it can be seen that the maximum increase in this component occurs in the south wall where the horizontal shear increases from 27.4 kips to 27.9 kips for an increase of 1.8%. The horizontal shear forces in the glulam to pilaster connections are shown in Figures 8.19b–c**.** The maximum increase in this force component due to vertical accelerations occurs at the ends of these walls and has a value of 11%.

This limited study has considered the effects of vertical accelerations on the connections of a long span roof (90 feet) to pilasters located on the perimeter. The results indicate that for the case study building, the vertical accelerations recorded at the site during the Big Bear earthquake did not have any significant effect on the performance. However, for stronger earthquakes having stronger recorded vertical ground accelerations, the effects can be significant for certain

connection force components. The most significant increases occurred in the vertical shear component in the connections along the longitudinal walls of the building. At these locations increases of more than 100% were obtained.

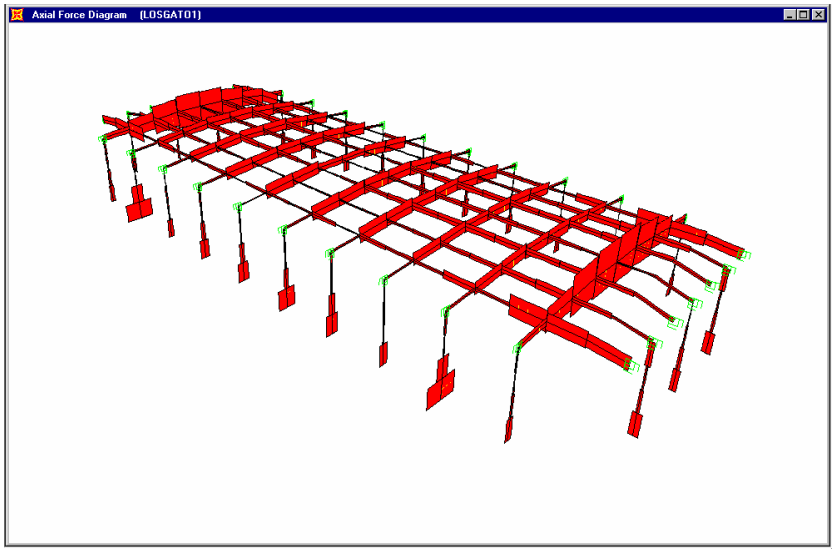

(a) Los Gatos ground motion — axial force

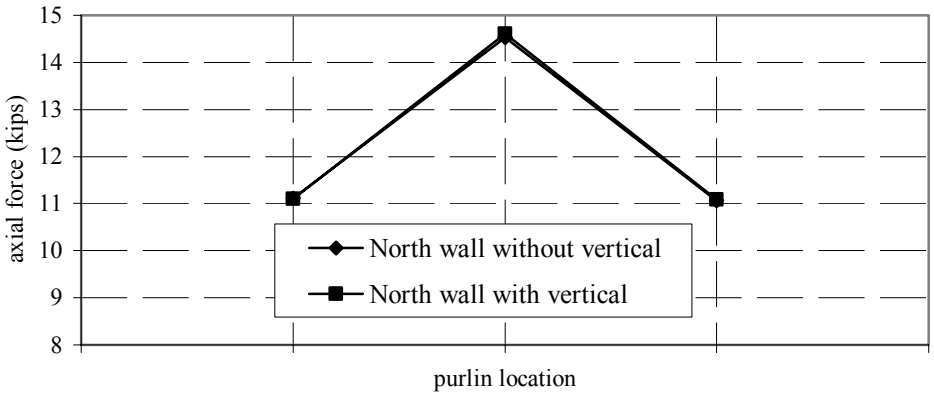

(b)

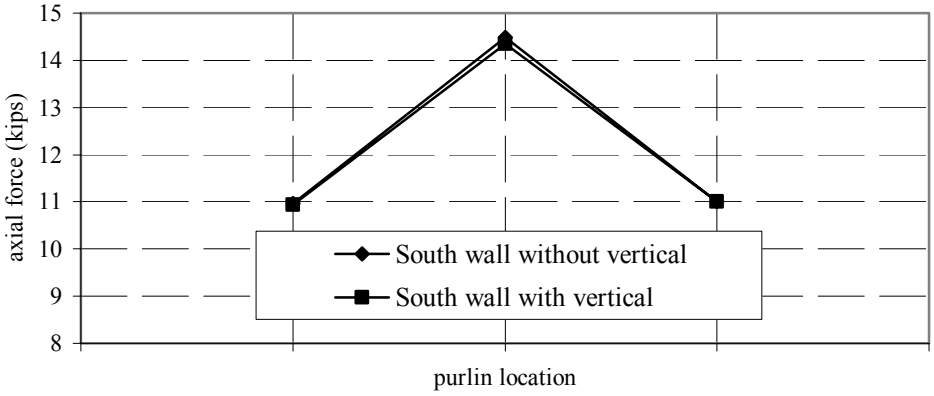

(c)

Fig. 8.14 Axial force component, end walls, Los Gatos

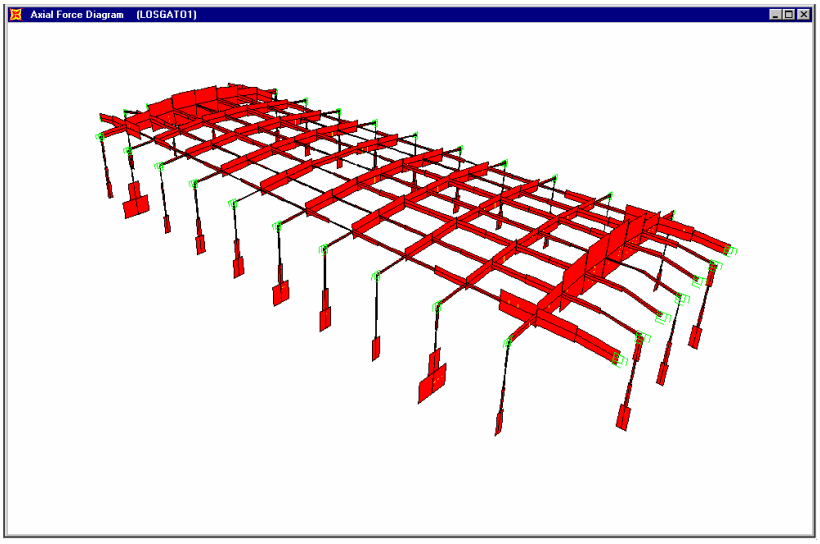

(a) Los Gatos ground motion — axial force

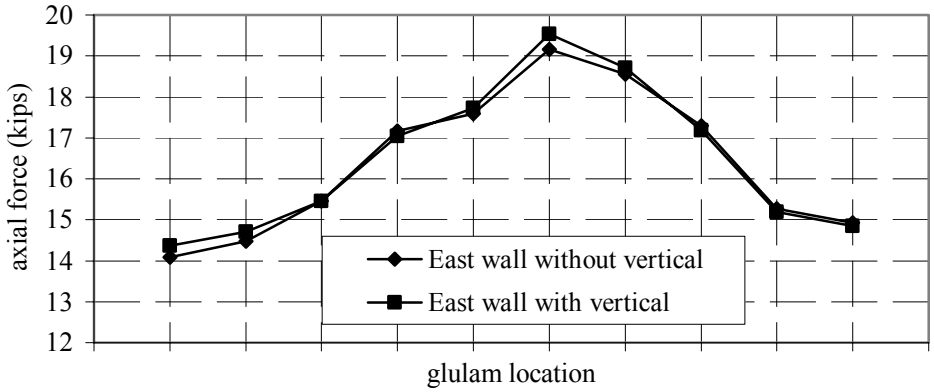

(b)

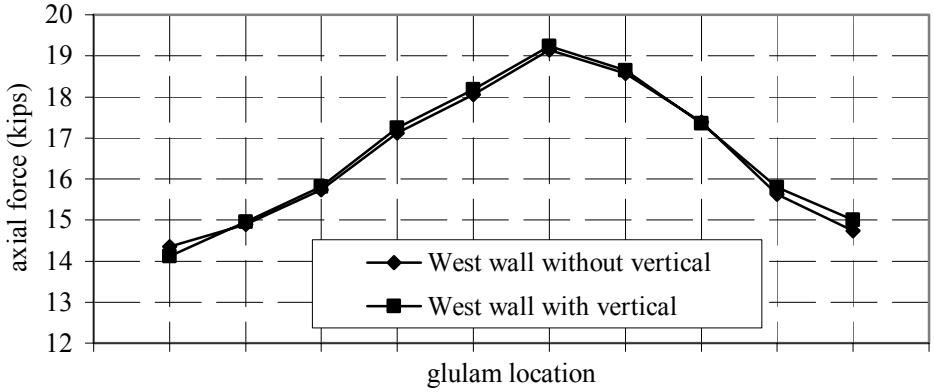

(c)

Fig. 8.15 Axial force component, longitudinal walls, Los Gatos

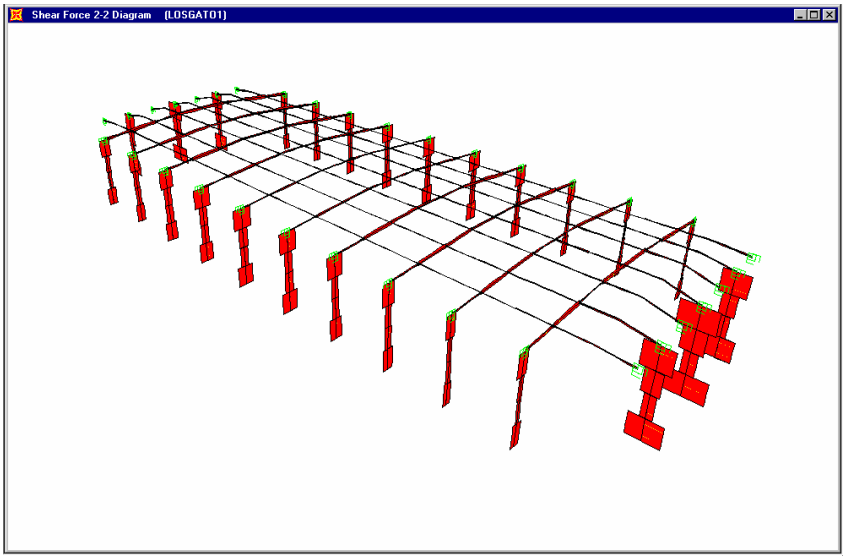

(a) Los Gatos ground motion, 2-2 shear

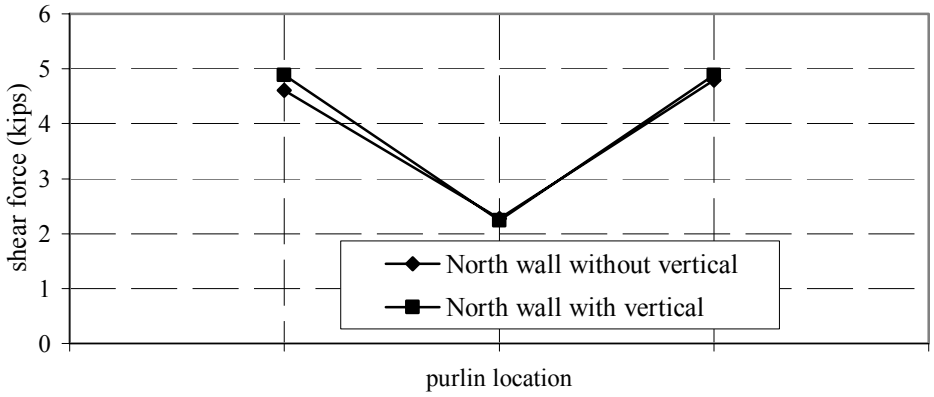

(b)

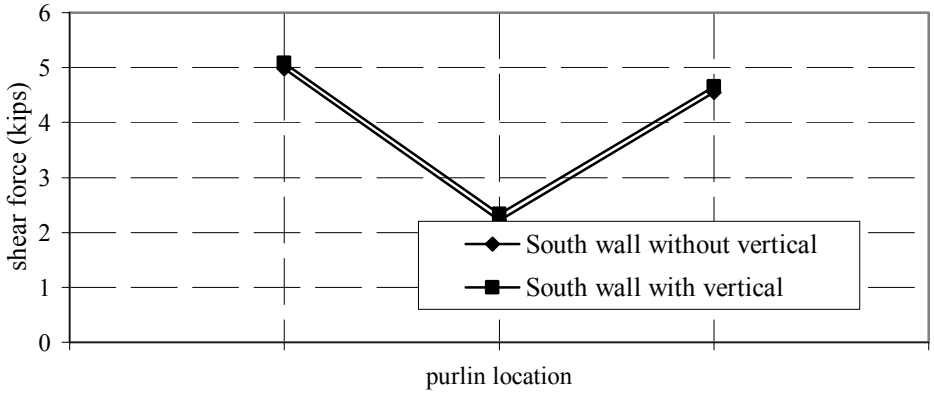

(c)

Fig. 8.16 Vertical shear component, end walls, Los Gatos

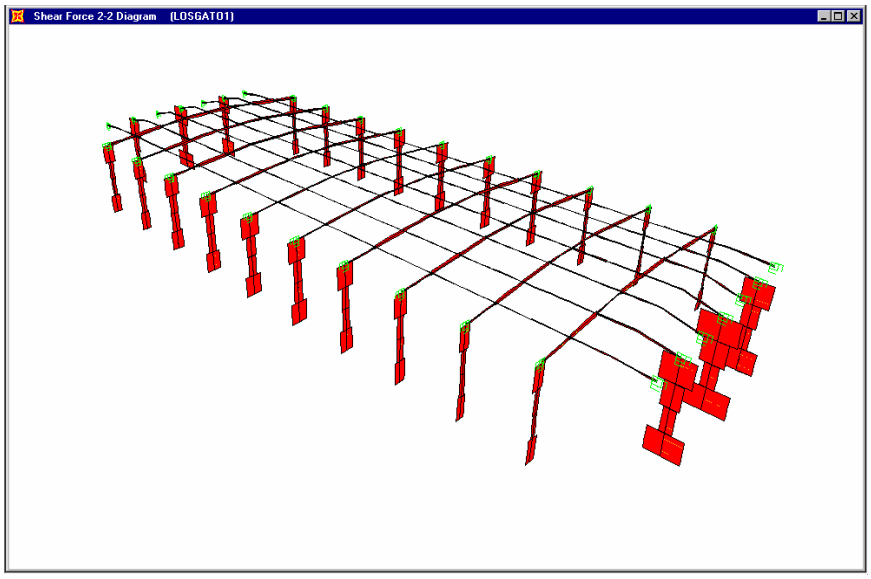

(a) Los Gatos ground motion, 2-2 shear

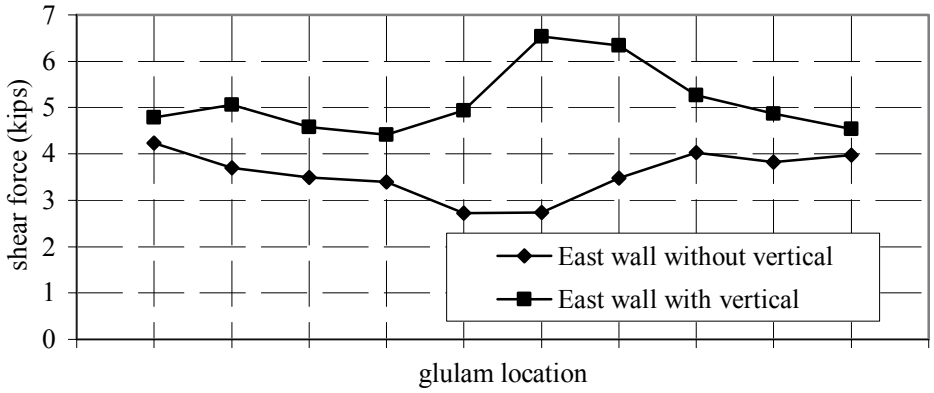

(b)

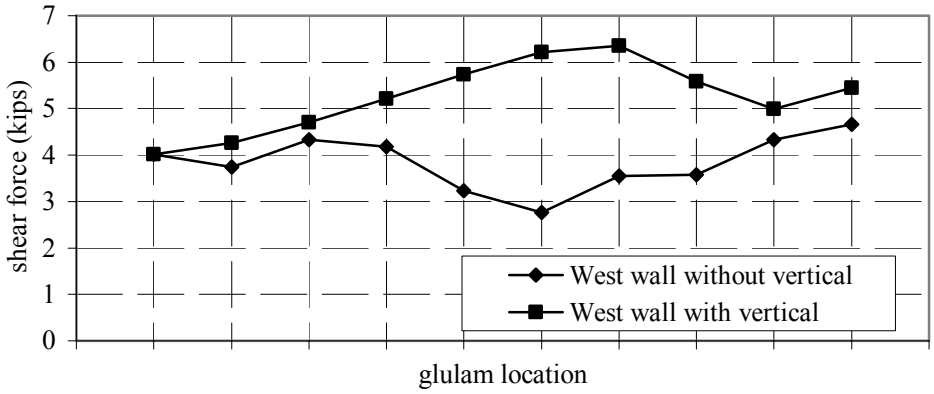

(c)

Fig. 8.17 Vertical shear force component, longitudinal walls, Los Gatos

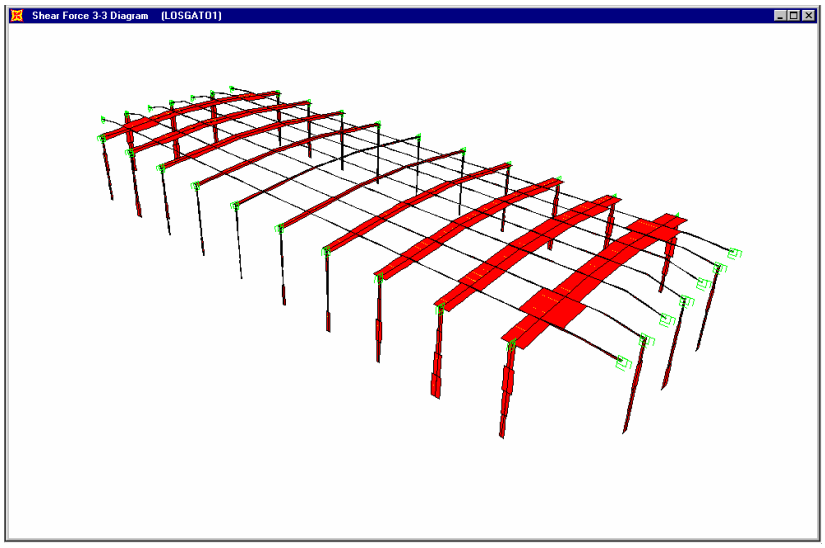

(a) Los Gatos ground motion, 3-3 shear

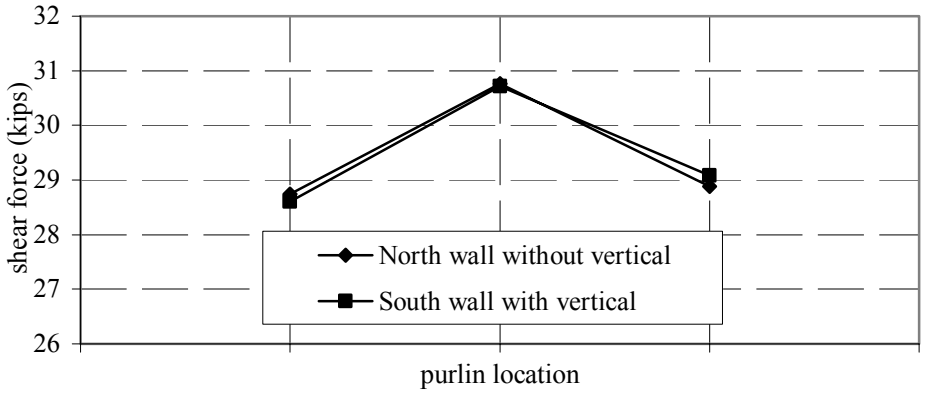

(b)

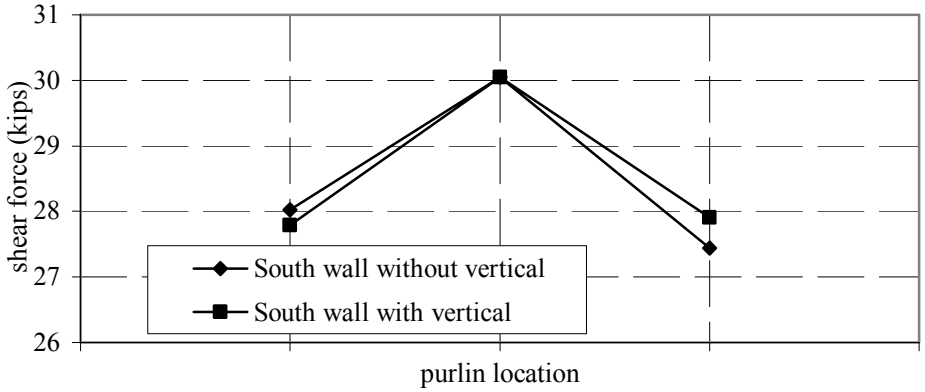

(c)

Fig. 8.18 Horizontal shear force component, end walls, Los Gatos

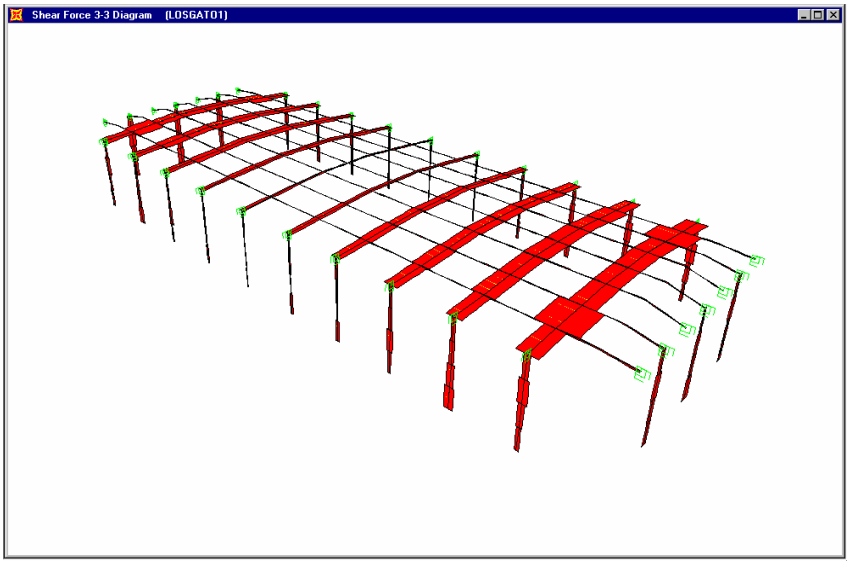

(a) Los Gatos ground motion, 3-3 shear

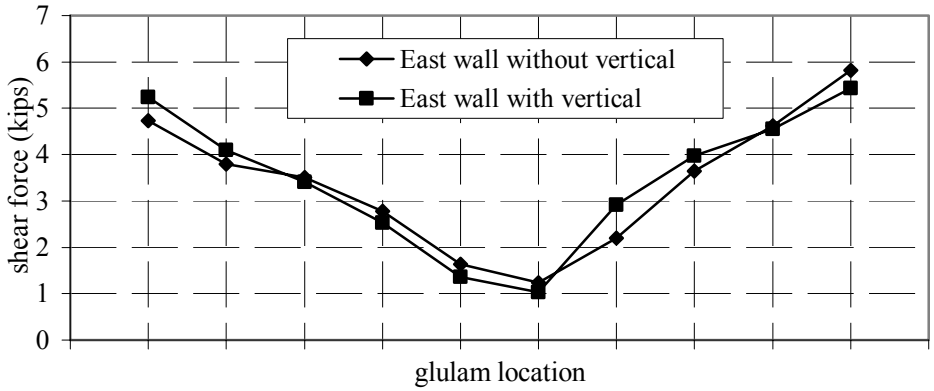

(b)

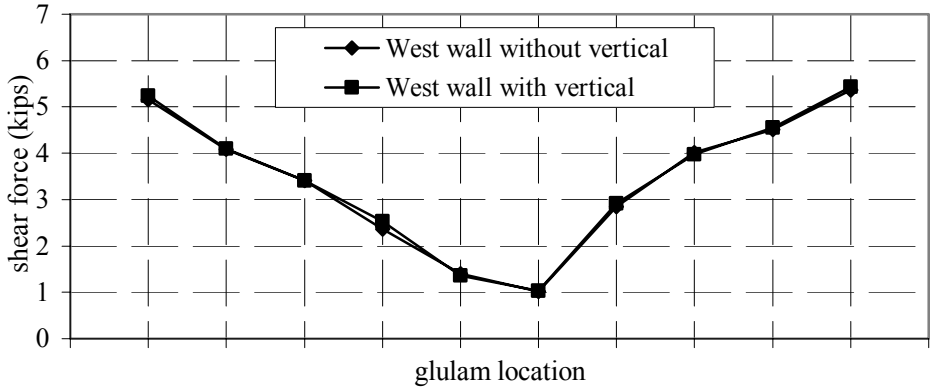

(c)

Fig. 8.19 Horizontal shear force component, longitudinal walls, Los Gatos

9 Conclusions

Analysis of Recorded Response

1. Data recorded in the building during previous earthquakes indicate that there is a significant amplification of the horizontal acceleration between the base and the roof in the direction out-of-plane to the walls. The acceleration at the roof level may be as high as 5.6 times the base acceleration.

2. Recorded data indicate there is almost no amplification of the horizontal base acceleration in the plane of the walls and that the acceleration at the roof level is approximately equal to the base acceleration.

3. The maximum measured drift at the roof level, which occurred in the out-of-plane direction during the Big Bear earthquake, was 0.81 inches. This resulted in an interstory drift index of 0.0025. Maximum measured drift in the in-plane direction was 0.028 inches for an IDI of 0.00014.

4. Comparisons of response spectra for different recordings along the top of the same wall indicate little change in the response over the entire period range for in-plane accelerations. For out-of-plane motions, these comparisons indicate an amplification of the accelerations for building periods of less than one second.

5. Analysis of the recorded accelerations from four earthquake records using Fourier transfer functions indicates a substantial increase in the period of the building. In the transverse direction, the period increases from 0.4–0.67 seconds in a sequential manner indicating the cumulative effect of the multiple shaking. This represents a 65% reduction in stiffness. In the longitudinal direction, the building period was increased from 0.35–

0.75 seconds by the ground motions from the Big Bear earthquake. For this building, the increase was probably due to a loosening of the nailing in the diaphragm and a loosening of the connections to the pilasters. In both cases it was not possible to include the effects of any repairs that may have been made. It is of interest to note that following the Big Bear earthquake, the period obtained from the Northridge earthquake record shortened to 0.6 seconds. These results clearly indicate that when assessing the vulnerability of an existing building that has been subjected to prior earthquake ground motions, it is necessary to conduct analysis considering models with at least two different stiffness values representing the initial condition and the current existing condition.

3D Dynamic Analyses (Elastic)

1. Using the limited information contained on the four sheets of plans that were made available, it was possible to construct a 3D elastic model of the building using SAP2000. This model contained 1000 beam elements, 2000 shell elements, and 500 spring elements. The results obtained gave a very close approximation to the periods of the fundamental modes in both principal directions, as the calculated modes were in good agreement with estimates of the periods obtained from the recorded data.

2. Participating mass for this building was calculated to be 46.3% in the transverse direction and only 15.5% in the longitudinal direction. Since the base shear is the product of the mass participation and the base acceleration, if the base accelerations in both directions are approximately equal, the base shear in the transverse direction will be almost three times larger. This unbalance will be even more if the predominate ground motion is in the transverse direction as it was for this building.

3. Periods of vibration for this building that were estimated using building code formulas showed poor correlation with periods obtained from the recorded data or calculated using the 3D analytical model and modal analysis. Prior to 1988, the estimated period depended upon the dimension of the building plan in the direction of the seismic forces ($T = .05h_n/\sqrt{D}$). For this building this results in periods of 0.14 seconds in the transverse direction and 0.09 seconds in the longitudinal. These values compare with 0.40 seconds and 0.33 seconds determined from the recorded data. Using the 1997 UBC, a single value

is determined that depends only on the building height and has a value of 0.23 seconds. It can be seen that the code values have little correlation with the actual values.

4. With the exception of sensor 9, transverse to the south wall, comparisons between recorded accelerations and calculated accelerations showed good agreement for all four recorded earthquake motions. Corresponding displacements determined from the recorded accelerations also correlated well with those obtained from the analytical model.

5. Base shear time histories calculated for the Palm Springs and Northridge earthquakes were well within the design value specified by the UBC '97, indicating predominantly elastic behavior. Similar time histories calculated for the Landers and Big Bear earthquakes exceeded the code lateral force requirement; however, this occurred only during a limited number of excursions. Changes in period noted in the analysis of the recorded data were probably due to loosening of the nailing in the roof diaphragm and some limited microcracking that was observed in the west wall of the building.

6. The Big Bear and Landers ground motions produce contours of in-plane shear force in the walls indicating demands that are more than twice code design requirements. However, calculations of estimated capacity indicate substantial overstrength for in-plane shear. Contours of out-of-plane moments in the walls indicate demands that are approximately half of capacity, and demands on the connections of glulam beams to pilasters are also approximately half of capacity. However, contours of in-plane shear in the roof diaphragm are twice as large as the estimated capacity. Hence, it can be concluded that for this building, the critical component under these recorded earthquakes was the roof diaphragm. Unfortunately this was the most difficult component to inspect during a site visit.

7. Although not shown on the limited set of building plans that were available, a site visit indicated that there was no continuity at the corners of the building. An analysis of the building with the corners disconnected for the Landers and Big Bear ground motions shows that this has limited effect on the accelerations and displacements. In the N-S direction, the base shears were increased by approximately 30% when the corners were disconnected. Force contours indicated a limited change in the in-plane shear in the walls

and the roof diaphragm. However, there was a significant increase in the out-of-plane moment in the corner panels of the TUW.

8. Pulse-type ground motions recorded in the free field during recent earthquakes place an extreme demand on this type of building structure. Three pulse-type motions representing different types of displacement pulses were considered and used for input for the building with pilasters and disconnected corners. All three records would have caused demands significantly higher than those for which the building was designed according to minimum code design requirements. Based on an examination of the force contours, the only building component with adequate capacity was the in-plane shear capacity of the walls. However, the out-of-plane moment capacity of the walls was exceeded by a factor of 4 and, therefore, the walls may have failed in this failure mode rather than in shear. The in-plane shear capacity in the roof diaphragm was exceeded by as much as a factor of 10, and the capacity of glulam beam to pilaster connections were exceeded by a factor of 2.6 considering old connections. These results indicate that the roof diaphragm seems to be the critical component under these severe pulse-type earthquake ground motions.

9. The results of the elastic analyses using the model with disconnected corners indicate that the axial force in the connection of the glulam to the pilaster at the midpoint along the length of the wall may be as much as 2.7 times the value at the end of the wall.

3D Dynamic Analyses (Nonlinear Connections)

1. Including the nonlinear behavior of the connections, with the diaphragm elastic, reduces the axial force in the glulam beams at the midlength of the wall to a maximum of 1.7 times the value at the end of the wall (Fig. 7.1). This is a reduction of 37% from the results obtained from the elastic analysis. It should also be noted that in the 1991 UBC, the required design anchorage force in the middle of the wall was increased by 50% relative to the anchorage force at the ends.

2. Under the Big Bear ground motion, the maximum axial forces in the connection of the glulam beams to the pilasters with elastic diaphragm exhibit weakly nonlinear behavior, with a displacement demand of 0.26 inches and a displacement ductility demand of 1.5 (Fig. 7.4). For the purlin to pilaster connection, the maximum axial force occurs near the

corner of the transverse wall, with a displacement demand of 0.20 inches and a ductility demand of 2.2 (Fig. 7.7).

3. One of the pulse-type motions (Los Gatos) develops an axial displacement demand in an old glulam beam connection with elastic diaphragm of 1 inch, with a displacement ductility demand of 4 (Fig. 7.11). Under the same conditions, the axial displacement demand in the purlin to pilaster connection increases to 10 inches, with a corresponding displacement ductility demand of more than 100. The old connections cannot sustain this type of deformation without failure. It was also shown that in addition to the axial force demands, these connections along the shorter side of the building also have high in-plane horizontal shear forces (30 kips) (Fig. 7.13) that are concurrent with the axial force. This has not been considered in any testing program known to the authors.

4. Under the Los Gatos ground motion, the new glulam beam-to-pilaster connections combined with elastic diaphragm have a similar displacement demand (1.25 in.) but the displacement ductility demand is reduced to 2.0 (Fig. 7.18). The new purlin-to-pilaster connections reduce the axial displacement demand to 0.5 inches and the displacement ductility demand to 3.3. This is a significant improvement in these types of connections.

5. Inclusion of the vertical ground accelerations in the analyses had a significant effect on the vertical shear force component of the glulam to pilaster connections, with increases of more than 100% obtained under pulse-type ground motions. However, this connection force component, including the increase, is approximately 33% of the more dominant axial force component. The axial force component in both the purlins and glulam beams is increased only by approximately 2% with the inclusion of vertical accelerations. The horizontal shear force component in the purlin to pilaster connection is increased by as much as 4%, whereas the same component in the glulam to pilaster connection is increased by up to 15%.

3D Static and Dynamic Analyses (Nonlinear Connections and Diaphragm)

1. The Hrennikoff model, which represents the continuum as a grid, can be used to model the inelastic behavior of the roof diaphragm. The major connections of the diaphragm to the glulam beam and the purlins can be modeled using nonlinear spring elements. These

changes converted the elastic building model to an inelastic building model with only the walls remaining elastic. However, it was noted that the inclusion of these nonlinear elements reduced the out-of-plane bending demand in the walls to near-capacity values. The nonlinear model proved to be effective in estimating the displacement and ductility demands in the connections.

2. It is shown that a nonlinear Hrennikoff truss model used to represent the diaphragm panel in a pushover analysis simulating the component test at UC Irvine produces a close approximation to the test results. This includes both dense nailing and sparse nailing, and elastic and inelastic behavior with unloading.

3. With the introduction of the nonlinear diaphragm into the 3D building model, the maximum base shear demand under the Big Bear ground motion decreased to 220 kips, which is below the code design shear requirement of 247 kips. All connection components (old connections) to the glulam beams remained either elastic or very weakly nonlinear. The purlin to pilaster connections had a maximum displacement demand of 1.0 inch and a displacement ductility demand of 7.6. This is less than the average displacement capacity of 1.22 inches for the old connections obtained in the UC Irvine tests. The ductility demand was also less than the estimated 13.5 obtained from the test results of the old connections. The Hrennikoff elements have a maximum displacement demand of 0.78 inches and a displacement ductility demand of 4.5. Based on the test results, the displacement ductility capacity of the diaphragm is estimated to be 4.5.

4. Considering a nonlinear diaphragm with dense nailing and old connections, the base shear in the E-W direction under the Los Gatos motion was approximately 2.4 times the code value. The connection of the glulam to pilaster has a displacement demand of 0.89 inches and a ductility demand of 3.6. These are less than the 2.5 inches and 6.8 ductility values obtained from the tests. The axial load in the purlin to pilaster connection had a displacement demand of 1.2 inches, which is close to the test value of 1.22 inches for the old connections. The ductility demand was 5.2 compared with the estimated capacity of 13.5 from the tests. It should be noted that the purlin connection near the corner of the transverse wall has a significant vertical shear demand (Fig. 7.45) and that this is without considering possible effects of the vertical component of the Los Gatos ground motion.

5. Combining the dense nailing with the new connections and nonlinear diaphragm results in a reduced base shear demand under Los Gatos that is almost equal to the code requirement. All components of the glulam to pilaster connections remain elastic (Figs. 7.56–7.57). The displacement demand in the purlin to pilaster connections is reduced to 0.58 inches (Fig. 7.59) and the ductility demand is reduced to 3.5, which is less than the 9.4 obtained from the test data. The ductility demand estimated for the diaphragm is a modest 4.3, which compares well with the capacities obtained in the tests. Hence the combination of new connections and dense nailing should enable a building of this type to withstand a strong pulse-type earthquake motion such as that recorded at Los Gatos Presentation Center.

6. The sparse nailing with the old connections results in a base shear that is 1.7 times the code requirement. The glulam to pilaster connection has a displacement demand of 1.7 in. (Fig. 7.69) that is less than the 2.5 inch capacity obtained in the tests. The ductility demand is 5.7 compared with a capacity of 6.8 from the test program. The purlin to pilaster connections are critical, having an axial displacement demand of 0.92 inches (Fig. 7.71) that is close to the 1.22 inch capacity from the tests. The estimated ductility demand is approximately 9, which is within the 13.5 maximum obtained from the tests; however, the ductility demand for the vertical shear component has a value of 48. Also, use of the sparse nailing with the old connections places high displacement and ductility demands on the roof diaphragm, estimated to be near 37 (Fig. 7.73), and may not be sustainable.

7. With the inclusion of the new connections with the sparse nailing, the base shear is reduced such that there are only a limited number of excursions above the code base shear requirements. The maximum displacement ductility demand for all force components of the glulam to pilaster connection is 2.4, which is not excessive. The purlin to pilaster connections near the corner of the transverse wall are critical and have an axial displacement demand of 0.54 inches (Fig. 7.81) that is less than the 1.13 inches obtained in the test results. The estimated ductility of 3.2 is also less than the 9.4 of the tests. However, the vertical shear is critical in these connections, with the displacement

ductility demand reaching 13. The ductility demands in the roof diaphragm are also high, reaching a maximum value of 13.2, which may not be sustainable.

Table 9.1 Connection force components (kips)

Los Gatos ground motion

	PURLIN TO PILASTER				GLULAM TO PILASTER		
Condition	Axial	Vertical	Horizontal		Axial	Vertical	Horizontal
Elastic	21.9	9.9	71.9		46	6.1	62
Old Connection*	13.2	5.	29		19	7.	5.5
New Connection*	18.5	7.1	39		34	5	7.5
Dense Nailing** Old Connection	4.9	11	2.8		18.0	8.5	2.8
Dense Nailing** New Connection	21.	26	7.0		35.	7.	6.7
Sparse Nailing** Old Connection	3.9	10.1	7.0		24.0	6.9	6.5
Sparse Nailing** New Connection	21.0	26.0	7.0		35.0	6.6	6.4

* Nonlinear Connections, Elastic Diaphragm

** Nonlinear Connections, Nonlinear Diaphragm (Hrennikoff model)

Table 9.2 Base shear (kips)

Los Gatos Ground Motion

Condition	Longitudinal (N-S)	Transverse (E-W)
Elastic	430	1430
Old Connections	346	820
New Connections	220	540
Code Required (UBC 1997)	247	247
Dense Nailing Old connections	350	810
Dense Nailing New Connections	220	530
Sparse Nailing Old Connections	150	320
Sparse Nailing New Connections	150	460

Table 9.3 Displacement ductility demand

Los Gatos ground motion

	GLULAM TO PILASTER			**PURLIN TO PILASTER**			**ROOF DIAPHRAGM**
Condition	Axial	Vert.	Hor.	Axial	Vert.	Hor.	Shear
Old Connection	4.0	E	E	100	13.1	E	E
New Connection	2.0	E	E	3.3	E	E	E
Dense Nailing Old Connection	3.6	E	E	8.0	56.7	E	18.3
Dense Nailing New Connection	E	E	E	3.5	7.4	E	4.3
Sparse Nailing Old Connection	5.7	E	E	9.0	48.0	E	36.8
Sparse Nailing New Connection	2.4	E	E	3.2	13.0	E	13.2

E = linear elastic

Maximum Ductility Capacities: Glulam to Pilaster: Old: 6.8 New: 3.1
Purlin to Wall: Old: 13.5 New: 9.4
Diaphragm: 4.5

10 Recommendations

1. **Connection Testing.** While the results from the tests conducted at UC Irvine were extremely useful for this study, they are not complete. Tests of the glulam to pilaster connections were conducted in the axial (parallel to grain) direction only. The results of this study indicate that similar tests considering the vertical shear (perpendicular to grain) and horizontal shear (parallel to wall and perpendicular to grain) are also required but not available. Also, the effects of combined loading on the connection may have a significant effect on the inelastic behavior. The same comments apply to the purlin to pilaster connections. In the case of the purlins, tests were conducted only in the axial direction (parallel to grain), and for these members the horizontal shear capacity may be important. It is strongly recommended that additional testing be conducted to verify the strength of these missing components. Newer construction of this type excludes the use of pilasters, with the connection of the glulam beams being made directly to the wall. Cyclic tests of this type of connection need to be conducted before further analytical studies. Analysis of recorded data indicates that the nailed connections may tend to loosen under cyclic loads. This aspect also needs to be investigated under controlled experiments.

2. **Diaphragm Testing.** These test results were also essential for the current study. Perhaps the biggest shortcoming of these tests was the lack of any documentation (photographs or sketches) of the failure modes of the tested panels. This would have been very useful for correlation with the analytical results obtained from the analytical models. In order to consider as many variations of roof panel configuration as could be accommodated within the test program, there was no evaluation of repeatability of the results, which may be important for this type of construction that is very dependent upon workmanship. Hence it is recommended that additional panel tests be conducted. It has also been noted

in this study that the timber diaphragm appears to be the weak link of this type of building system.

3. **Pushover Analysis.** Use of a static three-dimensional pushover analysis for determining the lateral resistance of a building system with a flexible diaphragm can be quite tedious and requires further investigation. The results of this study have indicated that such an analysis can be highly dependent upon the location and magnitude of the lateral forces, since the diaphragm may not be capable of distributing these forces to the lateral-resisting elements. The procedure of applying the lateral loads at the distributed masses of a detailed finite element model appears to work well but additional studies are necessary to fully develop the procedure.

4. **TUW Panels.** This study has placed emphasis on the behavior of a TUW building with cast-in-place pilasters between adjacent panels, since a building of this type was instrumented with accelerometers and had recorded the response of four previous earthquakes. Current design practice for TUW buildings excludes the use pilasters, resulting in a series of wall segments that are interconnected by chord steel located just below the roofline. In addition, an intermediate shear plate connector is often included midheight between the panels. A cursory analysis of a building of this type was considered in this study by modifying the existing model of the TUW building; however, a detailed analysis was beyond the scope of the current work. This analysis in which the tops of the panels were connected by the roof diaphragm showed no significant changes in the building performance due to the modified construction; however, a more detailed analysis of this type of system should be undertaken to verify these results and to investigate the connections in detail.

5. **Instrumentation Program.** To the best of the authors' knowledge, there is no instrumented TUW building with segmental wall panels representative of current construction practice. Hence it would be very helpful if the CSMIP Program would instrument one or two of these building systems as soon as possible.

References

ACI (1998), "Practitioner's Guide to Tilt-Up Concrete Construction," American Concrete Institute, PP-3, Farmington, Michigan.

Applied Technology Council, 1995, "Structural response modification factors," ATC-19, Redwood City, CA.

Bouwkamp, J. G., Hamburger, R. O. and Gillengerten, J. D. (1994), "Degradation of Plywood Roof Diaphragms Under Multiple Earthquake Loading," Data Utilization Report CSMIP/94-02, CSMIP, Sacramento, CA.

Bower, Warren H. (1974), "Lateral Analysis of Plywood Diaphragms," Journal of the Structural Division, ASCE, Vol. 100, No. ST4, April.

Carter, III, J. W., Hawkins, N. M. and Wood S. L. (1993), "Seismic Response of Tilt-Up Construction," Civil Engineering Studies, Structural Research Series No. 581, Dept. of Civil engineering, University of Illinois at Urbana-Champaign, Urbana, IL.

CSI (1998), "SAP2000, Version 7, Integrated Finite Element Analysis and Design of Structures,", Computers & Structures Inc., Berkeley, CA.

EERI (1996), "Tilt-Up-Wall Buildings," *Northridge Earthquake of January 17, 1994 Reconnaissance Report*, Vol. 2, Earthquake Engineering Research Institute, Oakland, CA.

Hall, J. (1999), "Seismic Response of Tilt-Up Buildings

Hamburger, R.O. and McCormick, D.L. (1994), "Implications of the January 17, 1994 Northridge Earthquake on tilt-up and Masonry Buildings With Wood Roofs, Proceedings, 1994 SEAOC Convention.

Hamburger, R.O., McCormick, D.L. and Hom, S. (1988), Performance of Tilt-up Buildings in the October 1, 1987 Whittier Narrows Earthquake, EERI Spectra 4, 1, Earthquake Engineering Research Institute, Oakland, CA.

Hawkins, N. M., Wood, S. L. and Fonseca, F. S. (1994), "Evaluation of Tilt-Up systems," Proceedings, Fifth National Conference on Earthquake Engineering, EERI, Vol. 3.

Hrennikoff, A. (1941), "Solution of Problems of Elasticity by the Framework Method," Transactions, ASME, Journal of Applied Mechanics, December.

Johnson, M. A., and Fonseca, F. S. (1998), "Seismic Response of Reinforced Concrete Tilt-Up Wall Panels," Proceedings, Sixth U.S. National Conference on Earthquake Engineering, EERI, Oakland, CA.

Lyons, R. T. and Gebhart, K. (1994), "Three Tilt-Up Buildings," Northridge Building Case Studies Project, California Seismic Safety Commission, Sacramento, CA.

Mehrain, M. and Graf, W. P. (1990), "Dynamic Analysis of tilt-Up Buildings," Proceedings, Fourth National Conference on Earthquake Engineering, EERI, May.

Scawthorn, C. and McCormick (2003), "Precast and Tilt-Up Buildings," Chapter 14 of the "Earthquake Engineering Handbook," edited by W-F. Chen and C. Scawthorn, CRC Press LLC, Boca Raton, FL.

SEAOC (2000), Seismic Design Manual, Volume 2, Building Design Examples, Light Frame, Masonry and Tilt-up, Structural Engineers Association of California, Sacramento, CA.

SEAONC (2001), "Guidelines for Seismic Evaluation and Rehabilitation of Tilt-up Buildings and other Rigid Wall/Flexible Diaphragm Structures," Structural Engineers Association of Northern California, San Francisco.

Szilard, R. (1974), "Theory and Analysis of Plates, Classical and Numerical Methods," Prentice-Hall, Inc., Englewood Cliffs, New Jersey.

Wallace, J. W., Stewart, J. P., and Whittaker, A. S., (1999), "Building Vulnerability Studies: Modeling and Evaluation of Tilt-Up and Steel Reinforced Concrete Buildings," Report No. PEER 1999/13, Pacific Earthquake Engineering Research Center, University of California, Berkeley, CA

.

Wood, S. L. and Hawkins, N. M. (1998), "Measured Response of Two Tilt-Up Buildings," The Loma Prieta, California, Earthquake of October 17, 1989-Building Structures, U.S. Geological Survey Professional Paper 1552-C, USGS , Denver, CO.

Appendix A: A Summary of the UC Irvine Tests

Stiffness of Timber Diaphragms and Strength of Timber Connections

OVERVIEW AND SUMMARY

To complement the ongoing analytical studies of tilt-up wall buildings, an experimental program was conducted to provide the following mechanical characteristics for typical timber roof diaphragms: stiffness of the diaphragm as well as strength for the timber roof to wall connection. Beside these two characteristics, the reviewers will comment about the maximum deformation, the mode of failure, the ductility, and the energy-dissipation capacity due to plastic deformation.

Stiffness Tests of the Roof Diaphragm Panel: They considered the cyclic load (resistance) vs. deflection characteristics of six representative roof diaphragm panels (five 16′ x 20′ and one 20′ x 16′) under different nail and stud (subpurlin) spacing conditions as well as under different time histories of the cyclic loading (hysteresis loops) (Tables A1–A2).

Strength Tests of the Timber Roof-Wall Connections: They considered the load-deflection characteristics for 12 different connections (representative of old and new construction methods) comprising the following test matrix.

1. Glulam beams (GLB) to column connection (4 tests) (Table A3)
2. Diaphragm to 3″x12″ ledger, (purlin-to-wall) connection (4 tests) (Table A4)
3. Diaphragm to 3″x6″ ledger (subpurlin to wall) connection (4 tests) (Table A5)

The six panels and the 12 connections that were tested were representative of configuration and conditions found in PG&E's Fremont, California, facility.

Summary of Results

Stiffness Tests of Roof Diaphragm: A general description of the roof diaphragm test matrix is given in Table A1**.** All diaphragms used ½″ structural I plywood with 10d (2-¼″x 0.148″ ϕ-9 gage) pneumatically driven nails.

Test Setup: Figure A1 shows a test setup schematic for sample roof diaphragm 2 (RD2). All the other samples (RD1, RD3, RD4, RD5, RD6) were tested by racking the 16′ edge rather than the 20′ edge as shown in Figure A1.

Test Protocol*:* All the samples except RD4 were subjected to a reversed cyclic deformation specified according to the ATC-4 displacement protocol shown in Figure A2. The sample RD4 was subjected to an ersatz fling displacement time history (Figure A3(d)).

Test Results: From analysis of the lateral load (resistance) – displacement diagrams shown in Figure A3, it is possible to extract from each recorded hysteretic diagram the following very important qualitative and quantitative data regarding the following important mechanical characteristics.

Lateral stiffness: The largest initial lateral stiffness of about 18 kips/in. has been provided by RD2 as shown in Figure A3(b). When the results obtained are normalized with respect to the racking edge length, the stiffness is slightly higher (10%) than that of sample RD1 (about 13.0 kips/in.). This 13 kips/in. is smaller (about 20%) than that provided by the specimen RD5 (about 10 kips/in.).

Yielding strength (load): Normalizing the observed (recorded) yielding loads (Fig. A3) as the load per foot of length of racking, the values given in Table A2 are obtained. The highest yield strength is provided by specimens RD3 and RD6 at 938 #/ft. These are the two specimens with the highest nailing density, which have a yield strength 2.3 times higher than the specimens RD1 (406 #/ft) and RD2 (500 #/ft), which had a lower nailing density.

Post-yield deformation: All the specimens showed deformation hardening after yielding. The rate of hardening is significantly higher for specimens RD3 and RD6 (i.e., the specimens with the higher density of nailing). RD1 had a post-yielding stiffness of about 13% of the initial lateral stiffness and RD3 had about 34% of the initial stiffness.

Maximum strength (resistance): The diagrams of Figure A3 clearly show that the specimens RD6 (about 24 kips) and RD3 (about 26 kips) had the larger maximum strength being their normalized maximum resistance about 1500 #/ft and about 1625 #/ft, respectively (Table A2). When the resistances are compared with that of specimen RD1 (about 1100 #/ft) that had a smaller density of nailing than the specimens RD6 and RD3, and with the resistance of specimen RD5 (about 719 #/ft), which had the smallest density of nailing, the advantage of the higher density of nailing is clear.

Maximum (ultimate) deformation (displacement): From analysis of the resistance-deformation diagrams shown in Figure A3, it is clear that the maximum deformation (displacement at what was considered to be the failure of the specimen) was provided by specimen RD4 (about 7.6 inches) that corresponds to a drift index of about 4%. This specimen was the only one that was subjected to a fling-type deformation. Of the remaining specimens that were deformed according to the test protocol of Figure A2, specimen RD6 (Fig. A3(f)) resisted the larger displacement (about 6 in.) but already with a degradation of the strength from 24 kips to 10 kips (i.e., a reduction of about 58%) at a displacement of about 5 inches (i.e., a drift index of about 2.6%). From the results it is clear that the test protocol had a significant influence on the maximum deformation. If it is considered that the fling (under negative loading) started at about 1.0 inches, the total deformation resisted to the fling was about 8.6 inches (i.e., about 8.6/5.0=1.72 times more than those specimens subjected to the test protocol of cyclic deformation).

Maximum ductility: By idealizing the envelopes of the resistance versus deformation diagram as a bilinear elasto-perfectly-plastic behavior, it is possible to estimate the maximum ductility for each specimen. For specimen RD4 tested by a fling, the maximum displacement ductility could be as large as 9.0, and is the largest of all the specimens tested, as shown in Figure A3(d). Among all the specimens tested under the cyclic deformation (according to the test protocol of Fig. A2), the largest ductility corresponds to specimens RD1 and RD5, with a value of about 4.5. The smallest ductility was 4.0 developed by specimen RD6.

Maximum energy dissipation due to plastic deformation: By considering the envelopes for the specimens that were submitted to the test protocol and then compared with the corresponding results of specimen RD4 tested under fling, it can be concluded that this $E_{h\mu}^{+}$ of RD4 is

somewhat larger than the $E_{h\mu}^-$ and the $E_{h\mu}^+$ (about 110 in.-kips for RD4 and 90 in.-kips for RD6 and RD3). These use very crude approximations and thus a better computation should be done. However, considering that the specimens deformed according to the test protocol at each of the three cycles to which they were subjected at each deformation step, and dissipated energy, it is obvious that the total $E_{h\mu}^-$ (as well as the $E_{h\mu}^+$) were larger than the $E_{h\mu}^-$ of specimen RD4. Specimen RD5 that was constructed with 50% fewer studs (subpurlins) and therefore smaller density of nails had the smallest $E_{h\mu}$ capacity among all the specimens tested. The envelope of $E_{h\mu}^+$ was approximately the same as that of $E_{h\mu}^-$ and was approximately 35 in.-kips (i.e., about 2.6 times smaller than that of specimen RD6 and RD3, and about 1.5 times smaller than the $E_{h\mu}^-$ of specimen RD1). This is a consequence of the 50% fewer studs and the consequence of smaller density of the nailing.

Modes of failure: The modes of failure of all roof diaphragms were characterized by a pop-out type of failure of the plywood. The out-of-plane separation occurred between some of the panel assemblies (2x4 subpurlins (studs) with the plywood cover) and the 4x12 purlins. The likelihood of this type of failure in the case of the behavior of the roof diaphragm in the real tilt-up building construction is considerably smaller than in the tests due not only to the effect of the gravity load of the plywood panel but also to the roofing material used in real construction.

Observations Regarding the Effects of the Different Variables Considered in the Tests:
From analysis of the above results, the following observations can be made regarding the effects:

The effect of the type of time-history on the hysteretic loops: Comparing the deformation of RD4 and RD1 it is clear that the fling deformation of RD4 rather than the repeated cyclic deformations required by the test protocol on specimen RD1 resulted in an increase in the maximum strength (25%) and in the displacement at failure (70%). The maximum ductility of RD4 was about two times that of RD1. The lateral stiffness is practically not affected.

The effects of the spacing of the studs (subpurlins): Comparing the results obtained in the test of RD5 that represents old construction with the results obtained in the test of RD1 representing new construction, with twice the number of studs than RD5, shows a decrease in lateral stiffness (33%), decreases in maximum strength, practically the same ultimate displacement at failure (5 in.), and about the same maximum ductility but significantly smaller $E_{h\mu}^+$ and $E_{h\mu}^-$. From

comparison of the results obtained in the tests of RD6 and RD3 with a significantly higher nailing density than the specimens RD5 and RD1, there was practically no effect of the spacing of studs on the lateral stiffness, the yield load, and the maximum resistance. Although there was practically no effect on the maximum (ultimate) displacement, specimen RD6 showed an early degradation of its strength (3 in. for RD6 and 3.5 in. for RD3). From these observations it can be concluded that the spacing or number of studs contributes more to the mechanical characteristics of a lightly nailed shear panel than to those of a densely nailed shear panel, and that the increase in edge and continuous edge nails had much more of an influence on this performance than the number of studs.

The effect of density of nailing: Based on the test results for the specimen RD1 with spacing of nails of 6 inches the initial lateral stiffness was 13 kips/in., the yield load was 6.5 kips, the maximum strength was 16 kips, and the ultimate displacement was about 5 inches, resulting in a ductility of about 4.5 and in a $E_{h\mu}^{+} = E_{h\mu}^{-} \cong 50$ kip-in. considering just the envelope. The test results for RD3 with a denser nailing pattern of 2 inches o.c. for ledger and continuous edges and 3 inches o.c. for other edges, the initial lateral stiffness, the yield load, the maximum strength, the ultimate displacement, the maximum ductility, and the $E_{h\mu}^{+} = E_{h\mu}^{-}$ (considering just the area under the envelope) were about 16.5 kips/in., 15 kips, 26 kips, 5 inches, 4.0 and 90 kip-in., respectively. Thus there is no doubt that the denser nailing pattern resulted in a significant improvement on the mechanical behavior of the shear panel.

Strength Tests of Glulam Beam-Column Connections

Specimens tested: To assess the effects of the connections between a GLB and a concrete column, two double-ended columns were constructed and tested. One column was constructed with an old GLB seat at each end, whereas the other column was constructed using a new GLB seat. The double-end construction thus provided an opportunity to test two of the same GLB seat connections from a single column. The old construction consisted of a 12″ x 12″ cross-section column and the new construction consisted of a 12″ x 16″ cross-section column. These two columns have the same type of reinforcement. While the GLB seat construction for the old column was a Simpson GLB-5A, for the new column the GLB seat was a Simpson GLB 512. Table A3 provides the construction details and results for the 4 GLB-column connection tests.

Test results: Figures A4 and A5, respectively, depict the monotonically increased displacement versus the displacement behavior of the beam-column connection with old and new connections, as well as the NDS (National Design Specifications) that are based on allowable stress design loads. From analysis of the resistance versus displacement plots, shown in Figures A4 and A5, the following qualitative and quantitative data regarding the following important mechanical characteristics are derived.

Qualitative overall performance: The new connection appears to have a more pronounced, idealized bilinear elasto-plastic behavior, with both a higher yield load and a higher maximum load than the old connection. Thus it would appear that the new construction is more attractive than the old. However, it must be noted that the ratio of the maximum resistance to the NDS design load was higher for the old (about 5.2) than for the new construction (about 4.4). Furthermore, the plots do not give any idea about the mode of failure. From the observations of the tests it was concluded that the old connection had a more ductile type of failure.

Quantitative performance: From a bilinear, elasto-perfectly-plastic idealization of the average curves of Figures A4 and A5, the following mechanical characteristics have been estimated.

> *Stiffness:* The old construction specimens showed an average stiffness of about 60 kips/in., which is 36% higher than the average stiffness of the two new specimens.
>
> *Yielding strength:* Although the idealized yielding of the old specimens was estimated to be about 26 kips, the actual yielding started at about 13 kips. The new specimens behaved practically elastically up to a load of 26 kips, and the idealized yielding strength was about 34 kips.
>
> *Type of deformation after yielding:* The old specimens showed significant deformation hardening after the yielding load of 13 kips. This deformation hardening continued up to reaching its maximum strength of about 31.4 kips. The new specimens after reaching their yielding strength of about 26 kips showed some deformation hardening up to its maximum strength of about 36.3 kips. After the old specimens reached their maximum strength, they showed significant softening, dropping their strength from 31.4 kips to about 24 kips. The new specimens after reaching their maximum values showed small softening.

Maximum strength (load): The average maximum strengths recorded for the old specimens were 32.8 kips and 29.9 kips, resulting in an average value of 31.4 kips, which is lower by about 13.5% than the average value of the maximum strength of the two new construction specimens [36.25 = (37.5+35.0)/2].

Maximum ultimate displacement: The two old specimens failed at 2.5 inches. The two new specimens failed at somewhat different displacements, one at 2.5 inches, the other at 2.3 inches.

Maximum ductility: Considering the idealized bilinear elasto-perfectly-plastic idealization, the maximum ductility of the old specimens (6.0) was 94% higher than the maximum ductility (3.1) of the new specimens.

Maximum energy dissipation: The approximate value of $(E_{h\mu})_{max}$ for the old specimens was 53 kip-in., which resulted in being about 5% lower than the $(E_{h\mu})_{max}$ of the new specimens (56 kip-in.).

Mode of failure: After straining the specimens beyond their maximum strength, the old connection never experienced complete failure or fracture of the GLB. However, the new connections experienced a fracture, i.e., a type of brittle fracture that was the result of cross tension induced by the rotation of the bolt couple relative to the GLB. The resulting split occurred along the lines of the bolts. The failure of the old connection was due to yielding of the bolts and localized crushing of the glulam beam at the bolt holes.

Conclusions: Although the new connection may have had slightly higher yielding resistance and offered a higher maximum strength and $E_{h\mu}$, the old connection may have had a more ductile behavior than the new. Thus there is a need to develop a connection that behaves in a reliable ductile fashion. This perhaps could be achieved by avoiding the splitting by using either the skewed bolt pattern and by using three smaller diameter bolts, rather than two, or by using stitch bolts as shown in Figure 5-31 of the SEAOC Guidelines [SEAOC, 2001].

Strength Tests of Purlin-to-Wall Connections

Specimens tested: A representative purlin to wall connection in the Fremont Meter Repair Facility entailed the connection of a 4″ x 12″ purlin to a 3″ x 12″ ledger. A typical purlin to wall connection was constructed to both the old (1970's era) and the new (mid to late 1980's era) construction details. Table A4 provides the test matrix for the purlin to wall strength tests. Figure A6 illustrates the Simpson PA-18 purlin to wall connection for the new construction.

Test results: Figures A7 and A8 depict, respectively, the monotonically increasing displacement-resistance (load) behavior for the purlin to wall connections with the old and new connections. By comparing the diagrams plotted in Figures 7 and 8, the following qualitative and quantitative observations can be made regarding the mechanical characteristics of the old and new connections:

Qualitative overall performance: The new connection exhibits both significantly higher yield resistance and maximum strength than the old connection. Additionally the new connection appears to have a more pronounced trilinear nonlinear behavior. While an elastic-perfectly-plastic idealization of each of the two diagrams seems to indicate that the old connection would provide a higher ductility, it is obvious that the amount of dissipated energy, $E_{h\mu}$, by the new connection is significantly higher than that provided by the old connection. Thus it might be concluded that the additional anchor bolts, the PA-18 strap and the "L" bracket in the new connection had a significant effect on the improvement of the performance with respect to the old.

Quantitative performance: From a bilinear elasto-perfectly-plastic idealization of the average curves of the plotted diagrams of Figures A7 and A8, the following mechanical characteristics have been estimated:

> *Stiffness, "k":* While the old connection has a stiffness of about 33 kips/in., the new had a stiffness of about 120 kips/in. (i.e., nearly 3.6 times that of the old).
>
> *Yield load:* The actual average yielding occurred at about 9 kips for the new and about 3 kips for the old. The idealized equivalent yielding for the new is about 18 kips versus 3.2 kips for the old.

Maximum strength: The actual average maximum strengths were 20.5 kips and 4.3 kips for the new and old connections, respectively. The idealized maximum strengths are about 18 kips and 3.3 kips, respectively.

Ultimate displacements: The average maximum displacements were 1.13 inches and 1.22 inches for the new and old connections, respectively.

Ductility: From the idealized load-displacement diagram, the μ_{max} were about 9.4 and 13.5 for the new and old connections, respectively.

Maximum hysteretic energy ($E_{h\mu}$): The ($E_{h\mu}$) of the idealized diagrams resulted in approximately 18 kip-in. for the new and only 3.6 kip-in. for the old.

Mode of failure: The failure in the two new specimens was not in the purlin-to-wall interface but rather at the subpurlin where the plywood was spliced. The old construction detailed panel failed by cross-grain splitting of the ledger.

Conclusion: From the above results it is concluded that there is no need to improve the presently used new connection if the nailing of the plywood to the subpurlin is not improved.

Strength Tests of Subpurlin-to-Wall Connections

Tested specimens: Four specimens very similar to those used in the tests of the purlin to wall connections were tested. Table 5 provides the test results for the four specimens tested. Figure 9 shows the subpurlin to wall connection hardware of the new construction specimen.

Test results: The performance of the new and old construction is illustrated in Figures 10 and 11, respectively. From a comparison of the diagrams plotted in these figures, qualitative and quantitative observations can be made that are very similar to those made for the purlin-to-wall connections that have been summarized above. The only significant difference is that the old construction samples failed at much lower displacement (an average of 1.0 inch) than the new construction samples (about 2 in.).

Conclusion: There is no need for improving the new type of connection if there is no improvement in the nailing of the plywood to their supporting elements.

Table A1 Stiffness tests: roof diaphragm characteristics

Sample	Height x Width	Edge Nailing	Continuous Edge Nailing	Sub-purlin Spacing
RD1	20 ft. x 16 ft.	6 in. o.c.	6 in. o.c.	2 x 4's @ 16 in. o.c.
RD2	16 ft. x 20 ft.	6 in. o.c.	6 in. o.c.	2 x 4's @ 16 in. o.c.
RD3	20 ft. x 16 ft.	3 in. o.c.	2 in. o.c.	2 x 4's @ 16 in. o.c.
RD4	20 ft. x 16 ft.	6 in. o.c.	6 in. o.c.	2 x 4's @ 16 in. o.c.
RD5	20 ft. x 16 ft.	6 in. o.c.	6 in. o.c.	2 x 4's @ 24 in. o.c.
RD6	20 ft. x 16 ft.	3 in. o.c.	2 in. o.c.	2 x 4's @ 24 in. o.c.

Note: All sheathing nails were 10d, 2-1/4" x 0.148" ϕ (9 gage)

Table A2 Stiffness tests: roof diaphragm loads; UBC, yield, ultimate

Sample	Height x Width	UBC Load (lb/ft)	Yield Load (lb/ft)	Ultimate Load (lb/ft)
RD1	20 ft. x 16 ft.	320	406	1000
RD2	16 ft. x 20 ft.	320	500	1100
RD3	20 ft. x 16 ft.	730	938	1625
RD4	20 ft. x 16 ft.	320	406	1250
RD5	20 ft. x 16 ft.	320	469	719
RD6	20 ft. x 16 ft.	730	938	1500

Table A3 Strength tests: glulam beam characteristics

Sample	Beam / Column Size	Beam Seat	Bolts	Ultimate / NDS Load (kips)
GLB1	5 1/8" x 12" / 12" x 12"	GLB-5A	(2) 5/8 in	29.9 / 5.99
GLB2	5 1/8" x 12" / 12" x 12"	GLB-5A	(2) 5/8 in	32.8 / 5.99
GLB3	5 1/8" x 12" / 12" x 16"	GLB-512	(2) ¾ in	35.0 / 8.26
GLB4	5 1/8" x 12" / 12" x 16"	GLB-512	(2) ¾ in	37.5 / 8.26

Table A4 Strength tests: purlin-wall connector characteristics

Sample	Length x Width	Ledger	Anchor Bolts	Straps	Edge Nailing @ Ledger	Edge Nailing @ 4x	Construction Era
PW1	8 ft. x 4 ft.	3 in. x 12 in.	(4) 5/8 in.	(2) PA-18	10d @ 6 in. o.c.	10d @ 6 in. o.c.	New
PW2	8 ft. x 4 ft.	3 in. x 12 in.	(4) 5/8 in.	(2) PA-18	10d @ 6 in. o.c.	10d @ 6 in. o.c.	New
PW3	8 ft. x 4 ft.	3 in. x 12 in.	(2) 5/8 in.	-	10d @ 2 in. o.c.	10d @ 3 in. o.c.	Old
PW4	8 ft. x 4 ft.	3 in. x 12 in.	(2) 5/8 in.	-	10d @ 2 in. o.c.	10d @ 3 in. o.c.	Old

Table A5 Simpson PA-18 purlin to wall connection

Sample	Length x Width	Ledger	Anchor Bolts	Straps	Edge Nailing @ Ledger	Construction Era
SW1	4 ft. x 4 ft.	3 in. x 6 in.	(1) 5/8 in.	(1) PAT-18	10d @ 6 in. o.c.	New
SW2	4 ft. x 4 ft.	3 in. x 6 in.	(1) 5/8 in.	(1) PAT-18	10d @ 6 in. o.c.	New
SW3	4 ft. x 4 ft.	3 in. x 6 in.	(1) 5/8 in.	-	10d @ 2 in. o.c.	Old
SW4	4 ft. x 4 ft.	3 in. x 6 in.	(1) 5/8 in.	-	10d @ 2 in. o.c.	Old

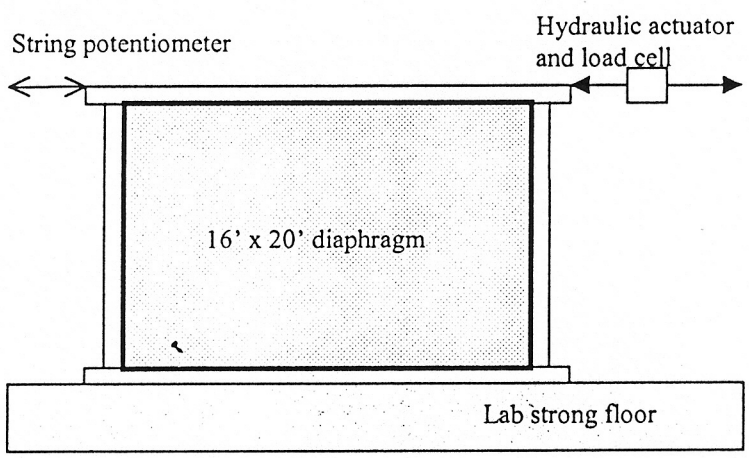

Fig. A1 Test setup for roof diaphragm 2

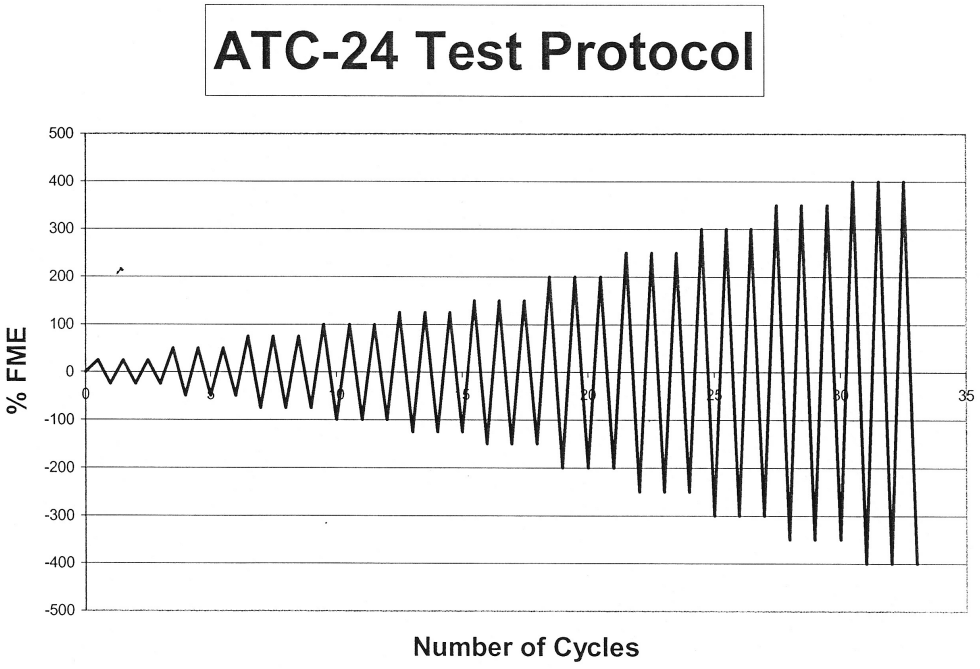

Fig. A2 ATC-24 test protocol for roof diaphragm tests

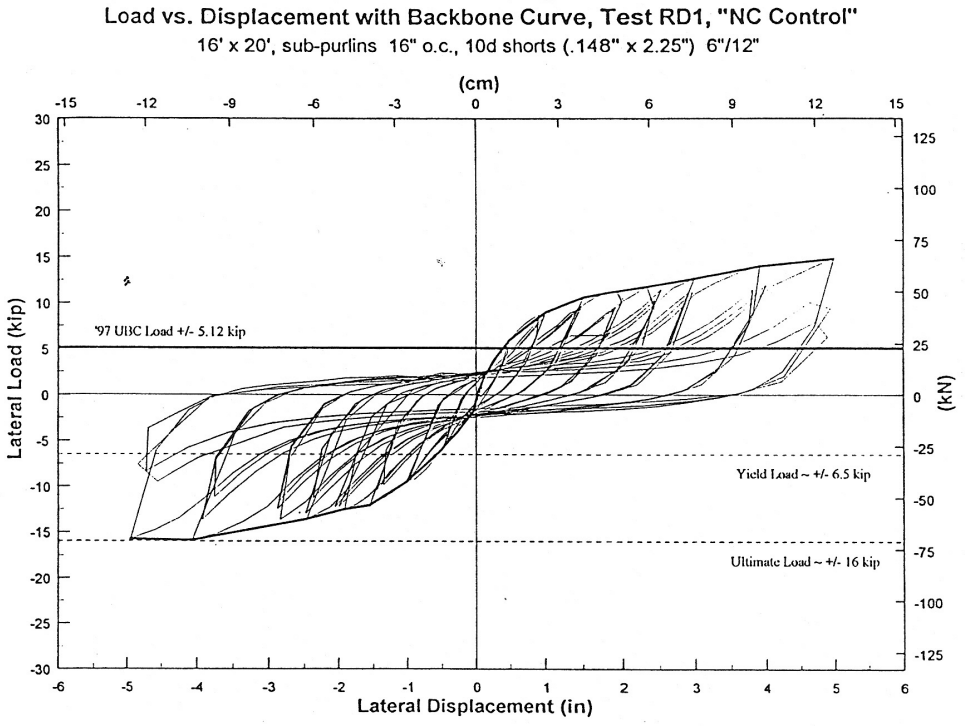

Fig. A3(a) Test RD1

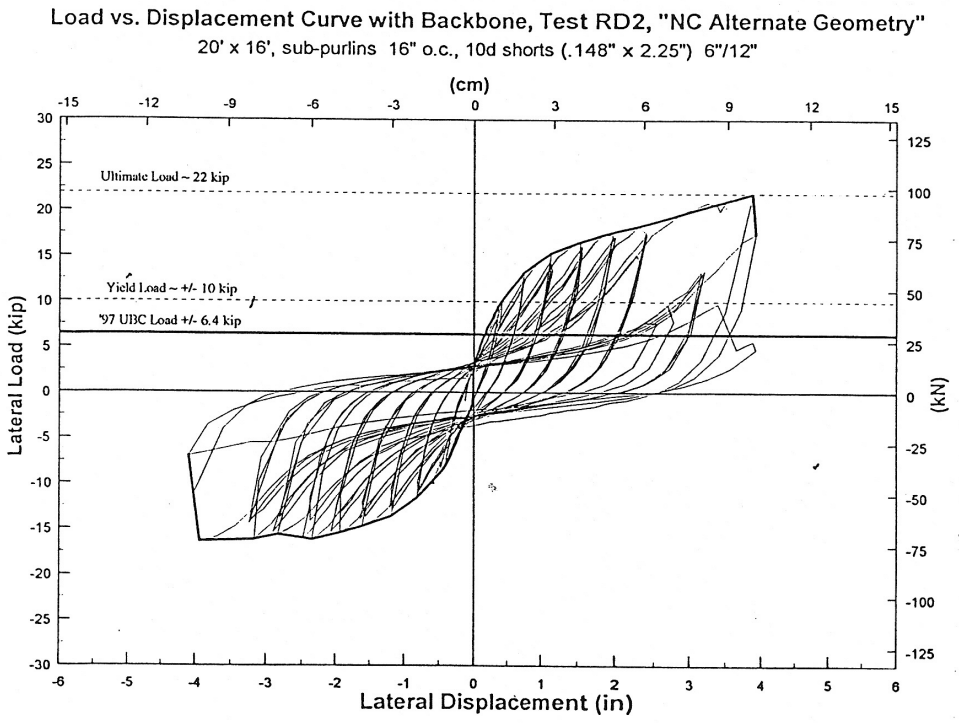

Fig. A3(b) Test RD2

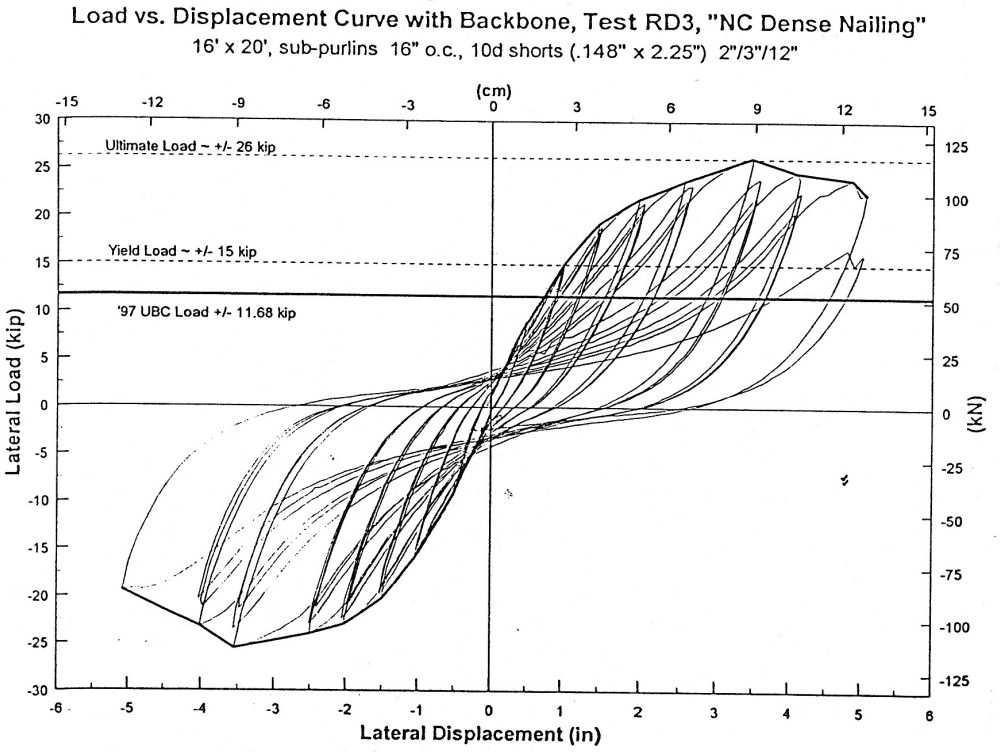

Fig. A3(c) Test RD3

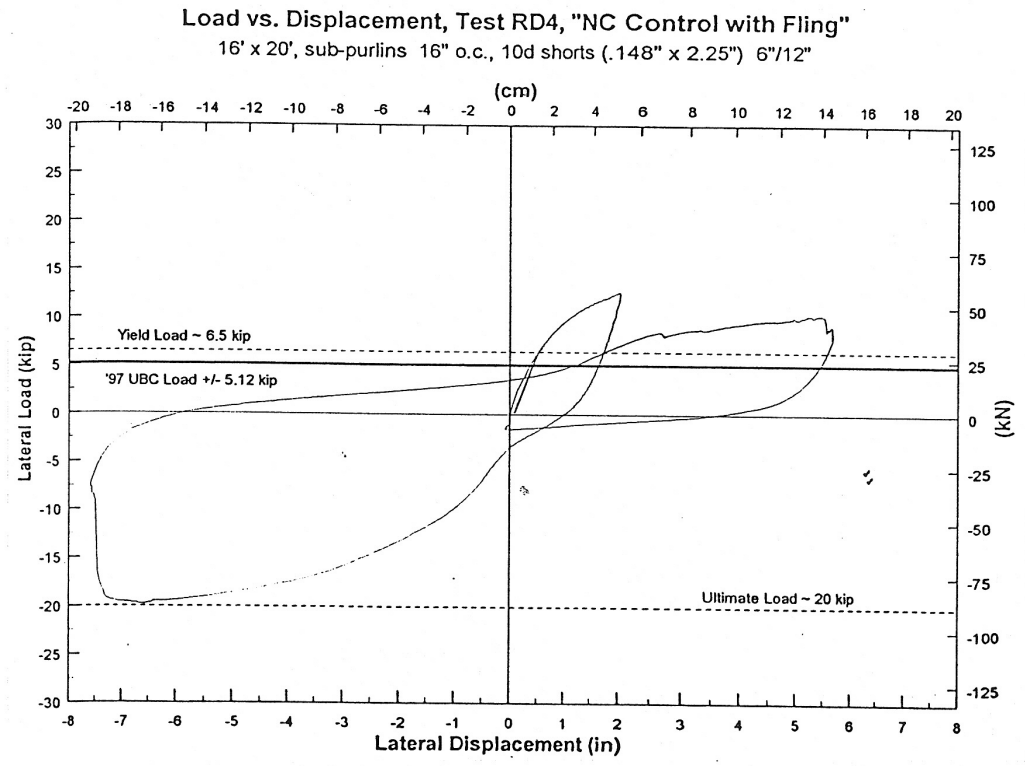

Fig. A3(d) Test RD4

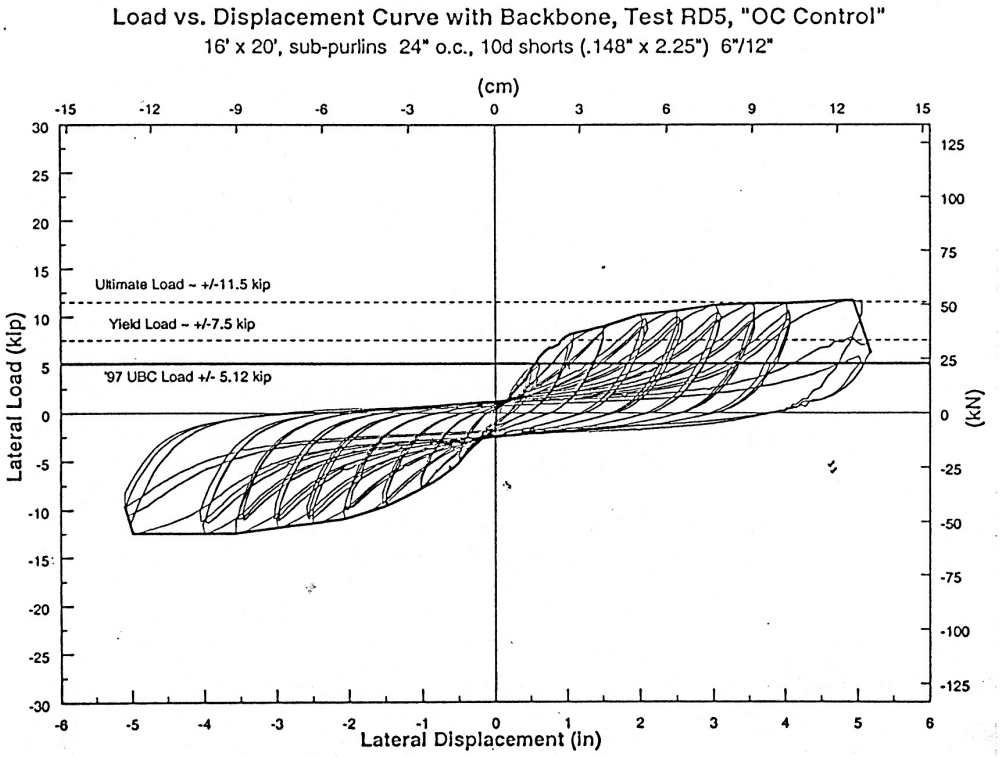

Fig. A3(e) Test RD5

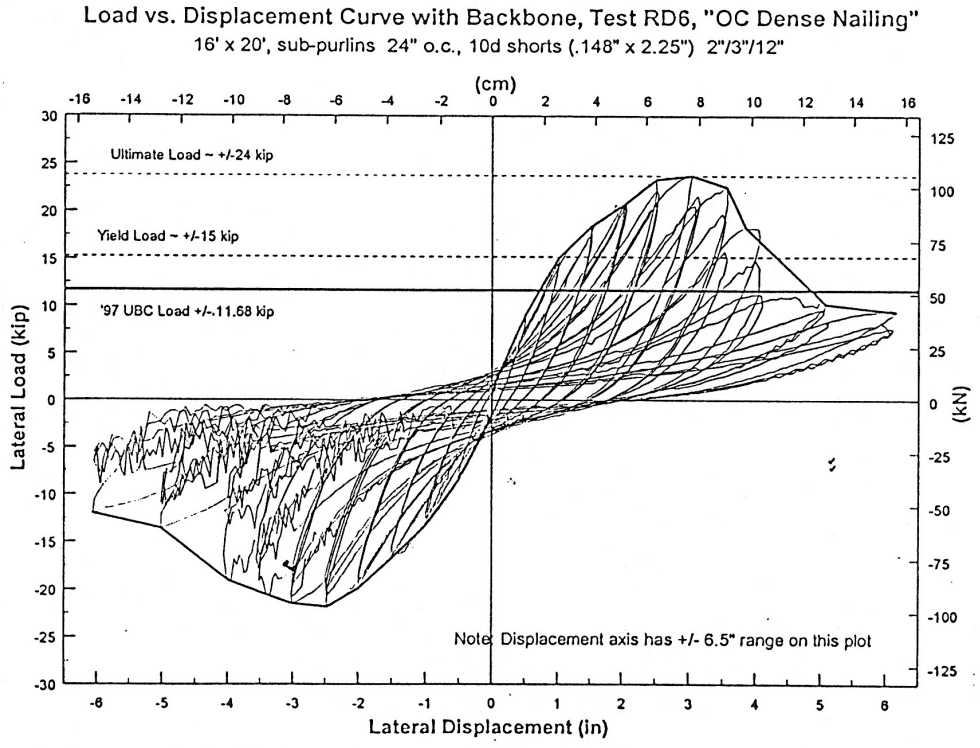

Fig. A3(f) Test RD6

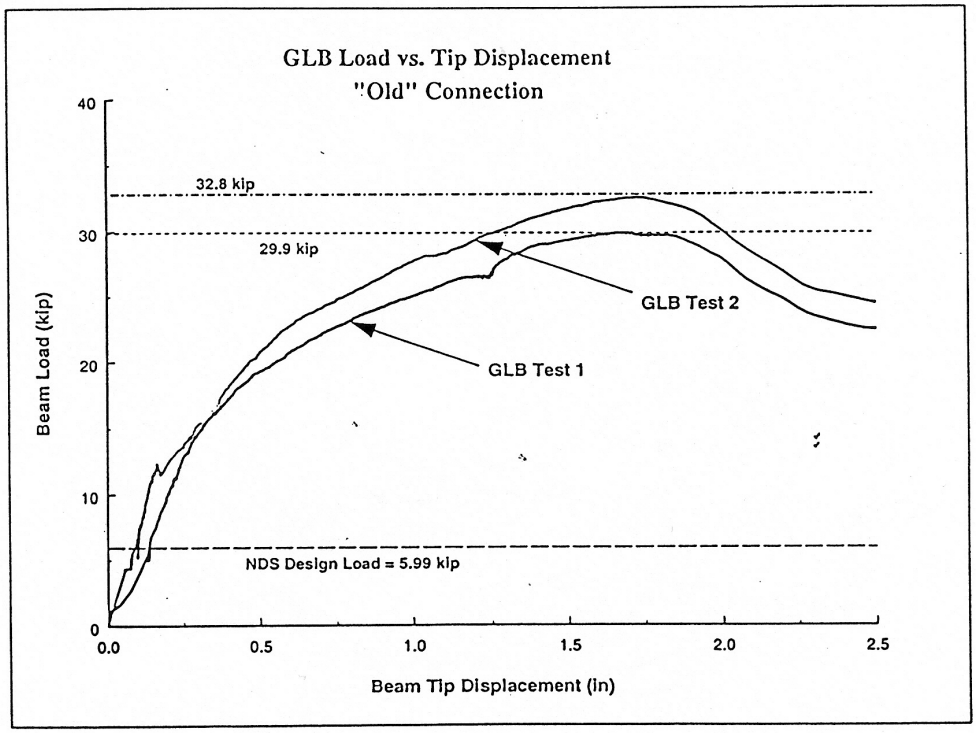

Fig. A4 GLB load vs. displacement (old)

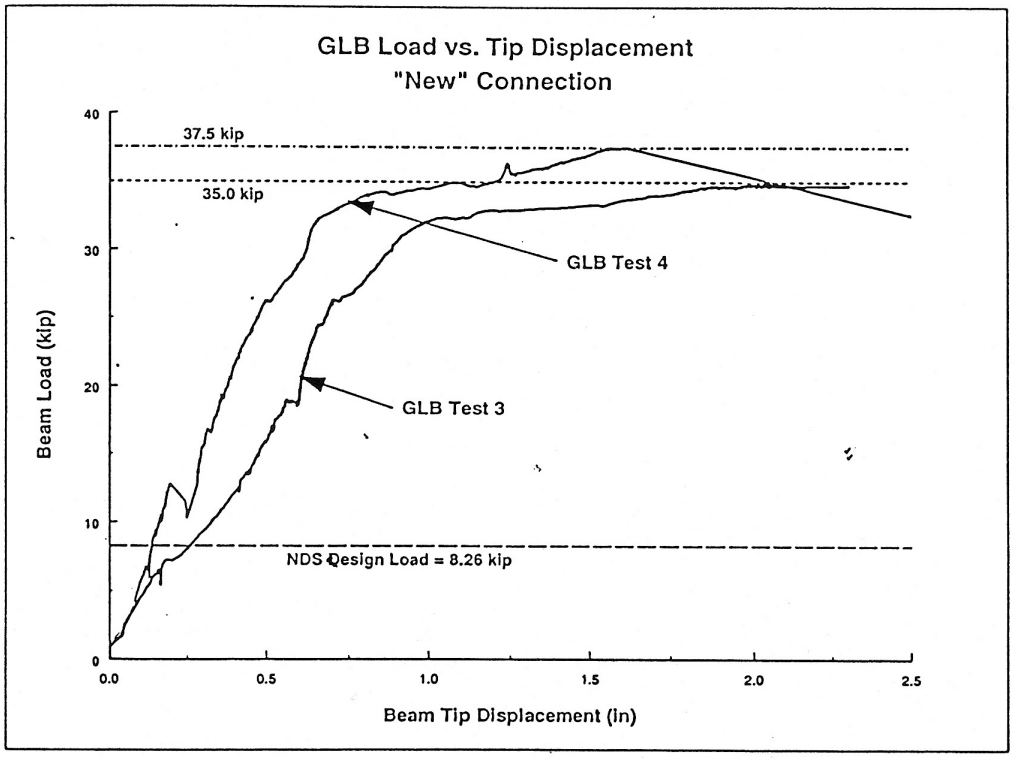

Fig. A5 GLB load vs. displacement (new)

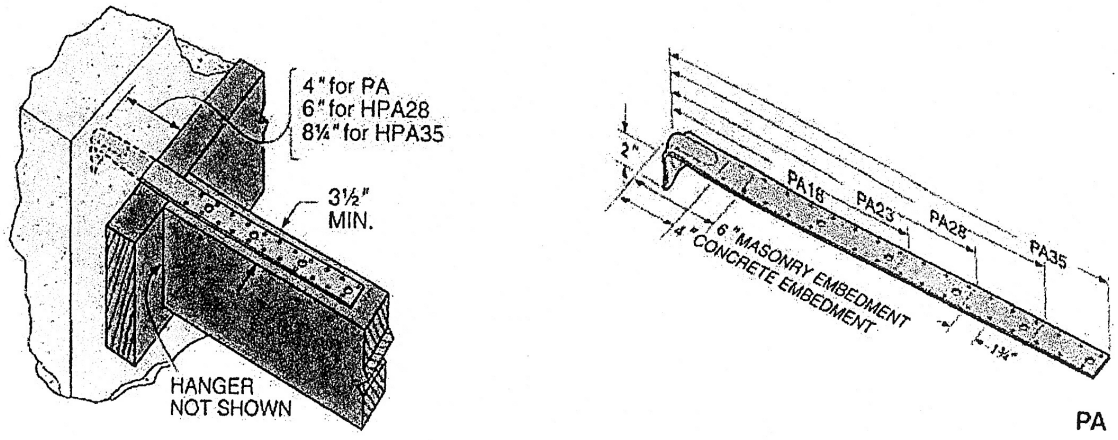

Fig. A6 Simpson PA-18 purlin to wall connection

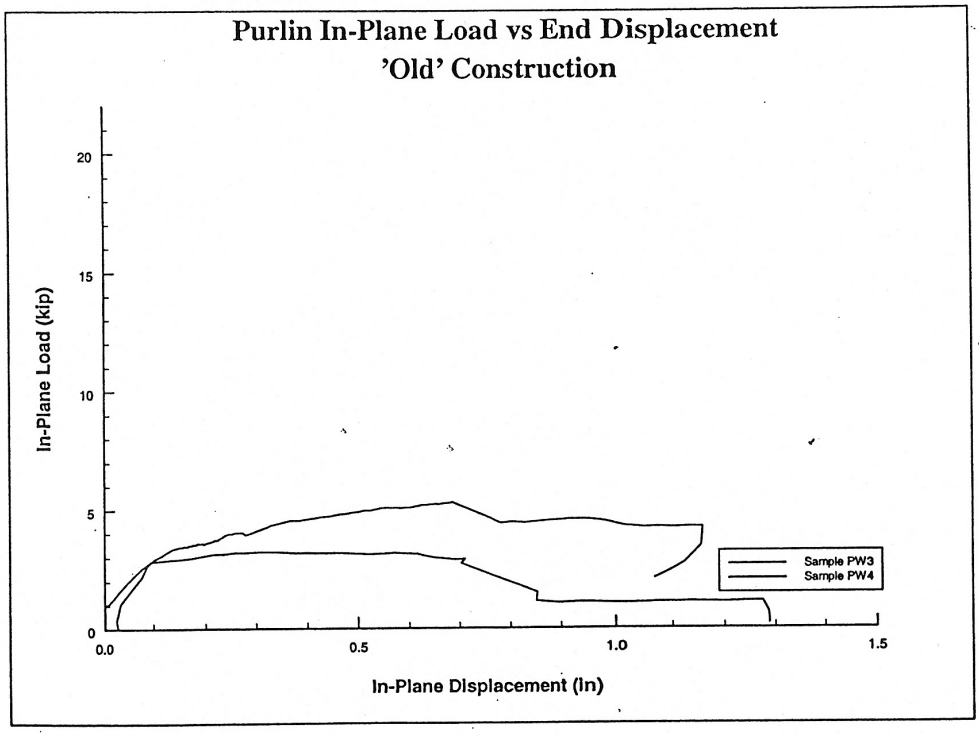

Fig. A7 Purlin in-plane load vs. displacement (old)

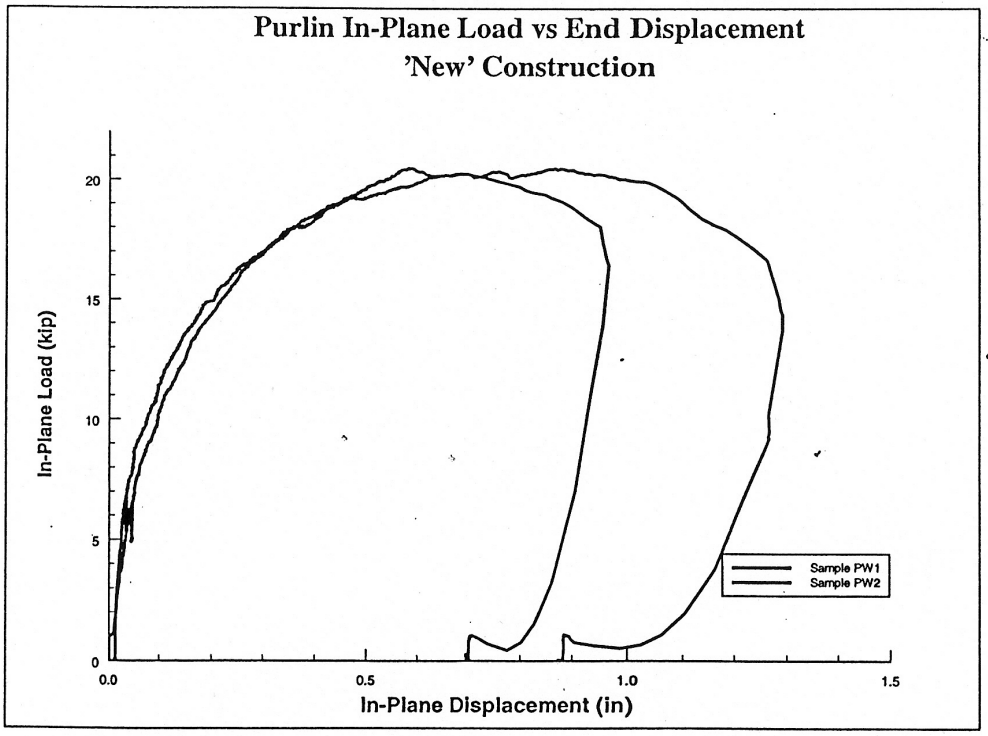

Fig. A8 Purlin in-plane load vs. displacement (new)

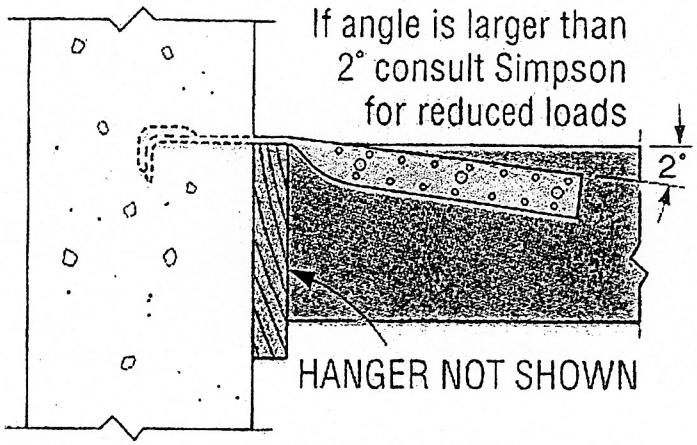

Typical PAT Installation

Fig. A9 Typical PAT installation

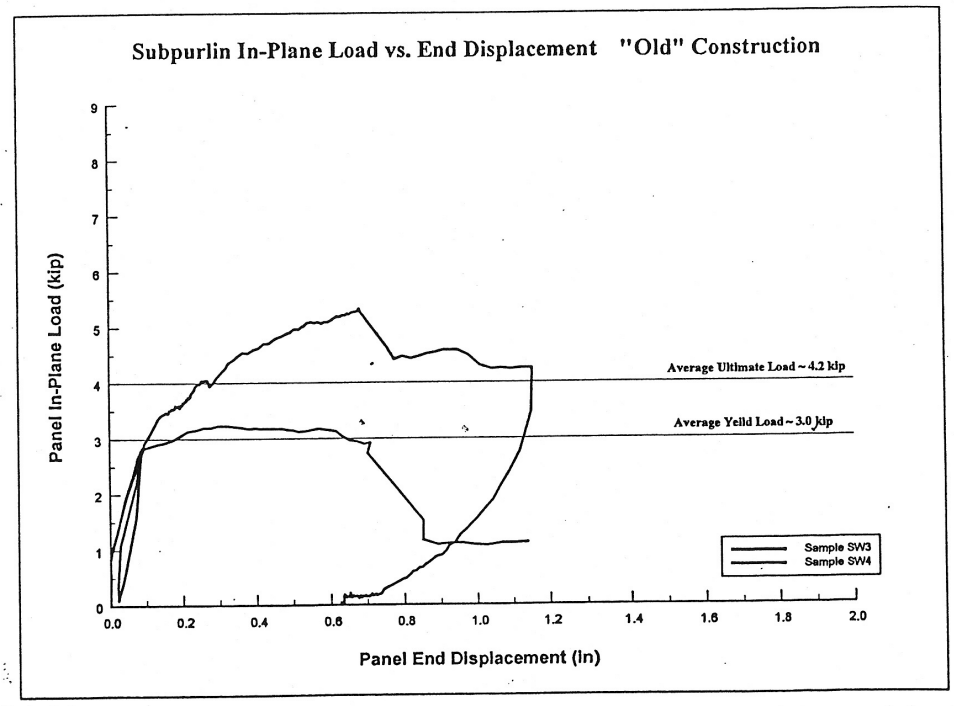

Fig. A10 Subpurlin in-plane load vs. displacement (old)

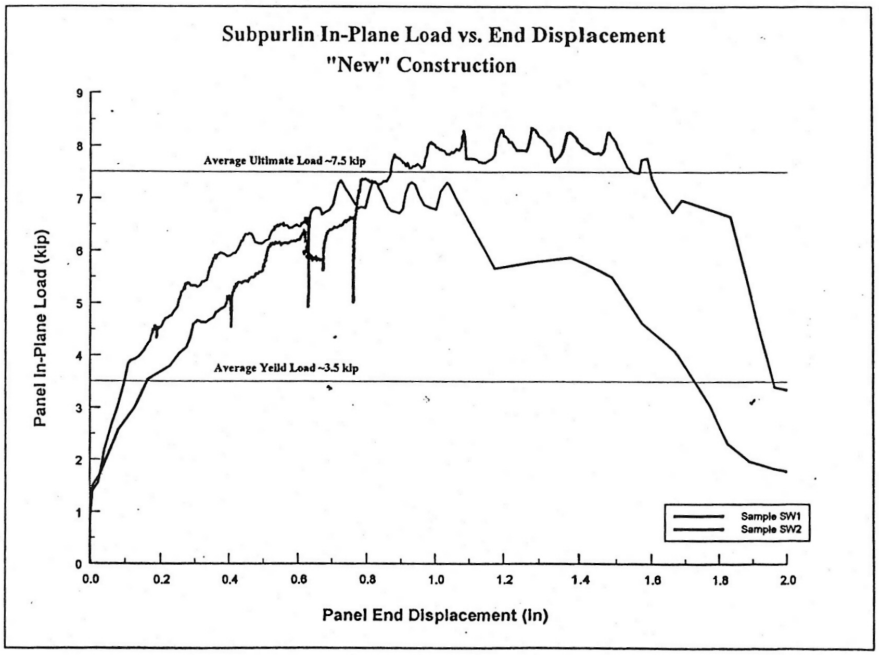

Fig. A11 Subpurlin in-plane load vs. displacement (new)

Appendix B: UBC 1997 Lateral Force Requirements

Since soil conditions are not known, Soil Type S_d will be used. The site is located in Seismic Zone 4 at a distance of approximately 6 Km from the San Jacinto fault, which is taken as a type-B fault. For these conditions, the near-fault factors are taken as: $N_a = 1.0$ and $N_v = 1.2$. Use of these parameters results in the following values for the seismic coefficients:

$$C_a = 0.44N_a = 0.44x1.0 = 0.44 \quad \text{and} \quad C_v = 0.64N_v = 0.64x1.2 = 0.768$$

The response reduction factor is taken as R = 4.5 and the occupancy importance factor is taken as I = 1.0. Using Method A, the fundamental period of the building is estimated as

$$T = C_t(h_n)^{3/4} = 0.02(27)^{3/4} = 0.23 \text{ seconds}$$

$$V = (C_vI/RT)\ W = (0.768x1.0/4.5x0.23)\ W = 0.742W$$

$$V \leq (2.5C_aI/R)\ W = (2.5x0.44x1.0/4.5) = 0.244W$$

$$V \geq (0.11C_aI)\ W = (0.11x0.44x1.0) = 0.0484W$$

$$V \leq (0.8xZxN_vxI/R)\ W = (0.8x0.4x1.2x1.0/4.5)W = 0.085W$$

Therefore, with the self weight estimated as W = 1013 kips, the design base shear is given as

$$V = 0.244W = 0.244x1013 = 247 \text{ kips}$$

Seismic Dead Load:

Glulam Beams:	80.87 kips
Purlins:	25.31 kips
Pilasters (half-height):	141.77 kips
Roof:	34.97 kips
Walls (half-height)	729.72 kips

Total Seismic Dead Load: 1012.64 kips

Appendix C: Recorded Earthquake Accelerations, Redlands Building

Palm Springs, July 8, 1986, M = 5.6

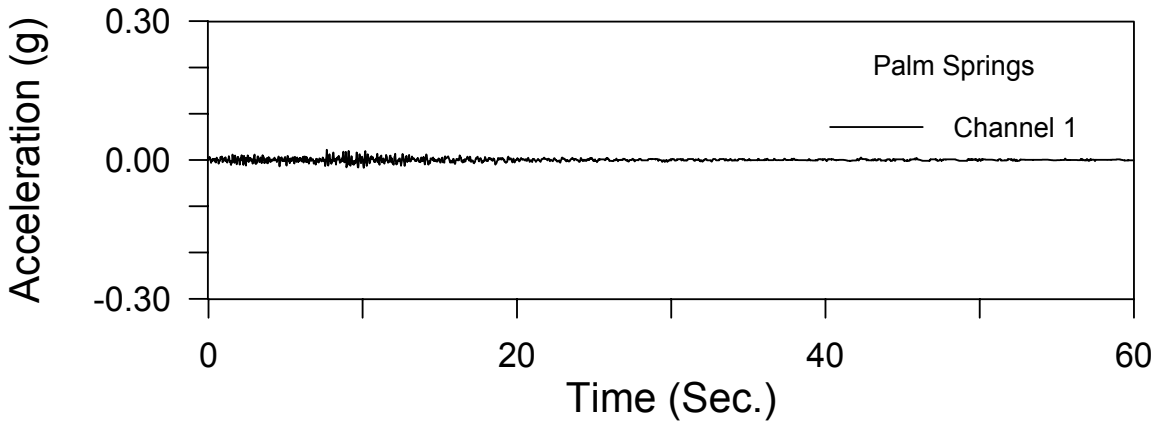

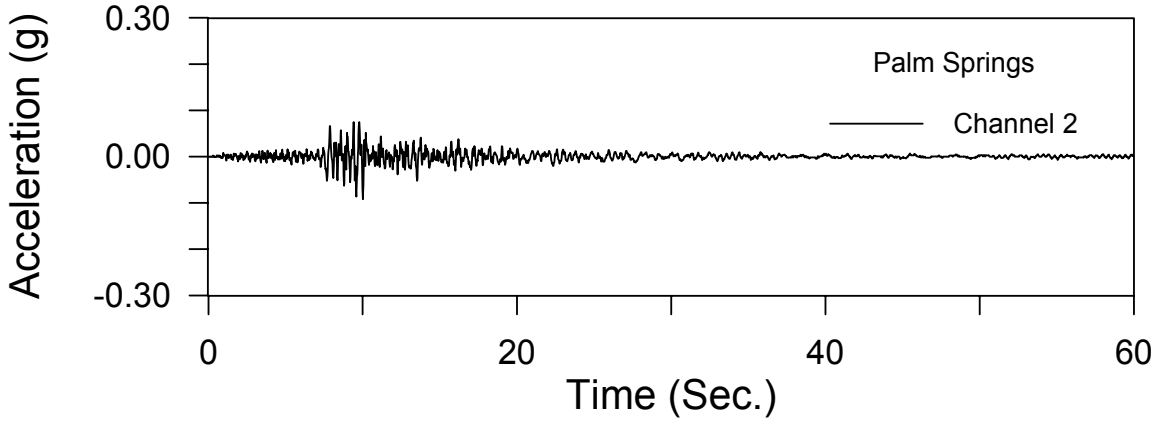

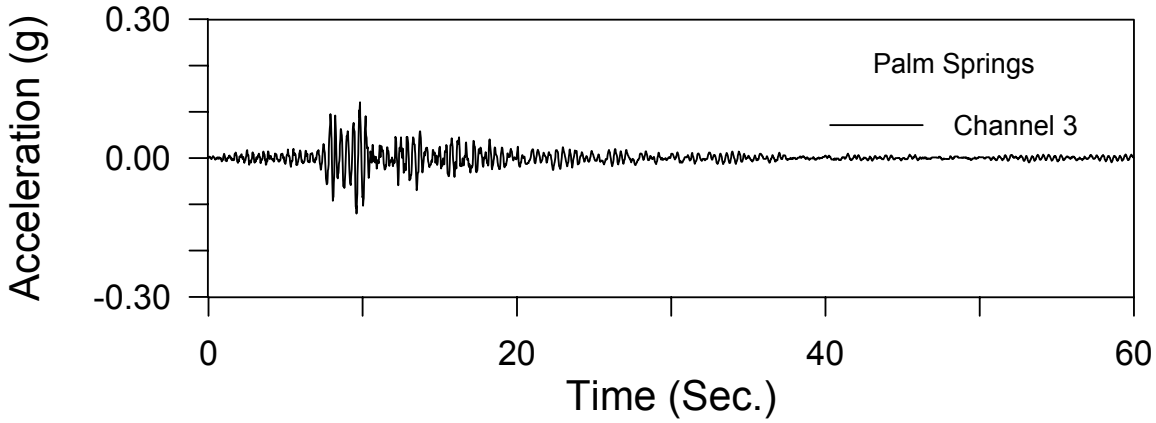
Acceleration (g)
0.30
0.00
-0.30
Palm Springs
Channel 3
0
20
40
60
Time (Sec.)

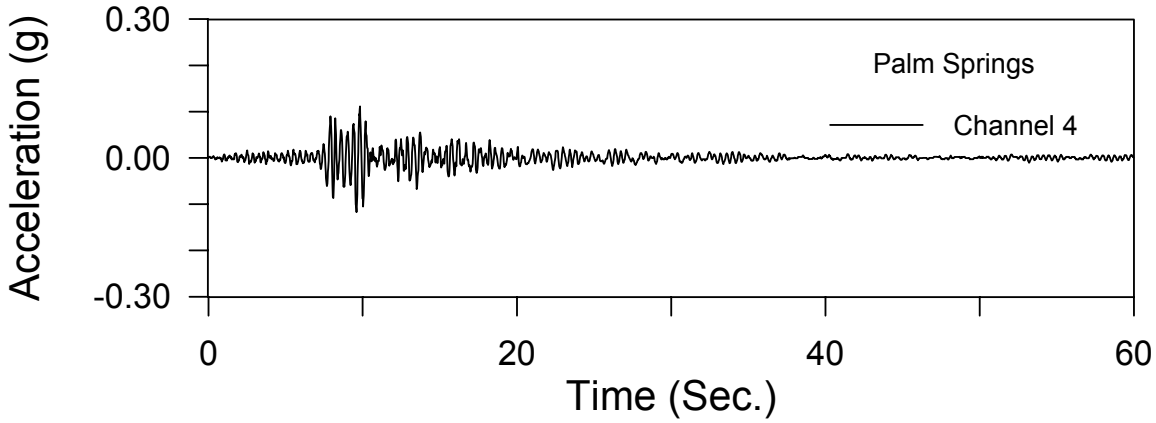
Acceleration (g)
0.30
0.00
-0.30
Palm Springs
Channel 4
0
20
40
60
Time (Sec.)

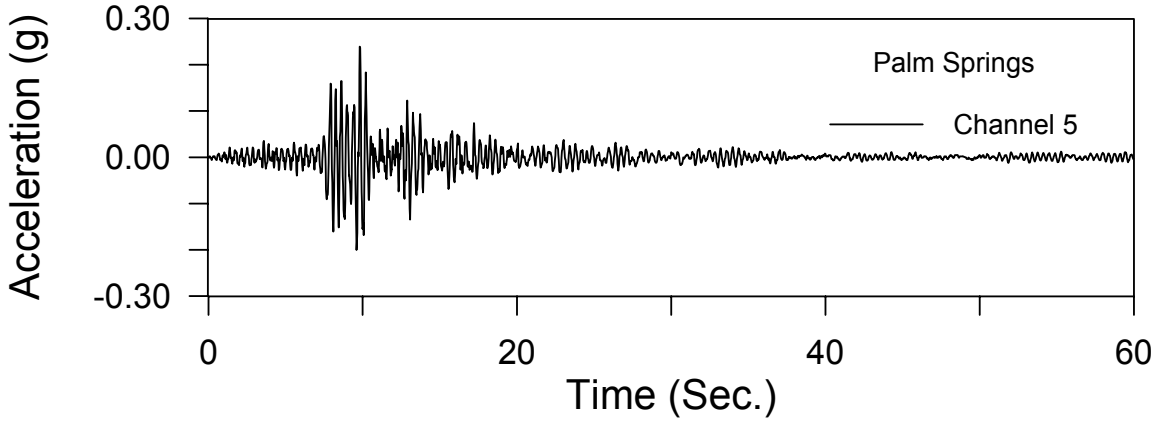
Acceleration (g)
0.30
0.00
-0.30
Palm Springs
Channel 5
0
20
40
60
Time (Sec.)

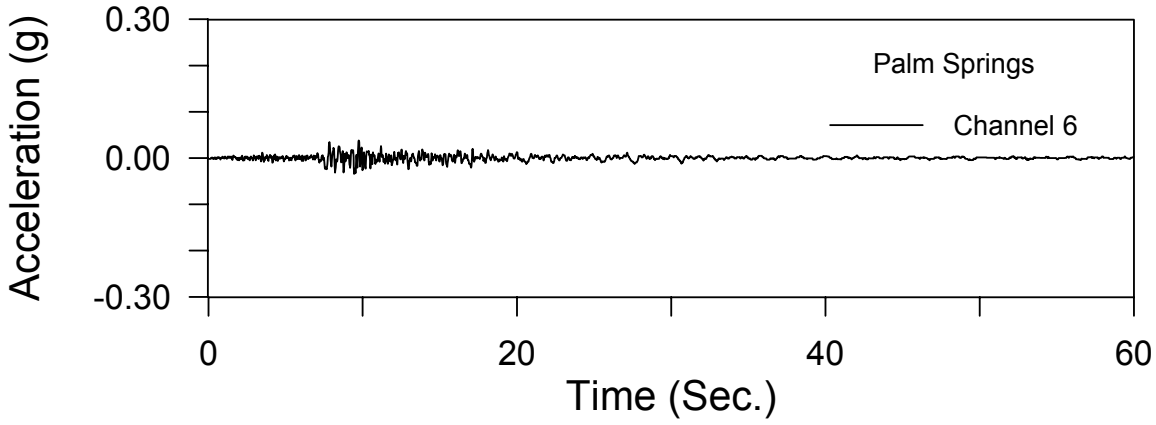
0.30
0.00
-0.30
Acceleration (g)
Palm Springs
Channel 6
0
20
40
60
Time (Sec.)

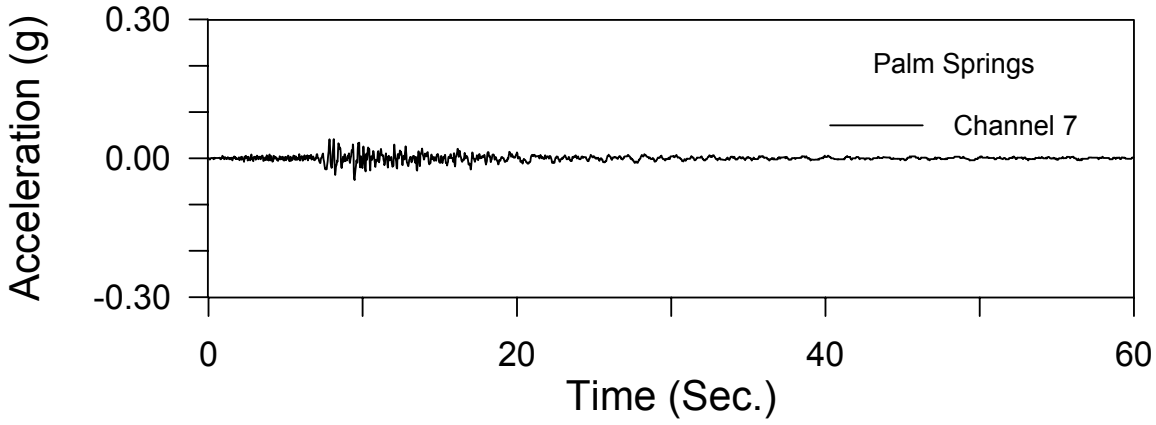
0.30
0.00
-0.30
Acceleration (g)
Palm Springs
Channel 7
0
20
40
60
Time (Sec.)

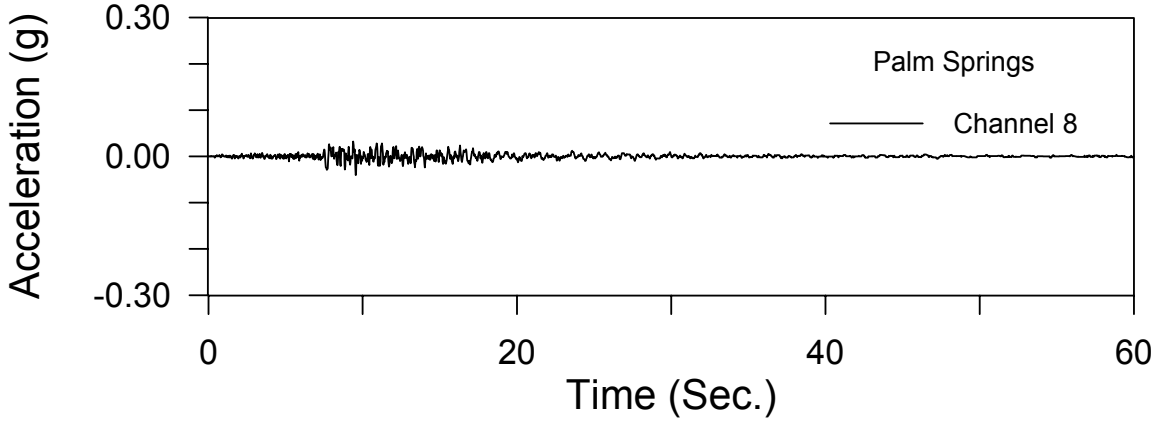
0.30
0.00
-0.30
Acceleration (g)
Palm Springs
Channel 8
0
20
40
60
Time (Sec.)

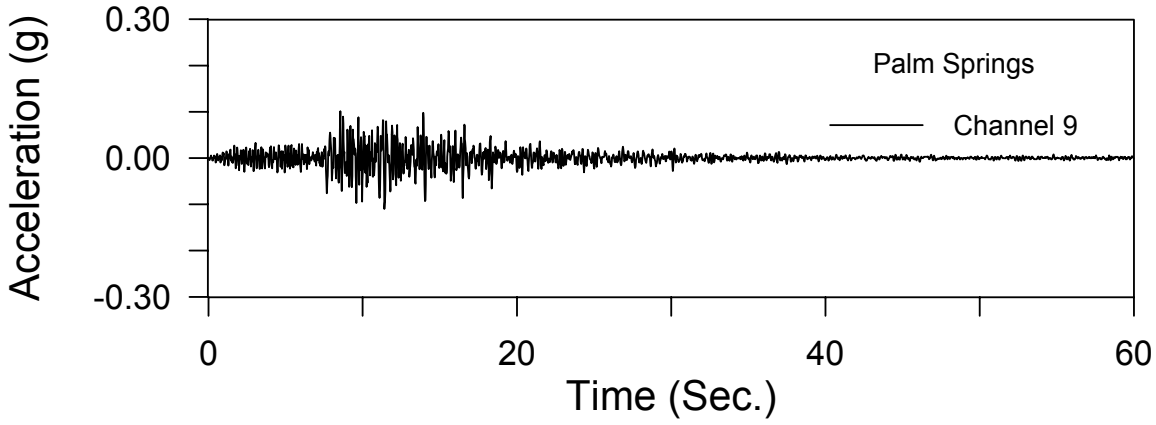
Acceleration (g)
0.30
0.00
-0.30
Palm Springs
Channel 9
0
20
40
60
Time (Sec.)

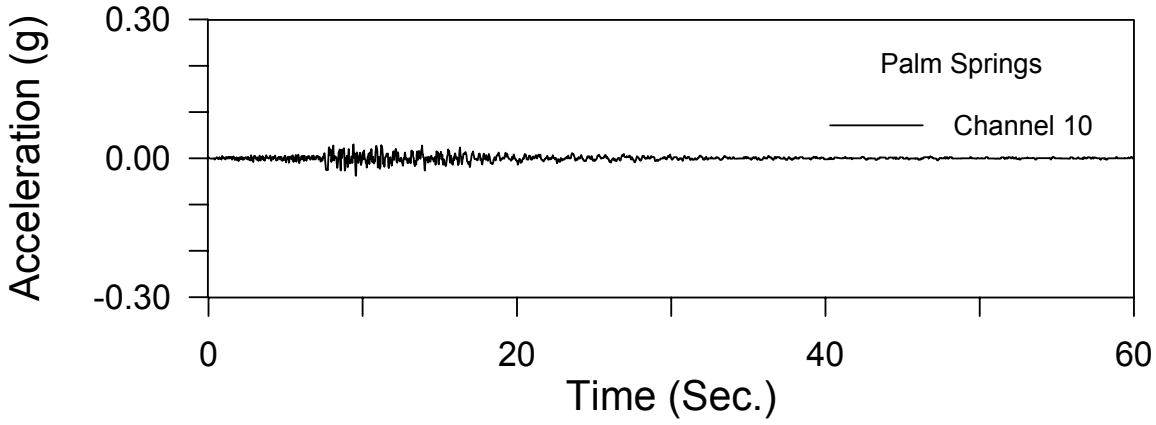
Acceleration (g)
0.30
0.00
-0.30
Palm Springs
Channel 10
0
20
40
60
Time (Sec.)

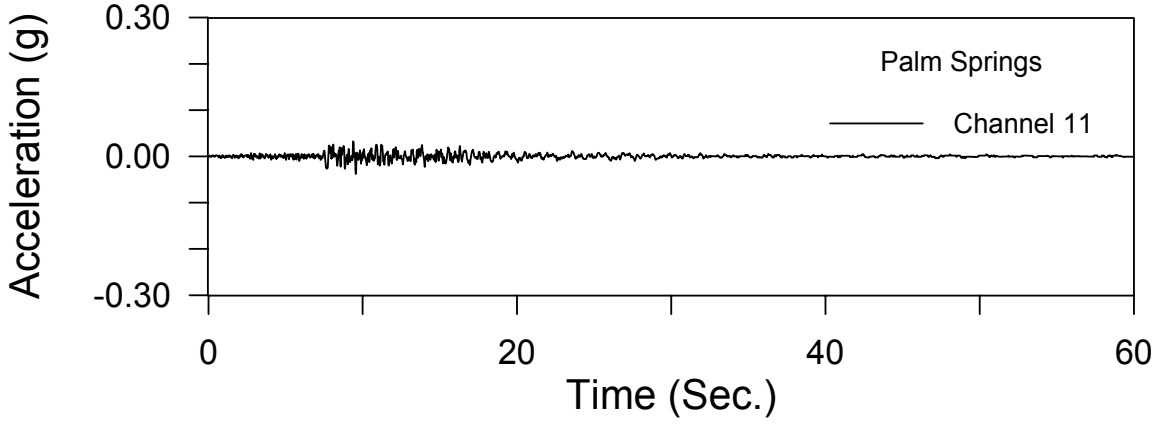
Acceleration (g)
0.30
0.00
-0.30
Palm Springs
Channel 11
0
20
40
60
Time (Sec.)

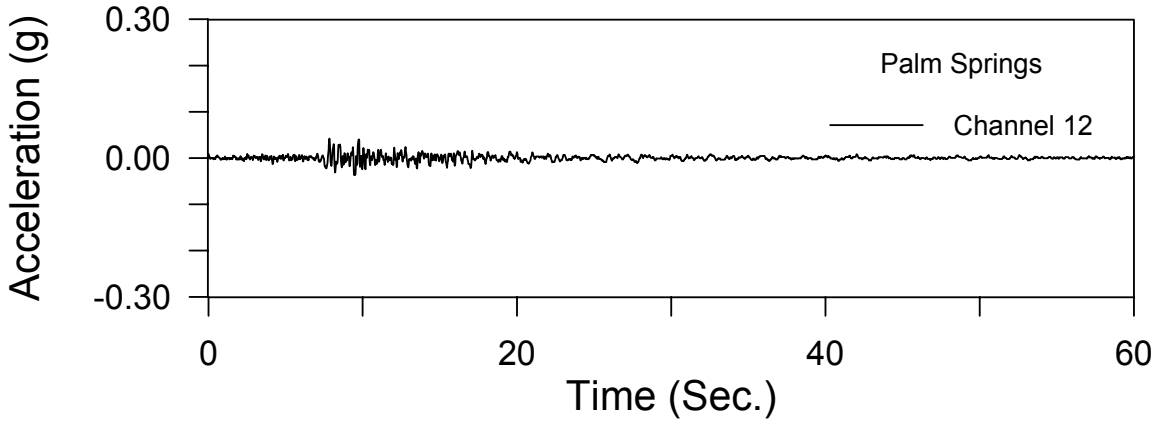

Landers Earthquake, June 28, 1992, M = 7.5

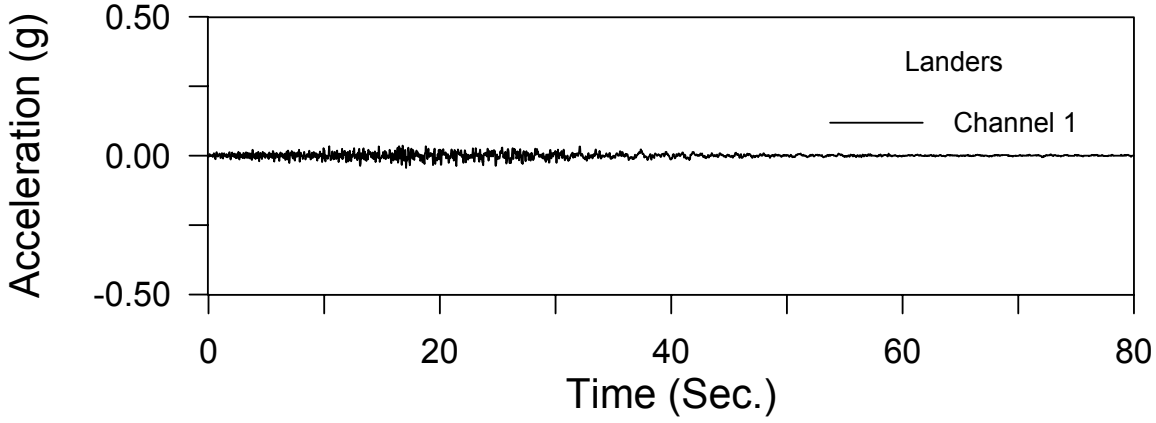

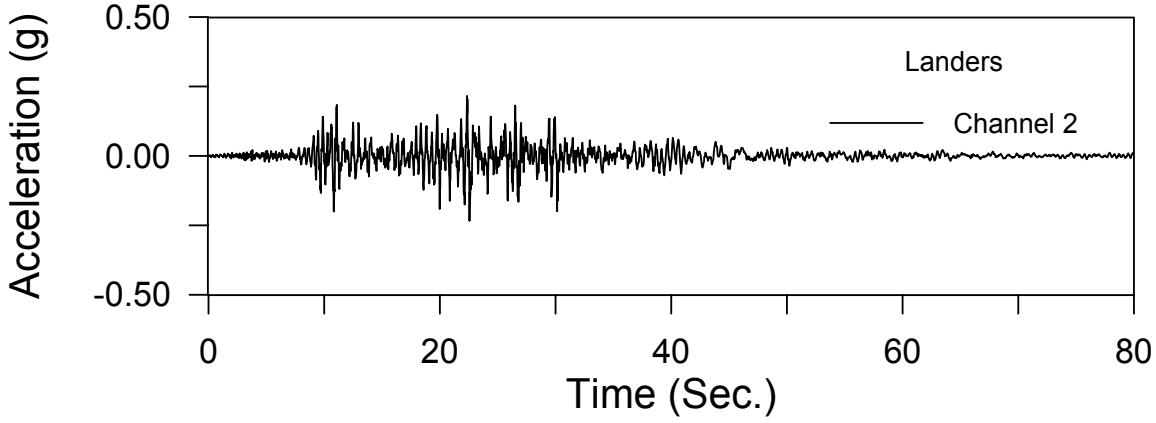

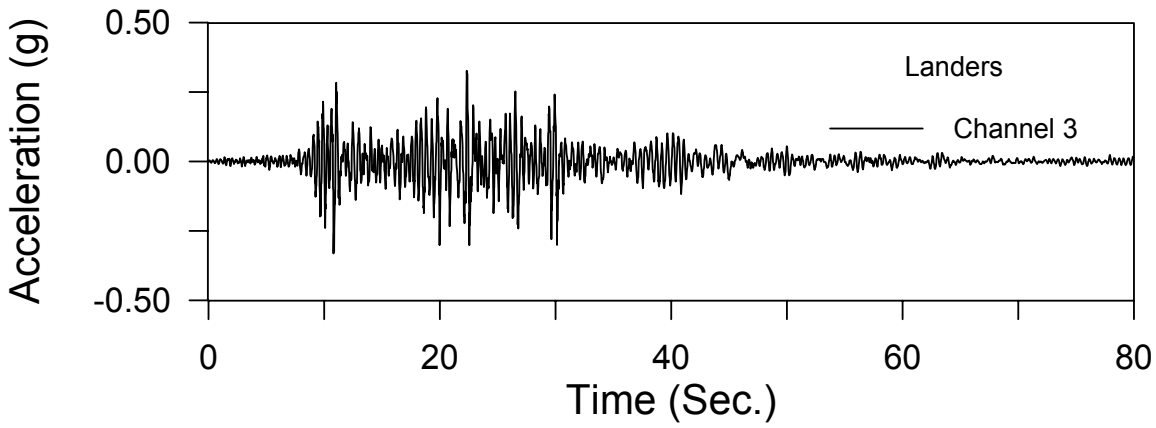
Acceleration (g)
0.50
0.00
-0.50
Landers
Channel 3
0
20
40
60
80
Time (Sec.)

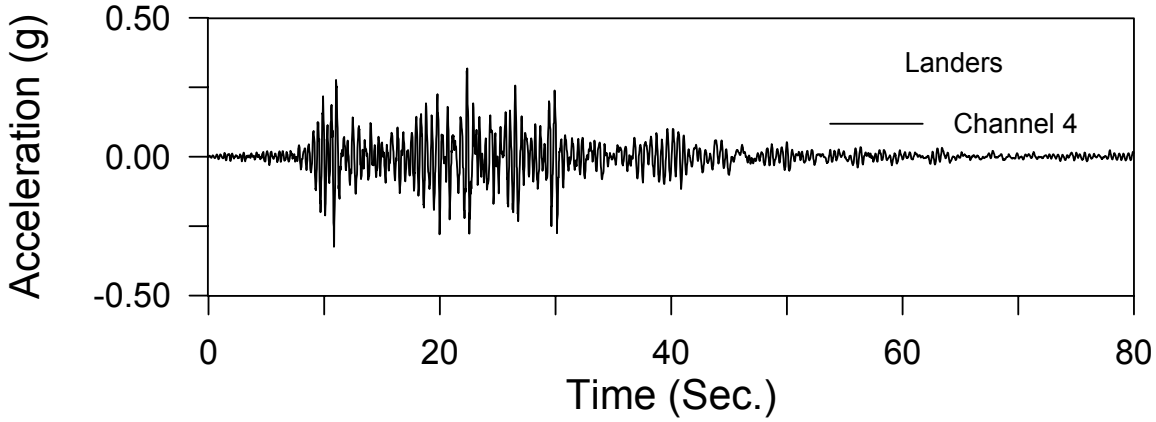
Acceleration (g)
0.50
0.00
-0.50
Landers
Channel 4
0
20
40
60
80
Time (Sec.)

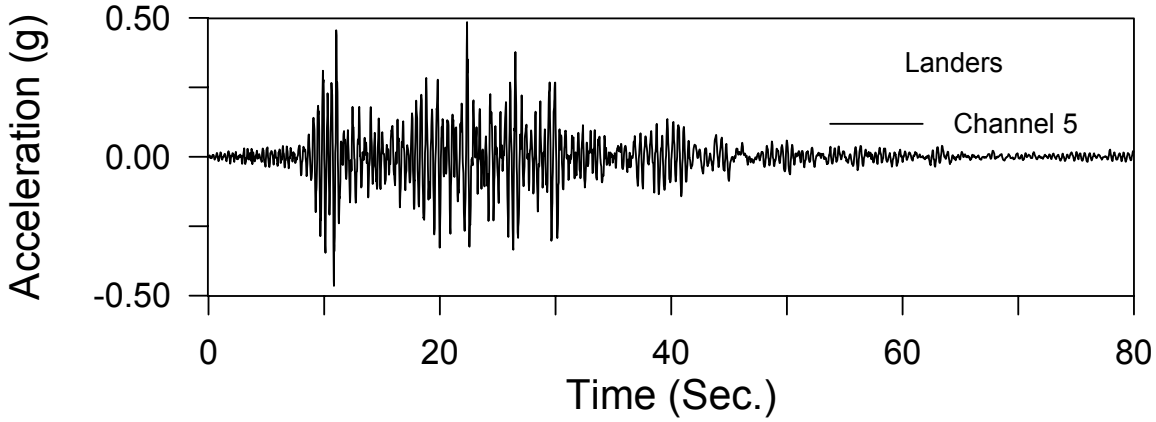
Acceleration (g)
0.50
0.00
-0.50
Landers
Channel 5
0
20
40
60
80
Time (Sec.)

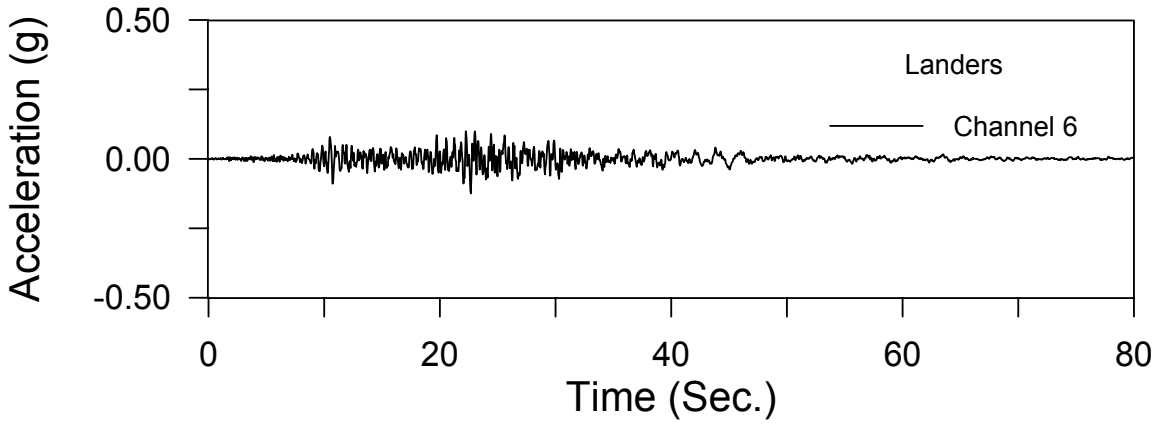
0.50
0.00
-0.50
Acceleration (g)
Landers
Channel 6
0
20
40
60
80
Time (Sec.)

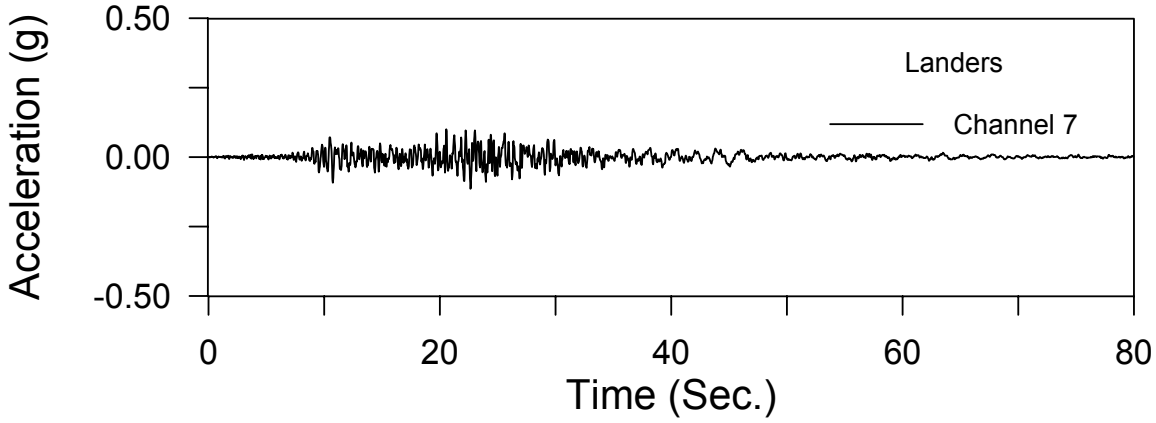
0.50
0.00
-0.50
Acceleration (g)
Landers
Channel 7
0
20
40
60
80
Time (Sec.)

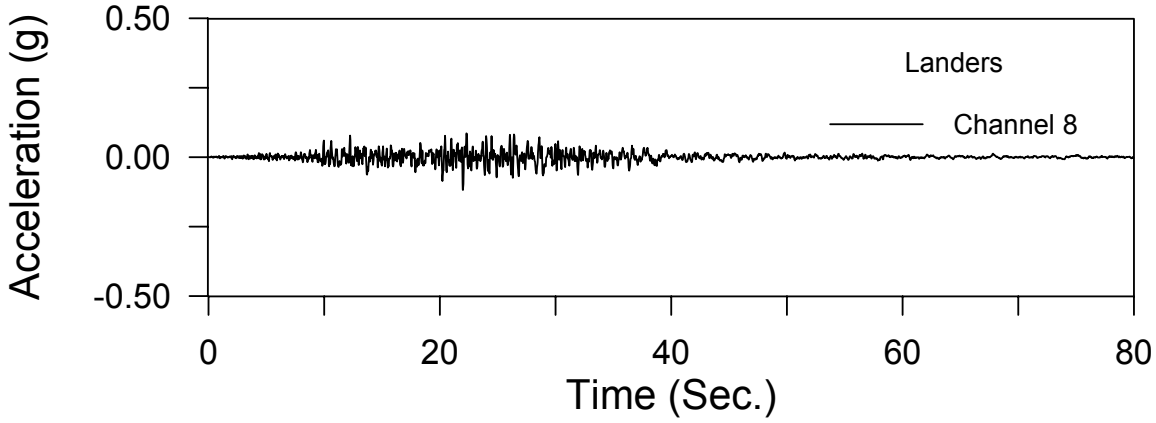
0.50
0.00
-0.50
Acceleration (g)
Landers
Channel 8
0
20
40
60
80
Time (Sec.)

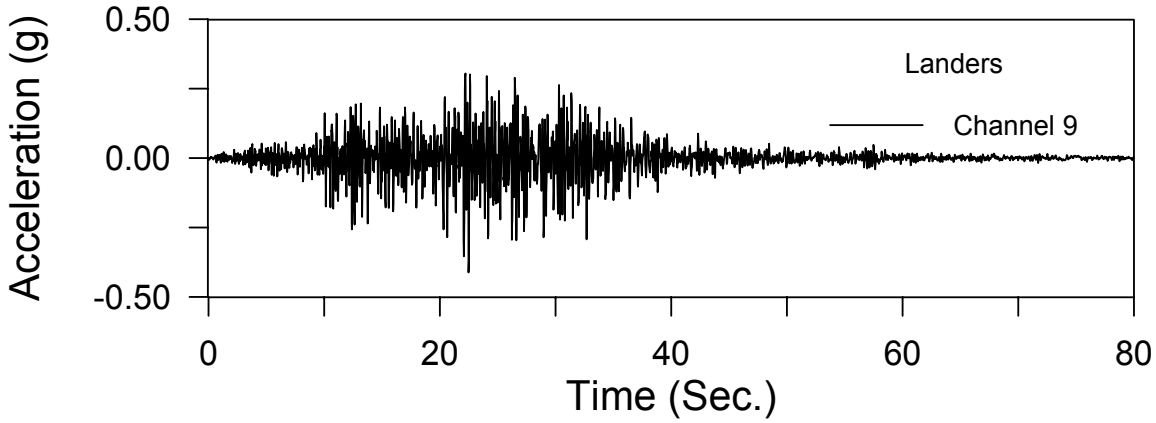
0.50
0.00
-0.50
Acceleration (g)
Landers
Channel 9
0
20
40
60
80
Time (Sec.)

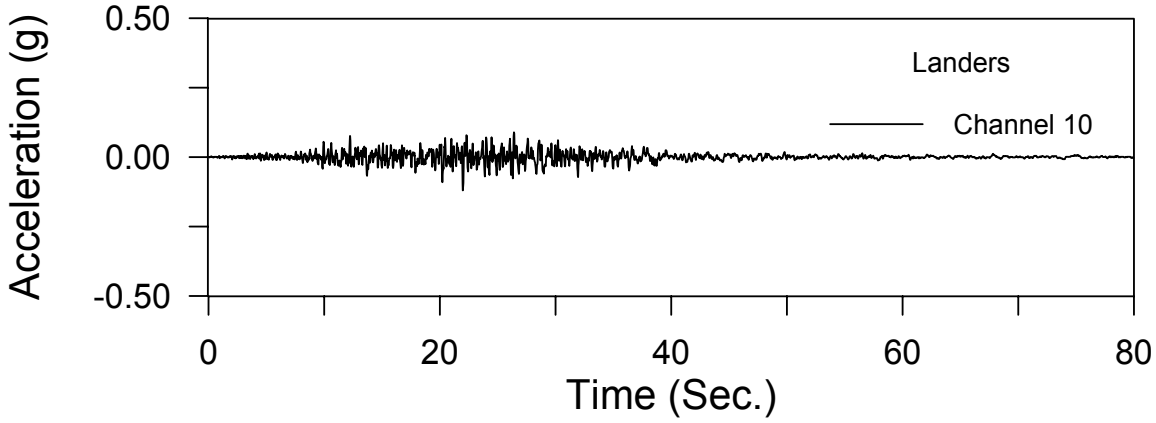
0.50
0.00
-0.50
Acceleration (g)
Landers
Channel 10
0
20
40
60
80
Time (Sec.)

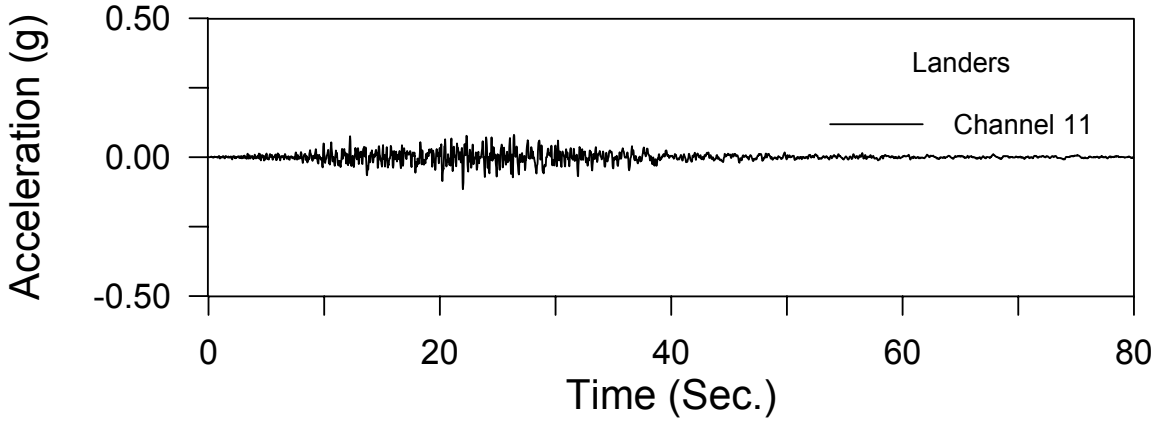
0.50
0.00
-0.50
Acceleration (g)
Landers
Channel 11
0
20
40
60
80
Time (Sec.)

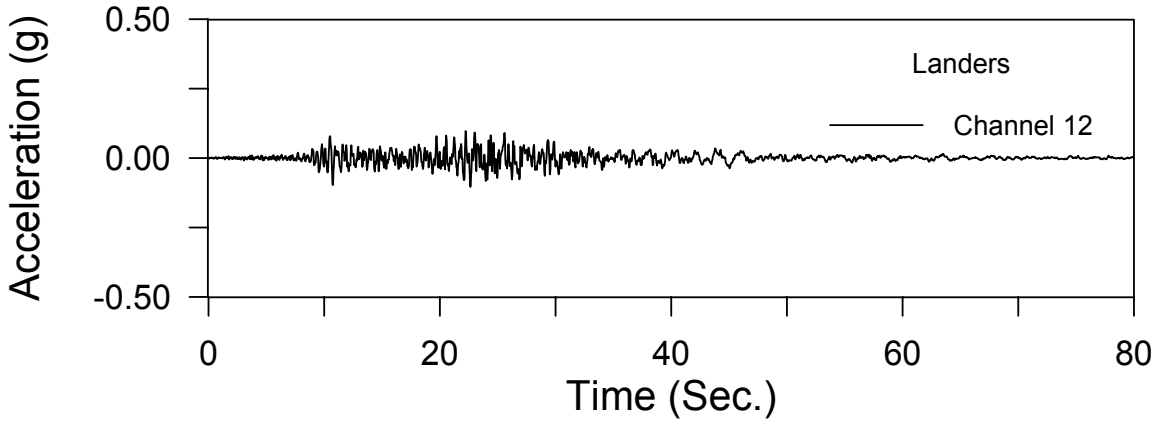

Big Bear Earthquake, June 28, 1992, M= 6.6

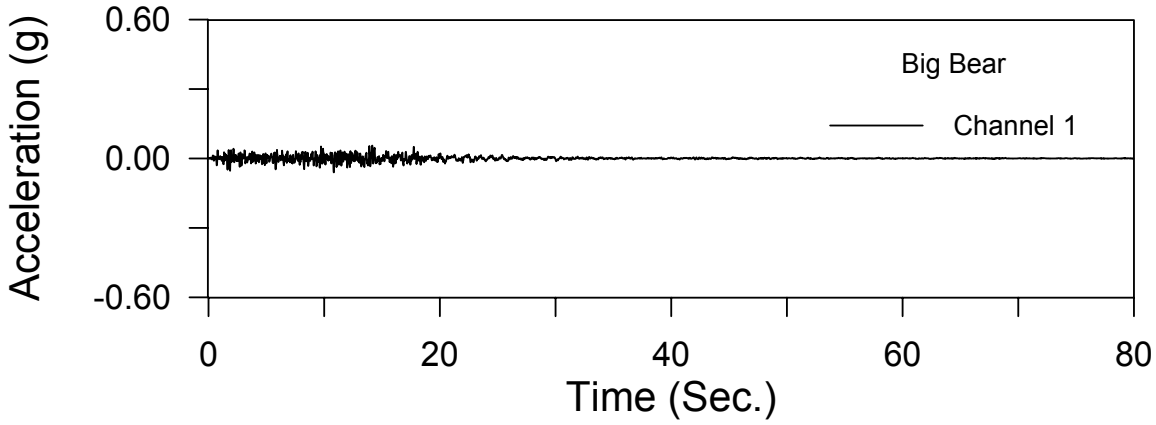

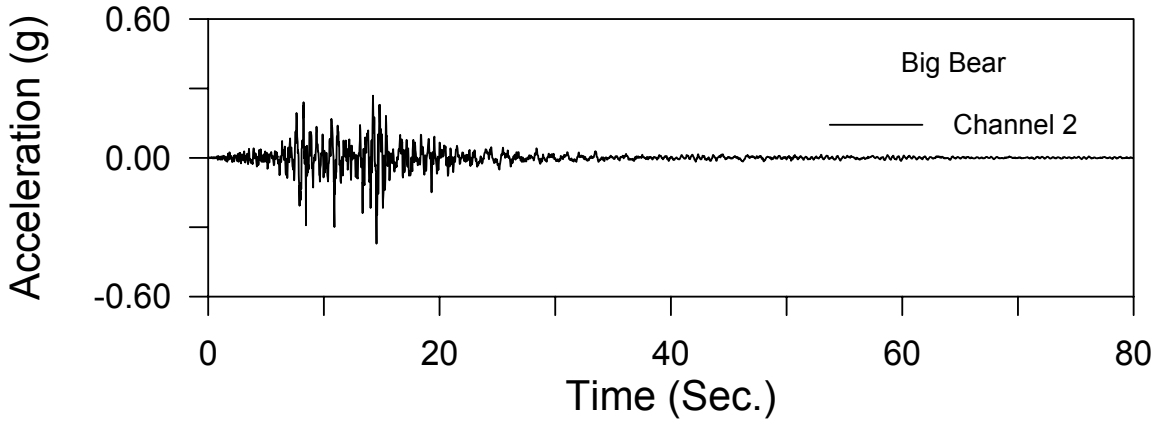

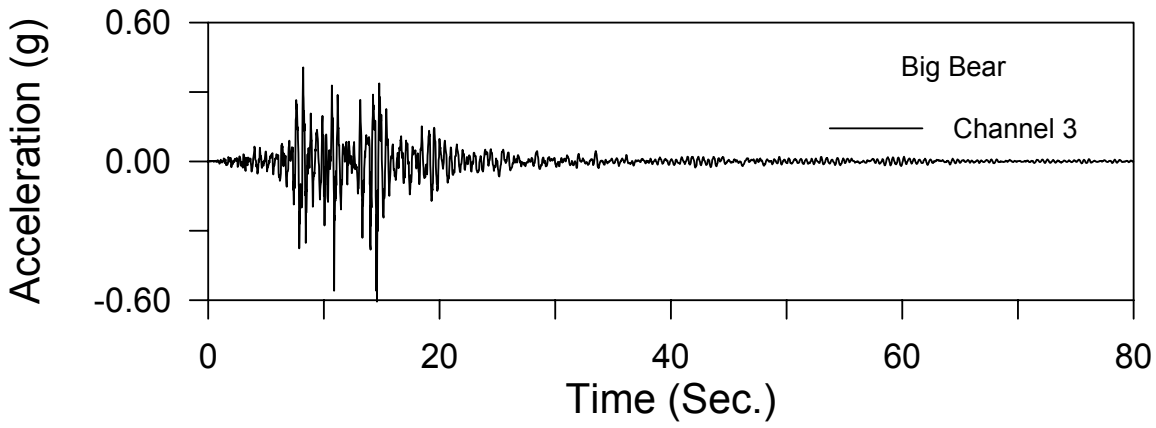
Big Bear
Channel 3
Acceleration (g)
0.60
0.00
-0.60
0
20
40
60
80
Time (Sec.)

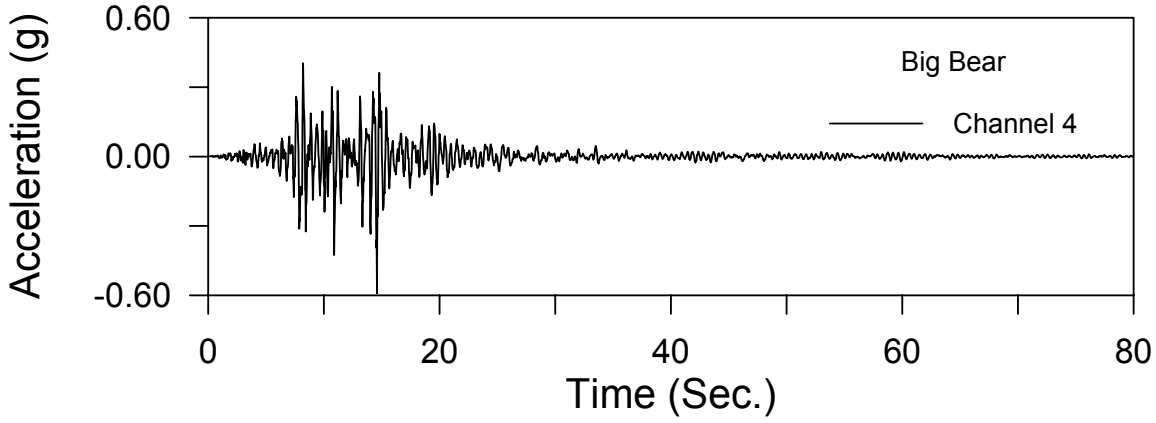
Big Bear
Channel 4
Acceleration (g)
0.60
0.00
-0.60
0
20
40
60
80
Time (Sec.)

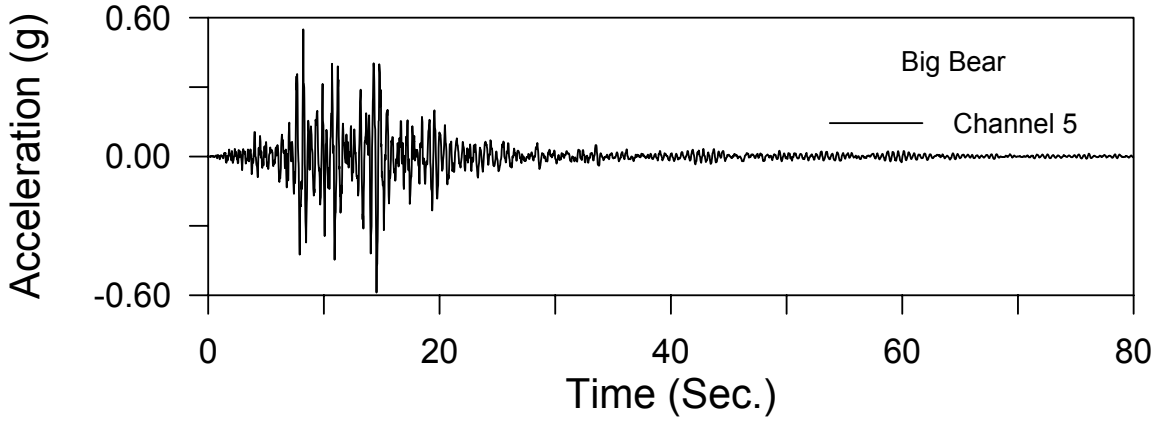
Big Bear
Channel 5
Acceleration (g)
0.60
0.00
-0.60
0
20
40
60
80
Time (Sec.)

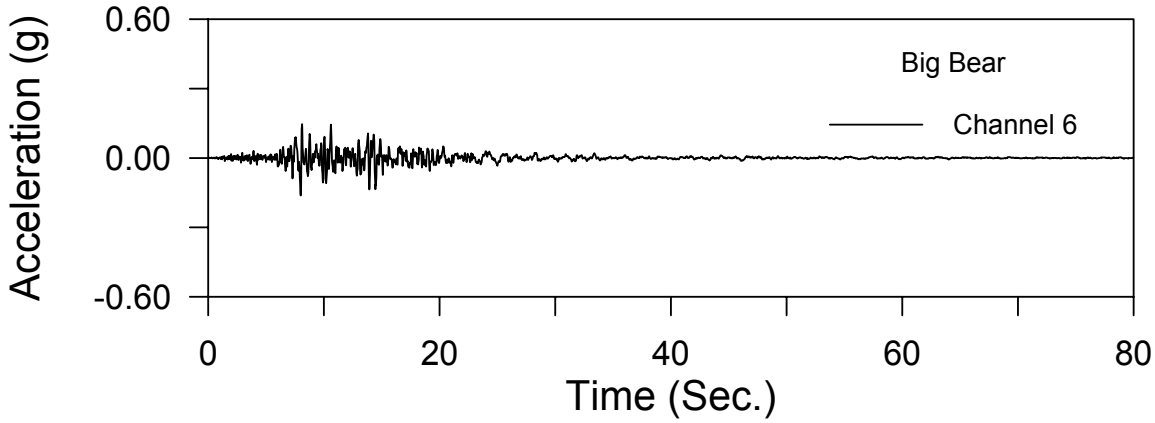
0.60
0.00
-0.60
Acceleration (g)
Big Bear
Channel 6
0
20
40
60
80
Time (Sec.)

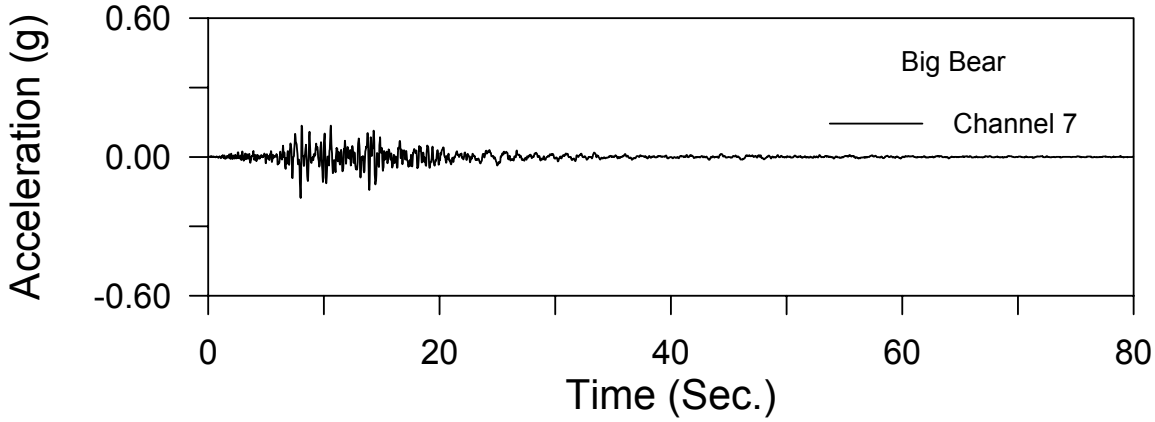
0.60
0.00
-0.60
Acceleration (g)
Big Bear
Channel 7
0
20
40
60
80
Time (Sec.)

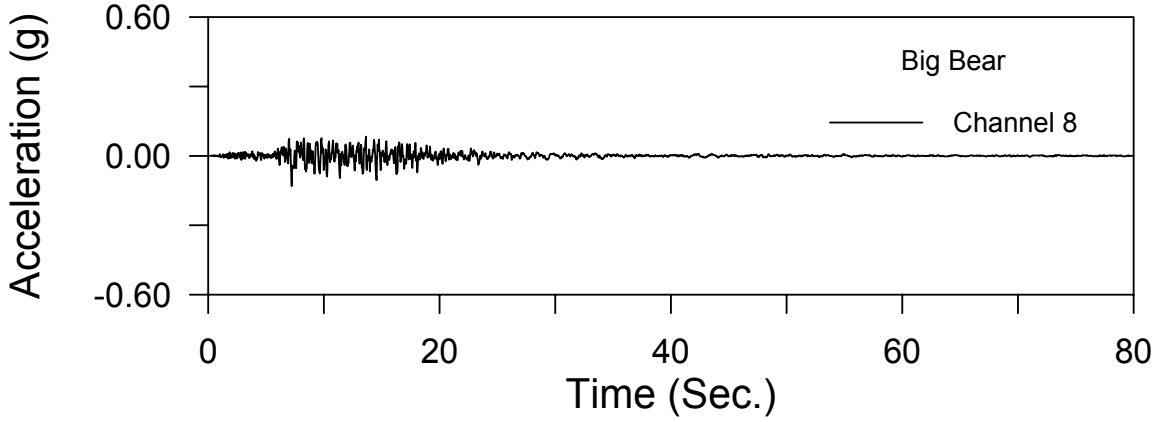
0.60
0.00
-0.60
Acceleration (g)
Big Bear
Channel 8
0
20
40
60
80
Time (Sec.)

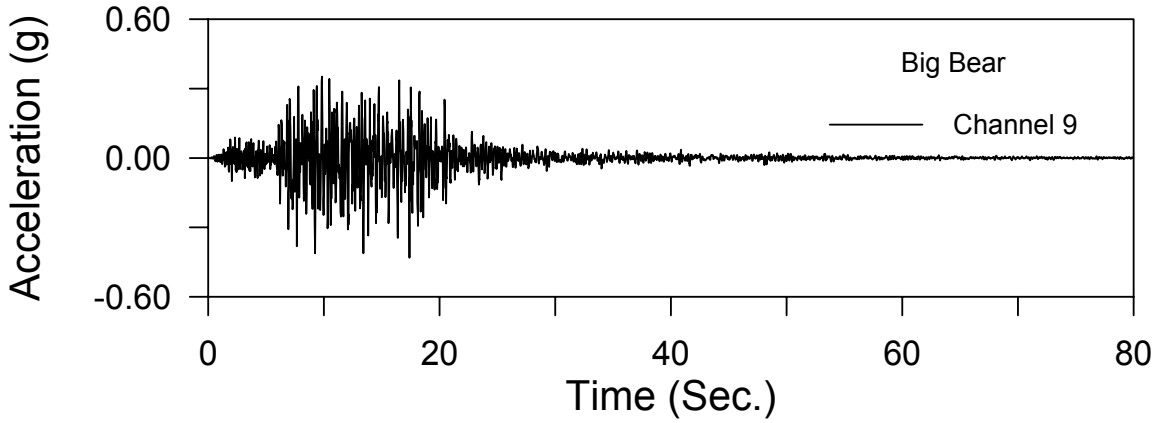
Big Bear
Channel 9
Acceleration (g)
0.60
0.00
-0.60
0
20
40
60
80
Time (Sec.)

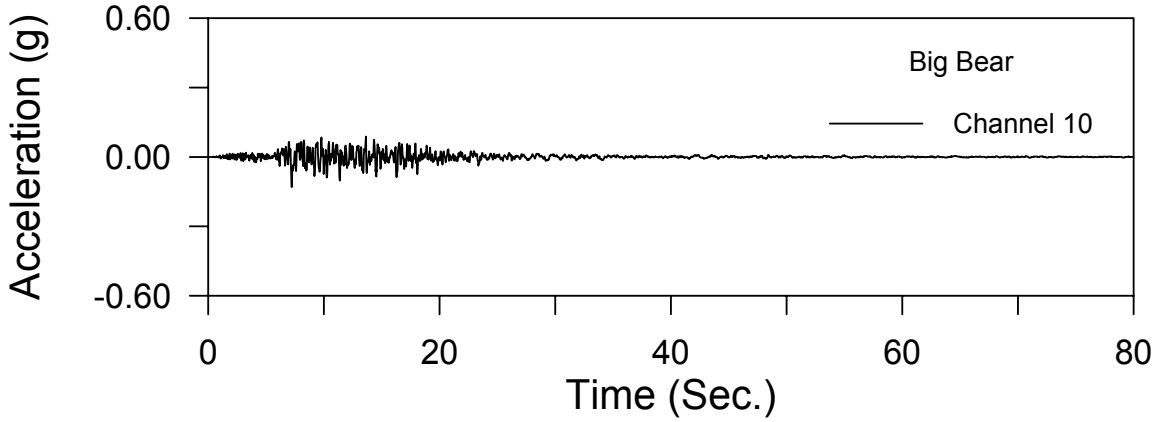
Big Bear
Channel 10
Acceleration (g)
0.60
0.00
-0.60
0
20
40
60
80
Time (Sec.)

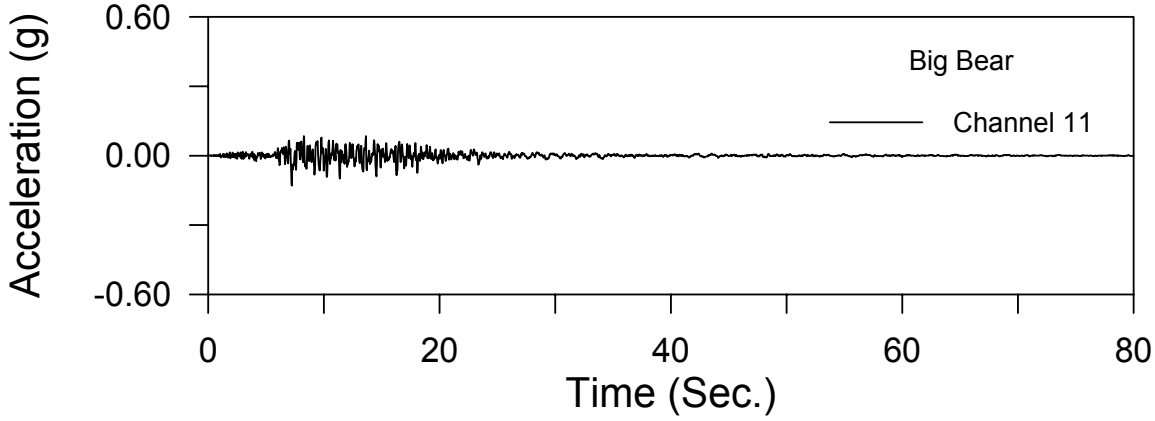
Big Bear
Channel 11
Acceleration (g)
0.60
0.00
-0.60
0
20
40
60
80
Time (Sec.)

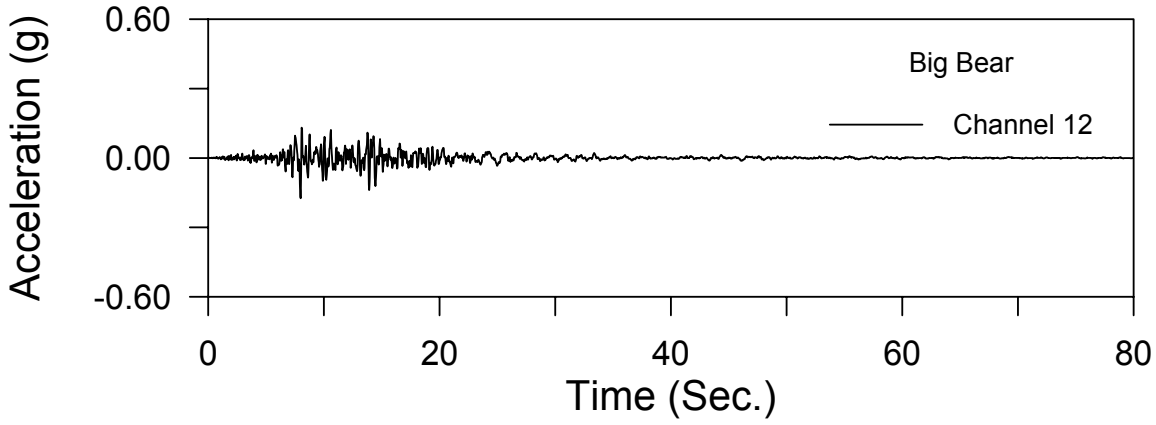

Northridge Earthquake, January 17, 1994, M=6.7

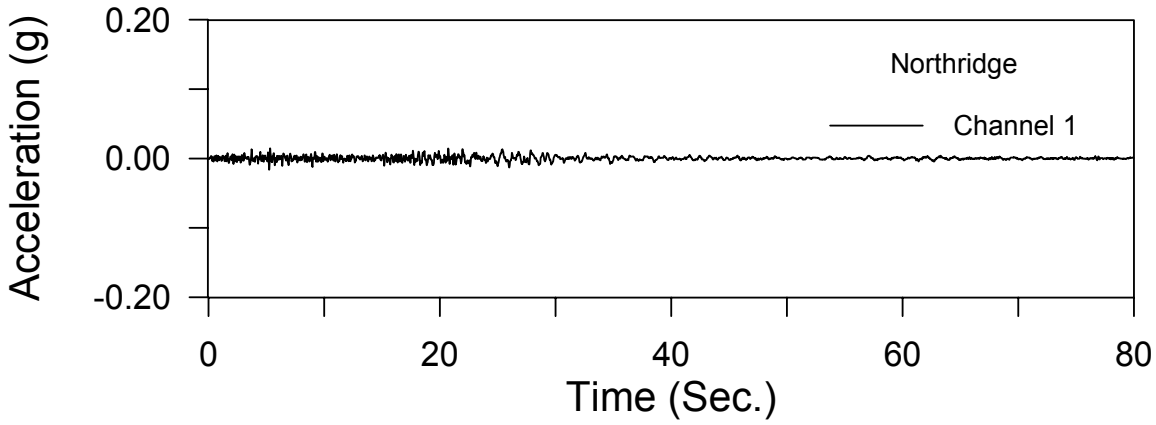

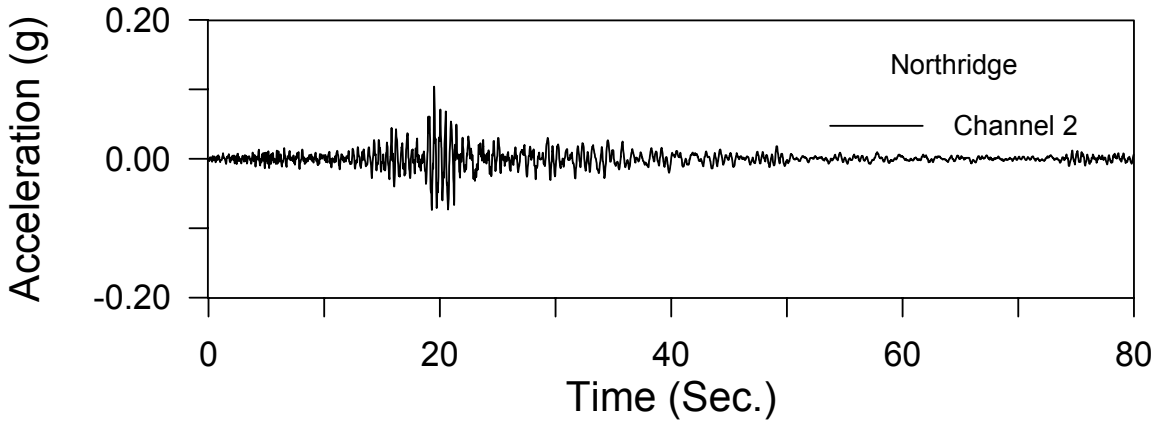

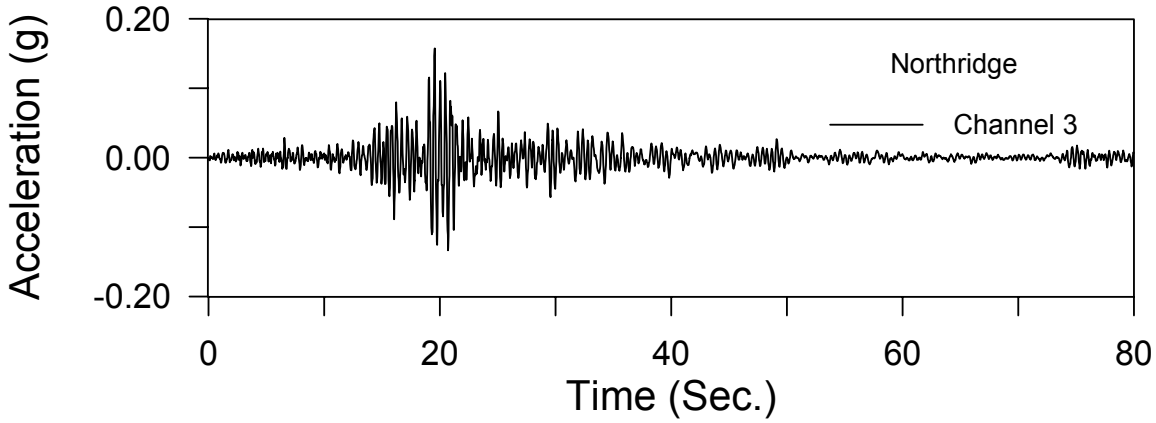
Acceleration (g)
0.20
0.00
-0.20
Northridge
Channel 3
0
20
40
60
80
Time (Sec.)

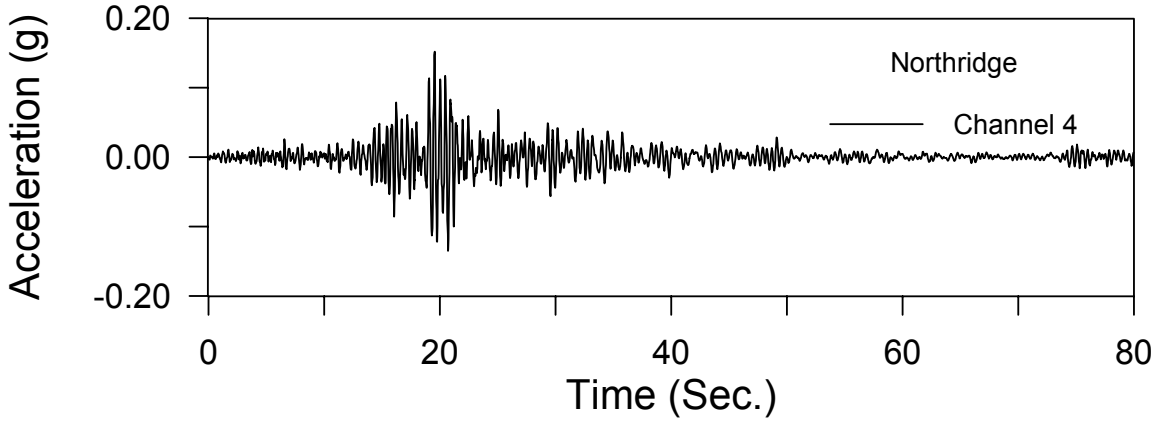
Acceleration (g)
0.20
0.00
-0.20
Northridge
Channel 4
0
20
40
60
80
Time (Sec.)

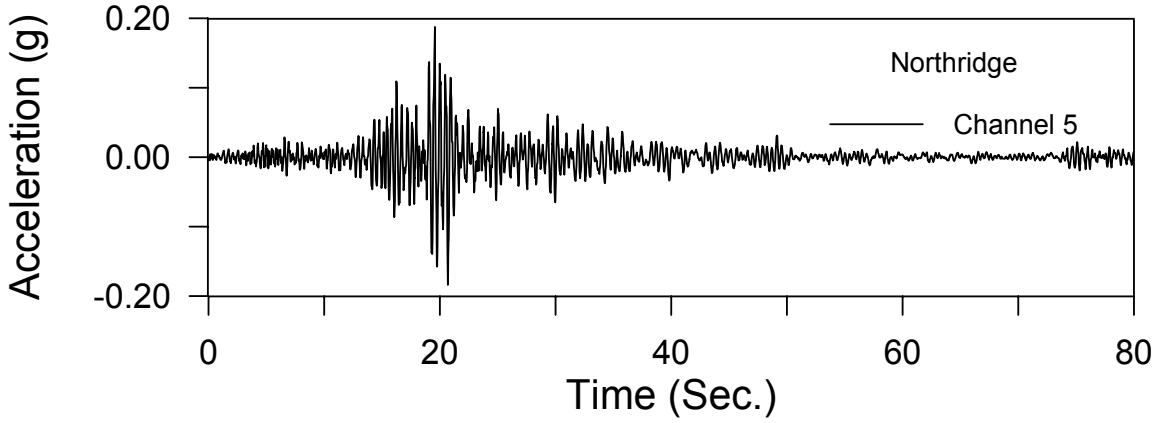
Acceleration (g)
0.20
0.00
-0.20
Northridge
Channel 5
0
20
40
60
80
Time (Sec.)

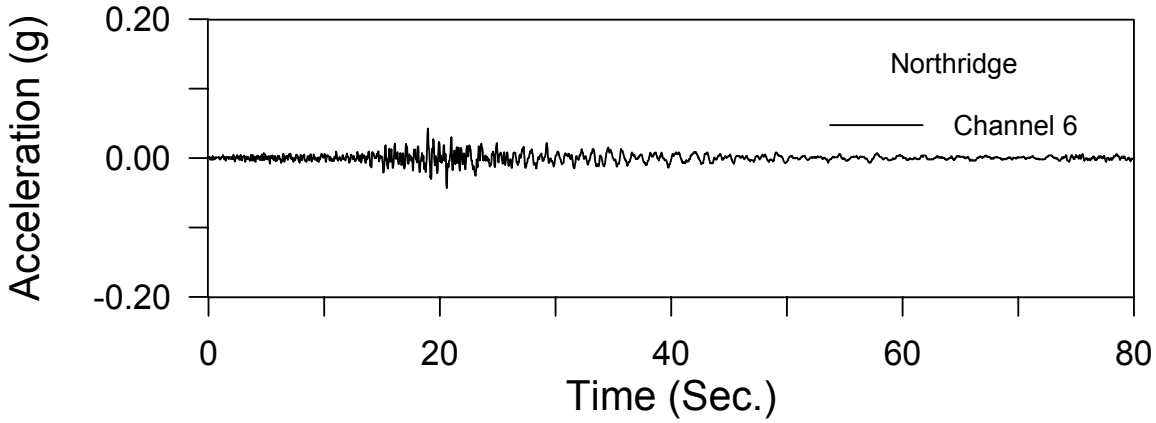
Acceleration (g)
0.20
0.00
-0.20
Northridge
Channel 6
0
20
40
60
80
Time (Sec.)

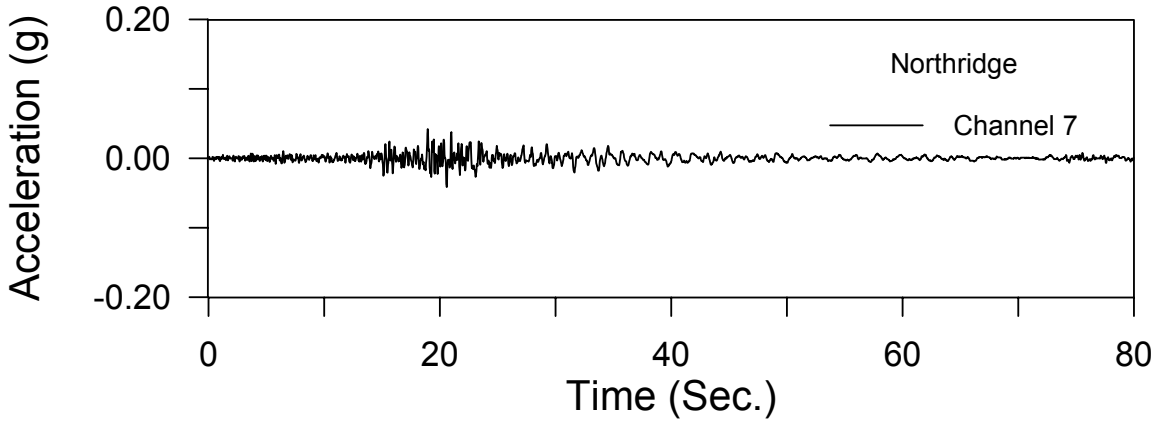
Acceleration (g)
0.20
0.00
-0.20
Northridge
Channel 7
0
20
40
60
80
Time (Sec.)

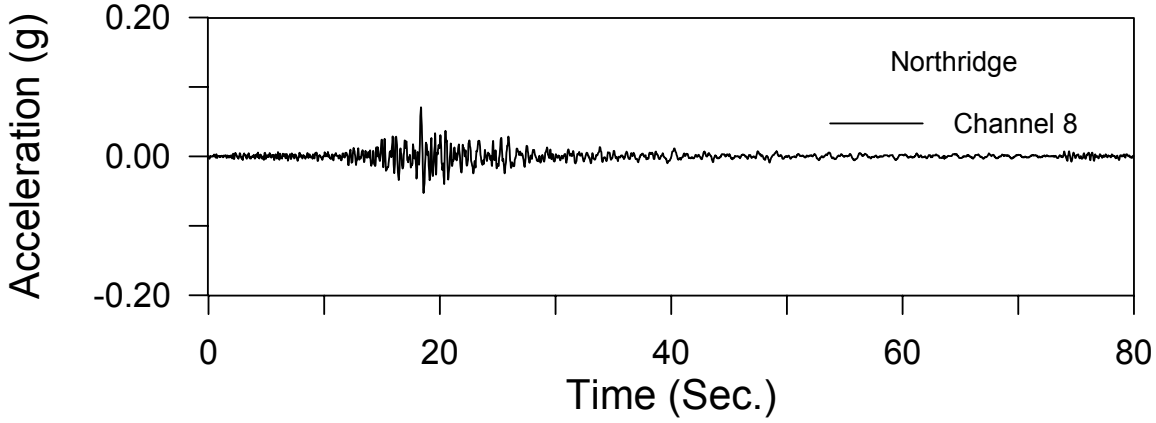
Acceleration (g)
0.20
0.00
-0.20
Northridge
Channel 8
0
20
40
60
80
Time (Sec.)

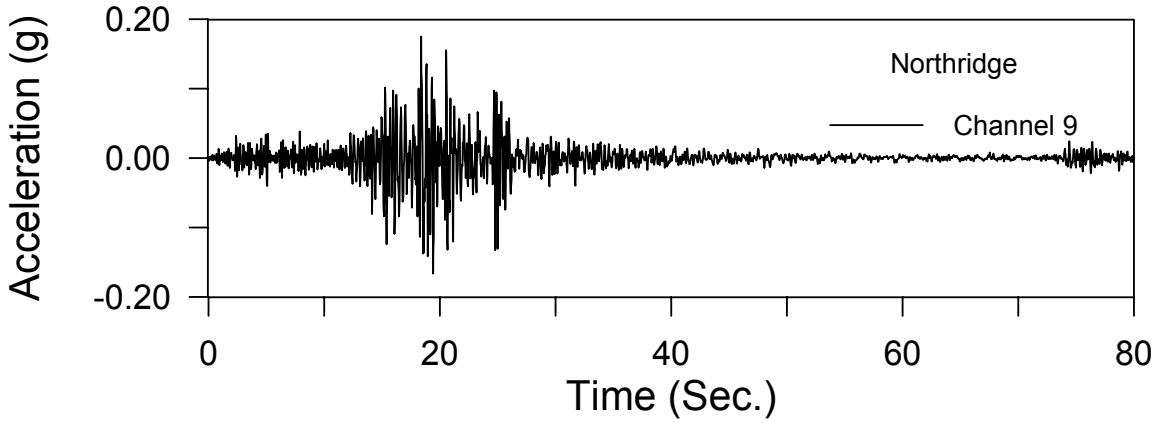
Acceleration (g)
0.20
0.00
-0.20
Northridge
Channel 9
0
20
40
60
80
Time (Sec.)

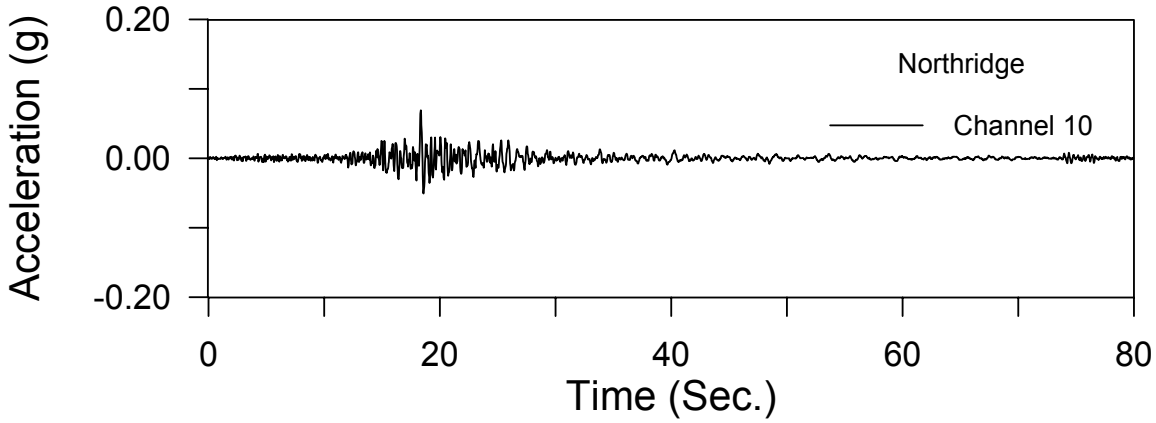
Acceleration (g)
0.20
0.00
-0.20
Northridge
Channel 10
0
20
40
60
80
Time (Sec.)

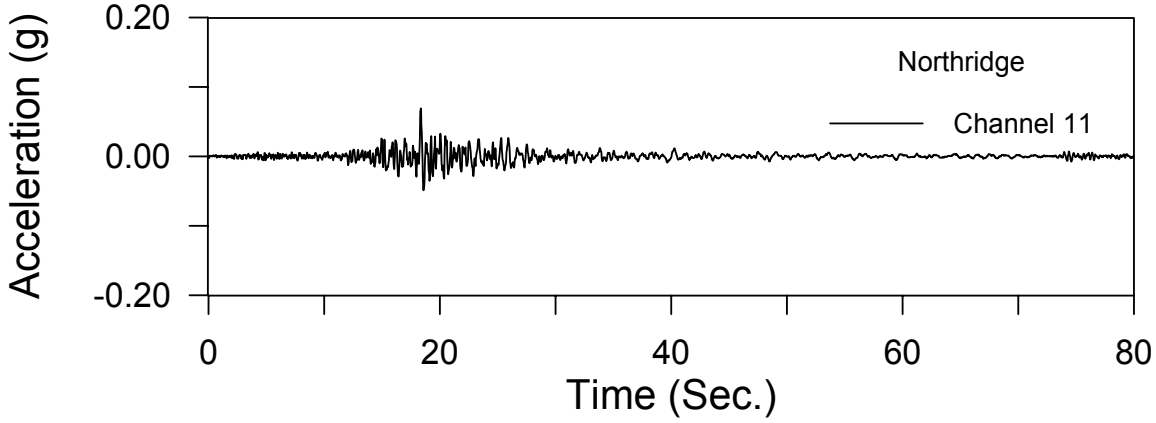
Acceleration (g)
0.20
0.00
-0.20
Northridge
Channel 11
0
20
40
60
80
Time (Sec.)

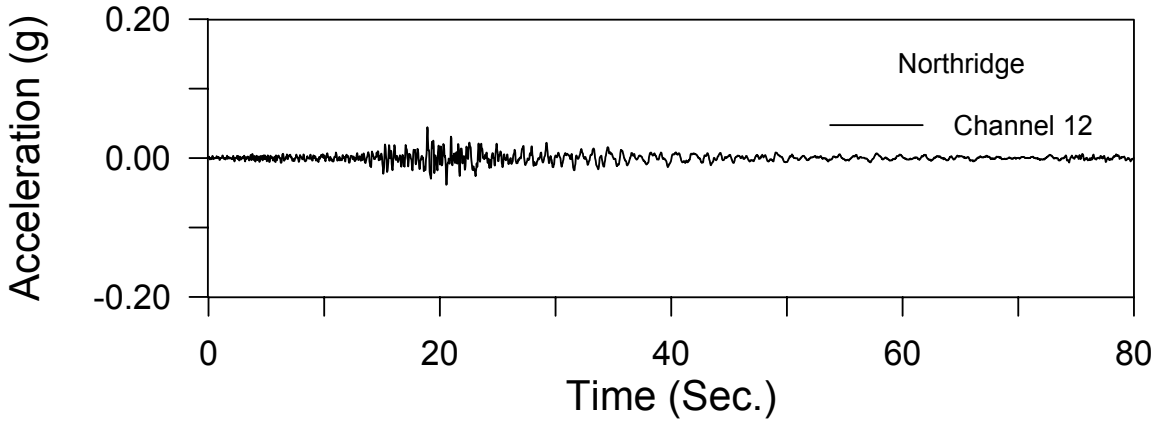
0.20
0.00
-0.20
Acceleration (g)
Northridge
Channel 12
0
20
40
60
80
Time (Sec.)

PEER REPORTS

PEER reports are available from the National Information Service for Earthquake Engineering (NISEE). To order PEER reports, please contact the Pacific Earthquake Engineering Research Center, 1301 South 46th Street, Richmond, California 94804-4698. Tel.: (510) 231-9468; Fax: (510) 231-9461.

PEER 2004/07 *Ground Motions for Earthquake Simulator Qualification of Electrical Substation Equipment.* Shakhzod M. Takhirov, Gregory L. Fenves, Eric Fujisaki, and Don Clyde. January 2005.

PEER 2004/06 *Performance-Based Regulation and Regulatory Regimes.* Peter J. May and Chris Koski. September 2004.

PEER 2004/05 *Performance-Based Seismic Design Concepts and Implementation: Proceedings of an International Workshop.* Peter Fajfar and Helmut Krawinkler, editors. September 2004.

PEER 2004/04 *Seismic Performance of an Instrumented Tilt-up Wall Building.* James C. Anderson and Vitelmo V. Bertero. July 2004.

PEER 2004/03 *Evaluation and Application of Concrete Tilt-up Assessment Methodologies.* Timothy Graf and James O. Malley. October 2004.

PEER 2004/02 *Analytical Investigations of New Methods for Reducing Residual Displacements of Reinforced Concrete Bridge Columns.* Junichi Sakai and Stephen A. Mahin. August 2004.

PEER 2004/01 *Seismic Performance of Masonry Buildings and Design Implications.* Kerri Anne Taeko Tokoro, James C. Anderson, and Vitelmo V. Bertero. February 2004.

PEER 2003/18 *Performance Models for Flexural Damage in Reinforced Concrete Columns.* Michael Berry and Marc Eberhard. August 2003.

PEER 2003/17 *Predicting Earthquake Damage in Older Reinforced Concrete Beam-Column Joints.* Catherine Pagni and Laura Lowes. October 2004.

PEER 2003/16 *Seismic Demands for Performance-Based Design of Bridges.* Kevin Mackie and Božidar Stojadinović. August 2003.

PEER 2003/15 *Seismic Demands for Nondeteriorating Frame Structures and Their Dependence on Ground Motions.* Ricardo Antonio Medina and Helmut Krawinkler. May 2004.

PEER 2003/14 *Finite Element Reliability and Sensitivity Methods for Performance-Based Earthquake Engineering.* Terje Haukaas and Armen Der Kiureghian. April 2004.

PEER 2003/13 *Effects of Connection Hysteretic Degradation on the Seismic Behavior of Steel Moment-Resisting Frames.* Janise E. Rodgers and Stephen A. Mahin. March 2004.

PEER 2003/12 *Implementation Manual for the Seismic Protection of Laboratory Contents: Format and Case Studies.* William T. Holmes and Mary C. Comerio. October 2003.

PEER 2003/11 *Fifth U.S.-Japan Workshop on Performance-Based Earthquake Engineering Methodology for Reinforced Concrete Building Structures.* February 2004.

PEER 2003/10 *A Beam-Column Joint Model for Simulating the Earthquake Response of Reinforced Concrete Frames.* Laura N. Lowes, Nilanjan Mitra, and Arash Altoontash. February 2004.

PEER 2003/09 *Sequencing Repairs after an Earthquake: An Economic Approach.* Marco Casari and Simon J. Wilkie. April 2004.

PEER 2003/08 *A Technical Framework for Probability-Based Demand and Capacity Factor Design (DCFD) Seismic Formats*. Fatemeh Jalayer and C. Allin Cornell. November 2003.

PEER 2003/07 *Uncertainty Specification and Propagation for Loss Estimation Using FOSM Methods.* Jack W. Baker and C. Allin Cornell. September 2003.

PEER 2003/06 *Performance of Circular Reinforced Concrete Bridge Columns under Bidirectional Earthquake Loading*. Mahmoud M. Hachem, Stephen A. Mahin, and Jack P. Moehle. February 2003.

PEER 2003/05 *Response Assessment for Building-Specific Loss Estimation*. Eduardo Miranda and Shahram Taghavi. September 2003.

PEER 2003/04 *Experimental Assessment of Columns with Short Lap Splices Subjected to Cyclic Loads*. Murat Melek, John W. Wallace, and Joel Conte. April 2003.

PEER 2003/03 *Probabilistic Response Assessment for Building-Specific Loss Estimation.* Eduardo Miranda and Hesameddin Aslani. September 2003.

PEER 2003/02 *Software Framework for Collaborative Development of Nonlinear Dynamic Analysis Program.* Jun Peng and Kincho H. Law. September 2003.

PEER 2003/01 *Shake Table Tests and Analytical Studies on the Gravity Load Collapse of Reinforced Concrete Frames.* Kenneth John Elwood and Jack P. Moehle. November 2003.

PEER 2002/24 *Performance of Beam to Column Bridge Joints Subjected to a Large Velocity Pulse.* Natalie Gibson, André Filiatrault, and Scott A. Ashford. April 2002.

PEER 2002/23 *Effects of Large Velocity Pulses on Reinforced Concrete Bridge Columns.* Greg L. Orozco and Scott A. Ashford. April 2002.

PEER 2002/22 *Characterization of Large Velocity Pulses for Laboratory Testing.* Kenneth E. Cox and Scott A. Ashford. April 2002.

PEER 2002/21 *Fourth U.S.-Japan Workshop on Performance-Based Earthquake Engineering Methodology for Reinforced Concrete Building Structures*. December 2002.

PEER 2002/20 *Barriers to Adoption and Implementation of PBEE Innovations.* Peter J. May. August 2002.

PEER 2002/19 *Economic-Engineered Integrated Models for Earthquakes: Socioeconomic Impacts.* Peter Gordon, James E. Moore II, and Harry W. Richardson. July 2002.

PEER 2002/18 *Assessment of Reinforced Concrete Building Exterior Joints with Substandard Details.* Chris P. Pantelides, Jon Hansen, Justin Nadauld, and Lawrence D. Reaveley. May 2002.

PEER 2002/17 *Structural Characterization and Seismic Response Analysis of a Highway Overcrossing Equipped with Elastomeric Bearings and Fluid Dampers: A Case Study.* Nicos Makris and Jian Zhang. November 2002.

PEER 2002/16 *Estimation of Uncertainty in Geotechnical Properties for Performance-Based Earthquake Engineering.* Allen L. Jones, Steven L. Kramer, and Pedro Arduino. December 2002.

PEER 2002/15 *Seismic Behavior of Bridge Columns Subjected to Various Loading Patterns.* Asadollah Esmaeily-Gh. and Yan Xiao. December 2002.

PEER 2002/14 *Inelastic Seismic Response of Extended Pile Shaft Supported Bridge Structures.* T.C. Hutchinson, R.W. Boulanger, Y.H. Chai, and I.M. Idriss. December 2002.

PEER 2002/13 *Probabilistic Models and Fragility Estimates for Bridge Components and Systems.* Paolo Gardoni, Armen Der Kiureghian, and Khalid M. Mosalam. June 2002.

PEER 2002/12 *Effects of Fault Dip and Slip Rake on Near-Source Ground Motions: Why Chi-Chi Was a Relatively Mild M7.6 Earthquake.* Brad T. Aagaard, John F. Hall, and Thomas H. Heaton. December 2002.

PEER 2002/11 *Analytical and Experimental Study of Fiber-Reinforced Strip Isolators*. James M. Kelly and Shakhzod M. Takhirov. September 2002.

PEER 2002/10 *Centrifuge Modeling of Settlement and Lateral Spreading with Comparisons to Numerical Analyses***.** Sivapalan Gajan and Bruce L. Kutter. January 2003.

PEER 2002/09 *Documentation and Analysis of Field Case Histories of Seismic Compression during the 1994 Northridge, California, Earthquake.* Jonathan P. Stewart, Patrick M. Smith, Daniel H. Whang, and Jonathan D. Bray. October 2002.

PEER 2002/08 *Component Testing, Stability Analysis and Characterization of Buckling-Restrained Unbonded Braces™.* Cameron Black, Nicos Makris, and Ian Aiken. September 2002.

PEER 2002/07 *Seismic Performance of Pile-Wharf Connections.* Charles W. Roeder, Robert Graff, Jennifer Soderstrom, and Jun Han Yoo. December 2001.

PEER 2002/06 *The Use of Benefit-Cost Analysis for Evaluation of Performance-Based Earthquake Engineering Decisions*. Richard O. Zerbe and Anthony Falit-Baiamonte. September 2001.

PEER 2002/05 *Guidelines, Specifications, and Seismic Performance Characterization of Nonstructural Building Components and Equipment*. André Filiatrault, Constantin Christopoulos, and Christopher Stearns. September 2001.

PEER 2002/04 *Consortium of Organizations for Strong-Motion Observation Systems and the Pacific Earthquake Engineering Research Center Lifelines Program: Invited Workshop on Archiving and Web Dissemination of Geotechnical Data, 4–5 October 2001*. September 2002.

PEER 2002/03 *Investigation of Sensitivity of Building Loss Estimates to Major Uncertain Variables for the Van Nuys Testbed.* Keith A. Porter, James L. Beck, and Rustem V. Shaikhutdinov. August 2002.

PEER 2002/02 *The Third U.S.-Japan Workshop on Performance-Based Earthquake Engineering Methodology for Reinforced Concrete Building Structures*. July 2002.

PEER 2002/01 *Nonstructural Loss Estimation: The UC Berkeley Case Study.* Mary C. Comerio and John C. Stallmeyer. December 2001.

PEER 2001/16 *Statistics of SDF-System Estimate of Roof Displacement for Pushover Analysis of Buildings.* Anil K. Chopra, Rakesh K. Goel, and Chatpan Chintanapakdee. December 2001.

PEER 2001/15 *Damage to Bridges during the 2001 Nisqually Earthquake.* R. Tyler Ranf, Marc O. Eberhard, and Michael P. Berry. November 2001.

PEER 2001/14 *Rocking Response of Equipment Anchored to a Base Foundation.* Nicos Makris and Cameron J. Black. September 2001.

PEER 2001/13 *Modeling Soil Liquefaction Hazards for Performance-Based Earthquake Engineering.* Steven L. Kramer and Ahmed-W. Elgamal. February 2001.

PEER 2001/12 *Development of Geotechnical Capabilities in OpenSees.* Boris Jeremić. September 2001.

PEER 2001/11 *Analytical and Experimental Study of Fiber-Reinforced Elastomeric Isolators*. James M. Kelly and Shakhzod M. Takhirov. September 2001.

PEER 2001/10 *Amplification Factors for Spectral Acceleration in Active Regions.* Jonathan P. Stewart, Andrew H. Liu, Yoojoong Choi, and Mehmet B. Baturay. December 2001.

PEER 2001/09 *Ground Motion Evaluation Procedures for Performance-Based Design.* Jonathan P. Stewart, Shyh-Jeng Chiou, Jonathan D. Bray, Robert W. Graves, Paul G. Somerville, and Norman A. Abrahamson. September 2001.

PEER 2001/08 *Experimental and Computational Evaluation of Reinforced Concrete Bridge Beam-Column Connections for Seismic Performance*. Clay J. Naito, Jack P. Moehle, and Khalid M. Mosalam. November 2001.

PEER 2001/07 *The Rocking Spectrum and the Shortcomings of Design Guidelines.* Nicos Makris and Dimitrios Konstantinidis. August 2001.

PEER 2001/06 *Development of an Electrical Substation Equipment Performance Database for Evaluation of Equipment Fragilities*. Thalia Agnanos. April 1999.

PEER 2001/05 *Stiffness Analysis of Fiber-Reinforced Elastomeric Isolators.* Hsiang-Chuan Tsai and James M. Kelly. May 2001.

PEER 2001/04 *Organizational and Societal Considerations for Performance-Based Earthquake Engineering.* Peter J. May. April 2001.

PEER 2001/03 *A Modal Pushover Analysis Procedure to Estimate Seismic Demands for Buildings: Theory and Preliminary Evaluation.* Anil K. Chopra and Rakesh K. Goel. January 2001.

PEER 2001/02 *Seismic Response Analysis of Highway Overcrossings Including Soil-Structure Interaction.* Jian Zhang and Nicos Makris. March 2001.

PEER 2001/01 *Experimental Study of Large Seismic Steel Beam-to-Column Connections.* Egor P. Popov and Shakhzod M. Takhirov. November 2000.

PEER 2000/10 *The Second U.S.-Japan Workshop on Performance-Based Earthquake Engineering Methodology for Reinforced Concrete Building Structures.* March 2000.

PEER 2000/09 *Structural Engineering Reconnaissance of the August 17, 1999 Earthquake: Kocaeli (Izmit), Turkey.* Halil Sezen, Kenneth J. Elwood, Andrew S. Whittaker, Khalid Mosalam, John J. Wallace, and John F. Stanton. December 2000.

PEER 2000/08 *Behavior of Reinforced Concrete Bridge Columns Having Varying Aspect Ratios and Varying Lengths of Confinement.* Anthony J. Calderone, Dawn E. Lehman, and Jack P. Moehle. January 2001.

PEER 2000/07 *Cover-Plate and Flange-Plate Reinforced Steel Moment-Resisting Connections.* Taejin Kim, Andrew S. Whittaker, Amir S. Gilani, Vitelmo V. Bertero, and Shakhzod M. Takhirov. September 2000.

PEER 2000/06 *Seismic Evaluation and Analysis of 230-kV Disconnect Switches.* Amir S. J. Gilani, Andrew S. Whittaker, Gregory L. Fenves, Chun-Hao Chen, Henry Ho, and Eric Fujisaki. July 2000.

PEER 2000/05 *Performance-Based Evaluation of Exterior Reinforced Concrete Building Joints for Seismic Excitation.* Chandra Clyde, Chris P. Pantelides, and Lawrence D. Reaveley. July 2000.

PEER 2000/04 *An Evaluation of Seismic Energy Demand: An Attenuation Approach.* Chung-Che Chou and Chia-Ming Uang. July 1999.

PEER 2000/03 *Framing Earthquake Retrofitting Decisions: The Case of Hillside Homes in Los Angeles.* Detlof von Winterfeldt, Nels Roselund, and Alicia Kitsuse. March 2000.

PEER 2000/02 *U.S.-Japan Workshop on the Effects of Near-Field Earthquake Shaking.* Andrew Whittaker, ed. July 2000.

PEER 2000/01 *Further Studies on Seismic Interaction in Interconnected Electrical Substation Equipment.* Armen Der Kiureghian, Kee-Jeung Hong, and Jerome L. Sackman. November 1999.

PEER 1999/14 *Seismic Evaluation and Retrofit of 230-kV Porcelain Transformer Bushings*. Amir S. Gilani, Andrew S. Whittaker, Gregory L. Fenves, and Eric Fujisaki. December 1999.

PEER 1999/13 *Building Vulnerability Studies: Modeling and Evaluation of Tilt-up and Steel Reinforced Concrete Buildings.* John W. Wallace, Jonathan P. Stewart, and Andrew S. Whittaker, editors. December 1999.

PEER 1999/12 *Rehabilitation of Nonductile RC Frame Building Using Encasement Plates and Energy-Dissipating Devices.* Mehrdad Sasani, Vitelmo V. Bertero, James C. Anderson. December 1999.

PEER 1999/11 *Performance Evaluation Database for Concrete Bridge Components and Systems under Simulated Seismic Loads.* Yael D. Hose and Frieder Seible. November 1999.

PEER 1999/10 *U.S.-Japan Workshop on Performance-Based Earthquake Engineering Methodology for Reinforced Concrete Building Structures.* December 1999.

PEER 1999/09 *Performance Improvement of Long Period Building Structures Subjected to Severe Pulse-Type Ground Motions*. James C. Anderson, Vitelmo V. Bertero, and Raul Bertero. October 1999.

PEER 1999/08 *Envelopes for Seismic Response Vectors.* Charles Menun and Armen Der Kiureghian. July 1999.

PEER 1999/07 *Documentation of Strengths and Weaknesses of Current Computer Analysis Methods for Seismic Performance of Reinforced Concrete Members.* William F. Cofer. November 1999.

PEER 1999/06 *Rocking Response and Overturning of Anchored Equipment under Seismic Excitations.* Nicos Makris and Jian Zhang. November 1999.

PEER 1999/05 *Seismic Evaluation of 550 kV Porcelain Transformer Bushings.* Amir S. Gilani, Andrew S. Whittaker, Gregory L. Fenves, and Eric Fujisaki. October 1999.

PEER 1999/04 *Adoption and Enforcement of Earthquake Risk-Reduction Measures.* Peter J. May, Raymond J. Burby, T. Jens Feeley, and Robert Wood.

PEER 1999/03 *Task 3 Characterization of Site Response General Site Categories*. Adrian Rodriguez-Marek, Jonathan D. Bray, and Norman Abrahamson. February 1999.

PEER 1999/02 *Capacity-Demand-Diagram Methods for Estimating Seismic Deformation of Inelastic Structures: SDF Systems*. Anil K. Chopra and Rakesh Goel. April 1999.

PEER 1999/01 *Interaction in Interconnected Electrical Substation Equipment Subjected to Earthquake Ground Motions.* Armen Der Kiureghian, Jerome L. Sackman, and Kee-Jeung Hong. February 1999.

PEER 1998/08 *Behavior and Failure Analysis of a Multiple-Frame Highway Bridge in the 1994 Northridge Earthquake*. Gregory L. Fenves and Michael Ellery. December 1998.

PEER 1998/07 *Empirical Evaluation of Inertial Soil-Structure Interaction Effects.* Jonathan P. Stewart, Raymond B. Seed, and Gregory L. Fenves. November 1998.

PEER 1998/06 *Effect of Damping Mechanisms on the Response of Seismic Isolated Structures.* Nicos Makris and Shih-Po Chang. November 1998.

PEER 1998/05 *Rocking Response and Overturning of Equipment under Horizontal Pulse-Type Motions.* Nicos Makris and Yiannis Roussos. October 1998.

PEER 1998/04 *Pacific Earthquake Engineering Research Invitational Workshop Proceedings, May 14–15, 1998: Defining the Links between Planning, Policy Analysis, Economics and Earthquake Engineering.* Mary Comerio and Peter Gordon. September 1998.

PEER 1998/03 *Repair/Upgrade Procedures for Welded Beam to Column Connections.* James C. Anderson and Xiaojing Duan. May 1998.

PEER 1998/02 *Seismic Evaluation of 196 kV Porcelain Transformer Bushings.* Amir S. Gilani, Juan W. Chavez, Gregory L. Fenves, and Andrew S. Whittaker. May 1998.

PEER 1998/01 *Seismic Performance of Well-Confined Concrete Bridge Columns.* Dawn E. Lehman and Jack P. Moehle. December 2000.